2025 ICU PADERBORN

INTERNATIONAL CONGRESS ON ULTRASONICS

SEPTEMBER 21–25, 2025
PADERBORN · GERMANY

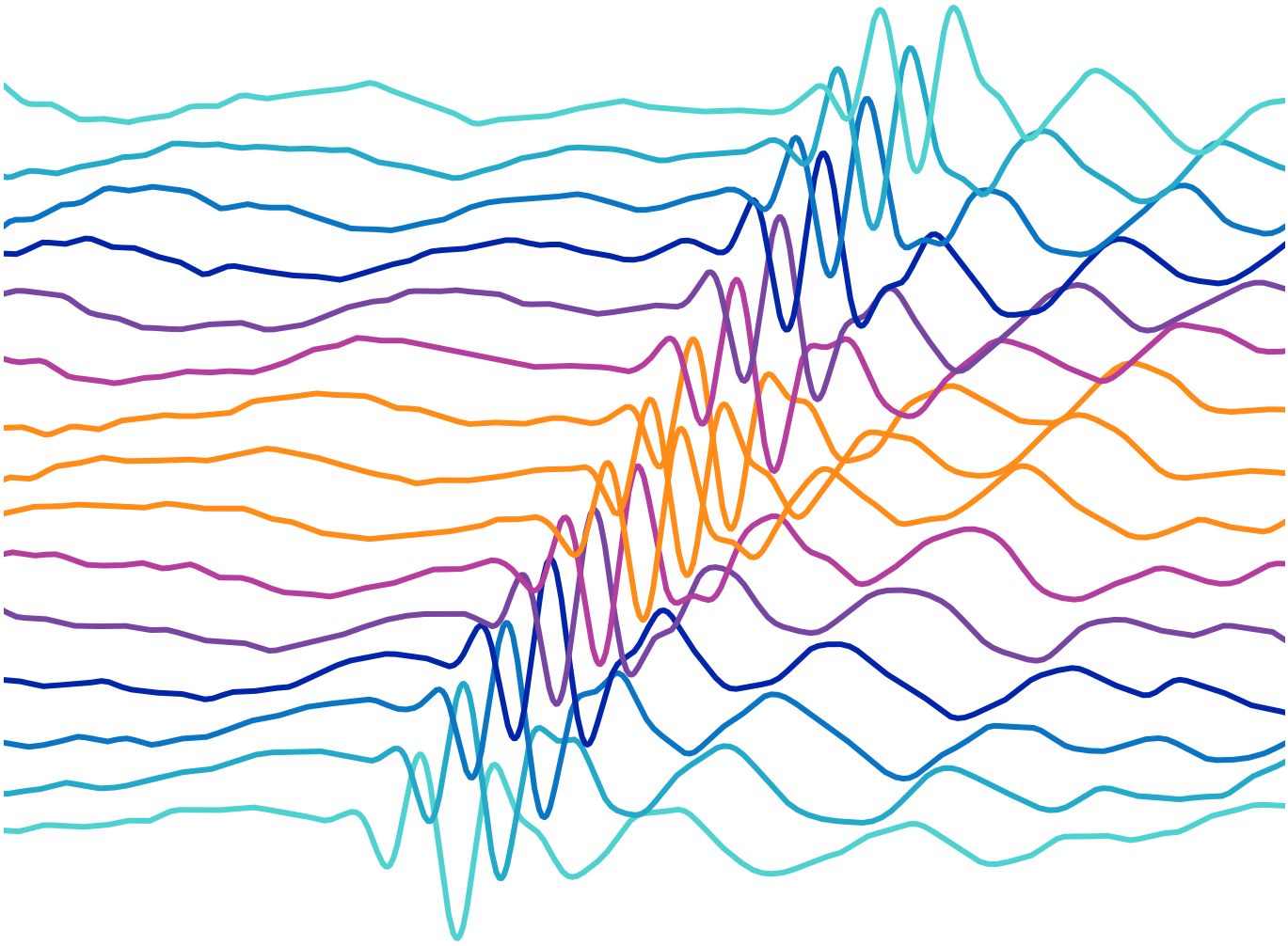

PROCEEDINGS

PADERBORN UNIVERSITY

Measurement Engineering

WWW.2025ICU.ORG

Proceedings

2025 ICU PADERBORN
9th International Congress on Ultrasonics – ICU
21 - 25 September 2025, Paderborn (Germany)

Scientific Leadership:
Prof. Dr. Bernd Henning, Paderborn University
Prof. Dr. Stefan J. Rupitsch, University of Freiburg
Dr. Leander Claes, Paderborn University

The authors are responsible for form and content of the papers.

AMA Service GmbH accepts no responsibility for the correctness and completeness of the details and the consideration of private rights of third parties.

Herausgeber / Publisher:

AMA Service GmbH
Von-Münchhausen-Str. 49
31515 Wunstorf / Germany
Tel. +49 5033 9639-0
info@ama-service.com
www.ama-service.com / www.sensor-test.com
www.ama-science.org / www.smsi-conference.com

ISBN 978-3-910600-08-9

Preface

On behalf of the organizing team, the ICU Board, and the International Scientific Committee, we warmly welcome you to the 2025 ICU PADERBORN, which takes place from September 21 to 25, 2025.

The International Congress on Ultrasonics (ICU), initiated by the ICU Board, in which leading representatives of acoustic societies from all over the world work closely together, has its roots in a congress series dating back to 1995, when the first congress, then known as the World Congress on Ultrasonics (WCU), took place in Berlin. Since then, leading scientists in the field of ultrasound have met every two years in locations on different continents. Other congress venues have included Yokohama, Copenhagen, Atlanta, and Paris. Continuing this long-standing tradition, the first ICU took place in Vienna in 2007. Further congresses followed in Santiago de Chile, Gdansk, Singapore, Metz, Honolulu, Bruges, and most recently in Beijing. It is therefore a particular pleasure to be able to continue this now 30-year-old successful tradition here in Paderborn.

Ultrasound is a key technology that has become indispensable in society, research and industry. Because this field of research is characterized by its exceptionally high level of interdisciplinary work, many technical and technological challenges still need to be overcome.

The aim of the 2025 ICU PADERBORN is to bring together scientists from research institutions and companies around the world to encourage open, creative and constructive discussions. The diversity of applications on the one hand, and the open atmosphere on the other, are intended to stimulate ideas and inspire innovative, visionary technical solutions, without, however, neglecting the responsibility entrusted to us in technological progress.

These conference proceedings comprise the latest scientific research results and key contributions presented at the 2025 ICU PADERBORN.

Our special thanks go to the members of the International Scientific Committee, the session chairs, and in particular the authors. We greatly appreciate your commitment in bringing together this congress and making the 2025 ICU PADERBORN a great event!

Bernd Henning
Paderborn University, Germany

Stefan J. Rupitsch
University of Freiburg, Germany

Leander Claes
Paderborn University, Germany

Member of International Scientific Committee (ISC)

Thierry Baasch	Lund University · Sweden
Carolin Birk	University of Duisburg-Essen · Germany
Leonard Bond	Iowa State University · USA
Jannis Bulling	BAM Berlin · Germany
Leander Claes	University of Paderborn · Germany
Nico F. Declercq	Georgia Tech Lorraine · France
Serge Dos Santos	INSA Centre Val de Loire · France
Klaus S. Drese	University of Applied Science Coburg · Germany
Flemming Forsberg	Thomas Jefferson University · USA
Hauke Gravenkamp	CIMNE Barcelona · Spain
Clemens Grünsteidl	RECENDT · Austria
Vitali Goussev	Université du Maine · France
Christian Hedeyat	Fraunhofer-Institute ENAS · Germany
Tobias Hemsel	University of Paderborn · Germany
Bernd Henning	University of Paderborn · Germany
Sigrun Hirsekorn	NDT Consultant · Germany
Klaus V. Jenderka	University of Applied Science Merseburg · Germany
Daniel A. Kiefer	ESPCI Paris · France
Christopher Kube	Pennsylvania State University · USA
Elfgard Kühnicke	Technical University BA of Freiberg · Germany
Christian Kupsch	Technical University BA of Freiberg · Germany
Peter Lewin	University Philadelphia · USA
Yubing Li	Chinese Academy of Sciences · China
Marko Liebler	Robert Bosch GmbH · Germany
Frieder Lucklum	Technical University of Denmark · Denmark
Jens Prager	BAM Berlin · Germany
Alan Pavlic	California Institute of Technology · USA
Stefan Radel	Technical University of Wien · Austria
Samuel Raetz	Le Mans Université · France
Jens Rautenberg	Endress+Hauser Flow · Germany
Stefan J. Rupitsch	University of Freiburg · Germany
Wolfgang Sachse	Cornell University · USA
Nooshin Saeidi	Fraunhofer Institute ENAS · Germany
Alexey Scherbakov	Technical University of Dortmund · Germany
Erik Starke	SICK Engineering GmbH · Germany
Chris Stöckel	Fraunhofer Institute ENAS · Germany
Ulrike Steinmann	University of Magdeburg · Germany
Zhongqing Su	The Hong Kong Polytechnic University · China
Alexander Sutor	UMIT Tirol · Austria
Dean Ta	Fudan University Shanghai · China
Koen Van Den Abeele	KU Leuven · Belgium
Andrea Walther	Humboldt University of Berlin · Germany
Xiuming Wang	Chinese Academy of Sciences · China
Oliver B. Wright	Hokkaido University · Japan
Xianmei Wu	Chinese Academy of Sciences · China
Bernhard Zagar	Montanuniversität Loeben · Austria
Xiumei Zhang	Chinese Academy of Sciences · China

Member of ICU Board

Leonard Bond · USA
Francisco Camarena · Spain
Younho Cho · Korea
Nico Declercq · Belgium, France, USA
Marc Deschamps · France
Jürg Dual · Switzerland
Luis Gaete-Garreton · Chile
Vitali Goussev · France
Bernd Henning · Germany (ICU President)
Sigrun Hirsekorn · Germany (ICU Secretary General)
Arkadiusz Jozefczak · Poland
Hiroshi Kanai · Japan
Peter A. Lewin · USA
Pai-Chi Li · Taiwan
Tim Mason · UK
Kentaro Nakamura · Japan
Nataliya Polikarpova · Russia
Stefan Radel · Austria
Wolfgang Sachse · USA
Oleg Sapozhnikov · Russia
Zhongqing Su · Hong Kong
Gail Ter Haar · UK
Koen Van Den Abeele · Belgium
Xiuming Wang · China (ICU Chairman)
Jens E. Wilhjelm · Denmark
Suk Wang Yoon · Korea

YSAC Members (non-voting):
Michael Neidrauer · USA
Yulia Petronyuk · Russia

PL1: Plenary Session 1

PL2: Plenary Session 2

PL3: Plenary Session 3

Lecture Sessions

A1-b: Acoustic and Elastic Metamaterials and Phononic Crystals

A2-b: Acoustic Tweezers and Particle Manipulation

A4-a: Bubbles and Cavitation

A5-a: Computational Acoustics for Complex Media and Structures

A6-a: Micromachined Ultrasonic Transducer (CMUT and PMUT) Technologies and Applications

A8-a: Nonlinear Acoustics and Ultrasonics

A9-a: Opto-Acoustics

A12-a: Surface Acoustic Waves and Guided Waves

A12-c: Surface Acoustic Waves and Guided Waves

A15-b: Ultrasonic Scattering

A15-c: Ultrasonic Scattering

A16-a: Ultrasonic Signal Processing and Instrumentation

A18-a: Nonlinear Properties of Piezoelectric Ceramics (FOR 5208)

B1-b: Biomedical Ultrasound for Therapy and Diagnosis

B1-c: Biomedical Ultrasound for Therapy and Diagnosis

B7-a: High-Frequency Ultrasound Imaging

B7-b: High-Frequency Ultrasound Imaging

B12-a: Ultrasonic Characterization of Tissues

B14-a: Ultrasound Elasticity Imaging

B15-a: Ultrasound Transducers for Medical Uses

C1-a: Acoustic Imaging and Beamforming Applications

C2-a: Acoustic Microscopy

C3-a: Acoustic Sensors

C6-a: Guided Waves and Their Applications in NDT and SHM

C6-b: Guided Waves and Their Applications in NDT and SHM

C9-a: NDT and NDE Transducers

C13-a: Ultrasonic Material Characterization

C13-b: Ultrasonic Material Characterization

C13-c: Ultrasonic Material Characterization

C13-d: Ultrasonic Material Characterization

D3-a: Laser Ultrasonics Applications in Industry and Aeronautics

D6-a: Power Ultrasound Cavitation and Cleaning

D6-b: Power Ultrasound for Fluid Manipulation

E2-a: Coupled acoustic/elastic/electromagnetic waves

E4-a: Machine Learning and Statistical Methods in Acoustics

E5-a: Reservoir Acoustics and Borehole Acoustic Logging

E5-b: Reservoir Acoustics and Borehole Acoustic Logging

Poster Session

DOI 10.5162/Ultrasonic2025/PL1.2

PL1.2 - Keynote

Photonic quantum systems

Prof. Dr. Christine Silberhorn

Paderborn University, Paderborn (Germany)

Abstract:

Quantum technologies promise a change of paradigm for many fields of application, for example in communication systems, in high-performance computing and simulation of quantum systems, as well as in sensor technology. Current efforts in photonic quantum science target the implementation of practical devices and scalable systems, where the realization of quantum devices for real-word deployment and controlled quantum network structures is key for many applications.

Here we review different approaches to advance current experimental approaches for scaling multi-dimensional photonic quantum systems and show our most advanced system for photonic quantum computing. Our research comprises integrated quantum circuits based on $\chi(2)$–materials, spectral-temporal engineering of quantum light and features all needed experimental functionalities for future photonic quantum technologies.

DOI 10.5162/Ultrasonic2025/PL2.1

PL2.1 - Keynote

Ultrasonics with EUV and x-ray lasers

Dr. Alexei Maznev

MIT, Cambridge · USA

Abstract:

The invention of the optical laser in the 20th century greatly advanced the field of ultrasonics: lasers are now widely used for both generation and detection of ultrasound. The beginning of the 21st century witnessed remarkable progress in the development of bright and ultrafast short wavelength sources, including free electron lasers operating in the extreme ultraviolet (EUV) and x-ray ranges. In this talk, I will provide an overview of recent advances achieved by using EUV and x-ray lasers for the generation and detection of acoustic fields on the ultrafast time scale. Much of the discussion will be focused on the transient grating technique, in which two short laser pulses are crossed in the sample to launch acoustic waves at the wave vector defined by the periodicity of the optical interference pattern. This technique has recently been extended to the EUV and x-ray spectral ranges [1-4]. The main advantage of using short wavelengths is that the transient grating period defining the acoustic wavelength can be very short: measurements with periods down to 10 nm have already been demonstrated [4]. We will also discuss diffuse scattering of EUV and x-ray radiation by acoustic waves with nanoscale wavelengths [5, 6]. A surprising recent finding [6] is the observation of dynamic circular fringe patterns in the EUV scattering from metal and semiconductor samples following femtosecond laser excitation. These patterns originate from spatially random but temporally coherent surface acoustic waves with wavelengths down to 60 nm whose excitation is facilitated by miniscule surface roughness. Other advances in using EUV and x-ray radiation in ultrasonics will also be briefly reviewed.uantum technologies promise a change of paradigm for many fields of application, for example in communication systems, in high-performance computing and simulation of quantum systems, as well as in sensor technology. Current efforts in photonic quantum science target the implementation of practical devices and scalable systems, where the realization of quantum devices for real-word deployment and controlled quantum network structures is key for many applications.

[1] F. Bencivenga, R. Mincigrucci, F. Capotondi et al., Sci. Adv. 5, eaaw5805 (2019).
[2] A. A. Maznev, F. Bencivenga, A. Cannizzo, et al., Appl. Phys. Lett. 113, 221905 (2018).
[3] A. A. Maznev, R. Mincigrucci, F. Bencivenga et al., Appl. Phys. Lett. 119, 044102 (2021).
[4] H. Li, N. Wang, L. Zhang et al., https://arxiv.org/abs/2506.03428
[5] Y. Huang, P. Sun, S. W. Teitelbaum et al., Phys. Rev. X 14, 041010 (2024).
[6] F. Capotondi, A. A. Maznev, F. Bencivenga et al., https://arxiv.org/abs/2502.18445

DOI 10.5162/Ultrasonic2025/PL2.2

PL2.2 - Keynote

Lessons Learned in (Micro-)Acoustic Sensing

Prof. Dr. Bernhard Jakoby

Johannes Kepler University, Linz (Austria)

Abstract:

This talk focuses on some general aspects that the author encountered in almost three decades of research in the area of acoustic and microacoustic sensing. Some of these works were applied and some were more fundamental with results being specific to the respectively considered problems. At the same time, there are insights that are of a more general relevance, which may be useful for one or the other fellow researcher in the field. In particular, the concept of “physical chemosensors” and “orthogonal sensors” as well as the selection of driving mechanisms (Lorentz-forces vs. piezoelectricity), operation frequency, and vibration modes will be discussed for selected fluidic sensing applications.

In these cases, also the consideration of the second coefficient of viscosity has proven to be beneficial. Challenges associated with highly viscous liquids can be turned into useful features when considering alternative sensing principles. Similarly, using weakly coupled acoustic systems can yield design advantages overcompensating the associated loss in signal level. Also, in terms of fabrication technologies as well as modeling techniques, one can benefit from using methods from neighboring disciplines introducing additional methodological flavors in one’s research. Finally, when it comes to applications, the relevance of algorithms and electronics must not be under-estimated. This exemplary list of aspects will be illustrated and discussed using examples from several ongoing and finalized research projects.

DOI 10.5162/Ultrasonic2025/PL3.1

PL3.1 - Keynote

Zero group velocity and backward guided elastic waves

Dr. Claire Prada

Institut Langevin, Paris (France)

Abstract:

Guided elastic waves involves the coupling of shear and compression waves at interfaces. Even in the simplest guides, such as homogeneous plates or cylinders, this complex interaction results in the existence of negative phase velocity branches. In the absence of attenuation or leakage, the minimum frequencies of such backward branches correspond to zero-group-velocity (ZGV) modes and are associated with narrow local resonances. These ZGV resonances are very well observed using non-contact laser ultrasonic techniques (LUS) [1] and are useful for assessing the local properties of materials such as thickness, Poisson's ratio [2] in particular at high temperatures [3] and, elastic anisotropy whether intrinsic [4] or induced by stress [5]. This presentation will review the remarkable properties of backward and ZGV resonances. Special attention will be given to anisotropic plates, for which ZGV points exist for some propagation directions at minima and saddle points of modal dispersion surfaces, whereas quasi-resonances with energy propagation perpendicular to the wave vector occur in other directions. These transverse-velocity modes and the associated extreme power flux skewing will be illustrated through measurements conducted on monocrystalline silicon plates [6] and on rolled steel plates.

[1] Prada, Balogun, Murray, Appl. Phys. Lett. (2005)
[2] Clorennec, Prada, Royer, J. Appl. Phys., 101 (3) (2007)
[3] Watzl, Kerschbaummayr,…, Grünsteidl, Acta Materiala 235 (2023).
[4] Prada, Clorennec, Murray, Royer, J. Acoust. Soc. Am. 126, (2009)
[5] Morales, Pathal, Lum, Kube, Murray, Stobbe, Appl. Phys. Lett. 124, 084101 (2024)
[6] Kiefer, Mezil, Prada, Science Advances 9, eadk6846 (2023)

DOI 10.5162/Ultrasonic2025/PL3.2

PL3.2 - Keynote

Dynamic Gravity

Prof. Dr. Jürg Dual

ETH Zurich, Zurich · Swiss

Abstract:

With many recent advances in multi-messenger astronomy, fully controlled transmitter receiver laboratory experiments on dynamic gravitational fields (DGFs) have become more important. This implies measuring their phase and amplitude behaviour and assessing any non-gravitational crosstalk. Here we will present two new experiments in this context. While there is consensus that static (i.e. mHz) gravitational fields cannot be attenuated, to the authors' knowledge, shielding effects for DGFs have not been experimentally investigated. Theoretically, the absorption cross-section is expected to be proportional to frequency squared. Usually, dynamic experiments consist of a periodically moving mass distribution (here two rotating tungsten bars). The detector system consists of a high Q (104), 42 Hz resonant titanium bending beam. Its gravitationally induced motion is analyzed using three laser Doppler vibrometers and multichannel lock-in amplifiers. Of paramount importance is a highly temperature stable environment and the vibration isolation of the detector from ambient noise and crosstalk from the transmitter. Here we present progress on several fronts: High precision gravitational interaction modeling, quantitative crosstalk assessment and transmitter characterization using neutron imaging. The laser interferometers are calibrated at the measurement frequency specifically for the extremely small displacements in the pm range. This results in an estimated measurement uncertainty of around 0.1% for Big G. In addition, we will present experimental results on shielding of DGFs using different metal shields with dimensions of about 1.4 × 0.3 × 0.1 m and mass of up to ~500 kg placed in between transmitter and detector. The signals for the two shield positions (with/without shield) are best analyzed by fitting a single degree of freedom response function in a ceteris paribus mode. At a frequency of more than four orders of magnitude higher than previous quasistatic shielding investigations, the relative change of amplitude and phase of the response signal is very small for both a 9 cm thick brass shield and a 10 cm thick lead shield.

[1] Brack, T., Zybach, B., Balabdaoui, F., Kaufmann, S., Palmegiano, F., Tomasina, J.-C.,Dual, J. (2022). Dynamic measurement of gravitational coupling between resonating beams in the hertz regime. Nature Physics, 18(8), 952. doi: 10.1038/s41567-022-01642-8
[2] Brack, T., Fankhauser, J., Zybach, B., Kaufmann, S., Palmegiano, F., Tomasina, J.-C.,Dual, J. (2023). Dynamic gravitational excitation of structural resonances in the hertz regime using two rotating bars. Communications Physics, 6(1), 270. doi: 10.1038/s42005-023-01389-5

*Corresponding author. Email: dual@imes.mavt.ethz.ch

DOI 10.5162/Ultrasonic2025/A1-b1

Guided Acoustic Waves on Periodic Structured Plates: from Theory to Application

Johannes Landskron[1], Conrad R. Wolf[1], and Klaus-Stefan Drese [1]
[1]Institute for Sensor and Actuator Technology, Coburg University of Applied Science, 96450 Coburg, Germany
Johannes.Landskron@hs-coburg.de, Klaus.Drese@hs-coburg.de

Abstract: Guided acoustic waves are well studied for unstructured plates. In the last years the view of researchers has been extended to phononic crystals consisting of periodic structured or combined materials in the direction of sound propagation. In this work, the influence of one-sided and two-sided structured geometries on Lamb waves is investigated by simulations and laser Doppler vibrometry. In addition to the analysis of band structures, the transmission, reflection and mode conversion behavior of Lamb waves is characterized for finite structures.

Keywords: Guided Acoustic Waves, Lamb Waves, Phononic Crystals, Finite Elements Method, Laser Doppler Vibrometry

Introduction

Guided acoustic waves (GAW), including Lamb, Rayleigh, and quasi-Scholte waves, are used in various sensor and actuator applications, such as deposit detection, flow rate measurement, and non-destructive testing or fluid manipulation [1]. Recent acoustic research focuses on phononic crystals (PCs) for the manipulation of acoustic waves [2]. These investigations are facilitated by advanced simulation methods. In particular, the finite element method (FEM) enables a fast characterization of various geometries. This development makes studies more efficient, reducing the need for extensive physical experiments. Nevertheless, this option has been observed to demonstrate the tendency of structures to be examined exclusively through simulation, yielding geometries which are difficult or impossible to manufacture [3]. In this work, the interaction of Lamb waves with structured metal plates is investigated. For the first analysis, the band structure diagrams for different symmetric and antisymmetric structures are calculated and characterized. For experimental validation, a laser Doppler vibrometer (LDV) is used. Additionally, the interaction of Lamb waves with a finite number of structure elements is investigated by frequency domain simulations. Here, the reflection, transmission, and mode conversion behavior of Lamb waves at such structures is calculated. Finally, challenging aspects of experimental validation as well as the possibilities of using such structures in combination with fluid exposure are discussed.

Methods

In this paper, a model based on a unit cell (UC) was used for the calculation of band structures [4]. In the case of an unstructured plate, the two-dimensional finite element model for the unit cell consists exclusively of a rectangle with height H_{uc} and width B_{uc}. Floquet boundary conditions can be utilized to calculate the cell dispersion behavior for predefined wave numbers k_x by means of eigenfrequency analysis. According to Eq. (1) the dimensionless parameter k has to be swept from 0 to 1 to evaluate all relevant values of k_x in the study.

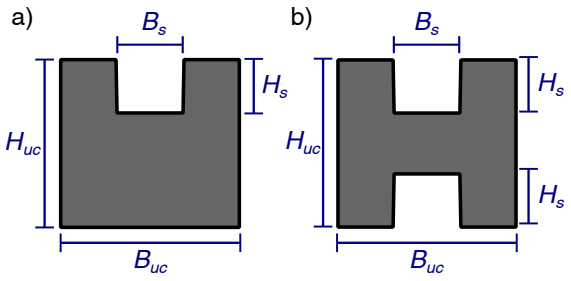

Fig. 1: Sketches of the unit cells used for the band structure analysis with a) single-sided and b) double-sided structures.

$$k_x = \frac{\pi}{B_{\mathrm{uc}}} k \quad \text{with} \quad k \in [0, 1] \tag{1}$$

Lamb waves, which ordinarily propagate on flat plates, are characterized according to their order of oscillation and the symmetry behavior in the plate. A standard distinction is made between symmetric and antisymmetric modes [5]. In order to investigate the influence of the symmetry behavior of the periodic structuring on the different Lamb waves, two types of UCs were investigated in this work. These grooves were denoted either single-sided or double-sided, depending on their orientation relative to the sample's

DOI 10.5162/Ultrasonic2025/A1-b1

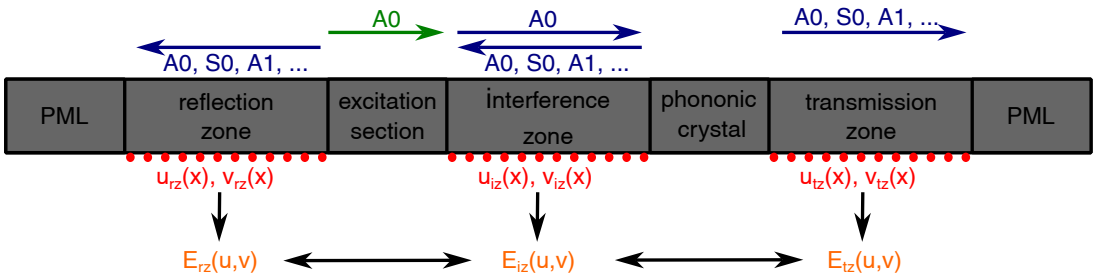

Fig. 2: Sketch of the simulation for the evaluation of the transmission and reflection behavior of limited structures.

surface. The parameters B_s (width) and H_s (height) were introduced to describe the structured geometries (Fig. 1). In the simulations, the dimensions of the geometry were gradually increased starting from the simple unstructured plate in order to be able to analyze the progressive changes in the derived band structure diagrams. The geometric parameters used for the UC are listed in Tab. 1.

The former considered band structure is theoretically only valid for infinitely long periodic PCs. To study the performance of limited structures, a new frequency domain model was built. Therefore, a long plate geometry was generated consisting of different zones (see Fig. 2). In these simulations, a right-wards traveling A0 mode was generated in the excitation zone. By passing the interference zone the limited PC was reached causing reflections, transmission, and mode conversion. Perfectly matched layers (PML) at both ends of the panel effectively suppress unwanted reflections. In the reflection, interference, and transmission zone the local magnitudes of the waves can be determined for each mode by Fourier transformation at the plate surface. In simulations, both amplitudes, the normal component *v(x)* and the in-plane component *u(x)*, can be determined. In addition, a cross section energy coefficient can be derived for each Lamb mode by Eq. (2) based on the eigenfrequency simulations for an unstructured plate. This coefficient allows to determine the wave energy in a plate cross section by evaluating the local magnitudes at the plate surface.

Tab. 1: Geometric parameters of the unit cells.

Parameter	Single-Sided UC	Double-Sided UC
B_{uc} / mm	2	2
H_{uc} / mm	1.5	1.5
B_{uc} / mm	1	1
H_{uc} / mm	0 - 0.5	0 - 0.25

$$E(f) = \frac{\int_0^{H_{\mathrm{uc}}} |E_{\mathrm{pot}}(f,h)| + |E_{\mathrm{kin}}(f,h)| \cdot \mathrm{d}h}{|u(f)|^2 + |v(f)|^2} \quad (2)$$

These energy values can be utilized to establish an energy balance for the model. The energy of the incident wave is equivalent to the sum of the energy of all transmitted and reflected modes of the PC. Furthermore, the interference zone facilitates a comparison between the data from the reflection and transmission zones. By evaluating this model for different frequencies, the response behavior of the PC can be precisely determined.

The energy coefficients calculated by Eq. (2) are displayed in Fig. 3 for three different Lamb modes. In contrast to the A0 and S0 modes, the A1 mode exists only above a cut-off frequency of about 1 MHz. Consequently, below this frequency the incoming A0 mode can only be converted into a S0 mode by the PC, while above the S0 mode has to be considered beside A0 and S0 modes.

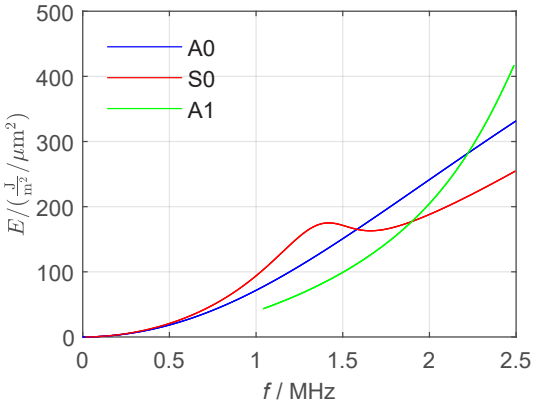

Fig. 3: Energy coefficient for squared surface elongation magnitude for different Lamb modes.

DOI 10.5162/Ultrasonic2025/A1-b1

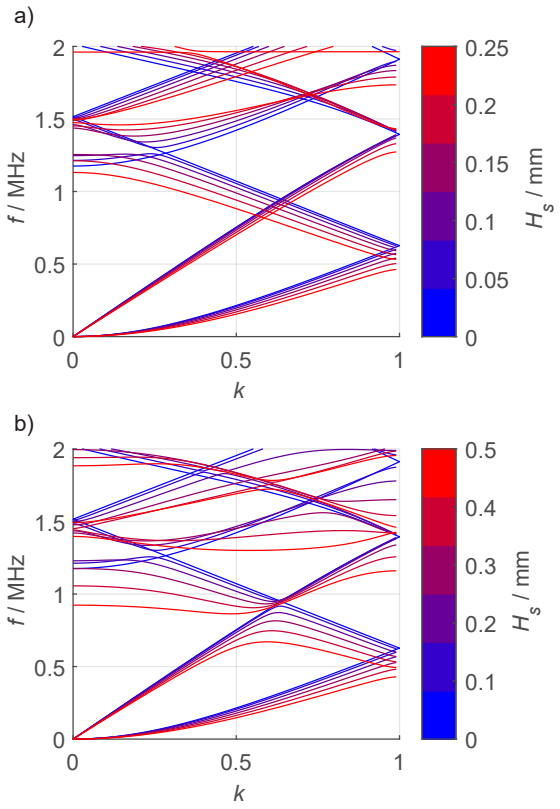

Fig. 4: Calculated band structure diagrams for a) double-sided and b) single-sided unit cells with varying parameter H_s based on a 1.5 mm aluminum plate.

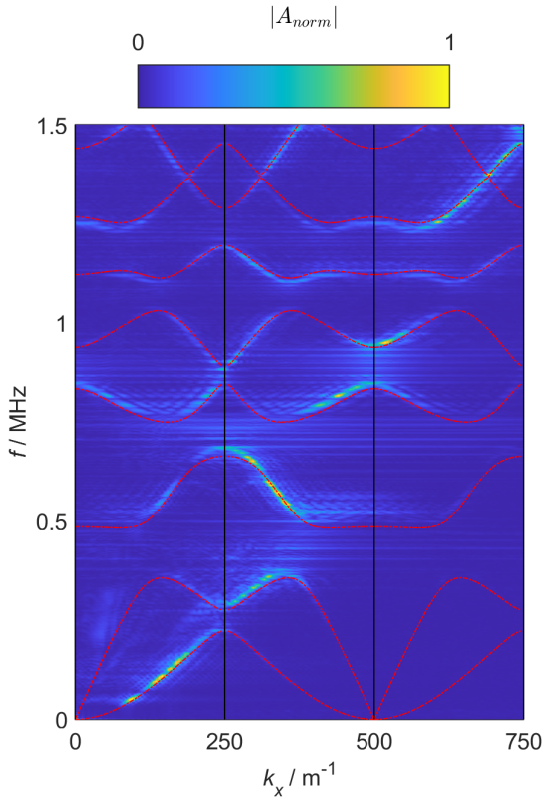

Fig. 5: Band structure measured on a 1.5 mm thick brass plate with 50 periodic milled single-sided PC (surface plot) overlaid with the simulated expanded band structure diagram (red line).

For experimental validation a single-sided structured plate with 50 milled grooves was prepared. The excitation of Lamb waves was generated by a piezoelectric transducer connected to a sine wave generator in combination with an amplifier for higher amplitudes. For characterization of the waves the local motion of the surface on the counter side of the structured area was sampled by a LDV. The evaluation of the band structure diagram was performed by 2-dimensional Fourier transformation [6].

Results

The influence of single-sided and double-sided PCs on the band structures of Lamb waves is illustrated in Fig. 4. In this graphs the depth of the structures has been gradually increased. In both diagrams, the structuring causes the mode branches to split at the edges $k = 0$ and $k = 1$. This phenomenon results in band gaps with no possible propagation inside. Furthermore, it can be observed in (Fig. 4a) that the implementation of a PC leads to uniform transitions between modes at the original intersection points between the A0 and A1 modes ($k = 0.25$, $f = 1.25$ MHz). A detailed examination using the fast Fourier transform (FFT) reveals the existence of multiple wavelengths occurring simultaneously on both branches. This phenomenon can be attributed to the transitions occurring in the diagrams. Consequently, the diagrams cannot be unfolded as for a flat plate to derive the dispersion relation. Therefore, the designations for Lamb waves, such as the A0 mode, cannot be adopted for PCs. In case of a single-sided structure (Fig. 4b), it can be observed that these interactions also occur between antisymmetric and symmetric modes ($k = 0.6$, $f = 0.9$ MHz) caused by symmetry break of the structure. This phenomenon can result in the formation of band gaps, which theoretically preclude the transmission of incident Lamb waves within specific frequency ranges.

This behavior can be confirmed in an experiment with a structured brass plate. As illustrated in Fig. 5, the measured band diagram is compared to the corresponding simulation periodically extended. As can be seen, the simulation is capable of accurately pre-

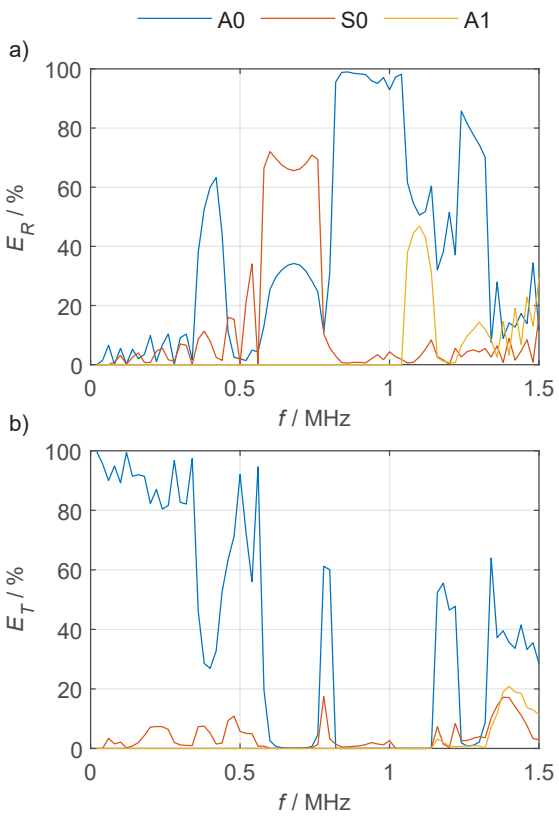

Fig. 6: Simulated relative (a) reflected and (b) transmitted energy of an inconming A0 Lamb mode by a single-sided PC of 10 elements.

dicting the band structure of PCs. As predicted, different wavelengths can be detected in the signals for the same frequencies related to the same simulated branches. However, the manner in which these crystals respond to incident waves can only be calculated from the second simulation.

Fig. 2 reveals the reflection and transmission behavior of 10 one-sided structured PCs to an incident A0 mode. This analysis is based on the band structure of Fig. 6. As assumed, low frequency A0 modes are able to pass the crystal. In the center of the displayed frequencies, an augmented reflection is observed, with the S0 mode predominating in the reflected signal. At frequencies exceeding 1 MHz, as anticipated, S0 mode components were excited by mode conversion.

Discussion and Outlook

The findings indicate that the behavior of PCs in combination with Lamb waves can be efficiently investigated through the utilization of the aforementioned methods. The simulated band structures have shown a strong correlation with the experimental data. However, it was demonstrated that a more detailed analysis of the interaction is necessary, particularly when considering finite crystals. The primary advantage of the method presented here is that, by employing suitable coefficients, an energy balance can be conducted using only the magnitudes at the surface. Consequently, the method can be applied to experiments with LDV data. However, this method requires the consideration of additional effects such as attenuation and the directivity of waves on real 3D plates. The subsequent step will involve the characterization of PCs with fluid loading, which promises to be a fascinating avenue of research. A particularly salient aspect of this study is the potential of extending the calculation to acoustic streaming, a development that promises to unlock a range of novel applications, including acoustically supported electroplating processes on structured electrodes.

Funding

This research was funded by: Technologie Allianz Oberfranken TAO; Bayerisches Staatsministerium für Wirtschaft, Landsentwicklung und Energie; Bayerisches Staatsministerium für Wissenschaft und Kunst; Bundesministerium für Bildung und Forschung and Gemeinsame Wissenschaftskonferenz GWK

References

[1] M. Philibert et al. "Lamb waves-based technologies for structural health monitoring of composite structures for aircraft applications". In: *European Journal of Materials* 2.1 (Dec. 31, 2022). DOI: 10.1080/26889277.2022.2094839.

[2] V. Laude. "Principles and properties of phononic crystal waveguides". In: *APL Materials* 9.8 (Aug. 1, 2021). DOI: 10.1063/5.0059035.

[3] L. Yuan et al. "Study on Lamb Waves in a Composite Phononic Crystal Plate". In: *Crystals* 10.9 (Sept. 9, 2020). DOI: 10.3390/cryst10090799.

[4] S. Van Den Boom, F. Van Keulen, and A. Aragón. "Fully decoupling geometry from discretization in the Bloch–Floquet finite element analysis of phononic crystals". In: *Computer Methods in Applied Mechanics and Engineering* 382 (Aug. 2021). DOI: 10.1016/j.cma.2021.113848.

[5] Z. Tian and L. Yu. "Lamb wave frequency–wavenumber analysis and decomposition". In: *Journal of Intelligent Material Systems and Structures* 25.9 (June 2014). DOI: 10.1177/1045389X14521875.

[6] L. Draudvilienė et al. "Accuracy Assessment of the 2D-FFT Method Based on Peak Detection of the Spectrum Magnitude at the Particular Frequencies Using the Lamb Wave Signals". In: *Sensors* 22.18 (Sept. 7, 2022). DOI: 10.3390/s22186750.

DOI 10.5162/Ultrasonic2025/A1-b2

Phononic Crystallography of Fibre-Reinforced Polymers using Broadband Acoustic Waves

Mareen Wippermann[1] *and Leander Claes*[1]
[1]*Measurement Engineering Group, Paderborn University, 33098 Paderborn, Germany*
wippermann@emt.uni-paderborn.de

Abstract: Assuming that fibre-reinforced polymers can be modelled as two-dimensional phononic crystals, the present study proposes an approach to experimentally determine their crystallographic properties. The results closely resemble classical crystallographic methods, such as X-ray diffraction, but allow for the characterisation of macroscopic structures by non-destructive, acoustic means. The proposed method is based on the evaluation of spatio-temporal measurement data of broadband guided acoustic waves in the frequency and wavenumber domain.

Keywords: Waveguides, Periodic structure, Phononic crystals, Crystallography, Fibre-reinforced polymers

Motivation

Fibre-reinforced polymers have attracted considerable interest due to their exceptional mechanical properties, including high strength-to-weight ratios, which renders them ideal for a broad spectrum of engineering applications. The material composition and orientation of the reinforcing fibres permit a flexible and application-specific design of the composite material for the respective use case. In addition, composites are distinguished by their high resistance to corrosion and fatigue. Fibre-reinforced polymers exhibit an orthogonal woven structure and are distinguished by variations in the number of crossed fibres or the fibre distribution [1]. Typically, fibre-reinforced polymers are fabricated as laminated composites, with multiple layers. However, during subsequent processing and forming operations, local deviations in periodicity and alterations in the geometry of the fibre weave can occur, potentially impacting the mechanical properties.

The present study employs pulsed laser radiation as a non-destructive technique to induce broadband acoustic waves within fibre-reinforced polymer samples. The samples are conceptualised as phononic crystals, wherein their internal structure and inherent periodicity influence their acoustic behaviour [2]. Whilst phononic crystals are typically deliberately designed to exhibit engineered band gaps for specific functional purposes, such as vibration isolation or wave guiding, this work is focused on analysis of existing structures. The proposed method of evaluating guided acoustic wave measurement data from these samples enables the determination of the phononic crystals properties, such as the unit cell geometry, by evaluating the material's periodicity, thereby providing a framework for the quantification of structural properties.

Experimental Procedure

The measurement setup shown in Fig. 1 is utilised for the analysis of the properties of guided acoustic waves in fibre-reinforced polymers. Pulsed ($1.5\,\mathrm{ns}$), infrared laser radiation is directed and focused onto a line on the sample by a cylindrical lens. The energy density is sufficiently low to prevent damage to the sample, resulting only in a fast, localised increase in temperature. The thermoelastic effect results in the excitation of broadband acoustic waves, which propagate through the sample. The excited acoustic waves are detected by a piezoelectric transducer, which utilises a strip-shaped piezoelectric ceramic as the active element. In order to analyse wave propagation in the spatial domain, the excitation location in x-direction is variable. A recorded dataset is two-dimensional, resolved in both space and time.

The transformation of the data into the wavenumber-frequency domain can be achieved applying a two-dimensional Fourier transform. [3] The result can then be interpreted similarly to a dispersion diagram, with ridges indicating propagating modes. In the dispersion diagrams of fibre-reinforced polymers, the propagating modes exhibit repetitions in the wavenumber range with a period of Δ_{k_x} (Fig. 2). This effect directly results from the periodic internal structure of the samples [5], [6]. The spatial period a of the sample can be calculated using the following reciprocal relationship [7]

$$a = \frac{2\pi}{\Delta_{k_x}}. \tag{1}$$

To evaluate the measurement data with respect to their periodicity, the autocorrelation of the dispersion diagrams is calculated in the direction of the wavenumber and averaged over the frequency (Fig. 3). Each

DOI 10.5162/Ultrasonic2025/A1-b2

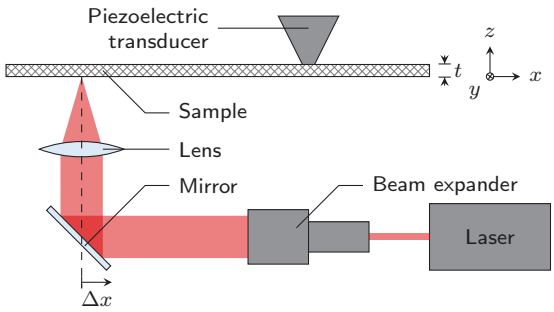

Fig. 1: Experimental setup for the excitation and detection of broadband acoustic waves in plate-like samples with variable excitation position [4].

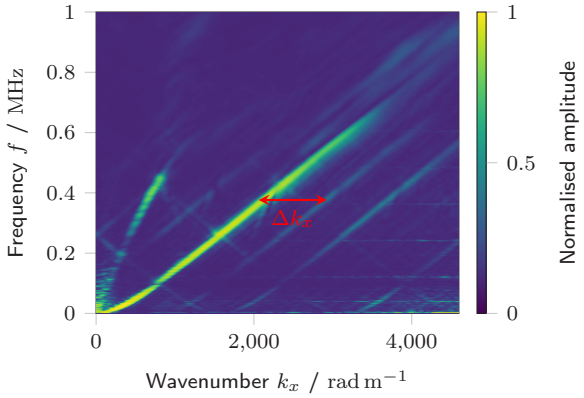

Fig. 2: Measured dispersion diagram of a fibre-reinforced polymer sheet with plain weave. The sample is three-layered and has a thickness of 1.5 mm.

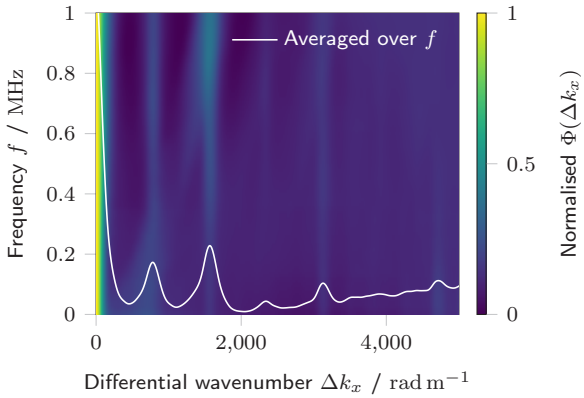

Fig. 3: Autocorrelation along the wavenumber direction of the dispersion diagram from a fibre-reinforced polymer with plain weave (Fig. 2), and averaged over the frequency. [8]

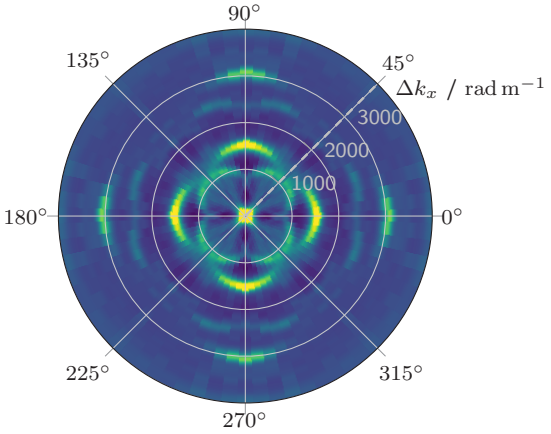

Fig. 4: Frequency-averaged autocorrelation functions as a function of the angel α from a sample with plain weave.

maximum thus represents a period of the measurement data in the wavenumber regime. The distances $\Delta_{k_x,i}$ of the maxima can be averaged and converted into the spatial period a using Eq. (1). Consequently, a robust methodology exists for determining the size of the unit cell [8].

Unit cell geometry

In order to ascertain the geometry of the unit cell, the proposed evaluation of the periodicity in wavenumber regime is conducted as a function of an angle α. α is defined as the angle between the measurement direction (x-direction) and the direction of one of the fibre bundles in the wave. The frequency-averaged autocorrelation functions (compare Fig. 3) as a function of the angle α for a sample with plain wave is shown in Fig. 4. Remapping the radial axis using the reciprocal relationship from Eq. (1) results in a depiction in the spatial regime (Fig. 5). The intensities of these peaks are indicative of the geometry of the present unit cell of a plain weave. The unit cell under consideration is square, with a side measuring $a = 8.1\,\mathrm{mm}$, which aligns well with optical measurements of the sample. Fig. 5 also shows a larger square that is rotated by $45°$. The current assumption as to why the square is visible is that these depictions visualise reflection planes in the samples, which also occur at an angle of $45°$.

The reciprocal relationship $a = \frac{2\pi}{\Delta k_x}$ to map the wavenumber data to the spatial domain is used instead of a Fourier transformation as an approximation because manual handling of the sample in the measurement setup currently does not yield reliable phase information. It is evident that this mapping does not result in the restoration of the original spatial signal; rather, it provides an intuitive spatial structure. A

DOI 10.5162/Ultrasonic2025/A1-b2

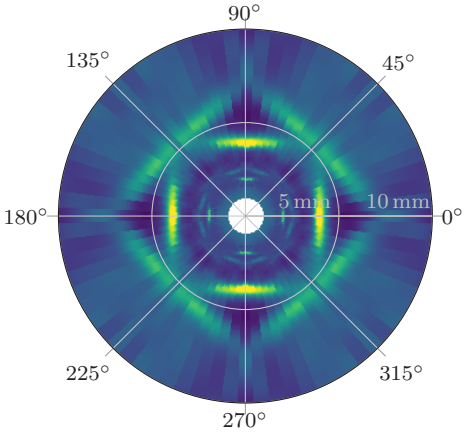

Fig. 5: Result of the proposed method to characterise the internal periodic structure of a sample with plain weave showing a symmetrical, square unit cell geometry.

consequence of the inverted mapping under consideration is that repetitions or artefacts at smaller values of a appear which are not interpretable.

The results of the proposed method for the analysis of the internal, periodic structure bear a strong resemblance with images from X-ray crystallography, which is a method of visualising the atomic arrangements of crystals by detecting diffraction patterns [9]. It is thus referred to as phononic crystallography, because it allows for the analysis of phononic crystals and their dispersive properties, like reflection planes and the unit cell geometry.

Results

To assess the capability of the proposed method to determine the structural properties of a given sample with internal periodic structure, it applied to detect fibre weave deformation. The samples consist of a single-layer of glass fibre 2/2 twill weave embedded in a polypropylene matrix. The measurements are conducted in a range of $0°..180°$ and then repeated due to the symmetry of the weave. As illustrated in Fig. 6, the applying the proposed method shows the quadratic unit cell of the twill wave, with a side length of $a = 9.58\,\mathrm{mm}$. This corresponds to the expected value, which can be determined visually.

In a 2/2 twill weave, fibres bundles in one direction always cross over two fibre bundles in the other direction. It is assumed, that reflection of acoustic waves occur when the fibres transition between layers. The dispersion diagram of the sample with plain weave shows repetitions at a and $\frac{a}{2}$ are discernible (respectively Δk_x and $2\Delta k_x$). The repetitions at a are more prominent in the measurement data and are thus evaluated. Furthermore, the ridges at $135°$

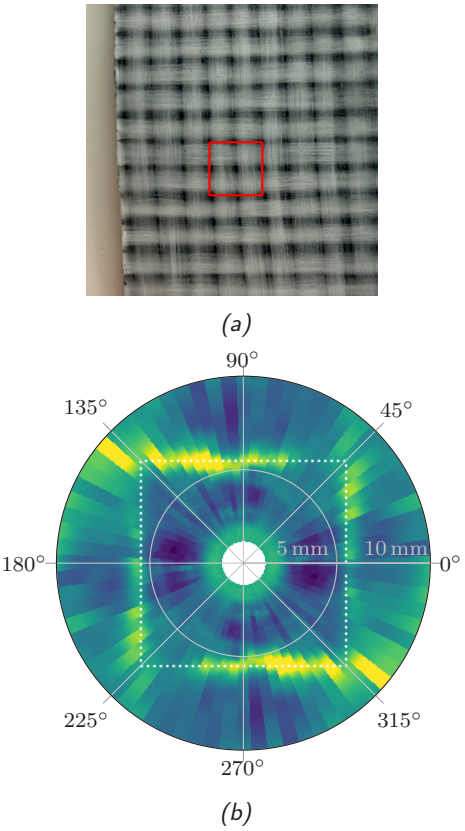

Fig. 6: Result of the proposed method to characterise the internal periodic structure of a sample with twill weave (a) showing a square unit cell geometry with asymmetric intensity (b).

are more pronounced than at $45°$; this phenomenon corresponds with the asymmetry of the weave with respect to rotations of $90°$. A comparison with the results from the plain weave (Fig. 5) shows that the proposed method can thus also infer basic properties of the pattern of the weave. The exact correspondence of weave pattern and the results are subject of future studies.

The same analysis is conducted on a distorted single-layer sample with twill weave (Fig. 7). The composition of this sample is identical to that of the reference sample. It is evident that the distortion of the weave in a single direction results in the unit cell assuming a parallelogram shape. It is imperative to demonstrate that the measurement results of the proposed method show this geometric change. The result (Fig. 7b) shows that the distortion of the unit cell is clearly detected and determined to be approximately $20°$.

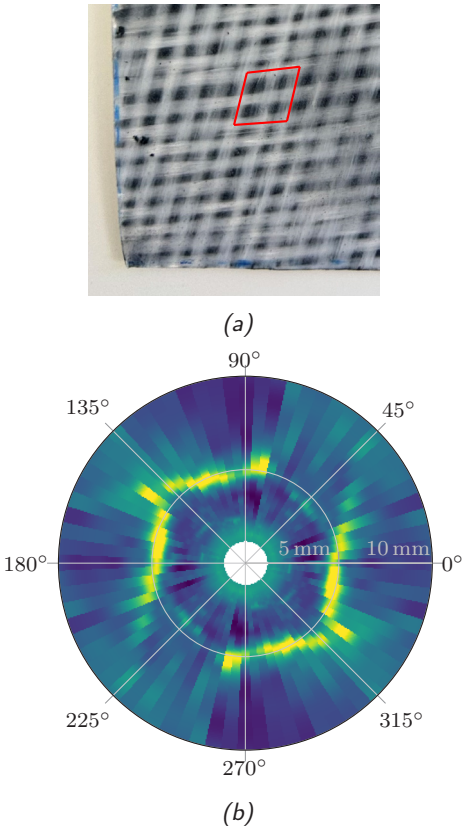

Fig. 7: Result of the proposed method to characterise the internal periodic structure of a sample with distorted twill weave (a) showing a unit cell with parallelogram shape with asymmetric intensity (b).

Conclusion

Using the proposed method, the geometry and size of unit cells of different weave patterns in fibre-reinforced polymers can be determined by evaluating the dispersive behaviour of acoustic plate waves. This is especially evident when evaluating samples with non-rectangular unit cells. Indications for the asymmetry of specific weave pattern can also be found in the results.

Subsequent research will investigate local distortion or changes in periodicity. Synthetically created periodic structures will be analysed to further validate the findings of this study. This facilitates the investigation of the influence of a small aperiodicity on phononic crystallography. A potential extension of the method is to quantitatively analyse the maxima in the autocorrelation of the dispersion data.

A full empirical band structure of the sample can also be inferred from the measurement data, which will be evaluated for material modelling purposes in future studies.

Acknowledgements

This research is funded by the Deutsche Forschungsgemeinschaft (DFG, German Research Foundation) – 495847374 (FaMOUS).

References

[1] R. A. Angelova, 'Design of weave patterns,' in *Advanced Weaving Technology*, Y. Kyosev and F. Boussu, Eds. Cham: Springer International Publishing, 2022, pp. 195–250, ISBN: 978-3-030-91515-5. DOI: 10.1007/978-3-030-91515-5_5. [Online]. Available: https://doi.org/10.1007/978-3-030-91515-5_5.

[2] A. Khelif and A. Adibi, *Phononic Crystals: Fundamentals and Applications*. Jan. 2015, pp. 1–245, ISBN: 978-1-4614-9392-1. DOI: 10.1007/978-1-4614-9393-8.

[3] D. Alleyne and P. Cawley, 'A 2-dimensional fourier transform method for the quantitative measurement of lamb modes,' in *IEEE Symposium on Ultrasonics*, IEEE, 1990. DOI: 10.1109/ultsym.1990.171541.

[4] L. Claes, T. Meyer, F. Bause, J. Rautenberg and B. Henning, 'Determination of the material properties of polymers using laser-generated broadband ultrasound,' *Journal of Sensors and Sensor Systems*, vol. 5, no. 1, pp. 187–196, 2016, ISSN: 2194-878X. DOI: 10.5194/jsss-5-187-2016.

[5] F. Bloch, 'Über die Quantenmechanik der Elektronen in Kristallgittern,' *Zeitschrift für Physik*, vol. 52, no. 7-8, pp. 555–600, 1929.

[6] L. Claes, 'Einfluss der periodischen Struktur auf geführte Wellen in gewebeverstärkten Polymeren,' in *Fortschritte der Akustik - DAGA 2024*, Deutsche Gesellschaft für Akustik e.V., Ed., 2024, pp. 620–623.

[7] J. D. Jackson, *Classical electrodynamics*. John Wiley & Sons, 2021.

[8] M. Wippermann, L. Claes, P. Brandes, E. Moritzer and B. Henning, 'Determination of the unit cell geometry in fibre-reinforced polymer sheets using guided acoustic waves,' 2025. DOI: 10.71568/DASDAGA2025.116.

[9] T. Oeser, 'Kristallstrukturanalyse durch Röntgenbeugung,' *Spektroskopiekurs kompakt/Thomas Oeser*, 2019.

DOI 10.5162/Ultrasonic2025/A2-b4

Acoustophoresis on Microfluidic Chips Made of Polymers and Glass: Experimental Comparison

E. De los Reyes[1], *I. González*[1], *L. Díez*[1], *and A. Pinto*[1]
[1]*Consejo Superior de Investigaciones Científicas CSIC, Institute of Physical Technologies and Information ITEFI, Madrid, Spain*
iciar.gonzalez@csic.es

Abstract: We present an experimental study to analyze the influence of the chip material on acoustophoresis processes induced by ultrasounds in microfluidic devices. Two materials with different acoustic properties were used for the chip structutre: glass and PMMA repectively. Different vibrations established in their respective structures give rise to diverse acoustic pressure patterns within the liquid phase of the channels, providing different particle collection efficiencies. Advantages and disadvantages of both types of chips have been tested.

Keywords: Ultrasounds, Microfluidics, Acoustophoresis, Sorting, Micromanipulation.

Background, Motivation and Objective

In last decades, the development of technology in the field of microfluidics has advanced considerably for sorting and separation applications, being Bulk Acoustic Wave actuation (BAW) one of the plattforms that can perform in this field. In these platform, an ultrasonic actuator is mechanically attached to a chip, generating a wave propagation throughout its structure. Different operating mechanisms of BAW actuators depend directly from the materials used in the chips and thus, of its acoustic impedance.

$$Z = \rho c \tag{1}$$

where Z is the material's acoustic impedance, ρ is the density and c is the sound velocity.

In chips made of materials with high acoustic impedance such as glass or silicon, a standing wave is established in the liquid phase between two rigid parallel walls separated by an integer number of half wavelengths. For a half wavelength-channel width, a pressure node is established at the central axis, collecting particles due to the radiation force induced by ultrasound [1]. This type of material presents low acoustic energy loss and high directivity.

In contrast, the polymeric chip materials have a low acoustic impedance, similar to that of the liquids. It is the entire chip structure that is involved in establishing complex three-dimensional vibration modes at any frequency [2, 3]. Acoustic energy is transferred to the liquid phase from the structural vibrations that generates these vibration modes. Due to the low acoustic impedance of these materials, energy loss is greater than that found in acoustically hard materials.

The process of acoustophoresis by which particle collection is achieved is governed by the radiation force, which is due to the nonlinear interaction between the incident and the scatered wave from the particles through the fluid medium. The expression for this radiation force for a one-dimensional standing wave was described by Gorkov [1] as:

$$F_R = \frac{-\pi P_0^2 \cdot V_p \cdot \beta_l}{2\lambda} \cdot \varphi(\rho_p, \beta_p, \rho_l, \beta_l) \cdot \sin\left(\frac{4\pi x}{\lambda}\right) \tag{2}$$

$$\varphi(\rho_\mathrm{p}, \beta_\mathrm{p}, \rho_\mathrm{l}, \beta_\mathrm{l}) = \frac{5\rho_p - 2\rho_l}{2\rho_p + \rho_l} - \frac{\beta_p}{\beta_l} \tag{3}$$

where V_p the volume of the particles, φ, is the acoustic contrast factor with ρ_p, β_p and ρ_l, β_l being the density and adiabatic compressibility of the particles and the fluid, respectively. The distance of the particles from the pressure node is given by *'x'*. The acoustic contrast factor determines whether the movement of the particles occurs toward the pressure nodes ($\varphi > 0$) or toward the antinodes ($\varphi < 0$).

Acoustically rigid materials, such as glass or silicon, have proven to be efficient in particle collection [4, 5, 6, 7] and present stable frequency resonances. However, the still high cost of these devices makes the use of polymer devices an attractive alternative.

In polymer chips, the expression described in Eq. (2) is no longer valid because the field transmitted to the liquid from the chip structure is a fully three-dimensional field. This makes the expressions much

DOI 10.5162/Ultrasonic2025/A2-b4

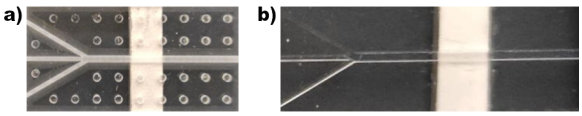

Fig. 1: Pictures of a) Glass Chip, b) PMMA Chip.

more complex, as has been described in recent literature [2]. Previous studies [3], have verified numerical and experimentally this complex behaviours of polymer chips. Results were obtained regarding particle collection along the longitudinal axis of the channel in polymeric-based chips.

However, another parameter is also involved in the particle collection: the flow rate generating drag viscous forces on the particles. The expression that defines these forces, exerted by the fluid on the particles along their trajectory toward the pressure nodes, is given by:

$$F_d = -6\pi\eta R_p(u - v) \tag{4}$$

where η is the dynamic fluid viscosity, R_p is the particle radius u is the particle velocity and v is the fluid velocity.

Laminar flow regime of microfluidics provides flow velocities with parabolic profiles, favouring particle entraintment toward the central axis. According to it, suitable combination of acousto-hydrodymic conditions have been found in this study for optimal particle collection [2, 8, 9, 10].

The objective and motivation of this study is to determine how two materials with very different acoustic impedances affect particle collection in chips and channels with identical cross-dimensions (Fig. 1) at the same frequency. An experimental comparison has been made to show the advantages and disadvantages of both materials.

Experimental setup

Two microfluidic chips were developed to perform the experiments of: i) Borosilicate Glass (Z≈13 MRayls) and ii) Polymethylmethacrylate (PMMA) (Z≈11,9 MRayls). They have the same width and thickness (15x1.5 mm) with identical channel cross-sections (800x500 μm). The channel is centered in both chips.

Piezoelectric PZ26 Ferroperm ceramics were used as ultrasonic actuator, attached underneath the chips, vibrating in Thickness mode at around 1 MHz. They were placed perpendicular to the channel and excited by an Agilent 33500B function generator connected to an E&I 240L amplifier; a continuous sinusoidal wave was used to excite the PZ26.

Polystyrene beads of 20 μm diameter (Dynoseeds TS 20, Microbeads) were used, diluted in deionized water filtered through 0.2 μm pore-size biological grade filters. For the injection of the particle suspension, a 2.5 ml syringe was employed, and the flow rate was regulated using a KDScientific KDS-260-CE syringe pump. Various flow rates were tested, ranging from 50 μl/min to 300 μm/min. Among them, Q = 80 μl/min was selected as the optimal flow rate to enhance particle collection efficiency.

The optical elements used in the laboratory are a ZEISS Axio Scope A1 microscope with a ZEISS EC EPIPLAN 5x/0.13 HD lens, and a Photron FASTCAM SA3 high-speed camera, configured with a frame rate of 2000 frames per second.

Results

The presence of cylindrical-shaped perforations within the glass chip structure, significantly disturbs the propagation of the incident wave from the vibrating surface of the piezoelectric ceramic. Due to the high rigidity of the glass material, wave propagation predominantly occurs along the direction of incidence. The perforations induce highly directed wave guidance toward the channel in the adjacent chip region. In the rest of the chip, these perforations induce acoustic short-circuiting, resulting in wave reflection and significant energy dissipation in areas farther from the channel. Regions in close proximity to the channel, experience more direct wave propagation, which would be equivalent to having a very narrow chip.

Several optimal collection frequencies were found for both chips in the range of 800 kHz to 1200 kHz, with 974 kHz chosen as representative. It is worth noting that, although the glass chip collects over a range that covers the studied interval, with small intervals in which collection is slightly impaired, this is not the case for the polymer chip, where these ranges are very intermittent and in some cases, nonexistent.

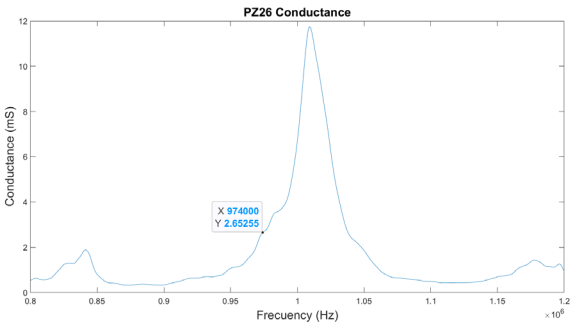

Fig. 2: Graph of the conductance of the PZ26 used in both the glass chip and the PMMA chip.

DOI 10.5162/Ultrasonic2025/A2-b4

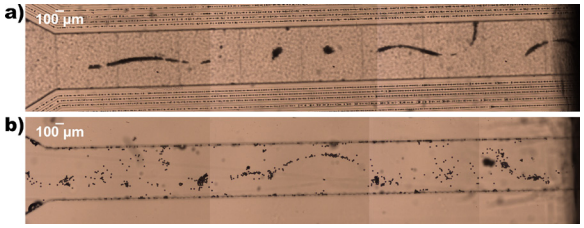

Fig. 3: Particle collection at 974 kHz obtained within the microchannel at stagnant conditions, drawing the pressure node pattern; a) In the glass chip, b) in the PMMA chip.

Under flow stangnant conditions, the acoustic pressure nodes draw a discontinuous line around the central axis of the channel. Instead, they form confined clusters of aggregates at different possitions of the channel width, including small areas beside the walls (Fig. 3). They appear more dispersed in the PMMA chip, showing more irregular and weaker pressure nodes spatially dispersed, due to the establishment of three-dimensional vibration modes within the solid structure of the chips, as described in the introduction.

However, under flow conditions, the parabolic flow velocity profile, with a maximum at the central axis and governed by viscous drag forces, favours circulation of particles along the central area once collected by the radiation force and by viscous drag forces in the same direction. It is, therefore, the acousto-hydrodynamic combination that enables both the collection and maintenance of the particles along the channel axis, even though the pressure nodes are not spatially regular along the channel. This phenomenon has been widely described in the litereature and repeatedly observed in video recordings obtained under flow conditions of our experiments, where circulating particles exhibit a well-defined alignment along this central axis or in its vicinity within small surrounding areas (Fig. 4).

Experiments were conducted with flow rates ranging from 50 to 300 μl/min. It was observed that, in polymer-based chips, flow rates exceeding 80 μl/min result in very poor particle collection, with significant dispersion of particles throughout the channel. On the contrary, particle collection in glass chips tolerate flow rates up to 100 μl/min, although this also leads to a slight reduction in collection efficiency. It is due to times unbalance, the time of circulation is shorter than that required to reach the central axis at these high flow rates, preventing particles circulating near the walls from reaching the center of the channel. Nevertheless, particle collection with efficiency degrees over 70% still occurs at this rate. A flow rate of 80 μl/min allows for particle collection in both types of chips and enables a comparison of their collection efficiency.

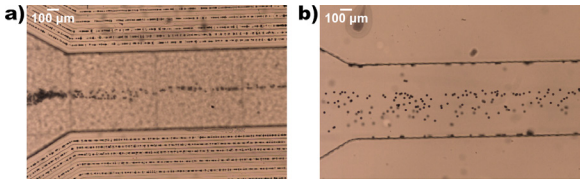

Fig. 4: Particle collection at 974 kHz obtained within the microchannel and a flow rate at the syringe pump of 80 μl/min; a) In the glass chip, b) in the PMMA chip.

Furthermore, particle trapping occurs more slowly in polymer chips, even in stangnant conditions. This suggests that, at a given frequency, the resulting acoustic radiation force is weaker in these materials, which can be explained by the high energy loss and establishment of three-dimensional complex vibrations in this acoustically soft structures described above. Lower flow rates are more favorable for effective collection in these polymer-based chips. In contrast, particle collection in glass chips is nearly instantaneous, both with and without flow.

However, the resulting temperature rise in the ceramic associated to higher voltages supplied, favours formation of bubbles within the channels and aggregation of particles, which adhere to the channel walls and bubble surfaces, thereby altering the acoustic conditions inside. These alterations lead to a significant decrease in collection efficiency.

In our experiments, a collection efficiency of 100% was achieved in the glass chip, whereas in the PMMA chip, the efficiency was approximately 70% although they collected in a wider central area.

Conclusions

In the polymer chip, the acoustophoretic process occurs with lower particle collection efficiency than in glass chips. The greater energy dissipation in acoustically soft materials like PMMA, and complex three-dimensional vibration modes established in this material, results in poorer particle collection in the polymer chips.

However, polymeric chips present the advantages of being lower in cost and are more versatile in establishing pressure nodes at different areas of the channel, they are also more versatile regarding the pressure nodes establishment. It does not occur in glass chips, which provide a wider frequency stability and a very high efficiency in collecting particles at fixed positions within the channels.

Acknowledgements

This work has been made within the framework of the eruopean project PM-HE-CL6-ONE-BLUE. Reference:101134929 – GAP (HORIZON): "Integrated approach to asses the levels and impact of contaminants of emerging concern on blue health and biodiversity modulated by climate change drivers", funded by the European Commission.

References

[1] L. Gor'kov. "On the forces acting on a small particle in an acoustic field in an ideal fluid". In: *Sov. Phys. Acoust.* 6 (1962), pp. 773–775.

[2] A. Vargas et al. "A 3D analysis of the acoustic radiation force in microfluidic channel with rectangular geometry". In: *Wave Motion* 101 (2021), p. 102701. DOI: 10.1016/j.wavemoti.2020.102701.

[3] E. de los Reyes et al. "Three-dimensional numerical analysis as a tool for optimization of acoustophoretic separation in polymeric chips". In: *The Journal of the Acoustical Society of America* 150 (2021), pp. 646–656. DOI: 10.1121/10.0005629.

[4] C. R. P. Courtney et al. "Manipulation of microparticles using phase-controllable ultrasonic standing waves". In: *The Journal of the Acoustical Society of America* 128 (2010), pp. 195–199. DOI: 10.1121/1.3479976.

[5] M. Evander et al. "Acoustophoresis in Wet-Etched Glass Chips". In: *Analytical Chemistry* 80 (2008), pp. 5178–5185. DOI: 10.1021/ac800572n.

[6] A. Haake and J. Dual. "Micro-manipulation of small particles by node position control of an ultrasonic standing wave". In: *Ultrasonics* 40 (2002), pp. 317–322. DOI: 10.1016/S0041-624X(02)00114-2.

[7] M. A. Şahin, B. Çetin, and M. B. Özer. "Investigation of effect of design and operating parameters on acoustophoretic particle separation via 3D device-level simulations". In: *Microfluidics and Nanofluidics* 24 (2020), 24:8. DOI: 10.1007/s10404-019-2311-1.

[8] Q. Wang, D. Yuan, and W. Li. "Analysis of Hydrodynamic Mechanism on Particles Focusing in Micro-Channel Flows". In: *Micromachines* 8 (2017), p. 197. DOI: 10.3390/mi8070197.

[9] I. González et al. "Influence of Hydrodynamics and Hematocrit on Ultrasound-Induced Blood Plasmapheresis". In: *Micromachines* 11 (2020), p. 751. DOI: 10.3390/mi11080751.

[10] Z. Liu et al. "Effects of fluid medium flow and spatial temperature variation on acoustophoretic motion of microparticles in microfluidic channels". In: *The Journal of the Acoustical Society of America* 139 (2016), pp. 332–349. DOI: 10.1121/1.4939737.

DOI 10.5162/Ultrasonic2025/A2-b5

Enhancing Air Purification: Ultrasound-Based Filtration of Ultrafine Aerosols and Gaseous Pollutants

Patrick Haas[1], *Sabrina Tietze*[1], *and Klaus Stefan Drese*[1]
[1]*Institute of Sensor and Actuator Technology (ISAT), University of Applied Sciences Coburg, Am Hofbräuhaus 1b, 96450 Coburg, Germany*
patrick.haas@hs-coburg.de

Abstract: Since COVID-19, clean indoor air has become more of a focus due to airborne viruses. Conventional filters often fail to capture ultrafine particles. This work investigates how standing ultrasonic fields manipulate aerosols for more efficient cleaning. Gor'kov theory and FEM simulations used to evaluate the acoustic forces on particles. Experiments by light refractive vibrometry and high-speed camera observations confirm the model quality.

Keywords: Acoustic manipulation, Gor'kov potential, FEM simulation, air purification, levitation

Introduction

Since the COVID-19 pandemic, the importance of clean indoor air has gained renewed attention due to airborne transmission of viruses and aerosols. Conventional air purifiers often struggle to effectively capture ultrafine particles and gaseous pollutants. In this work, we explore the use of ultrasound not merely for filtration enhancement, but specifically to manipulate aerosol particles within an airstream. By generating standing acoustic waves, particles can be influenced and concentrated at defined positions, enabling novel approaches to air purification. In the first step, the study investigates the behavior of particles in acoustic fields based on the analytical Gor'kov model and finite element simulations (FEM). Theoretical investigations are compared with experiments. Our aim is to demonstrate how acoustic forces can be used to actively control aerosol distribution in airflows and thus create the basis for advanced cleaning technologies.

Methods and Calucations

To set the parameters for the calculations in a first step, a wind tunnel including an acoustic resonator chamber was designed. The top of the wind tunnel of Fig. 1 consisted of an inlet (1), a flow straightener (2), the acoustic resonator chamber (4) with connecting pieces (3) and the fan (5), which drew in the air. With the wind tunnel, it was possible to generate disturbance velocities from 0 $\frac{\mathrm{m}}{\mathrm{s}}$ to 9 $\frac{\mathrm{m}}{\mathrm{s}}$.
The resonator chamber has been designed so that the interior of the resonator can be observed using a camera (VW 600C, Keyence Deutschland GmbH, Frankfurt am Main, Germany) and a vibrometer (PSV 400M, Polytec GmbH, Waldbronn, Germany).

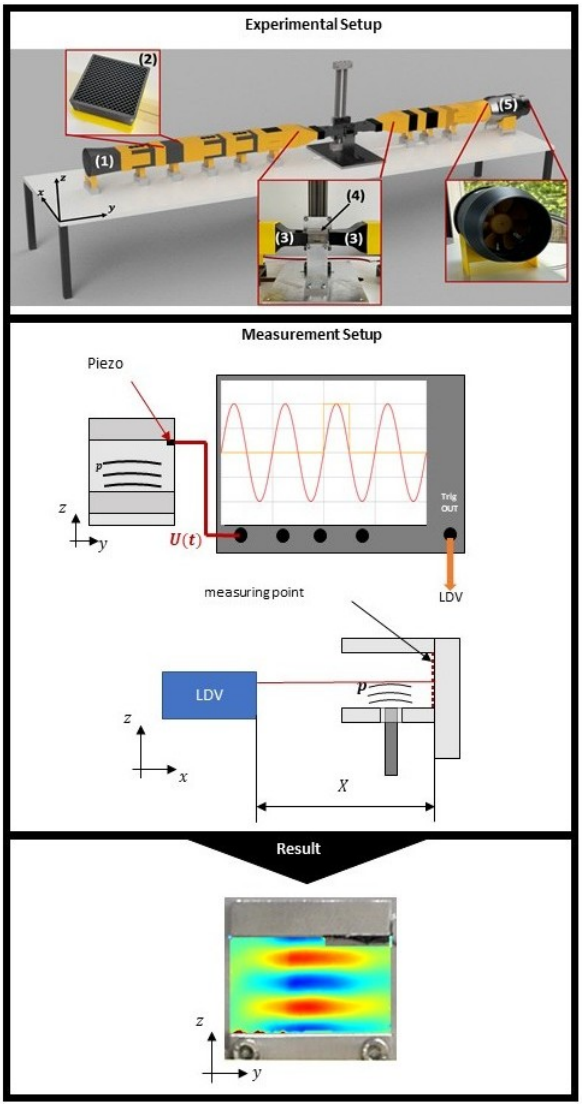

Fig. 1: Measurement setup for measuring the pressure fields in the resonator chamber with the Laser Doppler Vibrometer.

DOI 10.5162/Ultrasonic2025/A2-b5

In addition, there is an external recess in the base of the resonator chamber to accommodate the ultrasonic horn (UP200S, Hielscher Ultrasonics GmbH, Teltow, Germany). The ultrasonic horn in conjunction with a reflector of steel on the opposite side of the wind tunnel is used to generate the standing wave field. The following considerations were made to determine the optimum distance between the reflector and the ultrasonic horn.

For the theoretical predictions, the analytical model of Gor'kov [1] is compared with FEM done by COMSOL Multiphysics version 6.1. For resonance to occur, the distance between the ultrasonic horn and the reflector l_z must be an integer multiple of half the wavelength of the acoustic wave λ. The wave number k for the direction are defined as [1]–[3]:

$$k = \frac{n\pi}{l_z}, n \in \mathbb{N} \tag{1}$$

The sound potential U, from which the acoustic pressure and velocity can be derived, is defined in the three spatial directions x, y, z as:

$$U(x,y,z,t) = \frac{\hat{\xi}\omega}{|\vec{k}|}\cos\left(\frac{n_x\pi}{l_x}x\right)\cos\left(\frac{n_y\pi}{l_y}y\right)\cos\left(\frac{2\pi}{\lambda}z\right)\sin(\omega t) \tag{2}$$

Whereas ω is the angular frequency. The acoustic velocity and pressure are then obtained by:

$$\vec{v} = \nabla U, \quad p = -\rho\frac{\partial U}{\partial t} \tag{3}$$

For small spherical particles $R \ll \lambda$, the time-averaged acoustic radiation force can be derived from the Gor'kov potential U_{rad}, given by [1], [4], [5]:

$$U_{rad} = \frac{4\pi}{3}R^3\left[\frac{f_1}{2\kappa_{\text{air}}}\langle p^2\rangle - \frac{3f_2}{4\rho_{\text{air}}}\langle v^2\rangle\right] \tag{4}$$

The contrast factors f_1 and f_2 depend on the material properties of the particle and the surrounding medium:

$$f_1 = 1 - \frac{\kappa_{\text{p}}}{\kappa_{\text{air}}}, \quad f_2 = \frac{2\left(\rho_{\text{p}/\rho_{\text{air}}}-1\right)}{2\rho_{\text{p}/\rho_{\text{air}}}+1} \tag{5}$$

Here R is the radius of the particle and the coefficients f_1 and f_2 are dimensionless coefficients that take into account the properties of the material (density ρ and compression modulus κ) of the particle (index *p*) and the surrounding medium (index *air*). The brackets $\langle\cdot\rangle$ in Eq. (4) indicate time averages. The first term in Eq. (4) $f_1/2 \cdot \kappa_{\text{air}}\langle p^2\rangle$ describes the effect of the pressure field on the drop, while the second term $3f_2/4\rho_{\text{air}}\langle v^2\rangle$ describes the dynamic effects due to the movement of the medium. The acoustic radiation force is then given by the gradient of the Gor'kov potential:

$$\vec{F}_{rad} = -\nabla U_{rad} \tag{6}$$

For larger particles, the acoustic force can be calculated as [6], [7]:

$$\vec{F}_{rad} = -\oint_{\partial\Omega_0}\left[\left(\frac{\rho\langle v^2\rangle}{2} - \frac{\langle p^2\rangle}{2\rho c^2}\right)\vec{n} - \rho\langle(\vec{n}\cdot\vec{v})\vec{v}\rangle\right]dA. \tag{7}$$

For the force in the z-direction, the force contribution F_z is considered in more detail. Furthermore, the spatial coordinates in the x- and y-directions are set to zero $F_z^{\text{rad}}(0,0,z) = F_z$. This writes the force in the z-direction [8]:

$$F_z = \underbrace{-\pi R^3\left(-\frac{1}{3}f_1\kappa_{\text{air}}p_{\text{max}}^2 - \frac{1}{2}f_2 v_{\text{max}}^2\rho_{\text{air}}\frac{k_z^3}{k^2}\right)}_{F_{\text{z, max}}=\text{const.}}\cdot\sin(2k_z z) \tag{8}$$

If one investigates Eq. (8), one can see that the force field in the z-direction has twice the frequency of the original pressure field [9]. Another statement can be derived from Eq. (8). The force curve shows that the acoustic force direction changes every $\lambda/4$. As a result, the acoustic force points sometimes in and sometimes against the weight force, which means that particles cannot form and accumulate in every area of the pressure field. Particles can only accumulate where the weight force is balanced by the acoustic force.

To verify theoretical predictions without air flow, standing wave fields are visualized using the refractive vibrometry method [10] and nodes are visualized using levitated droplets and a camera.

Results

To validate the FEM, the pressure field between the ultrasonic horn and the resonator plate is first simulated at various distances, including distances outside the resonance condition. In addition, the pressure field is determined experimentally using the light refractive vibrometry method. The results can be found in Fig. 2. As this is a qualitative comparison of the pressure fields, no colour bar has been used. The pressure free areas are shown in green. As can be seen, a standing wave field is formed for the distances $l_z = \lambda$ and $l_z = 2\lambda$ (Fig. 2 third and fourth lines), because of the pressure bulges or pressure troughs. At a distance of $l_z = 8$ mm (Fig. 2 first line) an asymmetric spatial mode seems to form. At a distance of $l_z = 12$ mm (Fig. 2 second line) a weak pressure bulge appears in the center. However, due to the distance $l_z = N \times \frac{\lambda}{2}$, the condition of a standing wave is not yet fulfilled, i.e. the pressure field has no pressure bulges or pressure troughs and nodes. The pressure fields of the experiments are in good agreement with the predicted pressure fields by FEM.

DOI 10.5162/Ultrasonic2025/A2-b5

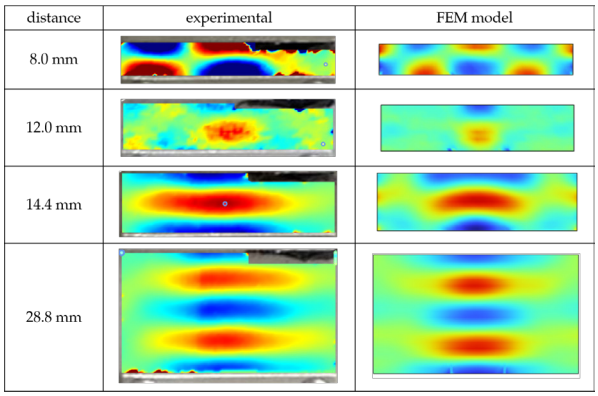

Fig. 2: Qualitative representation of the pressure fields at different distances left from the experiment, right from FEM model at various distances of the resonator plates. The missing measurement window in the right-hand corner of each experimental measurement was removed from the measurement because the trigger piezo was attached at this point and therefore no measurement was possible at these points.

A closer look at the pressure fields predicted by the analytical model and the FEM reveals a high degree of similarity when compared with the experiments for a resonator length of $l_z = \lambda$ or $l_z = 2\,\lambda$. Similar values were found for the z-coordinates of the pressure bellies and nodal points of the standing compression spring. The compared values can be seen in Tab. 1.
Last particles in the form of water droplets are introduced into the resonator. The arrangement of the water droplets in the resonator can be seen at the level of the nodal points if the FEM data is placed next to them, see Fig. 3.

Tab. 1: Calculated node and extrema positions (in λ) for different models and resonator lengths l_z.

Model	**z positions (in λ)**
FEM $l_z{=}\lambda$	**Nodes:** 0.232, 0.751
	Extrema: 0.492
Analytical $l_z{=}\lambda$	**Nodes:** 0.25, 0.75
	Extrema: 0.5
LDV $l_z{=}\lambda$	**Nodes:** 0.24, 0.79
	Extrema: 0.52
FEM $l_z{=}2\lambda$	**Nodes:** 0.254, 0.737, 1.24, 1.76
	Extrema: 0.496, 0.987, 1.50
Analytical $l_z{=}2\lambda$	**Nodes:** 0.25, 0.75, 1.25, 1.75
	Extrema: 0.5, 1.0, 1.5
LDV $l_z{=}2\lambda$	**Nodes:** 0.25, 0.75, 1.25, 1.76
	Extrema: 0.5, 1.0, 1.51

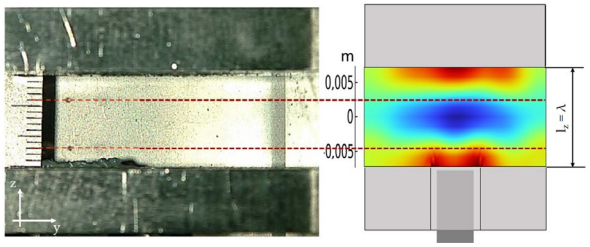

Fig. 3: Levitated droplets in their stability points (left) compared with the FEM pressure field $l_z = \lambda$ (right).

Discussion

When analyzing the two-dimensional pressure fields in Fig. 2 and comparing the LDV measurements with the FEM, a good qualitative agreement between the LDV measurements and the FEM simulation can be observed. For the distance of 8 mm in Fig. 2, there is a slight deviation between the FEM and the LDV measurement. This deviation is due to the limitation of the calculation space in the FEM model, which does not prevail in the measurement.
The deviations in the position of the zero points (nodes) and the extreme values (bellies) between the theoretical pressure fields and the simulations listed in Tab. 1 occur at all distances considered ($l_z = \lambda$ and $l_z = 2\lambda$). The pressure field from the analytical model assumes that the propagating waves are excited by the entire width of the lower resonator plate and thus have flat wave fronts over the entire width and interfere from a standing wave in the resonator.

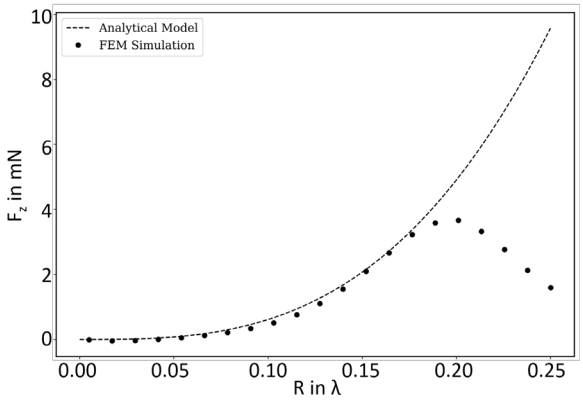

Fig. 4: The force curves as a function of the radius of the droplet are shown for each of the models. The force resulting from the Gor'kov potential is shown as a dashed line, with the dots representing the forces resulting from the FEM model. Both forces curves were evaluated at the point ($x = 0\,m$, $y = 0\,m$, $z = \frac{5\lambda}{8}$).

In the pressure fields from the FEM and the pressure fields from the LDV measurement, the pressure field is excited by the tip of the ultrasonic horn with a limited diameter of 14 mm, which causes waves with curved wave fronts to propagate and thus waves with curved wave fronts to intefere into a standing wave field. This can be a cause that leads to the differences in the model. Fig. 3 shows that the droplets accumulate in the nodal points. However, a further estimation between the Gor'kov model and the FEM (Fig. 4) shows that with increasing particle size, an estimation using Gor'kov is no longer possible to determine the force influence on the droplets.

Conclusion

The aim of this work was to achieve acoustic air purification. For this purpose, a test rig was constructed, the dimensions of which were then used to set up analytical models, FEM and experiments to verify the theoretical models. It was shown that the theoretical pressure field can also be verified using light refractive methods, which confirms the theory. It was also possible to observe the influence of droplets using a camera. Furthermore, it was shown that Gorkov's model can be used for the design of small particles or droplets, while FEM must be used for larger particles. The next step will be to set up several or longer resonators based on these results and generate an air flow charged with water dropletes in the test set-up.

Acknowledgement

The authors would like to thank the team of the Institute of Sensor and Actuator Technology especially Siegfried Vorister for his expertise in constructing the resonator and for his technical guidance throughout the design of the test rig. The support of this research by 'Technologieallianz Oberfranken (TAO)' is gratefully acknowledged. The work was financial supported by the Alfred Kärcher Foundation.

References

[1] L. Gor'Kov, 'On the forces acting on a small particle in an acoustical field in an ideal fluid,' *Soviet Physics Doklady*, vol. 6, pp. 773–775, 1962.

[2] S. Weinzierl, *Handbuch der Audiotechnik*. Berlin, Germany: Springer Science & Business Media, 2008.

[3] M. Dewar, 'Einführung in die moderne chemie: Lehrbuch für naturwissenschaftler und mediziner in den anfangssemestern,' in *Einführung in die moderne Chemie*, Berlin, Germany: Springer Berlin Heidelberg, 1970, pp. 57–70.

[4] L. Worstmann, 'Stability of a particle levitated in an acoustic field,' *Acoustic Levitation*, vol. 5, 2016.

[5] G. Simon, M. Andrade, M. Desmulliez, M. Riehle and A. Bernassau, 'Numerical determination of the secondary acoustic radiation force on a small sphere in a plane standing wave field,' *Micromachines*, vol. 10, p. 431, 2019, 10.3390/mi10070431.

[6] M. Barmatz and P. Collas, 'Acoustic radiation potential on a sphere in plane, cylindrical, and spherical standing wave fields,' *Journal of the Acoustical Society of America*, vol. 77, pp. 928–945, 1985, 10.1121/1.392061.

[7] H. Bruus, 'Acoustofluidics 7: The acoustic radiation force on small particles,' *Lab on a Chip*, vol. 12, pp. 1014–1021, 2012, 10.1039/C2LC21068A.

[8] C. Devendran, D. R. Billson, D. A. Hutchins and A. Neild, 'Optimisation of an acoustic resonator for paricles manipulation in air,' *Sensors and Actuators B: Chemical*, vol. 224, pp. 529–538, 2016, 10.1016/j.snb.2015.10.068.

[9] L. V. King, 'On the acoustic radiation pressure on spheres,' *Proc. R. Soc. Lond. A*, vol. 147 (861), pp. 212–240, 1934, 10.1098/rspa.1934.0215.

[10] S. Tietze and G. Lindner, 'Visualization of the interaction of guided acoustic waves with water by light refractive vibrometry,' *Ultrasonics*, vol. 99, p. 105 995, 2019, 10.1016/j.ultras.2019.105955.

DOI 10.5162/Ultrasonic2025/A4-a1

Influence of Changes in Static Pressure on Sonoluminescence

Shuta Nakamura[1] and Ken Yamamoto[1]
[1]Department of Pure and Applied Physics, Kansai University Graduate School of Science and Engineering, 3-3-35 Yamate-cho, Suita-shi, Osaka, 564-8680, Japan
k610651@kansai-u.ac.jp

Abstract: Experimental observations and theoretical numerical calculations on the primary Bjerknes force were performed to determine the effect of static pressure changes on sonoluminescence (SL). The intensity of SL increased with increasing static pressure. The numerical calculations showed that under high static pressure, bubbles in standing waves are trapped at higher sound pressures. Bubbles trapped under higher sound pressure collapse more violently and the temperature inside the bubble increases.

Keywords: acoustic cavitation, sonoluminescence, static pressure, standing wave, primary Bjerknes force

1. Introduction

Ultrasonic cavitation is a phenomenon in which microscopic bubbles are generated by irradiation of ultrasonic waves into a liquid. Sonoluminescence (SL)[1] is known to depend on several parameters, including frequency, acoustic power, type of solute, type of dissolved gas, and liquid temperature. In this study, we focused on the parameter static pressure. Various experimental and theoretical studies have examined the effects of large static pressure changes (several MPa) on SL [2], but there are few studies on small changes in static pressure (several tens of kPa). Therefore, the purpose of this study was to clarify the effect of minute static pressure changes on SL and its associated factors.

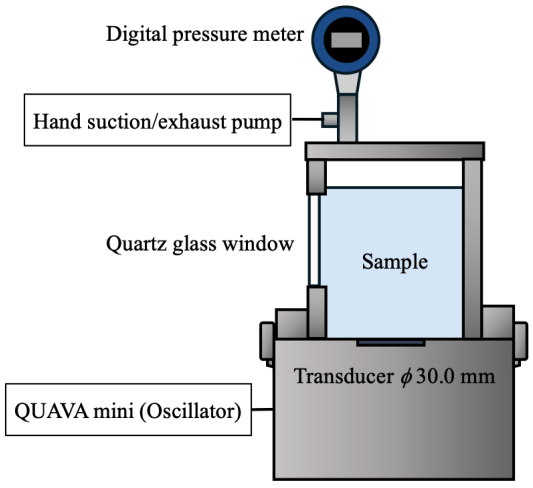

Fig. 1: Schematic diagram of the experimental system.

2. Materials and Methods

2.1. Experiment

Fig.1 shows a schematic diagram of the experimental system. A rectangular stainless steel sample chamber $(60 \times 60 \times 100\ mm)$ is attached to an ultrasonic generator (QUAVA mini, KAIJO Co., Ltd.) with a frequency of 430 kHz. A quartz glass window is installed in the side to allow measurement of SL. A digital pressure gauge (KDM30-α, Krone Corporation) and a hand suction exhaust pump are attached to the lid of the sample chamber to control the internal static pressure. Purified water was used as the test liquid, which was degassed by stirring under reduced pressure of 0.1 MPa for 1 h and then was stirred under an Ar atmosphere at ambient pressure for 1 h. The temperature of the samples was maintained at 13 ± 1°C by circulating cooling water outside the sample bath. Acoustic power was kept constant at 10 ± 1 W using the calorimetry method. SL spectra were measured with a spectrometer (SP2300i, Princeton Instruments) and CCD detector (Pixis100, Princeton Instruments). SL photographs were taken using a digital SLR camera (α7S, Sony Corporation) with an exposure time of 2 min.

2.2. Numerical calculation

Numerical calculations were performed for the vibration of a single bubble, neglecting interactions between bubbles. The bubble is assumed to always be spherical and its center is not displaced during one cycle. The bubble oscillations are described by the Keller-Miksis equation[3]:

DOI 10.5162/Ultrasonic2025/A4-a1

$$\left(1-\frac{\dot{R}}{c}\right)R\ddot{R}+\frac{3}{2}\dot{R}^2\left(1-\frac{1}{3}\frac{\dot{R}}{c}\right) = \left[1+\frac{\dot{R}}{c}+\frac{R}{c}\frac{d}{dt}\right]\frac{P_B}{\rho} \quad (1)$$

Here, R is the instantaneous bubble radius, t is time, an overdot denotes the time derivative, ρ is the density of the liquid, and c is the speed of sound in the liquid. The nonlinear term P_B can be expressed as

$$P_B=\left(P_0+\frac{2\sigma}{R_0}\right)\left(\frac{R_0}{R}\right)^{3\gamma}-\frac{2\sigma}{R}-\frac{4\mu}{R}\dot{R}-P_0+P_\infty \quad (2)$$

where R_0 is the initial radius of the bubble; σ and μ are the surface tension and viscosity in the liquid, respectively; P_0 is the static pressure; P_∞ is the external sound pressure; f is the ultrasonic frequency; and γ is the specific heat ratio of the gas in the bubble. The external sound pressure P_∞ assumes a standing wave and is represented by

$$P_\infty=-P_S\cos(kz)\sin(2\pi ft) \quad (3)$$

Here, k is the wavenumber, z is the position in the height direction, and $z=0$ is the position of the belly of the standing wave. The acoustic amplitude P_S was estimated from the acoustic power. Using the bubble radius R calculated by the Keller-Miksis equation, the primary Bjerknes force was calculated as follows[4]:

$$\vec{F_B}=-\langle\vec{F_p}\rangle=-\langle V\nabla p\rangle \quad (4)$$

Here, $\vec{F_p}$ is the instantaneous radiant force acting on the bubble and $\langle\ \rangle$ indicates the time average. The force $\vec{F_p}$ is given by

$$\vec{F_p}=\left(-\frac{4\pi}{3}\right)R^3kA\sin(kz)\sin(\omega t)\vec{e_z} \quad (5)$$

The change in bubble diameter was treated as an adiabatic process, and the maximum temperature inside the bubble was calculated using the following equation:

$$T_{max}=T_0\left(\frac{R_0}{R_{min}}\right)^{3(\gamma-1)} \quad (6)$$

here T_0 is the initial temperature inside the bubble The above equations were solved using MATLAB's ODE45s solver, with absolute and relative tolerances of 1×10^{-9}. The gas inside the bubble was assumed to be Ar. The initial conditions were as follows: $R(0)=R_0$, $\dot{R}(0)=0$, $T_0=286.15$ K, $f=430$ kHz, $\rho=1000\ \mathrm{kg/m^3}$, c=1482 m/s , σ=72.75×10^{-3} N/m, μ=1.002×10^{-3} Pa·s, γ=1.67,and P_w=10 W.

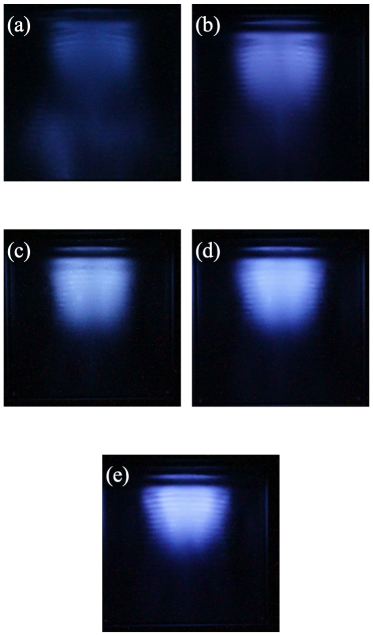

Fig. 2: Photographs of SL taken under different static pressures. All photographs were taken with an exposure time of 2 min.

3. Results and Discussion

3.1. SL Observations

Changes in SL intensity and emission distribution in response to variations in static pressure were observed. Fig. 2 show photographs of SL observed under different static pressures. As the static pressure was increased, stronger light emission was observed near the liquid surface. Conversely, as the static pressure was decreased, the emission distribution extended further toward the bottom of the sample chamber. Previous studies have also reported that light emission is concentrated near the liquid surface, which can be explained by the ratio of standing wave and traveling wave components [5]. A standing wave arises from the interference between a traveling wave and its reflected wave. In regions farther from the liquid surface, attenuation of the sound wave causes the reflected wave to become weaker than the traveling wave, hindering formation of a standing wave. As a result, the traveling wave component becomes dominant. In areas where the traveling wave component is strong, bubbles experience radiation force from the traveling wave and move toward the liquid surface. In such regions, bubble collapse events capable of generating SL are less likely to occur. On the other hand, near

DOI 10.5162/Ultrasonic2025/A4-a1

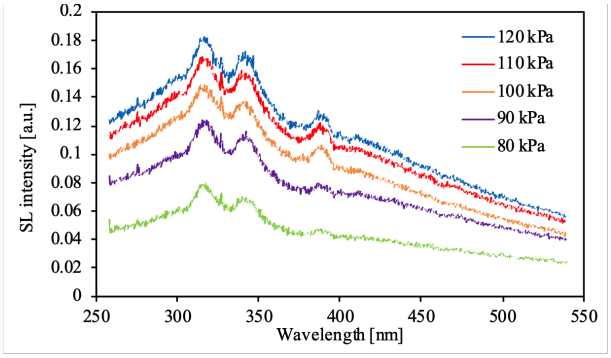

Fig. 3: SL spectra in Ar saturated water at different static pressures.

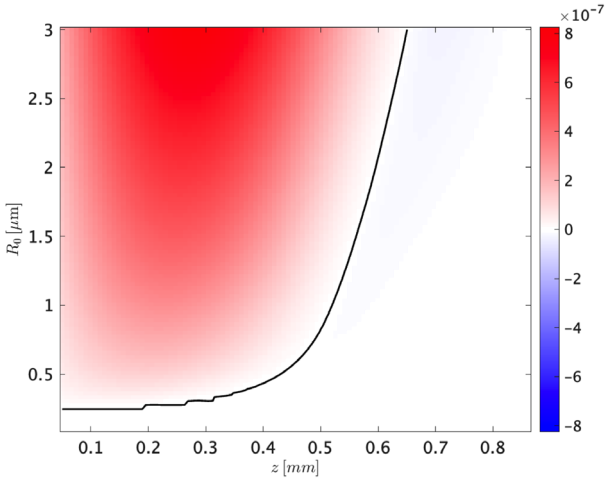

Fig. 4: Heat map showing the magnitude of the primary Bjerknes force for at position z and for initial bubble radius R_0. Static pressure is 100 kPa. The line indicates the point where $\vec{F}_B$=0.

the liquid surface, the attenuation of the traveling and reflected waves is roughly the same, leading to a stronger standing wave component. In regions with a strong standing wave component, bubbles are trapped within the standing wave due to the primary Bjerknes force [4] and oscillate in stable positions. As a result, SL is concentrated in these regions. Fig. 3 shows the measurement results of SL intensity. Based on the SL spectrum, the intensities of both the broadband component and the OH radical peak were calculated. As the static pressure was increased, the intensities of both the broadband emission and the OH radical peak increased accordingly.

3.2. Numerical Calculation of the Primary Bjerknes force

To examine the equilibrium positions of bubbles within a standing wave, a numerical calculation of the primary Bjerknes force was conducted. The time average over one acoustic cycle was taken, where a force pushing the bubble away from (resp. toward) the pressure antinode was taken as positive (resp. negative). Fig.4 shows a heat map representing the magnitude of the primary Bjerknes force as a function of position z and initial bubble radius R_0 under a static pressure of 100 kPa. When a bubble is located far from the pressure antinode, it experiences a negative radiation force pulling it toward the antinode. However, as it approaches the antinode, it eventually experiences a positive radiation force, pushing it away. As this occurs, the bubble continues to expand even into the second half of the acoustic cycle, making the contribution of the latter half dominant. As a result, the bubble becomes trapped at the position where the Bjerknes force is zero $\left(\vec{F}_B = 0\right)$. The trapping position depends on the initial bubble radius R_0, with smaller bubbles tending to be trapped closer to the pressure antinode.

Fig. 5 shows the dependence of the bubble trapping position on static pressure. Numerical calculations revealed that, for all initial bubble radii, the bubbles become trapped closer to the pressure antinode with increasing static pressure. This indicates that the bubbles are trapped in regions with higher acoustic pressure. The bubbles move closer to the antinode because the time required for the bubbles to collapse becomes shorter with increasing static pressure. As a result, the contribution from the latter half of the acoustic cycle becomes smaller, leading to trapping positions closer to the antinode.

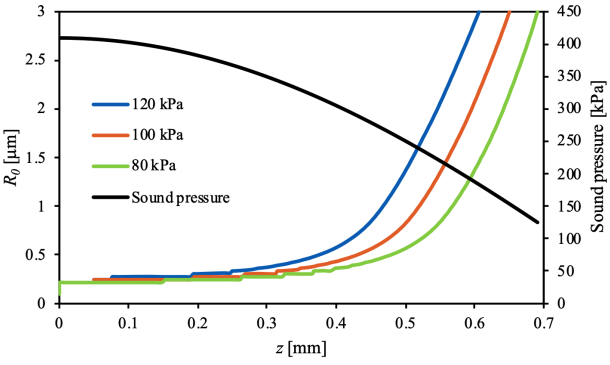

Fig. 5: Size of bubbles trapped at position z under different static pressures. The second vertical axis shows the sound pressure that the bubble at position z receives from the standing wave.

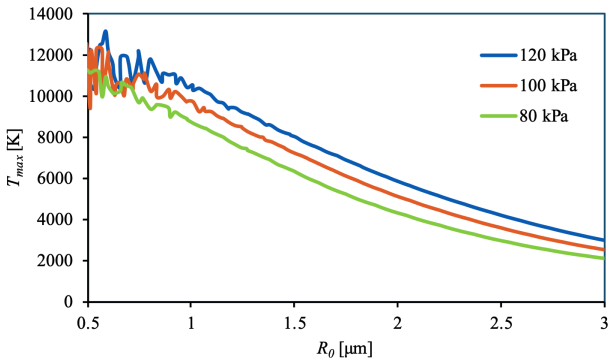

Fig. 6: Maximum temperature inside the bubble at the bubble trap position. z corresponding to R_0 was determined from Fig. 5.

Fig. 6 shows the maximum temperature inside the bubble at the trapping position. Based on the results from Fig. 5, the acoustic pressure corresponding to each initial bubble radius R_0 and static pressure P_0 was determined. The maximum temperature increased with rising static pressure. The reason for this was that the change in bubble position due to the increase in static pressure caused the bubble to experience higher acoustic pressure, resulting in more violent collapse. The internal bubble temperature is a crucial parameter in determining SL intensity, and its dependence on static pressure shows a trend similar to that observed in Fig.3. These results suggest that the equilibrium position of the bubble in the standing wave may be one of the key factors influencing SL intensity.

4. Conclusion

An increase in SL intensity and a change in the emission distribution were observed with increasing static pressure. Numerical calculations revealed that, with increasingstatic pressure increases, bubbles become trapped closer to the pressure antinode of the standing wave. Bubbles subjected to stronger acoustic pressure undergo more violent collapse and reach higher maximum temperatures. This study enhances our understanding of static pressure as a key parameter in ultrasonic cavitation and contributes to the determination of efficient operating conditions for industrial applications such as ultrasonic cleaning and sterilization.

References

[1] P.-K. Choi and *et al.* "Na emission and bubble instability in single-bubble sonoluminescence". In: *Ultrasonics Sonochemistry* 38 (2017), pp. 154–160. DOI: 10.1016/j.ultsonch.2017.03.015.

[2] S. Merouani and *et al.* "Review on the impacts of external pressure on sonochemistry". In: *Ultrasonics Sonochemistry* 106 (2024), p. 106893. DOI: 10.1016/j.ultsonch.2024.106893.

[3] J. B. Keller and *et al.* "Bubble oscillations of large amplitude". In: *Journal of the Acoustical Society of America* 68 (1980), pp. 628–633. DOI: 10.1121/1.384720.

[4] T. J. Matula and *et al.* "Bjerknes force and bubble levitation under single-bubble sonoluminescence conditions". In: *Journal of the Acoustical Society of America* 102 (1997), pp. 1522–1527. DOI: 10.1121/1.420065.

[5] J. Lee and *et al.* "Spatial Distribution Enhancement of Sonoluminescence Activity by Altering Sonication and Solution Conditions". In: *Journal of Physical Chemistry B* 112 (2008), pp. 15333–15341. DOI: 10.1021/jp8060224.

DOI 10.5162/Ultrasonic2025/A4-a2

Ultrasonic Guided Waves for Gas Bubble Removal on Optical Sensor Surfaces

Oliver Blaschke[1], Dennis Bernhardt-Famulla[2], Stephanie Holz[2], and Klaus Stefan Drese[1]
[1]Coburg University of Applied Sciences and Arts, Institute for Sensor and Actuator Technology, Coburg, Germany
[2]Dr. Küke GmbH, Wedemark, Germany
oliver.blaschke@hs-coburg.de

Abstract: This study demonstrates a method for gas bubble removal from glass surfaces using acoustic standing wave fields. Piezoelectric transducers generate targeted frequencies, creating radiation forces that move bubbles toward antinodes. By incorporating bubble resonance frequencies, detachment efficiency is enhanced. Simulations and experiments confirmed effective wave formation and bubble migration. A burst-mode excitation minimized thermal load, providing a non-invasive solution for maintaining optical sensor performance in liquid environments.

Keywords: bubbles, ultrasonic bubble manipulation, ultrasonic transducers, acoustics, standing waves

Introduction

The presence of gas bubbles adhering to glass surfaces in water poses a critical issue for optical sensors utilized in the context of water quality measurements. These bubbles induce distortions in light paths through the process of refraction, thereby leading to inaccuracies in parameter estimation. The presence of even small bubbles has the capacity to significantly alter sensor readings by introducing optical artifacts that interfere with the transmission and detection of light. Therefore, the objective of this study is to explore the use of ultrasonic guided acoustic waves as a means to effectively remove bubbles from glass surfaces. This technique utilizes the interaction of ultrasonic acoustic waves with the water-glass interface, forming standing wave fields, thereby inducing radiation forces that influence bubble motion. A further point of this study is whether the excitation of the bubbles at their resonance frequency at the same time can improve the manipulation of the bubbles due to reduced bonding to the adhering surface.

Method

Acoustic waves that propagate along the solid-water interface at specific frequencies and wavelengths generate an acoustic standing wave field in the adjacent fluid. Fluctuations in pressure within the acoustic field create stationary nodes and fluctuating antinodes. The wavelength necessary for a standing wave field to form depends on the width of the system. This results in a set of wavelengths that are integer divisors of twice the width of the system:

$$\lambda = \frac{2L}{n};\ n = 1, 2, 3, ... \tag{1}$$

The acoustic radiation force in the standing wave field causes the gas bubbles to move toward the antinode positions within the fluid region. This leads to increased movement and eventually causes the bubbles to move away from the glass surface [1].

The radiation force is defined with the time-averaged first-order pressure $\langle p \rangle$ and velocity $\langle v \rangle$ as [2], [3]:

$$F_{rad} = \int_{\partial\Omega} \left\{ \left[\frac{1}{2}\kappa_0 \langle p^2 \rangle - \frac{1}{2}\rho_0 \langle v^2 \rangle \right] n + \rho_0 \langle (n \cdot v) v \rangle \right\} \tag{2}$$

With κ_0 as the compressibility of the bulk fluid as $\kappa_0 = 1/(\rho_0 c_0^2)$ where ρ_0 and c_0 are the density and velocity of sound of the fluid, respectively.

While the acoustic field is active, the bubbles are trapped within the antinodes. When the field is shut off, buoyancy effects transport the bubbles away. To increase the effect, the resonance characteristic of the gas bubbles themselves was used. Depending on their size, bubbles have resonance frequencies at which they oscillate. This oscillating movement reduces the bubbles' adherence to the glass surface, allowing them to be more efficiently removed by the acoustic radiation force of the standing wave field. For constrained gas bubbles, for which the influence of surface tension is not negligible, the resonance frequency can be derived from the Rayleigh-Plesset equation, as described in [4]:

DOI 10.5162/Ultrasonic2025/A4-a2

$$R\ddot{R} + \frac{3\dot{R}^2}{2} = \frac{1}{\rho}\left\{\left(p_0 + \frac{2\sigma}{R_0} - p_v\right)\left(\frac{R_0}{R}\right)^{3\gamma} + p_v - \frac{2\sigma}{R} - \frac{4\eta\dot{R}}{R} - p_0 - P(t)\right\} \tag{3}$$

Here, the oscillating bubble radius R in an acoustic field depends on its first- and second-order time derivatives $\dot{R}$ and $\ddot{R}$ as well as the surface tension acting on the bubble σ, the fluid density ρ_0 and the viscosity η, as well as the hydrostatic pressure p_0 and the vapor pressure inside the bubble p_v and the initial bubble radius R_0. $P(t)$ is the time-dependent pressure variation from the acoustic field and γ is the polytropic index.

For the assumption of small amplitude variations in bubble radius, the resonance frequency ω_0 can be calculated with [4]:

$$\omega_0 = \frac{1}{R_0\sqrt{\rho}} \sqrt{\left\{3\gamma\left(p_0 + \frac{2\sigma}{R_0} - p_v\right) - \frac{2\sigma}{R_0} + p_v - \frac{4\eta^2}{\rho R_0^2}\right\}} \tag{4}$$

The material properties as can be seen in table 1. According to Figure 1 the resonance frequency for bubbles of the size in the range between 100 µm and 2 mm ranges from 0.5 kHz to 13 kHz.

Tab. 1: Material properties of gas bubbles and water at 20°C.

$\rho/\frac{\mathrm{kg}}{\mathrm{m}^3}$	998
$\sigma/\frac{\mathrm{N}}{\mathrm{m}}$	0.0728
$\eta/\mathrm{Pa}\cdot\mathrm{s}$	1.001×10^{-3}
p_0/Pa	101 325
p_v/Pa	2340
γ	1.4

For the experimental setup, a measurement chamber with dummy sensors as optical sensors was constructed in order to serve as a basis for gas bubble removal. The housing is depicted in Figure 2. For the generation of ultrasonic frequencies, piezoelectric transducers were considered because they can act on a wide range of frequencies and can be driven at high voltages for large deflections. Since the space for attaching the transducers was limited, they were placed directly on the top side of the quartz glass

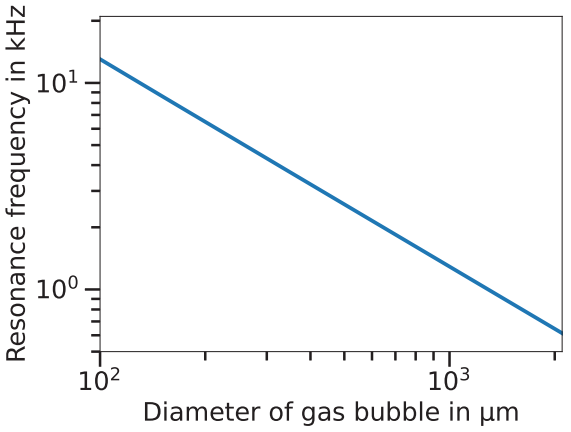

Fig. 1: Resonance frequency of gas bubbles in water for different bubble diameters.

surface, next to the optical sensor dummy. Lead zirconate titanate (PZT) transducers (PIC 255 material, PI Ceramic GmbH, Lederhose, Germany), measuring 25 mm $\times$ 2 mm $\times$ 1 mm were used. Two transducers were placed in a row on both sides of the dummy to span its entire length, reaching a total length of 50 mm. The goal was to remove any gas bubbles from the glass surface under the dummy elements. The same procedure was carried out on the back of the housing because there is another dummy element there. The prepared measurement chamber is depicted in Figure 2.

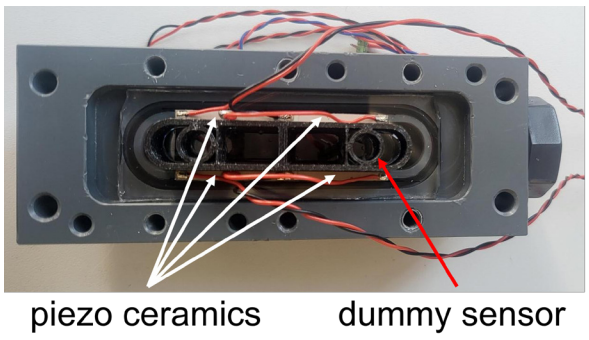

Fig. 2: Measurement chamber with dummy sensor and prepared glass surface with piezo transducers.

The necessary wavelengths for the standing wave fields were found using equation (1) where the system's width, L, was 12 mm. This resulted in a set of wavelengths and with the speed of sound in water being 1480 m/s, distinct frequencies were determined. FEM simulations were conducted in COMSOL Multiphysics software to prove the excitation concept on

DOI 10.5162/Ultrasonic2025/A4-a2

the geometry of the measurement chamber in beforehand. The three-dimensional simulations included the chamber's fluid volume as well as the 3 mm thick quartz glass plates. The excitation of the standing wave fields with the related driving frequencies was modeled on top of the glass plates to emulate the actuation with the piezo ceramics in the experimental stage. To demonstrate standing wave excitation in a fluid volume, a special measurement chamber was constructed. The side walls were cut out and replaced with glass plates, one of which was coated with a primer. The experimental setup involved continuously exciting the standing wave field at a frequency of 370 kHz and measuring the pressure field inside the fluid with a laser Doppler vibrometer (PSV-400M, Polytec GmbH, Waldbronn, Germany). The results were then compared with those of the associated finite element method (FEM) simulation. Figure 3 compares the standing wave fields from the experiment and the simulation, showing that the results agree qualitatively. This indicates that the generation of the standing wave field and the corresponding radiation force, which moves the gas bubbles toward the fluid volume and away from the glass surface, operated as intended. The final step was to optimize the actuation to remove the bubbles faster and more efficiently.

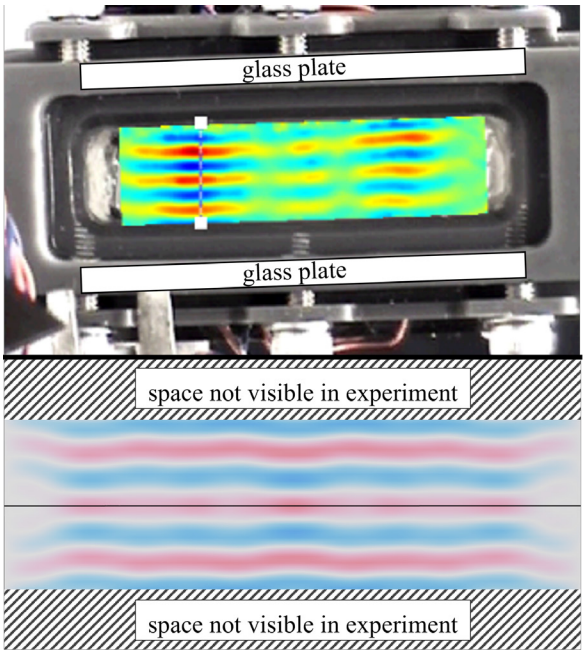

Fig. 3: Laser Doppler vibrometer measurement of pressure field inside measurement chamber (top). FEM simulation of same excitation at 370 kHz (bottom).

The final driving signal for the transducers was designed to fulfill two tasks. First, a standing wave field had to be generated. Second, the resonance frequency of the different bubble sizes had to be met. To this end, a chirp signal was designed to encompass the frequency range between 0.5 kHz and 7 kHz, striking a balance between the findings of Figure 1 and the overall signal length and, consequently, the thermal load on the piezo ceramics. The chirp signal was alternated with continuous high-frequency sinusoidal signals at the following frequencies: 308.33 kHz, 370.00 kHz, 431.67 kHz and 493.33 kHz. For clarification, the excitation signal and the resulting frequency spectrum are depicted in Figure 4. The signal was driven in burst mode, and the burst delay was chosen to be 112 ms to ensure that the piezo ceramics would not overheat, even with long-term usage. In the experimental setup the signal was generated with a function generator (33521A, Agilent Technologies, Waldbronn, Germany) and amplified to 288 Vpp with a voltage amplifier (A 1230-02, Dr. Hubert GmbH, Bochum, Germany) before being fed into the piezo ceramics.

Results

The experimental investigation of gas bubble removal revealed that combining the resonance frequency and the standing wave approach significantly optimizes bubble migration, enabling efficient removal across the relevant sensor surface. Figure 5 shows the initial gas-bubble-contaminated surface, as well as the stages of the cleaned surface after up to three burst cycles of the excitation signal shown in Figure 4. Most of the adhering gas bubbles detached during the first burst cycle, which occurred after 40 µs. The last few bubbles detached after the third cycle, which occurred after about 340 µs. The final image on the right in Figure 5 shows the bubble-free surface after the bubbles in the fluid were driven away by buoyancy.

For cases involving excitation at only the resonance frequencies of the gas bubbles or the excitation of only the standing wave field, the bubble removal results were much lower than those in the combined, alternating case presented in the Methods section. The frequencies for the standing wave field were chosen based on their effectiveness. Frequencies lower than 300 kHz did not significantly affect the bubbles. Frequencies higher than 500 kHz were also not suitable for this task because increased overall power consumption resulted in a lower maximum voltage to prevent thermal destruction of the piezo ceramics. In this case, frequencies higher than 500 kHz did not offer an increase in bubble manipulation.

DOI 10.5162/Ultrasonic2025/A4-a2

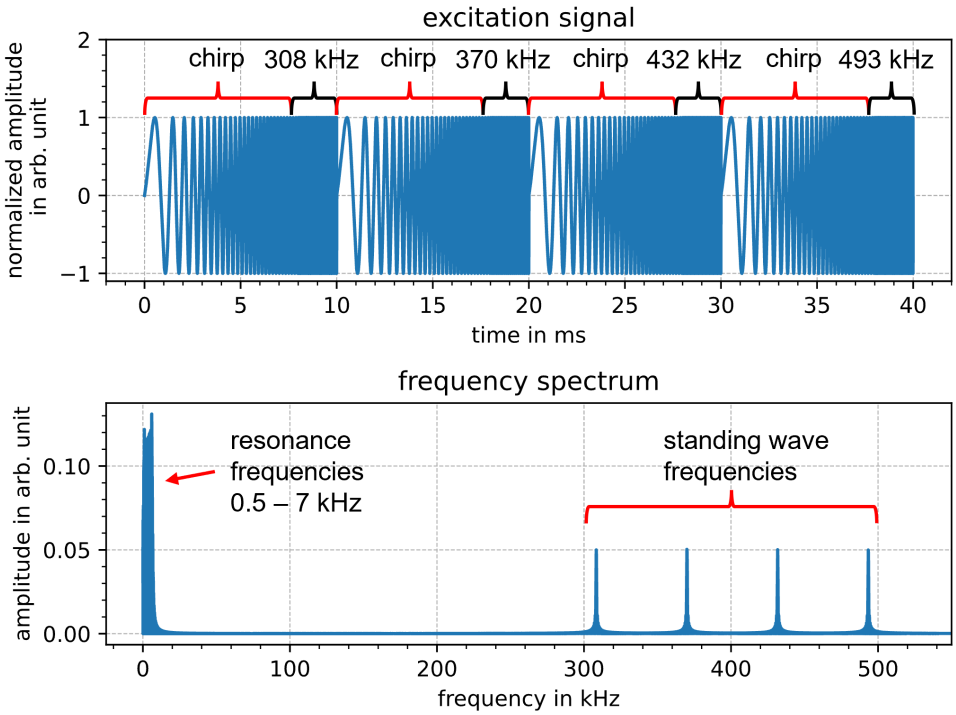

Fig. 4: One period of the excitation signal (top). Corresponding multi-band frequency spectrum (bottom).

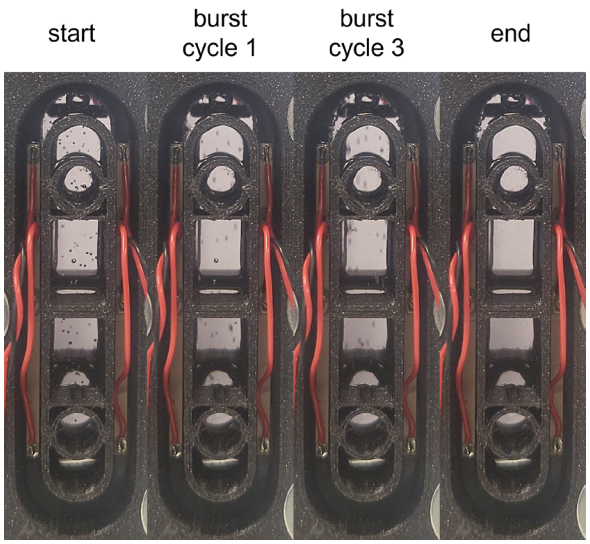

Fig. 5: Applied strategy for bubble removal. Left to right: start with no actuation, few bubbles on surface after the first burst cycle, no bubbles on surface after three burst cycles, result after shutting off.

Conclusion

The brief cleansing period and low power usage of burst mode actuation offer an energy-efficient, non-invasive method that maintains long-term precision and reliability of optical sensors in liquid environments. Unlike mechanical or chemical cleaning, this approach avoids sensor degradation or contamination. Additionally, ultrasonic wave parameters can be adjusted in real time to adapt to changes in temperature and flow conditions. This makes acoustic bubble removal a scalable solution for water quality monitoring and advances acoustic bubble migration technology, enhancing optical sensor performance.

Acknowledgment

This research was funded by the German Federal Ministry of Research, Technology and Space (BMFTR) within the program "KMU-innovativ" under grant number 02WQ1677B.

References

[1] X. Xi, F. B. Cegla, M. Lowe *et al.*, 'Study on the bubble transport mechanism in an acoustic standing wave field,' *Ultrasonics*, vol. 51, no. 8, 2011.

[2] H. Bruus, 'Acoustofluidics 7: The acoustic radiation force on small particles,' *Lab on a Chip*, vol. 12, no. 6, 2012.

[3] W. Lauterborn and T. Kurz, 'Physics of bubble oscillations,' *Reports on Progress in Physics*, vol. 73, no. 10, 2010.

[4] T. G. Leighton, *The acoustic bubble*. London San Diego New York [etc.]: Academic press, 1994.

DOI 10.5162/Ultrasonic2025/A4-a3

Multiple non-spherical acoustic cavitation bubbles in high-power ultrasonic field

Yaorong Wu[1], *Zhaokang Lei*[1], *Rui Liu*[1], *and Chenghui Wang*[1]
[1]*Institute of shaanxi key Laboratory of Ultrasonics,shaanxi Normal university,shaanxi China,710119*
corresponding.wangld001@snnu.edu.cn

Abstract: Based on the interaction among non-spherical bubbles, this study investigated the dynamic behavior and internal temperature changes of non-spherical oscillating bubbles in a high-intensity sound field from a theoretical perspective. Under the condition of the same initial parameters, when the sound field frequency approaches megahertz, the research found that in liquids with different viscosities and surface tensions, the temperature inside the bubbles is difficult to reach the high temperature required for sonoluminescence..

Keywords: Non-spherical deformation, High frequency,Temperature, Viscosity,Surface tension.

Background, Motivation and Objective

Ultrasonic waves propagating in liquid media can cause cavities and bubbles within the medium to grow and collapse under their influence. This phenomenon is known as acoustic cavitation [**Azadegan2025**]. Cavitation bubbles exhibit the characteristics of slow expansion and rapid collapse during the oscillation process. This phenomenon can trigger various physical effects, such as microflow, impact waves and shear forces. These acoustic cavitation effects have been widely applied in fields such as biomedicine and sonochemistry [**Wei2023**]. The cavitation phenomenon caused by ultrasonic waves, especially its stable state and inertial state, plays an important role in the sonochemical process. Therefore, by controlling the applied power or adjusting the driving frequency, the expected sonochemical effect can be effectively achieved [**Avramovic2025**].

To date, most analyses on the prediction of cavitation effects have mainly been based on spherical bubble dynamics. However, the shape of the bubbles may deviate from spherical, especially near the interface of different media or in the cavitation bubbles around the bubbles. This deviation in shape can lead to non-spherical oscillations, which in turn may cause the light intensity emitted by sonoluminescent bubbles to be significantly lower than that of spherical bubbles, or form high-speed jets in the liquid[**Liu2025**]. The high temperature generated inside the collapsing bubble (i.e., the "hot spot") is the trigger factor for most sonochemical reactions. Therefore, under different solution compositions and conditions, accurately measuring this temperature is particularly important. At a frequency of 20 kHz, even in the presence of alcohol, the bubble temperature did not show a significant change. The cause of this phenomenon may be related to the transient characteristics of cavitation bubbles [**Rae2005**]. Furthermore, it was observed that at higher frequencies, as the alcohol concentration increased, the average bubble temperature (i.e., the aforementioned chemical temperature) did indeed decrease [**Ashokkumar2011**]. With the increase of alcohol concentration, the measured temperature of cavitation bubbles shows a decreasing trend. In alcohol of the same concentration, the influence of long-chain alcohols is more significant. The reason for the decrease in bubble temperature under high-frequency conditions lies in that the high-temperature environment generated when cavitation bubbles collapse promotes the evaporation and decomposition of volatile solutes, thereby leading to the accumulation of hydrocarbon products [**Ashokkumar1999**]. The above-mentioned research mainly focuses on the variation of bubble temperature with frequency in alcohol solutions, while the mechanism of temperature variation with time within non-spherical oscillating bubbles in high-intensity sound fields is still under further exploration.

The main purpose of this study is to numerically investigate the non-spherical bubble dynamic behavior of three bubbles in left-right symmetrical and asymmetrical environments in a high-intensity sound field, as well as the relationship between the internal temperature of the bubbles and fluid parameters, by applying the published three-bubble model[**Wu12022**, **Wu22022**].

Results

In order to deeply study the oscillation phenomenon of multiple non-spherical bubbles in a high-intensity sound field, this section will adopt the formula (23) of the theoretical model proposed in the previous

DOI 10.5162/Ultrasonic2025/A4-a3

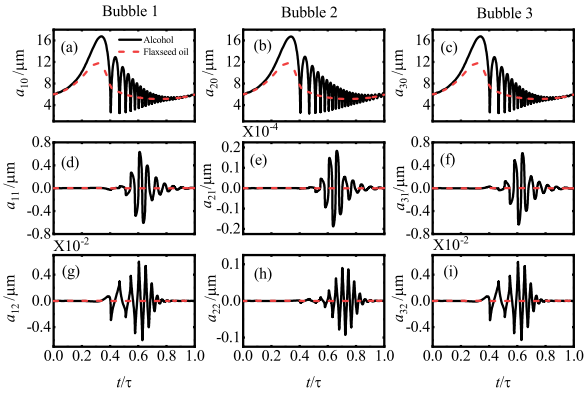

Fig. 1: The evolution of spherical and aspherical components of three identical bubbles at uniform distances in alcohol and flaxseed oil.

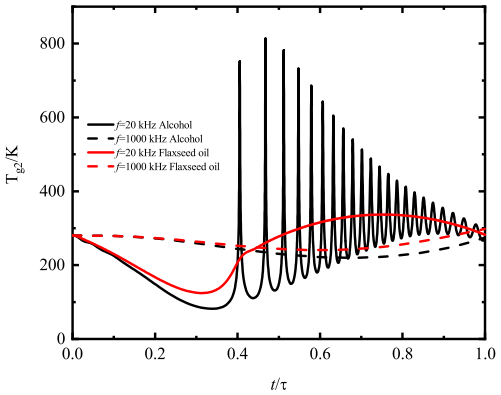

Fig. 2: The temperatures inside the bubbles in alcohol and flaxseed oil liquids at different frequencies.

literature[**Wu12022**, **Wu22022**] to numerically simulate the interaction of non-spherical oscillating bubbles in different liquids of a high-intensity sound field. Previous work on the interaction among three non-spherical bubbles has mainly focused on the interaction of bubbles in water. Based on the study of non-spherical oscillating bubbles in water, this paper further explores the oscillation phenomena of three non-spherical bubbles in alcohol and castor oil, as shown in Fig. 1. Firstly, we set the viscosities of alcohol and castor oil as h=0.0011 Pa·s and h=0.033 Pa·s respectively, with the initial radii and distances of bubbles are $a_{10}(0) = a_{20}(0) = a_{30}(0) = 6\ \mu m$, $D_{12}(0) = D_{23}(0) = 500\ \mu\mathrm{m}$. Other parameters refer to the previous literature. We also set sound waves with a pressure amplitude of 1.1 bar and a frequency of $f = 1/\tau = 20$ kHz to simulate the oscillation behavior of three bubbles. The research results show that when the middle bubble is in the left-right symmetrical mode, the oscillation of its non-spherical even symmetrical mode is more obvious, while the odd symmetrical mode approaches zero (see Fig. 1(e) and (h)), which is consistent with the research results in water. Meanwhile, the study also found that the spherical and non-spherical oscillation patterns of the three bubbles in alcohol were significantly greater than those in castor oil, as shown in Fig. 1. This further indicates that as the viscosity increases, both the volume of the bubbles and the amplitude of the non-spherical oscillation decrease.

Based on the research results in Fig. 1, this study aims to conduct an in-depth analysis of the temperature changes within three non-spherical oscillating bubbles located in a left-right symmetrical environment. The driving frequencies were set to 20 kHz and 1000 kHz respectively to predict the relationship between the internal temperatures and frequencies of the three bubbles immersed in alcohol and flaxseed oil with different viscosities, as shown in Fig. 2. At a driving frequency of 20khz, the temperature of the oscillating bubbles in the alcohol reaches a peak of approximately 800k. Conversely, when the frequency increased to the megahertz range, the temperatures observed in both alcohol and flaxseed oil were close to 280 K. This result indicates that achieving sonoluminescence temperatures in liquids of different viscosities under a megahertz sound field is challenging.

Figure 1 mainly discusses the oscillation phenomena of three non-spherical bubbles in alcohol and flaxseed oil in a 20 kHz sound field. To further investigate the oscillation influence of the megahertz sound field on these three non-spherical bubbles, we analyzed the evolution of the spherical and non-spherical components of the bubbles in alcohol and flaxseed oil over time at a frequency of 1000 kHz, as shown in Fig. 3. The initial distance is set to be consistent with the other parameters in Fig. 1. The research results show that when the three bubbles in alcohol and flaxseed oil are in a left-right asymmetric pattern, the non-spherical component of bubble 3 is the smallest (see Figs. 3(f) and (i)), which is consistent with the relevant research results conducted in water. Compared with Fig. 1, the initial distances and initial radii of bubble 1 and bubble 2 are the same. However, when the frequency approaches megahertz, both the spherical and non-spherical components of the bubbles decrease significantly. This further indicates that as the frequency increases, the oscillation behavior of non-spherical bubbles in alcohol and flaxseed oil becomes increasingly close to a spherical state.

The research results in Fig. 2 indicate that viscos-

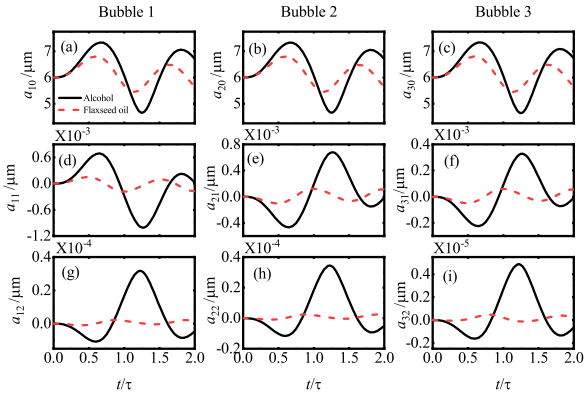

Fig. 3: The influence of megahertz sound fields in alcohol and flaxseed liquids on non-spherical oscillating bubbles.

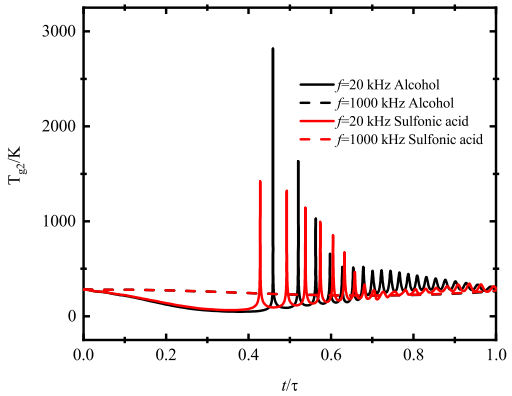

Fig. 4: The influence of surface tension on thetemperature inside the bubble in alcohol and sulfonic acid solutions.

ity has a significant influence on the temperature of non-spherical bubbles. However, fluid parameters are also closely related to surface tension. The temperatures within three non-spherical bubbles in alcohol and sulfonic acid with different surface tensions under a megahertz sound field are shown in Fig. 4. The surface tensions of alcohol and sulfonic acid are $\sigma = 0.022$ N/m and $\sigma = 0.055$ N/m respectively. To better control the variables, we adopted the same viscosity parameters in the experiment, and the other initial parameters were consistent with those in Fig. 3. The research results show that when the driving frequency is 20 kHz, the temperature of the oscillating bubbles in the alcohol reaches the maximum value, approaching 3000 K. When the frequency was raised to megahertz, the temperatures in both alcohol and sulfonic acid were close to 280 K. This result indicates that under the megahertz sound field, it is difficult to achieve the high temperature required for sonoluminescence in liquids with different surface tensions.

Conclusion

In a high-power ultrasonic field, the prediction of the internal temperature of non-spherical bubbles is helpful to achieve the expected sonochemical effect by adjusting the driving frequency. Studies show that in liquids such as alcohol and flaxseed oil, the oscillation trends of non-spherical bubbles are similar to those of spherical and non-spherical bubbles in water. Furthermore, when viscosity and surface tension change, as long as the driving frequency reaches the megahertz level, the internal temperature of the bubble is difficult to reach the high temperature required for sonoluminescence.

Acknowledgments

This work was supported by the National Natural Science Foundation of China (Grant No. 12374441), and the Fundamental Research Funds for the Central Universities of Education of China (Grant No. GK20246034),and the Project Supported by Natural Science Basic Research Plan in Shaanxi Province of China (Program No.2025JC-YBQN-066).

References

References

[1] M. Azadegan, B. Rahmatizadeh and M. T. H. Beheshti, et al. "Control of acoustic cavitation yield bydual frequency sonication: A Lyapunov exponent analysis". In: Applied Acoustics 239 (2025), pp. 1 10829. DOI:10.1016/j.apacoust.2025.110829.

[2] W. Wei, Y. Wang, Z. Wang, et al. "Microscale acoustic streaming for biomedical and bioa- nalytical applications". In: TrAC Trends in Analytical Chemistry, 160, (2023), pp. 116959. Doi.org/10.1016/j.trac.2023.116958.

[3] V. Avramovic, L. Hallez and C. Inserra, et al. "Acoustic spectra processing for the determination of cavitation threshold in a high-frequency sonoreactor in water and PEG mixtures from 1 to 54 mPa.s". In: Ultrasonics Sonochemistry, 119, (2025) pp. 107388. Doi: 10.1016 /j.ultsonch. 2025. 107388.

[4] Y. Liu, X. He and C. Huang, et al. "Interaction dynamics between cavitation bubbles and compressible air bubbles in an infinite domain". In: International Journal of Heat and Mass

Transfer, 249, (2025), pp. 127214. Doi:10.1016 /j.ijheatmasstransfer.2025.127214.

[5] J. Rae and M. Ashokkumar, O. Eulaerts, et al. "Estimation of ultrasound induced cavitation bubble temperatures in aqueous solutions". In: Ultrasonics Sonochemistry, 12, (2005), pp 325-329. Doi: 10.1016/j.ultsonch.2004.06.007.

[6] M. Ashokkumar."The characterization of acoustic cavitation bubbles – An overview". Ultrasonics Sonochemistry, 18, (2011), pp. 864-872, Doi: 10.1016/j.ultsonch.2010.11.016.

[7] M. Ashokkumar, P. Mulvaney and F. Grieser. "The effect of pH on multibubble sonoluminescence from aqueous solutions containing simple organic weak acids and bases". In: Journal of the American Chemical Society, 121 (1999), pp. 7355–7359.Doi: 10.1021/ja990482i.

[8] Y. Wu , W. Chen and L. Zhang, et al. "The left-right symmetrical and asymmetrical deformations in a three-bubble system". In: Journal of the American Chemical Society, 152. (2022), pp. 2446-2455, Doi: 10.1121/10.0014905.

[9] Y. Wu, Z. Lei and R. Liu, et al. "The oscillations of non-spherical bubbles in liquid,Ultrasonics Sonochemistry". 114, (2025), pp. 107262, Doi: 10.1016/j.ultsonch.2025.107262.

DOI 10.5162/Ultrasonic2025/A5-a1

Acoustic Wave Propagation in Porous Piezoelectric Media

Zhixiang Sun[1,2], *Yinqiu Zhou*[1,2], *Xiuming Wang*[1,2], *Lin Liu*[1,2], *Xiao He*[1,2], *and Yonghao Lu*[1,2]
[1]*Institute of Acoustics, Chinese Academy of Sciences, Beijing 100190, China*
[2]*University of Chinese Academy of Sciences, Beijing 100049, China*
zhouyinqiu@mail.ioa.ac.cn

Abstract: Porous piezoelectric media are heterogeneous complex materials composed of a piezoelectric solid skeleton with fluid-filled pores, holding significant value in transducer optimization and understanding bone regeneration mechanisms. However, existing studies are predominantly theoretical, lacking rigorous full-wavefield numerical simulations, particularly accurate treatment of the coupled poroelastic and piezoelectric effects. To address this issue, this work develops a high-fidelity staggered-grid finite-difference time-domain (FDTD) framework for simulating acoustic wave propagation in anisotropic porous piezoelectric media. A mechanical-electrical coupled staggered grid rigorously handles electromechanical coupling by solving Poisson's equation at each time step. Numerical results are validated against analytical solutions from the Christoffel equation, demonstrating superior accuracy compared to simplified coupling schemes.

Keywords: Porous piezoelectric media, FDTD, Biot theory, Poisson's equation, Staggered grid

Introduction

Porous piezoelectric media (PPMs) consist of a piezoelectric solid skeleton with fluid-filled pores, such as porous piezoelectric ceramics and human bone tissue. Compared to traditional dense piezoelectric materials, PPMs exhibit advantages including low density, low acoustic impedance, and low mechanical quality factor, making them valuable for optimizing the acoustic performance of porous piezoelectric composites and transducers, as well as understanding the regeneration mechanisms of piezoelectric bone tissue [1].

Currently, theoretical research on PPMs is primarily based on classical Biot theory [2, 3]. Vashishth and Gupta combined Biot theory with piezoelectric effects, deriving the Christoffel equation for transversely isotropic PPMs [4]; Sharma investigated the effects of piezoelectricity on wave velocities [5]. Regarding numerical simulations, methods have been developed for non-porous piezoelectric materials [6, 7] and non-piezoelectric porous media [8], but rigorous full-wavefield simulations for PPMs remain scarce. Meanwhile, under quasi-static approximation, some numerical studies have employed oversimplified electromechanical coupling treatments, which actually introduce artificial stiffening effects and break the intrinsic anisotropic symmetry of the material [9, 10].

To address these issues, this work proposes a mechanical-electrical coupled staggered-grid FDTD framework for simulating wave propagation in porous piezoelectric media. The method rigorously couples mechanical and electrical fields by solving Poisson's equation at each time step, ensuring numerical stability and physical accuracy. We validate numerical results against analytical solutions based on the Christoffel equation, demonstrating that the rigorous Poisson-based coupling scheme is essential for accurate simulation, particularly for quasi-shear wave propagation.

Acoustic Wave Propagation Theory

Following the framework established by Vashishth and Gupta [4, 11], wave propagation in porous piezoelectric media is governed by a coupled system combining Biot's poroelasticity theory with piezoelectric constitutive relations. The governing equations consist of:

Biot's equations of motion describe the mechanical motion of the coupled solid skeleton and pore fluid:

$$\begin{aligned} \sigma_{ij,j} &= \rho_{ij}^{11}\ddot{u}_j + \rho_{ij}^{12}\ddot{u}_j^* + b_{ij}(\dot{u}_j - \dot{u}_j^*) \\ \sigma_{,i}^* &= \rho_{ij}^{12}\ddot{u}_j + \rho_{ij}^{22}\ddot{u}_j^* - b_{ij}(\dot{u}_j - \dot{u}_j^*) \end{aligned} \tag{1}$$

where σ_{ij} and σ^* are stress components for solid and fluid phases, u_i and u_i^* denote the displacement vectors, ρ_{ij}^{11}, ρ_{ij}^{12}, and ρ_{ij}^{22} are dynamic density coefficients accounting for inertial coupling, and b_{ij} represents the dissipation function related to fluid viscosity and permeability.

Piezoelectric constitutive equations relate the mechanical and electrical fields on the basis of Biot's theory:

$$\begin{aligned} \sigma_{ij} &= c_{ijkl}u_{k,l} + m_{ij}u_{k,k}^* - e_{kij}E_k \\ \sigma^* &= m_{ij}u_{i,j} + Ru_{i,i}^* \\ D_i &= e_{ikl}u_{k,l} + \xi_{ij}E_j \end{aligned} \tag{2}$$

DOI 10.5162/Ultrasonic2025/A5-a1

where c_{ijkl} are elastic stiffness coefficients, m_{ij} and R represent coupling parameters between solid and fluid phases, e_{ikl} are piezoelectric constants, ξ_{ij} are dielectric permittivity components, D_i is electric displacement, and E_i is the electric field.

Quasi-static approximation and Gauss's law assume the magnetic field is negligible, allowing the electric field to be expressed as the negative gradient of electric potential. With zero free charge density inside the medium, the electric field equations are:

$$\begin{aligned} E_i &= -\phi_{,i} \\ D_{i,i} &= \rho_e = 0 \end{aligned} \tag{3}$$

where ϕ is the electric potential and ρ_e is the free charge density. Equations (1)–(3) together constitute the complete system of governing equations.

For plane harmonic wave propagation, we seek solutions of the form:

$$(u_i, u_i^*, \phi) = (B_i, F_i, G) \exp\left[i\omega\left(\frac{n_i x_i}{v} - t\right)\right] \tag{4}$$

where ω is angular frequency, v is phase velocity, x_i denote spatial coordinates, and n_i are direction cosines of the propagation vector. Substituting the plane wave solution (4) into the governing equations (1)–(3) yields an algebraic eigenvalue problem, leading to the Christoffel equation:

$$|\mathbf{M}_{7\times7}| = 0 \tag{5}$$

This equation predicts the existence of four propagating wave modes in the medium. The analytical phase and group velocities obtained by solving Eq. (5) serve as benchmark solutions for validating the numerical FDTD scheme presented in the next section.

Numerical Simulation Framework

To simulate full wavefield propagation in porous piezoelectric media, we develop a high-order staggered-grid FDTD method that rigorously handles electromechanical coupling. We focus on a transversely isotropic medium in the 2D x_1-x_3 plane.

Beyond the mechanical equations (Eqs. (1)–(2)), the electrical field is governed by the Poisson equation derived from Gauss's law $\nabla \cdot \mathbf{D} = 0$:

$$\begin{aligned} \xi_{11}\frac{\partial^2 \dot{\phi}}{\partial x^2} + \xi_{33}\frac{\partial^2 \dot{\phi}}{\partial z^2} = \frac{\partial}{\partial x}\left[e_{15}\left(\frac{\partial v_x}{\partial z} + \frac{\partial v_z}{\partial x}\right)\right] \\ + \frac{\partial}{\partial z}\left[e_{31}\frac{\partial v_x}{\partial x} + e_{33}\frac{\partial v_z}{\partial z}\right] \end{aligned} \tag{6}$$

where $\dot{\phi}$ is the time derivative of electric potential. The right-hand side couples the mechanical velocity field to the electric potential. Solving this equation

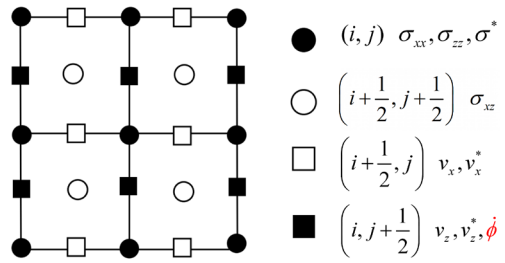

Fig. 1: Schematic of the electro-mechanical coupled staggered grid.

at every time step captures the complete dynamic electromechanical interaction. This rigorous approach differs fundamentally from simplified schemes that assume $\partial D_i/\partial t = 0$, which effectively decouples the system and introduces artificial stiffening effects [9, 10].

To implement this rigorous scheme, we design an electro-mechanical coupled staggered grid. Our key innovation is the strategic co-location of the electric potential rate $\dot{\phi}$ with the vertical velocity v_z at grid position $(i, j+\frac{1}{2})$, as shown in Fig. 1. This arrangement ensures that all spatial derivatives in both the stress-update equations (Eq. (2)) and the Poisson equation (Eq. (6)) can be computed using the same high-order stencils, preserving coupling physics with high-order accuracy and numerical stability.

Based on this grid arrangement, the time-marching algorithm proceeds in three stages at each time step.

Stage 1: Velocity Update. Velocities are updated from stress gradients using Eq. (1). For the horizontal velocity of the solid skeleton:

$$\begin{aligned} v_{x(i+1/2,j)}^{(n+1/2)} = v_{x(i+1/2,j)}^{(n-1/2)} + \Delta t\Big[\gamma_{11}\Big(D_x\sigma_{xx(i+1/2,j)}^{(n)} \\ + D_z\sigma_{xz(i+1/2,j)}^{(n)}\Big) + \gamma_{12}D_x\sigma_{(i+1/2,j)}^{*(n)} \\ + b(\gamma_{12}-\gamma_{11})\left(v_{x(i+1/2,j)}^{(n-1/2)} - v_{x(i+1/2,j)}^{*(n-1/2)}\right)\Big] \end{aligned} \tag{7}$$

where D_x and D_z denote spatial difference operators. Similar expressions apply to other velocity components. This stage follows the standard Biot poroelastic formulation without piezoelectric terms.

Stage 2: Electric Potential Solution. The Poisson equation is solved for $\dot{\phi}$ using the updated velocity

DOI 10.5162/Ultrasonic2025/A5-a1

Tab. 1: Material parameters for PZT-2 porous piezoelectric medium.

Parameter	Value	Parameter	Value
ρ_{11} (kg/m^3)	5082	c_{11} (GPa)	148.0
ρ_{12} (kg/m^3)	-1155	c_{13} (GPa)	74.2
ρ_{22} (kg/m^3)	4928	c_{33} (GPa)	131.0
e_{31} (C/m^2)	-2.324	c_{44} (GPa)	25.3
e_{33} (C/m^2)	10.99	R (GPa)	20.0
e_{15} (C/m^2)	9.3	m_{11} (GPa)	8.8
ξ_{11} (nF/m)	3.984	m_{33} (GPa)	5.2
ξ_{33} (nF/m)	2.081		

field:

$$\begin{aligned}\xi_{11}D_x^2\dot{\phi}^{(n+1/2)}_{(i,j+1/2)} + \xi_{33}D_z^2\dot{\phi}^{(n+1/2)}_{(i,j+1/2)} \\ = D_x\left[e_{15}\left(D_z v_x + D_x v_z\right)\right]^{(n+1/2)}_{(i,j+1/2)} \\ + D_z\left[e_{31}D_x v_x + e_{33}D_z v_z\right]^{(n+1/2)}_{(i,j+1/2)}\end{aligned} \tag{8}$$

The grid arrangement ensures that the source term velocities, after undergoing second-order differentiation, are naturally located at $(i, j+1/2)$, coinciding with the center position of the second-order derivatives on the left-hand side. The sparse coefficient matrix is pre-computed once, and the linear system is solved directly at each time step.

Stage 3: Stress Update. After computing the electric potential rate $\dot{\phi}$, stresses are updated from velocity and electric potential gradients using Eq. (2). For σ_{xx}:

$$\begin{aligned}\sigma^{(n+1)}_{xx(i,j)} = \sigma^{(n)}_{xx(i,j)} \\ + \Delta t\Big[c_{11}D_x V^{(n+1/2)}_{x(i,j)} + c_{13}D_z V^{(n+1/2)}_{z(i,j)} \\ + m_{11}\left(D_x v^{*(n+1/2)}_{x(i,j)} + D_z v^{*(n+1/2)}_{z(i,j)}\right) \\ + e_{31}D_z\dot{\phi}^{(n+1/2)}_{(i,j)}\Big]\end{aligned} \tag{9}$$

The term $e_{31}D_z\dot{\phi}$ represents the piezoelectric contribution. Similar expressions apply to other stress components.

Results and Validation

To validate the proposed FDTD framework and demonstrate the necessity of rigorous electromechanical coupling, we perform theoretical calculations and numerical simulations for wave propagation in transversely isotropic porous piezoelectric media. We select PZT-2 type porous piezoelectric ceramic as the representative material, with parameters listed in Tab. 1.

We first establish the analytical benchmark by solving the Christoffel equation (Eq. (5)) to obtain velocities for all wave modes as functions of propagation angle θ. As shown in Fig. 2, the theory predicts four distinct wave modes: the fast quasi-longitudinal wave (qP1), quasi-shear wave (qSV), and horizontally polarized shear wave (SH) characteristic of anisotropic elastic media, plus the slow quasi-longitudinal wave (qP2) arising from solid-fluid coupling in the porous microstructure. For transversely isotropic media with 6mm symmetry, the 7×7 Christoffel system decouples into a 2×2 system governing the SH wave (velocity independent of piezoelectric coupling) and a 5×5 system governing the three in-plane coupled modes (qP1, qSV, qP2) where electromechanical effects are significant [11]. The phase and group velocity polar plots (Fig. 2a,b) exhibit strong anisotropic characteristics reflecting material symmetry. These analytical solutions serve as rigorous benchmarks for numerical validation.

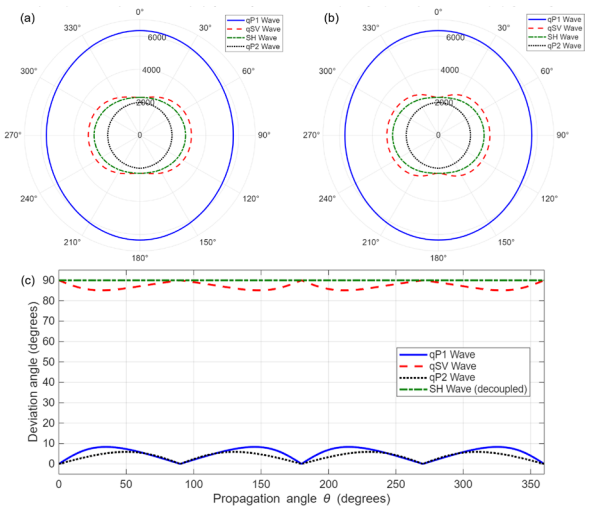

Fig. 2: Analytical solutions for PZT-2 porous piezoelectric medium: (a) Phase velocity polar plot, (b) Group velocity polar plot, (c) Skewing angle as a function of propagation angle.

The numerical FDTD simulations are performed on a 10 mm $\times$ 10 mm computational domain with spatial grid size $\Delta x = \Delta z = 25$ μm and time step $\Delta t = 2\times10^{-9}$ s. The spatial discretization employs eighth-order accuracy while time integration maintains second-order accuracy. An impulse source with center frequency $f_0 = 6$ MHz is applied at the domain center. Dirichlet boundary conditions are enforced at all boundaries.

Fig. 3 presents snapshots of multiple physical fields computed by the rigorous FDTD approach at $0.7\,\mu$s, demonstrating the comprehensive capability of the numerical framework. Clear concentric wave fronts corresponding to different modes are visible: the out-

DOI 10.5162/Ultrasonic2025/A5-a1

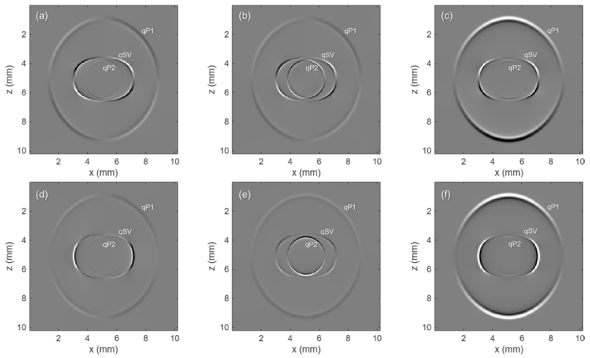

Fig. 3: Snapshots of multiple physical fields from FDTD simulations at $0.7\,\mu$s: (a) Horizontal velocity v_x of solid skeleton, (b) Horizontal velocity v_x^* of pore fluid, (c) Normal stress σ_{zz}, (d) Shear stress σ_{xz}, (e) Pore pressure σ^*, (f) Electric potential ϕ.

ermost front represents the fast qP1 wave, followed by qSV, with the slower qP2 wave in the interior. Note that the SH wave, which vibrates out of plane, cannot be captured by this two-dimensional implementation. The numerical wave speeds extracted from these wave fronts show excellent agreement with the analytical solutions in Fig. 2, confirming the accuracy of the staggered-grid FDTD method.

Having validated the numerical framework against analytical solutions, we now investigate the fundamental importance of rigorous electromechanical coupling treatment. Two approaches are compared: the simplified approach assumes $\partial D_i/\partial t = 0$, effectively decoupling the system; the rigorous approach solves the full Poisson equation (Eq. (6)) at each time step, maintaining complete dynamic coupling.

Fig. 4 presents a direct comparison between these two approaches alongside theoretical predictions. The rigorous method (center) faithfully reproduces all theoretical wave characteristics, with wave front positions matching the analytical benchmarks. Conversely, the simplified treatment (left) produces visible deviations in the wavefield structure, with the qSV wave showing the most pronounced discrepancies while qP1 and qP2 modes remain relatively unaffected.

The underlying physical mechanism stems from the constraint imposed by $\partial D/\partial t = 0$, which prevents the electric field from dynamically responding to time-varying mechanical strain. This artificially enhances the effective elastic stiffness in certain crystallographic directions, distorting wave velocities and disrupting the intrinsic anisotropic symmetry. The rigorous Poisson equation treatment, by contrast, allows the electric potential to evolve naturally in response to the instantaneous strain state, preserving both Gauss's law and correct electromechanical coupling physics.

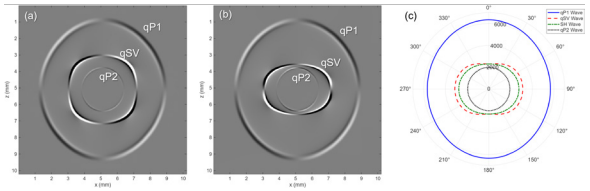

Fig. 4: Comparison of electromechanical coupling schemes: (a) Simplified approach with $\partial D/\partial t = 0$, (b) Rigorous Poisson equation approach, (c) Analytical velocity distribution from Christoffel equation.

The superior performance of the rigorous approach is fundamentally enabled by the proposed electromechanical coupled staggered grid design, ensuring numerical consistency and physical coupling accuracy.

Conclusion

This work presents an FDTD framework based on an electro-mechanical coupled staggered grid for simulating wave propagation in porous piezoelectric media. By rigorously solving the complete Poisson equation at each time step, the method accurately captures all wave modes and achieves excellent agreement with analytical solutions derived from the Christoffel equation. Compared to traditional simplified coupling schemes, the proposed method accurately simulates quasi-shear wave propagation while avoiding noticeable velocity deviations and wavefield distortions. The framework provides a robust numerical tool for investigating electromechanical wave phenomena in anisotropic porous piezoelectric materials, with applications in transducer design and piezoelectric tissue characterization.

Acknowledgment

This work was supported by the National Natural Science Foundation of China (NSFC) under Grant Nos. 42127807, 12274432, and 52227901.

References

[1] E. Mercadelli, A. Sanson, and C. Galassi. "Porous piezoelectric ceramics". In: *Piezoelectric ceramics* (2010), pp. 111–128.

[2] M. A. Biot. "Theory of Propagation of Elastic Waves in a Fluid-Saturated Porous Solid. I. Low-Frequency Range". In: *The Journal of the Acoustical Society of America* 28.2 (1956), pp. 168–178.

[3] M. A. Biot. "Theory of propagation of elastic waves in a fluid-saturated porous solid. II. Higher frequency range". In: *The Journal of the acoustical Society of america* 28.2 (1956), pp. 179–191.

[4] A. K. Vashishth and V. Gupta. "Wave propagation in transversely isotropic porous piezoelectric materials". In: *International Journal of Solids and Structures* 46.20 (2009), pp. 3620–3632.

[5] M. Sharma. "Piezoelectric effect on the velocities of waves in an anisotropic piezo-poroelastic medium". In: *Proceedings of the Royal Society A: Mathematical, Physical and Engineering Sciences* 466.2119 (2010), pp. 1977–1992.

[6] E. Filoux et al. "Modeling of piezoelectric transducers with combined pseudospectral and finite-difference methods". In: *The Journal of the Acoustical Society of America* 123.6 (2008), pp. 4165–4173.

[7] S. Rahman, H. Langtangen, and C. Barnes. "A finite element method for modelling electromechanical wave propagation in anisotropic piezoelectric media". In: *arXiv preprint physics/0510175* (2005).

[8] L. Liu, X.-M. Zhang, and X.-M. Wang. "Theoretical analysis and numerical simulation of acoustic waves in gas hydrate-bearing sediments". In: *Chinese Physics B* 30.2 (2021), p. 024301.

[9] F. Chagla and P. M. Smith. "Finite difference time domain methods for piezoelectric crystals". In: *IEEE transactions on ultrasonics, ferroelectrics, and frequency control* 53.10 (2006), pp. 1895–1901.

[10] Y.-y. Zhao et al. "Finite difference time domain analysis of two-dimensional piezoelectric phononic crystals". In: (2012), pp. 1–4. DOI: 10.1109/SPAWDA.2012.6464021.

[11] A. K. Vashishth and V. Gupta. "Decoupling of plane waves in porous piezoelectric materials". In: *Proceedings of the Royal Society A: Mathematical, Physical and Engineering Sciences* 470.2169 (2014), p. 20140172.

DOI 10.5162/Ultrasonic2025/A5-a3

Numerical Analysis of Wave Propagation in Partially Saturated Porous Formations for CO_2 Geological Sequestration

Xiumei Zhang[1,2,3], *Yujuan Qi*[1,2,3], *and Lin Liu*[1,2,3]
[1]*State Key Laboratory of Acoustics, Institute of Acoustics, Chinese Academy of Sciences, Beijing 100190, China*
[2]*School of Physics Sciences, University of Chinese Academy of Sciences, Beijing 100049, China*
[3]*Beijing Engineering Research Center of Sea Deep Drilling and Exploration, Institute of Acoustics, Chinese Academy of Sciences, Beijing 100190, China*
zhangxiumei@mail.ioa.ac.cn

Abstract: Understanding elastic wave propagation in unsaturated porous media, critical for geophysical exploration, especially in hydrocarbon reservoirs and CO_2 storage formations, demands accurate numerical frameworks. This study introduces a numerical model based on Lo's three-phase theory to analyze wave dynamics in two-fluid saturated porous media. The governing equations are reformulated into a velocity-stress form and solved using a hybrid algorithm that combines the time-splitting scheme and staggered-grid finite-difference method (FDM), effectively addressing stiffness issues in porous media simulations. Our findings reveal four distinct wave modes: three compressional waves (P1, P2, P3) and one shear wave (S). Notably, slow compressional waves (P2, P3), driven by solid-fluid and fluid-fluid relative motions, show strong dependence on fluid viscosity and frequency. Although these waves are rarely observable at seismic frequencies, their energy distribution and conversion into propagating P1/S waves at interfaces are crucial. Wavefield snapshots demonstrate complex mode conversions among all four waves, reflecting intricate solid-wetting/nonwetting fluid coupling. Key contributions include the algorithm's robustness in simulating multi-wave phenomena, the fluid-phase energy dominance in slow waves, and the complexity of interface-induced mode conversions.

Keywords: numerical simulation, wave propagation, CO_2 geological sequestration, porous media

Introduction

Numerical simulation serves as a vital approach for investigating the acoustic properties of underground reservoirs [1]. Particularly, the staggered-grid finite-difference method (FDM), with high efficiency and low numerical dispersion, has emerged as a primary approach for simulating spatiotemporal characteristics of acoustic wave propagation in complex heterogeneous media.

The porous media framework, considering the solid-fluid coupling effects, provides more accurate representations of acoustic wave propagation in actual geological formations. The efficacy of staggered-grid FDM has been well established through seminal works by Dai et al. [2]. However, significant challenges remain when studying more complex three-phase porous media, such as CO_2 storage reservoirs. Although Lo et al. established a wave theory for unsaturated porous media based on Eulerian formulation [3], which has been successfully applied by other scholars in fluid-containing complex materials and CO_2 geological storage monitoring, numerical simulation research on its acoustic propagation characteristics remains inadequate. Current analyses of spatiotemporal responses in Lo's theory primarily rely on analytical solutions, proving insufficient for practical reservoirs with strong heterogeneity or complex geometries [4]. Therefore, developing a numerical algorithm based on Lo's theory for acoustic responses in porous reservoirs holds substantial theoretical and practical value.

Numerical arithmetic based on Lo's theory

$$\begin{aligned} v_{s(i,j+1/2)}^{x(n+1/2)} &= v_{s(i,j+1/2)}^{x(n-1/2)'} + B_{11} dt D_x \tau_{xx(i,j+1/2)}^{(n)} \\ &\quad + B_{11} dt D_z \tau_{xz(i,j+1/2)}^{(n)} + B_{12} dt D_x \sigma_{1(i,j+1/2)}^{(n)} \\ &\quad + B_{13} dt D_x \sigma_{2(i,j+1/2)}^{(n)}, \\ \tau_{xz(i,j)}^{(n+1)} &= \tau_{xz(i,j)}^{(n)} + \mu dt D_x v_{s(i,j)}^{z(n+1/2)} \\ &\quad + \mu dt D_z v_{s(i,j)}^{x(n+1/2)}, \end{aligned} \tag{1}$$

Based on the previous work of Qi et al., a numerical simulation algorithm for acoustic fields in porous media based on Lo's model was developed using the time-splitting method and the staggered grid finite

DOI 10.5162/Ultrasonic2025/A5-a3

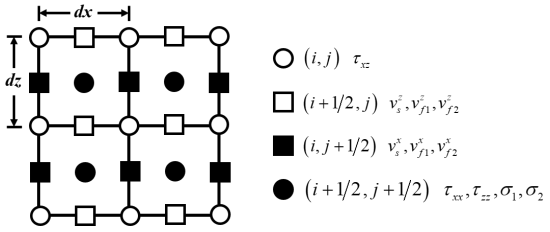

Fig. 1: Spatial distribution of the field variables.

difference method [5][6]. The format of the modified model in two dimensions can be expressed as Eq. (1) and Eq. (2).

$$\begin{aligned}\tau^{(n+1)}_{xx(i+1/2,j+1/2)} &= \tau^{(n)}_{xx(i+1/2,j+1/2)} \\ &+ (a_{11} + 4/3\mu)\, dt D_x v^{x(n+1/2)}_{s(i+1/2,j+1/2)} \\ &+ (a_{11} - 2/3\mu)\, dt D_z v^{z(n+1/2)}_{s(i+1/2,j+1/2)} \\ &+ a_{12} dt \left(D_x v^{x(n+1/2)}_{1(i+1/2,j+1/2)} + D_z v^{z(n+1/2)}_{1(i+1/2,j+1/2)} \right) \\ &+ a_{13} dt \left(D_x v^{x(n+1/2)}_{2(i+1/2,j+1/2)} + D_z v^{z(n+1/2)}_{2(i+1/2,j+1/2)} \right),\end{aligned} \tag{2}$$

where v_g^i indicates the macroscopic average velocity of phase g in i direction; subscript s indicates the phase of solid grain, subscript 1 denotes the phase of nonwetting fluid, and subscript 2 represents the phase of wetting fluid; τ_{ij} indicates the force components of solid grain; σ_i indicates the fluid stress of phase i; a_{ij}, B_{ij} are the coefficients related to Lo's work[3] and Qi's work[6]; dt denotes the time step; Dx and Dz denote the discretized difference operators in the x- and z-directions, respectively. The spatial distribution of the field variables in the staggered-grid finite-difference algorithm is depicted in Fig. 1.

Numerical calculations and analysis

To investigate the spatiotemporal propagation characteristics of waves in unsaturated porous media, the time-splitting staggered-grid finite-difference algorithm is applied to the wave numerical simulation, with the parameters shown in Tab. 1. In the numerical simulation, the model size is 500 m × 500 m, with $dx = dz = 0.2$ m and $dt = 10$ μs. A Ricker wavelet with the dominant frequency of 50 Hz is located at the point (250 m, 250 m), loading on the vertical particle velocity of each phase. Moreover, to mitigate spurious reflections caused by the limited computational domain, the Perfectly Matched Layer (PML) was implemented around the model. Snapshots of the velocity components of the solid grain, the nonwetting and wetting pore fluid at 90 ms are shown in Fig. 2, with a proportional amplitude ratio of each phase. In this case, the influence of fluid viscosity was neglected

Tab. 1: Parameters of unsaturated porous media.

Type	Parameters	Value
Solid grain	grain bulk modulus, K_s (GPa)	40
	frame bulk modulus, K_m (GPa)	7.12
	shear modulus, μ (GPa)	9.986
	grain density, ρ_s (kg/m^3)	2573
	porosity, ϕ	0.135
	permeability, κ (D)	0.706
Nonwetting fluid - CO_2	density, ρ_1 (kg/m^3)	384
	bulk modulus, K_1 (GPa)	0.018
	viscosity, η_1 (mPa · s)	0.028
Wetting fluid - Brine	density, ρ_2 (kg/m^3)	1034
	bulk modulus, K_2 (GPa)	2.65
	viscosity, η_2 (mPa · s)	0.70

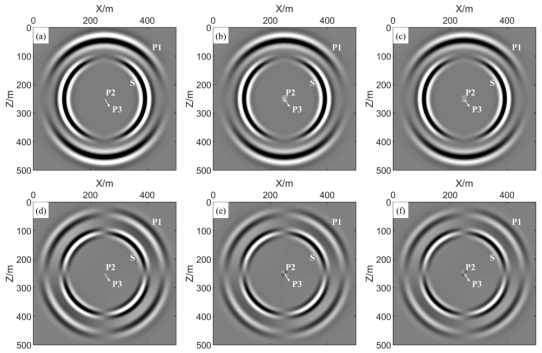

Fig. 2: Snapshots of the vertical particle velocity component of (a) solid grain, (b) nonwetting fluid, and (c) wetting fluid, and the horizontal particle velocity component of (d) solid grain, (e) nonwetting fluid, and (f) wetting fluid at 90 ms.

to magnify the characteristics of the slow compressional waves. It is obviously shown that the P1, S, P2, and P3 waves can be sequentially observed from outer to inner regions. Especially, the energy of the P3 wave is concentrated near the source, due to its slow velocity. Additionally, the phase contrast reveals that the P2 wave is generated by the relative motion between the solid grain and pore fluids, while the P3 wave is generated due to the relative motion between the nonwetting fluid and wetting fluid. The P2 and P3 waves concentrate their energy in the phase of pore fluids.

To clarify the conversion process of acoustic waves at the interface, a two-layer unsaturated porous media model is constructed, and the model parameters are shown in Tab. 2. To ensure that the results are

DOI 10.5162/Ultrasonic2025/A5-a3

Tab. 2: Parameters for modeling two-layer, three-phase porous media

Type	Parameters	Upper layer	Lower layer
Solid grain	grain bulk modulus, K_s (GPa)	40	40
	frame bulk modulus, K_m (GPa)	1.37	9.50
	shear modulus, μ (GPa)	0.82	6.20
	grain density, ρ_s (kg/m^3)	2600	2800
	porosity, ϕ	0.36	0.2
	permeability, κ (D)	1.6	8
Non-wetting fluid	density, ρ_1 (kg/m^3)	498	860
	bulk modulus, K_1 (GPa)	0.025	1.3
	viscosity, η_1 (mPa · s)	0.035	300
	Saturation, S_1 (%)	80	50
Wetting fluid	density, ρ_2 (kg/m^3)	1036	1036
	bulk modulus, K_2 (GPa)	2.64	2.64
	viscosity, η_2 (mPa · s)	0.77	0.77
	Saturation, S_2 (%)	20	50

accurate with the boundary conditions of layered interfaces, the parameters at the interfaces are effectively averaged[7].

In the numerical simulations, a P-wave source with a dominant frequency of 30 kHz is applied at (0.4 m, 0.3 m) to excite the vertical particle velocity in each phase. Fig. 3 displays snapshots of the vertical particle velocity across different phases, clearly showing direct P1 and P2 waves, along with various converted waves, including reflected waves and transmitted waves. The comparison between solid and fluid wavefields reveals that converted slow waves exhibit stronger signatures in the fluid phase, demonstrating significant phase-dependent energy conversion at the interface. Notably, the P3 wave remains localized near both the source and interface due to its slow propagation velocity. Furthermore, when the slow compressional wave crosses the interface, it converts into fast compressional and shear waves that continue to propagate normally, highlighting the complex wave conversion processes occurring in the unsaturated porous media.

Vertical Seismic Profiling (VSP) is a seismic monitoring technique, provides higher resolution and finer details of the subsurface structure due to the receivers being located inside the well. Therefore, the time-lapse VSP surveys are modeled. The classical block model saturated with brine is established with Tab. 3. Layers A and C represent formations with poor porosity and permeability, and layer B represents the target

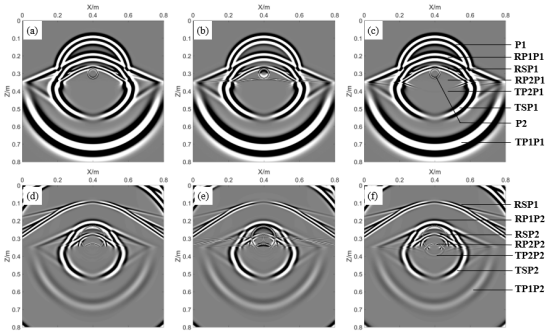

Fig. 3: Snapshots of the vertical particle velocity component of (a, d) solid grain, (b, e) nonwetting fluid, and (c, e) wetting fluid at 0.2 ms and 0.5 ms, respectively.

Tab. 3: Parameters of the solid grain of a horizontally laminated formation.

Layer Number	A	B	C
grain bulk modulus, K_s (GPa)	40.33	40	40
frame bulk modulus, K_m (GPa)	12.6	7.12	23.9
shear modulus, μ (GPa)	12.3	9.986	16
grain density, ρ_s (kg/m^3)	2704	2226	2670
porosity, ϕ	0.019	0.135	0.016
permeability, κ (D)	0.1472	0.7063	0.0001

reservoir for CO_2 injection.

In numerical simulations, a single P-wave source is used, with receivers located at depths 100 m - 1260 m, spaced 4 m apart. Fig. 4 shows the corresponding seismograms as the injected S_{CO2} is 0.4. Both the upgoing and the downgoing wavefields are observed. The intersection point of wave conversion matches the positions of the layer interfaces, which can be used for stratigraphic calibration.

The waveforms from depths of 700 m and 1000 m are subject to decimation for detailed analysis. Fig. 5 shows the comparison under different injected S_{CO2}. The variation of CO_2 can be observed by time-lapse arrival times of the reflected and transmitted waves, particularly the compressional waves. In this scenario, the difference between injected S_{CO2} is 0% and 5% is minimal. At this time, CO_2 is mainly dissolved into the brine, resulting in lower free S_{CO2}. Additionally, the acoustic response becomes more pronounced while free S_{CO2} increases, particularly showing the decrease in compressional velocity and the delay of travel time. As expected, the acoustic methods can effectively

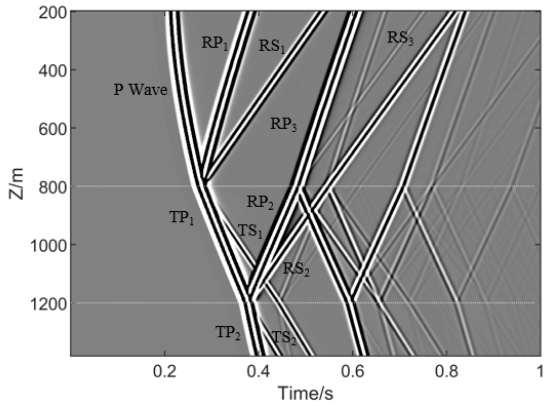

Fig. 4: Corresponding seismograms with $S_{CO2} = 0.4$ in layer B

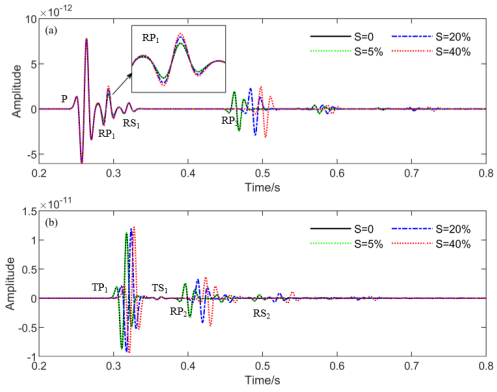

Fig. 5: Received waveforms for different injected S_{CO2} in layer B: (a) Z = 700 m; (b) Z = 1000 m.

detect the migration of free-phase CO_2. However, the process of dissolution seems impossible to detect.

Conclusion

In this paper, we analyze the wave propagation characteristics in porous media saturated with CO_2 and brine. Using the time-splitting staggered-grid finite-difference algorithm, we efficiently obtained the wavefield snapshot and waveforms in unsaturated porous media. The energy distribution and generation mechanism of various types of waves in unsaturated porous media, as well as the acoustic wave mode conversion at the interface, have been systematically analyzed. Synthesizing the study, we undertake a comparative exploration of VSP responses within saline aquifers, while considering variations in CO_2 saturation.

The proposed numerical algorithm allows us to effectively illustrate the transmission process of four waves in unsaturated porous media. At seismic frequencies, only P1 and S waves are considered propagating waves, while P2 and P3 waves are identified as diffusion waves influenced by the viscous coefficient. The propagation behavior and energy distribution at the interface vary significantly across different components, highlighting the strong coupling between the solid grain, wetting fluid, and non-wetting fluid. This coupling must be considered when assessing wave attenuation. Moreover, a series of waveforms for VSP monitoring has been modeled to account for both CO_2 saturation and dynamic fluid effects. The results indicate that an increase in free S_{CO2} corresponds to a time delay in arrivals.

References

[1] J. M. Carcione, C. Morency, and J. E. Santos. "Computational poroelasticity—A review". In: *Geophysics* 75.5 (2010), 75A229–75A243. DOI: 10.1190/1.3474602.

[2] N. Dai, A. Vafidis, and E. Kanasewich. "Wave propagation in heterogeneous, porous media: A velocity-stress, finite-difference method". In: *Geophysics* 60.2 (1995), pp. 327–340. DOI: 10.1190/1.1443769.

[3] W. C. Lo, C. L. Yeh, and J. W. Lee. "Effect of viscous cross coupling between two immiscible fluids on elastic wave propagation and attenuation in unsaturated porous media". In: *Advances in water resources* 83 (2015), pp. 207–222. DOI: 10.1016/j.advwatres.2015.06.002.

[4] Y. Zhang and P. Ping. "Nonmonotonic traveling waves in an unsaturated medium induced by a solid force and fluid mass sources". In: *Advances in Water Resources* 142 (2020), p. 103633. DOI: 10.1016/j.advwatres.2020.103633.

[5] J. M. Carcione and G. Quiroga-Goode. "Some aspects of the physics and numerical modeling of Biot compressional waves". In: *Journal of Computational Acoustics* 3.04 (1995), pp. 261–280. DOI: 10.1142/S0218396X95000136.

[6] Y. Qi, X. Zhang, and L. Liu. "The elastic wave propagation in Lo's three-phase porous media theory-based time-splitting staggered-grid finite-difference method". In: *Journal of Geophysics and Engineering* 22.2 (2025), pp. 399–416. DOI: 10.1093/jge/gxaf012.

[7] W. Guan and H. Hu. "The parameter averaging technique in finite-difference modeling of elastic waves in combined structures with solid, fluid and porous subregions". In: *Communications in Computational Physics* 10.3 (2011), pp. 695–715. DOI: 10.4208/cicp.020810.161210a.

DOI 10.5162/Ultrasonic2025/A6-a1

Development of a method to characterize CMUT receiver behavior

M. Städler[1], J. Kober[1], T. Trittler[1], M. Kircher[2], M. Herzog[1], H. Heuer[3], and J. Hampe[1]
[1] TUD Dresden University of Technology, Else Kröner Fresenius Center for Digital Health, Dresden, Saxony, Germany
[2] Fraunhofer, Institute for Photonic Microsystems, Dresden, Saxony, Germany
[3] Fraunhofer, Institute for Ceramic Systems and Technologies, Dresden, Saxony, Germany
merit.staedler@tu-dresden.de

Abstract: This study presents a method of characterizing the performance of a capacitive micromachined ultrasound transducer (CMUT) as receiver using a chirp signal on the transmitter. This approach enables the spectral analysis of key characterization parameters - sensitivity, bandwidth, and noise equivalent pressure within a single-shot measurement. To assess the effectiveness of the chirp-based approach relative to conventional single-tone excitation, both signal types were applied in a pitch-and-catch experiment involving two distinct CMUT probes. The results demonstrate a higher-resolved bandwidth and improved robustness against uncorrelated acoustic noise when employing the chirp excitation signal.

Keywords: Capacitive Micromachined Ultrasonic Transducers, Ultrasound, Receiver Characterization, Experimental Setup, Synchronized Swept-Sine Technique

Introduction

Capacitive micromachined ultrasound transducers (CMUTs) are attracting increasing interest due to their design flexibility, cost-effective mass production and their capability of monolithic integration within receiver electronics. With high receive sensitivity and broad bandwidth, they are particularly promising for use as receive elements in ultrasonic sensing and imaging applications. To evaluate the influence of different designs on their performance, a characterization of their receiver behavior is essential. To isolate and analyse the receiving performance, the “pitch-and-catch” setup adapted from Klemm et. al [1] is employed. This setup includes two line-of-sight configurations: one with a CMUT and a transmitter facing each other, and another where a hydrophone captures the emitted pressure from the transmitter. This dual approach allows comprehensive sensitivity assessment by comparing the CMUT output with the hydrophone-recorded pressure. In contrast to other studies, particular emphasis is placed on characterizing the receive behavior across a wide frequency spectrum, which is critical for broadband sensitivity analysis and the evaluation of the noise equivalent pressure (NEP). As these information are vital for optimizing CMUTs as the ultrasound transduction mechanism for a wide range of applications [2]. To cover the desired frequency range, common pulse and single-tone (ST) for discrete frequencies or a broadband chirp signal can be used. Whereby multiple STs and a chirp signal can be better compared due to the precisely controlled frequency of a ST [3]. In this work, we present an exponential chirp excitation as an efficient alternative, enabling broadband characterization in a single measurement. This method reduces the need for multiple tone-by-tone acquisitions, allowing sensitivity and NEP to be derived from a single dataset. Two CMUT probes, differing in their diameter of the membrane, are used to be characterized with both signal methods in the "pitch-and-catch" configuration. The results obtained using the exponential chirp are compared with those from conventional ST measurements, using the generated derived characteristics sensitivity, bandwidth and NEP as metric.

Methods

Two excitation signals were employed in the pitch-and-catch experiments: an exponential chirp spanning a bandwidth of 1...16 MHz with a duration of 1 ms, and 32 single sinusoidal tones ranging from 1...16 MHz in 500 kHz steps, each with a duration of 100 µs. Both signal types were recorded using the CMUT probes and a hydrophone. The experimental configuration, illustrated in Fig. 1, consists of a water tank and two independent pitch-and-catch configurations. In both setups, a piezoelectric transmitter (SONOTEC SONOSCAN IK-10-6) was used, driven by a high-bandwidth power amplifier (Mini-Circuits ZHL-32A+) in combination with coaxial fixed attenuators (Mini-Circuits VAT-A-SERIES). As receivers, either a hydrophone (HGL-0400, preamplifier: AH-2010-100; ONDA Corporation) or one of the CMUT

DOI 10.5162/Ultrasonic2025/A6-a1

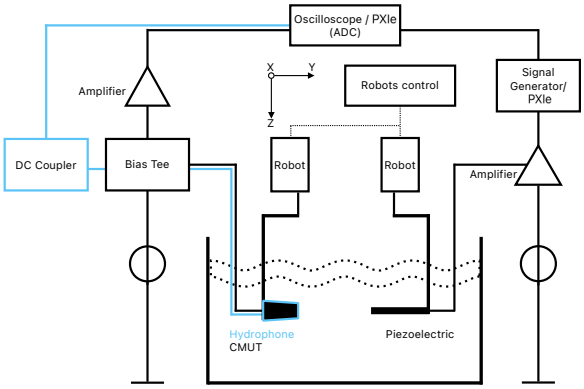

Fig. 1: Schematic presentation of the "pitch-and-catch" measurement setup with both line-of-sight options either an applied hydrophone (in blue) or a CMUT (in black). Figure adapted [1].

probes was aligned with the transmitter at a distance and depth of 60 mm. Each CMUT probe, provided by Fraunhofer IPMS, featured an active area of 250 µm × 250 µm and included an integrated circuit. Therefore, this characterization method inherently reflects the combined performance of both the integrated circuit and the CMUT. Two CMUT variants were evaluated: *CMUT1*, with a nominal frequency (f_0) of 6.5 MHz and a DC bias of 64 V, and *CMUT2*, with a nominal frequency of 8 MHz and a bias voltage of 72 V. These nominal frequencies were determined based on impedance measurements. For consistent comparison, both CMUTs were supplied with 90% of their maximum bias voltage using a custom-designed Eval-Kit ($R = 50\ \Omega$) [4]. Signal generation and data acquisition for the chirp measurements were performed using a National Instruments system consisting of an FPGA controller (NI PXIe-8133) and a FlexRIO transceiver module (NI FlexRIO-5781R). To automate the ST measurements, we used Python-controllable devices. A signal generator (SDG 1062X, SIGLENT) transmitted sinusoidal excitation signals with an amplitude of 1 V_{pp}, while a digital oscilloscope (PicoScope 3406B, Pico Technology) handled data acquisition. Both instruments were synchronized via a trigger. Each ST measurement was recorded 32 times and averaged to reduce noise, whereas the chirp measurement was recorded only once. As the applied chirp signal includes fade-in and fade-out phases, the data corresponding to the first and last frequencies were excluded. This led to a bandwidth range of 2...14 MHz ($[f_1;f_2]$) being considered for the comparison. The chirp data was analyzed using the synchronized swept-sine technique (SST) as described by Novak et al. [5], which allows the separation of individual harmonic orders in the CMUT response. The sensitivity was determined based on the first harmonic to isolate the linear response and eliminate nonlinear effects. It is defined as the ratio between the CMUT's recorded output signal and the reference pressure measured by the hydrophone (Eq. (1)) [1]. The pressure values were derived from the measured voltage, converted to pressure using the calibration data specific to the hydrophone employed.

$$S = \frac{U_{CMUT}}{P_{hydrophone}} \tag{1}$$

To determine the 6 dB bandwidth, the sensitivity spectrum was converted into the dB domain, and the frequency range within 6 dB of the peak sensitivity was calculated as schematically presented in Fig. 2 b) with eq. (2).

$$FBW = \frac{f_{high} - f_{low}}{f_0} \tag{2}$$

The NEP was derived as the ratio of the recorded noise level to the calculated sensitivity and the recorded frequency range ($f_{PXIe} = 100MHz, f_{PicoScope} = 125MHz$) (Eq. (3), Fig. 2).

$$NEP = \frac{U_{noise}}{S \cdot \sqrt{\Delta f}} \tag{3}$$

Noise measurements were conducted in the same water tank environment, with no excitation signal applied. The noise levels observed for the two signal types differ due to variations in the electronic acquisition configurations and the applied averaging methods. Since the absolute noise level of the PXIe system is three times higher than that of the Picoscope, the chirp-based measurement acquired with the PXIe was normalized by a factor of three to ensure comparability. Both spectra, sensitivity and NEP, of both signal types are compared through a deviation calculation. Therefore, the ST dataset is interpolated, and for each frequency in the recorded chirp signal, the difference between the ST amplitude and the chirp amplitude is calculated. Finally, the average of these deviations is computed. As the difference between the sensitivity and NEP spectrum is only a constant factor, only the deviation of the sensitivity spectrum is considered.

Results

The SST of Novak et al. [5] showed that only a second harmonic component was present in the CMUT probe signals, located around the –30 dB level. As a result, no separation of higher harmonic orders was conducted in subsequent calculations. Fig. 2 presents the sensitivity and NEP spectra for both signal excitation methods. Over the full recorded bandwidth,

DOI 10.5162/Ultrasonic2025/A6-a1

a) Sensitivity

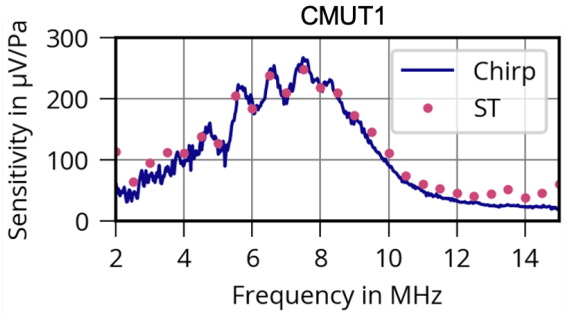

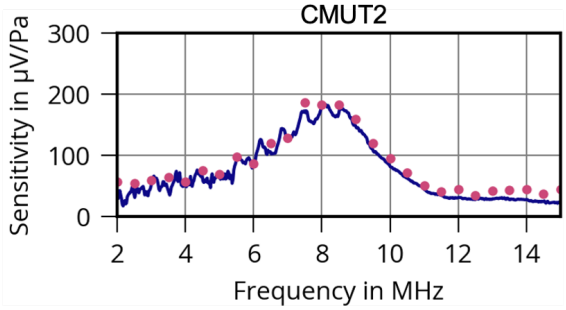

b) NEP

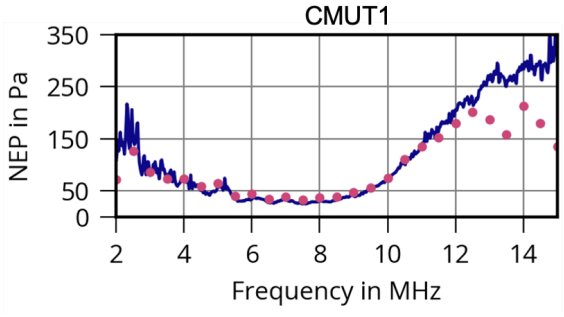

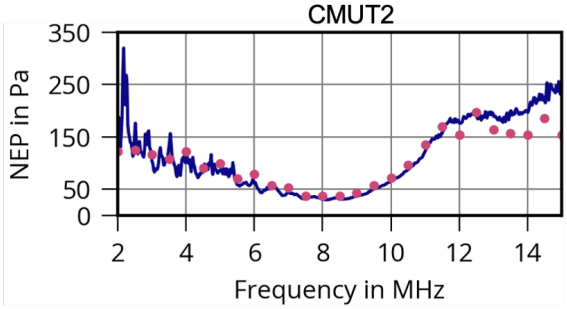

c) Characterization parameters

	CMUT1		CMUT2	
	Chirp	ST	Chirp	ST
S in $\frac{\mu V}{Pa}$	267.35	247.7	183.35	187
f_0 in MHz	7.5	7.5	8.11	7.5
B_{-6dB} in %	63.73	53.33	47.84	46.67
B_{-6dB} range	[4.74; 9.52]	[5.5; 9.5]	[6.08; 9.96]	[6.5; 10]
NEP in $\frac{mPa}{\sqrt{Hz}}$	3.40	3.73	4.13	4.35

d) Bandwidth calculation

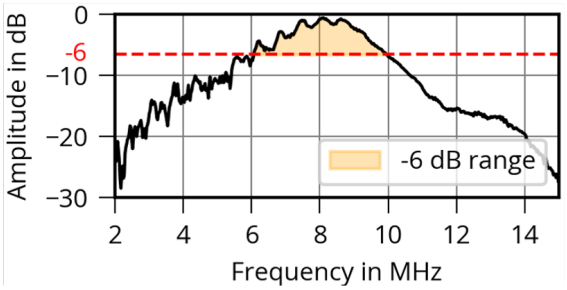

Fig. 2: Comparison of both signal types recorded by the two CMUT probes. Results of the sensitivity (a) and the NEP (b) calculation based on Equation(1) (3) and the characterization parameters (c). (d) Schematic presentation of the bandwidth calculation.

the difference between the signal types amounts to 19.3 % for the *CMUT1* and 14.6 % for the *CMUT2*. When the bandwidth is restricted to a ±4 MHz range around the resonance frequency, the probes exhibit a deviation of 8.9 % and 11.5 %. Even closer, within a ±2 MHz range, the *CMUT1* shows a deviation of 1.7%, and the *CMUT2* showed a deviation of 7.5%. The maximum recorded sensitivity values differed by 7.3% for the *CMUT1*, with both signals showing the maximum at 7.5 MHz. For the *CMUT2*, the deviation in maximum sensitivity between signal types was 1.9% but the resonance frequencies differ. A broader bandwidth was conducted by *CMUT1* (10.4%) and by *CMUT2* (1.17%) when the chirp signal was used. After applying a linear correction factor, the NEP values for *CMUT1* differed by 0.33 mPa/$\sqrt{Hz}$, and for *CMUT2*, by 0.22 mPa/$\sqrt{Hz}$.

Discussion

The chirp-based measurement offers higher frequency resolution within a single acquisition, enabling a more precise determination of the absolute characterization parameters such as resonance frequency and bandwidth range, as illustrated in Fig. 2a. In contrast, the ST measurement required averaging over 32 individual acquisitions to achieve comparable accurate values at a reduced frequency resolution. Despite this, the level of disruption in the lower frequency range is comparable, suggesting that the disturbances are inherent to the measurement setup or probe behavior rather than random noise. In the higher frequency

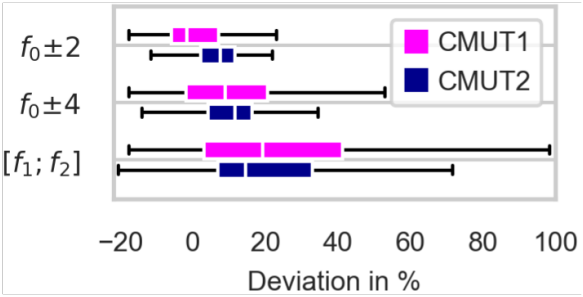

Fig. 3: The percentage deviation of the calculated sensitivity from ST and chirp signal measurements of the CMUT probes is shown in box plots across different frequency ranges.

range, the ST method appears more susceptible to disturbances, leading to a higher number of outliers in the recorded data. Although using smaller frequency steps in the ST approach could improve resolution, it would also significantly increase measurement time. As the improvement of the resolution by a factor of n would require n × m measurements, where m is the number of repetitions for each measurement. Furthermore, from a practical implementation and noise robustness perspective, it is important to note that chirp-based measurements require an excitation and acquisition system with sufficient transmission buffer capacity and an adequately high sampling rate to generate, transmit, and accurately capture chirp waveforms. These requirements may not be met in all hardware setups, potentially limiting feasibility.

Conclusion

The measurements using the chirp signal proved beneficial in terms of reduced acquisition time and higher spectral resolution, enabling a more precise analysis of parameters relevant for receiver behavior characterization. The observed response of the CMUT receivers was consistent across both excitation methods, suggesting that the use of a chirp signal represents a valid and effective alternative for CMUT receiver characterization.

Acknowledgment

This research was supported by the European Union and tax revenues on the basis of the budget adopted by the Saxon State Parliament as part of the project HYBRIDECHO under the grant number 100689694.

References

[1] M. Klemm. *Acoustic simulation and characterization of capacitive micromachined ultrasonic transducers*. en. Dresdner Beiträge zur Sensorik Band 66. Dresden: TUDpress, 2017. ISBN: 978-3-95908-100-9.

[2] J. Joseph, B. Ma, and B. T. Khuri-Yakub. "Applications of Capacitive Micromachined Ultrasonic Transducers: A Comprehensive Review". In: *IEEE Transactions on Ultrasonics, Ferroelectrics, and Frequency Control* 69.2 (2022), pp. 456–467. DOI: 10.1109/TUFFC.2021.3112917.

[3] S. Caporale et al. "Excitation and Deconvolution in Ultrasound Nondestructive Testing Systems". In: *Ultrasonic Nondestructive Evaluation Systems: Industrial Application Issues*. Ed. by P. Burrascano et al. Cham: Springer International Publishing, 2015, pp. 85–140. ISBN: 978-3-319-10566-6. DOI: 10.1007/978-3-319-10566-6_4. URL: https://doi.org/10.1007/978-3-319-10566-6_4.

[4] Fraunhofer-IPMS. *Evaluation kit for CMUTs*. URL: %5Curl % 7Bhttps : / / www . ipms . fraunhofer . de / content / dam / ipms / common / documents / 2024 - 2 / Fraunhofer % 20IPMS % 20 - %20Evaluation % 20Kit % 20for % 20Capacitive % 20micromachined % 20ultrasonic%20transducers.pdf%7D (visited on 06/23/2025).

[5] A. Novak, L. Simon, and P. Lotton. "Synchronized Swept-Sine: Theory, Application, and Implementation". In: *Journal of the Audio Engineering Society* 63.10 (Nov. 2015), pp. 786–798. DOI: 10.17743/jaes.2015.0071. URL: https://hal.science/hal-02504321.

DOI 10.5162/Ultrasonic2025/A6-a2

Design and Technology for Cavity SOI Piezoelectric Micromachined Ultrasonic Transducers (PMUTs) with an Infinite Cell Array Design.

Shubham Mulay[1], *Chris Stoeckel*[1,2], *Falk Schwenzer*[1,2], *and Jörn Bankwitz*[1,2]
[1] *Fraunhofer Institute for Electronics Nano Systems (ENAS), Chemnitz, Germany*
[2] *Technical University of Chemnitz, Center for Micro and Nano Technologies, Chemnitz, Germany*
shubham.mulay@enas.fraunhofer.de

Abstract: Piezoelectric micromachined ultrasonic transducers (PMUTs) using aluminum nitride (AlN) as the active piezoelectric layer represent a powerful and compact alternative to conventional bulk piezoelectric elements. Due to their CMOS compatibility, high mechanical robustness, and strong potential for miniaturization. This paper presents a detailed insight into the design and fabrication and characterization of PMUTs utilizing cavity SOI technology and a unique infinite cell design for improved channel shape and size development.

Keywords: PMUTs, Cavity, SOI, AlN, Cell

Introduction and Motivation

Ultrasound technology is currently undergoing a fundamental transformation, shifting away from bulky, discrete components toward highly integrated, miniaturized systems [1], [2]. In particular, micromachined ultrasonic transducers (MUTs) are enabling entirely new applications in the fields such as medical imaging technology, automotive systems, and consumer electronics due to their compact design and low-voltage electronics integration.

MUTs generate acoustic signals using thin film membranes; these signals can be analyzed through reflection and interaction with objects for both imaging and actuation/sensing purposes. When arranged in arrays, MUTs enable spatially resolved detection and high-resolution ultrasound and photoacoustic imaging [3], [4].

The development of piezoelectric MUTs provides powerful, CMOS-compatible alternatives to traditional bulk piezoelectric elements. AlN has proven to be a particularly well-suited active piezoelectric material, offering excellent thermal stability, low dielectric losses, and outstanding process compatibility with modern silicon technologies [3], [5], [6], [7] [8].

The PMUTs presented in this paper are based on cavity SOI-based membranes and utilize AlN for the generation and detection of ultrasound signals. Fabricated using well established, wafer-based MEMS processes, they enable highly miniaturized, scalable, and cost-effective production. Due to their compact size, low operating voltage, and high integration capability, these PMUTs are ideal for use in portable devices, industrial inline measurement systems, as well as in medical diagnostic equipment.

Operating Principle

PMUTs consist of numerous oscillating membranes that generate ultrasonic waves. Their operation is based on the unimorph principle, wherein a piezoelectric layer is sandwiched between top and bottom electrode and is bonded to a thin, silicon membrane. When an electrical voltage is applied, the membrane deforms due to the inverse piezoelectric effect, generating ultrasonic waves. In contrast, an incoming acoustic wave causes mechanical deformation which is then converted into an electrical signal [2], [7], [8]. This dual functionality enables both the transmission and sensing of ultrasound signals. Figure 1 shows the cross section of a PMUT, after applying a signal between the top and bottom electrode.

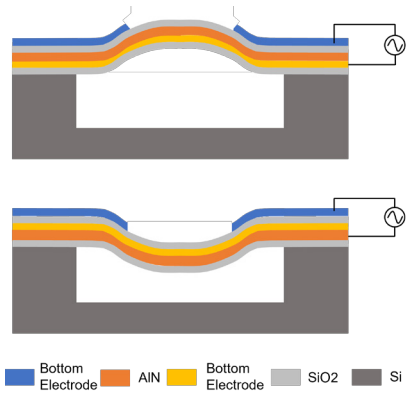

Fig. 1: Cross-section of a PMUT showcasing the operating principle

DOI 10.5162/Ultrasonic2025/A6-a2

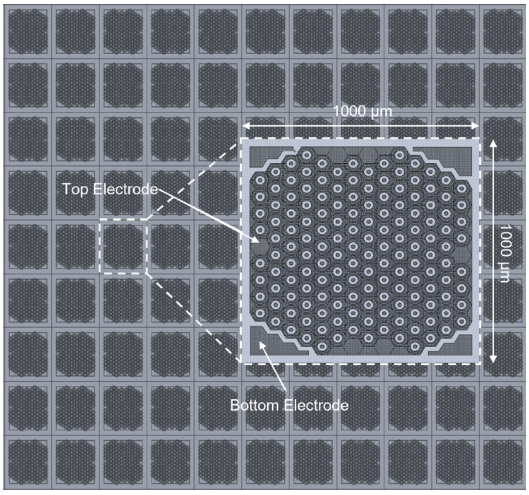

Fig. 2: The design of a PMUT cell array with an enlarged PMUT cell and dimensions

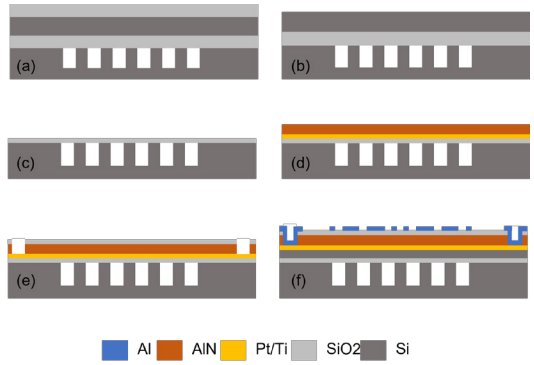

Fig. 3: Process flow of PMUTs for formation of cavities (a) Wafer Bonding (b) Si grinding and etching (c) SiO2 wet etching (d) Deposition of Ti/Pt and AlN (e) via etching for contact to bottom electrode (f) Al depostion and patterning

PMUT Design

A key innovation of this work lies in its patented cell architecture, which offers a high degree of application flexibility. These PMUTs wafer consist of numerous individual cells structures of 1 x 1 mm², each comprising 150 circular membranes. Each PMUT cell can be operated independently or interconnected via wire bonding to form arrays. By adapting the wire bonding layout, the geometry, size, and number of acoustic channels can be freely configured without requiring any changes to the silicon chip design itself. Whether a linear, circular, or complex array configuration is needed, the PMUT chip can be easily tailored to the specific application using automated wire bonding technology.

This post-fabrication reconfiguration of the channel layout enables fast prototyping and modular system integration. The design of the PMUT cell array is shown in Figure 2, The figure shows a small part of the wafer along with a enlarged sketch of the individual PMUT cell. The Four corner areas act as the contact for bottom electrode whereas the top electrode covers the full center area of chips (except for the membranes). The top electrode covers 60 % of the total membrane area for optimal output.

Fabrication

The fabrication of PMUT cells is carried out on two 150 mm wafers which are then bonded together using direct bonding. The PMUTs were fabricated using a simple three mask process.Figure 3 shows a cross-sectional representation of the fabrication process. The fabrication process begins with the deposition of the resist to create cavities in the handle wafer. The resist is then patterned accordingly, followed by DRIE process for etching 25µm Si. These cavities define the position of each PMUT membrane. For the device wafer fabrication, the process begins with the growth of 3 µm thermal oxide on both sides of the Si.

The bonding of the two wafers was performed using direct bonding. To find the optimum bonding parameters the wafers were bonded at room temperature both in atmospheric pressure and in vacuum, step (a). The wafers are then subsequently annealed at 1000 °C to enhance the bond strength and the quality of the interface between the bonded wafers. Figure 4 presents IR images depicting the conditions of the wafers before and after annealing, specifically for those bonded through direct bonding at room temperature in vacuum and under atmospheric pressure.

After bonding, the SiO2 is etched using a wet etch process, step (b). The wafer is then thinned down until 40 µm Si is remaining on top of the SiO2 using a grinding step. This Si is then removed using a dry etching process. The 3000 nm SiO2 is further reduced down to 1500 nm using wet etching forming a thin SiO2 membrane on top of the cavities, step(c).

The Ti/Pt stack is subsequently deposited using a PVD process. 20 nm Ti is deposited which functions as an adhesion layer between Pt and SiO2, while the 100 nm deposited Pt serves two functions, it acts primarily as the bottom electrode for the PMUTs as well as functions as a seed layer for the AlN. Then 600 nm AlN is deposited using PVD, step (d). A thin layer of SiO2 is deposited using PE-CVD, this SiO2 layer acts a hard mask for the AlN etching.

After the SiO2 deposition, the second mask is used to define vias to the bottom electrode through dry etching of the SiO2 and AlN, step (e). Once the vias are etched a final 500 nm of Al top electrode is deposited. In the final step the thrid mask is used

DOI 10.5162/Ultrasonic2025/A6-a2

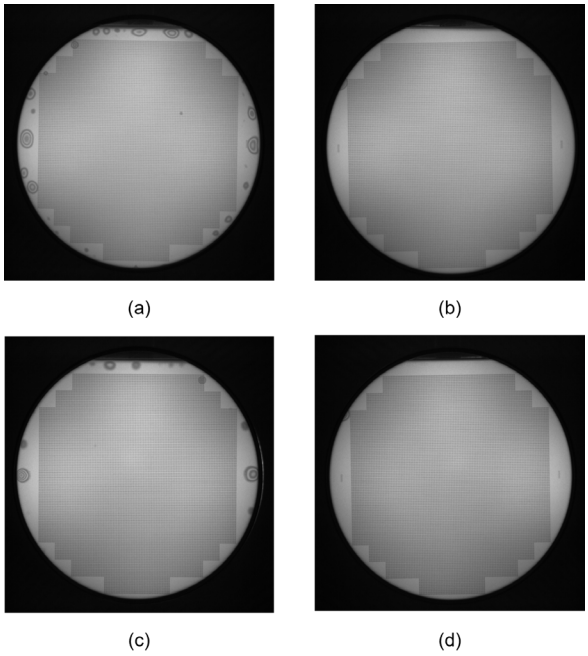

Fig. 4: IR Images of the PMUT wafers after bonding at (a) atmospheric pressure and (b) in vacuum and post annealing IR images of wafers bonded at (c) atmospheric pressure and (d) in vacuum

to pattern the top electrodes of PMUTs. The Al is etched using a wet etch process, step (f). PMUTs with a membrane diameter of 50 µm were fabricated with an overall cell size of 1000 µm x 1000 µm. An optical microscope image of part of the fabricated PMUT array form the wafer is shown in Figure 5.

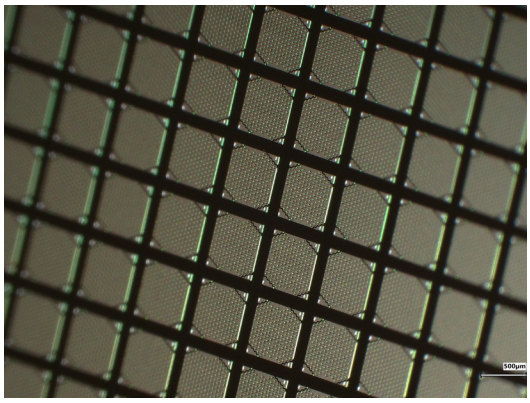

Fig. 5: A microscopic image of a part of a fabricated array from a PMUT wafer

Characterization

The wafer-level electrical characterization of a PMUT cell arrays was carried out.The out-of-plane membrane deflections are recorded at the center using a Polytech

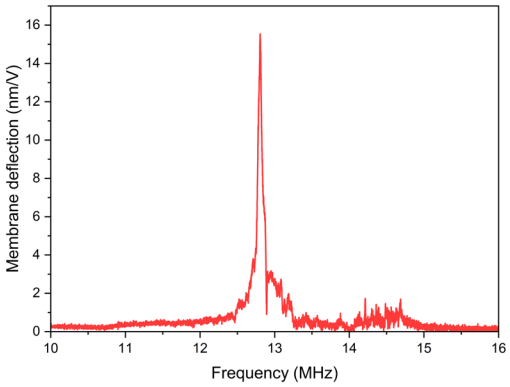

Fig. 6: LDV measurement for the membrane delfrction and frequency of the PMUTs

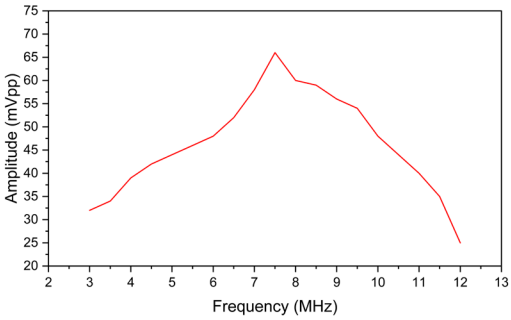

Fig. 7: The Frequency vs Amplitude plot of the PMUTs in an oil bath.

MSA-100 3DLaser Doppler Vibrometer (LDV) with an ACTR-110 axis controller. The PMUTs were actuated with a chirp signal with a voltage amplitude of 1 V and the resonance frequency as well as the membrane deflections were recorded.

These PMUTs exhibit a resonance frequency of around 12.7 MHz in air with a out of plane membrane deflections of 14 nm/V. The resonance frequency varies slightly over the wafer with a standard deviation of 3.1 %. The dynamic membrane deflection of the PMUT membrane is plotted in Figure 6. The electrical capacitance of each cell over the wafer is measured using a an automatic prober (Karl Suss PA-200) and an LCR meter (Keysight, E4980A) and was found to be around 57 pF.

The transmit performance of the PMUT array was measured using an acoustic hydrophone (Müller Instruments, Germany) in an oil bath. A 3 mm x 1 mm linear PMUT array was fistly diced, mounted and wire bonded to a PCB. The PMUT linear array was excited by connecting it to the function generator and actuating it with a square burst wave of 5 cycles of 10 V and the frequency response was recorded at 10

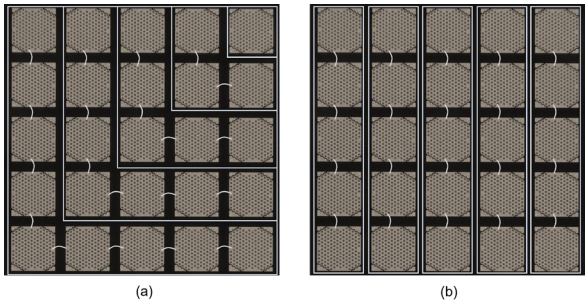

Fig. 8: Wire bond plans for (a) Matrix arrangement of cells (b) linear arrangement of cells

mm. The output of the hydrophone was connected to an oscilloscope through a preamplifier. The maximum pressure was recorded at 7.5 MHz. Figure 7 shows the frequency vs amplitude of PMUTs in Oil.

Modular Chip and Cell array design

A significant advancement of this technology is its PMUT cell architecture, which provides extreme flexibility for various applications. As the entire wafer consists of numerous PMUT cells, allowing for flexible chip configuration and customized form factors by adapting custom wafer dice plans. Furthermore, each PMUT cell can function independently or be connected through wire bonding to create various array shape and size.

By adapting the wire bonding layout, it is possible to customize the geometry, dimensions, and quantity of acoustic channels without necessitating alterations to the design of the silicon chip. The PMUT chip can be readily adapted to accommodate various configurations, including linear, circular, or intricate arrays, utilizing automated wire bonding technology. This ability to reconfigure the channel layout after fabrication facilitates rapid prototyping and supports modular system integration. Figure 8 show two of these custom array geometry.

Conclusion

The design, fabrication and characterization PMUTs based on cavity SOI platform with an infinite cell design was discussed in this paper. A simple 3-mask fabrication process for the development of AlN based PMUT was developed and PMUTs with 50 µm membrane diameter were successfully fabricated. This cavity SOI-based process enables fabrication of smaller diameter membranes, overcoming the challenges of high aspect ratios faced in traditional DRIE-based Si back etching for small membranes.

The post fabrication mechanical electrical and acoustic characterization was carried out to evaluate the performance of the PMUT cell arrays. These PMUTs exhibit a resonance frequency of 13 MHz in air and the frequency shifts to 7.5 MHz in liquids with an overall bandwidth of 110 % in liquids. The capacitance/cell of the PMUTs is 57 pF.

The advanced PMUT cell architecture design offers exceptional flexibility in chip configuration, enabling the customization of acoustic channels without altering the silicon chip design. This adaptability allows for the creation of various array shapes and sizes, facilitating rapid prototyping and seamless integration into modular systems.

References

[1] J. Wang, Z. Zheng, J. Chan and J. T. Yeow, 'Capacitive micromachined ultrasound transducers for intravascular ultrasound imaging,' *Microsystems & nanoengineering*, vol. 6, no. 1, p. 73, 2020.

[2] Y. Lu and D. A. Horsley, 'Modeling, fabrication, and characterization of piezoelectric micromachined ultrasonic transducer arrays based on cavity soi wafers,' *Journal of Microelectromechanical Systems*, vol. 24, no. 4, pp. 1142–1149, 2015.

[3] J. Cai et al., 'Beyond fundamental resonance mode: High-order multi-band aln pmut for in vivo photoacoustic imaging,' *Microsystems & nanoengineering*, vol. 8, no. 1, p. 116, 2022.

[4] A. Dangi et al., 'A photoacoustic imaging device using piezoelectric micromachined ultrasound transducers (pmuts),' *IEEE transactions on ultrasonics, ferroelectrics, and frequency control*, vol. 67, no. 4, pp. 801–809, 2019.

[5] S. Shelton et al., 'Cmos-compatible aln piezoelectric micromachined ultrasonic transducers,' in *2009 IEEE International Ultrasonics Symposium*, IEEE, 2009, pp. 402–405.

[6] R. J. Przybyla et al., 'In-air rangefinding with an aln piezoelectric micromachined ultrasound transducer,' *IEEE Sensors Journal*, vol. 11, no. 11, pp. 2690–2697, 2011.

[7] C. B. Karuthedath, A. T. Sebastian, P. Helistö, T. Sillanpää and A. Kärkkäinen, 'Development of scaln pmuts for medical applications,' *Journal of microelectromechanical systems*, vol. 32, no. 5, pp. 505–512, 2023.

[8] C. Stoeckel, K. Meinel, M. Melzer and T. Otto, 'Thin film piezoelectric aluminum nitride for piezoelectric micromachined ultrasonic transducers,' in *2018 IEEE SENSORS*, 2018, pp. 1–4. DOI: 10.1109/ICSENS.2018.8589845

DOI 10.5162/Ultrasonic2025/A6-a3

New manufacturing technique based on microsystems technology for flexible polymer ultrasonic arrays

A. Jakob[1], W. Haberer[1], M.O. Krob[1], P. Weber[1], and F. Tiefensee[1]
[1]Fraunhofer-Institut für Biomedizinische Technik IBMT, Joseph-von-Fraunhofer-Weg 1, 66280 Sulzbach, Germany
anette.jakob@ibmt.fraunhofer.de

Abstract: This work presents a top-down manufacturing technology for the fabrication of flexible ultrasonic arrays made of polymer PMUTs. The top-down fabrication allows all contacting from the backside of the PMUTs and thus the aperture area stays free from any electrical contacts. The PMUTs of the fabricated array and test structures have center frequencies between 100 kHz and 450 kHz and an average 6 dB bandwidth of 8 %. The maximum amplitude in air for any membrane was 100 nm with a sinusoidal excitation of 10 Vpp. The bending radius of the array was 10 mm.

Keywords: flexible array, top-down fabrication, polymer PMUT

Introduction

The international state of the art in the fabrication of ultrasonic transducers is currently still dominated by the application of the piezoelectric ceramic PZT. Increasing demands on the environmental compatibility of the applied materials, energy efficiency, design options for the array, low manufacturing costs and increased demand have led to the development of PMUTs (piezoelectric micromachined ultrasonic transducers) and CMUTs (capacitive micromachined ultrasonic transducers). Both types of transducers are fabricated using microsystems technology. The state of the art in CMUTs corresponds to the developments in Prof. Khuri-Yakub's working group at Stanford University in California. Many publications on this topic can be found at https://profiles.stanford.edu/butrus-khuri-yakub. Prof. Khuri-Yakub is considered as the inventor of CMUTs and his work over the last 30 years describes the development of CMUTs. While this research group develops CMUTs with silicon technology, Gerardo et al [1] built an array of polymer CMUTs. Other works on polymer CMUTs are mainly focused on flexibility or transparency [2];[3];[4]. Although PMUTs can generate a higher sound pressure, have a higher sensitivity and do not require an additional bias voltage, the development of micromachined ultrasonic transducers was focused on CMUTs for a long time. The development of PMUTs was in the background because a high bandwidth is easier to achieve with CMUTs and this feature is necessary for a clear ultrasound imaging. This disadvantage was overcome with the work of Hajati et al [5] and Dausch et al [6]. Using innovative membrane designs, they succeeded in increasing the bandwidth to up to 170% . These two working groups are building PMUT arrays with silicon technology. The research groups of Paul Heremans and Jan Genoe at the Catholic University of Leuven and at imec in Leuven are working in the field of PMUTs made of polymer. However, they mostly produce PMUTs according to the conventional down-top principle. So far only one of their publications reports on the fabrication of PMUTs using the top-down method [7]. However, the fabrication route described there does not appear to benefit from the advantages of the top-down approach, as the PMUTs are contacted in the aperture area. The present work describes the manufacturing of flexible polymer PMUTs using the top-down approach. The PMUTs are contacted from their rear side and the aperture area remains free of electrical contacts.

Simulation

The micromachined manufacturing of PMUTs requires several masks for photolithographic structuring. To determine the necessary manufacturing steps and the dimensions of the masks required for this, the shapes of the PMUTs were simulated at the beginning.The simulations of the oscillation behavior of a single PMUT were performed using the finite element method with Ansys software. The following material parameters were used for the simulations with Ansys: polymer photoresist dry film ADEX™ from DJ MicroLaminates, Inc. (E = 4 GPa, density = 1.5 g/cm^3, Poisson number = 0.22), zinc oxide (ZnO) (E = 120 GPa, density = 5.68 g/cm^3, Poisson number = 0.34), polyimide (E = 2.6 GPa, density = 1.29 g/cm^3, Poisson number = 3.5). The finite element model for the simulation with ANSYS was a two-dimensional, rotationally symmetrical model, so that the entire three-dimensional geometry was taken into account. Figure 1 shows the

DOI 10.5162/Ultrasonic2025/A6-a3

results of the simulation in comparison with the measured center frequencies from Table 1. For disc-shaped ZnO and electrodes on the membranes a good agreement between the measurements and the simulation can be seen. For the ring-shaped ZnO and electrodes on the membranes, there was a deviation at lower frequencies. But at higher frequencies the geometry of PMUTs with ring-shaped ZnO and electrodes can be simulated with sufficient accuracy.

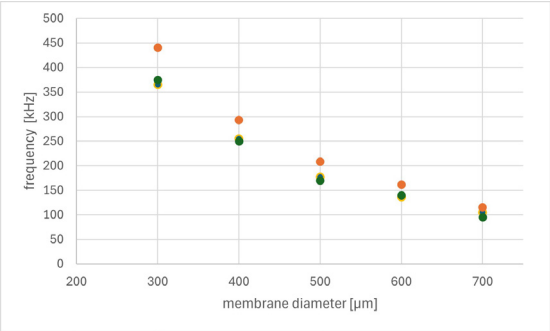

Fig. 1: green dots for measurement results of disc-shaped ZnO and eletrodes and orange dots for mesurement results of ring-shaped ZnO and electrodes, yellow dots for simulation results of disc-shaped ZnO and eletrodes.

Fabrication

With the results of the simulations the shape and dimensions of test structures and a linear array with 32 elements and a center frequency of 300 kHz were determined. Each element of the array should have 2 x 70 PMUTs. The linear array was placed in the center of a wafer and the remaining area was filled with test structures of 2 x 2 PMUTs of different diameters and thus different frequencies. The diameters of the PMUTs of the test structures were 300 µm, 400 µm, 500 µm, 600 µm and 700 µm. The PMUTs were manufactured according to the fabrication steps described below:

1) Application of a 5 µm thick layer of polyimide (PI) with additives on a silicon wafer using spin coating. 2) Application of a second 5 µm thick layer of PI on the first PI layer. 3) Deposition of a 300 nm thick platinum ground electrode by sputtering. The pads for contacting the array with an electronic were placed after the first and last PMUTs of an array element. The vias for contacting the top electrode were positioned between the array elements at approx. 100 µm from the PMUT's edge of an array element. 4) Sputtering of the piezoelectric zinc oxide (ZnO) and its photolithographic structuring using a wet etching process. The dimensions of the ZnO layer were kept slightly smaller than those of the ground electrode. In this way, the ZnO could be applied exclusively to the ground electrode. 5) Deposition and structuring of the platinum top electrode with titanium as an adhesion aid on the structured ZnO using a lift-off process and sputtering. The ZnO and the top electrode were made disc-shaped and ring-shaped. Figure 2a schematically shows the status after fabrication step 5).

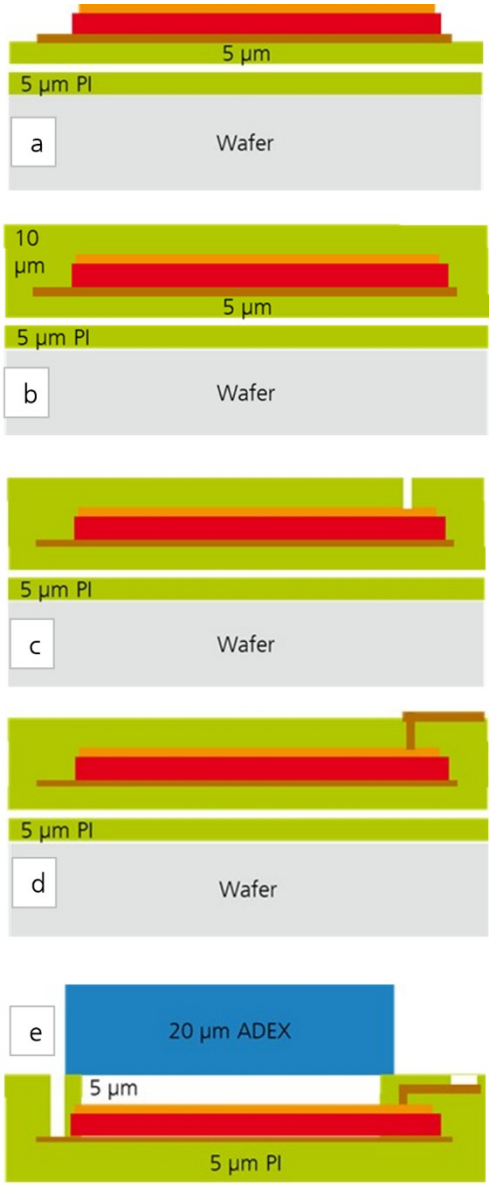

Fig. 2: schematical description of the steps involved in the new top-down PMUT manufacturing process.

6) Application of a 10 µm thick layer of PI using spin coating and structuring the via holes for contacting the top electrode using reactive ion etching. Figures 2b and c schematically show these fabrication steps. 7) The 70 via holes of one element were connected to each other. The contact was routed to the outside

DOI 10.5162/Ultrasonic2025/A6-a3

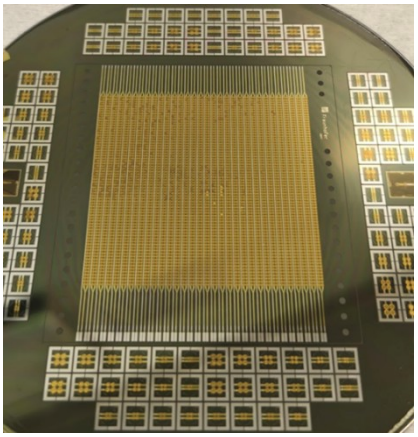

Fig. 3: photo of the 32-element linar array in the center and test structures araound on a wafer.

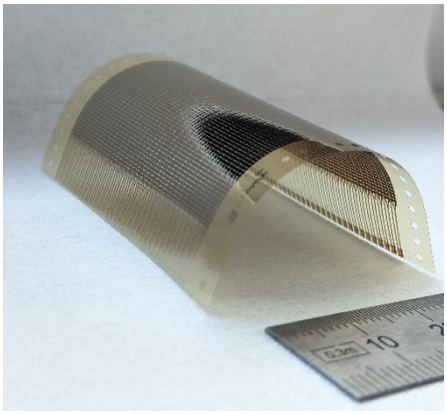

Fig. 4: photo the flexible array with a bending radius of 10 mm.

of the array. The deposition and structuring of the platinum was carried out using a lift-off process and sputtering. Figure 2d schematically shows the status after the step 7). 8) Application of a further 5 µm thick PI layer. 9) The cavity and the electrical contacts were structured using reactive ion etching. 10) Lamination and structuring of a 20 µm thick ADEX film on the cavity for stabilization. The ADEX was laminated onto the entire surface of the wafer and then structured lithographically. The array and the test structures are detached between the first and second 5 µm PI layer. Figure 2e shows the structure of the resulting PMUT cell.

Results

Figure 3 shows a photo of the wafer with the finished linear array and test structures and figure 4 demonstrates the flexibility of the array with a bending radius of 10 mm.

The bandwidth and the oscillation behavior of the

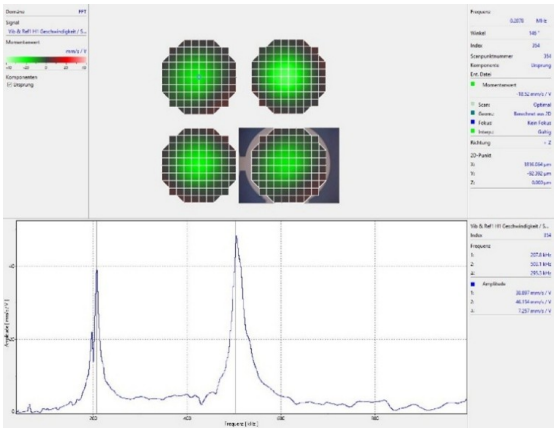

Fig. 5: averaged spectrum of a 500 µm test structure, fundamental oscillation 208 kHz, first harmonic 503 kHz.

Tab. 1: frequencies of the fundamental oscillation of the test structures.

Diameter µm	disc-shaped structure kHz	ring-shaped structure kHz
300	365	440
400	255	293
500	177	208
600	136	161
700	105	115

test structures and the array were determined using the UHF-120 vibrometer from Polytec GmbH. Circuit boards for contacting and holding the foil-like structures were designed and commissioned externally. The center frequency and the 6dB bandwidth were determined with a pulse-shaped electrical excitation and a Fast Fourier Transformation. Figure 5 shows an example of the frequency spectrum of a 2 x 2 test structure with 500 µm diameter membranes. The fundamental oscillation is at 208 kHz and the first harmonic at 503 kHz. Table 1 shows the frequencies of the fundamental oscillation of the test structures as a function of the membrane diameter. In all cases, the max. 6 dB bandwidth was approx. 8 %.

For the examination of the oscillation behavior, the membranes were excited with a sine burst with 50 cycles and 10 Vpp. The surface of the membranes was scanned with approx. 100 measuring points. Figure 6 shows an example of the oscillation behavior of a 500 µm membrane with a ring-shaped ZnO layer and electrodes. The amplitudes of the fundamental oscillation at 10 Vpp were 100 nm for all membranes

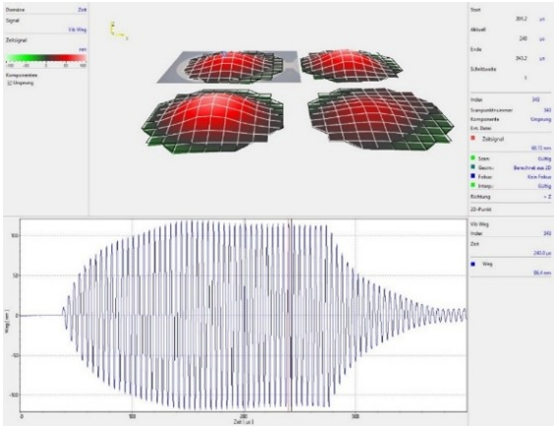

Fig. 6: oscillation of a 500 µm membrane excited with a sine burst of 10 Vpp and 50 cycles.

regardless of the shape of the ZnO and the electrodes.

Summary

The top-down manufacturing technology presented here enables the fabrication of flexible arrays made of polymer PMUTs. The advantage of top-down fabrication is the contacting from the backside of the array and therefore the free array aperture. The PMUTs have center frequencies between 100 kHz and 450 kHz according to the selected dimensions. The measured average 6 dB bandwidth of 8 % is too small for ultrasound imaging and further work must be invested to increase bandwidth. In this context alternative membrane geometries could be tested. The developed simulation tool calculates the geometries of PMUTs with disc-shaped ZnO and electrodes with good accuracy. Higher frequencies over 1 MHz for medical imaging can be easily achieved with smaller membrane diameters. The maximum amplitude in air for each membrane was 100 nm with a sinusoidal excitation of 10 Vpp. The bending radius of the flexible array was 10 mm. Further investigations into beam forming are planned once the driving electronics have been finalized. With the piezoelectric polymer PVDF or thin translucent ZnO and electrodes made of transparent indium tin oxide, transparent PMUTs could also be produced in the future.

References

[1] C. D. Gerardo, E. Cretu, and R. Rohling. "Fabrication and testing of polymer-based capacitive micromachined ultrasound transducers for medical imaging". In: *Microsystems & nanoengineering* 4 (2018), p. 19. DOI: 10.1038/s41378-018-0022-5.

[2] A. Omidvar et al. "Flexible Polymer-based Capacitive Micromachined Ultrasound Transducers (polyCMUTs): Fabrication and Characterization". In: *IEEE IUS 2021*. Piscataway, NJ, USA: IEEE, 2021, pp. 1–4. ISBN: 978-1-6654-0355-9. DOI: 10.1109/IUS52206.2021.9593645.

[3] A. Omidvar et al. "Flexible PolyCMUTs: Fabrication and Characterization of a Flexible Polymer–Based Capacitive Micromachined Ultrasonic Array for Conformal Ultrasonography". In: *Advanced Materials Technologies* 8.5 (2023). ISSN: 2365-709X. DOI: 10.1002/admt.202201316.

[4] M. Ghavami, M. R. Sobhani, and R. Zemp. "Transparent Dual-Frequency CMUT Arrays for Photoacoustic Imaging". In: *IEEE transactions on ultrasonics, ferroelectrics, and frequency control* 70.12 (2023), pp. 1621–1630. DOI: 10.1109/TUFFC.2023.3331356.

[5] A. Hajati et al. "Monolithic ultrasonic integrated circuits based on micromachined semi-ellipsoidal piezoelectric domes". In: *Applied Physics Letters* 103.20 (2013). ISSN: 0003-6951. DOI: 10.1063/1.4831988.

[6] D. E. Dausch et al. "In vivo real-time 3-D intracardiac echo using PMUT arrays". In: *IEEE transactions on ultrasonics, ferroelectrics, and frequency control* 61.10 (2014), pp. 1754–1764. DOI: 10.1109/TUFFC.2014.006452.

[7] S. V. Joshi, S. Sadeghpour, and M. Kraft. "Bendable Polymer-Based High-Frequency pMUTs on Transparent SU8 and Polyimide Substrates". In: *2023 22nd International Conference on Solid-State Sensors, Actuators and Microsystems (Transducers)*. 2023, pp. 849–852.

DOI 10.5162/Ultrasonic2025/A8-a1

Sixty-Seven Years in Nonlinear Acousto-Optics

Laszlo Adler[1]
[1] The Ohio State University, Integrated Systems Engineering
Clearwater, Florida, United States of America

Abstract: In the late 1950s the Ultrasonic Group at Michigan State University introduced light diffraction to study distortion of ultrasonic waves in liquids under the direction of Professor Egon Hiedemann. In this paper, some results of these studies will be presented (with a detailed description of the author's measurements of B/A). The rate at which the harmonics are developed (the wave distortion is an indication of the harmonics present) during the propagation of the initially sinusoidal ultrasonic wave depends on the nonlinearity of the medium. The light which is diffracted by the distorted wave results in an asymmetric pattern contrary to Raman–Nath theoretical prediction. From the light intensity measurements due to the generated second harmonics—filtered out by a metal plate—the Nonlinearity Parameter B/A was determined. In the 1970s at the University of Tennessee, a similar filtering technique was also applied to study imaging mechanisms in the Bragg diffraction region of finite amplitude waves. Developments in studying finite amplitude standing ultrasonic waves in a liquid filled cavity will be also discussed. Using light diffraction measurements, it was observed that above a threshold amplitude, fractional harmonics of the driver transducer are also generated in addition to the generated harmonics. Some of these fractional harmonics are lower and some of them are higher frequencies than the frequency of the driver. The generation mechanism of the fractional harmonics is explained based on parametric resonance. It was recently observed that above a second threshold value of the driver's amplitude, the system undergoes chaotic behavior. Further increase of the driver's amplitude returns the system from chaos to stable oscillation.

Keywords: Nonlinear, Acousto-Optics, Subharmonics, Chaos, Liquids

Introduction and Background

Diffraction of Light by Ultrasonic Waves

Ever since it was predicted by Brillouin [1] in 1922 that light will be scattered by ultrasound in transparent materials, thousands of investigators studied the interaction of light with ultrasound. In 1932 Debye and Sears [2] in the USA and Lucas and Biquard [3] in France independently observed that when a monochromatic light beam propagates perpendicularly through an ultrasonic beam, the light will diffract into several orders (Brillouin actually predicted that the light will produce only a single order after the interaction with the ultrasound). A theoretical model was suggested by Sir Raman and Nath [4] (it is known today as Raman–Nath theory). They proposed that the ultrasonic wave behaves like a diffraction grating for the light which will produce the diffraction orders. Starting with the electromagnetic wave equation and introducing a variable refractive index for the light, they were able to predict the intensity of each order as well as the positions of the orders. The intensity of the diffracted light in the nth order is given in Eq. (1),

$$I_n = \mathrm{J}_n^2(v). \tag{1}$$

J_n is the nth order Bessel function with the argument v, which is called the Raman–Nath parameter related to the pressure of the ultrasonic wave.

$$v = \frac{2\pi\mu a}{\lambda}, \tag{2}$$

where a is the width of the sound field, λ is the wavelength of the light, and μ is the variation of the refractive index of the liquid due to the density variation caused by the ultrasonic pressure. The angle Θ of the diffracted light is given by

$$\sin(\Theta) = \frac{n\lambda}{\lambda^*} \tag{3}$$

where λ^* is the wavelength of the sound.

Diffraction of Light by Finite Amplitude Ultrasonic Waves

For higher ultrasonic frequencies the spacing between orders is larger than for the smaller ones. The intensity distribution of the diffracted light is symmetrical, i.e. the intensity of the first diffracted light to the right from the incident light is the same as to the left, because it is the square of the Bessel functions. The theory of Raman and Nath was in good agreement

DOI 10.5162/Ultrasonic2025/A8-a1

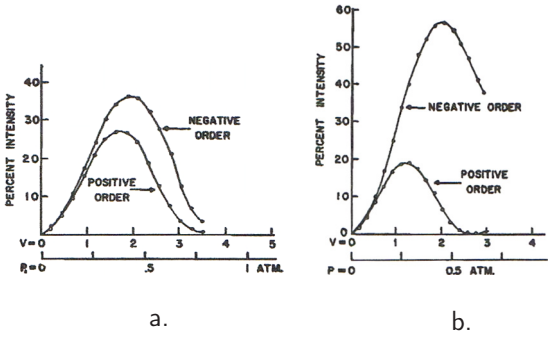

Fig. 1: Intensity of light measured in the first order for a $4\,\mathrm{MHz}$ *ultrasonic wave in water as a function of the pressure at a distance from the source: a. at* $10\,\mathrm{cm}$ *and b. at* $50\,\mathrm{cm}$.

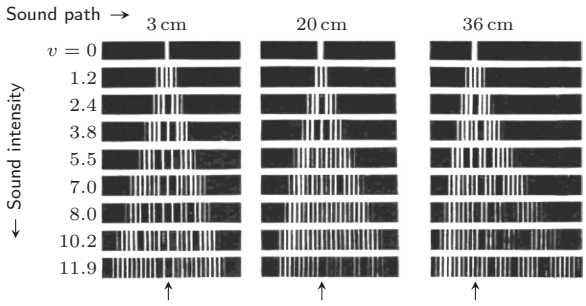

Fig. 2: Light diffraction by ultrasonic waves in water with frequency of $1.76\,\mathrm{MHz}$ *at* $3\,\mathrm{cm}$, $20\,\mathrm{cm}$, *and* $36\,\mathrm{cm}$.

with the experimental results for low-intensity ultrasound, i.e. for infinitesimally small ultrasonic amplitudes. Ken Zankel [5] observed asymmetry in the diffraction pattern. One possible explanation was the non-normal incidence of the light to the sound field. This was eliminated by proper alignment. There could have been another explanation for the asymmetry in the diffraction pattern—frequency range, width of the sound field—however it was demonstrated that the major effect of the asymmetry is due to the large amplitude of the ultrasonic waves or the so-called finite amplitude, in contrast with the infinitesimal amplitude. As a sinusoidal wave propagates with finite amplitude the ultrasonic wave form distorts due to the nonlinearity of the medium, producing harmonics, thus causing the asymmetry in the light diffraction pattern. The asymmetry in the first orders (the difference in the negative and positive order) of the measured light intensity is increasing with distance, as shown in Fig. 1, illustrating that the wave distortion increases with distance. The asymmetry in the diffraction pattern also increases with the increase of fundamental pressure as illustrated on a photograph in Fig. 2, which was taken by Mack Breazeale [6]. The asymmetry in the diffraction pattern is increasing with increasing distance of the ultrasound and with increasing sound intensity as illustrated in Fig. 2. The distortion of the ultrasonic waveform will be explained after a brief review of nonlinear acoustics which is described briefly in the next section.

Nonlinear Acoustics in Fluids

In general, a sound beam changes the wave shape as it propagates in a fluid (as well as in solids), whose pressure-density relationship does not obey Hooke's law. This means that harmonics are generated as the wave progresses. For infinitesimal amplitudes, the change in wave shape is so small that it can be neglected, however, it has to be considered for finite amplitude waves. The distortion of a finite amplitude wave is due to the nonlinear property of the medium in which the wave propagates. The positive and negative increment in pressure is impressed on the medium. The change in the volume of the mass not being equal, the volume change for positive pressure will be less than the volume change for negative pressure. Thuras, Jenkins, and O'Neil [7] in 1935 studied finite amplitude effects in gases. They have pointed out that the equation of state for adiabatic processes (such as sound propagation) shows that the linear relationship between pressure and volume does not hold and consequently leads to distortion of the wave. They derived a nonlinear wave equation and obtained an approximate solution for the generation of harmonics as a function of distance, fundamental pressure and frequency. Fox and Wallace [8] in 1959 following the same argument for liquids assumed a power series of relation between pressure and density

$$P = P_0 + A\frac{\rho-\rho_0}{\rho_0} + \frac{B}{2}\left(\frac{\rho-\rho_0}{\rho_0}\right)^2, \qquad (4)$$

where P and ρ are the instantaneous pressure and density of the liquid respectively, P_0 and ρ_0 are the pressure and density of the undisturbed liquid, and B/A is called the Nonlinearity Parameter for liquids. They derived a nonlinear wave equation for liquids, given in Eq. (5) for a one dimensional dissipationless case for the particle displacement ξ

$$\frac{\partial^2\xi}{\partial t^2} = c^2\frac{\partial^2\xi}{\partial x^2}\Bigg/\left(1+\frac{\partial\xi}{\partial x}\right)^{(B/A+2)}, \qquad (5)$$

where ξ is the particle displacement and c is the velocity of sound in the liquid.

DOI 10.5162/Ultrasonic2025/A8-a1

For infinitesimal amplitude waves the value of $\partial\xi/\partial x$ is much less than 1, and it can be neglected and Eq. (5) reduces to the linear wave equation as expected. Fox and Wallace also suggested a graphical analysis of the distorted wave. As they pointed out, the gradually steepening wave front would ultimately form a discontinuity without some stabilizing mechanism. This stabilizing mechanism is the attenuation of the ultrasound in the medium. Fox and Wallace also evaluated the Nonlinearity Parameters B/A for some liquids from compressibility data. Fubini-Ghiron [9] in 1935 used an analytical method to obtain an exact solution of the nonlinear wave equation, the paper which was published in Italian in the Alta Frequenza was not discovered before the same solutions were obtained independently by Hargrove [10] (at Michigan State University) and Keck and Bayer [11] (Brown University) in 1960. The solutions of Eq. (5) for the pressure amplitudes P_n of the nth harmonic of the distorted wave is given as,

$$P_n(k) = \frac{2P_1(0)}{nk} \mathrm{J}_n(nk), \tag{6}$$

where J_n is the nth order Bessel function, $k = x/L$, the ratio of the propagation distance x to the discontinuity distance L, that is the distance in a dissipationless liquid where the distorted wave slope will become infinite. The value of L is given by

$$L = c^3 \rho_0 \left(2 \left(\frac{B}{2A} + 1 \right) P_1(0) f \right)^{-1}, \tag{7}$$

where $P_1(0)$ is the peak acoustic pressure amplitude of the initial sinusoidal wave with frequency f.

Determination of the Nonlinearity Parameter B/A for Liquids [12]

One can calculate an expression for the amplitude of the second harmonic at any distance x from the source by expanding the Bessel function in a power series and dropping higher-order terms

$$P_2(x) = \frac{\pi}{2} \frac{B/A + 2}{\rho_0 c^3} x f P_1^2(0). \tag{8}$$

From Eq. (8), the Nonlinearity Parameter B/A is given by

$$B/A = \frac{2c^3 \rho_0}{\pi f} \frac{P_2(x)}{x P_1^2(0)} - 2. \tag{9}$$

Curves representing $P_2(x)/P_1^2(0)$ for a given medium, temperature, and frequency, and for various distances and initial pressures should extrapolate with zero slope to a common point for $xP_1(0) = 0$. The Nonlinearity Parameter B/A may then be determined from

$$B/A = \frac{2c^3 \rho_0}{\pi f} \left[\frac{P_2(x)}{x P_1^2(0)} \right]_{xP_1(0)=0} - 2. \tag{10}$$

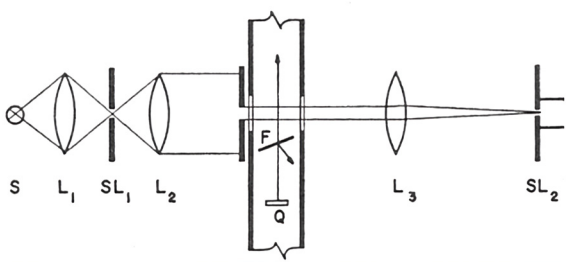

Fig. 3: Schematic diagram of the experimental arrangement.

As can be seen from Eq. (10), the amplitude of the second harmonic $P_2(x)$ and the amplitude of the fundamental $P_1(0)$ need to be measured to obtain the value of B/A for a given liquid and at a given frequency of the initial ultrasonic waves.

Experimental Arrangement and Procedure to Determine B/A

The experimental arrangement is shown schematically in Fig. 3. Light from the Hg-vapor lamp S is condensed by lens L_1 onto the source slit SL_1. The lens L_2 is adjusted by autocollimation to render the light parallel. The collimated light beam passes through a specially designed tank, and lens L_3 produces an image of the source slit SL_1 in the plane of the entrance slit SL_2 of the photomultiplier microphotometer P. A filter which passes the $5461\,$Å Hg line is located inside the photomultiplier. The transducer Q is an air-backed $1\,\mathrm{in} \times 1\,\mathrm{in}$ quartz excited at its fundamental frequency. The acoustic filter F is a stainless steel plate with a $1\,\mathrm{mm}$ thickness. When light passes through an ultrasonic wave in the liquid, various orders of diffraction are observed in the plane of the photomultiplier entrance slit. The peak change of refractive index μ is related to the peak sound pressure amplitude, a is the distance the light travels through the sound field and λ is the wavelength of light. From measurements of light intensity in the diffracted orders v may be determined from Eq. (2). To determine the pressure amplitude P from v the relationship between the change of refractive index μ and change in pressure P must be known. It is common usage to express the relationship between the change of refractive index and pressure by means of the theoretically derived expression obtained in 1880 by Lorentz–Lorenz [13]. They assumed that the molecules are optically isotropic. It is known, however, that it is not true for most liquids. In this work we used a formula obtained by Eykman [14] in 1895:

$$\mu = \frac{(\mu_0 - 1)(\mu_0 + 1.4\mu_0 + 0.4)}{\mu_0^2 + 0.8\mu_0 + 1} P, \tag{11}$$

DOI 10.5162/Ultrasonic2025/A8-a1

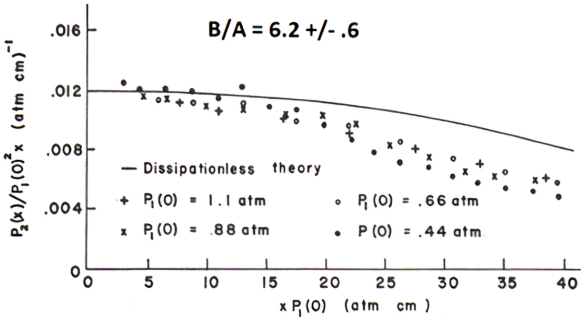

Fig. 4: Plot of reduced variables for determination of B/A in water.

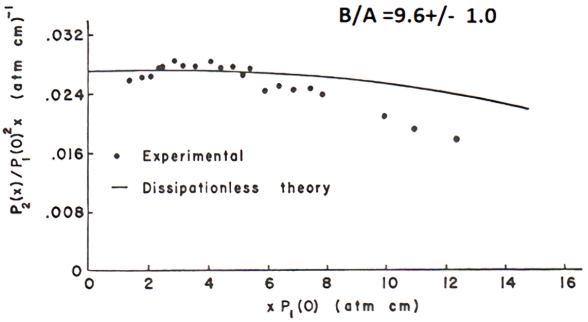

Fig. 5: Plot of reduced variables for determination of B/A in m-xylene.

where μ_0 is the refractive index of the undisturbed medium and P is the change of pressure.

Using Eq. (11) we obtain the relationship between P and v:

$$P = 0.56v/a\,\mathrm{atm} \tag{12}$$

for water and

$$P = 0.25v/a\,\mathrm{atm} \tag{13}$$

for m-xylene, where a is in cm.

Determinations of $P_1(0)$ were made from diffraction order light intensities for small sound amplitudes and near the transducer, where the waveform is undistorted (a necessary condition to use Raman–Nath theory, Eq. (1)). It was then assumed that the voltage across the transducer and $P_1(0)$ are linearly related. Values of $P_1(0)$ were obtained from the voltage across the transducer. For certain angles of incidence of the ultrasonic wave on the acoustic filter plate the fundamental component of the ultrasonic wave is reflected, and the second harmonic is transmitted [5, 15]. Using a weak ultrasonic wave with fundamental frequency corresponding to the second harmonic frequency of the finite amplitude wave to be investigated, measurements of the second harmonic component of the finite amplitude ultrasonic waves were made in water and in m-xylene for a $3.0\,\mathrm{MHz}$ fundamental frequency.

Fig. 4 shows $P_2(x)/(xP_1^2(0))$ vs. $xP_1(0)$ for water and Fig. 5 is a similar plot for m-xylene. From extrapolation of these data to $xP_1(0) = 0$ and using Eq. (10) $B/A = 6.2$ for water and $B/A = 9.6$ for m-xylene were determined. The estimated errors are within $10\,\%$.

The value of B/A for water is about $15\,\%$ higher than what is reported later. One source of error of the optical measurement is due to the conversion from refractive index variation μ to the acoustic pressure P.

Bragg Diffraction and Imaging of Light Through Finite Amplitude Ultrasonic Waves

When light interacts with an ultrasonic wave the light diffracts into several orders because the ultrasonic waves behave as a diffraction grating. This phenomenon is often referred to as Raman–Nath diffraction. In addition, there is another type of diffraction mechanism called Bragg diffraction which is more analogous to the diffraction of x-rays by a crystalline lattice. There is a region of overlap of the two mechanisms defined by the so-called Cook–Klein [16] parameter. A new means of studying Bragg diffraction was introduced by Korpel [17] in 1966, who demonstrated by using an infinitesimal ultrasonic amplitude that the first Bragg diffraction order contains an image of the ultrasonic wavefront, as well as an object placed in the ultrasonic beam. When finite amplitude ultrasonic waves are used, the problem becomes nonlinear [18]. The schematic of the experimental system is shown in Fig. 6. The RF signal is generated by a controlled oscillator. An X-cut square quartz transducer of $1\,\mathrm{in}$ in diameter was excited by using the harmonics of a $2\,\mathrm{MHz}$ fundamental frequency. The optical system consisted of a laser source and a cylindrical optical

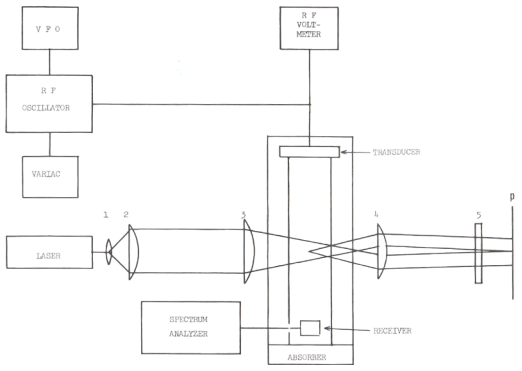

Fig. 6: Experimental system to observe Bragg imaging.

DOI 10.5162/Ultrasonic2025/A8-a1

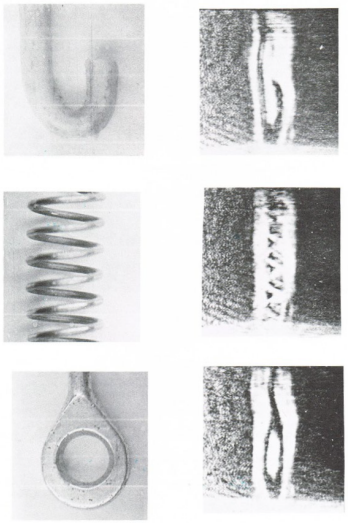

Fig. 7: Photographs of objects and their Bragg diffraction images.

system to obtain a wedge of light. This way the positive and negative Bragg diffraction orders would be observed simultaneously. Bragg imaging was obtained by placing an object to be imaged in the ultrasonic field between the transducer and the light beam. In Fig. 7 the objects and the corresponding Bragg images are shown. The images were made with an $18\,\mathrm{MHz}$ ultrasonic transducer ($2\,\mathrm{MHz}$ transducer was driven at the 9th harmonic).

As the amplitude of the ultrasonic wave increased multiple orders of Bragg diffraction are produced and multiple images of the objects were obtained, two in the second order, three in the third order as shown in Fig. 8. When finite amplitude ultrasonics was used, the ultrasonic wave got distorted and harmonics were generated. Using a transmission plate (like to measure B/A) to filter out the fundamental from the harmonics, images of double size images were obtained, since the magnification of the image is proportional to the frequency. In Fig. 9a, the double images of the hook are shown in second order. In Fig. 9b, the single image with twice the size is shown in the second order when only the second harmonics are present.

Subharmonic Generation in Water-Filled One Dimensional Cavity

While studying finite amplitude standing waves in a liquid filled cavity bounded at one end by a rigid reflector and the other end by a quartz transducer, extra orders in the diffraction pattern were observed [19, 20]. The extra orders appear only above a certain threshold voltage of the driver transducer. In Fig. 10, the diffraction pattern is shown for below the threshold value of parametric excitation in Fig. 10a, and above the threshold in Fig. 10b.

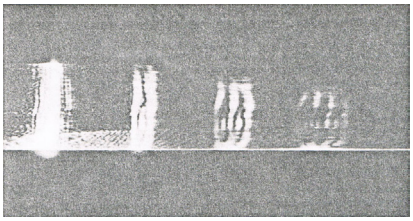

Fig. 8: Photograph of first, second and third order images of the loop.

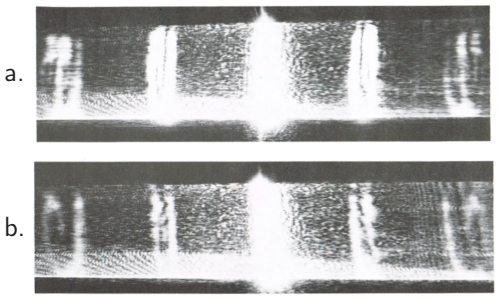

Fig. 9: Photographs of first and second order Bragg images a. without filter and b. with filter.

The extra diffraction orders shown in Fig. 10b were obtained due to the subharmonics generated at approximately half the frequency of the driver. The acoustical frequency spectrum shown on Fig. 11 corresponds to the optical diffraction pattern in Fig. 10b. It was taken by the spectrum analyzer. The driver frequency is called $2f$, which is $4\,\mathrm{MHz}$ in this case and the driver voltage is $100\,\mathrm{V}$. The other frequencies are

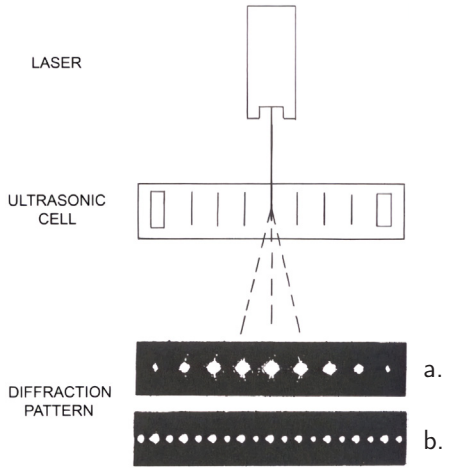

Fig. 10: Schematic diagram of the diffraction pattern below the threshold a. and above threshold b.

DOI 10.5162/Ultrasonic2025/A8-a1

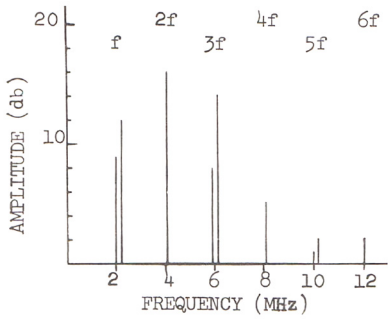

Fig. 11: Frequency spectrum at driver's voltage $100\,\mathrm{V}$.

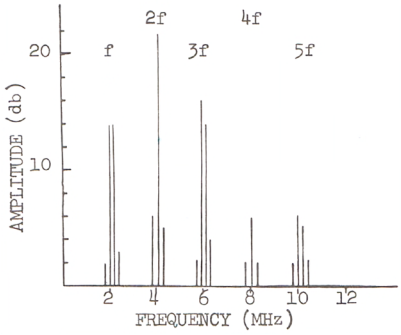

Fig. 12: Frequency spectrum at driver's voltage $200\,\mathrm{V}$.

grouped as follows: 1: $4f$, $6f$—these are the second and third harmonics of the driver. These components are present even below the threshold value of the parametric excitation and are due to the nonlinearity of the liquid. 2: The frequency pairs at f, $3f$ and $5f$, i.e. about one half, three halves and five halves the driver frequency, are sometimes called more appropriately fractional harmonics. These components are affected by the amplitude of the driver and other parameters e.g. the liquid used, geometry, the system etc.. With increased amplitude of the driver, the complexity of the spectrum increases as shown in Fig. 12 and Fig. 13, where the driver voltage increased to $200\,\mathrm{V}$ and $300\,\mathrm{V}$ respectively (it has been recognized only recently that the cascade of bifurcation leads essentially to chaos in the system, this will be discussed in the next section).

The theory to describe the generation of the subharmonics was based on a model used as a parametric system. In Fig. 14 the schematic of this system is shown. It implies that the cavity length is not constant, but it is a function of time. The variation of the cavity length is determined by the frequency as well as by the amplitude of the driver transducer. This resonant system has resonant frequencies which are themselves time dependent quantities.

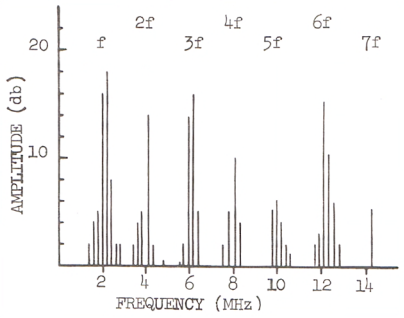

Fig. 13: Frequency spectrum at driver's voltage $300\,\mathrm{V}$.

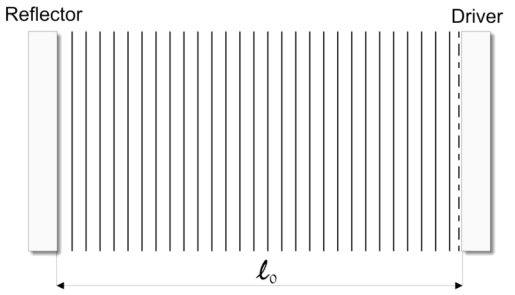

Fig. 14: Periodically varying cavity.

If the amplitude of the driver is A and the frequency is 2ω, the time dependent cavity length may be expressed as

$$l(t) = l_0(1 + h\cos(2\omega t)), \tag{14}$$

where $h = A/l_0$. The resonant frequency of the cavity takes its time dependent form

$$\omega_n(t) = \omega_n(1 + h\cos(2\omega t)). \tag{15}$$

Such vibration is not predicted by the standard normal mode solution. As a matter of fact, one cannot speak in a real sense about normal modes any more because the cavity length variation causes a fluctuation of the modes. This leads to instabilities as the source of parametric excitation of the fractional harmonics.

From the wave equation the solutions were obtained in terms of damped Mathieu functions [21] with a condition to obtain unstable solution as

$$h > c\alpha/\omega, \tag{16}$$

where c and α are the velocity and the absorption coefficient of the ultrasonic wave in the liquid. Eq. (16) relates the vibration amplitude to the other parameters of the system, and it is interpreted as the threshold condition to obtain parametric resonance. This means that parametric excitation

DOI 10.5162/Ultrasonic2025/A8-a1

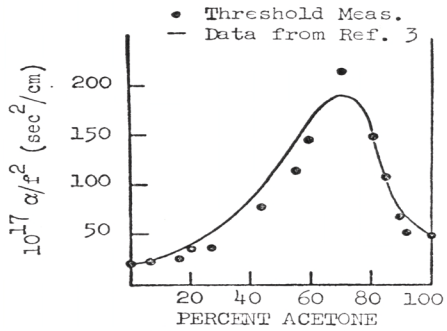

Fig. 15: Relative Absorption Coefficient as function percentage in a Water-Acetone mixture.

is a cumulative phenomenon. It is possible only if the energy input to the system, owing to a periodic variation of its resonant frequency, is greater than the energy dissipated by the system. This is the physical significance of the threshold. It was suggested to use the threshold condition in Eq. (16) to measure attenuation coefficients α for liquids [22]. In Fig. 15 the relative absorption coefficient is shown as a function of acetone concentration in water-acetone mixture as measured from the threshold of parametric excitation in the liquid mixture, and it compared very well with conventional absorption measurement.

Chaos and Beyond in a Liquid-Filled Ultrasonic Resonant System

As was pointed out in the previous section, discussing the mechanism of subharmonic generation, an increase of the driver's amplitude produces a cascade of bifurcation, see Fig. 11, 12, and 13. The problem was recently revisited with an improved experimental system shown in Fig. 16. It consists of an interferometer with optical precision controls used to adjust the positions of the piezoelectric transducer ($1\,\mathrm{MHz}$ – $10\,\mathrm{MHz}$ driven by a powerful amplifier) and a receiving transducer attached to an aligned reflector with lapped, flat, and parallel surfaces used to measure the generated frequency components in the cavity.

A visual assessment of the phenomena is obtained by passing laser light through the ultrasonic beam as indicated in Fig. 17. The laser light is diffracted into various orders n at angles given by Eq. (3).

Fig. 17 shows the diffraction patterns obtained for various transducer drive amplitudes (voltages): a. low amplitude ultrasonic waves ($5\,\mathrm{V}$); b. finite amplitude waves ($50\,\mathrm{V}$) resulting in an asymmetric diffraction pattern; and c. parametric resonance ($150\,\mathrm{V}$) producing extra diffraction orders due to the generation of the subharmonics.

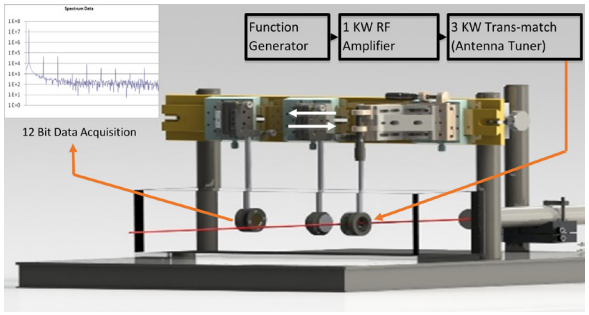

Fig. 16: Experimental system.

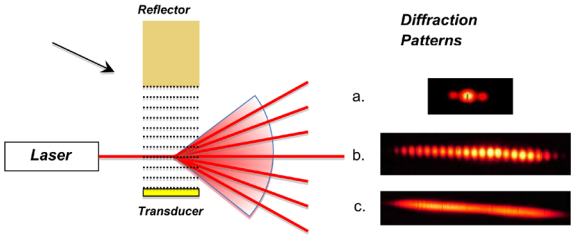

Fig. 17: Laser beam diffraction by ultrasonic wave: a. Linear Region, b. Nonlinear Region, c. Subharmonic Region.

Path to Chaos

A significantly higher transducer drive voltage ($450\,\mathrm{V}$) in the parametric resonance region leads to a cascade of bifurcations with increasing drive amplitudes that culminates in the generation of the chaotic pattern shown in Fig. 18a. Instead of distinct diffraction orders, the laser produces a smeared-out image due to the chaotic oscillations. Further increases in the transducer drive voltage (to $500\,\mathrm{V}$) lead to a second region of stability following the region of chaotic instability. The diffraction pattern in the second region of stability is shown in Fig. 18b. The pattern is similar to that of Fig. 17c, indicating the presence of stable subharmonics.

The chaotic behavior in the liquid-filled ultrasonic resonant system is generated at a second threshold (it was pointed out earlier that subharmonic generation requires a threshold power input). It is significant to notice from Fig. 18b that at an additional power level the chaos reverses into stable oscillation, i.e. beyond chaos. This observation is quite rare in chaotic systems, although some theoreticians are predicting the reversal of chaos. It should be mentioned that hysteresis is also observed when the power level changes from chaos to beyond and back to chaos. The question that remains unanswered is the physical mechanism involved when chaos is produced. One possible mechanism is "turbulence" which may take place in water at high power. Another possibility is phase transforma-

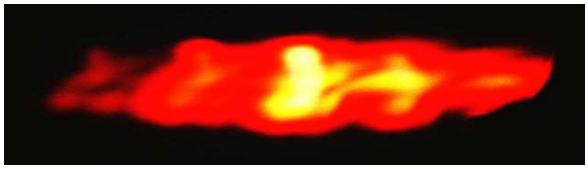

a. Chaos

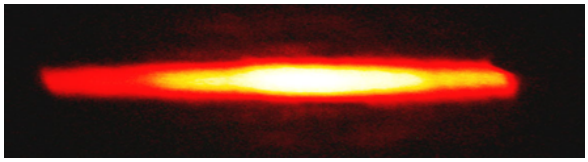

b. Beyond Chaos

Fig. 18: Laser Beam Diffraction Ultrasonic Waves: a. In the Chaotic Region ($450\,\mathrm{V}$) b. Beyond Chaotic Region ($500\,\mathrm{V}$).

tion in water, i.e. boiling, and subsequent formation of bubbles. Both of these mechanisms are examples of chaotic behavior. Additional work is required to evaluate the source of chaos in this system.

Summary

It was demonstrated that diffraction of light through ultrasonic waves with finite amplitudes provided many new observations and better understanding in nonlinear acoustics:

1. Measurements of the Nonlinearity Parameter B/A in liquids. It is important to describe the equation of state in liquids. It was found better evaluation of soft tissues.

2. Bragg Imaging with Second Harmonics. Provides an increased magnification of the images.

3. Observation of fractional harmonics in a one dimensional liquid filled ultrasonic cavity. The system was modelled as parametric resonance. The threshold condition is used to measure relative attenuation coefficient of liquids.

4. Observation of multilevel bifurcation of subharmonics, a path to chaos at a second threshold level. At an increased amplitude level the chaotic behavior reverses for stable subharmonics.

Acknowledgements

This work was partially supported by the Emeritus Academy at Ohio State University.

References

[1] L. Brillouin. "Diffusion de la lumière et des rayons X par un corps transparent homogène: Influence de l'agitation thermique". In: *Annales de Physique* 9.17 (1922), pp. 88–122. ISSN: 1286-4838. DOI: 10.1051/anphys/192209170088.

[2] P. Debye and F. W. Sears. "On the Scattering of Light by Supersonic Waves". In: *Proceedings of the National Academy of Sciences* 18.6 (June 1932), pp. 409–414. ISSN: 1091-6490. DOI: 10.1073/pnas.18.6.409.

[3] R. Lucas and P. Biquard. "Propriétés optiques des milieux solides et liquides soumis aux vibrations élastiques ultra sonores". In: *Journal de Physique et le Radium* 3.10 (1932), pp. 464–477. ISSN: 0368-3842. DOI: 10.1051/jphysrad:01932003010046400.

[4] C. V. Raman and N. S. Nagendra Nath. "The diffraction of light by high frequency sound waves: Part I." In: *Proceedings of the Indian Academy of Sciences - Section A* 2.4 (Oct. 1935), pp. 406–412. ISSN: 0973-7685. DOI: 10.1007/BF03035840.

[5] L. E. Hargrove, K. L. Zankel, and E. A. Hiedemann. "Effects of a Progressive Ultrasonic Wave on a Light Beam of Arbitrary Width". In: *The Journal of the Acoustical Society of America* 31.10 (Oct. 1959), pp. 1366–1371. ISSN: 1520-8524. DOI: 10.1121/1.1907636.

[6] M. A. Breazeale. "Experimental Studies of the "Least Stable Waveworm."" In: *The Journal of the Acoustical Society of America* 33.6 (June 1961), pp. 857–857. ISSN: 1520-8524. DOI: 10.1121/1.1936919.

[7] A. L. Thuras, R. T. Jenkins, and H. T. O'Neil. "Extraneous Frequencies Generated in Air Carrying Intense Sound Waves". In: *Bell System Technical Journal* 14.1 (Jan. 1935), pp. 159–172. ISSN: 0005-8580. DOI: 10.1002/j.1538-7305.1935.tb00688.x.

[8] F. E. Fox and W. A. Wallace. "Absorption of Finite Amplitude Sound Waves". In: *The Journal of the Acoustical Society of America* 26.6 (Nov. 1954), pp. 994–1006. ISSN: 1520-8524. DOI: 10.1121/1.1907468.

[9] E. Fubini Ghiron. "Anomalie nella propagazione di onde acustiche di grande ampiezza". In: *Alta frequenza: rivista di elettronica* 4 (1935), pp. 530–581.

[10] L. E. Hargrove. "Fourier Series for the Finite Amplitude Sound Waveform in a Dissipationless Medium". In: *The Journal of the Acoustical Society of America* 32.4 (Apr. 1960), pp. 511–512. ISSN: 0001-4966. DOI: 10.1121/1.1908127.

[11] W. Keck and R. T. Beyer. "Frequency Spectrum of Finite Amplitude Ultrasonic Waves in Liquids". In: *The Physics of Fluids* 3.3 (May 1960), pp. 346–352. ISSN: 0031-9171. DOI: 10.1063/1.1706039.

[12] L. Adler and E. A. Hiedemann. "Determination of the Nonlinearity Parameter B/A for Water and m-Xylene". In: *The Journal of the Acoustical Society of America* 34.4 (Apr. 1962), pp. 410–412. ISSN: 0001-4966. DOI: 10.1121/1.1918142.

[13] H. A. Lorentz. "Ueber die Beziehung zwischen der Fortpflanzungsgeschwindigkeit des Lichtes und der Körperdichte". In: *Annalen der Physik* 245.4 (Jan. 1880), pp. 641–665. ISSN: 1521-3889. DOI: 10.1002/andp.18802450406.

[14] M. J. F. Eykman. "Recherches réfractométriques (suite)". In: *Recueil des Travaux Chimiques des Pays-Bas* 14 (1895), p. 177. DOI: https://doi.org/10.1002/recl.18950140702.

[15] V. A. Krassilnikov, V. V. Shklovskaya-Kordy, and L. K. Zarembo. "On the Propagation of Ultrasonic Waves of Finite Amplitude in Liquids". In: *The Journal of the Acoustical Society of America* 29.5 (May 1957), pp. 642–647. ISSN: 1520-8524. DOI: 10.1121/1.1908994.

[16] W. Klein, B. Cook, and W. Mayer. "Light diffraction by ultrasonic gratings". In: *Acta Acustica united with Acustica* 15.2 (1965), pp. 67–74.

[17] A. Korpel. "Visualization of the cross section of a sound beam by Bragg diffraction of light". In: *Applied Physics Letters* 9.12 (Dec. 1966), pp. 425–427. ISSN: 0003-6951. DOI: 10.1063/1.1754639.

[18] R. T. Beyer. "10 - Nonlinear Acoustics". In: *Properties of Polymers and Nonlinear Acoustics*. Ed. by W. P. Mason. Vol. 2. Physical Acoustics. Academic Press, 1965, pp. 231–264. DOI: https://doi.org/10.1016/B978-0-12-395662-0.50014-X.

[19] A. Korpel and R. Adler. "Parametric phenomena observed on ultrasonic waves in water". In: *Applied Physics Letters* 7.4 (Aug. 1965), pp. 106–108. ISSN: 1077-3118. DOI: 10.1063/1.1754311.

[20] L. Adler and M. Breazeale. "Excitation of subharmonics in a resonant ultrasonic wave system". In: *Die Naturwissenschaften* 55.8 (1968), pp. 385–385. DOI: 10.1007/BF00593285.

[21] L. Adler and M. A. Breazeale. "Generation of Fractional Harmonics in a Resonant Ultrasonic Wave System". In: *The Journal of the Acoustical Society of America* 48.5B (Nov. 1970), pp. 1077–1083. ISSN: 0001-4966. DOI: 10.1121/1.1912245.

[22] J. H. Cantrell, L. Adler, and W. T. Yost. "Subharmonic generation, chaos, and subharmonic resurrection in an acoustically driven fluid-filled cavity". In: *Chaos: An Interdisciplinary Journal of Nonlinear Science* 25.2 (Feb. 2015), p. 023115. ISSN: 1089-7682. DOI: 10.1063/1.4913521.

DOI 10.5162/Ultrasonic2025/A8-a2

Quaternion Differential Equation for the $(2+1)D$ and $(3+1)D$ NDT

Sadataka Furui[1] and Serge Dos Santos[2]
[1] Teikyo University, Faculty of Science and Engineering, 2-17-12 Toyostodai, Utsunomiya, Japan
[2] INSA Centre Val de Loire; INSERM, Imaging Brain & Neuropsychiatry iBraiN U1253, F-41034 Blois Cedex, France
furui@umb.teikyo-u.ac.jp

Abstract: In Non-Destructive Testing (NDT), Ultrasonic (US) wave scattering positions are detected by interference of reflected original wave and reflected time-reversed (TR) wave. TR-US waves are produced by using the memristor. Transducers and detectors are located in a 2D plane and hysteresis effects are measured. We analyze the spectrum data of Wire Arc Additive Manufacturing (WAAM) sample obtained by Quaternion Excitation Symmetry Analysis Method (QESAM) using the conformally invariant quantum mechanical variables of de Alfaro-Fubini-Furlan. Depending on the relative position of the transducer and receivers, we observed conformality of spectra on different receivers. We review phonetic wave analysis of memristors, and show our lattice simulation data, which could contain chaotic behaviors. The (2+1)D analysis is extended to (3+1)D, by replacing quaternions to biquaternions and split-quaternions and discuss their lattice simulation

Keywords: Nonlinear Elastic Wave Spectroscopy, Biquaternion, Split-Quaternion, Conformal Symmetry, Encryption/Decryption

Introduction

In the Time Reversal based Nonlinear Elastic Wave Spectroscopy(TR-NEWS) [1] we use the non-commutativity of Quaternions to take into account nonclassical nonlinearity (hysteresis properties) of US wave propagation on a 2D plane. In the relativistically invariant propagation of waves in (1+1)D, Tomonaga[2] proposed defining time as a function of 3D space. In (3+1)D Quantum Chromo Dynamics, DeGrand et al.[3] simulated propagation of gluons in Dirac fermions sitting on 3D lattice sites using the Fixed Point action. We replaced gluons to phonons and Dirac fermions to Weyl fermion and simulated (2+1)D wave propagation[4].

In analysis of stochastic processes expressed by correlation/convolution processes, it is necessary to optimize the US wave propagation in materials. The stochastic processes follow the Langevin equation [5], and Lattice simulations can be applied[6].

The optimization of paths can be achieved by the minimal action, and we use Machine Learning tools for an extended Excitation Symmetry Analysis Method (ESAM) [7] signal processing.

(2+1)D US wave propagation

We perform WAAM sample data analysis by TR-NEWS. US waves produced by a transducer T_X are scattered in materials, and signals $s_1(t) = N_1x(t), s_2(t) = N_2x(t)^2$, $s_3(t) = N_3x(t)^3$ are received by 12 receivers $R_1, \cdots, R_{12}$ The received signal R_6 and R_{12} are shown in Fig.2 de Alfaro, Fubini and Furlan[8] considered (1+1)D Lagrangian $L = \frac{1}{2}(\dot{Q}^2 + \frac{g}{Q^2})$ and Hamiltonian $H = \dot{Q}\frac{\partial L}{\partial \dot{Q}}L$, dilatation D and conformal operator K obeys the algebra

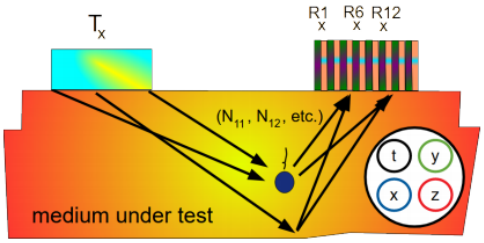

Fig. 1: The experimental setup of TR-NEWS using WAAM sample.

$$[H, D] = \sqrt{-1}H, [K, D] = -\sqrt{-1}K, [H, K] = 2\sqrt{-1}D \quad (1)$$

and constructed operators of $O(2,1)$ group by introducing R and S defined as

$$R = \frac{1}{2}(\frac{1}{a}K + aH), S = \frac{1}{2}(\frac{1}{a}K - aH) \quad (2)$$

DOI 10.5162/Ultrasonic2025/A8-a2

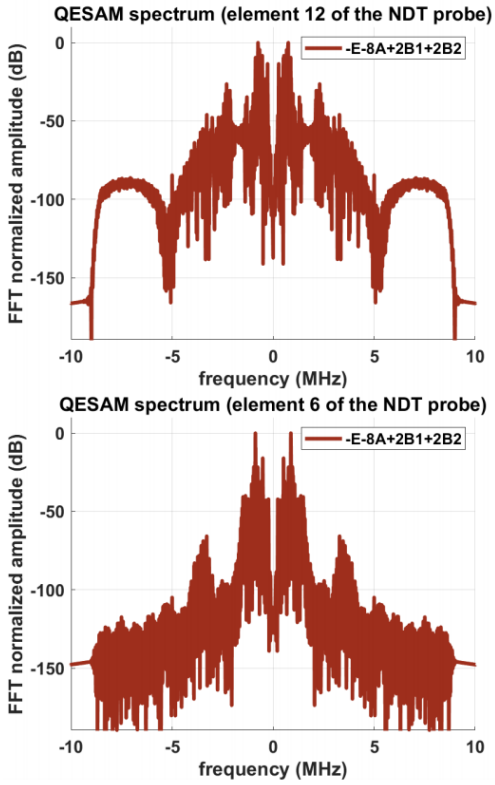

Fig. 2: The spectra of QESAM received at R12(top) and at R6(bottom).

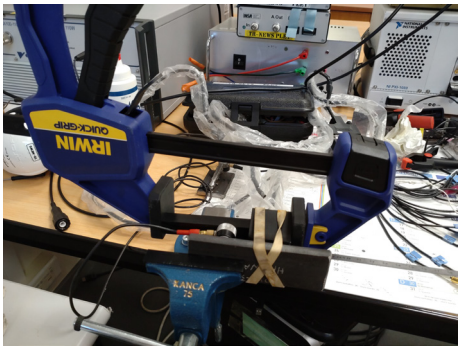

Fig. 3: The experimental setup.

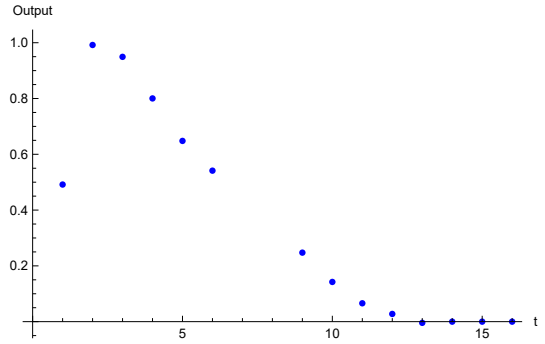

Fig. 4: Output calculated by the weight function at the 4000th cycle and the fixed point action at $t = 2, \cdots, 16$. The outputs in the range $t = 2, \cdots, 6$ are shifted upward by 0.5.

where a is a constant length, and conformal relation

$$[D, R] = \sqrt{-1}S, [S, R] = -\sqrt{-1}D, [S, D] = -\sqrt{-1}R \tag{3}$$

Godberashvili[9] defined a split quaternion

$$\begin{aligned} q &= q_0 + q_1 i + q_2 j + q_3 k \\ &= q_0 + q_1 i + (q_2 + q_3 i) j \\ q^* &= q_0 - q_1 i - q_2 j - q_3 ij \end{aligned} \tag{4}$$

In (2+1)D, $k = ij$ can be taken as the time axis, which induces the conformal $O(2,1)$ symmetry.

(3+1)D US wave propagation

The Godberashvilli's formula can be extended to

$$\begin{aligned} q &= q_0 + q_2 j + (q_3 + q_1 j) k \\ q^* &= q_0 - q_2 j - q_3 k - q_1 jk \\ q &= q_0 + q_3 k + (q_1 + q_2 k) i \\ q^* &= q_0 - q_3 k - q_1 i - q_2 ki \end{aligned} \tag{5}$$

Garling[10] defined biquaternions from quaternions e_1, e_2, e_3, e_4 as e_2e_3, e_3e_1, e_1e_2 as spacelike unit vectors and e_1e_4, e_2e_4, e_3e_4 as spacelke time.

In the (3+1)D lattice simulation, there are time shifts $\pm e_i e_4 (i = 1, 2, 3)$ on each paths that start from origin and return to the origin in 16 steps. There are 7 paths and their weight functions are fixed by an extension of Echo State Network(ESN). Extension means, the matrices that connect reservoir and output W_{ro} is obtained from the Fixed Point action and not fixed as in standard ESN,

The output of ESN are stable after 3000th cycle till 4000th cycle. The output has the Möbius band structure. When the outputs of $0 < t < 8$ are shifted upward by 0.5, the whole outputs become smooth [11].

Chaos in (3+1)D and its application

In (3+1)D, there are chaotic paths, which can be used in encrypting and decrypting[12]. We solved the differential equation of Chen's system using Mathematica and from $x(t) = (x_1(t), x_2(t), x_3(t))$ obtained masked signal $s_M(t)$ and encrypted signal $e(s_M(t)) = (f_1(f_1(f_1(f_1(s_M(t), k(t)), k(t)), k(t)), k(t)) = c(t)$

DOI 10.5162/Ultrasonic2025/A8-a2

where

$$f_1(x,k) = \begin{cases} (x+k)+2h, & -2h \le (x+k) \le -h \\ (x+k), & (x+k) < h \\ (x+k)-2h, & h \le (x+k) \le 2h. \end{cases} \quad (6)$$

The decrypted signal is $s_R(t) = d(c(t)) = f_1(f_1,(f_1(f_1(c(t),-\hat{k}(t)),-\hat{k}(t)),-\hat{k}(t)),-\hat{k}(t))$. $s_M(t)$ and $s_R(t)$ are sensitive to the initial conndition, and in a certain range, the difference of $s_M(t)$ and $s_R(t)$ are negligible.

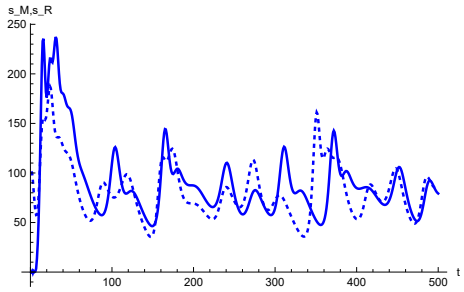

Fig. 5: The 4th step $s_M(t) = s_R(t)$ of Chen system. Solid line is calculated from $x(t)$, dashed line is calculated from $\hat{x}(t)$. $420 \le t \le 500$ can be used for encrypting/decrypting.

Dirac's bi-quaternion and Triality

Dirac applied Lorentz transformation to quaternions[13]. He expressed bi-quaternion as a ratio $q = uv^{-1}$, and for any quaternion λ, $q = u\lambda\lambda^{-1}v^{-1} = u\lambda(v\lambda)^{-1}$. Let $Q_1 = u\bar{v}$ where $\bar{v}$ is the conjugate quaternion, '$Q_2 = u\bar{u}$, $Q_3 = v\bar{v}$, and 4D vectors X_1, X_2, X_3 and X_4 are related by $Q_1 = X_0 + X_1 i + X_2 j + X_3 k$, $Q_2 = X_4 - X_5$, $Q_3 = X_4 + X_5$. The relatiion $Q_1\bar{Q}_1 = u\bar{v}v\bar{u} = uQ_3\bar{u} = Q_2Q_3$ leads to a constraint $X_0^2 + X_1^2 + X_2^2 + X_3^2 = X_4^2 - X_5^2$

Elgindy[14] tranformed the parameter $X_4 = t$ to $\tau = t(1-y^{1/\alpha})$ or $t - \tau = ty^{1/\alpha}$ and proposed use of fractional-order shifted Gegenbauer polynomial $\hat{G}_\alpha^\lambda(\tau)$ instead of Gegenbauer polynomial $G_\alpha^\lambda(x)$ with weight function $w^\lambda(x) = (1-x^2)^{\lambda-1/2}$.

The branch of Gegenbauer Polynomial is analogous to that of Productlog[z] function of Mathematica, which is the main solution of $z = we^w$, which on a complex plane posess a cut from $-\infty$ to $-1/e$ as shown in Fig.7. The split quaternion suggests the interchange of u to v, $\bar{v}$ to $\bar{u}$ changes the branch line of the ProductLog[z] function. Existence of three symmetric states is not equal to triality of octonions, we need to optimize the path on the multi-complex plane.

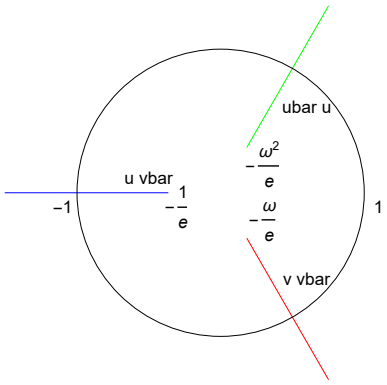

Fig. 6: The complex plane with three branch lines $z = u\bar{v}$, $z = v\bar{v}$ and $z = \bar{u}u$.

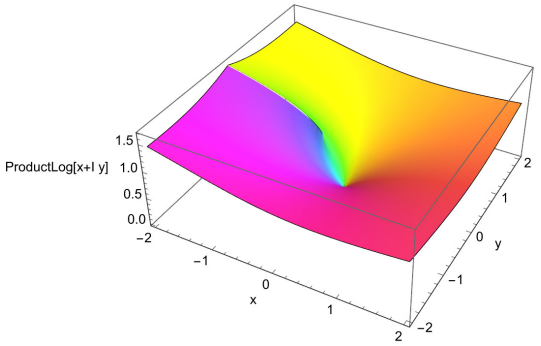

Fig. 7: The 3D plot of the ProductLog[z] function.

Hysteresis from Stochastic Differential Equation

In Preisach-Mayergoyz model[4], for input u, we define $x_n = u + X_n$, including the noise X_n., The output f_t is given by a solution of Itō's stochastic differential equation[15]

$$dX_t = b(X_t)dt + \sigma(X_t)dW_t, \quad (7)$$

where $b(X_t) = \delta\dot{X}_t$ and $\sigma(X_t)$ is a nondegenerate square matrix.

The output is

$$f_t = \int\int_{\alpha\ge\beta} \mu(\alpha,\beta)E\{\hat{\gamma}_{\alpha\beta}x_t\}d\alpha d\beta. \quad (8)$$

The function $\mu(\alpha,\beta)$ is approximately Gaussian function as Fig.8. The expectation value $E\{\hat{\gamma}_{\alpha\beta}x_n\} = P\{\hat{\gamma}_{\alpha\beta}x_n = +1\} - P\{\hat{\gamma}_{\alpha\beta}x_n = -1\}$. The probability $P\{\hat{\gamma}_{\alpha\beta}x_n = +1\} + P\{\hat{\gamma}_{\alpha\beta}x_n = -1\} = 1$, and its hysteresis effects can be seen for a fixed α change of f as u increases, as shown in Fig.9..

Discussion and Outlook

We showed that TR-NEWS method using quaternion is successful in (2+1)D NDT, and conformal prop-

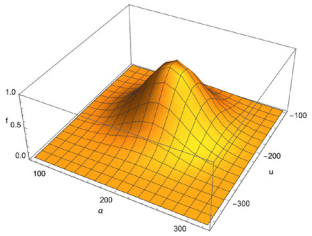

Fig. 8: The $\mu(\alpha, \beta)$ of the Preisach Model

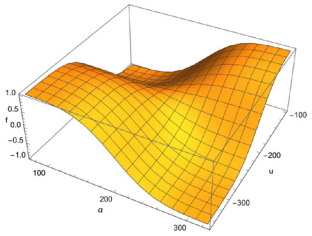

Fig. 9: The function $f(\alpha, u)$ derived from $\mu(\alpha, \beta)$

erty was observed. In (3+1)D NDT, biquaternion or split quaternion bases are necessary. On hypercomplex plane, the triality symmetry suggests that there are branching from $-\frac{1}{e}, -\frac{\omega}{e}, -\frac{\omega^2}{e}$,($\omega = e^{\sqrt{-1}\pi/3}$) to infinity exist.

The superposition of pure quaternion allows the total spectra $1 + \omega + \omega^2 = 0$, but the in (3+1)D as in (2+1)D[16], chaos occurs. The spacelike time proposed by Tomonaga is important for analysis of paths which contain ordinary delay and TR delays.

Efficient algorithm for performing (3+1)D NDT whose medical application is anticipated is under investigation.

Acknowledgement

S.F. is grateful to the Laboratory for Industrial Research (Nissanken) for the financial aid to the travel expense to the ICU2025 Congress, Prof. M. Arai and Prof. K. Hamada for allowing the use of workstations as a research collaborator.

References

[1] T. Goursolle et al. "A two-dimensional pseudospectral model for time reversal and nonlinear elastic wave spectroscopy". In: *J. Accoust. Soc. Am* 122(6) (2007), pp. 3220–3229.

[2] S. Tomonaga. "On a Relativistically Invariant Formulation of the Quantum Theory of Wave fields". In: *Prog. Theor. Phys. 1 (2) 27-40 (1946).* 1(2) (1946), pp. 27–40.

[3] T. DeGrand et al. "Non-perturbative tests of the fixed point action for SU(3) gauge theory". In: *Nucl. Phys. B* 454 (1995), pp. 615–637. DOI: arXiv:9506031[hep-lat]..

[4] S. Furui and S. Dos Santos. "Application of Quaternion Neural Network to Time Reversal Based Nonlinear Elastic Wave Spectroscopy". In: *INAE* 8 (2023), pp. 183–199.

[5] I. Mayergoyz. *Mathematical Models of Hysteresis and Their Applications*. Elsevier, 2003.

[6] H.Nakajima and S.Furui. "A new algorithm for numerical simulation of Langevin equations". In: *Nucl. Phys. B (Proc. Suppl.)* 53 (1997), pp. 983–986.

[7] S. Dos Santos and C. Plag. "A new algorithm for numerical simulation of Langevin equations". In: *Int. J. Non-Linear Mech.* 43 (2008), pp. 164–169.

[8] V. de Alfaro, S. Fubini. and G. Furlan. "Conformal Invariance in Quantum Mechanics". In: *Nuovo Cim.* A34 (2008), p. 561.

[9] M. Gogberashvili. "Split quaternions and particles in (2+1)D-space". In: *Eur. Phys. J. C* 74 (2014), p. 3200.

[10] D.J.H. Garling. *Clifford Algebras: An Introduction*. Cambridge University Press, 2011.

[11] S. Furui and S. Dos Santos. "Analysis of (2+1)D and (3+1)D Nonlinear Ultrasonic Waves using Conformal Invariance". In: *arXiv 2412.08655 v1[physics.optics]* (2024).

[12] K. Fallahi et al. "An application of Chen system for secure chaotic communication based on extended Kalman filter and multi-shift cipher algorithm". In: *Comm. in Nonlinear Science and Numerical simulation* 13 (2008), pp. 763–781.

[13] P.A.M. Dirac. "Application of Quaternions to Lorentz Transformations". In: *Proc R.I.A.* L, SECT. A (1945), pp. 261–270.

[14] K.T. Elgindy. "Super-Exponential Apprication of the Riemann-Liouville Fractional Integral via Gegenbauer-Based Fractional Approximation Methods". In: *Algorithms 2025* 18 (2025), pp. 395–425.

[15] K. Itoh. *The Probability Theory (In Japanese)*. Iwanami Shoten, 1991.

[16] S.Furui and T.Takano. "On the amplitude of external perturbation and chaos via devil's staircase and hidden attractors". In: *Int. J. of Bifurcations and Chaos* 23 (2013), p. 1350136.

DOI 10.5162/Ultrasonic2025/A8-b2

Numerical study of nonlinear guided waves in composite laminate with matrix crack

Nan Tao[1], Michal Dziendzikowski[2], Ran Tao[1], Roger M. Groves[1], and Nan Yue[1]
[1]*Department of Aerospace Structures and Materials, Delft University of Technology, Kluyverweg 1, 2629 HS, Delft, the Netherlands*
[2]*Air Force Institute of Technology, ul. Ks. Boleslawa 6, 01-494 Warszawa, Poland*
n.tao@tudelft.nl, n.yue@tudelft.nl

Abstract: This work studies nonlinear guided waves for the detection of matrix cracks in composites. Finite element modelling is used to simulate a 2 mm-thick unidirectional GFRP with a 2 mm-long crack. The fundamental symmetric (S0) mode propagating perpendicular to the crack surface is investigated. The influence of different crack depths on the nonlinear guided waves is studied. Current results show that nonlinear responses only happen when a crack exists and that the nonlinear responses differ between a half-thickness and a through-thickness crack.

Keywords: Nonlinear guided waves, unidirectional composites, numerical study, matrix crack, through-thickness crack

Introduction

The use of composite materials for safety-critical structures is increasing in various industrial sectors [1, 2, 3]. This poses an urgent challenge to non-destructive testing (NDT) and structural health monitoring (SHM) in assessing different defects and damage [1, 3, 4]. The nonlinear ultrasonic guided wave method [5, 6, 7] is an emerging SHM technique that has been shown to be effective in the detection of fatigue cracks in metals. The main sources of acoustic nonlinearity include material nonlinearity and contact acoustic nonlinearity (CAN). In recent years, the use of the CAN for manifesting damage such as closed cracks or delaminations in composites is receiving growing attention from researchers [8, 9]. This work aims to study the nonlinear guided wave response to a single matrix crack in a unidirectional composite laminate using finite element modelling (FEM). A 2 mm-thick unidirectional GFRP laminate with a 2 mm-long crack under symmetric excitation was modelled. The influence of various crack depths (i.e., no crack, half-thickness crack, and through-thickness crack) on nonlinear guided waves is investigated with a focus on primary frequency (1f) and superharmonics (2f, 3f).

Material description and modelling scenarios

A 300 $\times$ 300 $\times$ 2 mm GFRP composite with a layup of $[0]_8$ was modelled in Abaqus (Fig. 1). The material properties of the GFRP laminate for modelling are available in [10]. The fundamental symmetric S0 mode (10-cycle, 250-kHz Hanning windowed tone burst) was excited by applying in-plane concentrated forces on both the top and bottom surfaces of the laminate (at the edge of circular areas). Three crack depths, i.e., no crack, half-thickness crack, and full-thickness crack, with a crack length of 2 mm, were simulated. The wave propagating perpendicular to the crack surface was investigated. The crack surface was parallel to the x-axis (fiber direction).

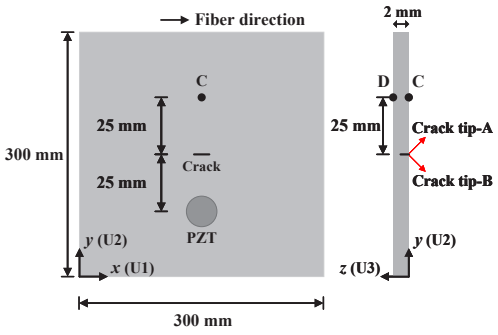

Fig. 1: Diagram of the unidirectional composite laminate. The crack is at the center of the plate along the x-axis (fiber direction). Wave propagating perpendicular to the crack surface was studied. Positions C and D are the corresponding sensing points.

Dispersion characteristics by DLR Dispersion Calculator

Fig. 2 shows the dispersion curve of the unidirectional GFRP laminate obtained from the DLR Dispersion Calculator. The Dispersion Calculator (DC) is a specialized tool for calculating the dispersion characteristics of the guided waves in isotropic and anisotropic materials using the stiffness matrix method [11]. The phase velocities and the wavelengths at 1f, 2f, and 3f are summarized in Tab. 1. It is good to note that

DOI 10.5162/Ultrasonic2025/A8-b2

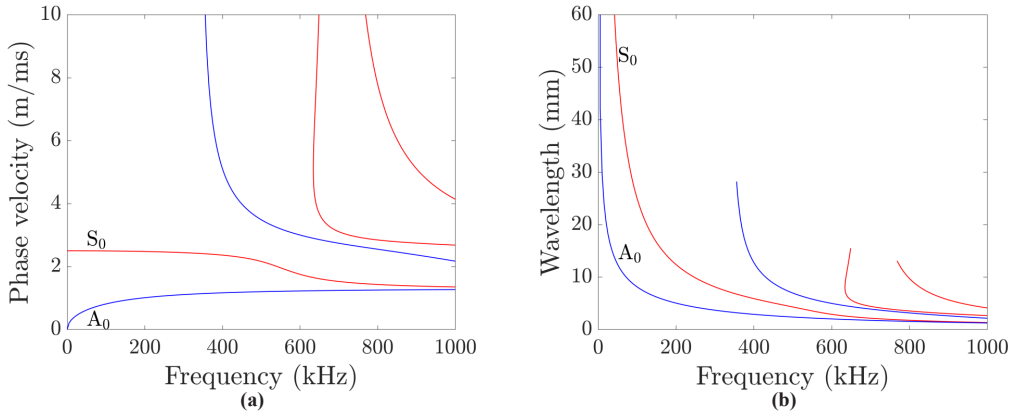

Fig. 2: The dispersion curve of the unidirectional GFRP laminate from the DLR Dispersion Calculator. (a) phase velocity, (b) wavelength. Wave propagation perpendicular to the fiber direction.

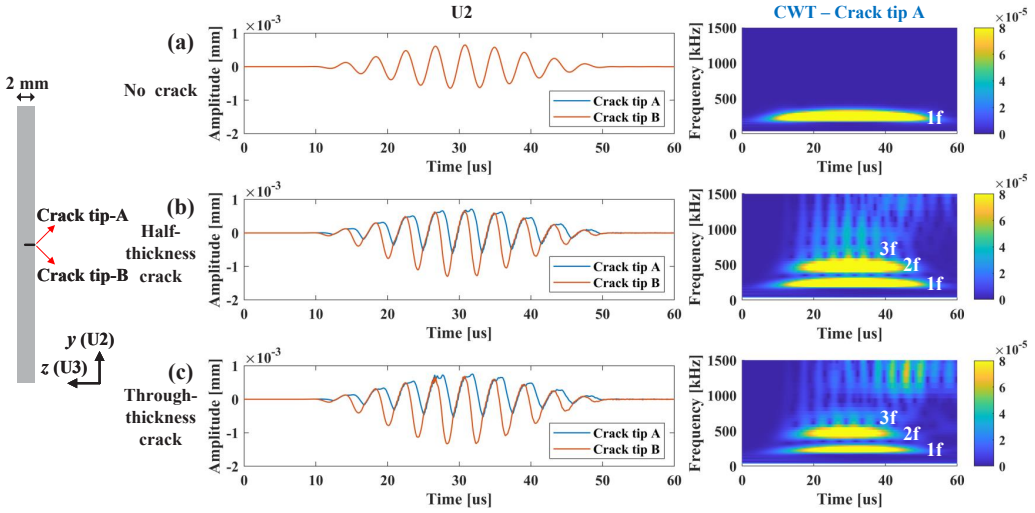

Fig. 3: The simulation results show the crack-wave interaction in the unidirectional composite. (a-c) are the displacements of crack tips A and B in the y-axis direction (U2) and the continuous wavelet transform (CWT) of the displacement U2 at crack tip A for no-crack, half-thickness, and through-thickness crack cases, respectively.

the ratio between the crack length (L=2 mm) and the wavelength of the excited fundamental S0 mode (λ=9.86 mm at 1f-250kHz) is around 0.2. To verify the FEM model, the phase velocities from FEM (1f) were calculated and compared with the DC, and their difference is 0.1%–0.2%.

Tab. 1: The phase velocities and the wavelengths of the guided waves in the unidirectional GFRP laminate obtained from the Dispersion Calculator.

		1f–250kHz	2f–500kHz	3f–750kHz
Phase velocity (m/ms)	S0	2.47	2.16	1.47
	A0	1.07	1.20	1.25
Wavelength (mm)	S0	9.86	4.33	1.96
	A0	4.28	2.40	1.67

Results

Fig. 3 shows the FEM results of the crack-wave interaction in the unidirectional composite. The in-plane displacements of the crack tips A and B in the y-axis direction (U2) are given for no-crack, half-thickness crack, and through-thickness crack cases, respectively. The corresponding continuous wavelet transform (CWT) of the displacements U2 at the crack tip A indicates the initial generation of nonlinearity due to the crack-wave interaction. It shows that for the no-crack case (Fig. 3(a)), only the primary frequency exists, and no super harmonics appear; for half- and through-thickness crack cases (Fig. 3(b-c)), the crack open-close phenomena are captured, resulting in nonlinear phenomena such as higher harmonic generation (2f and 3f components in the CWT maps).

DOI 10.5162/Ultrasonic2025/A8-b2

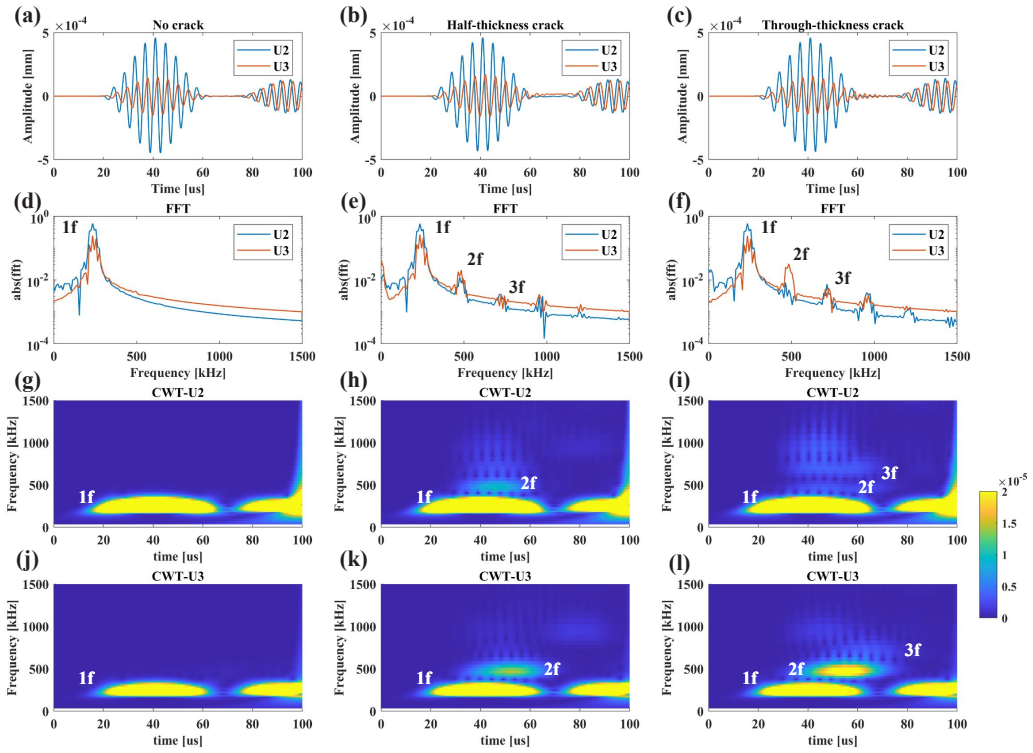

Fig. 4: The amplitude, FFT, and CWT plots (U2 and U3) at the sensing position C for no crack, half-thickness crack (crack depth 1 mm) and full-thickness crack (crack depth 2 mm) scenarios.

Fig. 4 shows the FEM results of a wave propagating at the sensing point C for no-crack, half-thickness and through-thickness crack cases. The position of point C is in Fig. 1. As the wave propagation is perpendicular to the crack surface, the deformations of U2 and U3 are dominant compared to U1. So here we focus on U2 and U3. The modelling results show that nonlinear responses (2f, 3f) happen when a crack exists (half- and through-thickness crack cases in Fig. 4(e, h, k) and 4(f, i, l), respectively); while for the no-crack case, it shows no nonlinear response (Fig. 4(d, g, j)). It also shows that the nonlinear responses differ between the half-thickness crack and the through-thickness crack.

The influence of the sensing points at the front and the back surface on the obtained nonlinear responses is also investigated. The amplitude, FFT, and CWT plots (using the out-of-plane displacement U3) at the sensing positions C (z=0 mm) and D (z=2 mm) for no crack, half-thickness crack (crack depth 1 mm) and full-thickness crack (crack depth 2 mm) scenarios are given in Fig. 5. It shows that for the no-crack and through-thickness crack cases, the out-of-plane displacement U3 of the sensing points at the front and back surfaces is symmetrical, so only symmetrical S mode waves exist; while for the half-thickness crack case, the U3 at the two sensing points is asymmetrical, which means that the new asymmetrical A mode waves also appear and propagate in the specimen.

Conclusions

This paper studied the nonlinear guided waves for the detection of a single matrix crack in composite laminates. Finite element modelling was used to simulate a 2 mm-thick unidirectional GFRP composite with a 2 mm-long crack. The fundamental symmetric (S0) mode propagating perpendicular to the crack surface was investigated. The influence of no crack, half-thickness crack, and through-thickness crack scenarios on the nonlinear guided waves was studied. The results show that the crack of 2 mm length in the composite laminate is possible to be detected using the nonlinear guided wave method, where the crack length is 1/5 of the primary guided wave's wavelength; the nonlinear responses only happen when a crack exists and that the nonlinear responses differ between a half-thickness crack and a through-thickness crack. Future work is to study different crack lengths and different composite layups on the nonlinear ultrasonic guided waves for matrix crack and microcrack detection.

Acknowledgment

This research was performed as part of the Horizon Europe COMP-ECO project (grant agreement 101079250).

DOI 10.5162/Ultrasonic2025/A8-b2

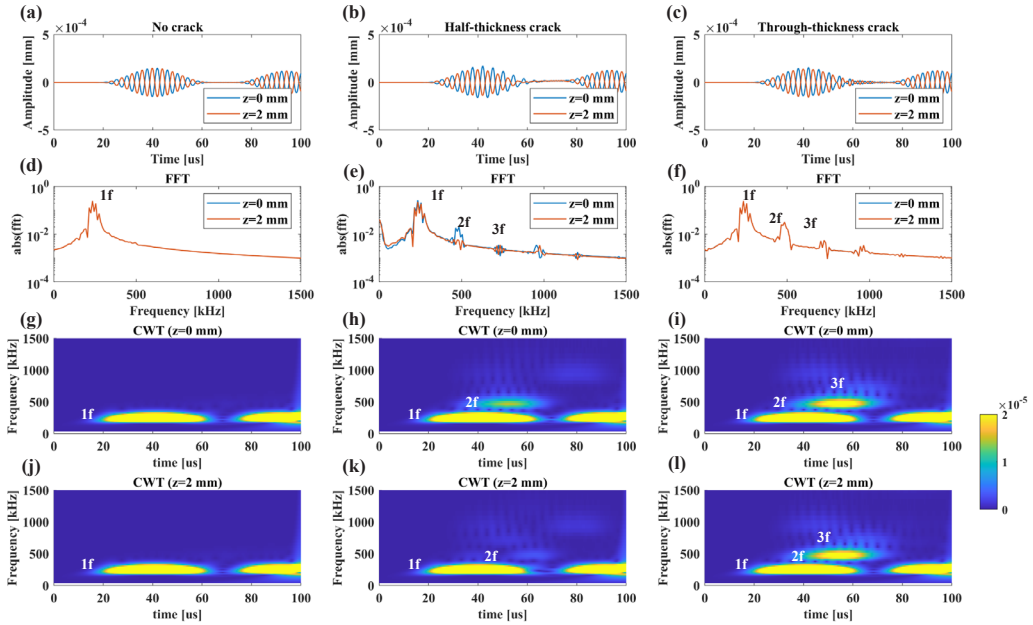

Fig. 5: The amplitude, FFT, and CWT plots (the out-of-plane displacement U3) at the sensing positions C (z=0 mm) and D (z=2 mm) for no crack, half-thickness crack, and full-thickness crack scenarios, respectively.

References

[1] M. Inês Silva, E. Malitckii, T. G. Santos, and P. Vilaça. "Review of conventional and advanced non-destructive testing techniques for detection and characterization of small-scale defects". In: *Progress in Materials Science* 138 (2023), p. 101155.

[2] E. J. Adler and J. R. Martins. "Hydrogen-powered aircraft: Fundamental concepts, key technologies, and environmental impacts". In: *Progress in Aerospace Sciences* 141 (2023). Special Issue on Green Aviation, p. 100922.

[3] R. M. Groves. "Inspection and Monitoring of Composite Aircraft Structures". In: *Comprehensive Composite Materials II*. Ed. by P. W. Beaumont and C. H. Zweben. Oxford: Elsevier, 2018, pp. 300–311.

[4] M. Ibrahim. "Nondestructive evaluation of thick-section composites and sandwich structures: A review". In: *Composites Part A: Applied Science and Manufacturing* 64 (2014), pp. 36–48.

[5] C. J. Lissenden. "Nonlinear ultrasonic guided waves—Principles for nondestructive evaluation". In: *Journal of Applied Physics* 129.2 (Jan. 2021), p. 021101.

[6] M. Mitra and S. Gopalakrishnan. "Guided wave based structural health monitoring: A review". In: *Smart Materials and Structures* 25.5 (Mar. 2016), p. 053001.

[7] D. Broda, W. Staszewski, A. Martowicz, T. Uhl, and V. Silberschmidt. "Modelling of nonlinear crack–wave interactions for damage detection based on ultrasound—A review". In: *Journal of Sound and Vibration* 333.4 (2014), pp. 1097–1118.

[8] C. Jiang, W. Li, M. Deng, and C.-T. Ng. "Numerical Simulation on Micro-damage Detection In CFRP Composites Based on Nonlinear Ultrasonic Guided Waves". In: *Materials Research Proceedings* 18 (2021).

[9] K. Wang, M. Liu, Z. Su, S. Yuan, and Z. Fan. "Analytical insight into "breathing" crack-induced acoustic nonlinearity with an application to quantitative evaluation of contact cracks". In: *Ultrasonics* 88 (2018), pp. 157–167.

[10] N. Tao, A. G. Anisimov, and R. M. Groves. "Shearography non-destructive testing of thick GFRP laminates: Numerical and experimental study on defect detection with thermal loading". In: *Composite Structures* 282 (2022), p. 115008.

[11] A. Huber. "The dispersion calculator: a free software for calculating dispersion curves of guided waves". In: *20th World Conference on Non-Destructive Testing (WCNDT 2024)*. Vol. 29. 6. NDT. net. 2024, pp. 1–17.

DOI 10.5162/Ultrasonic2025/A9-a1

Thermo-Elastic Coupling in Transient Grating Spectroscopy

Jakub Kušnír[2], Kristýna Repček[2], Tomáš Grabec[1], David Mareš[1], Pavla Stoklasová[1], Petr Sedlák[1], and Hanuš Seiner[1]
[1]*Institute of Thermomechanics of the Czech Academy of Sciences, Prague, Czechia*
[2]*Faculty of Nuclear Sciences and Physical Engineering, Czech Technical University in Prague, Prague, Czechia*
kusnir@it.cas.cz

Abstract: Characterization of the thermal diffusivity on the micrometer-thick film on a substrate by transient grating spectroscopy was investigated. The experiment was performed on a thin film of NiTi at 120°C, when the film is in the austenitic phase and exhibits cubic crystallographic symmetry. Apparent anisotropy of thermal diffusivity was observed in the experimental results, as confirmed by finite-element model (FEM). However, the calculation confirmed that the measurement was only sensitive to the thermal diffusivity of the film, omitting the substrate.

Keywords: transient grating spectroscopy, elasticity, thermal diffusivity, finite elements method

Introduction

Transient grating spectroscopy (TGS) is an opto-acoustic technique used to characterize the elastic and thermal properties of solids [1, 2, 3]. TGS, also known as impulsive stimulated thermal scattering (ISTS) [4, 5] or transient thermal grating (TTG) [6], is a non-destructive and contactless method that was used successfully to determine the elastic properties of a single-crystalline thin film of NiTi on an MgO substrate [7] and to measure the thermal diffusivity of the cubic single-crystals [8].

TGS uses two pulsed laser beams interfering on the sample surface that create spatially harmonic thermo-elastic excitation. Because of the excitation pattern, thermal and acoustic transient gratings are created – forming a dynamic surface-displacement grating on which the probe laser diffracts. The probe laser is continuous, and the optical geometry ensures recombination of the probe beams in a heterodyne detection setup [1]. The relative phase shift of the probe beams (the heterodyne phase) then influences the information obtained: Without a phase shift, the signal depends solely on thermal reflectivity; with a non-zero phase shift, it reflects both thermal reflectivity and surface displacement, combining acoustic oscillations with thermal decay [9]. An ideal signal is obtained in the 'phase-grating' mode with the heterodyne phase $\theta_{\mathrm{het}} = (\pm\pi/2)$. Acoustic oscillations can be characterized directly from the frequency spectrum, while fitting the signal with a formula from analytical models allows extracting the thermal diffusivity [10, 11].

However, as described in Ref. [8], when thermal diffusivity is measured on elastically anisotropic samples, the result of the fitting formula is influenced by the elastic properties, and a correction is needed to find the true thermal diffusivity of the measured sample. To characterize the influence of the elastic anisotropy on the apparent thermal anisotropy determined by the fitting formula, a quasi-static FEM model of the TGS experiment was used [8].

In this work, we show that TGS allows us to determine the thermal diffusivity of micrometer-thick films without the influence of the substrate. The sensitivity to thermal properties is depth dependent on the wavelength λ of the interference pattern as

$$L = \frac{\lambda}{\pi}, \tag{1}$$

where L is the thermal diffusion length [11]. Therefore, thermal properties are obtained up to this depth. Here we present its potential to determine the thermal properties of a single-crystalline sample that cannot be manufactured in bulk but only as a thin film.

Methods - Transient Grating Spectroscopy

Transient grating spectroscopy, illustrated in Fig. 1, is based on diffracting pump and probe lasers on the transmission phase grating and projecting ± 1 diffraction order beams on the sample surface using the 4F imaging system. Projected pump beams interfere on the sample surface, creating a spatially harmonic excitation pattern. The fringes spacing, and thus the acoustic wavelength λ, is set by the incidence angle of the beams and the laser light wavelength. Acoustic wavelength can thus be easily changed by changing the transmission phase grating. Each interference fringe acts as thermo-elastic source, launching

DOI 10.5162/Ultrasonic2025/A9-a1

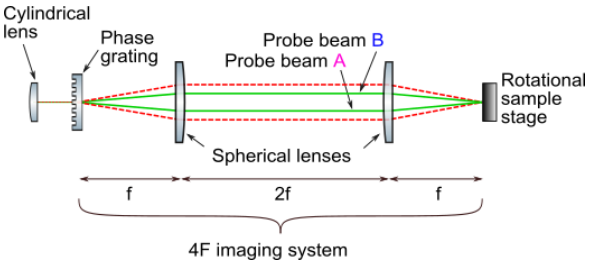

Fig. 1: Top-view schematic of the simplified optical setup of the TGS method.

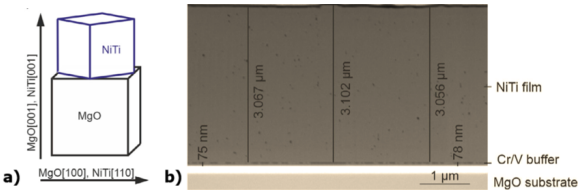

Fig. 2: a) Schematic showing B2 austenite unit-cell orientations of the film with respect to the substrate, b) cross-sectional SEM thickness measurement of the supported 3 µm thick NiTi layer on MgO substrate.

acoustic waves with a well-defined wave vector in a direction perpendicular to the excitation lines.

The probe beams go through the same optical setup as the pump beams. The beams are diffracted on the transient grating created on the sample surface after the excitation. The optical setup is in the Littrow configuration, where each probe beam diffracts in the reflection direction of the other, enabling heterodyne detection. Detection is carried out in the 'phase-grating' mode (heterodyne phase $\theta_{\mathrm{het}} = (\pm\pi/2)$), which maximizes sensitivity to out-of-plane displacement.

The measurement setup was similar to that used in the previous work of the authors [2]. The pump laser was a Nd:YAG pump laser (1064 nm, 0.54 ns, 200 µJ, 1 kHz) where the mean power on the sample surface was 17 mW. The probe beams were from the continuous-wave laser at 532 nm (120 mW) with mean power on detector around 15 mW. The optical setup was such that the resulting acoustic wavelength was $\lambda = 7\mu$m. The signal-to-noise ratio and sensitivity are further enhanced by measuring the intensity using differential Si photodiodes with a 60 dB amplifier. The differential setup further enhances the signal quality by removing phase-insensitive influences [4, 11].

The heterodyne probe signal was recorded by WaveRunner 640Zi oscilloscope (4 GHz bandwidth, vertical resolution of 8 bits, sampling rate 5 GS /s). The signal was averaged 50 thousand times in the time-domain for enhanced resolution and further reduced noise. Fourier analysis then reveals the dominant SAW frequencies, from which the SAW velocities were obtained using $v = f\lambda$, where λ is the excitation grating period, and were used to determine elastic constants [2].

To determine the thermal diffusivity, the fitting of an analytical function in the time-domain was used [10, 11]:

$$I(t) = A\left[\mathrm{erfc}\left(q\sqrt{\alpha t}\right) - \frac{\beta}{\sqrt{t}}\exp\left(q^2\alpha t\right)\right] + B\sin\left(2\pi f t + \varphi\right)\exp\left(-\frac{t}{\tau}\right) + C, \quad (2)$$

with A, B and C being constants, $q = 2\pi/\lambda$ is the acoustic wave number, α is thermal diffusivity, β describes the displacement and reflectivity contribution ratio, f frequency of the acoustic wave, τ the acoustic decay and ϕ the phase of the acoustic wave.

The experimental results were compared with the simulated results from the FEM simulation of the TGS experiment described in detail in [8].

Study case

The sample used in this study was a thin film of a NiTi shape memory alloy. The film was epitaxially grown by DC magnetron sputtering on a single-crystalline MgO(100) substrate [12]. To reduce epitaxial stress, buffer layers of vanadium and chromium were used, with a combined thickness of around 50 nm.

The epitaxial relationship between the NiTi austenite (B2 structure) and the MgO substrate was MgO(100)[001] ∥ V/Cr(100)[011] ∥ NiTi B2(100)[011]. This indicates that the austenite unit cell is rotated by 45° around the substrate normal relative to the film, such that of MgO aligns with of the austenite (as shown in Fig. 2a). The film thickness was measured by scanning electron microscopy (SEM) on a cross-section prepared by focused ion beam (FIB) milling using a FEI Helios NanoLab 600i, with the determined value of 3060 nm (Fig. 2b).

Results and Discussion

We carried out a 45° angular scan (with a step of 1°) of TGS measurement with $\lambda \approx 7\mu$m. The sample was measured at an elevated temperature of 120 °C at which the film was in a single crystalline austenite phase. The obtained time-domain signal is shown in Fig. 3 (top) with a strong acoustic and thermal

DOI 10.5162/Ultrasonic2025/A9-a1

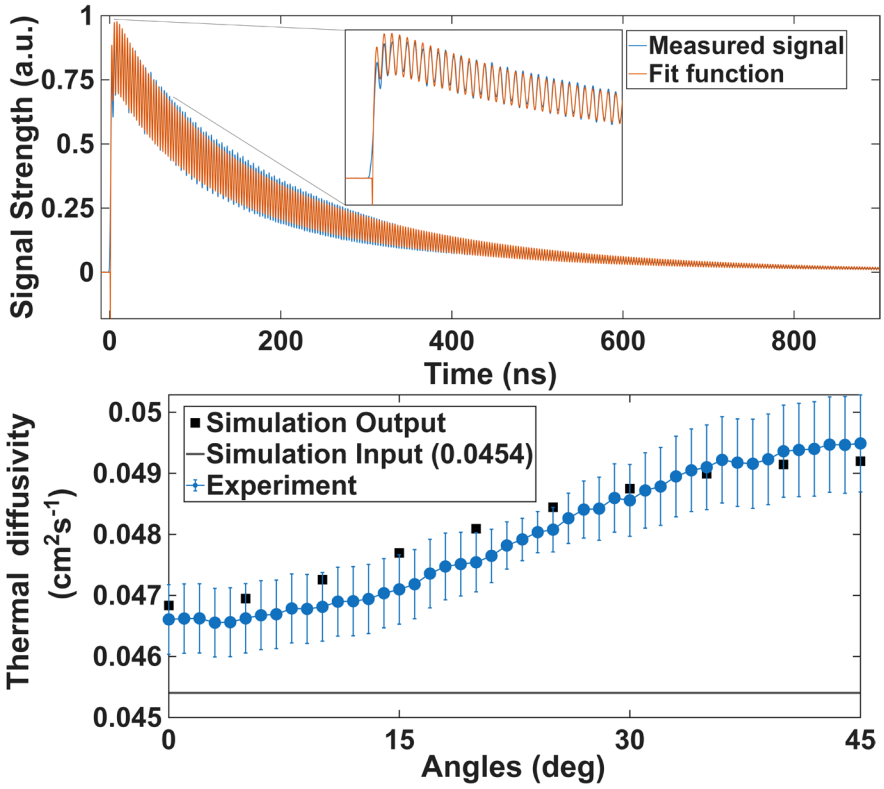

Fig. 3: Top: Time-domain signal in the 'phase-grating' measurement mode for epitaxial NiTi(001)[100] ($3\mu m$) on MgO(001)[110], with the measured signal in solid blue and calculated signal from the fitting function Eq. (2)*. Bottom: Comparison of experimentally measured (blue circles), simulated (black squares) and simulation input (black line) thermal diffusivity of thin film of NiTi on MgO. The black line is the true thermal diffusivity of the austenite phase of NiTi at 120 °C [8].*

response. The measured signal was fitted by Eq. (2), orange line, to obtain the thermal diffusivity.

Although the film is crystallographically cubic and therefore the thermal properties should be isotropic anisotropy of the thermal diffusivity was measured as shown in Fig. 3 (bottom) as blue circles with error bars (obtained from the fitting formula). This anisotropy results from the elastic anisotropy, which the derivation of the fitting formula (2) omits, and it is thus only apparent – as described in detail in Ref. [8]. However, quasi-static FEM simulation of the TGS experiment was used to find the true isotropic thermal diffusivity of the studied material by comparing the results of the FEM simulation with the experimental results, where isotropic thermal diffusivity was used as input. The input value for the FEM simulation is the considered the sought thermal diffusivity of the austenite phase of the NiTi at 120 °C, resulting in $\alpha = 0.0454\ \mathrm{cm^2 s^{-1}}$.

Note that the magnitude of λ was chosen so that the thermal properties would be probed only in the NiTi film – based on Eq. (1), the thermal-diffusion depth should be approximately $2.2\mu\mathrm{m}$. This was confirmed by the agreement of the experiment with the simulation, which was performed for considering bulk NiTi and omitting the substrate altogether.

Conclusion

Characterization of thermal diffusivity of epitaxial NiTi film was performed by TGS. The acoustic wavelength of 7 microns allowed us to probe only the film (with the thickness of 3 micrometers), omitting the influence of the MgO substrate. Although the film was crystallographically cubic and should be isotropic in thermal properties, anisotropic results were obtained by fitting the TGS signals. This is in agreement with earlier findings of the influence of elastic anisotropy on the TGS signals and the rate of the slow decay which corresponds with the thermal diffusivity. These results were confirmed by FEM simulations, allowing us to determine the true value of the thermal diffusivity of an elastically anisotropic thin supported film.

References

[1] A. A. Maznev, K. A. Nelson, and J. A. Rogers. "Optical heterodyne detection of laser-induced gratings". In: *Opt. Lett.* 23.16 (1998), pp. 1319–1321. DOI: 10.1364/OL.23.001319.

[2] P. Stoklasová et al. "Laser-Ultrasonic Characterization of Strongly Anisotropic Materials by Transient Grating Spectroscopy". In: *Experimental Mechanics* (2021). DOI: 10.1007/s11340-021-00698-6.

[3] K. Repček et al. "Compliant Lattice Modulations Enable Anomalous Elasticity in Ni–Mn–Ga Martensite". In: *Advanced Materials* 36.39 (2024), p. 2406672. DOI: 10.1002/adma.202406672.

[4] B. Verstraeten et al. "Determination of thermoelastic material properties by differential heterodyne detection of impulsive stimulated thermal scattering". In: *Photoacoustics* 3.2 (2015), pp. 64–77. DOI: 10.1016/j.pacs.2015.05.001.

[5] T. Grabec et al. "In-situ Characterization of Local Elastic Properties of Thin Shape Memory Films by Surface Acoustic Waves". In: *Smart Materials and Structures* 25.12 (2016). DOI: 10.1088/0964-1726/25/12/127002.

[6] J. A. Johnson et al. "Non-diffusive thermal transport in GaAs at micron length scales". In: *Journal of Applied Physics* 118.15 (2015), p. 155104. DOI: 10.1063/1.4933285.

[7] T. Grabec et al. "Guided acoustic waves in thin epitaxial films: Experiment and inverse problem solution for NiTi". In: *Ultrasonics* 138 (2024). DOI: 10.1016/j.ultras.2023.107211.

[8] J. Kušnír et al. "Apparent anisotropic thermal diffusivity measured in cubic single crystals by transient grating spectroscopy". In: *Journal of Applied Physics* 133.12 (2023), p. 125108. DOI: 10.1063/5.0136850.

[9] J. A. Johnson et al. "Phase-controlled, heterodyne laser-induced transient grating measurements of thermal transport properties in opaque material". In: *Journal of Applied Physics* 111.2 (2012), p. 023503. DOI: 10.1063/1.3675467.

[10] C. A. Dennett and M. P. Short. "Thermal diffusivity determination using heterodyne phase insensitive transient grating spectroscopy". In: *Journal of Applied Physics* 123.21 (2018), p. 215109. DOI: 10.1063/1.5026429.

[11] O. W. Käding et al. "Transient thermal gratings at surfaces for thermal characterization of bulk materials and thin films". In: *Applied Physics A* 61.3 (1995), pp. 253–261. DOI: 10.1007/BF01538190.

[12] K. Lünser et al. "How to grow single-crystalline and epitaxial NiTi films in (100)- and (111)-orientation". In: *Journal of Physics: Materials* 6.3 (2023), p. 035002. DOI: 10.1088/2515-7639/acd604.

Acknowledgments

This work was financially supported by the Czech Science Foundation [Project No. 22-13462S], Operational Program Johannes Amos Comenius of the Ministry of Education, Youth and Sport of the Czech Republic, within the frame of project Ferroic Multifunctionalities (FerrMion) [Project No.CZ.02.01.01/00/22_008/0004591], co-funded by the European Union and by the Grant Agency of the Czech Technical University [No. SGS25/168/OHK4/3T/14].

DOI 10.5162/Ultrasonic2025/A12-b1

Methods for Computing Quasi-Guided Waves in Plate Structures Coupled to Unbounded Media

Hauke Gravenkamp[1], Bor Plestenjak[2], and Daniel A. Kiefer[3]
[1]Institute of Materials, Technologies and Mechanics, Otto von Guericke University Magdeburg, 39106 Magdeburg, Germany
[2]IMFM and Faculty of Mathematics and Physics, University of Ljubljana, Jadranska 19, SI-1000 Ljubljana, Slovenia
[2]Institut Langevin, ESPCI Paris, Université PSL, 75005 Paris, France
hauke.gravenkamp@ovgu.de

Abstract: Using semi-analytical methods for modeling waves in layered structures, the thickness direction is discretized straightforwardly by finite elements. However, the coupling to adjacent acoustic or elastic half-spaces leads to a nonlinear eigenvalue problem (NLEP) for the wavenumbers and mode shapes. We demonstrate how this NLEP can be solved in two very different ways, either by recasting it as a multiparameter eigenvalue problem or by the concept of exponential residual relaxation in conjunction with standard Runge-Kutta solvers.

Keywords: guided waves, semi-analytical methods, leaky waves, multiparameter eigenvalue problems, Zhang Neural Networks

Problem statement

We address the problem of elastic waves propagating along a plate of constant thickness h with a (generally complex) wavenumber k, see Fig. 1. If the plate surfaces are traction-free or fixed, this setup corresponds to the classic Lamb wave problem [1], and various methods exist for the computation of wave modes and dispersion curves; see, e.g., [2, 3] and the references therein. In particular, it is common to discretize the plate thickness using finite elements, yielding a quadratic eigenvalue problem for the wavenumbers at a given frequency ω. If, on the other hand, the plate is in contact with fluid or solid half-spaces at either or both of its surfaces, the situation becomes significantly more complicated, as the interaction with the half-spaces results in additional nonlinear terms in the eigenvalue problem, involving the free-field longitudinal and transversal wavenumbers κ, γ in the half-spaces [4, 5, 6]. Specifically, the nonlinear eigenvalue problem is of the form

$$\left(\mu\,\mathbf{M} - \mathbf{E}_2 + \mathrm{i}k\,\mathbf{E}_1 - k^2\,\mathbf{E}_0 + \mathbf{R}(k,\mu)\right)\phi = \mathbf{0} \quad (1)$$

which we abbreviate as

$$\mathbf{L}(k,\mu)\,\phi = \mathbf{0} \quad (2)$$

with $\mu = \omega^2$. Here, $\mathbf{M}, \mathbf{E}_0, \mathbf{E}_1, \mathbf{E}_2$ are finite element matrices, and ϕ denotes the eigenvector, representing the amplitudes of displacements in the plate as well as the pressure or displacements in the unbounded domains. Furthermore, $\mathbf{R}(k,\mu)$ denotes the nonlinear terms stemming from the coupling to the half-spaces:

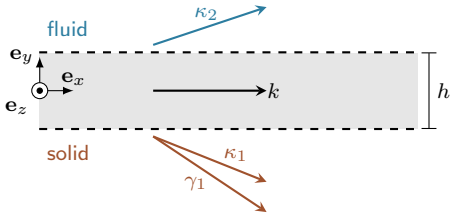

Fig. 1: Schematic of a homogeneous plate of thickness h between a fluid and a solid half-space.

$$\mathbf{R}(k,\mu) = \sum_{j=1}^{6} b_j\,\xi_j\,\mathbf{R}_j \quad (3)$$

with

$$b_j = \begin{cases} \mathrm{i} & j \in \{1,2\} \quad \text{fluid half-space,} \\ k & j \in \{3,4,5,6\} \quad \text{solid half-space.} \end{cases} \quad (4)$$

We denote by ξ the vertical wavenumbers of partial waves in the unbounded domains:

$$\xi_j(k,\mu) = \pm\sqrt{\frac{\mu}{c_j^2} - k^2} \quad (5)$$

with the corresponding wave speed c_j. The notation in Eq. (3) includes all six possible partial waves, while for any half-space not present in the current model, we set the corresponding $\mathbf{R}_j$ matrices to $\mathbf{0}$.

Solving the multiparameter eigenvalue problem

Equation (1) can be posed as a linear *multiparameter* eigenvalue problem in the parameters k, k^2, ξ_j. For brevity, we show the simplest case involving only one partial wave. This scenario may represent a plate coupled to a fluid either on one surface only or the same fluid on both surfaces. In this case, solutions to Eq. (1) satisfy the following system:

$$\begin{gathered}(\mu\,\mathbf{M}-\mathbf{E}_2+\mathrm{i}k\,\mathbf{E}_1+\xi_0\,\mathbf{E}_0+\mathrm{i}\xi_1\mathbf{R}_1)\,\phi=\mathbf{0},\\ \left(\begin{bmatrix}0 & -\kappa_1^2\\ 1 & 0\end{bmatrix}+\mathrm{i}\xi_1\begin{bmatrix}1 & 0\\ 0 & 1\end{bmatrix}+\xi_0\begin{bmatrix}0 & -1\\ 0 & 0\end{bmatrix}\right)\mathbf{x}_1=\mathbf{0},\\ \left(\begin{bmatrix}0 & 0\\ 0 & 1\end{bmatrix}+\mathrm{i}k\begin{bmatrix}0 & 1\\ 1 & 0\end{bmatrix}+\xi_0\begin{bmatrix}1 & 0\\ 0 & 0\end{bmatrix}\right)\mathbf{x}_2=\mathbf{0},\end{gathered}$$

where

$$\xi_1^2:=\kappa_1^2-k^2,\quad \xi_0=-k^2 \tag{6}$$

and $\mathbf{x}_1\neq 0$, $\mathbf{x}_2\neq 0$. Note that the determinants of the matrices in the second and third equations equal $\kappa_1^2-k^2-\xi_1^2$ and ξ_0+k^2, respectively; hence, these equations incorporate the relations (6). If the half-space consists of a solid elastic material, the system is slightly different. Considering again only one partial wave in the unbounded domain, we obtain

$$\begin{gathered}(\mu\,\mathbf{M}-\mathbf{E}_2+\mathrm{i}k\,\mathbf{E}_1+\xi_0\,\mathbf{E}_0+k\xi_3\mathbf{R}_1)\,\phi=\mathbf{0},\\ \left(\begin{bmatrix}0 & -\kappa_1^2\\ 0 & 0\end{bmatrix}+k\xi_3\begin{bmatrix}1 & 0\\ 0 & 1\end{bmatrix}+\xi_0\begin{bmatrix}0 & -1\\ 1 & 0\end{bmatrix}\right)\mathbf{x}_1=\mathbf{0},\\ \left(\begin{bmatrix}0 & 0\\ 0 & 1\end{bmatrix}+\mathrm{i}k\begin{bmatrix}0 & 1\\ 1 & 0\end{bmatrix}+\xi_0\begin{bmatrix}1 & 0\\ 0 & 0\end{bmatrix}\right)\mathbf{x}_2=\mathbf{0}.\end{gathered}$$

Introducing several partial waves or both a solid and a fluid half-space coupled to the same plate can be achieved straightforwardly by extending the system of equations accordingly. Details are found in [5]. Nowadays, established algorithms exist for the solution of multiparameter eigenvalue problems of this type [7, 8]. We make use of the approach implemented in the Matlab toolbox MultiParEig [9]. It requires the solution of a linear generalized eigenvalue problem involving the so-called operator determinants, which are constructed from Kronecker products of the matrices defining the multiparameter eigenvalue problem. While this approach allows the accurate computation of all solutions at any given frequency, the computational costs can be significant, as the operator determinants are square matrices of size $2^{n_\xi+1}n$, where n denotes the size of the finite element matrices, and n_ξ is the total number of partial waves in the half-spaces. Hence, in the most challenging case of a plate coupled to two different elastic half-spaces, the operator determinants are of size $32n\times 32n$.

Solution by exponential residual relaxation

The concept of exponential residual relaxation, also known as Zhang Neural Networks [10, 11, 12], is the following. Say we want to minimize some parameterized objective function, i.e., we are interested in solving

$$\mathbf{f}(\mathbf{y}(\mu),\mu)=0 \tag{7}$$

with a given parameter μ, defined on some interval $\mathcal{I}$. The idea is to postulate an exponentially decreasing residual of the above equation, such that

$$\mathbf{f}'(\mathbf{y}(\mu),\mu)=-\chi\,\mathbf{f}(\mathbf{y}(\mu),\mu),\quad \mu\in\mathcal{I} \tag{8a}$$

$$\mathbf{y}(\mu_0)=\mathbf{y}_0, \tag{8b}$$

where $\mathbf{f}'$ denotes the derivative with respect to μ, and χ is an algorithmic constant, defining the decay rate. In this form, Eqs. (8) pose an initial value problem that can be solved using standard algorithms, typically of the Runge-Kutta type. To apply this idea to our nonlinear eigenvalue problem, we define the objective function

$$\mathbf{f}(\phi,k,\mu)=\begin{bmatrix}\mathbf{L}(k,\mu)\,\phi\\ \phi^{\mathrm{H}}\phi-1\end{bmatrix}, \tag{9}$$

where the second row introduces a normalization required to obtain unique eigenvectors. The total derivative with respect to the parameter μ is given as

$$\mathbf{f}'(\phi,k,\mu)=\begin{bmatrix}\mathbf{L}(k,\mu)\phi'+\mathbf{L}'(k,\mu)\phi\\ 2\phi^{\mathrm{H}}\,\phi'\end{bmatrix}. \tag{10}$$

Substituting $\mathbf{f}$ and $\mathbf{f}'$ into Eq. (8)a yields

$$\begin{bmatrix}\mathbf{L} & \mathbf{L}_{,k}\,\phi\\ 2\phi^{\mathrm{H}} & 0\end{bmatrix}\begin{bmatrix}\phi'\\ k'\end{bmatrix}=-\begin{bmatrix}\chi_1\,\mathbf{L}\,\phi+\mathbf{L}_{,\mu}\,\phi\\ \chi_2\,(\phi^{\mathrm{H}}\phi-1)\end{bmatrix}, \tag{11}$$

which can be solved numerically starting from some known solution ϕ_0, k_0. The decay parameters are chosen as

$$\chi_1=100\frac{h^2}{c_t^2},\quad \chi_2=10\frac{h^2}{c_t^2} \tag{12}$$

with h and c_t denoting the plate's thickness and transversal wave speed, respectively. This approach requires reasonably accurate initial values at some μ_0, which can be computed either by the method described in the previous section or by suitable approximations [6], such as those obtained by replacing the exact boundary conditions by simple dashpots [13]. To solve Eq. (11), we employ a Runge-Kutta-based solver optimized for stiff differential equations with a variable step size implemented in Matlab's function *ode15s*.

DOI 10.5162/Ultrasonic2025/A12-b1

Numerical example

To demonstrate the capabilities of both approaches and compare their results, we present a challenging yet somewhat academic example, namely a titanium plate between an acoustic and an elastic half-space, consisting of water and Teflon, respectively. The material parameters are listed in Tab. 1. Figure 2 shows the phase velocity and attenuation of lowly attenuated modes (less than 4 dB/mm) up to a frequency of 8 MHz, computed using both proposed algorithms. For conciseness, we only show those solutions for which all wave vectors in the unbounded domains point away from the plate. In addition, there are solutions with one or more wave vectors pointing towards one of the plate surfaces. In practical applications, one is usually more interested in the direction of the power flux, which can be used as a criterion for distinguishing modes, see [5]. Applying the solution procedure based on multiparameter eigenvalue problems, we compute solutions at 120 predefined frequency steps, resulting in a total computational time of about 30 s on a current laptop computer. Employing the concept of exponential residual relaxation, we use the solution obtained by the first approach at 8 MHz and trace each of the shown modes towards $\mu = 0$. This computation takes about 1 s in total and requires an average of 74 steps per mode as chosen automatically by the solver when setting the solver's relative tolerance to 0.01. The results of both approaches are in excellent agreement. In addition, we show the wave field of an arbitrarily selected mode, which is obtained directly by computing the eigenvector ϕ, as it includes the amplitudes of displacements and pressure both inside the plate and in the unbounded domains. Specifically, we selected the third propagating mode (roughly corresponding to the A_1 mode in a free plate). Note that, while the results directly provide amplitudes along the plate's thickness, the wave field anywhere inside the plate and the unbounded domains can be computed in a postprocessing step. A detailed discussion of the accuracy and performance, as well as further examples, can be found in [5, 6]. The method based on multiparameter eigenvalue problems is also implemented in the free Matlab toolbox SAMWISE [14].

Tab. 1: Material parameters used in the example.

	density ρ	wave speeds c_ℓ, c_t	
Teflon	2.20 g/cm^3	1.35 km/s	0.55 km/s
titanium	4.46 g/cm^3	6.06 km/s	3.23 km/s
water	1.00 g/cm^3	1.48 km/s	

Conclusion

The proposed approaches help overcome a previous obstacle in applying semi-analytical methods to the case of plate structures coupled to unbounded domains. We provide two highly robust methods for solving the nonlinear eigenvalue problems that arise in this context. These techniques allow the computation of mode shapes, wavenumbers, and modal attenuation for arbitrarily layered plate structures coupled to solid and/or acoustic fluid media.

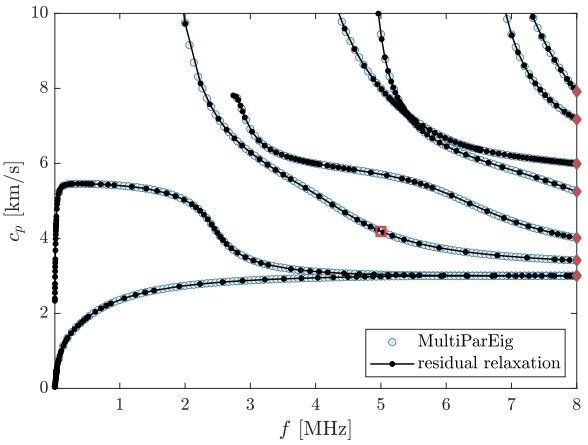

(a) phase velocity

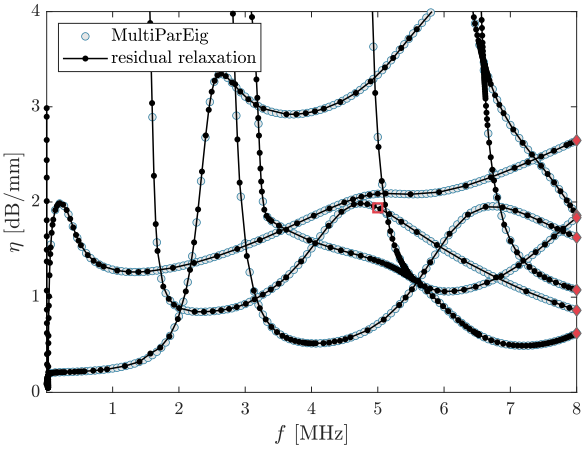

(b) attenuation

Fig. 2: Dispersion curves of a 1-mm-thick titanium plate between a solid and a fluid half space. Results are obtained using the framework of multiparameter eigenvalue problems as well as the proposed approach based on exponential residual relaxation. The symbol □ marks the solution selected for plotting the wave field in Fig. 3.

References

[1] H. Lamb. "On waves in an elastic plate". In: *Proceedings of the Royal Society of London* 93.648 (1917), pp. 114–128. DOI: 10.1098/rspa.1917.0008.

[2] M. J. S. Lowe. "Matrix techniques for modeling ultrasonic waves in multilayered media". In: *IEEE Transactions on Ultrasonics, Ferroelectrics and Frequency Control* 42.4 (1995), pp. 525–542. DOI: 10.1109/58.393096.

[3] H. Gravenkamp, C. Song, and J. Prager. "A numerical approach for the computation of dispersion relations for plate structures using the scaled boundary finite element method". In: *Journal of Sound and Vibration* 331.11 (2012), pp. 2543–2557. DOI: 10.1016/j.jsv.2012.01.029.

[4] H. Gravenkamp, C. Birk, and C. Song. "Numerical modeling of elastic waveguides coupled to infinite fluid media using exact boundary conditions". In: *Computers & Structures* 141 (2014), pp. 36–45. DOI: 10.1016/j.compstruc.2014.05.010.

[5] H. Gravenkamp et al. "Computation of leaky waves in layered structures coupled to unbounded media by exploiting multiparameter eigenvalue problems". In: *Journal of Sound and Vibration* 596 (2025), p. 118716. DOI: 10.1016/j.jsv.2024.118716.

[6] H. Gravenkamp, B. Plestenjak, and D. A. Kiefer. "Computing leaky waves in semi-analytical waveguide models by exponential residual relaxation". In: *ArXiv e-prints* (2025). DOI: 10.48550/arXiv.2505.04735.

[7] B. Plestenjak, C. I. Gheorghiu, and M. E. Hochstenbach. "Spectral collocation for multiparameter eigenvalue problems arising from separable boundary value problems". In: *Journal of Computational Physics* 298 (2015), pp. 585–601. DOI: 10.1016/j.jcp.2015.06.015.

[8] E. Ringh and E. Jarlebring. "Nonlinearizing two-parameter eigenvalue problems". In: *SIAM Journal on Matrix Analysis and Applications* 42.2 (2021), pp. 775–799. DOI: 10.1137/19M1274316.

[9] B. Plestenjak. *MultiParEig*. 2023. URL: www.mathworks.com/matlabcentral/fileexchange/47844-multipareig.

[10] Y. Zhang and J. Wang. "Recurrent neural networks for nonlinear output regulation". In: *Automatica* 37.8 (2001), pp. 1161–1173. DOI: 10.1016/S0005-1098(01)00092-9.

[11] F. Uhlig and Y. Zhang. "Time-varying matrix eigenanalyses via Zhang Neural Networks and look-ahead finite difference equations". In: *Linear Algebra and Its Applications* 580 (2019), pp. 417–435. DOI: 10.1016/j.laa.2019.06.028.

[12] F. Uhlig. "Zhang neural networks: An introduction to predictive computations for discretized time-varying matrix problems". In: *Numerische Mathematik* 156 (2024), pp. 691–739. DOI: 10.1007/s00211-023-01393-5.

[13] H. Gravenkamp, C. Birk, and C. Song. "Computation of dispersion curves for embedded waveguides using a dashpot boundary condition". In: *The Journal of the Acoustical Society of America* 135.3 (2014), pp. 1127–1138. DOI: 10.1121/1.4864303.

[14] H. Gravenkamp. *SAMWISE: Semi-Analytical Modeling of Waves in Structural Elements*. 2024. DOI: 10.5281/zenodo.13830671. URL: https://github.com/haukegravenkamp/SAMWISE.

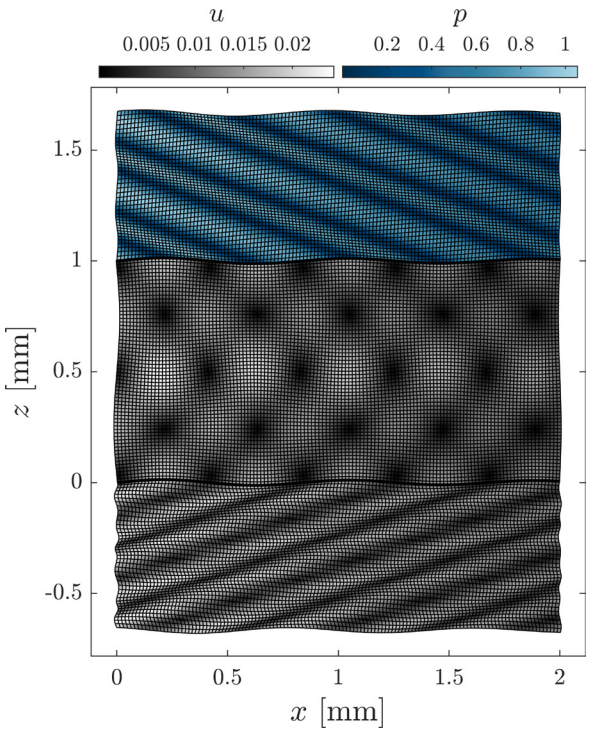

Fig. 3: Wave field of the third propagating mode at a frequency of 5 MHz.

DOI 10.5162/Ultrasonic2025/A12-b3

Ultrasonic Flow Measurement Using Guided Acoustic Waves: Application of Cylindrical Modes in Pipe Systems

Alexander Backer[1] *and Klaus Stefan Drese*[1]
[1] *Institute for Sensor and Actuator Technology (ISAT), Coburg University of Applied Sciences and Arts, Am Hofbräuhaus 1B, 96450 Coburg, Germany*
Alexander.Backer@hs-coburg.de

Abstract: This paper explores an alternative approach to ultrasonic flow measurement using guided acoustic waves in cylindrical modes. Unlike conventional methods with diagonal sound propagation, the entire pipe including the fluid is excited to vibrate, reducing path-dependent correction factors. A ring-shaped sensor was developed for a DN15 steel pipe. Results show a signal time shift 2.5 times greater than with Lamb wave-based sensors, adjustable over distance. This approach enables precise, non-invasive flow measurement across various pipe diameters.

Keywords: Flow metering, non-invasive flowmeter, ultrasonic flow measurement, guided acoustic waves, cylindrical modes

Introduction

Ultrasonic flow measurement in pipes has been established in industrial environments for many years. It is a precise, cost-effective and, above all, non-invasive method for measuring volume flows. In addition to variants with piston transducers and wedge transducers, in which sound is transmitted diagonally through the fluid once with and once against the direction of flow, guided acoustic waves are also used that couple out into the fluid [1, 2]. An essential common feature of these methods is the measurement along a sound path, which means that there are dependencies on the flow profile and correction factors are therefore required. The angle of the sound path directly influences the measured signal time shift. This means that the sensitivity of the measuring device when using guided waves is media-specific and can hardly be influenced by design. An approach that differs from the diagonal sound paths is the use of guided acoustic waves in the form of cylindrical modes. This involves sound propagation along the pipe, whereby the entire pipe and the fluid are excited to oscillate. Interaction with the entire fluid eliminates the need for path-dependent correction factors. In addition, this results in a much longer effective measurement path compared to diagonal transmission. This is not determined by the flowing medium but by the sensor distance, which also increases the signal time shift to be analysed. Due to the longer effective measuring distance, the cylindrical modes are already used for measuring the smallest flow rates in very thin pipes and cannulas [3]. The possibility of extending the approach to significantly larger pipe diameters has now been tested on a DN15 pipe.

Selection of suitable modes

For most common ultrasonic flow sensors with piston or wedge transducers, the angle of the sensors or wedge used is particularly important. In addition, a frequency suitable for the fluid and the pipe geometry must be selected. With Lamb wave-based flow sensors, on the other hand, the propagation and decoupling behaviour of the different Lamb modes must be taken into account. The selection of a suitable mode and measuring frequency is crucial here. The sensitivity of the sensor to a fluid flow resulting from the choice of operating point and can be determined by the convection coefficient [2]. This is shown for the material and fluid properties specified in Tab. 1 in figure 1.

Tab. 1: Sensor geometries and material parameters at $20\ ^\circ\mathrm{C}$ *[4].*

Tube Geometry		
Inner diameter	b	$15\ \mathrm{mm}$
Wall thickness	d	$1.5\ \mathrm{mm}$
Tube Properties		
Young's modulus	E	$193.8\ \mathrm{GPa}$
Poisso's ratio	ν	0.294
Density	ρ	$7969.0\ \mathrm{kg/m^3}$
Water Properties		
Speed of Sound	c_f	$1481.5\ \mathrm{m/s}$
Density	ρ	$998.2\ \mathrm{kg/m^3}$

A typical operating point of a Lamb wave ultrasonic flow sensor is marked with a red circle in Fig. 1.

DOI 10.5162/Ultrasonic2025/A12-b3

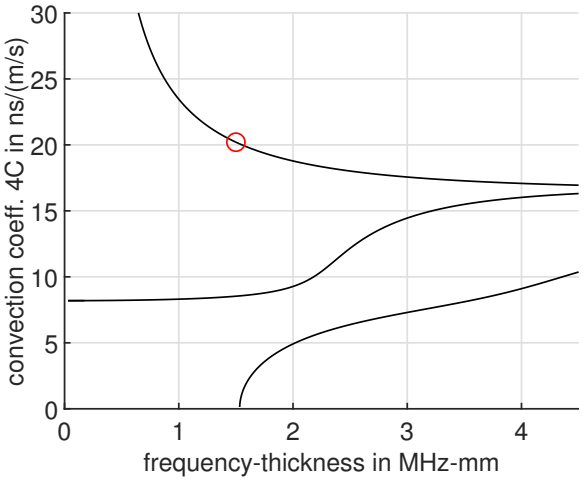

Fig. 1: Convection Coefficient for a Lamb wave based ultrasonic flow meter.

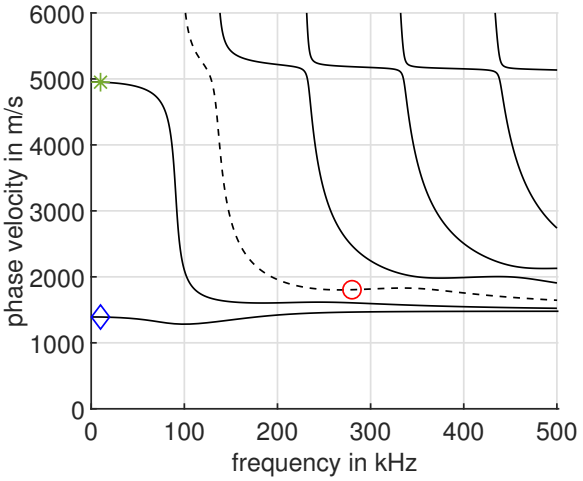

Fig. 2: Phase velocity diagramm of a fluid filled steel pipe. 0th circumferential order.

The example used represents a sensor with water flowing through it, which consists of two $1.5\ \mathrm{mm}$ thick, parallel steel plates, with $15\ \mathrm{mm}$ distance to each other. The mode used here is the A0 mode at an excitation frequency of $1\ \mathrm{MHz}$. The convection coefficient is calculated for a V-path configuration. The fluid is therefore sonicated twice in and twice against the flow direction. At a flow velocity of $1\ \mathrm{m/s}$, this results in a transit time difference of approx. $20\ \mathrm{ns}$.

In contrast to Lamb waves on plates, acoustic waves propagate on pipes in the form of cylindrical modes. There are longitudinal, flexural and torsional modes (L-, F-, T-modes). Due to the ring-shaped closed system of a pipe, azimuthal vibrations can also occur. These are numbered with the circumferential order starting at 0. In the case of a pipe filled with liquid, the interaction with the fluid and the sound propagation in the fluid results in additional modes with different vibration modes inside the fluid [5].
With the large number of possible modes, it is now necessary to find a suitable mode for the flow measurement. This paper focuses on the 0th circumferential order. The phase velocity is shown in Fig. 2 and the group velocity of the modes forming in a steel pipe filled with water is shown in Fig. 3. The exact material properties and pipe geometries are listed in Tab. 1.

When selecting a suitable mode and operating frequency, three points are particularly important. The first is the mode purity in the received signal. In addition to a dominant excitation by an optimised sensor geometry, this can be achieved by selecting a suitable operating point in the dispersion diagram of the group velocity and thus the time separation from other modes. Three operating points selected as examples are labelled red, green and blue in Fig. 2. The second point is the excitability and detectability of the mode. This is directly related to the third point, the sensitivity of the mode to a fluid flow. An initial estimate of this can be made using the axial power flow. Like the dispersion diagrams, this was calculated using the DISPERSE software [5]. It shows the spatial distribution of the axial power flow along the pipe across the pipe cross-section. In Fig. 4, this is shown for the positions marked in colour in Fig. 2 resp. Fig. 3.

The green and blue markings and the green and blue lines represent two extreme situations. In the former, the energy of the wave is transported almost exclu-

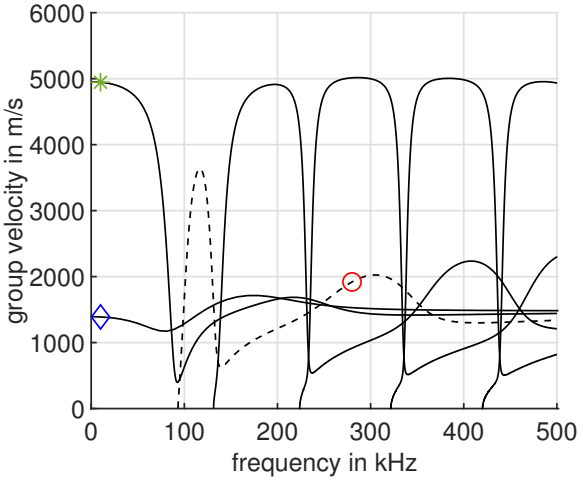

Fig. 3: Group velocity diagramm of a fluid filled steel pipe. 0th circumferential order.

DOI 10.5162/Ultrasonic2025/A12-b3

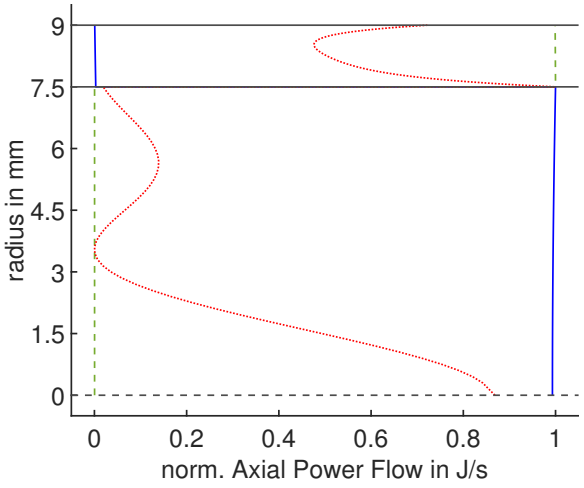

Fig. 4: Axial Power Flow of a fluid filled steel pipe.

sively in the pipe wall. This enables good excitability and detectability of the mode by an ultrasonic sensor attached to the pipe. However, since almost no energy is transported in the fluid, the mode hardly reacts to a fluid flow and is therefore unsuitable for a flow sensor. The blue curve represents the second extreme. Here, almost the entire energy of the mode is transported in the fluid. Although this means excellent sensitivity to fluid flow, it makes the mode extremely difficult to excite and detect. As shown in [3], it is possible to build a flow sensor with this mode, but it requires high signal amplification and at the same time massive attenuation of unwanted modes. The latter is difficult to realise with a DN15 pipe.
The third, red operating point represents a compromise between excitability and detectability as well as sensitivity to a fluid flow. In combination with excitation that is as mode-pure as possible through the sensor geometry and separation from other modes through a suitable group velocity, all conditions for the construction of an ultrasonic flow sensor are thus fulfilled.

Sensor configuration and measurement setup

Since the selected mode is one of the 0^{th} circumferential order, a ring-shaped sensor configuration was used. The sensor shown in Fig. 5 consists of 22 square piezoceramics. The sensors manufactured by PI Ceramic GmbH from PIC255 have an edge length of $2.54\ \mathrm{mm}$ and are equally distributed around the tube. A $100\ \mu\mathrm{m}$ thick indium foil is located between the tube surface and the piezoceramic, which deforms when the piezoceramics are pressed against it by tightly wrapping it with dental floss and enables good sound transmission between the tube and the sensor. Electrical contact was made via the tube and a copper wire wrapped in the dental floss.

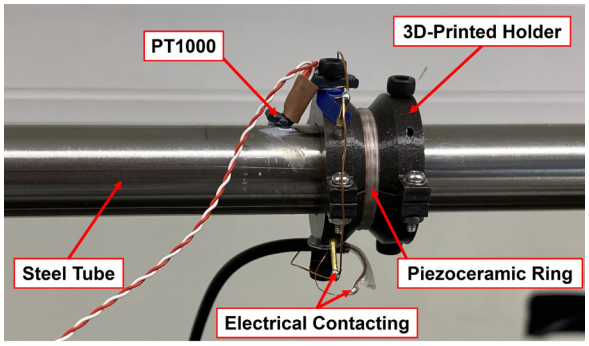

Fig. 5: One side of the ultrasonic flow meter with electrical connections and PT1000 temperature sensor.

Two of these sensors were attached to the $1.6\ \mathrm{m}$ long DN15 pipe at a distance of $200\ \mathrm{mm}$. The pre-flow distance between the first sensor and the nearest pipe coupling was $1\ \mathrm{m}$. The assembled measuring tube was then measured in the water test rig shown in Fig. 6. The flow rate was controlled via the speed control of a centrifugal pump. The Promass Q Coriolis sensor from Endress+Hauser was used as the reference sensor. A Keysight 33500B function generator was used to simultaneously excite the two sensors and a Teledyne LeCroy HDO6054B oscilloscope was used to detect the received signals. Switching between transmitting and receiving was realised by a two-channel multiplexer. A $20\ \mathrm{V_{peak-peak}}$, $280\ \mathrm{kHz}$, 10-fold sine burst with Hanning windowing was used as the transmission signal.

Measurement results and discussion

The two simultaneously recorded received signals were cross-correlated with each other and the time shift was determined. Fig. 7 shows the flow rate determined by the Coriolis sensor and varied via the pump speed on the left y-axis. The corresponding displacement of the ultrasonic signal is plotted on the right y-axis. Before the start and at the end of each measurement, the flow was completely stopped by closing the valves in order to obtain a zero line and thus a reference.

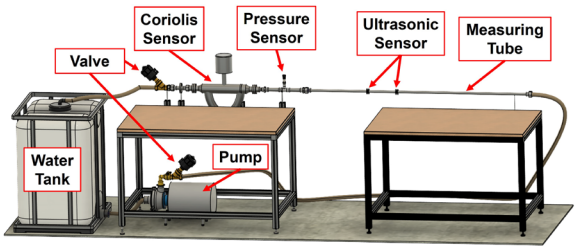

Fig. 6: Water test rig.

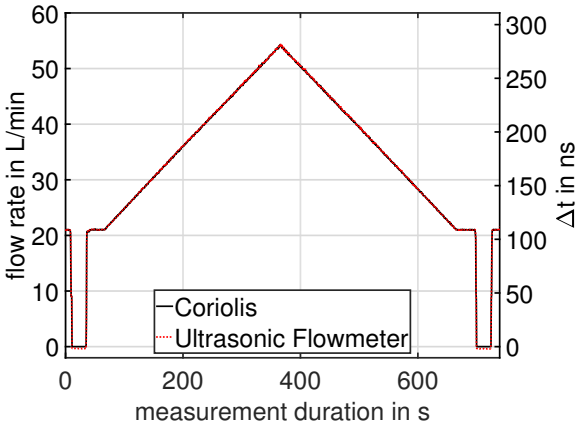

Fig. 7: Comparison of Coriolis and Ultrasonic Flow meter.

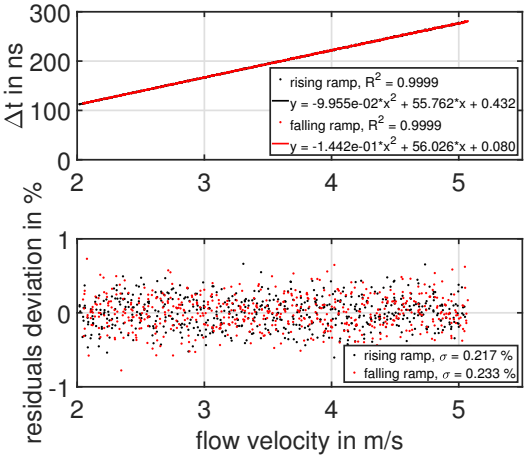

Fig. 8: Flow rate dependent signal shift.

As can be clearly seen in the figure, it is possible to achieve an almost perfect match between the Coriolis sensor and the ultrasonic flow sensor by appropriately scaling the right y-axis. It should be noted that the data had to be shifted by -1.8 ns in the y-direction in order to achieve a match between the curves. This leads to a slight offset in the area without flow. The cause of this is not yet clear and is therefore not discussed further.

In Fig. 8 at the top, the determined signal transit time shift of the rising and falling ramp is plotted against the mean flow velocity determined from the flow rate and a 2nd-order polynomial regression was performed. The relative deviation of the residuals is shown below. From the linear term of the regression, a signal transit time shift comparable to the convection coefficient and dependent on the mean flow velocity can be determined. This is around $55.9\ \mathrm{ns/(m/s)}$ and is therefore 2.5 times larger than a comparable lamb wave-based ultrasonic flow sensor with a V-path. It should be mentioned here that the resulting signal propagation time shift can be adjusted almost arbitrarily depending on the selected sensor distance. It is therefore possible to obtain a more compact sensor with a smaller distance or to increase the signal transit time shift and thus also the accuracy with a larger distance. This reduces the dependence on the pipe and fluid properties and thus opens up new design possibilities for ultrasonic flow sensors.
Although the significantly higher number of existing cylindrical modes compared to Lamb waves with a similar geometry represents a challenge in sensor development, it also opens up new possibilities with regard to disturbance compensation. Future investigations and experiments will have to show the scope of potential applications and the limits of cylindrical modes for ultrasonic flow measurement.

Funding

This research was funded by the German Federal Ministry of Research, Technology and Space (BMFTR) under the funding program Forschung an Fachhochschulen for the project "HydrAmess" under grant number 13FH094KX1.

References

[1] O. Fiedler. *Strömungs- und Durchflussmesstechnik*. München; Wien: Oldenbourg, 1992. 360 pp. ISBN: 3-486-22119-1.

[2] D. A. Kiefer, A. Benkert, and S. J. Rupitsch. "Transit Time of Lamb Wave-Based Ultrasonic Flow Meters and the Effect of Temperature". In: *IEEE transactions on ultrasonics, ferroelectrics, and frequency control* 69.10 (Sept. 2022), pp. 2975–2983. DOI: 10.1109/TUFFC.2022.3201106.

[3] A. Backer et al. "NON-INVASIVE ULTRASONIC FLOW MEASUREMENT METHOD FOR THE DETECTION OF FLOW RATES IN THE MICROLITER RANGE". In: *The 5th Conference on MicroFluidic Handling Systems (MFHS 2024)*. Munich, Germany, Feb. 21, 2024, pp. 29–32.

[4] *COMSOL Multiphysics®*. Version 6.1. Stockholm, Sweden. URL: www.comsol.com.

[5] M. Lowe and B. Pavlakovic. *DISPERSE - A System for Generating Dispersion Curves*. Version 2.0.20f. London, Nov. 14, 2019.

DOI 10.5162/Ultrasonic2025/A12-b4

Development of a continuous ultrasonic sensor for monitoring the fill level of existing separating layers

Miriam Piechaczek[1], Alexander Backer[1], Tobias Roß[1], Sabrina Tietze[1], and Klaus Stefan Drese[1]
[1]Institute of Sensor and Actuator Technology, Coburg University of Applied Sciences and Arts, Coburg, Germany
Miriam.Piechaczek@hs-coburg.de

Abstract: A sensor based on guided acoustic waves (GAW) to enable simultaneous detection of fill levels and phase boundaries in heterogeneous media is presented. By exciting longitudinal, flexural, and torsional modes in a polymer based cylindrical waveguide, level measurement, interface detection, and temperature compensation are achieved within a single system. The integration of multiple modes into one sensor reduces system complexity and cost while offering robust performance for industrial applications.

Keywords: Guided Acoustic Waves (GAW), multimodal waveguide, level measurement, multiphase media

Introduction

Level detection in liquid-filled containers is crucial for various industrial applications, such as wastewater treatment, chemical processing, and oil–water separation. Accurate and continuous monitoring of fluid conditions is essential to ensure process safety, operational efficiency, and environmental compliance. However, current sensor technologies suffer from several practical limitations, including sensitivity to foam or sediments, reduced accuracy in multiphase or inhomogeneous media, and incompatibility with aggressive or corrosive fluids [1]. Additionally, most conventional systems are unable to detect internal phase boundaries or sediment layers, particularly under conditions of mechanical fouling or chemical exposure.

Hence, the objective of this study is to present the use of guided acoustic waves (GAW) in polymer waveguides for the reliable detection of fill levels, phase boundaries, and bottom sediments in such challenging environments. Numerical simulations were conducted to explore the mode-specific sensitivities of a multimodal waveguide made from high-density polyethylene (HD-PE). The findings form the foundation for a novel sensor concept that enables not only level measurement, but also temperature compensation and identification of multiphase interfaces through multimode excitation. This approach offers a compact, chemically robust, and cost-effective solution for advanced industrial sensing applications.

Guided acoustic waves offer a promising alternative. Previous studies have shown that acoustic modes propagating in solid rods, particularly longitudinal (L) and flexural (F) modes, are suitable for level measurement. Metallic waveguides made of aluminum or steel have already been used to determine immersion depth through attenuation effects (L(0,2)) or time-of-flight measurements (L(0,1)) [2]. However, metals are costly and prone to corrosion, which limits their use in aggressive environments. Although corrosion-resistant alloys are available, they are often prohibitively expensive. As a result, polyethylene and other polymers are considered attractive alternatives due to their chemical resistance and low cost, and their suitability for acoustic wave excitation is widely discussed in the literature [3] [4]. Despite these advantages, polymers pose specific challenges, particularly modal dispersion and signal attenuation, which complicate the interpretation of acoustic signals [5] [6]. Building on recent developments in waveguide-based sensing technologies [1], this work proposes a multimodal excitation strategy to leverage the distinct physical characteristics of L-, F-, and T-modes. To investigate these properties, finite element simulations were conducted to model wave propagation in a polyethylene rod submerged in water. The simulations aim to evaluate the sensitivity of longitudinal, flexural, and torsional modes to changes in fluid fill level, internal phase boundaries, and temperature. Particular attention is given to the interaction between the waveguide surface and the surrounding medium, as this is expected to affect the modal behavior. The numerical investigation of the different mode sensitivities thus provides a solid foundation for a multimodal sensor concept and practical sensor design.

Materials and Methods

To assess the mode-specific sensitivity of guided acoustic waves in polymer-based waveguides, three-

DOI 10.5162/Ultrasonic2025/A12-b4

dimensional finite element simulations were conducted using COMSOL Multiphysics version 6.1 [7]. To simulate acoustic wave propagation within the HD-PE waveguide, a five-cycle sine burst modulated by a Hanning window at a center frequency of 6 kHz was applied. The generated acoustic wave propagates through the waveguide, reflectes at the opposite end, and returns to the transducer point by which a signal evaluation can be done. The simulation model consists of a cylindrical waveguide (length: $2\,\mathrm{m}$, diameter: $40\,\mathrm{mm}$) that is fully immersed in water to realistically model fluid-structure interactions. The objective of the simulations was to quantify reflection, attenuation, and propagation time variations of individual modes under varying fill levels and temperatures.
The geometry of the rod is based on commercially available dimensions and was adopted from prior investigations [1]. The material properties of high-density polyethylene (HD-PE) at room temperature are summarized in Table 1:

Tab. 1: Material properties of HD-PE at room temperature (20°C).

Parameter	Symbol	Value
Young's modulus	E	$2.2 \times 10^9\,\mathrm{Pa}$
Density	ρ	$960\,\mathrm{kg/m^3}$
Poisson's ratio	ν	0.38

To account for temperature-dependent effects, the Young's modulus was implemented as a function of temperature. The function is based on the COMSOL Multiphysics material database for HD-PE and was normalized to the reference values above [7]. The applied polynomial approximation leading to a Youngs Modulus in GPa and using temperatures provided in K is given by:

$$E(T) = 5{,}770 \times 10^{10} - 4{,}029 \times 10^{8} \cdot T + 9{,}505 \times 10^{5} \cdot T^2 - 7{,}573 \times 10^{2} \cdot T^3 \quad (1)$$

Temperature-dependent fluid properties of water were also taken into account using the COMSOL material database.
To analyze the sensitivity of the modes with respect to the fill level, a parameter sweep was performed for the heights $0\,\mathrm{m}$, $0.5\,\mathrm{m}$, $1\,\mathrm{m}$, $1.5\,\mathrm{m}$, and $2\,\mathrm{m}$. An excitation was introduced using a surface source applied to the top face of the rod, and the response signal was measured at a fixed point along the rod's circumference on the same surface.
Additionally, to assess the propagation behavior, dispersion diagrams were generated for the L(0,1), F(1,1), and T(0,1) for a high-density polyethylene (HD-PE) waveguide under two environmental conditions: vacuum and water immersion.

Results and Discussion

The results of the dispersion calculations indicate that both the longitudinal and flexural modes exhibit sensitivity to the surrounding medium (Fig. 1).

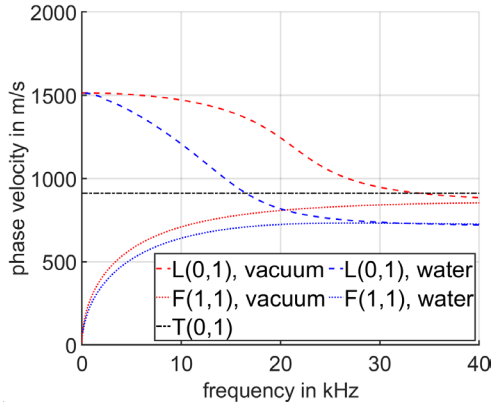

Fig. 1: Dispersion curves for the L(0,1), F(1,1), and T(0,1) modes in vacuum and water.

Specifically, their phase velocities are significantly higher in vacuum (red lines) than in water (blue lines), suggesting a strong interaction with the external fluid. This observation implies that these two modes are well-suited for detecting variations in fluid contact along the waveguide, such as changes in fill level. In contrast, the torsional mode T(0,1) (black line) shows no appreciable difference in phase velocity between vacuum and water, nor across the frequency range considered, as can be seen in Fig. 2.

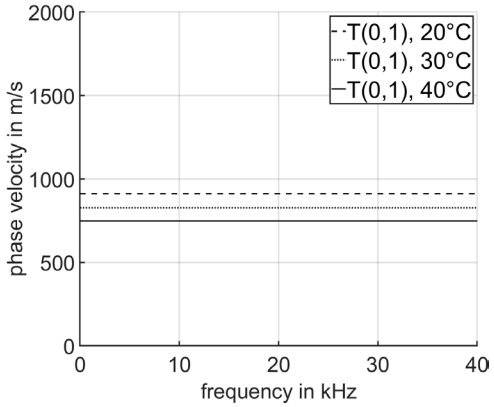

Fig. 2: Dispersion behavior of the T(0,1) mode at different temperatures.

Its velocity profile remains constant and unaffected by the external medium. This non-reactive behavior indicates that the T-mode is insensitive to immersion

DOI 10.5162/Ultrasonic2025/A12-b4

depth or fluid properties and may therefore serve as a stable reference in multimodal sensing configurations due to its remaining sensitivity to temperature variations.

To evaluate the influence of both the surrounding medium and temperature, further dispersion curves were generated for the L(0,1) and F(1,1) modes at 20 °C, 30 °C, and 40 °C, each in vacuum and in water. The results show a clear reduction in phase velocity not only when transitioning from vacuum to water, but also with increasing temperature for the longitudinal and flexural modes. Specifically, the F(1,1) mode exhibits a reduction of approximately 75 m/s in phase velocity for a temperature increase of 20 °C, both in vacuum and in water, at an excitation frequency of 6 kHz (Fig. 3).

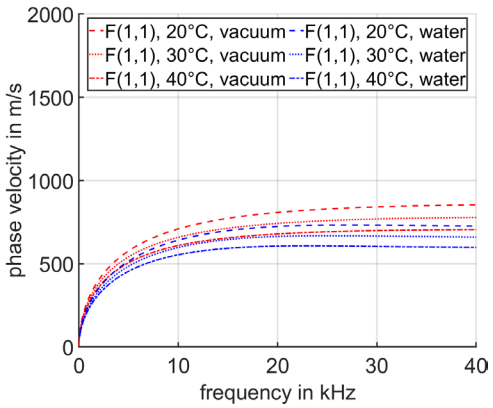

Fig. 3: Dispersion behavior of the F(1,1) mode at different temperatures and medium conditions.

In comparison, the L(0,1) mode shows a stronger reduction of about 280 m/s in vacuum and 250 m/s in water over the same temperature range at 6 kHz. (Fig. 4)

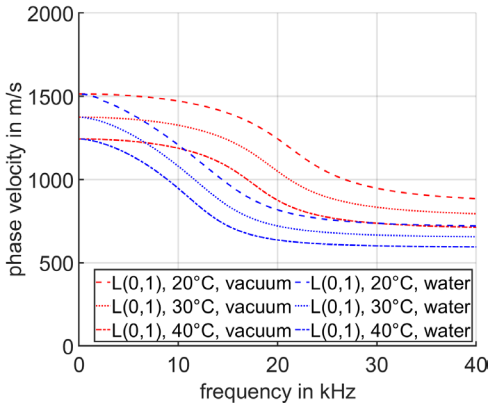

Fig. 4: Dispersion behavior of the L(0,1) mode at different temperatures and medium conditions.

This dual sensitivity toward both medium and temperature indicates that changes in environmental conditions affect wave propagation significantly. Consequently, accurate fill level determination using these modes requires temperature compensation to avoid erroneous interpretations.

To further verify the mode sensitivities, time-domain signal analyses were conducted. The torsional mode was first examined under vacuum conditions at various temperatures (Fig. 5).

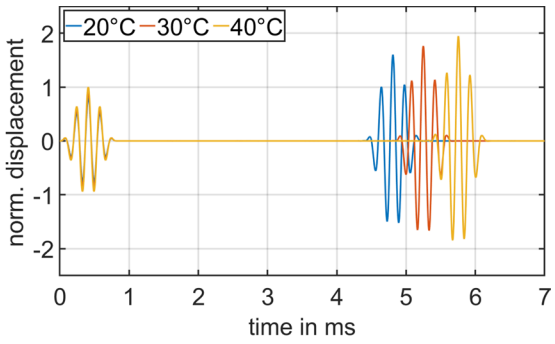

Fig. 5: Time signals of the torsional mode at 20°C, 30°C and 40°C in vacuum.

While the initial excitation pulses (left) overlap perfectly across all three temperatures (20°C, 30°C, and 40°C), the respective and reflected end signals (right) show a clear temporal shift. Specifically, the arrival time increases with temperature: the signal at 20°C arrives earliest, followed by 30°C and 40°C. This confirms the temperature-dependent propagation velocity of the T(0,1) mode, as proven by the examination of the dispersion (Fig. 2).

For the final analysis, time-domain signal evaluations of the three wave modes were performed at room temperature with varying fluid levels of the surrounding water(Fig. 6).
For the longitudinal (L) and flexural (F) modes, intermediate signal reflections were observed between the initial excitation (left) and the final reflection (right), after the wave had traversed the entire length of the waveguide. These intermediate reflections are attributed to interactions with the fluid medium, where higher filling levels lead to earlier reflection events corresponding to the fluid's upper boundary. In comparison, the flexural mode exhibits higher reflection amplitudes than the longitudinal mode, suggesting a potentially greater suitability for detecting fill level variations or identifying phase boundaries in stratified media. Specifically, the longitudinal mode returns approximately 4% of the excitation amplitude as a

reflection signal, whereas the flexural mode reflects about 14%, further highlighting its stronger sensitivity to fluid interaction.

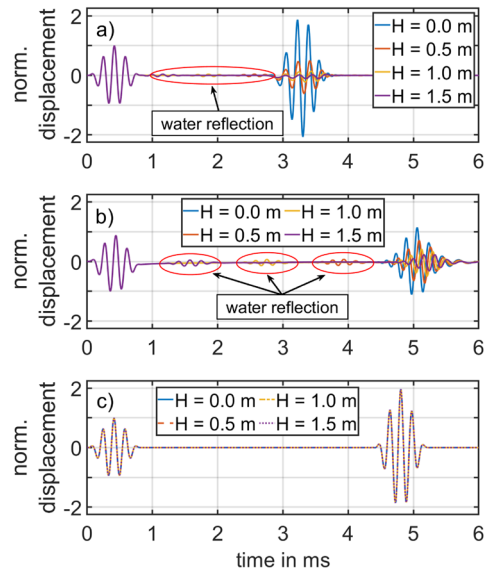

Fig. 6: Signal analysis for a) longitudinal mode b) flexural mode and c) torsional mode at different fluid levels (T=20°).

The varying arrival times of the end reflections are explained by the different group velocities of the wave modes, with the longitudinal mode (L) propagating fastest, followed by the torsional and flexural modes. The larger amplitude of the reflected end signals compared to the initial excitation signal can be attributed to constructive interference occurring at the rod termination during wave reflection.

Conclusion and Outlook

This study presents a numerical investigation of guided acoustic wave propagation in a polymer-based waveguide for simultaneous sensing of fill level, temperature, and phase boundaries. By selectively exciting and analyzing longitudinal, flexural, and torsional wave modes in a high-density polyethylene rod, distinct sensitivities toward environmental conditions were identified.
The results demonstrate that:

- The torsional mode T(0,1) is unaffected by contact with water and exhibits only temperature-dependent propagation characteristics, making it a reliable basis for temperature compensation.
- The longitudinal mode L(0,1) responds to both fill level and temperature changes, with measurable reflections at fluid interfaces, suitable for coarse interface detection.
- The flexural mode F(1,1) shows the highest sensitivity to fill level and phase boundaries, with strong signal modulation depending on immersion depth and surrounding medium.

These findings highlight the potential of a multimodal sensing strategy using guided acoustic waves in low-cost, chemically robust polymer materials. The integration of multiple wave modes within a single sensing element enables a compact and versatile sensor design capable of compensating for environmental cross-sensitivities. In the next steps, experiments will validate the theoretical findings. This includes the experimental characterization of mode behavior under varying fluid conditions and comparison of measured data with simulation results.

Acknowledgement

This research was funded by the German Federal Ministry of Research, Technology and Space (BMFTR) for the project KonUsT under grant number 02P24K111.

References

[1] K. Lutter, A. Backer, and K. S. Drese. "Guided Acoustic Waves in Polymer Rods with Varying Immersion Depth in Liquid". In: *Sensors* 23 (2023), p. 9892. DOI: 10.3390/s23249892.

[2] N. Subhash and B. Krishnan. "Fluid level sensing using ultrasonic waveguides". In: *Insight* 56 (2014), pp. 607–612. DOI: 10.1784/insi.2014.56.11.607.

[3] J. Shah, S. El-Hawwat, and H. Wang. "Guided Wave Ultrasonic Testing for Crack Detection in Polyethylene Pipes: Laboratory Experiments and Numerical Modeling". In: *Sensors* 23 (2023), p. 5131. DOI: 10.3390/s23115131.

[4] J. S. Egerton et al. "Ultrasonic attenuation and phase velocity of high-density polyethylene pipe material". In: *The Journal of the Acoustical Society of America* 141 (2017), pp. 1535–1545. DOI: 10.1121/1.4976689.

[5] H. Kwun, K. A. Bartels, and C. Dynes. "Dispersion of longitudinal waves propagating in liquid-filled cylindrical shells". In: *The Journal of the Acoustical Society of America* 105.5 (1999), pp. 2601–2611. DOI: 10.1121/1.426876.

[6] P. D. Wilcox. "A rapid signal processing technique to remove the effect of dispersion from guided wave signals". In: *IEEE Transactions on Ultrasonics, Ferroelectrics, and Frequency Control* 50.4 (2003), pp. 419–427. DOI: 10.1109/tuffc.2003.1197965.

[7] COMSOL Inc. *COMSOL Multiphysics: Simulate Real-World Designs, Devices, and Processes with Multiphysics Software*. https://www.comsol.com. Accessed: 2025-07-11. 2025.

DOI 10.5162/Ultrasonic2025/A12-c5

A Measurement Setup for the Determination of Temperature-Dependent Viscoelastic Material Parameters Using an Ultrasonic Pulse-Echo Technique

Dmitrij Dreiling[1], *Dominik Itner*[2], *Hauke Gravenkamp*[3], *Carolin Birk*[2], *and Bernd Henning*[1]
[1]*Paderborn University, Measurement Engineering Group, Paderborn, Germany*
[2]*University of Duisburg-Essen, Structural Analysis, Essen, Germany*
[3]*Otto von Guericke University Magdeburg, Institute of Materials, Technologies and Mechanics, Magdeburg, Germany*
dreiling@emt.uni-paderborn.de

Abstract: Ultrasonic methods facilitate a non-destructive characterisation of mechanical properties, such as Young's modulus or shear modulus, based on the propagation time and attenuation of ultrasonic signals. This contribution presents an ultrasonic measurement setup for determining temperature-dependent viscoelastic material parameters of polymers within a frequency range of $0.75\,\mathrm{MHz}$ to $2.5\,\mathrm{MHz}$. The system is based on a pulse-echo technique and features a temperature-controlled specimen chamber that enables precise and reproducible heating of hollow cylindrical specimens. To span the frequency range, a broadband ultrasonic transducer and a burst signal with a variable centre frequency are used for transmission. By systematically varying the temperature while measuring ultrasonic time-of-flight and attenuation, elastic and viscous properties can be identified across a temperature range of $20\,^{\circ}\mathrm{C}$ to $55\,^{\circ}\mathrm{C}$. Initial values are estimated from the measured signals, and the resulting viscous material parameters are determined using an inverse approach. The proposed method thus offers a time-efficient, non-invasive approach for characterising thermally sensitive, frequency-dependent material parameters.

Keywords: viscoelastic material parameters, temperature-dependent, inverse approach, pulse-echo measurement, polymers

Motivation

The determination of temperature-dependent viscoelastic material parameters is of crucial importance for understanding the behaviour of polymers in dynamic or harsh environments. Design, simulation and testing must be particularly accurate when polymers are subjected to continuous stress. However, the material parameters provided by manufacturers are often insufficient for simulation purposes, as they are typically measured using quasi-static and destructive methods. To address this limitation, acoustic methods have emerged as a viable alternative for non-destructive measurement [1, 2].

Our recent studies described the potential of an ultrasonic pulse-echo measurement setup and a guided wave approach for characterising viscoelastic properties of hollow cylindrical polymer specimens [3, 4]. The proposed framework, an inverse procedure, is presented in our work [5], where we demonstrate rapid convergence. The present study extends this methodology by systematically varying the ambient temperature between $20\,^{\circ}\mathrm{C}$ and $55\,^{\circ}\mathrm{C}$ of a specimen during measurements. Changing the thermal state perturbs a polymer's viscoelastic parameters e.g., elastic moduli, yet the specimen geometry remains (mostly) the same. Therefore, each temperature step results in a distinct pulse-echo measurement from the same physical specimen. By applying our inverse algorithm to this set of measurements, we can verify that the determined parameters evolve consistently with the imposed temperature changes, thereby demonstrating the robustness and repeatability of the method under varying operational conditions.

Forward Model of a Specimen with Viscoelastic Material Parameters

The forward model of the specimen is briefly introduced in the following. A hollow cylinder of inner radius r_i, outer radius r_o and length l is considered. Due to the extrusion process during the fabrication of polymer rods, a transversely isotropic viscoelastic material behaviour is assumed. The properties along the plane perpendicular to the cylinder length axis (indices $1, 2$) are assumed isotropic, while the properties along the longitudinal direction (index 3) differ. The polymer is assumed to behave linearly elastic for small strains and the constitutive relationship between the

DOI 10.5162/Ultrasonic2025/A12-c5

strains $\boldsymbol{\varepsilon}$ and the stresses $\boldsymbol{\sigma}$ is given by Hooke's law:

$$\boldsymbol{\sigma} = \mathbf{D}\,\boldsymbol{\varepsilon} \tag{1}$$

Considering transverse isotropy, the elasticity matrix $\mathbf{D}$ contains only five independent entries and can be expressed in terms of the five elastic parameters $E_1, E_3, \nu_{12}, \nu_{13}, \mu_{13}$, the Young's moduli, the Poisson's ratios and the shear modulus, respectively [3].

Further, a finite-element discretisation of the hollow cylinder gives the semi-discrete dynamic equilibrium

$$\mathbf{M}\,\ddot{\boldsymbol{u}}(t) \;+\; \mathbf{C}\,\dot{\boldsymbol{u}}(t) \;+\; \mathbf{K}\,\boldsymbol{u}(t) \;=\; \mathbf{0}\,, \tag{2}$$

where $\boldsymbol{u}(t)$ is the nodal displacement vector, $\mathbf{M}$ the consistent mass matrix and $\mathbf{K}$ the stiffness matrix built from the elasticity matrix as $\mathbf{K} = \int_{\Omega} \mathbf{B}^{\top}\mathbf{D}\mathbf{B}\,\mathrm{d}\Omega$. In this study, $\mathbf{C}$ denotes the damping matrix, which is modelled using the Rayleigh damping law

$$\mathbf{C} = \alpha_{\mathrm{M}}\,\mathbf{M} \;+\; \alpha_{\mathrm{K}}\,\mathbf{K}\,, \tag{3}$$

where α_{M} (mass-proportional) and α_{K} (stiffness-proportional) are scalar coefficients. Substituting the stiffness matrix and the Rayleigh damping (3) into the equation of motion (2) yields a governing relation for the hollow-cylindrical, transversely-isotropic polymer specimen subjected to a prescribed displacement. This relation can be solved with any standard time-integration scheme to obtain the displacement, velocity and stress fields needed for further analysis or for inverse property identification. The vector of all relevant viscoelastic parameters is given by

$$\boldsymbol{\gamma} = [E_1,\, E_3,\, \nu_{12},\, \nu_{13},\, \mu_{13},\, \alpha_{\mathrm{M}},\, \alpha_{\mathrm{K}}]\;. \tag{4}$$

Predicting ultrasonic wave propagation under viscoelastic constitutive laws can be computationally demanding, particularly in 3D finite element analyses at high frequencies and during parameter estimation in inverse procedures. To address this, the semi-analytical scaled boundary finite element method (SBFEM) is employed for efficient computation [6]. This method leverages a combination of radial discretisation, analytical solutions along the axis, and Fourier decomposition in the circumferential direction, thus efficiently handling arbitrary excitation patterns and the cylindrical geometry. The SBFEM formulation further enables the computation of sensitivities, i.e., derivatives of the simulated output with respect to the viscoelastic parameters $\boldsymbol{\gamma}$ [7]. Consequently, a single forward simulation results in both the time-dependent displacement response and its sensitivity to the underlying viscoelastic parameters, facilitating gradient-based optimisation.

So far, the descriptions refer only to modelling of the specimen. To set up a full forward model, the hardware of the measurement setup must also be modelled. For this purpose, analytical models are employed, which provide a swift yet sufficient representation of the hardware and are further introduced in [3].

Measurement Setup

Fig. 1 depicts the measurement setup including a USB oscilloscope, two custom-designed current-feedback amplifiers, switching electronics, a broadband ultrasonic transducer, and a thermal chamber with integrated radiator. Besides two inputs for data acquisition, the USB oscilloscope also features an arbitrary signal generator and an additional interface to trigger the switching electronics. The broadband amplifiers provide precise signal amplification of $6\,\mathrm{dB}$ when transmitting and $46\,\mathrm{dB}$ when receiving. The

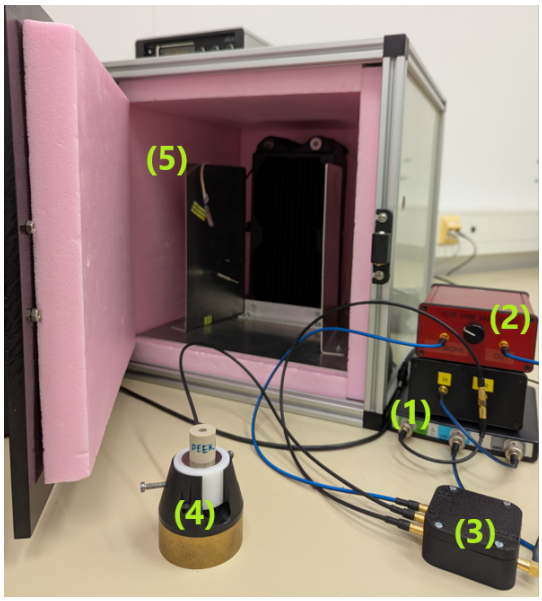

Fig. 1: (1) shows the USB oscilloscope (HS5-540XM, TiePie), (2) the custom transmitting and receiving voltage amplifier, (3) is the switching electronics with low on resistance, (4) is a broadband ultrasonic transducer with a specimen above, (5) is the thermal chamber with radiator.

wide bandwidth of the self-manufactured transducers allows excitation of variable center frequencies from $0.75\,\mathrm{MHz}$ to $2.5\,\mathrm{MHz}$, enabling the study of frequency effects on material parameters without the need to re-couple the specimen. Further, the specimen is coupled using a viscous medium applied by screen printing. The thermal chamber shown in Fig. 1 is connected to a cooling circulator (Julabo MAGIO MS-310F), which ensures fast and stable regulation of the temperature inside the chamber in a range from $20\,^{\circ}\mathrm{C}$ to $55\,^{\circ}\mathrm{C}$. In addition, the experimental setup is located in a temperature-controlled room

DOI 10.5162/Ultrasonic2025/A12-c5

that is maintained at $21 \pm 1\,^{\circ}\mathrm{C}$ to minimize external influences on the electronics.

Three different polymers are considered, with all specimens having the same dimensions. Polyetheretherketone (PEEK), polyamide 6 (PA6) and polypropylene (PP) are investigated. The specimens', inner radius $r_\mathrm{i} = 3\,\mathrm{mm}$, the outer radius $r_\mathrm{o} = 9\,\mathrm{mm}$ and length $l = 20\,\mathrm{mm}$ are considered.

Inverse Approach

This work employs an inverse approach for estimating the elastic material parameters of hollow-cylindric polymers in the ultrasound regime at different temperatures. A more detailed introduction to the method can be found in [5] and is briefly presented here. The method formulates material parameter identification as a nonlinear least-square-type optimisation problem, seeking to minimise the deviation between simulation and measurement by adjusting the model parameters $\hat{\boldsymbol{\gamma}}$. Leveraging a modification of the Levenberg-Marquardt method, based on geometric insights of the least-squares objective, this approach enhances convergence rates and reduces the required number of forward model evaluations. A key innovation is the objective function based on the autocorrelation of the signal's envelope in the frequency domain and can be written as:

$$\boldsymbol{\gamma} = \arg\min_{\hat{\boldsymbol{\gamma}}} \frac{1}{2} \left\| \arg_{\mathrm{stable}}(a) - \arg_{\mathrm{stable}}(\hat{a}(\hat{\boldsymbol{\gamma}})) \right\|^2$$

where a and $\hat{a}(\hat{\boldsymbol{\gamma}})$ are the autocorrelations of the measured and simulated envelopes, respectively. Further, $\arg_{\mathrm{stable}}(\cdot)$ denotes the stable, unwrapped phase extraction with damping for numerical stability. This transformation leads to a more convex optimisation landscape, effectively mitigating local minima and increasing the robustness and reliability of parameter estimation.

The initial estimates of the elastic parameters of $\boldsymbol{\gamma}$ are obtained from the group velocities of longitudinal and transverse sound $c_{\mathrm{g,L}}$ and $c_{\mathrm{g,T}}$, respectively (see, e.g., [3]). These are obtained from cross-correlation of the transmitted and received signals. The initial Rayleigh damping parameters are estimated in the frequency domain by evaluating the measured damping ratios α_{att} across a range of centre frequencies f_c to determine the corresponding α_M and α_K values:

$$\frac{\alpha_M}{4\pi f_\mathrm{c}} + \alpha_K \pi f_\mathrm{c} = \frac{\alpha_{\mathrm{att}}(2\pi f_\mathrm{c}) c_{\mathrm{g,L}}(2\pi f_\mathrm{c})}{2\pi f_\mathrm{c}} \,.$$

Results and Conclusion

Fig. 2 and Fig. 3 show the measured group velocities from the temperature and frequency dependent measurements of PEEK and PA6. While $c_{\mathrm{g,L}}$ increases with frequency, conversely it decreases with increasing heat. However, the selected temperature range and the heating of PA6 (same for PP) result in difficulties when determining $c_{\mathrm{g,T}}$. Similar observations are made in [8, 9] for PA6 and other polymers, discussing the glass transition temperature as the cause and subsequently restricting the temperature range significantly. Near the glass-transition temperature, the polymer's elastic moduli and viscosity change rapidly, causing strong dispersion and a large increase in ultrasonic attenuation that invalidates the simple linear-elastic assumptions used for parameter identification. Consequently the propagating wave is highly damped and scattered. As such, the transmitted signal is too distorted to extract reliable sound velocity or attenuation data. In order to provide only reliable estimates of the parameters, the temperature range from $20\,^{\circ}\mathrm{C}$ to $40\,^{\circ}\mathrm{C}$ is evaluated in the follow-

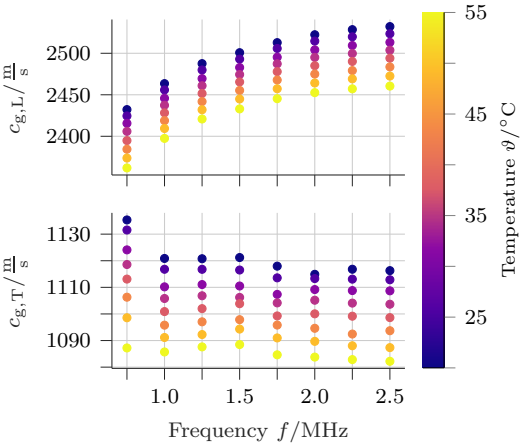

Fig. 2: Measured group sound velocities of PEEK.

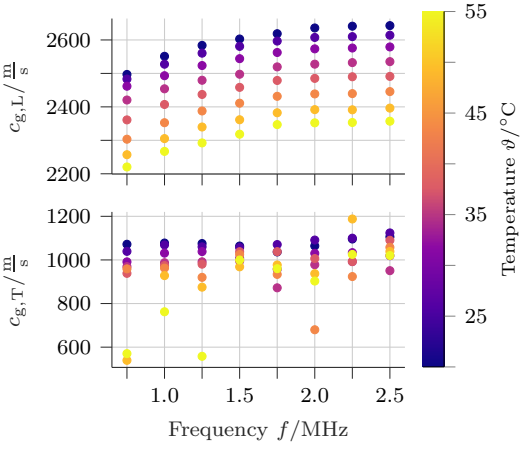

Fig. 3: Measured group sound velocities of PA6.

Tab. 1: Estimated material parameters of PEEK, PA6 and PP at temperatures ϑ.

Parameters			$\vartheta/°\mathrm{C}$		
PEEK	20	25	30	35	40
E_1/GPa	4.43	4.38	4.36	4.31	4.24
E_3/GPa	4.70	4.71	4.60	4.57	4.56
ν_{12}	0.37	0.37	0.37	0.37	0.37
ν_{13}	0.38	0.38	0.38	0.38	0.38
μ_{13}/GPa	1.57	1.56	1.55	1.54	1.53
$\alpha_\mathrm{M}/10^3$	127.2	124.0	130.2	130.6	131.1
$\alpha_\mathrm{K}/10^{-9}$	0.35	0.38	0.41	0.42	0.45

Parameters			$\vartheta/°\mathrm{C}$		
PA6	20	25	30	35	40
E_1/GPa	3.80	3.66	3.55	3.54	3.02
E_3/GPa	3.97	3.78	3.62	3.62	3.25
ν_{12}	0.39	0.39	0.40	0.41	0.40
ν_{13}	0.40	0.40	0.40	0.39	0.42
μ_{13}/GPa	1.26	1.19	1.08	0.96	0.99
$\alpha_\mathrm{M}/10^3$	157.5	174.5	182.8	195.9	217.1
$\alpha_\mathrm{K}/10^{-9}$	1.52	1.49	1.65	2.04	2.12

Parameters			$\vartheta/°\mathrm{C}$		
PP	20	25	30	35	40
E_1/GPa	3.87	3.43	3.44	3.41	3.21
E_3/GPa	4.03	4.08	3.40	3.42	3.16
ν_{12}	0.32	0.32	0.35	0.33	0.34
ν_{13}	0.33	0.34	0.34	0.33	0.34
μ_{13}/GPa	1.41	1.24	1.32	1.27	1.22
$\alpha_\mathrm{M}/10^3$	310.4	322.3	354.8	376.3	358.7
$\alpha_\mathrm{K}/10^{-9}$	1.93	1.97	2.00	2.04	2.01

ing. Tab. 1 shows the parameters of the materials determined at $f_\mathrm{c} = 1\,\mathrm{MHz}$ using the inverse method. Heating the test specimen to shift the operating point and test the robustness of the algorithm has been successfully implemented, particularly for PEEK. The identified parameters change approximately linearly with temperature. It is reasonable to conclude that the identified parameters are plausible, given the change in the respective sound velocities. For instance, an increase in temperature is associated with a decrease in the measured transversal sound velocity, whilst the identified shear modulus also decreases. PA6 and PP differ more at higher temperatures, as measured sound velocities differ by hundreds of metres per second, see Fig. 3. This indicates that no minor alteration in the operating point has been attained in this instance, and the parameter shift must be comparatively high. The results and the trend of the parameters presented is comparable qualitatively with the results of [8, 9]. In our case, transverse isotropy is assumed, but there is good agreement with the literature regarding the change in sound velocities. The consideration of other temperature-stable polymers can further illustrate the robustness of the measurement method and is the goal for further research.

Acknowledgements

The authors would like to thank the German Research Foundation (DFG) for financial support of the research project 409779252.

References

[1] L. Claes et al. "Determination of the material properties of polymers using laser-generated broadband ultrasound". In: *Journal of Sensors and Sensor Systems* 5.1 (2016), pp. 187–196. DOI: 10.5194/jsss-5-187-2016.

[2] M. Held et al. "Determination of Isotropic Elastic Constants from Dispersion Images Based on Ultrasonic Guided Waves by Using Neural Networks". In: *Ultrasonics* 143 (July 2024), p. 107403. DOI: 10.1016/j.ultras.2024.107403.

[3] D. Dreiling et al. "A pulse-echo measurement setup to determine viscoelastic material parameters". In: vol. 2822. 1. 2024. DOI: 10.1088/1742-6596/2822/1/012169.

[4] D. Dreiling et al. "Increasing the Sensitivity of Ultrasonic Transmission Measurements for Elastic Material Parameter Estimation". In: *Measurement Science and Technology* (May 2025). DOI: 10.1088/1361-6501/add9b6.

[5] D. Itner et al. "A modified Levenberg-Marquardt method for estimating the elastic material parameters of polymer waveguides using residuals between autocorrelated frequency responses". In: *arXiv* (2025). DOI: 10.48550/arXiv.2507.01706.

[6] D. Itner et al. "Efficient semi-analytical simulation of elastic guided waves in cylinders subject to arbitrary non-symmetric loads". In: *Ultrasonics* 114 (2021). DOI: https://doi.org/10.1016/j.ultras.2021.106389.

[7] M. S. Chowdhury, C. Song, and W. Gao. "Shape sensitivity analysis of stress intensity factors by the scaled boundary finite element method". In: *Engineering Fracture Mechanics* 116 (2014), pp. 13–30. DOI: 10.1016/j.engfracmech.2013.12.007.

[8] N. Lagakos et al. "Frequency and temperature dependence of elastic moduli of polymers". In: *Journal of Applied Physics* 59.12 (June 1986), pp. 4017–4031. DOI: 10.1063/1.336707.

[9] M. Webersen. "Zerstörungsfreie Charakterisierung der elastischen Materialeigenschaften thermoplastischer Polymerwerkstoffe mittels Ultraschall". PhD thesis. Universität Paderborn, 2021. DOI: 10.17619/UNIPB/1-1088.

DOI 10.5162/Ultrasonic2025/A15-b3

Design and performance analysis of a fiber ultrasonic hydrophone based on a phase-shifted fiber Bragg grating-thin plate coupled structure

Z.Li[1,2], *X.Wu*[1,2], *and B.An*[1,2]
[1] *State Key Laboratory of Acoustics, Institute of Acoustics, Chinese Academy of Sciences, Beijing, China*
[2] *University of Chinese Academy of Sciences, Beijing, China*
wuxm@mail.ioa.ac.cn

Abstract: To improve the sensitivity of a phase-shifted fiber Bragg grating (PS-FBG) for ultrasonic sensing, a coupled structure is proposed innovatively. The coupled structure is composed of a PS-FBG and a thin plate. The coupling mechanism between the plate's bending modes and the fiber's strain response have been studied theoretically and numerically. Experimental results further demonstrate sensitivity improvement across a broad ultrasonic frequency range. The proposed structure exhibits significant potential for ultrasonic sensing.

Keywords: PS-FBG,thin plate,sensitivity improvement,ultrasonic hydrophone,bending vibration

Introduction

Fiber optic acoustic sensors have shown broad application prospects in many fields such as oil exploration[1], structural health monitoring[2, 3] and medical diagnosis[4, 5] due to their unique advantages of anti-electromagnetic interference, small size, light weight and long-distance transmission. As a typical fiber optic sensing element, phase-shifted fiber Bragg grating (PS-FBG) has become the core component because of its narrow-band reflection spectrum characteristics and extremely high strain sensitivity. However, in practical applications, due to the rigid material and small size of the optical fiber, when the acoustic pressure acts directly on the bare optical fiber, the resulting strain response is extremely weak, which leads to insufficient acoustic pressure sensitivity, especially in high-frequency band.

To solve the above problems, this study innovatively designs a FBG-plate coupled structure, aiming to improve the sensor's sensitivity through the mechanical amplification effect of the structure. In this paper, the vibration theoretical model of the thin plate under the action of sound waves was established, especially for sound waves in the high frequency band. Numerical method was also used to analyze the improvement effect of the structure on the acoustic pressure reception sensitivity. Experimental results also proved that the structure can improve the sensitivity. This research work provides a theoretical and technical basis for the design of high-sensitivity fiber optic acoustic sensors.

Sensor Structure and Theoretical Analysis

The schematic diagram of the FBG-plate coupled structure proposed in this study is shown in Fig. 1. The planar circular thin plate is fixed on the support substrate, and the PS-FBG area is axially pasted on the surface of the thin plate with optical UV glue to sense the wavelength drift caused by ultrasonic waves. The fiber tail is fixed in the groove at the center of the support substrate and protected by a fiber sheath. When ultrasonic waves act on the planar circular thin plate, the plate will undergo bending vibration, so that the incident acoustic energy is efficiently converted into in-plane strain, and the strain is directionally transferred to the axial sensitive direction of the fiber through the high-stiffness adhesive layer, resulting in the drift of the central wavelength of the fiber Bragg grating, thus realizing the significant improvement of the acoustic pressure-strain conversion efficiency. This is the working principle of the structure.

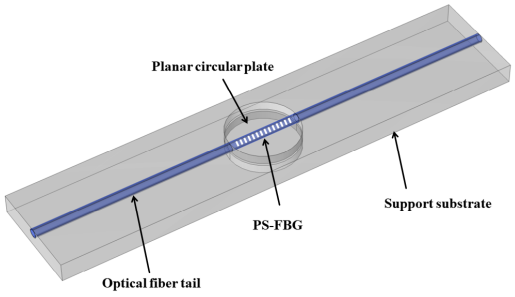

Fig. 1: Schematic diagram of the FBG-plate coupled structure.

Fig. 2 shows the deformation schematic diagram of a planar circular thin plate structure fixed around under uniform acoustic pressure P. The bending vi-

DOI 10.5162/Ultrasonic2025/A15-b3

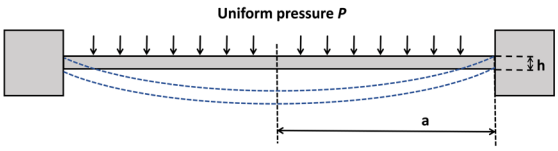

Fig. 2: Deflection of a clamped plate under uniform pressure.

bration of the thin plate under the incidence of plane sound waves belongs to small deflection vibration, which can be analyzed by Kirchhoff-Love plate theory[6]. It is assumed that the radius of the thin plate is a, the thickness is h, and the density is ρ; the thin plate is caused forced vibration by a plane sound wave with pressure amplitude P_0 and frequency of ω_0, and the corresponding equation can be expressed as

$$D\nabla^4 w + \rho h \frac{\partial^2 w}{\partial t^2} = P_0 e^{i\omega_0 t} \tag{1}$$

where $D = \frac{Eh^3}{12(1-\nu^2)}$ is the bending stiffness of thin plate, E is the Young's modulus of the plate, ν is the Poisson's ratio of the plate, $w = w(r, \theta, t)$ is the plate deflection.

For a circular plate fixed around, its deformation and rotation angle are both 0 at the boundary, so the boundary conditions are as follows:

$$\begin{cases} w|_{r=a} = 0 \\ \left.\dfrac{\partial w}{\partial r}\right|_{r=a} = 0 \end{cases} \tag{2}$$

The homogeneous solution of Eq. (1) can be expressed as follows

$$w_{nm}(r, \theta, t) = G_{nm} \cdot \mathcal{F}(r) \cdot \cos(n\theta) e^{i\omega_{nm} t} \tag{3}$$

where $\mathcal{F}(r) = J_n(k_{nm}\, r) - \frac{J_n(k_{nm}\, a)}{I_n(k_{nm}\, a)} I_n(k_{nm}\, r)$, $k_{nm}^4 = \frac{\omega^2 \rho h}{D}$ and ω represents the natural frequency of the free vibration of the thin plate. G_{nm} is the dimensionless maximum amplitude at any point in the thin plate and n,m represents that the circular thin plate is in the (n, m) order vibration mode. When considering the incidence of a plane ultrasound wave, the thin plate vibrates in the axisymmetric mode, that is $n = 0$.

Next, on the basis of the solution of the above free vibration, the analytical solution of the vibration response of the thin plate under the action of plane sound waves can be obtained

$$w(r, t) = \frac{P_0 e^{i\omega_0 t}}{\rho h} \sum_m \frac{F_m(r) W_m(r)}{\omega_m^2 - \omega_0^2} \tag{4}$$

where $F_m = \left(\int_0^a W_m(r)\, r\, dr\right) / \left(\int_0^a W_m^2(r)\, r\, dr\right)$.

When the optical fiber is axially pasted on the surface of the thin plate, the radial strain of the thin plate in the state of ultrasonic wave-induced bending vibration will be converted into the axial strain of the optical fiber. At the same time, since the central π phase shift of the PS-FBG is the most sensitive to the response of the sound wave when the ultrasonic wave is vertically incident on the PS-FBG[7], the axial strain at the center of the thin plate determines the sensitivity of the acoustic pressure of the PS-FBG. Under the action of acoustic pressure, the axial strain at the center of the thin plate can be expressed as

$$\begin{aligned} \varepsilon_r(r, t)|_{r=0} &= -z \left.\frac{\partial^2 w(r, t)}{\partial r^2}\right|_{r=0} \\ &= \frac{P_0 e^{i\omega t}}{4\rho} \sum_{m=1}^{\infty} \frac{F_m(0) k_m^2 G_m \left(1 + \frac{\mathrm{J}_0(k_m a)}{\mathrm{I}_0(k_m a)}\right)}{\omega_m^2 - \omega^2} \end{aligned} \tag{5}$$

The above theoretical analysis ignores the influence of damping. While a thin plate vibrates in water, the damping effect of water to the vibration system cannot be ignored. Then a damping factor ζ_m is introduced, the axial strain at the center of the thin plate can be expressed as

$$\varepsilon_r(r, t)|_{r=0} = \frac{P_0 e^{i\omega_0 t}}{4\rho} \sum_{m=1}^{\infty} \frac{F_m(0) k_m^2 G_m \left[1 + \frac{\mathrm{J}_0(k_m a)}{\mathrm{I}_0(k_m a)}\right]}{\omega_m^2 - \omega_0^2 + i\, 2\zeta_m \omega_m \omega_0} \tag{6}$$

When the ultrasonic wave is vertically applied to the PS-FBG, the optical fiber can be regarded as a cylindrical elastic body. It is assumed that both ends of the optical fiber are free, and the axial strain caused by the ultrasonic wave is

$$\varepsilon_z = -\nu_0 \frac{p}{E_0} \tag{7}$$

where $\nu_0 = 0.17$ is the Poisson's ratio of the fiber and $E_0 = 70\,\mathrm{GPa}$ is the Young's modulus of the fiber.

By comparing the central axial strain of the thin-plate structure ε_z with the axial strain ε_r generated by the bare optical fiber directly under the action of ultrasonic waves, the improvement effect of the structure on ultrasonic wave sensing can be analyzed.

Numerical Analysis

On the basis of the theoretical analysis of the coupled structure, the strain amplification characteristics can be further revealed through numerical calculation method. According to the derived analytical solution of the axial strain of the planar circular thin plate under the action of sound waves, the amplification factor of the axial strain of the coupled structure relative to the axial strain of the bare fiber directly under the action of sound waves can be quantitatively

DOI 10.5162/Ultrasonic2025/A15-b3

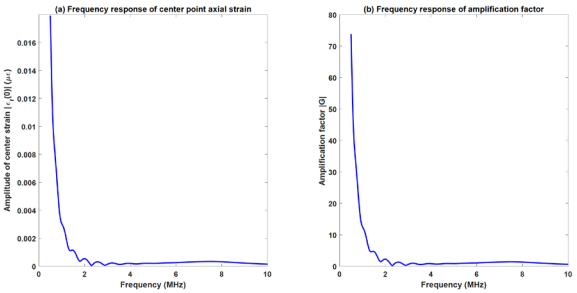

Fig. 3: (a)Frequency response of center point axial strain and (b)Frequency response of amplification factor.

obtained through numerical calculation, so as to intuitively evaluate the sensitivity improvement effect of the structure.

The material of the thin plate is resin. Its Poisson's ratio is 0.3, Young's modulus is 1.25GPa , the radius of the circular plate is 3.75mm, and the thickness is 0.25mm. Considering the material internal consumption and fluid radiation damping effect, the damping ratio ζ_m of the thin plate in water is taken as 0.2, and the optimal damping ratio will be subsequently determined by inversion of the experimental results. The numerical method is applied to simulate the dynamic response of the circular thin plate under the excitation of ultrasonic wave. In order to calculate the frequency response of the axial strain at the center point, the acoustic pressure P_0 is selected as 100 Pa, and the sound wave with a frequency range of 0.5-10 MHz are calculated. The calculation results are shown in Fig. 3. It can be seen from Fig. 3 that in the low-frequency 0.5-0.8 MHz frequency band, the amplification factor exceeds 1000 times at the highest, and the amplification effect is remarkable; in the high-frequency 1-10 MHz frequency band, the frequency response of the amplification factor is relatively gentle, and the amplification effect is stable.

The response to 1 MHz sound-wave excitation is calculated. The strain response of the bare fiber is $2.429\times10^{-4}\mu\varepsilon$, and the axial strain at the center point of the thin plate is $0.003\mu\varepsilon$, with an amplification factor of 12.4 times, which verifies the improvement effect of the thin plate structure on the acoustic pressure sensing of the fiber.

Experiment and Result

The structure of the sensor system established in this study is shown in Fig. 4. During the experiment, the fiber ultrasonic sensor is placed in a water tank, and the signal generator is used to apply excitation to the ultrasonic transducer in the water tank to generate an acoustic signal, which propagates through the water to the PS-FBG. After the wavelength shift is generated, it is converted into a phase change by a Mach-Zehnder interferometer (MZI), and finally three cosine signals with a phase difference 120° are output after passing through a coupler and a photodetector. The three signals collected in the experiment are demodulated by the arc tangent demodulation algorithm to obtain the phase signal. According to the linear relationship between the phase and wavelength of the MZI, the obtained phase signal can represent the response of the sensor.

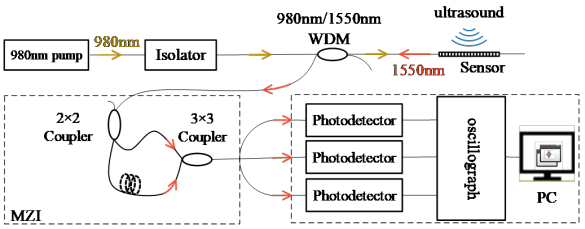

Fig. 4: The schematic diagram of the sensor system.

In the experiment, the position of the transducer was kept unchanged, and the bare fiber and the fiber packaged with the sensitivity improvement structure were placed at the same position in the water tank to ensure that the two received the same sound field. The experimental device is shown in Fig. 5.

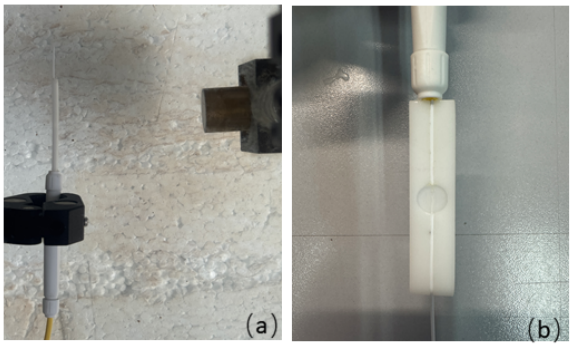

Fig. 5: (a) Experimental diagram of a sound wave incident vertically on PS-FBG and (b) Physical diagram of the sensitized structure package.

The amplification effect of the sensitivity improvement structure can be known by comparing the signal responses of the two. An ultrasonic transducer with central frequency 1 MHz was applied in the experiments to generate an ultrasonic pulse train with 20 cycles. The experimental results are shown in Fig. 6. It can be found that the responses of both to the sound wave show a process from oscillation down to stability, which is consistent with the sensing characteristics of PS-FBG to the non-uniform strain field caused by

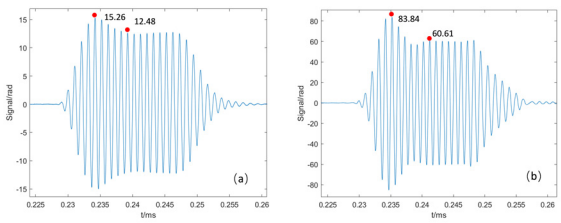

Fig. 6: Acoustic signal obtained by demodulation of (a) bare fiber and (b) sensitized structure.

ultrasonic waves. The maximum value of the oscillatory response and the amplitude of the response after stabilization are marked in the results. It can be found that the maximum value of the sensitivity improvement structure is 5.49 times that of the bare fiber, and the stable value of the sensitivity improvement structure is 4.86 times.

This result fully verifies that the structure can improve the acoustic pressure reception sensitivity of PS-FBG. There is an error between this result and the theoretical calculation value. The main reason is that in the packaging process, the optical fiber is pasted on the surface of the thin plate with UV glue, and the adhesive layer has a great influence on the strain transfer between the thin plate and the optical fiber, so there is a difference from the theoretical value. In the future, the strain transfer efficiency between the thin plate and the optical fiber needs to be inversed through experiments.

Fig. 7 amplifies the stable part of the demodulated signal, and it can be further observed that both structures can accurately measure the acoustic signal without waveform distortion, which indicates that the sensitivity enhancement structure can stably improve the acoustic pressure reception sensitivity.

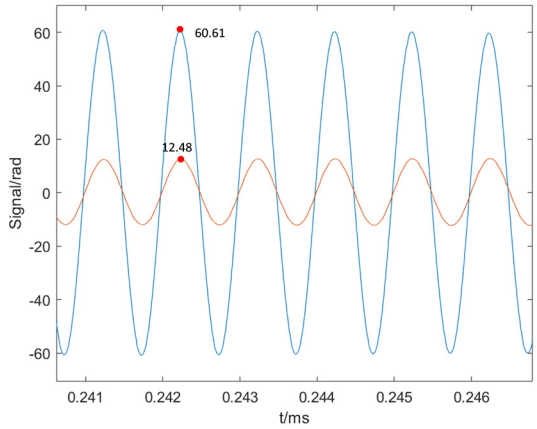

Fig. 7: Enlarged view of acoustic stabilization section.

Conclusion

In order to address the problem of insufficient sensitivity in the high-frequency band of the bare fiber ultrasonic hydrophone, this study designs and tests a coupled sensitivity improvement sensor. In this paper, the vibration theoretical model of the thin plate under the action of ultrasound is established. Based on this model, numerical calculation shows that under the excitation of 1 MHz ultrasound, the axial strain at the center of the thin plate is increased by about 12.4 times compared with that of the bare fiber,and the sensitivity improvement effect was further verified experimentally. However, there are still optimization directions, such as exploring the multi-objective optimization of thin plate materials. The next step will continue to carry out in-depth research.

References

[1] Q. Rong and X. Qiao. "FBG for oil and gas exploration". In: *Journal of Lightwave Technology* 37 (2018), pp. 2502–2515. DOI: 10.1109/JLT.2018.2866326.

[2] H. Zhang, T. Liu, J. Lu, et al. "Static and ultrasonic structural health monitoring of full-size aerospace multi-function capsule using FBG strain arrays and PSFBG acoustic emission sensors". In: *Optical Fiber Technology* 78 (2023), p. 103316. DOI: 10.1016/j.yofte.2023.103316.

[3] M. Majumder et al. "Fibre Bragg gratings in structural health monitoring—Present status and applications". In: *Sensors and Actuators A: Physical* 147 (2008), pp. 150–164. DOI: 10.1016/j.sna.2008.04.008.

[4] D. Gurkan, D. Starodubov, and X. Yuan. "Monitoring of the heartbeat sounds using an optical fiber Bragg grating sensor". In: *SENSORS, 2005 IEEE*. 2005, 4–pp. DOI: 10.1109/ICSENS.2005.1597697.

[5] K. Ogawa et al. "Simultaneous measurement of heart sound, pulse wave and respiration with single fiber bragg grating sensor". In: *2018 IEEE International Symposium on Medical Measurements and Applications (MeMeA)*. 2018, pp. 1–5. DOI: 10.1109/MeMeA.2018.8438629.

[6] S. Timoshenko and S. Woinowsky-Krieger. *Theory of Plates and Shells*. 2nd ed. New York: McGraw-Hill, 1959.

[7] B. An, X. Wu, Z. Li, et al. "Sensing characteristics of π-phase-shifted fiber Bragg grating for ultrasonic induced non-uniform strain field". In: *Acta Acustica* 48 (2023). In Chinese, pp. 119–127. DOI: 10.15949/j.cnki.0371-0025.2023.01.027.

DOI 10.5162/Ultrasonic2025/A15-c3

A Full-Focusing Ultrasound Phased Array Imaging Method Based on MDMAS

Yiming Wang[1], *Jichao Xu*[1], *Qian Lubin*[1], *GuoPeng Fan*[1], *Weiwei Qi*[1], *Haiyan Zhang*[2], *Hui Zhang*[1], *and Wenfa Zhu*[1]
[1]*Shanghai University of Engineering Science, Shanghai and China*
[2]*Shanghai University, Shanghai and China*
jcxu@sues.edu.cn

Abstract: To address the limited contrast and poor noise suppression of conventional Delay Multiply and Sum (DMAS) beamforming, this paper proposes a correlation-guided nonlinear beamforming method. Multiplication is applied only to highly correlated signal pairs to suppress incoherent noise, and a Modified Coherence Factor is introduced to enhance image contrast. Experiments on rail specimens with artificial defects show improved flaw visibility and image clarity over DMAS, demonstrating the proposed method's potential for reliable phased array ultrasonic imaging.

Keywords: Phased array ultrasonic, Beamforming, Correlation, MDMAS, Contrast.

Introduction

Phased array ultrasonic imaging has been widely applied in industrial non-destructive testing and medical diagnostics [1-3]. However, during wave propagation in a medium, scattering and absorption-induced attenuation often lead to severe energy loss [4–5], causing the imaging results to be overwhelmed by noise and resulting in degraded image quality and ineffective defect identification [6–7]. Consequently, enhancing overall imaging performance, which depends on multiple factors such as noise suppression, contrast and signal coherence, has become both a pressing challenge and a central topic in recent ultrasonic imaging research.

The Full Matrix Capture (FMC)-based Total Focusing Method is a typical beamforming algorithm [8]. Based on the Delay and Sum (DAS) strategy, this method reconstructs ultrasonic images, enhancing imaging quality. However, DAS cannot effectively suppress interference signals, the SNR of Total-Focusing images is still insufficient [9-11]. In recent years, the Delay Multiply and Sum (DMAS) algorithm, a type of nonlinear beamforming method, has been introduced for use in medical imaging applications [12]. The distinction between coherent signals (e.g., defect echoes) and incoherent noise is emphasized in DMAS through the multiplication and accumulation of delayed signals., improving SNR by leveraging the spatial coherence of ultrasound signals. While DMAS has shown notable advantages, its performance can still be constrained by incoherent noise and reduced contrast in challenging imaging conditions.

To more effectively improve the SNR and image contrast, a phased array ultrasonic imaging method based on the nonlinear DMAS beamforming algorithm is investigated in this study. The proposed method introduces a threshold value to identify highly correlated signals, applying multiplication only to these signal pairs to adaptively suppress incoherent noise based on their Correlation Coefficient (CC). Since the reduction in multiplied pairs may degrade image contrast, a Modified Coherence Factor (MCF) further applied selectively to the highly correlated signals to enhance contrast. These enhancements collectively define the MDMAS beamforming method.

Methodology

DAS

The signal delayed at the *i*-th element in a phased array consisting of N uniformly spaced elements is represented as $s_i(t-\tau_i(x,z))$ .The DAS beamforming method reconstructs the image without any complex processing of the scattered signals. By summing the delayed signals, this method constructs the final image:

$$y_{DAS}(x,z)=\sum_{i=1}^{N} s_i(t-\tau_i(x,z)) \tag{1}$$

Characterized by simplicity in computation and effective suppression of clutter and noise, DAS is a commonly used data-independent beamforming technique. However, the weights in DAS are independent of the input signal. As a result, images reconstructed using DAS often suffer from high sidelobe levels and low contrast [14-15].

DMAS and Coherence Factor (CF)

$$\begin{aligned}\hat{s}_{ij}(x,z)&=s_i(t-\tau_i(x,z))s_j(t-\tau_j(x,z))\\ y_{DMAS}(x,z)&=\sum_{i=1}^{N-1}\sum_{j=i+1}^{N}\hat{s}_{ij}(x,z)\end{aligned} \tag{2}$$

The DMAS beamforming method achieves better sidelobe suppression and improved contrast by multiplying delayed signals. Eq. (2) illustrates the DMAS algorithm, where and are the delayed signals received by the i-th and j-th elements, respectively. Each pair of delayed signals is multiplied.

$$CF(x,z)=\frac{\left|\sum_{i=1}^{N} s_i(t-\tau_i(x,z))\right|^2}{N\sum_{i=1}^{N}\left|s_i(t-\tau_i(x,z))\right|^2} \tag{3}$$

A band-pass filter is used at the final stage to preserve the second harmonic signal [16], forming the DMAS beamformer. The CF is an adaptive weighting factor that reflects the ratio between coherent and incoherent signal energy. The traditional CF is defined as Eq. (3).
CF can be used to weight the output of DMAS beamforming, as shown in Eq. (4):

$$y_{DMAS}'(x,z) = CF(x,z) \times y_{DMAS}(x,z) \tag{4}$$

MDMAS and MCF
The CC is computed for every possible pair of received signals, denoted as ρ . In other words, $\rho(s_i, s_j)$ represents the CC between the ultrasound signals received by the *i*-th and *j*-th elements:

$$\rho(s_i, s_j) = \frac{COV(s_i, s_j)}{\sigma(s_i)\sigma(s_j)} \tag{5}$$

In this context, the delayed signals received by the *i*-th and *j*-th elements are denoted as s_i and s_j , respectively. $COV(s_i, s_j)$ serves as a measure of the covariance between the two signals, and $\sigma(s_i)$, $\sigma(s_j)$ are their standard deviations.
In Eq. (6), ultrasound signals with CC values lower than a predefined threshold value are excluded. The MDMAS beamforming method which doesn't have MCF can be expressed as:

$$y_{MDMAS}'(x,z) = \sum_{i=1}^{N-1} \sum_{j=i+1}^{N} \hat{s}_{ij}(x,z) \quad subject\ to \quad \rho(s_i, s_j) \geq threshold\ value \tag{6}$$

By applying the MCF to the MDMAS beamforming method (without MCF), the image contrast is enhanced and sidelobes are suppressed. The MCF can be expressed as:

$$MCF(x,z) = \frac{\left|\sum_{j \in E} s_j(t - \tau_j(x,z))\right|^2}{M \sum_{j \in E} \left|s_j(t - \tau_j(x,z))\right|^2} \tag{7}$$

Let *M* denote the length of *E*, representing the number of ultrasound signals satisfying the threshold value. The MCF is then incorporated into the beamforming scheme based on the proposed DMAS. The resulting beamforming formulation is expressed as:

$$y_{MDMAS}(x,z) = y_{MDMAS}'(x,z) \times MCF(x,z) \tag{8}$$

The structural overviews of DAS, DMAS, and MDMAS beamforming methods are illustrated in Fig. 1.

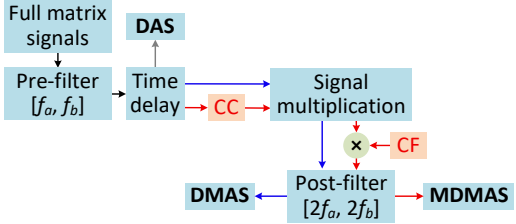

Fig. 1 Flowcharts of the DAS, DMAS, and MDMAS beamforming methods and their combinations with the MCF.

Contrast (CR) [17] and Signal-to-Noise Ratio (SNR) [18] served as quantitative metrics for evaluating the performance of the proposed method.

$$CR = 20\log_{10}\left(\frac{S_i}{S_o}\right) \tag{9}$$

$$SNR = 20\log_{10}\left(\frac{S_i}{\sigma_o}\right) \tag{10}$$

where S_i denotes the average signal amplitude in the target defect region at the same imaging depth, S_o and σ_o represent the average signal amplitude and standard deviation of the background region at the same imaging depth, respectively.

Experimental Setup

The experimental data in this study were acquired using a 32-channel ultrasonic phased array inspection system manufactured by M2M (France). Parameter configuration and signal visualization were carried out using the Multi2000 software, as shown in Fig. 2. The test specimen was a rail sample containing artificial defects with a diameter of 5 mm. A 16-element phased array probe manufactured by Shantou Ultrasound Co., Ltd. (China) was used in the experiment. With each element measuring 1.8 mm in width and spaced 0.2 mm apart, the array yields a total aperture of 31.8 mm. The center frequency of probe is about 1 MHz.

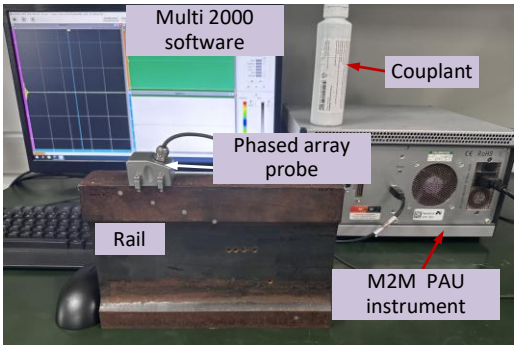

Fig. 2 Experimental system setup.

As shown in Fig. 3, the tested rail specimen contains artificial defects, all of which have a diameter of 5 mm. Region 1 includes a single defect, whereas Region 2 contains two defects with a vertical spacing of 10 mm. These two regions correspond to the imaging scenarios for single and double defects, respectively.

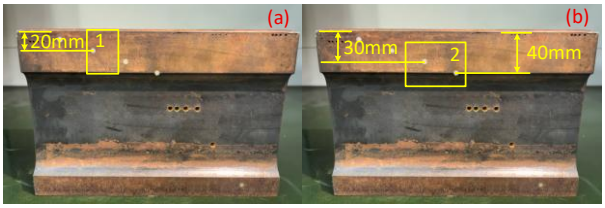

Fig. 3 Tested rail samples: (a) single artificial defect; double artificial defects.

Imaging Results

Imaging Results for One Defect
DAS, DMAS, and MDMAS beamforming methods were applied to the FMC data collected from Region 1 for ultrasonic imaging. The imaging results are shown in Fig.

4. The DAS result contains significant artifacts, due to conventional Total Focusing imaging relies solely on amplitude information, which is susceptible to noise. The DMAS algorithm improves image quality by enhancing the energy of defect signals through multiplication, thereby improving contrast and clarity. MDMAS further improves image quality by adaptively enhancing signal coherence.

The CR and SNR for the three methods were calculated, as shown in Tab.1. In terms of CR, the trend is $CR_{DAS}<CR_{DMAS}<CR_{MDMAS}$; MDMAS improves contrast by 78.72% compared to DAS, and DMAS improves it by 56.79%. In terms of SNR, the trend is $SNR_{DAS}<SNR_{DMAS}<SNR_{MDMAS}$; MDMAS increases SNR by 34.36% over DAS, while DMAS improves it by 22.63%.

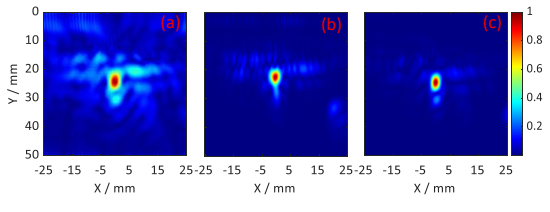

Fig. 4 Imaging results for one defect: (a) DAS; (b) DMAS; (c) MDMAS.

Tab.1 The CR and SNR of one defect's imaging results.

Method	CR (dB)	SNR (dB)
DAS	18.84	19.53
DMAS	29.54	23.95
MDMAS	33.67	26.24

Imaging Results for Two Defects

Ultrasound signals collected from Region 2 were used to image by DAS, DMAS, and MDMAS methods. The results are shown in Fig. 5. It is evident that image quality improves progressively with each algorithm enhancement.

The CR and SNR values of three methods are listed in Tab. 2. In terms of CR, the trend remains $CR_{DAS}<CR_{DMAS}<CR_{MDMAS}$. Both DMAS and MDMAS significantly improve image contrast, such as DMAS improving CR by 39.80% over DAS, and MDMAS improving CR by 9.04% over DMAS. Regarding SNR, the relationship holds $SNR_{DAS}<SNR_{DMAS}<SNR_{MDMAS}$. Specifically, DMAS increases SNR by 14.03% relative to DAS, while MDMAS further enhances SNR by 9.12% compared to DMAS.

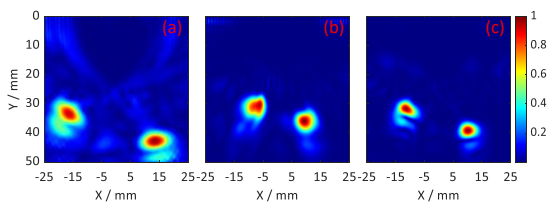

Fig. 5 Imaging results for two defects: (a) DAS; (b) DMAS; (c) MDMAS.

Tab.2 The CR and SNR of two defect's imaging results.

Method	CR (dB)	SNR (dB)
DAS	19.55	17.11
DMAS	27.33	19.51
MDMAS	29.80	21.29

Conclusion

In this study, a modified beamforming method (MDMAS) is proposed to address the problems that insufficient contrast and poor noise suppression of the conventional DMAS algorithm. The proposed method adaptively applies multiplication only to signal pairs with high correlation, which effectively suppresses incoherent components while preserving flaw-related signals. In addition, a MCF is introduced and selectively applied to these pairs of coherent signals, aiming to further improve image contrast. Experimental validation was conducted on rail specimens. Quantitative results showed that, compared to DMAS, the MDMAS method improved the CR by at least 9.04% and the SNR by at least 9.12%. These enhancements result in clearer flaw boundaries and more reliable defect characterization, demonstrating the method's practical potential in rail defect detection and maintenance.

Acknowledgments

This research was funded by the National Natural Science Foundation of China (Grant Nos. 12474457, 12174245, 12374443, 12304514, and 12104290), the National Key Research and Development Program of China (2022YFF0605600), the National Natural Science Foundation of China (Grant No. 12304514) and the Shanghai Municipal Natural Science Foundation (Grant No.24ZR1427300).

References

[1] Mohammadkhani R, Zanotti Fragonara L, Padiyar M J, et al. Improving depth resolution of ultrasonic phased array imaging to inspect aerospace composite structures[J]. *Sensors*, 2020, 20(2): 559.

[2] Fadnes S, Wigen M S, Nyrnes S A, et al. In vivo intracardiac vector flow imaging using phased array transducers for pediatric cardiology[J]. *IEEE transactions on ultrasonics, ferroelectrics, and frequency control*, 2017, 64(9): 1318-1326.

[3] Lin L, Cao H, Luo Z. Total focusing method imaging of multidirectional CFRP laminate with model-based time delay correction[J]. *Ndt & E International*, 2018, 97: 51-58.

[4] Van Pamel A, Brett C R, Lowe M J S. A methodology for evaluating detection performance of ultrasonic array imaging algorithms for coarse-grained materials[J]. *IEEE transactions on ultrasonics, ferroelectrics, and frequency control*, 2014, 61(12): 2042-2053.

[5] Ono K. A comprehensive report on ultrasonic attenuation of engineering materials, including metals, ceramics, polymers, fiber-reinforced composites, wood, and rocks[J]. *Applied Sciences*, 2020, 10(7): 2230.

[6] Villaverde E L, Robert S, Prada C. Ultrasonic imaging in

highly attenuating materials with Hadamard codes and the decomposition of the time reversal operator[J]. *IEEE Transactions on Ultrasonics, Ferroelectrics, and Frequency Control*, 2017, 64(9): 1336-1344.

[7] Jiao J, Ma T, Hou S, et al. A pulse compression technique for improving the temporal resolution of ultrasonic testing[J]. *Journal of Testing and Evaluation*, 2018, 46(3): 1238-1249.

[8] Holmes C, Drinkwater B W, Wilcox P D. Post-processing of the full matrix of ultrasonic transmit–receive array data for non-destructive evaluation[J]. *NDT & e International*, 2005, 38(8): 701-711.

[9] Lines D, Mohseni E, Javadi Y, et al. Using coded excitation to maintain signal to noise for FMC+ TFM on attenuating materials[C]//2019 *IEEE International Ultrasonics Symposium (IUS)*. IEEE, 2019: 635-638.

[10] Da T, Jichao X, Yanxun X, et al. Ultrasonic phased array TFM detection in highly attenuating materials based on modified Golay-coded excitation[C]//2018 *IEEE International Ultrasonics Symposium (IUS)*. IEEE, 2018: 1-4.

[11] Shen C C, Hsieh P Y. Ultrasound baseband delay-multiply-and-sum (BB-DMAS) nonlinear beamforming[J]. *Ultrasonics*, 2019, 96: 165-174.

[12] Lim H B, Nhung N T T, Li E P, et al. Confocal microwave imaging for breast cancer detection: Delay-multiply-and-sum image reconstruction algorithm[J]. *IEEE Transactions on Biomedical Engineering*, 2008, 55(6): 1697-1704.

[13] Deylami A M, Asl B M. Low complex subspace minimum variance beamformer for medical ultrasound imaging[J]. *Ultrasonics*, 2016, 66: 43-53.

[14] Zhu W, Wei Z, Fan G, et al. Ultrasonic guided wave array imaging detection of rail defects based on the symbolic coherent factor total focusing method[J]. *Nondestructive Testing and Evaluation*, 2025: 1-22.

[15] Xing Y, Zhu W, Xu J, et al. Ultrasonic imaging of near-surface blind defects based on WSAttnGAN network[J]. *Measurement*, 2025, 245: 116577.

[16] Matrone G, Savoia A S, Caliano G, et al. The delay multiply and sum beamforming algorithm in ultrasound B-mode medical imaging[J]. *IEEE transactions on medical imaging*, 2014, 34(4): 940-949.

[17] Zheng C, Wang H, Xu X, et al. An adaptive imaging method for ultrasound coherent plane-wave compounding based on the subarray zero-cross factor[J]. *Ultrasonics*, 2020, 100: 105978.

[18] Holmes C, Drinkwater B W, Wilcox P D. Post-processing of the full matrix of ultrasonic transmit–receive array data for non-destructive evaluation[J]. *NDT & e International*, 2005, 38(8): 701-711.

DOI 10.5162/Ultrasonic2025/A16-a2

RF Signals from the Superficial Tissues as Stability Index of Ultrasonic Transducer Mounting

R. Jurkonis[1], *J. Grajauskaitė*[2], *and M. Jucevičius*[1]
[1]*Kaunas University of Technology, Biomedical Engineering Institute, Kaunas, Lithuania*
[2] *Kaunas University of Technology, Interdisciplinary Prototyping Laboratory Centre - M-Lab, Kaunas, Lithuania*
rytis.jurkonis@ktu.lt

Abstract: Body-mounted ultrasonography stability is critical, as transducer displacement creates RF data artifacts. We quantify mounting stability by analyzing superficial RF signals. Frame-by-frame RF differences were quantified via RMS, defining Instability Waveforms (IW) and depth profiles. Waveforms varied with depth and mounting, exibiting various intensities and regularities, in some cases showing periodicity, potentially from vessel pulsation. A consolidated superficial IW index could be indicative of optimal mounting, improving artifact-free detection of endogenous tissue dynamics.

Keywords: blood vessel, on-body mounted, endogenous pulsation, dynamics imaging.

Introduction

Accurately positioning and sustaining the sensor over a focus area can be difficult and skill-dependent. Such challenges get even more complicated with patient movement or unintentional shifts by the operator, which can compromise data integrity [1]. This instability is critical because the time delays for image reconstruction are directly linked to the distance between the probe and the region of interest. Any movement creates uncertainty [2]. Innovative solutions, such as flexible skin patches, are helping to stabilize wearable ultrasonography devices [1]. However, other broader concerns about maintaining data quality with real-time synchronization and storage plus advanced image processing tools continue to dominate discussions [2]. The areas of reliability, ease of use, and regulatory standards are also areas that remain under-addressed. Given these challenges, the continuous monitoring of mounting stability becomes paramount for ensuring the high quality and reliability of ultrasonography data. In this paper, we propose a new way to measure transducer stability. Our method focuses on analyzing RF signals from the skin's surface and the uppermost tissue layers, an area that's often overlooked. By targeting this specific signal segment, we aim to develop a stability index that reduces artifacts and enhances the accuracy of detecting natural tissue movements.

Background, Motivation and Objective

Body mounted ultrasonic imaging is becoming a new trend [3]. With the body mounted transducer, the in vivo assessment of blood vessels by ultrasonography relies on the stability of acoustic contact. Despite dedicated mounting, the ultrasonic transducer has potential displacements with respect to tissues in vivo, increasing the considerable artifacts in ultrasonic RF data. Special attention to potential instability is considered when dynamic features are characterized in soft tissues. Thus, the monitoring of mounting stability is explored. The objective of the paper is to quantify the stability of transducer mounting by extracting RF data from the skin surface and the superficial tissues. There are published examples of transducer mounting on tissues, but not many provide characteristics of echoscopy signals that are gathered with on-body mounted sensing, particularly in ultrasonography.

Equipment

Signals were obtained with a research-dedicated scanner, Ultrasonix SonixTouch (Analogic Ultrasound, Richmond, BC, Canada), equipped with a 5–14 MHz linear array probe. The application surface area of the linear array transducer was 13 mm x 47 mm. During the ultrasonography on the wrist medial side, imaging was with harmonic 6.6 MHz waves at a frame rate, imaging depth, and focus of 65 fps, 2 cm, and a single focal distance of 0.8 cm, set in the scanner accordingly. During the ultrasonography on the thigh medial side, imaging was with harmonic 5.0 MHz waves at the frame rate, imaging depth, and focus of 66 fps, 3.5 cm, and single focal distance of 0.8 cm, set in the scanner accordingly. A cine-loop stored the data in the form of consecutive frames and RF arrays of digitalized signals for later offline analysis. The holder of the ultrasonic transducer was laboratory-made from hard foam, gluing it with a flexible plastic sheet. The plastic sheet or applicator was 10 cm in length and 16 cm in width.

DOI 10.5162/Ultrasonic2025/A16-a2

In the plastic sheet's central part, the hole was made 20 mm x 55 mm in size. Through this hole, the transducer working surface was coupled to skin. The total weight of the assembled probe was 80 g. On the wrist, the only ultrasonic transducer was stabilized with the laboratory stand, keeping more than 2 mm of gap to the skin. This gap was filled with acoustic coupling gel. The wrist was placed beneath the transducer to ensure blood vessel patterns in the central part of the ultrasonography images. The blood vessels are observed in a transversal direction. Another variant of imaging on the wrist was applying the assembled probe on the wrist to contact the skin with a semirigid surface: 10 cm along the forearm and 6 cm in the transversal direction of the wrist. In the case of imaging in thigh tissues, the whole surface of the applicator was contacting skin. The applicator was applied to the medial side of the thigh to obtain a pattern of femoral blood vessels. The applicator's longer dimension (16 cm) was directed on the thigh in a circumferential direction. Two belts around the thigh were holding the applicator. Belts were possible to bring to adjust compression on tissues.

Methods

We propose analyzing the often neglected part of the RF signal backscattered from the superficial tissue zone as a data source on stability. RF signals from three echolines – central and from both sides of the B-mode – were analyzed from the very first sample. The inter-frame difference was calculated for each echoscopy line Eq. (1).

$$D_L(i) = RF_{L,n}(i) - RF_{L,n+1}(i), \qquad (1)$$

here, RF is an array of radiofrequency data of one ultrasonography frame, L – the index of echoscopy lines, and n – is index of frames in sequence. The time waveforms of interframe difference were evaluated with depth windowing Eq. (2) to estimate depth profiles of activity:

$$Wz_{i,n} = rms(D_{[i-\frac{z}{2}:i+\frac{z}{2},n]}), \qquad (2)$$

here rms(*) – function calculating the root mean square of data; i – the index of locations dividing the first 5 mm depth of imaging into ten zones; z – length of one zone in space, which was 26 RF samples (or 0.5 mm).

Extraction of offset from waveform was made by substracting the mean value Eq. (3):

$$W_{i,n} = Wz_{i,n} - mean(Wz_{i,n}), \qquad (3)$$

here, mean(*) – a function calculating the arithmetic average value of data; Dividing imaging depth into zones enables analysis of tissue dynamics activity at specific depth locations. Estimating the inter-frame differences of RF signals in a sequence of frames provides a dynamic waveform as a function of time. So dynamic waveforms of instability are characterizing tissue activity in any of the locations. Locations in a B-mode image can be arranged with a rectangular grid of any density. In this example the twenty zones are covering the total depth of 5 mm in superficial tissues.

Imaging data

Application sites of the ultrasonic probe with holder were two locations on the researcher's body: the medial side of the wrist and the medial side of the thigh. The first location was preferred because of very superficial blood vessels. The radial artery and two veins were observed in the center of the images. The second location was on massive soft tissues of the thigh, where blood vessels are deep, surrounded by muscles. The great saphenous vein and femoral artery were observed in the image. The sample images from both locations are presented in Fig. 1.

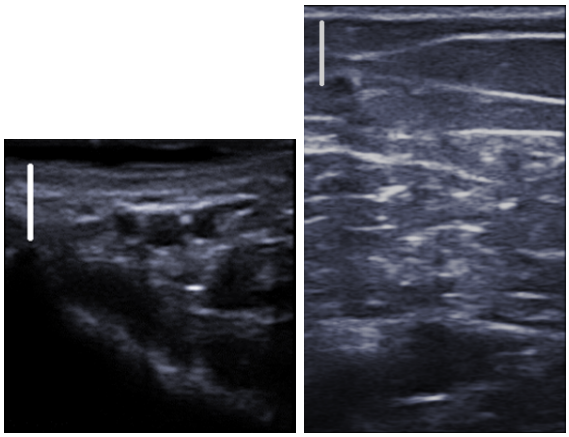

Fig. 1: Tissues and vessels images: a) without direct transducer contact to wrist skin; b) in direct transducer contact to thigh skin. The white line represents the 5 mm scale.

Imaging data for analysis of dynamics in superficial tissues was collected with two fixation options of array transducer. One fixation was on the laboratory stand when the transducer was stabilized in respect to the tabletop. The arm was also stabilized on the tabletop beneath the transducer facing downwards. Acoustic coupling of the medial side of the wrist was with an excessive amount of gel, so the transducer working surface did not touch skin. Transmission of ultrasound waves was established through a gap filled with acoustic coupling gel. The resulting image example is depicted in Fig. 1a.The thickness of the acoustic

DOI 10.5162/Ultrasonic2025/A16-a2

coupling gel was more than 2 mm. The wrist was placed beneath the transducer to ensure blood vessel patterns in the central part of the images. The blood vessels are observed in a transversal view. One, the central vessel appeared to be an artery, as its regular pulsation was observed. With a large applicator on thigh tissues, tightening with belts was interchanged from weak to stronger so that the great saphenous vein initially was observed at 9 mm depth, but after tightening, it was observed at 6 mm depth. The later case of tightening resulted in the image as the example provided in Fig. 1b.

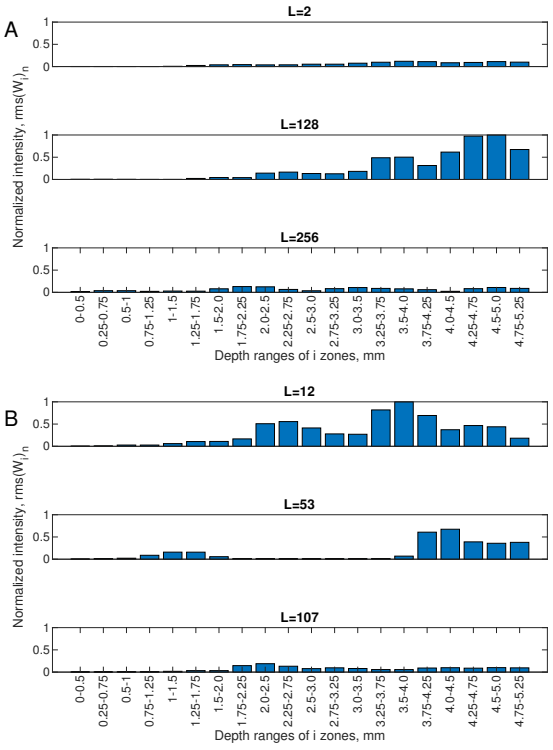

Fig. 2: Intensity of W_i in wrist tissues activity depth profiles at zones of depth: a) coupling with gel-filled gap 2mm; b) no gap coupling.

Results on dynamics of tissues

Common view of pattern in tissues is still grayscale B-mode images as in Fig. 1. We propose diagrams depicting in vivo activity of tissues.

The overview of tissue activity in space of imaging is provided by analyzing $D_L(i)$ at central and at both sides of the B-mode. The activity depth profiles calculated at these three echoscopy lines are presented in Fig. 2. The strongest magnitudes of activity are observed at echoscopy line L=128, z=[4.25-4.75] mm (see Fig. 2a) and at L=12, z=[3.5-4.0] mm (see Fig. 2b). Only the magnitude of activity is depicted, while waveform shapes themselves are addressed in Fig. 3.

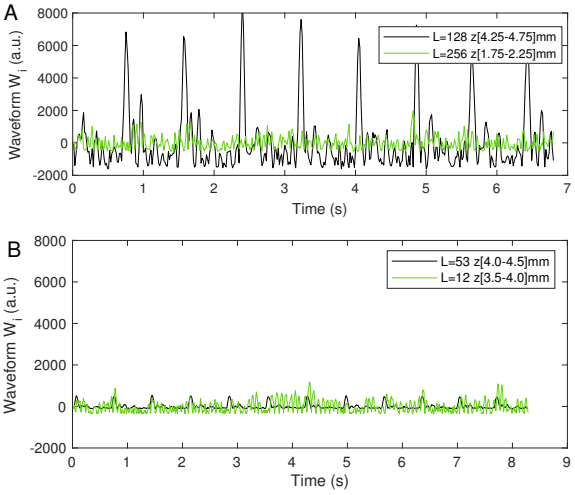

Fig. 3: Instability waveforms evaluated at depth ranges in the wrist: a) with more 2 mm gap at echoscopy line L=128; b) with no gap at L=53.

Comparing tissue activity magnitudes when imaging through a gel-filled gap and when the transducer is in direct coupling to the skin, we observe $D_L(i)$ magnitudes with a ratio around 10 times (5500 vs 520). With a large applicator on thigh tissues, tightening with belts was interchanged from weak to stronger so that the great saphenous vein initially was observed at 9 mm depth, but after tightening, it was observed at 6 mm depth. The intensity-depth profiles in tissues of the thigh are shown in Fig. 4. Identified the most active locations are at L=113, z=[1-1.5] mm (Fig. 4a weak compression with applicator) in case of weakest compression, and L=212, z=[2.25-2.75] mm (Fig. 4b thight compression). Observing the waveforms in Fig. 5 at these locations, we obtain that with weaker applicator compression, we get stronger in vivo activity waveforms with a ratio around 2 times (300 vs 150). The intensity-depth profiles in all cases (Fig. 2 and Fig. 4) accounts for the random activity in tissues, not only physiological pulsing waveforms presented in Fig. 3 and Fig. 5 in black color lines. The random motion artifacts corrupted waveforms are presented in green color lines (see Fig. 3 and Fig. 5), these waveforms are possibly of the magnitude order comparable to physiological waveforms magnitude.

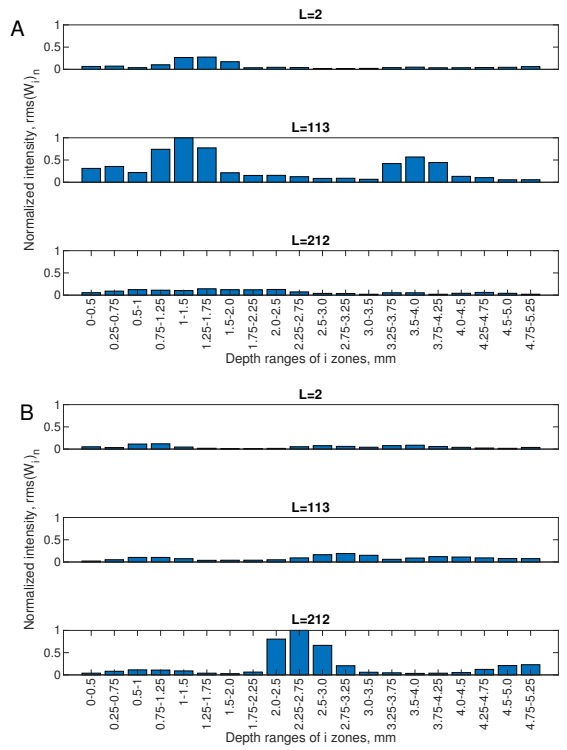

Fig. 4: Intensity of W_i at zones of depth in thigh tissues: a) weak compression (distance to saphenous vein 9 mm); b) stronger compression (distance to saphenous vein 6 mm)

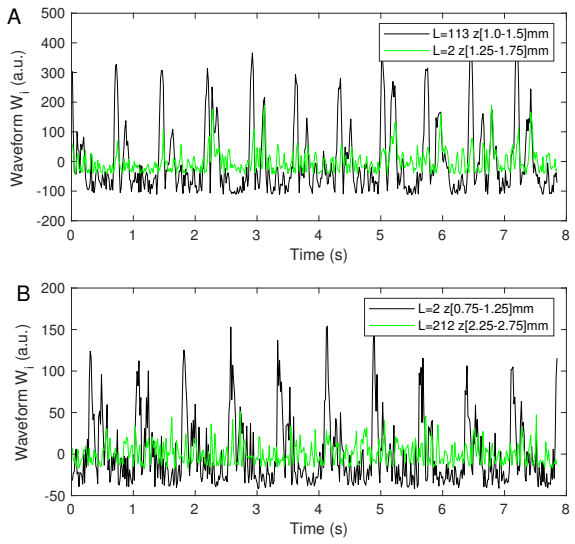

Fig. 5: Instability waveforms evaluated at particular depth ranges in the thigh: a) weak compression (distance to saphenous vein 9 mm); b) stronger compression (distance to saphenous vein 6 mm)

Discussions

Summarizing, instability depth profiles were compared in a few fixing variants of imaging transducers for acoustic coupling to the human body. Instability waveforms appeared to depend on location in tissues and on mounting variants. When the imaging probe is softly mounted physiologically, the arteries induce waveforms of pulsing that are observed. In these cases, high-intensity and highly repeatable in rhythm and shape waveforms are beneficial for the quality of ultrasonography data. But in generalized cases, the instability waveforms $W_{i,n}$ should be analyzed considering their random character. If it is not possible to find a regular rhythm or the inter-waveform correlation is too weak, then it is worth aggregating the calculation of the index of mounting stability. Instability magnitudes $Wz_{i,n}$ at a few echoscopy lines aggregated as a minimal index could be indicative of the maximum mounting stability. But it is important to not compromise the possible damping of highly repeatable waveforms that could be physiological pulsing in tissues induced by arteries.

References

[1] Amado-Rey et al. "Towards ultrasound wearable technology for cardiovascular monitoring: from device development to clinical validation". In: *IEEE Reviews in Biomedical Engineering* (2024). DOI: 10.1109/RBME.2024.3410399.

[2] E. Bianchini et al. "Wearable Ultrasound: Are We Ready to Take This Chance for Vascular Ageing Assessment?" In: *Artery Research* 31.1 (2025). DOI: 10.1007/s44200-025-00069-9.

[3] P. Song et al. "Clinical, Safety, and Engineering Perspectives on Wearable Ultrasound Technology: A Review". In: *IEEE Transactions on Ultrasonics, Ferroelectrics, and Frequency Control* 71.7 (2024), pp. 730–744. DOI: 10.1109/TUFFC.2023.3342150.

DOI 10.5162/Ultrasonic2025/A16-a4

Enhancing Air-coupled Ultrasonic Inspection: Resolving Signal Overlapping in Long-duration Chirp Signals

Muhammad Tayyib[1], *Musyyab Yousufi*[2], *Paulius Tervydis*[1], *and Linas Svilainis*[1]
[1] *Department of Electronics Engineering, Kaunas University of Technology, Lithuania*
[2] *Centre of Real Time Computer Systems, Kaunas University of Technology, Lithuania*
muhammad.tayyib@ktu.edu

Abstract: Air-coupled ultrasound investigations are crucial for non-destructive testing of thin and delicate materials. Conventional pulse excitation yields suboptimal signal-to-noise and narrow bandwidth. Chirp signals improve these parameters, however, requires long duration to do so, which results in overlapping of reflections. To solve the overlapping this paper proposed the use of residual deep learning approach using convolutional UNet1D architecture and composite loss function. Results show successful separation of overlapping reflections.

Keywords: Chirp signals, 1D convolutional neural network, overlapping reflections, air-coupled ultrasound, residual UNet.

Introduction

The use of air-coupled ultrasound is gaining traction in non-destructive testing (NDT), due to its adaptability across various mediums and non-contact investigations. Short-duration pulse excitation signals are commonly used because of their high temporal resolution and simple interpretation [1]. The main problem with pulse signals is limited bandwidth and low signal-to-noise ratio (SNR), especially in air-coupled ultrasound, where a high impedance mismatch between air and sample leads to losses in energy transmission [1]. An alternative approach involves the use of long-duration chirp signals (linear frequency modulation (LFM)), which offers the ability to increase the bandwidth and duration of signals (Fig. 1), as in [2] it was demonstrated that the longer the signal, the better the ability to compensate for spectral losses.

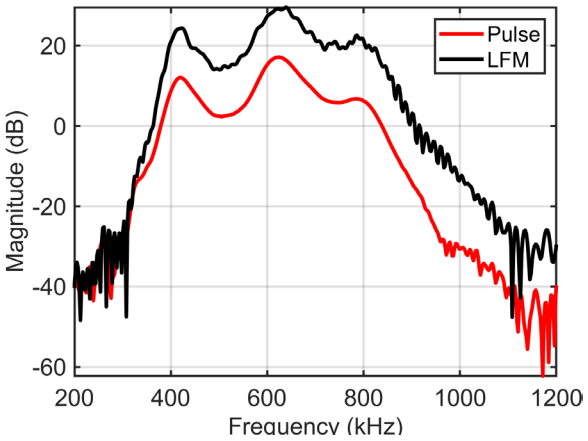

Fig. 1: Spectral response of pulse compared with LFM chirp signal

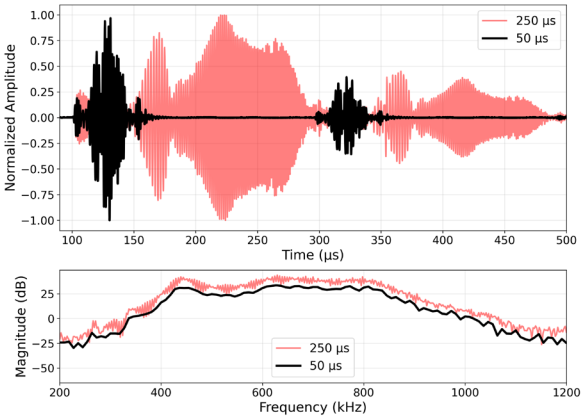

Fig. 2: Temporal response (top), spectral response (bottom) of $50\,\mu s$ *chirp compared with* $200\,\mu s$ *chirp*

The typical air-coupled ultrasound system is composed of transmitting and receiving transducers that cannot be too far from each other; thus, for short durations $10\,\mu s$ to $100\,\mu s$, the investigation could be carried out without acquisition problems; however, in longer signals, i.e. $150\,\mu s$ onward reflections begin to overlap in the received signals (Fig. 2 Top), making it extremely difficult to isolate and interpret individual reflections. Moreover, overlapping signals in the spectral domain (Fig. 2 bottom) results in a serrated response that makes it difficult to use the signal for parameter estimation.

Signal overlapping is traditionally solved by manual gating [3], matched filtering [4], or through frequency domain processing. Manual gating requires selection of time windows to isolate the reflections; however, it becomes ineffective if the signal overlaps and there is

DOI 10.5162/Ultrasonic2025/A16-a4

no distinction between reflections. Matched filtering or inverse filtering provides improved temporal resolution based on the assumption that the system is linear and the impulse response is known, which is almost impractical in air-coupled systems.

Moreover, in the case of time-localized reflection, they suffer from leakage and are not reliable. Deep neural networks (DNN) have been applied for signal separation in recent studies [5, 6], in [5], a deep learning approach classification task was achieved for modulation recognition, while the methodology was evaluated using only simulated data. Similarly, in [6], the results were also calculated with simulated data. Compared to these approaches, real-world experimental methods are needed that not only have the ability to train on experimentally obtained data but, instead of only classification, predict for the data which was not even part of the training.

In the air-coupled ultrasound received signals, if the reflections overlap and there is no gating, the spectral response contains too much interference making it difficult to interpret, as shown in Fig. 2(bottom). The overlapping signal scenario was experimented with using $650\,\mathrm{kHz}$ center frequency air-coupled transducers of different duration of LFM ($10\,\mu\mathrm{s}$ to $350\,\mu\mathrm{s}$). From visible interpretation of even the time domain signal, it was clear that signals up to $100\,\mu\mathrm{s}$ exhibit separate reflections, while longer signals, that is, $150\,\mu\mathrm{s}$, were affected by reflection overlapping. Thus, a novel approach is required to solve the overlapping in reflections to extract meaningful information from long-duration excitation signals.

In this work, a residual deep learning-based approach is proposed that focuses on the solution of overlapping in long-duration excitation signals. The model was trained on short-duration $10\,\mu\mathrm{s}$, $20\,\mu\mathrm{s}$, $50\,\mu\mathrm{s}$ gated signal (only the first reflection was preserved), for overlapped long-duration signals $150\,\mu\mathrm{s}$, $200\,\mu\mathrm{s}$, $300\,\mu\mathrm{s}$, and $350\,\mu\mathrm{s}$. The excitation voltage on the transducers was measured and considered as the input to the model, the output of the deep learning model was the calibration signal with only first reflection, the target function was L_2 norm in both time and frequency domains between the predicted signal and the actual signal. Thus, ensuring both temporal and spectral information for the modeling, the aim was to train the model in such a way that it can predict the non-overlapping reflection from the long-duration overlapping reflections using the knowledge learned during short-duration signals training.

To the best of our knowledge, this is the first application of residual UNet with 1D convolutions (Res-UNet1D) to separate overlapping reflections in experimentally obtained time-domain air-coupled ultrasound signals.

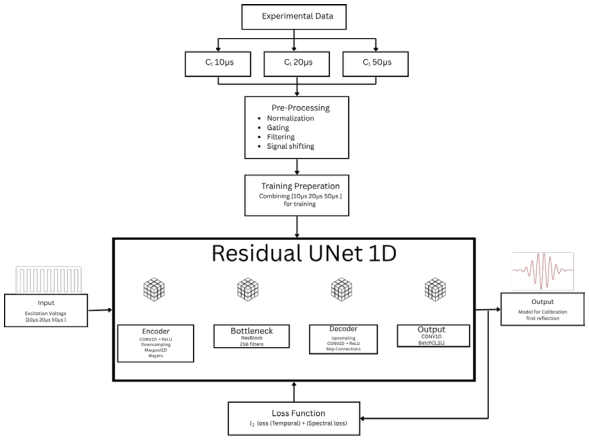

Fig. 3: Proposed Res-UNet1d based training flow diagram

2. Materials and Methods

Data was partitioned in such a way, as for training $10\,\mu\mathrm{s}$, $20\,\mu\mathrm{s}$ and $50\,\mu\mathrm{s}$ signals were used while long durations $150\,\mu\mathrm{s}$, $200\,\mu\mathrm{s}$, $250\,\mu\mathrm{s}$, $300\,\mu\mathrm{s}$, $350\,\mu\mathrm{s}$, were used for the testing where reflections are already overlapping. Data collected and stored in mat format where 100 repetitions were measured for each duration for a better statistical analysis of a diverse training set.

The methodology is shown in Fig. 3. As the excitation voltage for obtaining these signals was based on rectangular chirp, both the excitation voltage and the calibration signals were normalized to ensure a smooth training process; moreover, band-pass filtering was done between $0.15 - 1.5\,\mathrm{MHz}$ to remove any unwanted noise.

The UNet was developed from scratch and the Res-UNet1D block was specifically designed for residual tasks involving air-coupled ultrasound modeling as 1D time-domain signals. The residual block consists of two 1D convolutional layers, followed by batch normalization and activated by leaky rectified linear unit (LReLU) functions. Encoding was achieved in four stages; each stage consists of dual residual blocks with progressively increasing dilation $(1\,,\,2\,,\,4\,,\,8\,)$. These dilation rates ensure that the models effectively capture complex temporal features on varying scales.

The bottleneck segment deepens the feature extraction with two residual blocks characterized by high dilation rates, that is $16\,$, capturing long-range dependencies in the signal. The decoder mirrors the encoder path with slight up-gradation of using ConvTranspose1D for up-sampling. The final output was generated by a sequence of a 1x1 convolution reducing feature channels from $64\,\mathrm{to}\,32\,$, a ReLU activation, and a subsequent 1x1 convolution projecting to a

DOI 10.5162/Ultrasonic2025/A16-a4

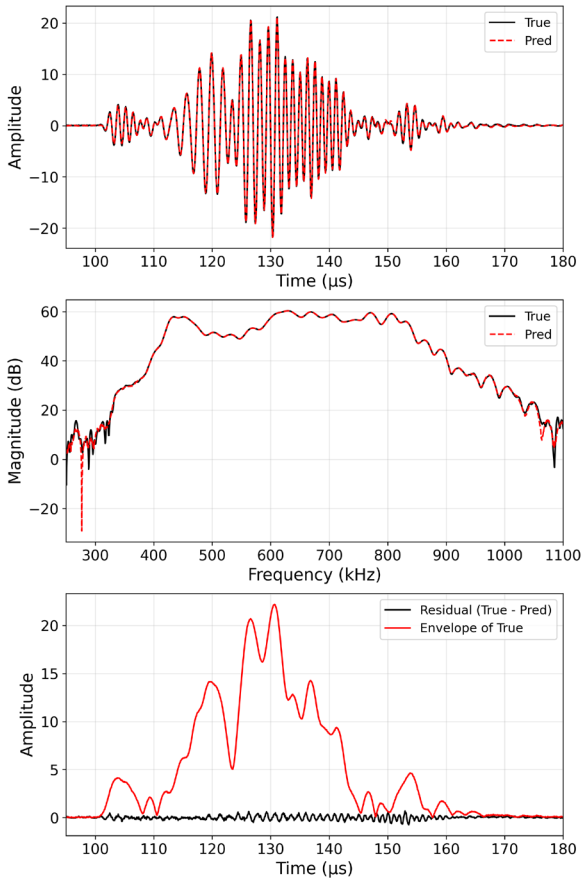

Fig. 4: Temporal (top), spectral (middle) and residual (bottom) response of $50\,\mu s$ *that was part of the training*

single-channel output, corresponding to the target residual signal

As training was achieved using short duration signals, the fitting results of modeling in comparison to the experiment are shown in Fig. 4, where both temporal (Fig. 4 (top)) and spectral (Fig. 4 (middle)) fitting results are in perfect match. Furthermore, the residual (Fig. 4 (bottom)) shows nearly perfect fitting results since the only remaining part contains noise content. The total loss function ($\mathcal{L}_{\text{total}}$) is described as fitting in both time ($\mathcal{L}_{\text{time}}$) and frequency ($\mathcal{L}_{\text{freq}}$) domains, as:

$$\mathcal{L}_{\text{total}} = \mathcal{L}_{\text{time}} + \alpha\,\mathcal{L}_{\text{freq}} \tag{1}$$

$$\mathcal{L}_{\text{time}} = \frac{1}{N}\sum_{n=1}^{N}(y_n - \hat{y}_n)^2 \tag{2}$$

$$\mathcal{L}_{\text{freq}} = \frac{1}{K}\sum_{k=1}^{K} w_k\,(|\mathcal{F}\{y\}_k| - |\mathcal{F}\{\hat{y}\}_k|)^2 \tag{3}$$

where $\alpha = 0.1$ is the trade-off weight (frequency loss scaling factor) for the total loss function that was set at such a value to obtain optimal or stable performance across our dataset after several validation experiments. y_n and $\hat{y}_n$ are the true experimental signal and predicted signals in sample n respectively, N is the total number of samples, $\mathcal{F}y_k$ is discrete Fourier transform (DFT) of y at frequency k and w_k is the weighting coefficient for the frequency bin k. The weight w_k is set to 1 for frequency bins within the range $[200, 1200]$kHz, and 0.5 outside this range, which results in a penalty for mismatch outside this passband region.

Results

The Res-UNet1D modeling was successfully achieved while training only for short-duration signals and testing for both short and long-duration signals (long-duration signals were not part of the model development, only part of the validation, i.e. prediction). Fig. 5 plots the time, freq and residual plots of $250\,\mu s$

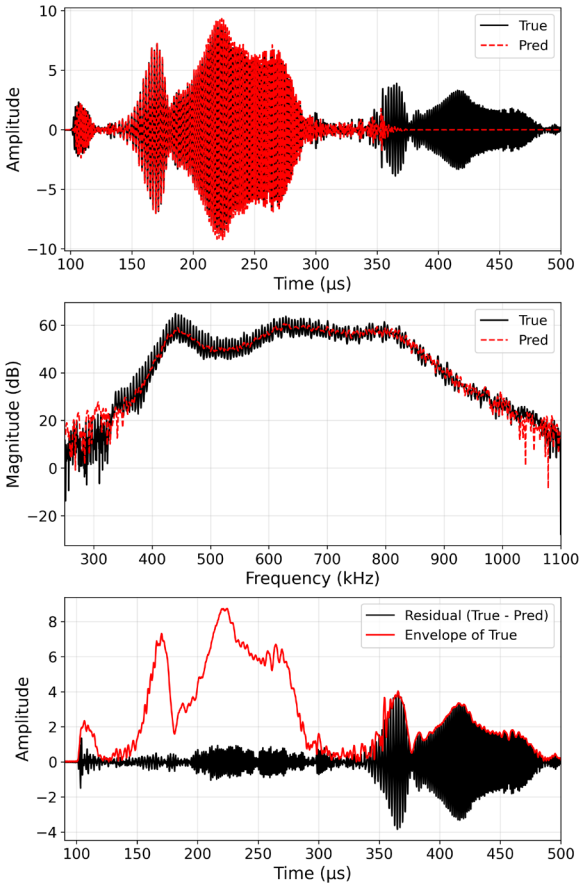

Fig. 5: Temporal (top), spectral (middle) and residual (bottom) response of $250\,\mu s$ *chirp signal, compared with the model (first reflection) of complete signal*

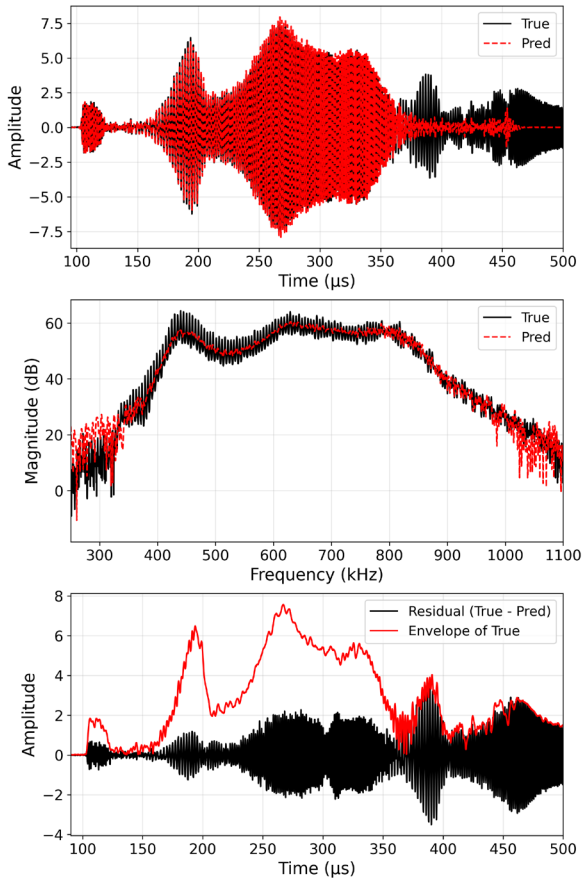

Fig. 6: Temporal (top), spectral (middle) and residual (bottom) response of $350\,\mu s$ *chirp signal, compared with the model (first reflection) of complete signal*

chirp signals, compared with $50\,\mu s$ (Fig. 4) the residual is a bit more, however it is important to note that $250\,\mu s$ was not in the training and the results are purely based on model prediction. Similarly, for the longest $350\,\mu s$ (Fig. 6), the visual results are also acceptable with minor losses of the modeling results.The residual part indicates that learning was successful for the first reflection region (Figs. 4–6 (bottom), under the envelope), while comparison with actual signal validates the proposed approach. Although for the long-duration signals there are some residuals, however, this is little sacrifice in order to achieve modeling.

Conclusion

Res-UNet1D based deep learning approach was proposed for the long-duration reflection overlapping in chirp signals used for air-coupled ultrasound. The results emphasize the importance of a deep learning architecture for modeling and predicting signals with significant overlap. The pre-processing, gating, scaling, normalization, and signal alignment ensured robust modeling of complex ultrasound reflections for experimental data. The close match between predicted and true signals in both the time and frequency domains highlights the model's capability to generalize across different excitation conditions and signal complexities.

Acknowledgment

This research was funded by a Grant No. S-MIP-23-133 from the Research Council of Lithuania.

References

[1] L. Fariñas et al. "Origin, development and applications of air-coupled broadband ultrasounds for the study of tissues and water relations in plant leaves: a review". In: *IEEE Open Journal of Ultrasonics, Ferroelectrics, and Frequency Control* 4 (2024), pp. 77–88. DOI: 10.1109/OJUFFC.2024.3433316.

[2] M. Tayyib and L. Svilainis. "Compensation function for enhanced bandwidth and improved SNR through programmable spectral shape signals". In: *2024 IEEE Ultrasonics, Ferroelectrics, and Frequency Control Joint Symposium (UFFC-JS)*. IEEE, 2024, pp. 1–5. DOI: 10.1109/UFFC-JS60046.2024.10793903.

[3] C. Bruckmann, S. Müller, and C. Zu Siederdissen. "Automatic, fast, hierarchical, and non-overlapping gating of flow cytometric data with flowEMMi v2". In: *Computational and Structural Biotechnology Journal* 20 (2022), pp. 6473–6489. DOI: 10.1016/j.csbj.2022.11.033.

[4] K. Dakic et al. "HybNet: a hybrid deep learning-matched filter approach for IoT signal detection". In: *IEEE Transactions on Machine Learning in Communications and Networking* 1 (2023), pp. 18–30. DOI: 10.1109/TMLCN.2023.3270131.

[5] G. Jajoo and P. Singh. "Modulation classification for overlapped signals using deep learning". In: *IEEE Open Journal of the Communications Society* (2024). DOI: 10.1109/OJCOMS.2024.3416750.

[6] R. Zhang et al. "A reference signal-aided deep learning approach for overlapped signals automatic modulation classification". In: *IEEE Communications Letters* 27.4 (2023), pp. 1135–1139. DOI: 10.1109/LCOMM.2023.3242690.

DOI 10.5162/Ultrasonic2025/A16-a5

Acoustic Energy Transmission on Mobile Sensors (AEToMS) in Closed (Pipe) Systems

Michael Simon[1], Felix Grimm[1], and Ulrike Steinmann[1]
[1] Otto-von-Guericke-University Magdeburg, Institute for Automation Technology, Chair for Measurement Technology, Universitätsplatz 2, Magdeburg, 39106, Germany
michael.simon@ovgu.de

Abstract: This paper investigates acoustic energy transmission for wirelessly charging mobile sensors in enclosed systems using focused ultrasound. A test setup with a 32-element ring array and a spherical sensor was used. The sensor was localized using time-of-flight measurements. Two focusing methods (phased array and time reversal) were implemented and experimentally compared. The charging signals were analysed in terms of amplitude and energy. The time-reversal approach achieved better focusing quality and higher energy transfer.

Keywords: Ultrasound, mobile sensors, localisation, focusing, energy harvesting

Background and Motivation

Mobile wireless sensor networks offer a promising solution for optimizing process control in closed systems through holistic, local monitoring. Unlike stationary sensors, mobile units move with the process medium, enabling spatially and temporally resolved data collection (even in otherwise inaccessible regions). Wireless transmission of the collected data provides real-time, location-specific insights to enhance system control.

While modern low-power systems consume minimal energy in standby, active modes (e.g. sensing, processing, and transmitting) can significantly increase power demand. Despite energy-saving strategies, battery depletion remains a limiting factor. This challenge can be addressed via energy harvesting, including external wireless energy transmission.

Unlike commonly used inductive methods, this work explores an acoustic approach using ultrasound. A key advantage is that the interaction range can be significantly increased, which is achieved either by controlled beam shaping or by utilising reflections at system boundaries. In order to efficiently transfer energy for charging a mobile sensor, the acoustic energy can be focussed on its position and converted in electrical energy by using a piezoelectric transducer.

This paper addresses the investigation of various methods for acoustic localisation and focusing e.g., time-of-flight (TOF), phased array (PA), time reversal (TR), to develop a feasible concept for efficient acoustic energy transmission with optimized energy yield.

Experimental Setup

Based on initial design decisions, a first experimental setup was developed, including a sensor prototype and a cylindrical test environment (see Fig. 1). The sensor is a 25 mm SLA-printed sphere with six flush-mounted piezoelectric transducers in a ring configuration. These serve both as receivers for acoustic energy and as transmitters for localisation (via burst signals) as well as communication (via frequency-modulated acoustic signals). The test cylinder (PMMA, 110 mm diameter, 200 mm height) contains 32 circumferential piezoelectric transducers mounted on outer facets for consistent coupling. These transducers are used for sensor localisation, acoustic energy focusing, and reception of communication signals. The piezoelectric elements used in both the sensor and cylinder are ceramic disks (PIC255, 10 mm diameter, 2 mm thickness).

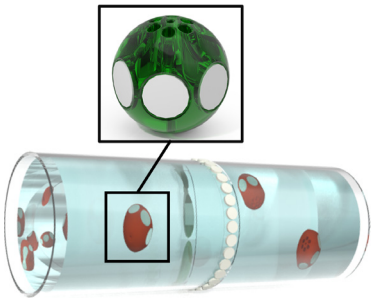

Fig. 1: Rendered image of the sensor (top) and multiple sensors in a pipe as sensor network (bottom).

Electronic components such as microcontroller, T/R switch, and energy management system (including signal conditioning, harvesting IC, and storage) are externally implemented at this stage. The transducers are connected via cables to the signal generation, measurement, or energy management systems. A detailed description of the sensor and its energy management system can be found in [1].

For accurate positioning, the sensor is fixed on a

DOI 10.5162/Ultrasonic2025/A16-a5

rigid wire and placed using a modified 3D printer. A MATLAB-based control software with a graphical user interface (GUI) was developed to operate the 3D positioning system, function generator, and digital oscilloscope, allowing automated measurement and frequency-modulated (FM) signal analysis for communication.

Signal acquisition is carried out using a four-channel digital oscilloscope, while synchronous output on 32 channels is generated via pulse-width modulation (PWM) using an FPGA evaluation board. Custom amplifier stages increase the signal amplitude to $\pm 30\,\mathrm{V}$ and apply low-pass filtering to reconstruct the acoustic waveforms. Additionally, COMSOL and LTSpice simulations are used for system analysis and optimisation. This setup provides the foundation for evaluating different localisation and focusing methods to improve focusing efficiency and charging performance.

Methods of Localisation and Focusing

Depending on the application, sensors may face constraints (e.g., limited space), requiring functional differentiation. The choice of acoustic energy transmission depends on whether the sensor actively transmits signals or functions passively. Initial tests confirmed that short acoustic transmissions are energetically feasible, motivating a focus on active signal emission. Two acoustic focusing methods are considered: phased array (PA) and time reversal (TR).

In PA, time-delayed signals from the external array produce constructive interference at a defined focal point [2] (as schematically shown in Fig. 2, step 3). This enables spatial selectivity without mechanical alignment, but requires precise knowledge of sensor position and medium properties. The method is sensitive to inhomogeneities and multipath effects.

Accurate localisation is thus essential. A common approach uses time-of-flight (TOF) or time-difference-of-arrival (TDOA) techniques. The sensor emits a signal through all its transducers, which is detected by external receivers (see Fig. 2, step 1). Based on signal arrival times and the known sound speed, the sensor position is estimated by triangulation or trilateration (Fig. 2, step 2). These methods are efficient, but their accuracy depends on precise time-picking and reliable sound speed. Reflections, multipath propagation, and medium inhomogeneities (e.g., temperature or concentration gradients) can obscure the direct signal and reduce accuracy. In sensor networks, mutual interference or occlusion can make signal interpretation even more difficult.

TR techniques provide a robust alternative in complex environments. Unlike PA, TR requires no prior localisation. Instead, the sensor emits a pulse, which is recorded over time by the external array, including

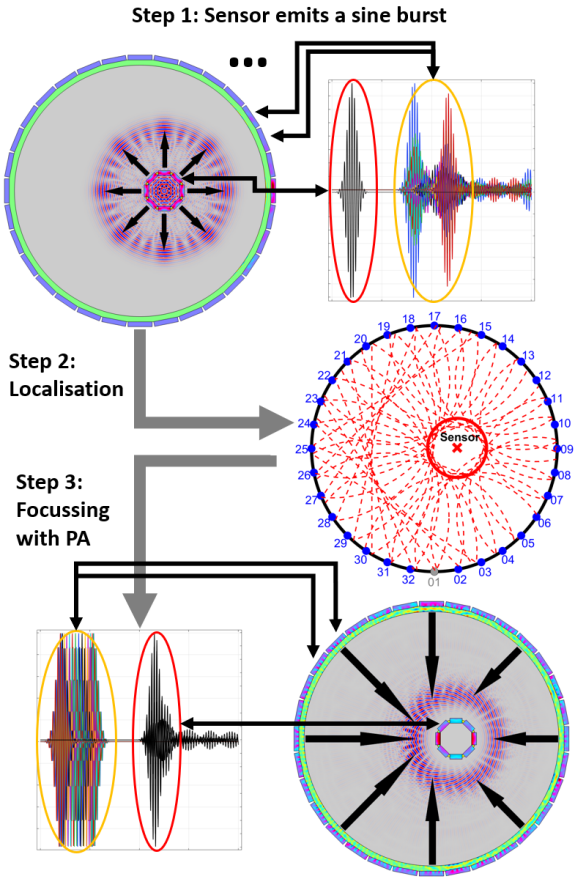

Fig. 2: Schematic procedure of the phased array focusing method: (Step 1) the sensor emits a pulse, (Step 2) the position is localized, (Step 3) acoustic energy is focused using time-delayed signals.

system-internal reflections (as schematically shown in Fig. 3, step 1). These signals are then time-reversed and re-emitted. Due to acoustic reciprocity, the wavefronts retrace their original paths and refocus at the source location [3] (Fig. 3, step 2).

This inherent property allows the method to compensate for inhomogeneities in the medium and to mitigate multipath effects, making it particularly well-suited for scattering or structurally complex environments [4]. Additionally, the presence of multiple reflections and scatterers can even enhance the focusing accuracy [5], which is advantageous for future applications in sensor networks. However, the method requires the initial calibration procedure and the time-reversed re-emission of the recorded signals, which inherently takes more time than phased array-based focusing. As a result, the achievable focusing rate (the number of focus events per second) is significantly lower.

DOI 10.5162/Ultrasonic2025/A16-a5

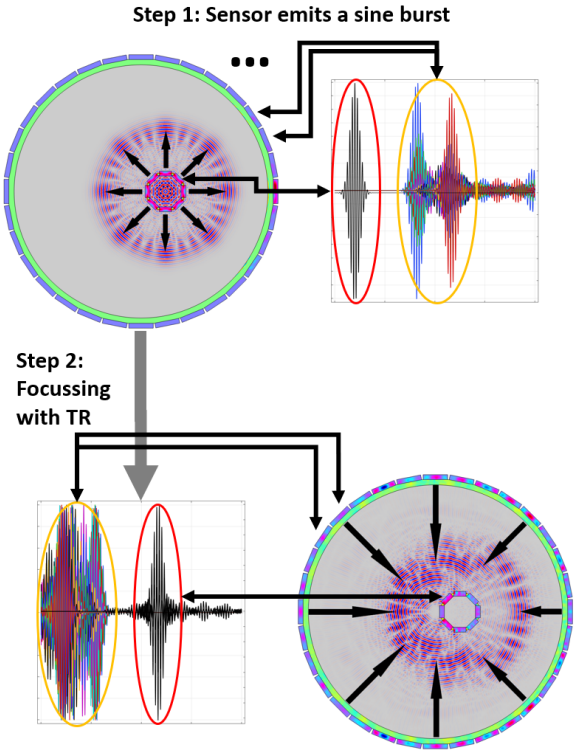

Fig. 3: Schematic procedure of the time reversal focusing method: (Step 1) the sensor emits a pulse, (Step 2) acoustic energy is focused using time-reversed signals.

Experimental investigations

For the experimental investigations, the sensor was positioned at various predefined locations along the x-axis within the water-filled cylinder, aligned with the plane of the external piezoelectric array. To enable acoustic focusing using either the PA or TR method, the sensor first emits a short sinusoidal burst signal (1 MHz, 5 cycles) simultaneously through all of its transducers. The resulting wave propagates radially through the medium and is recorded by the surrounding receiver array. The recorded signals are subsequently used for both localisation and TR-based focusing. Since accurate localisation is a prerequisite for the phased array approach, the sensor position was estimated based on the measured TOF of the received signals.

Tab. 1 presents the localisation results for selected sensor positions. To assess accuracy, the Euclidean distance between the true and estimated positions was calculated, yielding errors ranging from 0.39 mm to 2.56 mm, correspond to approximately 0.26 to 1.73 times the wavelength of the 1 MHz signal in water ($\lambda \approx 1.48$ mm). Relative to the cylinder's diameter (maximum possible error), this corresponds to deviations between 0.75 % and 4.92 %. This indicates that subwavelength localisation is achievable under favourable conditions, while worst-case deviations remain within approximately two wavelengths. These results demonstrate a spatial resolution that is consistent with the expected limits of TOF-based localisation methods.

Tab. 1: Localisation with TOF.

True position [mm] (x/y)	Estimated position [mm] (x/y)	Euclidean error [mm]
0/0	2.55/0.26	2.56
10/0	9.63/0.3	0.39
20/0	18.62/−0.87	1.52

To ensure the comparability of the results, the PA technique was applied using the actual target position instead of the calculated one, which was subject to errors. A time-shifted sinusoidal burst with a frequency of 1 MHz and 5 cycles was used for the PA focusing signal. This choice accounts for the duty cycle used during the calibration of the TR signals and enables a fair comparison between both methods. Depending on the position, the transmission of the time-delayed PA signals was completed after approximately 50 µs. In contrast, a time window of 500 µs was selected for the calibration of the TR signals, corresponding to approximately three complete round trips of the acoustic wave across the cylinder. Fig. 4 compares the signal amplitudes of all transducers of the sensor at the position (10/0) at the respective focusing times. While the moment of maximum focusing occurred at around 43 µs for the PA method, it was observed at approximately 503 µs when using the TR method.

When comparing results, the maximum peak value (voltage amplitude) across all transducers is considered as a primary indicator of spatial and temporal energy concentration. Higher peak amplitudes reflect more effective constructive interference of acoustic waves at the focal point, which correlates with improved focusing quality. Tab. 2 presents the maximum peak values obtained for selected focal positions. For these representative cases, the TR method achieves a substantial increase in amplitude, ranging from 53.1 % to 80.6 % compared to the PA approach.

However, the maximum amplitude does not directly reflect the amount of energy available at the focal point. To more robustly characterise the performance of energy transfer, this comparison is supplemented by evaluating the root mean square (RMS) over a defined time window. Since the sensor is equipped with six

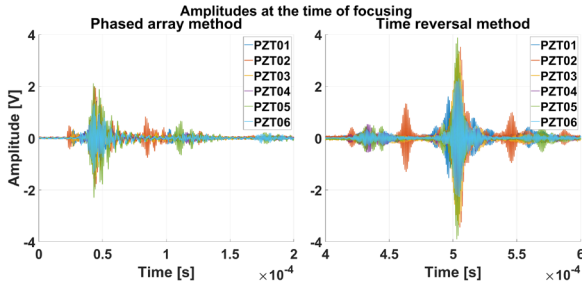

Fig. 4: Signal amplitudes of all transducers of the sensor at the position (10/0) at the time of focusing for two methods: phased array (left) and time reversal (right).

Tab. 2: Comparison of the maximum peak value.

Position (x/y) [mm]	Max amplitude PA [V]	Max amplitude TR [V]
0/0	3.25	5.09
10/0	2.17	3.91
20/0	2.5	3.82

transducers, the RMS value is calculated for each transducer within a 10 µs window centred around the individual peak amplitude and subsequently averaged. Tab. 3 presents the results of this RMS analysis. Again, the TR method shows a consistent advantage across all focal positions, with relative increases in RMS between 100.86 % and 129.23 % compared to the PA approach. This indicates that more usable energy is concentrated within the analysed time window, suggesting improved energy harvesting potential.

Summary and Outlook

This work explored two acoustic focusing techniques (phased array and time reversal) for wireless energy transmission to mobile sensors in enclosed systems. PA-based focusing requires prior localisation, for which a TOF-based algorithm achieved subwavelength accuracy. Both methods were theoretically analysed and experimentally tested in a 2D setup. TR showed consistently higher peak amplitudes and RMS values across all sensor transducers, indicating more effective focusing and greater energy availability within a defined time window. These results lay the groundwork for optimising charging performance and assessing system efficiency in future studies.

Tab. 3: Comparison of the averaged RMS value.

Position (x/y) [mm]	Averaged RMS PA [V]	Averaged RMS TR [V]
0/0	1.03	2.08
10/0	0.68	1.56
20/0	0.48	0.99

Further research will extend the current 2D system to 3D. To achieve this, chaotic cavities or acoustic lenses may be employed to increase transducer aperture. Under such conditions, conventional TOF localisation and PA focusing become unreliable, motivating the use of data-driven approaches such as machine learning [6]. Additionally, iterative time reversal [2] offers adaptive, tracked focusing without explicit localisation, with potential for selective targeting via decomposition of the time-reversal operator (DORT) in multi-sensor systems. The long-term objective of this work is the development of a robust, energy-autonomous mobile sensor network.

References

[1] Felix Grimm, Michael Simon, Stephan Adler and Ulrike Steinmann, Eds., *Mobile Sensor Concept with Energy Harvesting through Focused Ultrasound Signals: DEGA e.V*, 2025. DOI: 10.71568/dasdaga2025.195.

[2] B. E. Anderson, M. Griffa, P. A. Johnson, C. Larmat and T. J. Ulrich, 'Time reversal,' 2008. [Online]. Available: http://hdl.lib.byu.edu/1877/2177.

[3] Mathias Fink, 'Time-reversed acoustics,' *Scientific American*, vol. 281, no. 5, pp. 91–97, 1999, ISSN: 00368733. Accessed: 7th Jul. 2025. [Online]. Available: http://www.jstor.org/stable/26058488.

[4] M. Fink, 'Time reversal of ultrasonic fields. i. basic principles,' *IEEE transactions on ultrasonics, ferroelectrics, and frequency control*, vol. 39, no. 5, pp. 555–566, 1992, ISSN: 0885-3010. DOI: 10.1109/58.156174.

[5] P.-Y. Le Bas, T. J. Ulrich, B. E. Anderson and J. J. Esplin, 'A high amplitude, time reversal acoustic non-contact excitation (trance),' *The Journal of the Acoustical Society of America*, vol. 134, no. 1, EL52–6, 2013. DOI: 10.1121/1.4809773.

[6] T. Sillanpää et al., 'Localizing a target inside an enclosed cylinder with a single chaotic cavity transducer augmented with supervised machine learning,' *AIP Advances*, vol. 11, no. 11, p. 115 104, 2021. DOI: 10.1063/5.0068803.

DOI 10.5162/Ultrasonic2025/A18-a1

Modeling and simulation of the behavior of piezoceramics with the discontinuous Galerkin method

Carsten Spieker[1], Jonas Hölscher[2], Leander Claes[2], Bernd Henning[2], and Jens Förstner[1]
[1] Theoretical Electrical Engineering Group, Paderborn University, 33098 Paderborn, Germany
[2] Measurement Engineering Group, Paderborn University, 33098 Paderborn, Germany
carsten.spieker@uni-paderborn.de

Abstract: This paper explores the use of the discontinuous Galerkin time domain method (DG) for simulating piezoceramics, which is essential in designing ultrasonic transducers. The DG method allows computational efficiency and provides good adaptability to three-dimensional structures. The study confirms the method's stability and accuracy, emphasizing the importance of proper boundary conditions and computational grids, which set the stage for future developments.

Keywords: Discontinuous Galerkin Time Domain Method, Piezoelectricity, Material characterization, Numerical flux, Parallelization

Motivation

Physics-based numerical simulations of piezoceramics are essential for the design of components such as ultrasonic transducers. In this work, we investigate the application of the discontinuous Galerkin time domain method (DG) to solve a system of partial differential equations describing the mechanical behavior. This approach promises various advantages: The unstructured grid allows for a good description of any geometry. Due to the possibility to divide the geometry into several subregions, the calculation can be carried out efficiently by a parallelization. The time-domain description will allow for the inclusion of non-linear properties in the future.

In an inverse design approach, the material parameters are determined on the basis of the electrical impedance of the respective piezoceramic by optimization with our software tool [1]. In order to be able to consider a freely selectable electrode structure, a three-dimensional structure without assumption of any symmetries is regarded in this work.

Here, the openCFS software [2] will be used to validate the results with respect to linear material dependencies of the electrical and mechanical properties and the required compute times. In order to compare the different methods, only a linear behavior on the electrical and mechanical quantity is considered.

Physical description of piezoceramics

The relationship between the mechanical (stress $\boldsymbol{T}$ and strain $\boldsymbol{S}$) and electrical (electric field strain $\boldsymbol{E}$ and flux density $\boldsymbol{D}$) components can be described by using the following linear system of equations in Voigt notation [3]:

$$\begin{aligned} \boldsymbol{T} &= \boldsymbol{c}^{\mathrm{E}}\boldsymbol{S} - \boldsymbol{e}^{\mathrm{t}}\boldsymbol{E} \\ \boldsymbol{D} &= \boldsymbol{e}\boldsymbol{S} + \boldsymbol{\varepsilon}^{\mathrm{S}}\boldsymbol{E} \end{aligned} . \tag{1}$$

The elastic stiffness matrix $\boldsymbol{c}^{\mathrm{E}}$, the piezoelectric constant $\boldsymbol{e}$ and the permittivity matrix $\boldsymbol{\varepsilon}^{\mathrm{S}}$ are required for the description. In this work the material parameter for PIC255 manufactured by PI Ceramic are used [4]. For general formulation, each node is given a set of material parameters.

The plane wave in the piezoceramic can be calculated and described with [5]

$$\begin{aligned} \rho_0 \frac{\partial^2 u_1}{\partial t^2} &= \frac{\partial T_1}{\partial x_1} + \frac{\partial T_6}{\partial x_2} + \frac{\partial T_5}{\partial x_3} \\ \rho_0 \frac{\partial^2 u_2}{\partial t^2} &= \frac{\partial T_6}{\partial x_1} + \frac{\partial T_2}{\partial x_2} + \frac{\partial T_4}{\partial x_3} \\ \rho_0 \frac{\partial^2 u_3}{\partial t^2} &= \frac{\partial T_5}{\partial x_1} + \frac{\partial T_4}{\partial x_2} + \frac{\partial T_3}{\partial x_3} \end{aligned} \tag{2}$$

with the mechanical stress

$$\boldsymbol{T} = \begin{bmatrix} c_{11}^{\mathrm{E}} \frac{\partial u_1}{\partial x_1} + c_{12}^{\mathrm{E}} \frac{\partial u_2}{\partial x_2} + c_{13}^{\mathrm{E}} \frac{\partial u_3}{\partial x_3} + e_{31} \frac{\partial \phi}{\partial x_3} \\ c_{12}^{\mathrm{E}} \frac{\partial u_1}{\partial x_1} + c_{22}^{\mathrm{E}} \frac{\partial u_2}{\partial x_2} + c_{23}^{\mathrm{E}} \frac{\partial u_3}{\partial x_3} + e_{32} \frac{\partial \phi}{\partial x_3} \\ c_{13}^{\mathrm{E}} \frac{\partial u_1}{\partial x_1} + c_{23}^{\mathrm{E}} \frac{\partial u_2}{\partial x_2} + c_{33}^{\mathrm{E}} \frac{\partial u_3}{\partial x_3} + e_{33} \frac{\partial \phi}{\partial x_3} \\ c_{44}^{\mathrm{E}} \left(\frac{\partial u_2}{\partial x_3} + \frac{\partial u_3}{\partial x_2} \right) + e_{15} \frac{\partial \phi}{\partial x_2} \\ c_{55}^{\mathrm{E}} \left(\frac{\partial u_1}{\partial x_3} + \frac{\partial u_3}{\partial x_1} \right) + e_{15} \frac{\partial \phi}{\partial x_1} \\ c_{66}^{\mathrm{E}} \left(\frac{\partial u_1}{\partial x_2} + \frac{\partial u_2}{\partial x_1} \right) \end{bmatrix} . \tag{3}$$

With Eq. (2) and Eq. (3), we obtain a system of equations that depend only on the mechanical displacement $\boldsymbol{u}$. With the special feature that terms consist of either double spatial or double temporal

DOI 10.5162/Ultrasonic2025/A18-a1

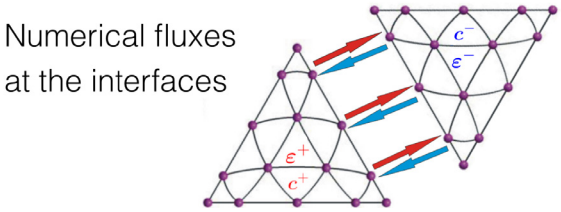

Fig. 1: Concept of the DG method with the numerical fluxes [7] (modified).

derivative terms. For the following numerical description, the sound velocity is introduced as the first time derivative of the mechanical displacement. This results in equations with first-order derivatives in space and time, which is necessary for the DG method.

Model

As an example, a piezoceramic cylinder ($r = 5\,\mathrm{mm}$, $h = 1\,\mathrm{mm}$) with full-surface electrodes is considered. For the simulations it is assumed that the piezoceramic can vibrate freely and does not experience any external forces. Therefore the following boundary condition is obtained:

$$\boldsymbol{N}^{\mathrm{t}}\boldsymbol{T} = 0, \tag{4}$$

where $\boldsymbol{N}^{\mathrm{t}}$ is the normal matrix of the respective boundary surface in Voigt notation.

Numerical scheme

This section provides an overview of the discontinuous Galerkin time domain method. The two main foundations are the DG operators and time stepping.

The DG method is related to two well-known methods: the Finite Element Method (FEM) and Finite Volume Method (FVM). The main difference is the range in which the shape functions extend. As in the FEM method, the computational domain is divided into triangles or tetrahedra. The shape functions of the DG method only apply locally in the computational domain. This allows local matrices to be set up, which have advantages in terms of individual calculation steps and parallelization [6]. The discontinuities between the neighboring volume elements can be corrected by the exchange of information with the so-called numerical fluxes f^*. This concept is illustrated in Fig. 1. The numerical flux is typically a function of internal and external values of the same coordinates. Where external describes the neighboring element or an external boundary condition and internal identifies the element in which the calculation takes place. Many different approaches for the numerical flux are presented in the literature [8]. Two fluxes are used in the following section. The central flux

$$f_{\mathrm{C}}^*(u) = \frac{f_-(u) + f_+(u)}{2} \tag{5}$$

can be interpreted mathematically as the mean value, this calculates the mean value of the two values present at the respective boundary node. To obtain a monotone solution, the central flux is extended to the Lax-Friedrichs flux as follows

$$f_{\mathrm{L}}^*(u) = \frac{f_-(u) + f_+(u)}{2} + \frac{C_{\mathrm{w}}}{2} n\,(u_- - u_+)\,, \tag{6}$$

where C_{w} describes the maximum speed of sound of the material.

To solve the piezoelectric equations, a first-order system is required in the DG method. To do this, the Eq. (2) and Eq. (3) are rewritten into the conservation form. The computational domain Ω is divided into K non-overlapping tetrahedra, where k indicates the k-th element.

$$\Omega = \bigcup_{i=1}^{K} D^k. \tag{7}$$

Eq. (8) describe the acoustics wave in the piezoceramic, which is approximated using the vectors u_i^k, which describe the DG approximation in the respective element k. In each element k, the function $u(x,t)$ is approximated as $u^k(x,t)$ using

$$u^k(x,t) = \sum_{i=1}^{N_p} u^k(x_i^k, t) l_i^k(x)\ \forall k \in K \tag{8}$$

with Lagrange polynomials $l_i^k(x)$ in the k-th node. In order to be able to apply the operators to every volume element k in general, a reference element is defined and an assignment is created. In this reference element, an unstructured grid with N_p

$$N_p = \frac{(N+1)\,(N+2)}{N} \tag{9}$$

nodes is generated, where N indicates the polynomial order of the basis functions.

In the DG method, the functions are implemented using operators. The mass matrix $\boldsymbol{M}$, the stiffness matrix $\boldsymbol{A}$ and the derivative operators $\boldsymbol{D_x}$ and $\boldsymbol{D_z}$ are required. The spatial derivatives can be approximated with the differentiation matrix:

$$\frac{\partial}{\partial x} \approx \boldsymbol{D_x} \tag{10}$$

In the DG method, the equation for the mechanical

DOI 10.5162/Ultrasonic2025/A18-a1

stress T_1 can be described for each node k using

$$\begin{aligned} T_1^k &= c_{11}^{\mathrm{E},k} D_{x_1}^k u_1^k + c_{12}^{\mathrm{E},k} D_{x_2}^k u_2^k \\ &\quad + c_{13}^{\mathrm{E},k} D_{x_3}^k u_3^k + e_{31}^k D_{x_3}^k \phi^k \\ &\quad - M_k^{-1} c_{11}^{\mathrm{E},k} \oint_{\partial D^k} n_{x_1}^k \left(u_1^k - u_{1\mathrm{C}}^{k*}\right) l^k \mathrm{d}x \\ &\quad - M_k^{-1} c_{12}^{\mathrm{E},k} \oint_{\partial D^k} n_{x_2}^k \left(u_2^k - u_{2\mathrm{C}}^{k*}\right) l^k \mathrm{d}x \\ &\quad - M_k^{-1} c_{13}^{\mathrm{E},k} \oint_{\partial D^k} n_{x_3}^k \left(u_3^k - u_{3\mathrm{C}}^{k*}\right) l^k \mathrm{d}x. \end{aligned} \tag{11}$$

Here D^k and $c^{\mathrm{E},k}$ represent the respective location-dependent values for node k. The central flux f_{C}^* is used for the mechanical stress. The other components of the mechanical stress $\boldsymbol{T}$ are described in the same way. The time derivative of the sound velocity $\boldsymbol{v}$ and the displacement $\boldsymbol{u}$ is described using

$$\begin{aligned} \frac{\partial v_1^k}{\partial t} &= \frac{1}{\rho^k} D_{x_1}^k T_1^k + \frac{1}{\rho^k} D_{x_3}^k T_5^k \\ &\quad - M_k^{-1} \frac{1}{\rho^k} \oint_{\partial D^k} n_{x_1}^k \left(T_1^k - T_{1\mathrm{L}}^{k*}\right) l^k \mathrm{d}x \\ &\quad - M_k^{-1} \frac{1}{\rho^k} \oint_{\partial D^k} n_{x_2}^k \left(T_6^k - T_{6\mathrm{L}}^{k*}\right) l^k \mathrm{d}x \\ &\quad - M_k^{-1} \frac{1}{\rho^k} \oint_{\partial D^k} n_{x_3}^k \left(T_5^k - T_{5\mathrm{L}}^{k*}\right) l^k \mathrm{d}x \\ \frac{\partial u_1^k}{\partial t} &= v_1^k. \end{aligned} \tag{12}$$

Here the Lax-Friedrichs flux is used.

Parallelization

To ensure efficient use of the simulation tool, emphasis is placed on computing time optimization and parallelization. The Message Passing Interface (MPI) library makes it possible to communicate between the processes and exchange data.

To optimally partition the entire computational domain into several smaller, non-overlapping subdomains, the Parallel Graph Partitioning and Fill-reducing Matrix Ordering library (ParMetis) is employed.

By combining these two libraries and the advantages of the DG method, the computing time can be reduced and the available computing resources can be fully exploited.

Time domain integration

The time step for the respective integration method is decisive for the numerical stability. In this case, the low storage explicit Runge Kutta (LSERK) [8] of the fifth order is used. To estimate a time step, the initial wave velocity v_{init}, the radius of the inner sphere of the volume element r_D and the distance between two parallelization elements Δr_i are required [9]

$$\Delta t \leq \frac{2}{3} \min\left(\Delta r_i\right) \min_{\Omega} \left(\frac{r_D}{|v_{\mathrm{init}}|}\right). \tag{13}$$

The interaction between the time step and the flux has a massive influence on the numerical stability. The stability can be positively influenced by the choice of the Lax-Friedrichs flux. Simulations involving higher-order shape functions typically exhibit greater instability.

Validation

In order to validate the results of the simulations, Hook's law is considered here. This represents the relationship between the mechanical stress $\boldsymbol{T}$ and the displacement $\boldsymbol{u}$.

The following distribution of the mechanical stress

$$T_3 = 10^9 \cdot e^{\left(-\frac{\left(z - 5\times10^{-4}\,\mathrm{m}^{-1}\right)^2}{10^{-8}}\right)} \cdot \sin\left(2 \times 10^3\,\mathrm{m}^{-1} \cdot \pi \cdot z\right) \tag{14}$$

is specified as the initial condition of the simulation. It is to be expected that the imprinted wave propagates within the model and is reflected at the edges of the computational domain. Consideration of the boundary conditions is essential here. The equation can be incorporated directly on the two cover surfaces. For the cladding of the piezoceramic, some modifications must first be made. The following equations

$$\begin{aligned} n_x T_1 + n_y T_6 + n_z T_5 &= 0 \\ n_x T_6 + n_y T_2 + n_z T_4 &= 0 \\ n_x T_5 + n_y T_4 + n_z T_1 &= 0 \end{aligned} \tag{15}$$

form the boundary conditions for the mechanical stress $\boldsymbol{T}$ in 3D. For the implementation, the mechanical stress is rotated so that the normal vector only has one nonzero component. The boundary condition is then imprinted and the mechanical stress is rotated back to its original state. This method proved to be robust.

During the tests, it became clear, that besides a well chosen time step, the underlying computational grid also has an huge influence on the simulation results. A high-quality grid in which the elements have uniform shapes and volumes, is necessary for a stable simulation.

Results

The work has shown that the advantages of the DG method can be used for the numerical simulation of the mechanical behavior. A stable simulation is possible by selecting a polynomial order and a suitable computational grid. Additionally, it is shown that the exact numerical consideration of the boundary conditions is important for numerical stability.

DOI 10.5162/Ultrasonic2025/A18-a1

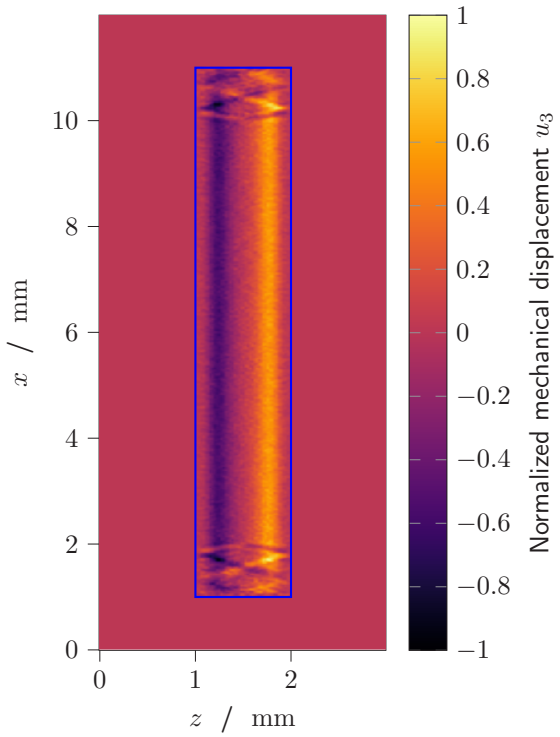

Fig. 2: Normalized simulation results in the x-z plane using the initial condition Eq. (14).

Fig. 2 shows the field of mechanical displacement in the x-z plane, i.e. a cross-section through the piezoceramic. The inner area of the blue rectangle indicates the piezoceramic, the outer area is used to imprint the boundary conditions. Reflections on the edges of the piezoceramic can be clearly recognised. In particular, the superimposition of the reflections on the cladding and the cover surfaces are well depicted. This is necessary for future calculations of the resonance frequencies, which is necessary for estimating the material properties [1].

It has been shown that stability decreases in simulations with a large number of time steps due to numerical instabilities. The geometry of the computational domain was varied in secondary work. In conclusion, it can be said that with the right choice of boundary conditions, the software tool can be used universally.

The work presented here shows the simulation of wave equation as a basis for the description of the mechanical waves in a piezoceramic. To summarize, the extension of the DG code provides a solid basis for further development in this field.

In future work, the coupling of the electrical quantity such as the electrical potential will be investigated.

Acknowledgements

The authors would like to thank the German Research Foundation (DFG) for funding the project 444955436 (NEPTUN). The authors would also like to express their gratitude to the Paderborn Center for Parallel Computing (PC^2) for access to the Noctua 2 cluster.

References

[1] N. Feldmann et al. In: *tm - Technisches Messen* 87.s1 (2020), s50–s55. DOI: doi:10.1515/teme-2020-0012. URL: https://doi.org/10.1515/teme-2020-0012.

[2] openCFS development team. *openCFS – open-source simulation tool for coupled field problems*. Accessed: 2025-06-16. 2025. URL: https://gitlab.com/openCFS/cfs.

[3] W. Voigt. *Lehrbuch der Kristallphysik (mit Ausschluss der Kristalloptik)*. Vieweg+Teubner Verlag, 1928. ISBN: 978-3-663-15316-0.

[4] C. Unverzagt. "Sensitivitätssteigerung durch Elektrodenmodifikation für die Materialparameterbestimmung von Piezokeramiken". PhD thesis. PhD thesis. Paderborn University, 2018. DOI: https://doi.org/10.17619/UNIPB/1-311.

[5] J. D. N. Cheeke. *Fundamentals and Applications of Ultrasonic Waves*. CRC Series in Pure and Applied Physics. Boca Raton, FL: CRC Press, 2002. ISBN: 0-8493-0130-0.

[6] Y. Grynko and J. Förstner. "Simulation of Second Harmonic Generation from Photonic Nanostructures Using the Discontinuous Galerkin Time Domain Method". In: *Recent Trends in Computational Photonics*. Springer International Publishing, 2017.

[7] Y. Grynko. *Numerical Simulations with the Discontinuous Galerkin Time Domain Method*. Lecture Slides, Paderborn University. 2021.

[8] T. W. Jan S. Hesthaven. *Nodal Discontinuous Galerkin Methods*. Springer New York, NY, 2007. DOI: https://doi.org/10.1007/978-0-387-72067-8.

[9] E. Brodal, J. S. Hesthaven, and F. Melandsø. "Numerical modeling of double-layered piezoelectric transducer systems using a high-order discontinuous Galerkin method". In: *Computers & Structures* (). DOI: https://doi.org/10.1016/j.compstruc.2008.02.006.

DOI 10.5162/Ultrasonic2025/A18-a2

Multiscale thermo-piezoelectric simulations using the finite element method

Jonas Hölscher[1], Olga Friesen[1], Carsten Spieker[2], Leander Claes[1], Jens Förstner[2], and Bernd Henning[1]
[1] Measurement Engineering Group, Paderborn University, 33098 Paderborn, Germany
[2] Theoretical Electrical Engineering Group, Paderborn University, 33098 Paderborn, Germany
hoelscher@emt.uni-paderborn.de

Abstract: The present study examines the simulation of coupled thermo-piezoeletric systems using a finite element method implementation applied to 2D axisymmetric models. Mechanical losses are calculated assuming Kelvin-Voigt type damping and are embedded in the thermal field as heat sources. Different approaches are explored to simulate the physical fields in both time and frequency domains. It is shown that frequency-domain simulations for harmonic excitations are particularly useful for the simulation of temperature-dependent piezoelectric systems.

Keywords: Piezoelectricity, Finite element method, Simulation, Thermal conduction, Coupled fields

Motivation

In the modern design process of piezoelectric actuators, simulations of the local mechanical and electrical fields play a crucial role. Those simulations enable the prediction of key characteristics such as resonant frequencies, thereby reducing the need for extensive prototyping. Accurate simulations of electro-mechanical fields require a thorough understanding of the underlying physical processes and material parameters. Since the material behavior of piezoelectric ceramics is generally temperature-dependent, it is necessary to consider temperature fields during the simulation process. Although well-established tools exist for the simulation of electrical and mechanical fields, no tools are known to the author which have the ability to efficiently simulate a coupled thermo-piezoelectric system. This paper proposes methods to determine the time-dependent temperature distribution within piezoelectric ceramics using the finite element method (FEM). To accomplish this, mechanical losses are calculated and incorporated into the thermal field as heat sources, assuming a Kelvin-Voigt type damping. Due to the different time scales of the fast changing electro-mechanical fields and the slow thermal fields, a multiscale problem occurs, which can be solved efficiently using frequency-domain simulations for the electro-mechanical subsystem. Finally, simulations with temperature-dependent material parameters are implemented and compared with experimental results.

Basic electro-mechanical and thermal fields

Assuming there are no forces applied on the piezoelectric material and there are no internal electric charges, the mechanical and electrical fields are described using a system of partial differential equations (PDEs) [1] and can be written as

$$\rho_0 \ddot{\boldsymbol{u}} - \mathcal{B}^{\mathrm{t}}\{\boldsymbol{C}^{\mathrm{E}}\mathcal{B}\{\boldsymbol{u}\} - \boldsymbol{e}^{\mathrm{t}}\nabla\phi\} = 0 \tag{1}$$

$$\nabla(\boldsymbol{e}\mathcal{B}\{\boldsymbol{u}\} - \boldsymbol{\epsilon}^{\mathrm{S}}\nabla\phi) = 0, \tag{2}$$

where $\boldsymbol{u}$ represents the mechanical displacement, ρ_0 the density, $\mathcal{B}\{\cdot\}$ the divergence operator in Voigt-Notation [2], ϕ the electric potential, $\boldsymbol{C}^{\mathrm{E}}$ the elasticity matrix at a constant electric field $\boldsymbol{E}$, $\boldsymbol{e}$ the piezoelectric coupling matrix, and $\boldsymbol{\epsilon}^{\mathrm{S}}$ describes the electrical permittivity matrix for a constant mechanical strain $\boldsymbol{S}$. This system of PDEs can be extended by a thermal field by considering the heat transfer equation in solid materials [3]

$$\rho_0 c_{\mathrm{P}} \dot{\vartheta} - \lambda\Delta\vartheta = \dot{W}, \tag{3}$$

where ϑ describes the local temperature, λ the thermal conductivity, c_{P} the specific heat capacity, ρ_0 the density and $\dot{W}$ the local loss density. The material is assumed to be thermally isotropic with temperature-independent thermal conductivity and specific heat capacity. Effects of thermoelasticity are not considered as they are assumed small compared to the mechanical losses. To couple the equations for the thermal and the electro-mechanical field, the mechanical loss density $\dot{W}$ is used. It can be calculated using [4]

$$\dot{W} = \boldsymbol{T}^{\mathrm{t}}\partial_t \boldsymbol{S}, \tag{4}$$

with the mechanical strain $\boldsymbol{S}$ and where the mechanical stress $\boldsymbol{T}$ is obtained through

$$\boldsymbol{T} = \boldsymbol{C}^{\mathrm{E}}(\tau\partial_t \boldsymbol{S} + \boldsymbol{S}) - \boldsymbol{e}^{\mathrm{t}}\boldsymbol{E}, \tag{5}$$

DOI 10.5162/Ultrasonic2025/A18-a2

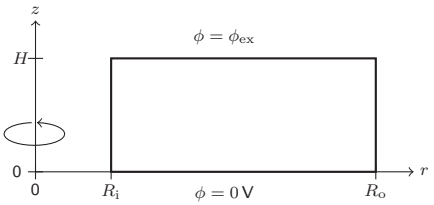

Fig. 1: 2D axisymmetric simulation model for a piezoelectric ring.

when a Kelvin-Voigt model is applied [1]. For this model a parameter τ is introduced and the piezoceramic is assumed to be adiabatic.

Finite element modeling

In this contribution piezoelectric rings with a thickness H, and inner and outer radii R_i and R_o are investigated. Therefore, it is sufficient to implement a 2D axisymmetric simulation in z using a corresponding model, as illustrated in Fig. 1. To apply an excitation, Dirichlet boundary conditions for the electric potential ϕ are implemented at the top and the bottom of the ring. The top boundary is set to the given excitation, and the bottom boundary is set to $0\,V$. Eq. (1), Eq. (2) and Eq. (3) can be transformed using the finite element method to the following system of linear equations [5]:

$$\boldsymbol{M}\begin{bmatrix}\ddot{\underline{u}}\\ \ddot{\underline{\phi}}\\ \ddot{\underline{\vartheta}}\end{bmatrix} + \boldsymbol{C}\begin{bmatrix}\dot{\underline{u}}\\ \dot{\underline{\phi}}\\ \dot{\underline{\vartheta}}\end{bmatrix} + \boldsymbol{K}\begin{bmatrix}\underline{u}\\ \underline{\phi}\\ \underline{\vartheta}\end{bmatrix} = \begin{bmatrix}0\\ \underline{f}_e\\ \underline{f}_\vartheta\end{bmatrix} = \underline{f}, \quad (6)$$

where $\boldsymbol{M}$ represents the finite element mass matrix, $\boldsymbol{C}$ the damping matrix, $\boldsymbol{K}$ the stiffness matrix. The load vector $\underline{f}$ consists of the load vector for the electric field $\underline{f}_e$ and the load vector of the thermal field $\underline{f}_\vartheta$. The underline indicates that these are nodal vectors. Using the *Newmark* algorithm the time derivatives from Eq. (6) can be resolved and an algebraic system of linear equations is given [5]. It is also assumed that the simulation model does not change with respect to the displacement $\boldsymbol{u}$ or the temperature ϑ.

Thermo-piezoelectric simulations

A thermo-piezoelectric simulation is performed for a hard piezoceramic ring (PIC181 by *PI Ceramic*) with a thickness of $1\,mm$, and inner and outer radii of $2.6\,mm$ and $6.35\,mm$, using the corresponding material parameters [6]. A sinusoidal excitation with an amplitude of $20\,V$ and a frequency of $2.23\,MHz$, corresponding to the first thickness resonance, is used. The simulation time step is $\Delta t = 20\,ns$, which is sufficient to model mechanical waves at this frequency. To ensure steady-state behavior, $80\,000$ time steps are simulated, and the resulting thermal field is shown in

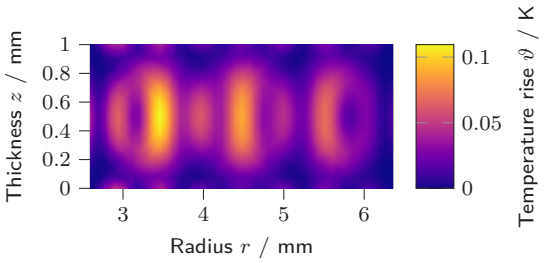

Fig. 2: Simulated thermal field of a PIC181 piezoceramic ring after $1.6\,ms$ with $20\,V$ amplitude at $2.23\,MHz$.

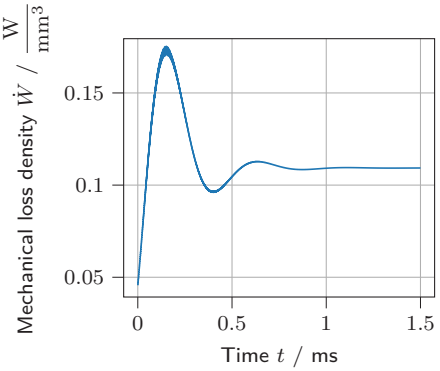

Fig. 3: Calculated time-averaged mechanical loss density of an example element of a PIC181 piezoceramic ring up until $1.6\,ms$.

Fig. 2. The temperature distribution shows several local maxima at areas with particularly high mechanical losses. The simulation outputs relative temperature increases in Kelvin units, which can be added to any arbitrary initial temperature.

Although a short time step length Δt is necessary to capture the high-frequency fields, the total simulation time is too short to obtain converged thermal quantities relevant for practical applications, in which the simulation should calculate temperatures after multiple seconds or minutes. To overcome this multiscale problem the periodicity of the excitation can be exploited: Due to the nature of the linear system a sinusoidal excitation also results in sinusoidal mechanical losses. Therefore, when the system becomes steady-state, the time-averaged mechanical losses do not change with respect to time anymore, as can be seen in Fig. 3. The time-averaged mechanical losses are thus calculated when the system is in steady-state and used in a separate thermal simulation with a larger time step length Δt. With $\Delta t = 1\,ms$ for the single thermal simulation and 1000 iterations, a thermal field after $1.0016\,s$ can be obtained, which is shown in Fig. 4. Here it can be seen that the temperature

DOI 10.5162/Ultrasonic2025/A18-a2

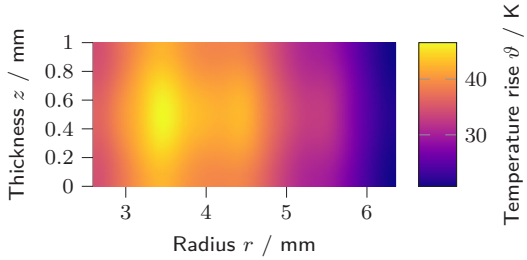

Fig. 4: Simulated thermal field of a PIC181 piezoceramic ring after $1.0016\,\mathrm{s}$ *with* $20\,\mathrm{V}$ *amplitude at* $2.23\,\mathrm{MHz}$.

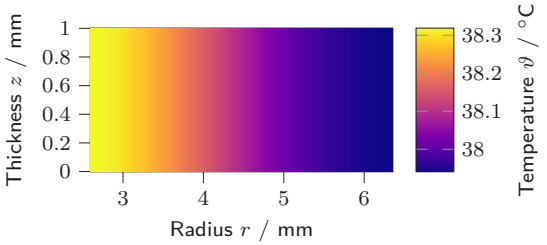

Fig. 5: Simulated thermal field using temperature-dependent material parameters of a PIC181 piezoceramic ring after $40\,\mathrm{s}$ *with* $4\,\mathrm{V}$ *amplitude at* $122.6\,\mathrm{kHz}$.

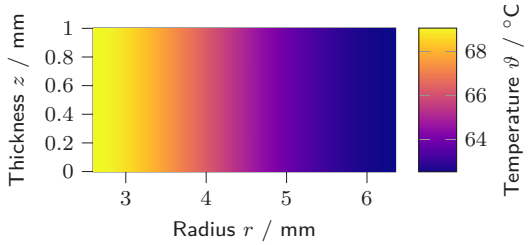

Fig. 6: Simulated thermal field using fixed material parameters of a PIC181 piezoceramic ring after $40\,\mathrm{s}$ *with* $4\,\mathrm{V}$ *amplitude at* $122.6\,\mathrm{kHz}$.

distribution is much more homogeneous across the ceramic, although local temperature maxima persist. Despite the relatively short simulation time of $1\,\mathrm{s}$, high temperatures are reached due to the high input power from the applied voltage and the low impedance at the resonance frequency.

Temperature-dependent material parameters

Since the thermal field is known at each time step, the temperature information can be used to update the material parameters during simulation. The time-averaged mechanical losses must be estimated for each set of material parameters, requiring multiple steady-state piezoelectric time-domain simulations which significantly increases the total simulation time. To overcome this issue, the usage of sinusoidal excitations can be exploited further: By performing the piezoelectric calculations in the frequency domain, the simulation directly yields the steady-state solution, from which the time-averaged mechanical losses can be calculated. By using a complex exponential ansatz for the solution vector

$$\begin{bmatrix} \underline{u} \\ \underline{\phi} \\ \underline{\vartheta} \end{bmatrix} = \underline{x}(t) = \underline{\hat{x}} \exp^{\mathrm{j}\omega t}, \tag{7}$$

the equation for solving the electro-mechanical problem in frequency domain can be derived:

$$(-\omega^2 \boldsymbol{M} + \mathrm{j}\omega \boldsymbol{C} + \boldsymbol{K})\underline{\hat{x}} = \underline{f} \cdot \exp^{-\mathrm{j}\omega t}. \tag{8}$$

This equation can be directly solved using standard solvers for linear systems of equations. Eq. (5) can be transformed to the frequency domain using a sinusoidal ansatz for the electrical and mechanical fields and thus the time-averaged mechanical loss density can be calculated using

$$\dot{W} = \mathrm{Re}\left\{ \frac{1}{2} \omega^2 \tau \hat{\boldsymbol{S}}^t \boldsymbol{C}^t \hat{\boldsymbol{S}} \right\}, \tag{9}$$

where $\hat{\boldsymbol{S}}$ represents the mode shapes of the mechanical strain in frequency domain.

The simulation procedure is as follows: A frequency-domain piezoelectric simulation is performed to calculate the time-averaged mechanical losses of the system, which are then embedded as heat sources into a separate time-domain thermal simulation. Whenever the temperature field changes significantly, the material parameters are updated, and the FEM matrices must be reassembled. This procedure is repeated until the desired simulation time is met.

This workflow is applied to the previously used PIC181 ring model with an excitation frequency set to the first radial resonance peak at $122.6\,\mathrm{kHz}$, and an excitation amplitude of $4\,\mathrm{V}$. Temperature-dependent material parameters estimated in [6] are used for this simulation. To match later experimental validation, the simulation runs over $40\,\mathrm{s}$ with an initial temperature of $25\,^{\circ}\mathrm{C}$ for the whole model. The resulting thermal field is shown in Fig. 5 and due to the given initial temperature in Celsius units, the simulated temperatures are given in Celsius units as well. For comparison, Fig. 6 shows the thermal field from the same simulation but with material parameters fixed at the initial temperature of $25\,^{\circ}\mathrm{C}$. It can be seen, that the simulation with temperature-dependent material parameters results in lower temperatures compared to the simulation using fixed parameters. This is due to a shift in the resonance frequency during operation caused by the temperature-induced changes in the

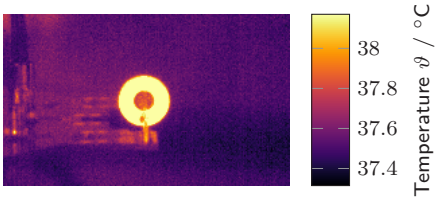

Fig. 7: Thermal image of a PIC181 piezoelectric ring after $40\,\mathrm{s}$ *with sinusoidal excitation with an amplitude of* $4\,\mathrm{V}$.

material parameters. Since the excitation frequency remains fixed, the system's impedance varies with temperature, leading to reduced input power and, consequently, lower heat generation.

Validation

The simulation results are validated by a comparison with thermal images. A signal generator excites a PIC181 piezoceramic ring at the desired resonance frequency and the surface temperature distribution is measured using a thermal camera (FLIR A68). To ensure high thermal emissivity, the specimen is painted black. The thermal image of the temperature distribution (Fig. 7) is captured after $40\,\mathrm{s}$ under the same excitation conditions as in the simulations. It can be seen, that the surface temperature in the thermal image closely matches the simulated temperature field obtained using temperature-dependent material parameters. Minor deviations remain, which can be attributed to uncertainties in emissivity estimation and measurement conditions. While the simulation predicts a slight radial temperature drop of approximately $0.4\,\mathrm{K}$ from the center to the outer edge, the measured temperature appears uniform across the ring. However, it is obvious that the simulations with temperature-dependent material parameters (Fig. 5) provides temperatures much closer to the physical observations than simulation with fixed material parameters (Fig. 6).

Conclusion

This study explores simulation approaches for coupled thermo-electro-mechanical material behavior in piezoceramic components using the finite element method. The simulation framework is implemented in Python and publicly available [7]. For sinusoidal excitation, the frequency-domain approach for the electromechanical subsystem proves especially efficient, as it allows the steady-state time-averaged mechanical loss density to be computed in a single step. This enables the incorporation of temperature-dependent material parameters into the simulation process. The simulation results show that such temperature-dependent modeling significantly affects the simulated temperature fields, as the changing material behavior leads to shifted resonance frequencies. A comparison with an experimental thermal image shows that the usage of temperature-dependent material parameter increases the plausibility of the simulation results, enabling for a more accurate prediction of temperature fields during operation. These findings highlight the importance of accurate simulation models that account for temperature-dependent behavior. Observed deviations between simulation and measurement may be attributed to deviations in the thermal material parameters, which are currently assumed to be isotropic and based on information from the manufacturer. Further, the thermal field is assumed to be adiabatic. The implementation of convective boundary conditions can lead to a more realistic prediction of the thermal behavior in future studies.

Acknowledgements

This research is funded by the Deutsche Forschungsgemeinschaft (DFG, German Research Foundation) – 444955436 (FOR 5208: NEPTUN).

References

[1] S. J. Rupitsch. *Piezoelectric Sensors and Actuators: Fundamentals and Applications*. Springer Berlin Heidelberg, 2019. ISBN: 978-3-662-57534-5.

[2] W. Voigt. *Lehrbuch der Kristallphysik (mit Ausschluss der Kristalloptik)*. Vieweg+Teubner Verlag, 1928. ISBN: 978-3-663-15316-0.

[3] H. D. Baehr and K. Stephan. *Wärme- und Stoffübertragung*. Springer Berlin Heidelberg, 2016. ISBN: 978-3-662-49676-3.

[4] B. Boley and J. Weiner. *Theory of Thermal Stresses*. Dover Publications, 2012. ISBN: 978-0-486-14386-6.

[5] M. Kaltenbacher. *Numerical simulation of mechatronic sensors and actuators*. Springer, 2007. ISBN: 978-3-540-71359-3.

[6] O. Friesen et al. "Estimation of temperature-dependent piezoelectric material parameters using ring-shaped specimens". In: 2024. DOI: 10.1088/1742-6596/2822/1/012125.

[7] J. Hölscher. *plutho 0.1.1 – Python library for coupled thermo-piezoelectric simulations*. Version v0.1.1. 2025. DOI: 10.5281/zenodo.15608545. URL: https://github.com/emtpb/plutho/releases/0.1.1.

DOI 10.5162/Ultrasonic2025/A18-a3

Identification of temperature-dependent material parameter functions in piezoelectricity

Raphael Kuess[1], Olga Friesen[2], Bernd Henning[2], and Andrea Walther[1]
[1]Humboldt-Universität zu Berlin, Unter den Linden 6, 10099 Berlin, Germany
[2]Paderborn University, Warburger Straße 100, 33098 Paderborn, Germany
raphael.kuess@hu-berlin.de

Abstract: We address the problem of identifying the temperature-dependent parameters of ring-shaped piezoelectric samples based on simulated data. For this purpose, we assume a polynomial structure of the material parameters with respect to the temperature. To increase stability and accuracy of the reconstruction, we apply adapted optimization and regularization strategies using regularized Newton-type methods in a block coordinate descent framework.

Keywords: Inverse Problems, Piezoelectricity, Temperature dependence, Parameter identification, Regularization

Introduction

Understanding the behavior of piezoelectric components is essential for various sensor and actuator applications, especially given their temperature-dependent characteristics. While piezoceramic elements undergo changes in properties due to heating during operation, it is imperative to develop a method for predicting these changes. This results in the assumption that the material parameters depend on temperature changes, where we do not consider thermal coupling effects. The elastic stiffness parameter c^{E} is not very sensitive to temperature changes, see [1]. Hence, we assume that this parameter is known, yielding that the required matrix valued parameter functions for the piezoelectric coupling e and the permittivity ε^{S} are dependent on a known temperature $\theta \in \Theta$:

$$e(\theta) := \begin{pmatrix} 0 & 0 & 0 & e_{15}(\theta) \\ e_{31}(\theta) & e_{31}(\theta) & e_{33}(\theta) & 0 \end{pmatrix}, \quad (1)$$

$$\varepsilon^{\mathrm{S}}(\theta) := \begin{pmatrix} \varepsilon_{11}(\theta) & 0 \\ 0 & \varepsilon_{33}(\theta) \end{pmatrix}, \quad (2)$$

where $\Theta \subset \mathbb{R}^+$ is a temperature interval of finite cardinality. Furthermore, we deduce from [1] that it is reasonable to assume a polynomial structure of the material parameters with respect to θ, i.e.,

$$(e(\theta), \varepsilon(\theta)) = \left(\sum_{j=0}^{k} a_j \theta^j, \sum_{j=0}^{k} b_j \theta^j \right), \quad (3)$$

where $(a_j, b_j) \in \mathbb{R}^{2\times 4} \times \mathbb{R}^{2\times 2}$ for $0 \leq j \leq k$. The coefficients in (3) are constant matrices and have the same structure as in the identities (1)-(2). This results in a transition of the parameter function space to a finite dimensional vector space, see [2].

The inverse problem

For $k = 1$, we have to reconstruct 10 parameters. Consequently, the parameter space X reads as

$$X := \Big\{ p \in \mathbb{R}^{10} : \; p_1 = a_{11_0} > 0, \; p_2 = a_{33_0} > 0, \; p_3 = b_{15_0}, \; p_4 = b_{31_0}, \; p_5 = b_{33_0}, \; p_6 = a_{11_1}, \; p_7 = a_{33_1}, \; p_8 = b_{15_1}, \; p_9 = b_{31_1}, \; p_{10} = b_{33_1} \Big\}.$$

As geometry we consider a thin annular piezoelectric element, where we exploit the symmetry of the geometry and use cylindrical instead of Cartesian coordinates. Consequently, we obtain a Lipschitz domain $\Omega \subset \mathbb{R}^2$ and assume that its boundary can be represented as the disjoint union $\partial\Omega := \Gamma_a \dot\cup \Gamma_0 \dot\cup \Gamma_n$. Thereby, Γ_a is the boundary segment electrically excited with an excitation signal independent of the spatial domain (equally distributed), Γ_0 is the grounded boundary segment and Γ_n is the remaining part of $\partial\Omega$. We introduce

$$H^2_{0,\Gamma}(\Omega, \mathbb{C}) = \left\{ f \in H^2(\Omega, \mathbb{C}) |\; f|_{(\Gamma_a \cup \Gamma_0)} = 0 \right\},$$

$$H^2_{\mathcal{B}}(\Omega, \mathbb{C}^2) = \Big\{ f \in L^2(\Omega, \mathbb{C}^2) |\; \|f\|_{H^2_{\mathcal{B}}(\Omega,\mathbb{C}^2)} := \|f\|_{L^2(\Omega,\mathbb{C}^2)} + \|\mathcal{B}f\|_{L^2(\Omega,\mathbb{C}^2)} + \left\|\mathcal{B}^T\mathcal{B}f\right\|_{L^2(\Omega,\mathbb{C}^2)} \Big\},$$

where

$$\nabla := \begin{pmatrix} \frac{\partial}{\partial r} \\ \frac{\partial}{\partial z} \end{pmatrix} \text{ and } \mathcal{B} := \begin{pmatrix} \frac{\partial}{\partial r} & 0 \\ \frac{1}{r} & 0 \\ 0 & \frac{\partial}{\partial z} \\ \frac{\partial}{\partial z} & \frac{\partial}{\partial r} \end{pmatrix},$$

with r denoting the radial and z the spatial element. Hence, we define the state space as

$$W := \left(H^2_{\mathcal{B}}(\Omega, \mathbb{C}^2) \times H^2_{0,\Gamma}(\Omega, \mathbb{C}) \right),$$

which coincides with the solution space of the following Fourier-transformed PDE-system

$$\forall\theta\in\Theta,\ \forall\omega\in\mathcal{W}:$$
$$-\rho\omega^2 d_1\hat{u}-\mathcal{B}^{\mathrm{T}}\big(d_2c^{\mathrm{E}}(\theta)\mathcal{B}\hat{u}+e^{\mathrm{T}}(\theta)\nabla\hat{\phi}_0\big)=\mathcal{B}^{\mathrm{T}}e^{\mathrm{T}}(\theta)\nabla\chi \quad \text{in } \Omega \quad (4)$$
$$-\nabla\cdot\Big(e(\theta)\mathcal{B}\hat{u}-\varepsilon^{\mathrm{S}}(\theta)\nabla\hat{\phi}_0\Big)=-\nabla\cdot\varepsilon^{\mathrm{S}}(\theta)\nabla\chi \ \text{ in } \Omega \quad (5)$$
$$n\cdot\Big(e(\theta)\mathcal{B}\hat{u}-\varepsilon^{\mathrm{S}}(\theta)\nabla\hat{\phi}_0\Big)=n\cdot\varepsilon^{\mathrm{S}}(\theta)\nabla\chi \quad \text{on } \Gamma_{\mathrm{n}} \quad (6)$$
$$\mathcal{N}^{\mathrm{T}}\big(d_2c^{\mathrm{E}}(\theta)\mathcal{B}\hat{u}+e^{\mathrm{T}}(\theta)\nabla\hat{\phi}_0\big)=-\mathcal{N}^{\mathrm{T}}e^{\mathrm{T}}(\theta)\nabla\chi \text{ on } \partial\Omega, \quad (7)$$

where $s=(\hat{u},\hat{\phi}_0)$ is the solution of the system, $\rho\in\mathbb{R}^+,\ d_1:=1-\mathrm{i}\frac{\alpha}{\omega},\ d_2:=1+\mathrm{i}\omega\beta$. We denote the space of frequencies with $\mathcal{W}\subset\mathbb{R}^+,\ |\mathcal{W}|<\infty$. Furthermore, n is the normal element corresponding to ∇ and $\mathcal{N}$ the normal element corresponding to $\mathcal{B}$. Additionally, we included the Rayleigh damping model, with $\alpha,\beta\in\mathbb{R}_0^+$ as Rayleigh damping parameters. The mixed Dirichlet boundary conditions, needed to model the excitation behavior, were homogenized using the Dirichlet lift Ansatz with Dirichlet lift function χ, see [2]. Consequently, we define the piezoelectric model operator $A_\omega^\theta: X\times W\to W^*$ for each $\theta\in\Theta$ and $\omega\in\mathcal{W}$ via

$$\begin{aligned}\langle A_\omega^\theta(p,s),(v,w)\rangle_{W^*,W}:=2\pi\int_\Omega\Big(&-d_1\rho\omega^2\hat{u}^{\mathrm{T}}\overline{v}\\&+\Big(d_2c^{\mathrm{E}}(\theta)\mathcal{B}\hat{u}+e^{\mathrm{T}}(\theta)\nabla\hat{\phi}_0\Big)^{\mathrm{T}}\overline{\mathcal{B}v}\\&+\Big(e(\theta)\mathcal{B}\hat{u}-\varepsilon^{\mathrm{S}}(\theta)\nabla\hat{\phi}_0\Big)^{\mathrm{T}}\overline{\nabla w}\\&+(e^{\mathrm{T}}(\theta)\nabla\chi)^{\mathrm{T}}\overline{\mathcal{B}v}-(\varepsilon^{\mathrm{S}}(\theta)\nabla\chi)^{\mathrm{T}}\overline{\nabla w}\Big)r\,\mathrm{d}(r,z)\,.\end{aligned} \quad (8)$$

To recover information on the parameter p, we need observed data with respect to the state s and the parameters p. Hence, we define the charge pulse $Q_\omega^\theta:\ X\times W\to\mathbb{C}$,

$$\begin{aligned}Q_\omega^\theta(p,s)&=\mathrm{Re}\left(Q_\omega^\theta(p,s)\right)+\mathrm{Im}\left(Q_\omega^\theta(p,s)\right)\\&=2\pi\int_{\Gamma_a}r\left(e(\theta)\mathcal{B}\hat{u}-\varepsilon^{\mathrm{S}}(\theta)\nabla\hat{\phi}\right)\cdot n\,\mathrm{d}(r,z)\end{aligned} \quad (9)$$

for each $\theta\in\Theta,\ \omega\in\mathcal{W}$, where $\mathrm{Re}(\cdot)$ denotes the real and $\mathrm{Im}(\cdot)$ the imaginary parts. We assume that $\left\|Q_\omega^\theta\right\|_{\mathbb{C}}>0$ and define the observation operator $C_\omega^\theta:\ X\times W\to\mathbb{R}$ for each $\theta\in\Theta,\ \omega\in\mathcal{W}$ as

$$C_\omega^\theta(p,z)=\log\left(\left\|Q_\omega^\theta\right\|_{\mathbb{C}}\right). \quad (10)$$

To model the inverse problem, we employ the reduced approach, meaning that we have to eliminate the model by introducing a so-called parameter-to-state map S_ω^θ for each $\omega\in\mathcal{W}$ and each $\theta\in\Theta$, which maps each parameter to the corresponding solution of the underlying PDE model (4)-(7). For existence and regularity of the parameter-to-state we need the following result, which includes regularities and important properties of the model and the observation operator.

Proposition 1. *For each $\omega\in\mathcal{W}$ and $\theta\in\Theta$, A_ω^θ as given in* (8) *is well-defined, bounded, bijective and continuously Fréchet differentiable on $X\times W$, C_ω^θ as given in (10) is well-defined, bounded and continuously Fréchet differentiable on $X\times W$ and S_ω^θ is well-defined, non-linear and continuously Fréchet differentiable on X.*

Proof. Due to Plancherel's Theorem, see [3], Chapter 7, the Fourier transform is continuously invertible on $L^2(0,T)$. Furthermore, the coordinate transformation is continuously invertible and $H^1(0,T)$ is isometrically isomorphic to $L^2(0,T)$. Hence, there exists a continuously invertible transformation between our setting and the setting in [2]. Lastly, $\left\|Q_\omega^\theta\right\|_{\mathbb{C}}>0$, $\|\cdot\|$ on $\mathbb{R}\setminus\{0\}$ and $\log(\cdot)$ on $\mathbb{R}^+$ are continuously Fréchet differentiable. □

As observed data is usually contaminated with noise, we consider noisy data $y^\delta\in\mathbb{R}^{|\mathcal{W}|\cdot|\Theta|}$. Then, the forward operator $F:X\to\mathbb{R}^{|\mathcal{W}|\cdot|\Theta|}$ reads as

$$F(p)=\begin{pmatrix}\left(C_\omega^{\theta_1}(p,S_\omega^{\theta_1}(p))\right)_{\omega\in\mathcal{W}}\\\vdots\\\left(C_\omega^{\theta_{|\Theta|}}(p,S_\omega^{\theta_{|\Theta|}}(p))\right)_{\omega\in\mathcal{W}}\end{pmatrix}.$$

Consequently, we want to identify $p\in X$ such that

$$F(p)=y^\delta. \quad (11)$$

This casts the problem into a single operator equation for the quantity p. As this inverse problem is ill-posed, see [4], we introduce a weakly lower semi-continuous regularizer $\mathcal{R}_\tau:X\to\mathbb{R}$ with regularization parameter $\tau>0$. Then, we address the inverse problem (11) similarly to [2] and [4] via an optimization approach, i.e., we aim at finding a minimizer of

$$J(p):=\frac{1}{2}\left\|F(p)-y^\delta\right\|^2_{\mathbb{R}^{|\mathcal{W}||\Theta|}}+\mathcal{R}_\tau(p), \quad (12)$$

which we assume to exist. As gradient computation for J in (12) is often done via adjoints, we note that the adjoint PDE is uniquely solvable for every state $(\hat{u},\hat{\phi}_0)\in W$, see Proposition 1 and [2].

Numerical realization and results

In praxis, sensitivities for different parameters vary considerably for solution methods to inverse problems in piezoelectricity, see [5]. To provide a better

handling of sensitivities, we propose a block coordinate descent (BCD) approach, similarly to [5]. This method iteratively minimizes the objective function over selected blocks of optimization variables while keeping the remaining optimization variables fixed, see [6]. We assume a cyclic selection, which means that the same partitions in a fixed order are cycled through, where in each step, one block is updated according to a sub-optimization method and then fixed while the next block is optimized. As [5] suggests to use BCD methods in combination with Newton-type methods as sub-optimization method, we apply a regularized structure exploiting Quasi-Newton update, see [7]. To ensure robustness we use the globalized approach (GRSE) of [7], which controls the regularization parameter such that it leads to globalization. Furthermore, we will use the partition $B_1 := \{a_{33_l}, b_{15_l}, b_{31_l}, b_{33_l} : l = 1, 2\}$ and $B_2 := \{a_{11_l} : l = 1, 2\}$. This choice is motivated by the corresponding sensitivities, since the forward operator is least sensitive to a_{11_0} for zeroth-order parameters and to a_{11_1} for first-order parameters. Consequently, it is reasonable to perform the optimization for B_1 first, while keeping B_2 fixed at the initial guess until convergence is reached to some extent, and then start with the alternating reconstruction of both blocks. As each block performs the GRSE method, they may have own regularization parameters $\tau^{B_1} > 0,\ \tau^{B_2} > 0$ corresponding to the respective block. The inverse problem will be numerically realized using the discretize-then-optimize approach, where we employ algorithmic differentiation (AD), see [8] and [9]. The space discretization is based on a finite element method, where we use FEniCS [10] in dolfin version 2019.2.0.dev0 and AD via the dolfin adjoint [11] library of FEniCS in version 2019.1.0. As domain Ω we consider a rectangle with vertices $(2.6, 0),\ (6.35, 0),\ (6.35, 1),\ (2.6, 1)$, where coordinates are given in mm. Furthermore, we use $10\,\mathrm{V}$ as excitation pulse and perform any numerical realization in kHz. This has the advantage of a better condition of the PDE system as the magnitudes of the material parameters differ significantly less. The temperature values considered in all numerical realizations will be $\Theta = \{50\,^\circ\mathrm{C},\ 70\,^\circ\mathrm{C}\}$. The damping parameters and the elastic stiffness parameter at $60\,^\circ\mathrm{C}$ are taken from [1]. The polynomial parameters serving as ground truth p^* are presented in Tab. 1 according to [1], rounded to two decimal places. Using FEniCS, specifying the Dirichlet lift function χ can be avoided, as it is possible to directly implement mixed Dirichlet conditions. Third-order elements with element size $h = 150\,\mu\mathrm{m}$ yield sufficiently reasonable simulation outcomes. From

Tab. 1: Target polynomial parameters.

Pol. par.	Value	Pol. par.	Value
a_{11_0}	2505.38	b_{15_1}	11.34
a_{11_1}	9.72	b_{31_0}	-5045.55
a_{33_0}	4975.13	b_{31_1}	-7.35
a_{33_1}	18.67	b_{33_0}	13 316.54
b_{15_0}	9174.08	b_{33_1}	23.82

[12] and computed sensitivities, conclusions can be drawn about reasonable frequency domains for the inverse problem. Due to the small sensitivities of the forward operator with respect to a_{11_0} and a_{11_1}, we will use a finer frequency grid in areas where the forward operator is more sensitive to those parameters and in resonance areas. Hence, we use $\mathcal{W} := \mathcal{W}_1 \cup \mathcal{W}_2 \cup \mathcal{W}_3$ as frequency domain, where

$$\mathcal{W}_1 := \{\omega \in \mathbb{N} :\ \omega \equiv 0 \bmod 3,\ 38 \leq \omega < 2600\},$$
$$\mathcal{W}_2 := \{\omega \in \mathbb{N} :\ \omega \equiv 0 \bmod 20,\ 2600 \leq \omega < 4500\},$$
$$\mathcal{W}_3 := \{\omega \in \mathbb{N} :\ \omega \equiv 0 \bmod 3,\ 4500 \leq \omega \leq 6000\}.$$

To generate the noisy data y^δ we contaminate the exact simulated data y, generated according to the parameters in Tab. 1, additively with uniformly distributed random noise with a noise level of 1%. We employ the hyperparameters $\mu = 0.5$, $\tau_0^{B_1} = \tau_0^{B_2} = 10^{-1}$, $\sigma = 4$, $c = a = 10^{-2}$ and scale the zeroth-order parameters with 10^2. Here, μ is the decay factor and σ is the growth factor of the regularization parameters for each block, see [7], and $c,\ a$ refer to $c,\ p$ in [7]. As initial Quasi-Newton matrices for each block we use scaled identities with scaling factor 10^{-4}. Finally, we choose an initial parameter guess p^0 that deviates by 5% from the parameters in Tab. 1. In Fig. 1, the parameter identification results using the BCD-GRSE method are shown, where every iteration step remained in the feasible set. For better visualization, the reconstructed parameter values have been normed by the ground truth, such that we aim for convergence to one. The reconstruction results in Fig. 1 show convergence, but the parameters to which the forward operator is least sensitive overall do not fully align with the respective ground truth. However, the charge computed with the reconstructed parameters aligns very well with the one obtained with the target parameters. The convergence of the data discrepancy term of the objective function to the target value confirms this behavior, see Fig. 2, where p^n denotes the reconstructed parameter at iteration n. Consequently, no further improvements can be expected, given the current objective function, since the occurrence of various

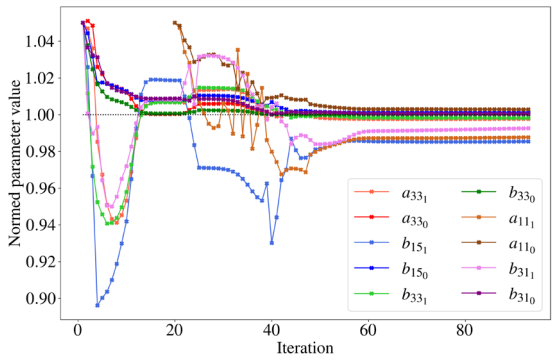

Fig. 1: Identification of the polynomial parameters.

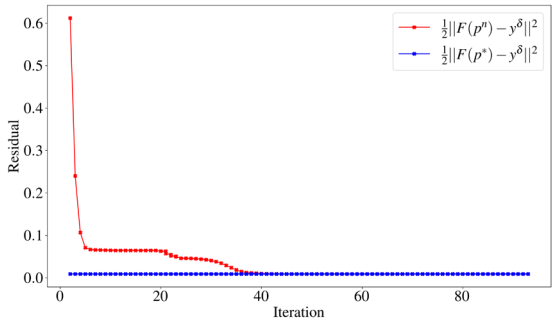

Fig. 2: Convergence of the data discrepancy.

local minima impairs uniqueness of reconstructed parameters. This behavior appears to occur due to the amplification of the discrepancy in sensitivities by the forward operator in the parameterized case. Consequently, selecting a suitable frequency range led to an improvement. If the material parameters are reconstructed separately for each individual temperature, this effect occurs significantly less.

Conclusion

We considered the problem of identifying temperature-dependent material parameters for piezoelectric rings, where we assumed a polynomial structure of the material parameters with respect to the temperature. To achieve reliable parameter identification, we used a block coordinate descent regularized Quasi-Newton method and adapted the frequency domain. The resulting methodology allowed a sufficient reconstruction of the polynomial parameters, as demonstrated by numerical results, but is prone to instability with respect to uniqueness. Furthermore, we note that this approach relies on a-priori knowledge of the parameter behavior, which is reasonable but may not always be available.

Acknowledgements

The authors thank the German Research Foundation (DFG) for financial support within the research group 5208 NEPTUN (444955436), support code JU 3254/1-1 and WA 1607/21-1. The work on this paper was partly funded by the DFG under Germany´s Excellence Strategy – The Berlin Mathematics Research Center MATH+ (EXC-2046/1, project ID: 390685689).

References

[1] O. Friesen et al. “Estimation of temperature-dependent piezoelectric material parameters using ring-shaped specimens”. In: *Journal of Physics: Conference Series* 2822.1 (2024), p. 012125.

[2] R. Kuess, D. Walter, and A. Walther. *Modelling and Analysis of an Inverse Parameter Identification Problem in Piezoelectricity*. Tech. rep. 2025.

[3] J. Cerdà. *Linear functional analysis*. Vol. 116. American Mathematical Soc., 2010.

[4] T. Lahmer. “Forward and Inverse Problems in Piezoelectricity”. doctoral thesis. Friedrich-Alexander-Universität Erlangen-Nürnberg, 2008.

[5] B. Jurgelucks. “Increased Sensitivity in Parameter Identification Problems for Piezoelectrics”. doctoral thesis. Paderborn University, 2019.

[6] S. Wright. “Coordinate descent algorithms”. In: *Math. Programming* 151.1 (2015), pp. 3–34.

[7] R. Kuess and A. Walther. *On regularized structure exploiting Quasi-Newton methods for ill-posed problems*. Tech. rep. 2025.

[8] R. Griesse and A. Walther. “Evaluating gradients in optimal control: continuous adjoints versus automatic differentiation”. In: *J. of Opt. Theory and App.* 122 (2004), pp. 63–86.

[9] A. Griewank and A. Walther. *Evaluating Derivatives*. Second edition. Society for Industrial and Applied Mathematics, 2008.

[10] M. Alnæs et al. “The FEniCS project version 1.5”. In: *Archive of Numerical Software* 3 (2015).

[11] S. Mitusch, S. Funke, and J. Dokken. “dolfin-adjoint 2018.1: automated adjoints for FEniCS and Firedrake”. In: *Journal of Open Source Software* 4.38 (2019), p. 1292.

[12] O. Friesen et al. “Estimation of piezoelectric material parameters of ring-shaped specimens”. In: *tm - Technisches Messen* (2024).

DOI 10.5162/Ultrasonic2025/A18-a4

Sensitivity Analysis and Material Parameter Estimation of a Pre-Stressed Langevin Transducer

Olga Friesen[1], Claus Scheidemann[2], Leander Claes[1], Tobias Hemsel[2], and Bernd Henning[1]
[1]Measurement Engineering Group, Paderborn University, 33098 Paderborn, Germany
[2]Dynamics and Mechatronics, Paderborn University, 33098 Paderborn, Germany
friesen@emt.uni-paderborn.de

Abstract: In this study, the stress-dependency of piezoelectric material parameters is investigated. A finite element model is developed to analyse the electrical impedance response of a mechanically pre-stressed Langevin transducer. The experimental data indicate a single dominant resonance, which limits the estimation of piezoceramic material parameters under different mechanical stresses. In addressing this issue, a sensitivity analysis is employed to identify the parameters with the greatest influence on the resonance. Based on this, a subset of the stress-dependent material parameters of the piezoelectric components can be identified in an inverse procedure.

Keywords: Piezoceramic rings, Langevin transducer, Sensitivity analysis, Parameter estimation

Motivation

Piezoelectric ceramics find application in high-power ultrasonic sensors and actuators, where they are subjected to significant electrical and mechanical stresses, leading to non-linear effects. An approach to analyse such non-linear behaviour involves shifting the operating points by varying the static mechanical load and characterising the linear behaviour in each operating point. This method allows for an approximation of the material's non-linear characteristics. Nevertheless, the realisation of a homogeneous mechanical load is still a considerable challenge [1, 2]. In Langevin transducers, which are typically employed in high-power applications, the piezoceramics are pre-stressed axially as homogeneously as possible in order to avoid mechanical tensile stresses. However, this approach increases the complexity of the simulation model, as it necessitates the consideration of additional metallic components and a second ceramic element.

The experimental measurements, and consequently the simulation results (cf. Fig. 4), demonstrate that only a single resonance is clearly discernible in the electrical impedance spectrum within the considered frequency range. This is due to the fact that radial and torsional modes are barely pronounced in this configuration. The resonance is a so-called thickness-extensional mode, which is located in a frequency range in which transducers of this kind are typically operating [3]. This limitation makes it difficult to estimate a complete set of piezoelectric material parameters in an inverse procedure, which requires additional resonances [4].

A two-dimensional simulation model is developed for the purpose of simulating the transducer's frequency-dependent electrical impedance. A detailed analysis of the resulting impedance data is performed, paying particular attention to the resonance behaviour, which is evidently different for a transducer constructed with multiple components than for a single, unconstrained piezoceramic ring. The material parameters with the greatest influence on the resonance are identified by means of a sensitivity analysis of the simulated impedance data. This, in turn, allows for a targeted parameter estimation process based on measurements under varying load conditions.

Numerical model

Mathematically, the behaviour of piezoelectric materials can be modelled as functions of electrical and mechanical quantities

$$\boldsymbol{T} = -\underline{\boldsymbol{e}}^{\mathrm{t}}\boldsymbol{E} + \underline{\boldsymbol{c}}^{\mathrm{E}}\boldsymbol{S} \tag{1}$$

$$\boldsymbol{D} = \underline{\boldsymbol{\varepsilon}}^{\mathrm{S}}\boldsymbol{E} + \underline{\boldsymbol{e}}\boldsymbol{S}, \tag{2}$$

where $\boldsymbol{T}$ represent the mechanical stress, $\boldsymbol{S}$ the mechanical strain, $\boldsymbol{E}$ the electrical field strength, and $\boldsymbol{D}$ the electrical displacement. The mechanical stiffness matrix $\underline{\boldsymbol{c}}^{\mathrm{E}}$, the permittivity matrix $\underline{\boldsymbol{\varepsilon}}^{\mathrm{S}}$, and the piezoelectric coupling matrix $\underline{\boldsymbol{e}}$ are the matrices of the material parameters of interest. Employing the Voigt notation [5] and taking into account the symmetry conditions of a transversely isotropic piezoceramic material, the material parameter matrices are given as follows:

$$\underline{\boldsymbol{c}}^{\mathrm{E}} = \begin{bmatrix} c_{11}^{\mathrm{E}} & c_{12}^{\mathrm{E}} & c_{13}^{\mathrm{E}} & 0 & 0 & 0 \\ c_{12}^{\mathrm{E}} & c_{11}^{\mathrm{E}} & c_{13}^{\mathrm{E}} & 0 & 0 & 0 \\ c_{13}^{\mathrm{E}} & c_{13}^{\mathrm{E}} & c_{33}^{\mathrm{E}} & 0 & 0 & 0 \\ 0 & 0 & 0 & c_{44}^{\mathrm{E}} & 0 & 0 \\ 0 & 0 & 0 & 0 & c_{44}^{\mathrm{E}} & 0 \\ 0 & 0 & 0 & 0 & 0 & \frac{(c_{11}^{\mathrm{E}} - c_{12}^{\mathrm{E}})}{2} \end{bmatrix} \tag{3}$$

DOI 10.5162/Ultrasonic2025/A18-a4

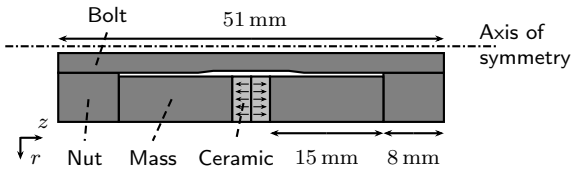

Fig. 1: Two-dimensional, rotationally symmetric simulation model for a Langevin transducer, composed of two oppositely polarised piezoceramic rings (light grey), steel masses, nuts and a hollow bolt.

$$\underline{\boldsymbol{e}} = \begin{bmatrix} 0 & 0 & 0 & 0 & e_{15} & 0 \\ 0 & 0 & 0 & e_{15} & 0 & 0 \\ e_{31} & e_{31} & e_{33} & 0 & 0 & 0 \end{bmatrix} \tag{4}$$

$$\underline{\boldsymbol{\varepsilon}}^{\mathrm{S}} = \begin{bmatrix} \varepsilon_{11}^{\mathrm{S}} & 0 & 0 \\ 0 & \varepsilon_{11}^{\mathrm{S}} & 0 \\ 0 & 0 & \varepsilon_{33}^{\mathrm{S}} \end{bmatrix}. \tag{5}$$

Including damping, e.g. Rayleigh damping, characterised by the parameters $\alpha_{\mathrm{M,p}}$ and $\alpha_{\mathrm{K,p}}$ [6], and the density ρ_{p} of the piezoelectric material, a total of 13 relevant piezoceramic parameters are given:

$$\boldsymbol{p}_{\mathrm{mat,piezo}} = \big[\rho_{\mathrm{p}}, c_{11}^{\mathrm{E}}, c_{12}^{\mathrm{E}}, c_{13}^{\mathrm{E}}, c_{33}^{\mathrm{E}}, c_{44}^{\mathrm{E}}, \varepsilon_{11}^{\mathrm{S}}, \varepsilon_{33}^{\mathrm{S}}, e_{15}, e_{31}, e_{33}, \alpha_{\mathrm{M,p}}, \alpha_{\mathrm{K,p}}\big]. \tag{6}$$

The calculation of frequency-dependent impedance for a given geometry and set of material parameters necessitates the employment of a simulation model. The results can be achieved by means of a finite element approximation [7], for instance, within the simulation tool openCFS (Coupled Field Simulation) [8]. The simulation model for the Langevin transducer implemented in this study is illustrated in Fig. 1. It includes a pair of piezoceramic rings, which are compressed by hollow, cylindrical steel masses, nuts and a hollow bolt made of steel. The thickness of the piezoceramic rings (PIC184, *PI Ceramic*, Germany) is $2.5\,\mathrm{mm}$, whilst the outer radius is $10\,\mathrm{mm}$ and the inner radius $4\,\mathrm{mm}$. Further dimensional information can be found in the figure. The electrical contact is facilitated by $0.1\,\mathrm{mm}$ copper plates, which are omitted in this model. The parameters in Eq. (6) are used for the description of the piezoceramic rings. The parameters for the steel components are as follows:

$$\boldsymbol{p}_{\mathrm{mat,steel}} = \big[\rho_{\mathrm{s}}, c_{\mathrm{L,s}}, c_{\mathrm{T,s}}, \alpha_{\mathrm{M,s}}, \alpha_{\mathrm{K,s}}\big]. \tag{7}$$

The density is denoted by ρ_{s}, the longitudinal velocity by $c_{\mathrm{L,s}}$, the transversal velocity by $c_{\mathrm{T,s}}$, and the damping parameters by $\alpha_{\mathrm{M,s}}$ and $\alpha_{\mathrm{K,s}}$, analogous to $\alpha_{\mathrm{M,p}}$ and $\alpha_{\mathrm{K,p}}$. An alternative description could be provided using the Young's modulus E, and the Poisson ratio ν of the steel components.

Tab. 1: Initial values for PIC184 piezoceramic material and for steel parameters.

Parameter	Value	Parameter	Value
c_{11}^{E}	$140.22\,\mathrm{GPa}$	$\varepsilon_{11}^{\mathrm{S}}$	$5.65\,\mathrm{nF\,m^{-1}}$
c_{12}^{E}	$76.19\,\mathrm{GPa}$	$\varepsilon_{33}^{\mathrm{S}}$	$5.58\,\mathrm{nF\,m^{-1}}$
c_{13}^{E}	$80.2\,\mathrm{GPa}$	$\alpha_{\mathrm{M,p}}$	$6.49 \cdot 10^{3}\,\mathrm{s^{-1}}$
c_{33}^{E}	$126.24\,\mathrm{GPa}$	$\alpha_{\mathrm{K,p}}$	$0.24\,\mathrm{ns}$
c_{44}^{E}	$25.41\,\mathrm{GPa}$	$c_{\mathrm{L,s}}$	$6130.86\,\mathrm{m\,s^{-1}}$
e_{15}	$10.65\,\mathrm{C\,m^{-1}}$	$c_{\mathrm{T,s}}$	$3277.08\,\mathrm{m\,s^{-1}}$
e_{31}	$-5.39\,\mathrm{C\,m^{-1}}$	$\alpha_{\mathrm{M,s}}$	$7.41 \cdot 10^{-8}\,\mathrm{s^{-1}}$
e_{33}	$14.2\,\mathrm{C\,m^{-1}}$	$\alpha_{\mathrm{K,s}}$	$0.1\,\mathrm{ns}$
ρ_{p}	$7750\,\mathrm{kg\,m^{-3}}$	ρ_{s}	$7700\,\mathrm{kg\,m^{-3}}$

Due to the transducer's design, two oppositely polarised piezoceramics are utilised. It is therefore essential that the polarisation direction is reflected in the material parameters. A straightforward calculation demonstrates that this can be denoted by a negative sign in the matrix of piezoelectric constants Eq. (4). The two-dimensional model is rotationally symmetric, as indicated by the dashed-dotted line situated along the longitudinal z-axis, which serves to reduce the computational time. An investigation of the vibration modes of this model reveals a certain degree of analogy to results from simpler models in previous studies [3], which indicates the reliability of the model used here.

Sensitivity analysis

The objective of a sensitivity analysis is to identify the material parameters that have a significant impact on the numerically calculated impedance. For these parameters, the probability of good estimation is higher using an inverse procedure, although the frequency range is limited. The numerical model of the transducer is evaluated using the finite element method [8] to simulate the complex impedance within the specified frequency range. The full set of material parameters is used, with each parameter being modified independently. The piezoceramic parameters for the simulation are obtained from the estimation of an unconstrained sample [4], and the parameters for steel are taken from data sheets [9]. The used parameters are given in Tab. 1. The deviation between two different simulated spectra is defined as a measure of sensitivity as follows:

$$\Upsilon = \left[\sum_i \big||Z_{\mathrm{ref},i}| - |Z_{\mathrm{var},i}|\big|^2\right]^{\frac{1}{2}}. \tag{8}$$

In this context Z_{ref} is the reference impedance vector that serves as a baseline against which other, varying

DOI 10.5162/Ultrasonic2025/A18-a4

Tab. 2: Resulting sensitivities of piezoceramic material and steel parameters.

Parameter	Sensitivity Υ / Ω	Parameter	Sensitivity Υ / Ω
c_{11}^{E}	9210	$\varepsilon_{11}^{\mathrm{S}}$	13
c_{12}^{E}	4920	$\varepsilon_{33}^{\mathrm{E}}$	20 079
c_{13}^{E}	39 865	$\alpha_{\mathrm{M,p}}$	59
c_{33}^{E}	44 893	$\alpha_{\mathrm{K,p}}$	17
c_{44}^{E}	347	$c_{\mathrm{L,s}}$	46 591
e_{15}	91	$c_{\mathrm{T,s}}$	124 320
e_{31}	6009	$\alpha_{\mathrm{M,s}}$	4706
e_{33}	31 284	$\alpha_{\mathrm{K,s}}$	$5 \cdot 10^{-8}$

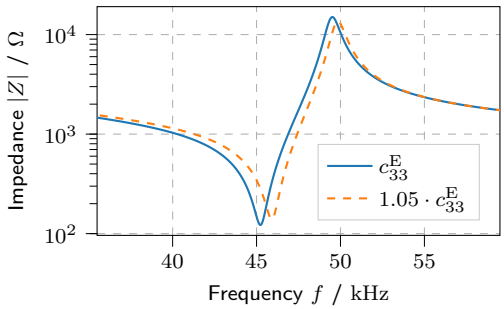

Fig. 2: Influence of an increase by 5 % of the c_{33}^{E} parameter on the electrical impedance of the simulated Langevin transducer.

impedances are compared. The impedance vector Z_{var} is any impedance vector with a material parameter that varies by 5 %. The index i is used to correspond to the sampled frequency points of the impedance vectors.

The resulting deviations are shown in Tab. 2 for each parameter. The absolute sensitivity offers limited interpretative value due to its dependence on the number of sampled frequency points. However, it can be interpreted relatively to other values. These deviations are attributed to shifts in the impedance, as illustrated exemplary for c_{33}^{E} in Fig. 2. It can be observed that the piezoceramic parameters in the longitudinal 33-direction, i.e. in the direction of the z-axis in Fig. 1, are the parameters with the highest sensitivity measure. This phenomenon also aligns with the fact that the exciting electrical field is primarily present in this direction. This observation indicates that, within the constrained frequency range, estimation of the piezoceramic parameters in 33-direction is a feasible option.

Material parameter estimation

The simulated impedance, using the initial values from Tab. 1, shows a significant deviation from the measurements (cf. Fig. 3). A possible explanation for this is the fact that the minimal mechanical load of 30 MPa is necessary for the parts of the transducer to be physically in a full contact [10]. As a consequence, the estimation of the steel parameters is performed first in an inverse procedure, with the parameters given priority according to their impact on the impedance. The sequence of parameters to be estimated is therefore firstly $c_{\mathrm{T,s}}$, subsequently $c_{\mathrm{L,s}}$, and finally the damping parameters (ref. Tab. 2). The resulting steel parameters from Tab. 3 are then used for the subsequent optimisation of the piezoceramic material parameters in 33-direction simultaneously, using measurements for different mechanical loads. The resulting estimated values for piezoceramic materials are presented in Tab. 4. It is evident that the values of the estimated material parameters successively increase with mechanical load. The application of the estimated parameters in simulating an impedance and subsequent comparison with measurement data reveals a high degree of agreement, as can be seen in Fig. 3.

Tab. 3: Estimated steel material parameters.

Parameter	Value	Parameter	Value
$c_{\mathrm{L,s}}$	$6123.79\,\mathrm{m\,s^{-1}}$	$\alpha_{\mathrm{M,s}}$	$3.99 \cdot 10^{-8}\,\mathrm{s^{-1}}$
$c_{\mathrm{T,s}}$	$3473.65\,\mathrm{m\,s^{-1}}$	$\alpha_{\mathrm{K,s}}$	5.46 ps

Tab. 4: Estimated piezoceramic material parameters in 33-direction for PIC184.

Parameter	Mechanical Stress		
	40 MPa	50 MPa	60 MPa
c_{33}^{E} / GPa	126.29	128.37	131.73
e_{33} / $\mathrm{C\,m^{-1}}$	16.23	17.77	18.31
$\varepsilon_{33}^{\mathrm{E}}$ / $\mathrm{nF\,m^{-1}}$	6.9	7.18	7.3

When simulating a wider frequency range, the problem of prominent resonances can be observed once more in Fig. 4. It is evident that, particularly in the case of simulated impedance, the first resonance can be adequately represented, while subsequent resonances are more challenging to assign and to interpret. These are assumed to be higher harmonics. Furthermore, there are modes which can not be captured by the 2D simulation model, including (like) bending and circumferential modes [11].

Conclusion

In this study, stress-dependent piezoelectric material parameters are identified. A simulation model of a Langevin transducer is created, which enables the nu-

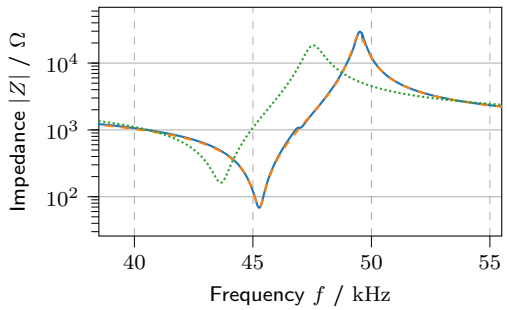

Fig. 3: Comparison of measured (——) and simulated impedance data of a Langevin transducer using the estimated (- - -) and initial (·····) material parameters for $40\,\mathrm{MPa}$.

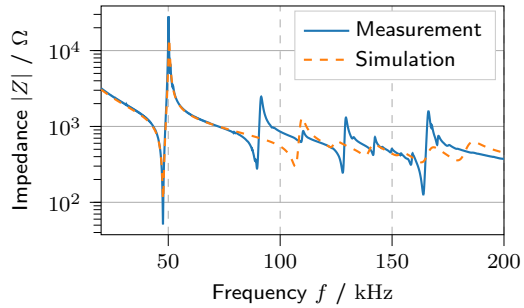

Fig. 4: Comparison of measured and simulated impedance data of a Langevin transducer for a mechanical stress of $60\,\mathrm{MPa}$ *using the estimated material parameters in a wider frequency range.*

merical calculation of electrical, frequency-dependent impedances. The use of numerical simulation is advantageous in this context, as it facilitates a more profound comprehension of the processes within the given structure. Consequently, it is feasible to investigate vibration modes in greater detail and to perform sensitivity studies to identify the most advantageous material parameters for estimation. The findings contribute to a more refined understanding of the role of mechanical pre-stress in piezoelectric transducers and provide a systematic approach for a parameter identification under constrained measurement conditions. Despite the restriction to a single resonance, it is possible to identify a subset of the piezoceramic material parameters. The results presented herein demonstrate a change in these material parameters with increasing mechanical load. It provides an impression of the non-linearities present in this operating case and can subsequently be used to model these non-linearities. Further research could investigate the potential for enhanced interpretation and utilisation of the less pronounced resonances to estimate additional material parameters.

Acknowledgement

This research is funded by the Deutsche Forschungsgemeinschaft (DFG, German Research Foundation) – 444955436 (FOR 5208: NEPTUN).

References

[1] C. Scheidemann et al. "Influence of Temperature and Pre-Stress on the Piezoelectric Material Behavior of Ring-Shaped Ceramics". In: *7th International Conference on Advanced Electromaterials (ICAE 2023) and International Conference on Functional Materials & Devices 2023 (ICFMD 2023)*. 2023.

[2] O. Friesen et al. "Untersuchung piezoelektrischer Materialeigenschaften unter hydrostatischer Last". In: *Fortschritte der Akustik - DAGA 2024*. Ed. by Deutsche Gesellschaft für Akustik e.V. 2024, pp. 1117–1120.

[3] A. Iula et al. "Finite element three-dimensional analysis of the vibrational behaviour of the Langevin-type transducer". In: *Ultrasonics* 40.1-8 (2002), pp. 513–517.

[4] O. Friesen et al. "Estimation of piezoelectric material parameters of ring-shaped specimens". In: *tm - Technisches Messen* (2024). DOI: 10.1515/teme-2024-0107.

[5] W. Voigt. *Lehrbuch der Kristallphysik (mit Ausschluss der Kristalloptik)*. 1966th ed. Vieweg+Teubner Verlag, Jan. 1928. ISBN: 978-3-663-15316-0.

[6] N. Feldmann et al. "Modelling damping in piezoceramics: A comparative study". In: *tm - Technisches Messen* 88.5 (2021), pp. 294–302. DOI: 10.1515/teme-2020-0096.

[7] M. Kaltenbacher. *Numerical simulation of mechatronic sensors and actuators*. Vol. 2. Springer, 2007.

[8] S. Schoder and K. Roppert. *openCFS: Open Source Finite Element Software for Coupled Field Simulation – Part Acoustics*. 2022. DOI: 10.48550/arXiv.2207.04443. arXiv: 2207.04443 [math.NA].

[9] G. Lucefin. "Lucefin steel". In: *Technical card, revision* (2013).

[10] F. Arnold and S. Mühlen. "The influence of the thickness of non-piezoelectric pieces on prestressed piezotransducers". In: *Ultrasonics* 41.3 (2003), pp. 191–196.

[11] B. S. Aronov. "Piezoelectric circular ring flexural transducers". In: *The Journal of the Acoustical Society of America* 134.2 (Aug. 2013), pp. 1021–1030. DOI: 10.1121/1.4812760.

DOI 10.5162/Ultrasonic2025/A18-a6

Estimation of third order elastic constants of piezoceramics using DC biased impedance measurements

Leander Claes[1], Jonas Hölscher[1], Olga Friesen[1], Claus Scheidemann[2], Tobias Hemsel[2], and Bernd Henning[1]
[1]Measurement Engineering Group, Paderborn University, Germany
[2]Dynamics and Mechatronics, Paderborn University, Germany
claes@emt.uni-paderborn.de

Abstract: Third order elastic constants of piezoceramics are estimated from electrical impedance measurements by leveraging the dependence of material parameters on a DC bias voltage induced constant mechanical strain. Linear (second order) piezoelectric material parameters are determined for the biased and non-biased sample by solving an inverse problem matching the frequency-dependent electrical impedance of the sample with the output of a simulation model. Estimates for third order elastic constants are derived from these results, enabling simulations with the estimated parameters and thus a comparison with observations.

Keywords: Piezoelectricity, third order elastic constants, acoustoelastic effect, inverse problem, material characterisation

Motivation

Piezoelectric ceramics are used in a wide range of application areas due to their advantageous electromechanical coupling properties. With design processes becoming increasingly simulation-driven, quantitative knowledge of the material behaviour is essential. While the material behaviour can be considered linear in sensory, small-signal applications, non-linear effects occur in the field of high-power acoustics. It includes applications such as ultrasonic cleaning, bonding, and welding, where the systems' behaviour can be considered primarily linear with superimposed nonlinear properties. With these effects typically not considered during the design phase, their influence can result in unforeseen behaviour in the physical system. In an approach to estimate of third order elastic constants of piezoelectric ceramics, this contribution demonstrates how the parameters of a quadratic mechanical material model, as well as the linear dielectric and piezoelectric coupling behaviour, can be identified.

Material modelling

Using tensor notation, the linear elastic behaviour of a rigid medium is modelled as

$$T_{ij} = c_{ijkl} S_{kl}, \tag{1}$$

using Einstein notation [1] where T_{ij} and S_{kl} are the mechanical stress and strain tensors and c_{ijkl} is the elastic stiffness tensor. This description is considered a linearisation of the material behaviour in a specific operating point. It can be expanded in polynomial terms to a quadratic description:

$$T_{ij} = c_{ijkl} S_{kl} + \tfrac{1}{2} c_{ijklmn} S_{kl} S_{mn}, \tag{2}$$

where c_{ijklmn} is the sixth rank tensor describing the quadratic elastic material behaviour. When describing linear material behaviour, Voigt notation [2] is used to reduce the rank of the elasticity tensor from four to two, i.e. from $3 \times 3 \times 3 \times 3$ to 6×6 by exploiting the symmetry of the stress and strain tensors, which are consequently restructured from 3×3 to 6×1. For the quadratic elastic material description, the dimensionality is reduced to [3]

$$T_i = c_{ij} S_j + \tfrac{1}{2} c_{ijk} S_j S_k, \tag{3}$$

with the third rank tensor c_{ijk} with dimensions $6 \times 6 \times 6$ describing the quadratic elastic material behaviour.

Because high-power acoustic devices are typically driven at resonance with comparatively small electric fields, linear relations are used for dielectric ε_{ij} and coupling e_{ij} behaviour, resulting the material equations [4]

$$T_i = c_{ij} S_j + \tfrac{1}{2} c_{ijk} S_j S_k - e_{ji} E_j \quad \text{and} \tag{4}$$
$$D_i = \varepsilon_{ij} E_j + e_{ij} S_j, \tag{5}$$

with the electric field E_i and the dielectric displacement D_i, each with dimensions 3×1.

Polarised piezoelectric ceramics can be modelled as transversely isotropic, coinciding with the 6mm crystal class, which has ten degrees of freedom for a quantitative, linear, undamped material description [5] and can be parametrised as follows:

$$c_{11}, c_{12}, c_{13}, c_{33}, c_{44},$$
$$\varepsilon_{11}, \varepsilon_{33}, e_{15}, e_{31}, \text{and } e_{33}. \tag{6}$$

DOI 10.5162/Ultrasonic2025/A18-a6

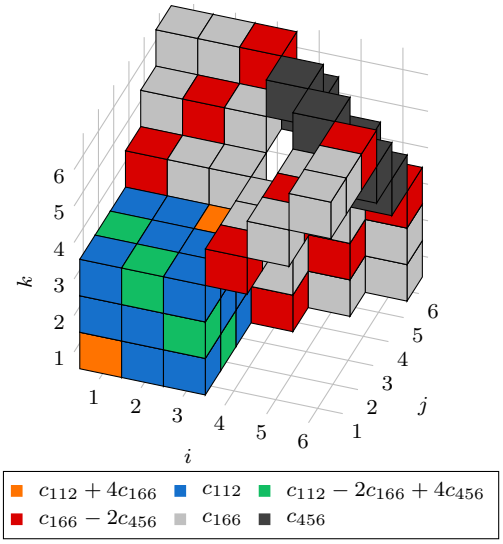

Fig. 1: Visualisation of the non-zero entries of c_{ijk} showing the symmetry of the quadratic elasticity tensor with respect to the indices i, j, and k.

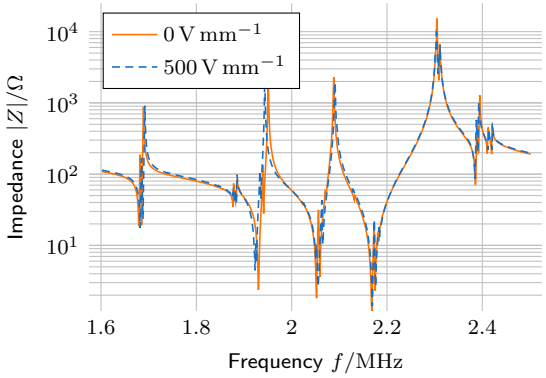

Fig. 2: Section of the electric impedance spectrum of a piezoceramic ring with and without superimposed static electric field.

For a transversely isotropic material, the tensor c_{ijk} has nine degrees of freedom [6]. As the purpose of the present study is, however, to model nonlinear effects that are small compared to the linear behaviour, it is assumed sufficient consider isotropic nonlinearity. This reduces the degrees of freedom of c_{ijk} to three, which can be parametrised with

$$c_{112}, c_{166}, \text{and } c_{456} \tag{7}$$

and allows for the application of established relationships from acoustoelastic theory to identify these parameters [7]. Fig. 1 shows a visual representation of the non-zero entries of c_{ijk}. As evident, six different numerical values occur, which can be derived from an arbitrary subset of three values [6, 3].

Experimental procedure

As a basis for the determination of third order elastic constants, linear piezoelectric material parameters are identified from voltage biased electric impedance measurements. This requires an experimental setup that enables the application of a sufficiently high, static voltage while impedance measurements are conducted [8]. Capacitors with adequate dielectric strength and size are used to decouple the bias voltage from the measurement voltage of an impedance analyser. A static voltage of $500\,\mathrm{V}$ is applied, resulting in a static electric field of $500\,\mathrm{V\,mm^{-1}}$ in the sample considered in this study: a hard piezoceramic ring (PIC181 by *PI Ceramic*) with a thickness of $1\,\mathrm{mm}$, and inner and outer radii of $2.6\,\mathrm{mm}$ and $6.35\,\mathrm{mm}$. The electric field is applied to coincide with polarisation direction of the samples. Electric impedance spectra with frequencies up to $8\,\mathrm{MHz}$ with and without static electric field are acquired. A section with particular sensitivity is shown in Fig. 2. As evident, the influence of the static field can be considered small, however specific resonance frequencies are affected. These impedance spectra are the basis of the subsequent linear material characterisation procedure and consequently for the estimation of third order elastic constants.

Material parameter identification

Based on the impedance measurements, the linear piezoelectric material parameters are identified for the biased and unbiased state by solving an inverse problem. The method applied here is identical to previous work [8]: An axisymmetric finite element model of the piezoelectric sample is implemented in openCFS [9] to acquire synthetic electric impedance spectra for given material parameters. The material parameters are adapted until measurement and simulation are in agreement using gradient-based local optimisation. The initial values required for the optimisation procedure are estimated using a modified convolutional neural network [10]. The results of this identification procedure for the sample in both electric field conditions are listed in Tab. 1 including the parameters of a Rayleigh damping model α_M and α_K. The density of the sample ($\rho = 7850\,\mathrm{kg\,m^{-3}}$) is measured directly and assumed constant. All parameters show an influence of the static electric field, however, the largest changes are observed in the damping parameters. For the subsequent estimation of c_{ijk} based on the acoustoelastic effect, only the changes in the linear elastic parameters c_{ij} are considered.

Approaches to determine third order elastic constants c_{ijk} based on the acoustoelastic effect are formulated relative to a static stress T_i [7]. In the

DOI 10.5162/Ultrasonic2025/A18-a6

Tab. 1: Identified linear parameters for the piezoelectric sample (PIC181) for the biased and unbiased state ($\rho = 7850\,\mathrm{kg\,m^{-3}}$).

Parameter	$0\,\mathrm{V\,mm^{-1}}$	$500\,\mathrm{V\,mm^{-1}}$
c_{11}/GPa	142.17	143.16
c_{12}/GPa	77.42	77.66
c_{13}/GPa	79.49	79.65
c_{33}/GPa	131.04	130.48
c_{44}/GPa	28.29	27.61
$\varepsilon_{11}/\mathrm{nF\,m^{-1}}$	9.39	8.41
$\varepsilon_{33}/\mathrm{nF\,m^{-1}}$	5.90	5.65
$e_{15}/\mathrm{C\,m^{-2}}$	12.33	12.19
$e_{31}/\mathrm{C\,m^{-2}}$	−5.25	−5.33
$e_{33}/\mathrm{C\,m^{-2}}$	14.25	14.03
$\alpha_\mathrm{M}/\mathrm{ms^{-1}}$	6.89	11.01
$\alpha_\mathrm{K}/\mathrm{ps}$	≈ 0	14.6

present study, no mechanical stress is induced. Instead, the sample shows strain resulting form the applied static voltage via the piezoelectric effect. To still evaluate the measurements using the acoustoelastic relation, the equivalent mechanical stress $T_{\mathrm{eq},i}$, which would result in the same strain is considered. For a given static, electric field E_j ($E_1 = E_2 = 0$ and $E_3 = 500\,\mathrm{V\,mm^{-1}}$), $T_{\mathrm{eq},i}$ is determined using previously identified piezoelectric coupling quantities:

$$T_{\mathrm{eq},i} = e_{ji} E_j, \tag{8}$$

thus assuming homogenous static fields. By exploiting the acoustoelastic relations, which in turn are based on a quadratic material model, the previously mentioned entries of c_{ijk} can be determined [7], where $c_{ij,0}$ and c_{ij} denote the properties of the unstressed and stressed material respectively:

$$c_{166} = \frac{\frac{3c_{11,0}-4c_{44,0}}{T_{\mathrm{eq},3}}(c_{33}-c_{11})+5c_{11,0}+4c_{44,0}-6\frac{c_{11,0}^2}{c_{44,0}}}{6\frac{c_{11,0}}{c_{44,0}}-8}, \tag{9}$$

$$c_{456} = \frac{c_{44,0}}{c_{11,0}-2c_{44,0}}\Big(\frac{3c_{11,0}-4c_{44,0}}{T_{\mathrm{eq},3}}(c_{31}-c_{44,0}) - 4c_{11,0} + 4c_{44,0} - c_{166}\Big), \tag{10}$$

and

$$c_{112} = \frac{1}{2}\Big((c_{33}+c_{11}-2c_{11,0})\frac{3c_{11,0}-4c_{44,0}}{T_{\mathrm{eq},3}} - 3c_{11,0} + 4c_{44,0} - 2\frac{c_{11,0}^2+c_{11,0}c_{116}}{c_{44,0}}\Big). \tag{11}$$

Applying these expressions with the equivalent stress $T_{\mathrm{eq},3}$ yields estimates for the third order elastic constants of the piezoelectric material listed in Tab. 2. The remaining entries of c_{ijk} are determined using the relations visualised in Fig. 1.

Tab. 2: Identified third order elastic constants for the piezoelectric sample (PIC181).

Parameter	Estimate	Parameter	Estimate
c_{166}/GPa	$-2.57 \cdot 10^4$	c_{111}/GPa	$-2.13 \cdot 10^5$
c_{456}/GPa	$7.67 \cdot 10^5$	c_{123}/GPa	$3.01 \cdot 10^6$
c_{112}/GPa	$-1.10 \cdot 10^5$	c_{144}/GPa	$-1.56 \cdot 10^6$

Validation

To assess whether the identified quantitative material model can serve as an adequate approximation of the physical material's dynamic nonlinear behaviour, the following experiment is conducted: The sample is excited with a continuous sinusoidal signal at the first local minimum in the impedance spectrum at $122.6\,\mathrm{kHz}$, which is assumed to be a close approximation for the first radial resonance frequency. The signal is applied with an amplitude of $10\,\mathrm{V}$ and the surface displacement at a point on the centre line of the ring's surface is measured with a laser Doppler vibrometer (VibroFlex QTec by *Polytec*). A displacement signal is recorded after the sample reaches a steady state. The spectrum of the measured displacement (Fig. 3) shows harmonic frequencies occurring at integer multiples of the excitation frequency, indicating nonlinear behaviour.

The described experimental setup is recreated in a 2D nonlinear, time-domain, piezoelectric finite element model assuming radial symmetry [11]. In each time step, the wave equation for elastic waves in solids, considering the nonlinear material behaviour, is solved using an iterative Newton-Raphson approach. The solution of the problem using linear material behaviour is used as initial values for the first time step. All subsequent time steps use the solution of the previous step. Due to the simplicity of the quadratic nonlinearity the Jacobian is calculated analytically. When using a sufficiently short time step in the simulation, the change in the displacement per iteration is small and thus the solution converges after few (typically two) iterations. The displacement simulation result is evaluated at the approximate position it is measured at in the experiment. The simulation is conducted with a sufficient number of time steps for the system to reach a steady state and the spectrum of the displacement is analysed (Fig. 3). The simulation result shows the formation of harmonics at multiples of the driving signal frequency, however, these are significantly less pronounced compared to the measurement results. While the first harmonic is clearly visible in the simulation, it is two orders of magnitude lower compared to the measurement result and would be below the noise floor of a physical system if accurate.

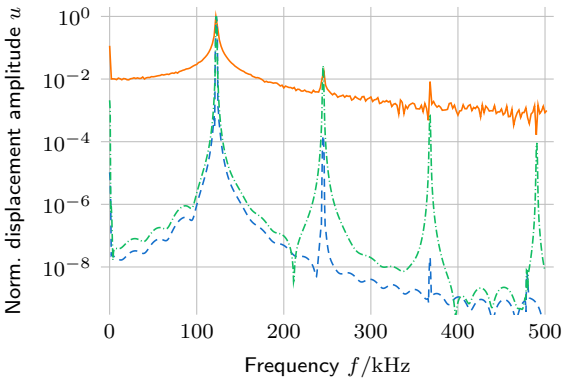

Fig. 3: Spectra of the surface displacement signals resulting from an excitation at the specimens first (linear) radial resonance frequency from measurements (——) and simulations with the estimates for c_{ijk} (- - - -) and the estimates scaled by a factor of 100 (-·-·-·).

The comparison indicates that the proposed approach based on acoustoelasticity clearly underestimates the nonlinear effects occurring in the analysed piezoelectric material. It can, however, be shown that the model is capable of quantitatively reproducing the first harmonic by scaling the nonlinear material parameters up e.g. by a factor of 100 (Fig. 3).

Conclusions

The described method to determine third order elastic constants for piezoceramics based on voltage-biased impedance measurements enables the identification of a quadratic and thus nonlinear elastic material model. However, the estimates provided by the method are shown to be too low to accurately describe nonlinear effects occurring in the sample. One option to rectify these results would be to again solve an inverse problem matching e.g. the simulation results to the measurement (Fig. 3). The deviations are, however, of a magnitude that suggests a revision of the estimation procedure to be more appropriate. An approach would be to assume cubic instead of quadratic material behaviour, which would lead to symmetric properties of the elastic system. A reason for the underestimation of the nonlinearities can also derive from the fact that in the present study, nonlinear effects are exclusive to the elastic behaviour of the material. Taking into account these effects for the dielectric or coupling behaviour can thus be an aspect of future studies.

Acknowledgements

This research is funded by the Deutsche Forschungsgemeinschaft (DFG, German Research Foundation) – 444955436 (FOR 5208: NEPTUN).

References

[1] A. Einstein. "Die Grundlage der allgemeinen Relativitätstheorie". In: *Annalen der Physik* 354.7 (Jan. 1916), pp. 769–822. ISSN: 1521-3889. DOI: 10.1002/andp.19163540702.

[2] W. Voigt. *Lehrbuch der Kristallphysik (mit Ausschluss der Kristalloptik)*. 1966th ed. Vieweg+Teubner Verlag, Jan. 1928. ISBN: 978-3-663-15316-0.

[3] Y. Zhang, J. Jin, and H. Hu. "Third-order elastic, piezoelectric, and dielectric constants". In: *Applied Mathematics and Mechanics* 40.12 (Nov. 2019), pp. 1831–1846. ISSN: 1573-2754. DOI: 10.1007/s10483-019-2550-7.

[4] R. C. Smith. *Smart Material Systems: Model Development*. Society for Industrial and Applied Mathematics, Jan. 2005. ISBN: 978-0-89871-747-1. DOI: 10.1137/1.9780898717471.

[5] W. Heywang, K. Lubitz, and W. Wersing. *Piezoelectricity: Evolution and future of a technology*. Vol. 114. Berlin: Springer, 2008. ISBN: 978-3-540-68680-4.

[6] I. J. Fritz. "Third-order elastic constants for materials with transversely isotropic symmetry". In: *Journal of Applied Physics* 48.2 (Feb. 1977), pp. 812–814. ISSN: 1089-7550. DOI: 10.1063/1.323647.

[7] J. K. Krüger et al. "Nonlinear elastic properties of solid polymers as revealed by Brillouin spectroscopy". In: *Colloid and Polymer Science* 269.8 (Aug. 1991), pp. 764–771. ISSN: 1435-1536. DOI: 10.1007/bf00657442.

[8] O. Friesen et al. "Estimation of piezoelectric material parameters under varying electric field conditions". In: *DAS / DAGA 2025 - 51st Annual Meeting on Acoustics*. 2025, pp. 994–997. DOI: 10.71568/DASDAGA2025.078.

[9] S. Schoder and K. Roppert. *openCFS: Open Source Finite Element Software for Coupled Field Simulation – Part Acoustics*. 2022. DOI: 10.48550/arXiv.2207.04443. arXiv: 2207.04443 [math.NA].

[10] K. Koch et al. "Neuronale Netze zur Startwertschätzung bei der Identifikation piezoelektrischer Materialparameter". In: *tm - Technisches Messen* (2024). DOI: 10.1515/teme-2024-0099.

[11] J. Hölscher. *plutho 0.1.1 – Python Library for coUpled THermo-piezOelectric simulations*. 2025. DOI: 10.5281/zenodo.15608545. URL: https://github.com/emtpb/plutho/releases/0.1.1.

DOI 10.5162/Ultrasonic2025/B1-b1

Passive Cavitation Mapping of Focused Ultrasound Induced Cavitation on Magnetic Nanoparticles

Christian Marinus Huber[1,2,*], *Helmut Ermert*[1], *Ingrid Ullmann*[2], *Martin Vossiek*[2], *and Stefan Lyer*[1]

[1] *Department of Otorhinolaryngology, Head and Neck Surgery, Section of Experimental Oncology and Nanomedicine (SEON), Professorship for AI-Controlled Nanomaterials (KINAM), Universitätsklinikum Erlangen, Glücksstrasse 10a, Erlangen, 91054, Bavaria, Germany*

[2] *Institute of Microwaves and Photonics (LHFT), Friedrich-Alexander-Universität Erlangen-Nürnberg, Cauerstrasse 9, Erlan-gen, 91058, Bavaria, Germany*

[*] *Christian.Ch.Huber@fau.de*

Abstract: Magnetic nanoparticles (MNPs) are utilized in Magnetic Drug Targeting (MDT) to treat tumors, for which it would be advantageous to develop a monitoring method. We aim to use the cavitation produced by MNPs in a focused ultrasonic (FUS) field for imaging via passive cavitation mapping (PCM), a novel approach for MNP mapping. MNP-PCM has the advantage of real-time imaging capability and compatibility with flow conditions over other MNP imaging modalities. Additionally, cavitation can enhance perfusion and drug release. We demonstrate a PCM system for MNPs using time domain Delay and Sum (DAS); Delay Multiply and Sum (DMAS); and the Robust Capon Beamforming (RCB). The code used is available at github.com/ChristianHuber555/ICU_MNP_PAM.

Keywords: Ultrasound Imaging, Magnetic Nanoparticles, Drug Delivery, Passive Imaging, Beamforming, Cavitation

Introduction

Nanomaterials are increasingly integrated into modern medicine for targeted therapy, diagnostics, or drug delivery [1]. Notably, lipid-based nanoparticles were employed in mRNA COVID-19 vaccines [2], highlighting the translational impact of nanoscale systems. Other nanocarriers—such as polymeric, gold, and magnetic nanoparticles (MNPs)—enable a broad range of biomedical applications, including tissue engineering, molecular imaging, and cancer therapy. MNPs offer unique advantages due to their responsiveness to external magnetic fields [3]. They are widely investigated for localized cancer treatments such as magnetic drug targeting (MDT) and magnetic hyperthermia [4]. In MDT, MNPs are accumulated magnetically to tumor regions, enabling site-specific chemotherapy. However, a critical limitation of this approach is the lack of real-time monitoring to assess particle distribution and treatment progression under physiological flow.

Ultrasound-based methods for imaging MNPs [5] have shown promise in MDT monitoring. However, most are inadequate for detecting MNPs in motion within vascular systems. In our previous work [6], [7], we demonstrated that lauric acid-coated MNPs (LA-MNPs) exhibit sonosensitivity, acting as cavitation nuclei under focused ultrasound (FUS). Cavitation is defined as the formation and dynamics of gas-filled bubbles and occurs as either stable cavitation (oscillatory behavior near equilibrium) or inertial cavitation (violent collapse). Acoustic cavitation enhances drug delivery through increased vascular permeability, localized drug release, and improved imaging contrast [8]. Cavitation can be used for imaging either by using the generated bubbles as high echogenic contrast in active cavitation mapping [9] or using acoustic cavitation emission in passive cavitation mapping (PCM) [10].

In this study, we utilize the sonosensitivity of our LA-MNPs to induce inertial cavitation under flow and apply PCM to map their spatial distribution. This approach has the potential to enable real-time monitoring of MNP transport during MDT, providing a foundation for ultrasound-guided, feedback-controlled nanoparticle therapy.

Methods and Materials

In time-domain Passive Cavitation Mapping (PCM) [10], the cavitation intensity at each spatial location $\mathbf{x} = (x, z)^T$ is quantified by integrating the squared source strength $q(\mathbf{x}, t)$ over a temporal window T

$$I(\mathbf{x}) = \frac{1}{\rho c} \int_{t_0}^{t_0+T} q(\mathbf{x}, t)^2 \mathrm{d}t, \tag{1}$$

where ρ is the density of the medium and c is the speed of sound.

The accuracy of PCM critically depends on the beamforming algorithm used to reconstruct $q(\mathbf{x}, t)$

and $I(\mathbf{x})$. In this work, we evaluate and compare the conventional Delay-and-Sum (DAS) beamformer [10], the non-linear Delay-Multiply-and-Sum (DMAS) beamformer [11], and the statistically adaptive Robust Capon Beamformer (RCB) [12]. Each method offers distinct trade-offs in resolution, robustness to noise, and sensitivity to cavitation signals.

For all beamforming methods, cavitation emissions must be passively recorded using multiple spatially distributed sensors—typically a linear array transducer. The positions of the N transducer elements are denoted as $\mathbf{x}_n = (x_n, z_n)^T = (x_n, 0)$, with received signals $s_n(t)$ for each element $n \in \mathcal{N}$, $1 \leq n \leq N$. As the acquisition is restricted to 2D imaging, the out-of-plane y-axis is neglected and set to $y = 0$ throughout all computations.

For a target location $\mathbf{x}$, the geometric distance between the pixel and each sensor element is given by

$$d_n(\mathbf{x}) = \sqrt{z^2 + (x_n - x)^2}. \tag{2}$$

Eq. (2) defines the propagation distance from each pixel to sensor n, and the corresponding time delay is $\tau(\mathbf{x}) = d_n(\mathbf{x})/c$. The DAS beamformer estimates the source strength by

$$q_{\mathsf{DAS}}(\mathbf{x}, t) = \frac{1}{N\alpha} \sum_{n=1}^{N} s_n(t + \tau_n(\mathbf{x})), \tag{3}$$

where α is the piezoelectric sensitivity coefficient of the array elements. The DMAS beamformer extends DAS by introducing pairwise nonlinear correlations

$$q_{\mathsf{DMAS}}(\mathbf{x}, t) = \frac{1}{(N^2 - N)\alpha} \sum_{n_1=1}^{N-1} \sum_{n_2=n_1+1}^{N} \widehat{s}_{n_1} \widehat{s}_{n_2}, \tag{4}$$

where the modified signal is defined as $\widehat{s}_n = \mathrm{sign}\{s_n(t)\} \cdot \sqrt{|s_n(t)|}$. To reduce computational complexity, Eq. (4) can be reformulated

$$q_{\mathsf{DMAS}}(\mathbf{x}, t) = \frac{1}{N(N-1)\alpha} \frac{e_1^2 - e_2}{2} \tag{5}$$

using power sums

$$e_j = \sum_{n=1}^{N} \widehat{s}_n^j. \tag{6}$$

To compute the cavitation intensity map using RCB the received signals are ordered to a vector

$$\mathbf{s}(\mathbf{x}, t) = \begin{bmatrix} s_1(t - \tau_1(\mathbf{x})) \\ \vdots \\ s_N(t - \tau_N(\mathbf{x})) \end{bmatrix}. \tag{7}$$

RCB is a statistically optimal beamforming approach that minimizes the total output power while constraining the beamformer weights $\mathbf{w}$ to remain close to a unity gain response. The beamforming weights are obtained by solving the constrained optimization problem

$$\min_{\mathbf{w}} \{\mathbf{w}^T \mathbf{R}_S(\mathbf{x})^{-1} \mathbf{w}\} \quad \text{subject to} \quad \|\mathbf{w} - \mathbf{1} \leq \epsilon\| \tag{8}$$

where $\mathbf{R}_S(\mathbf{x}) = \mathbf{U}\mathbf{V}\mathbf{U}^T$ is the eigenvalue decomposition of the sample covariance matrix, $\mathbf{1}$ is a all-ones vector, and ϵ is a user-defined robustness parameter. The solution of Eq. (8) yields the beamforming weights used to compute the cavitation intensity

$$I(\mathbf{x}) = \frac{1}{\alpha^2 \rho c} \frac{1}{\widehat{\mathbf{a}}_0 \mathbf{U}\mathbf{V}(\lambda^2 \mathbf{I} + 2\lambda^{-1}\mathbf{V} + \mathbf{V}^2)^{-1}\mathbf{U}^T \widehat{\mathbf{a}}_0}, \tag{9}$$

with $\mathbf{I}$ as an all-ones matrix, λ as Lagrange multiplied and $\widehat{\mathbf{a}}_0 = \widehat{\mathbf{a}}N/\|\widehat{\mathbf{a}}\|$ with $\widehat{\mathbf{a}} = \mathbf{1} - \mathbf{U}(\mathbf{I} + \lambda\mathbf{V})^{-1}\mathbf{1}$. The Lagrange multiplier can be found by solving

$$\|(\mathbf{I} + \lambda \mathbf{R}_S^{-1}\mathbf{1})\| - \epsilon = 0. \tag{10}$$

The experimental setup is illustrated in Fig. 1. A tissue-mimicking phantom containing a 2 mm diameter flow channel was fabricated from 2 wt% agarose, 1 wt% silica gel, and 97 wt% ultrapure water, following the procedure described in [13]. The flow channel was aligned with the focal region of a focused ultrasound (FUS) field (center frequency $f = 835$ kHz, pulse duration $t_{\mathsf{on}} = 200$ μs, mechanical index = 1, 10 pulses per acquisition).

A suspension of LA-MNPs at a concentration of 3 mg Fe/mL was circulated through the channel. Cavitation emissions were passively captured using 64-elements of the 128 element linear array transducer (Verasonics 64 LE, L11-5v; center frequency 7.6 MHz, relative bandwidth 77%) positioned orthogonally to the FUS propagation axis and mounted above the phantom.

Signals were recorded at a sampling rate of 31.25 MHz and subsequently upsampled to 55.11 MHz. A comb notch filter was applied to suppress the FUS fundamental and harmonic frequencies. The preprocessed array signals were reconstructed using the DAS, the DMAS, and the RCB. Cavitation intensity maps were computed and averaged over all 10 FUS pulses. For quantitative evaluation, the contrast ratio (CR) between cavitating and non-cavitating regions was used.

Results and Discussion

Using the described setup, cavitation on magnetic nanoparticles was successfully induced via focused

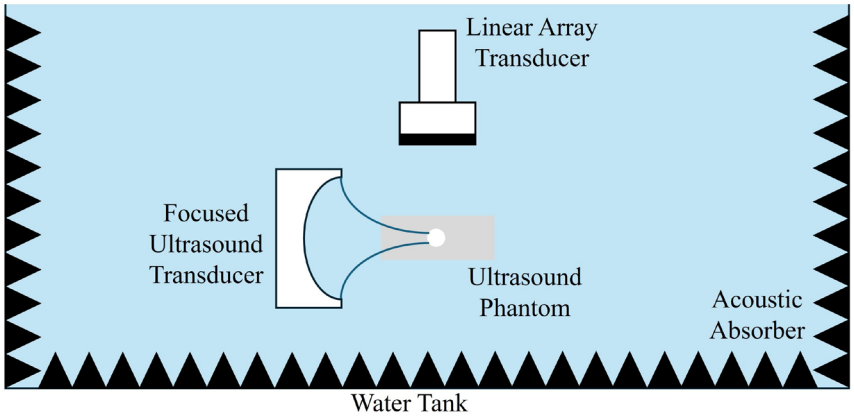

Fig. 1: Measurement setup used for passive cavitation mapping of focused ultrasound induced cavitation on magnetic nanoparticles.

ultrasound. The resulting acoustic emissions were passively received by the linear array transducer and processed using DAS, DMAS, and RCB beamforming algorithms. The reconstructed cavitation maps are shown in Fig. 2.

All beamformers were able to localize cavitation activity within the phantom. However, notable differences in spatial specificity and artifact suppression were observed. The DAS reconstruction shows widespread intensity outside the flow channel, indicating poor spatial confinement. In contrast, RCB provides improved localization, effectively suppressing off-target signal but introducing artifacts near the bottom boundary of the phantom, likely due to reflections. DMAS offers a balance between spatial resolution and artifact suppression, producing a confined cavitation region without the lower-edge artifacts seen in RCB.

Quantitatively, the contrast ratio was used to evaluate performance: DAS yielded a CR of -7.79 dB, RCB -7.17 dB, and DMAS - 5.91 dB. Among the three, DMAS demonstrated the best overall performance in terms of both CR and artifact-free localization.

These results confirm that passive cavitation mapping can effectively visualize FUS-induced cavitation on MNPs under flow conditions, and that DMAS offers the most robust imaging performance in this context.

Conclusion

This study demonstrates the feasibility of using PCM to monitor FUS-induced cavitation on MNPs under flow conditions. By utilizing the sonosensitive properties of LA-coated MNPs, we enabled cavitation-based imaging that can be used for real-time monitoring of MDT.

The DAS, DMAS, and RCB were evaluated for their ability to reconstruct MNP-cavitation intensity maps from passively received acoustic signals. While all methods successfully localized cavitation activity, DMAS provided the best balance of contrast, spatial confinement, and artifact suppression, achieving the highest CR. RCB improved localization but exhibited boundary artifacts, whereas DAS was limited by poor spatial resolution.

These findings demonstrate PCM as a promising tool for real-time, non-invasive monitoring of MNP transport during MDT. Future work will focus on in vivo validation, optimization for 3D imaging, and integration with feedback control systems for image-guided therapy.

Acknowledgments

The authors gratefully acknowledge the financial support of the German Research Foundation (DFG) - project number 452821018, and the Julitta und Richard Müller Stiftung.

References

[1] J. Damodharan, 'Nanomaterials in medicine – an overview,' *Materials Today: Proceedings*, vol. 37, pp. 383–385, 2021. DOI: 10.1016/j.matpr.2020.05.380.

[2] R. S. Shapiro, 'Covid-19 vaccines and nanomedicine,' *International Journal of Dermatology*, vol. 60, no. 9, pp. 1047–1052, 2021. DOI: 10.1111/ijd.15673.

[3] A. S. Thalmayer, K. Götz, M. Lübke and G. Fischer, 'Experimental and simulative analysis of magnetic nanoparticle accumulation using various halbach arrays,' *Current Directions in Biomedical Engineering*, vol. 10, no. 4, pp. 649–652, 2024. DOI: 10.1515/cdbme-2024-2159.

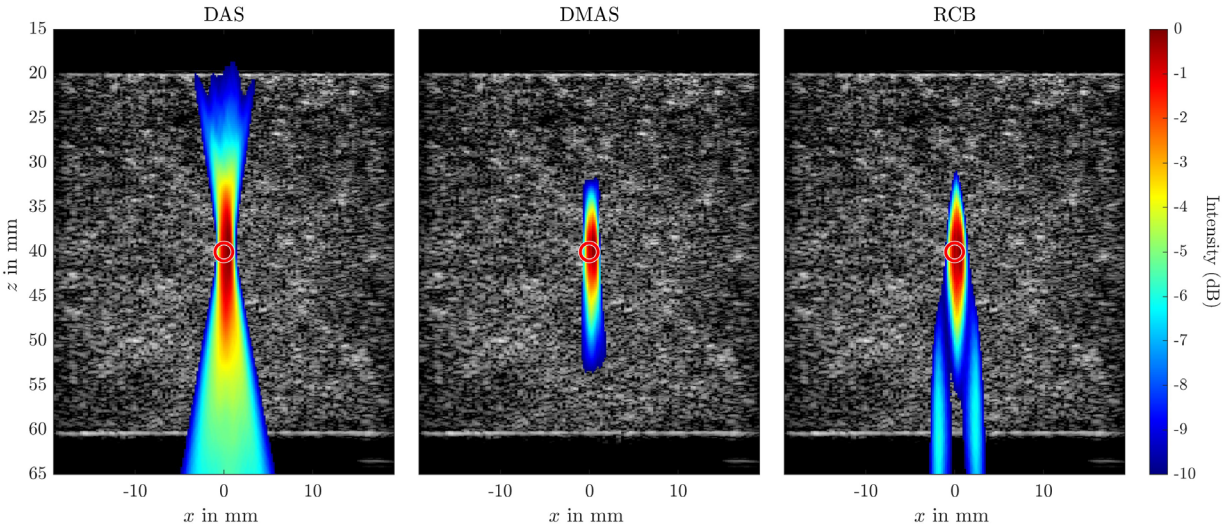

Fig. 2: Resulting cavitation intensity maps overlaid on the B-mode image using the Delay and Sum (DAS), Delay Multiply and Sum (DMAS), and Robust Capon Beamformer (RCB). $\epsilon = 10$ *was used for the RCB. The flow channel is shown as red circle in each plot.*

[4] R. Tietze et al., 'Efficient drug-delivery using magnetic nanoparticles–biodistribution and therapeutic effects in tumour bearing rabbits,' *Nanomedicine : Nanotechnology, Biology, and Medicine*, vol. 9, no. 7, pp. 961–971, 2013. DOI: 10.1016/j.nano.2013.05.001.

[5] C. M. Huber et al., 'A review on ultrasound-based methods to image the distribution of magnetic nanoparticles in biomedical applications,' *Ultrasound in Medicine & Biology*, vol. 51, no. 2, pp. 210–234, 2025. DOI: 10.1016/j.ultrasmedbio.2024.10.007.

[6] C. Huber et al., 'Ultrasound-mediated cavitation of magnetic nanoparticles for drug delivery applications,' *Current Directions in Biomedical Engineering*, vol. 8, no. 2, pp. 568–571, 2022. DOI: 10.1515/cdbme-2022-1145.

[7] C. M. Huber et al., 'Ultrasound-induced stable and inertial cavitation of magnetic nanoparticles for drug delivery applications,' *Current Directions in Biomedical Engineering*, vol. 10, no. 4, pp. 328–331, 2024. DOI: 10.1515/cdbme-2024-2080.

[8] Z. Shen, J. Shao, J. Zhang and W. Qu, 'Ultrasound cavitation enhanced chemotherapy: In vivo research and clinical application,' *Experimental Biology and Medicine (Maywood, N.J.)*, vol. 245, no. 14, pp. 1200–1212, 2020. DOI: 10.1177/1535370220936150.

[9] T. Ding et al., 'Spatial-temporal three-dimensional ultrasound plane-by-plane active cavitation mapping for high-intensity focused ultrasound in free field and pulsatile flow,' *Ultrasonics*, vol. 69, pp. 166–181, 2016. DOI: 10.1016/j.ultras.2016.04.010.

[10] M. Gyöngy and C.-C. Coussios, 'Passive spatial mapping of inertial cavitation during hifu exposure,' *IEEE Transactions on Biomedical Engineering*, vol. 57, no. 1, pp. 48–56, 2010. DOI: 10.1109/TBME.2009.2026907.

[11] S. Lu, R. Li, X. Yu, D. Wang and M. Wan, 'Delay multiply and sum beamforming method applied to enhance linear-array passive acoustic mapping of ultrasound cavitation,' *Medical Physics*, vol. 46, no. 10, pp. 4441–4454, 2019. DOI: 10.1002/mp.13714.

[12] C. Coviello et al., 'Passive acoustic mapping utilizing optimal beamforming in ultrasound therapy monitoring,' *The Journal of the Acoustical Society of America*, vol. 137, no. 5, pp. 2573–2585, 2015. DOI: 10.1121/1.4916694.

[13] C. M. Huber, N. Dorsch, H. Ermert, M. Vossiek, I. Ullmann and S. Lyer, 'Passive cavitation mapping for biomedical applications using higher order delay multiply and sum beamformer with linear complexity,' *Ultrasonics*, vol. 153, p. 107 653, 2025. DOI: 10.1016/j.ultras.2025.107653.

DOI 10.5162/Ultrasonic2025/B1-c3

UTMD-Mediated Nano-Stem Cells for the Treatment of Ischemic Stroke

Mingxuan Li[1], *Fan Li*[2], *and Lianfang Du*[1]
[1]*Department of Medical Ultrasound, Shanghai General Hospital, Shanghai Jiao Tong University School of Medicine, Shanghai, 201620, China*
[2]*Department of Medical Ultrasound, Shanghai Chest Hospital, Shanghai Jiao Tong University School of Medicine, Shanghai, 200030, China*
medicineli@163.com

Abstract: Ischemic stroke, a leading cause of global disability and death, affects about 15 million annually[.] Current therapies face limitations from narrow treatment windows and the blood-brain barrier (BBB), which restricts drug delivery[1]. Nanotechnology offers promising solutions: copper-selenium nanoparticles (Cu2-xSe) combine biocompatibility with antioxidant/anti-inflammatory effects, scavenging ROS and modulating ferroptosis[2,3]. Selenium upregulates GPX4 via TFAP2c/Sp1, inhibiting lipid peroxidation[4]. Similar Cu-based nanozymes have shown anti-inflammatory effects in osteoarthritis by modulating macrophage polarization[5]. Stem cell therapy, particularly BMSCs, promotes neurorepair through differentiation and neurotrophic factor secretion[6]. Our innovation combines UTMD technology - which transiently opens the BBB via microbubble cavitation[7,8] - with engineered Cu2-xSe@BMSCs. This multimodal strategy simultaneously addresses BBB penetration, oxidative stress, inflammation, apoptosis, and neural regeneration.

Keywords: ischemic stroke, copper selenium nanoparticles, mesenchymal stem cells, blood-brain barrier, ultrasound therapy

Cu2-xSe Nanoparticle Synthesis and Characterization

Cu2-xSe nanoparticles (NPs) were successfully synthesized using a modified method based on previous reports. TEM analysis revealed that Cu2-xSe NPs exhibited a uniform spherical morphology with distinct copper and selenium element distribution, confirming the successful formation of Cu2-xSe NPs.

In Vitro Hypoxia Protection Study

The cytotoxicity of Cu2-xSe NPs was evaluated using the CCK-8 assay. At concentrations up to 10 μg/mL, Cu2-xSe NPs showed low cytotoxicity. In CoCl2-induced hypoxic models, Cu2-xSe NPs significantly improved cell survival rates and reduced oxidative stress. Fluorescence staining revealed that cells treated with Cu2-xSe NPs exhibited stronger green fluorescence (indicating live cells) compared to untreated hypoxic cells, highlighting their protective effect against hypoxic injury. Furthermore, Cu2-xSe NPs effectively reduced reactive oxygen species (ROS) accumulation, as evidenced by DCFH-DA staining. Lipid peroxidation levels, assessed by C11-BOdipy 581/591 staining, were significantly reduced in the Cu2-xSe-treated group, particularly at a concentration of 4 μg/mL. These findings suggest that Cu2-xSe NPs attenuate oxidative damage and lipid peroxidation in hypoxic cells.

Iron Death Inhibition

Western blot analysis showed that Cu2-xSe NPs restored the expression of GPX4 and FTH, which were downregulated in the CoCl2-induced hypoxia group. Simultaneously, the expression of ACSL4, a marker of ferroptosis, was decreased. These results indicate that Cu2-xSe NPs could protect against ferroptosis by modulating oxidative stress and iron homeostasis under hypoxic conditions.

In Vivo Neuroprotective Effect

The neuroprotective efficacy of Cu2-xSe nanoparticles (NPs) was systematically evaluated in a transient middle cerebral artery occlusion (tMCAO) mouse model. Behavioral assessments revealed that combination therapy with UTMD and BMSC-loaded Cu2-xSe NPs significantly improved neurological functional recovery compared to model controls. Treated animals demonstrated markedly enhanced performance in adhesive removal, water maze, and rotarod tests, indicating substantial improvements in sensory-motor function, spatial learning, and motor coordination. Neuroimaging and histopathological analyses provided compelling evidence for the therapeutic effects, showing dramatic reductions in cerebral infarct volume and neuronal apoptosis. These findings collectively demonstrate

that Cu2-xSe NPs confer comprehensive neuroprotection through multiple mechanisms, including oxidative stress mitigation and neuronal survival promotion, highlighting their potential as a novel therapeutic agent for ischemic stroke.

References

1.Campbell BCV, De Silva DA, Macleod MR, Coutts SB, Schwamm LH, Davis SM, et al. Ischaemic stroke. Nat Rev Dis Primers. 2019;5(1):70.
2.Baldinotti R, Fronza MG, Fetter J, Silva L, Bender CB, Lüdtke DS, et al. Protective effects of octylseleno-xylofuranoside in a streptozotocin-induced mouse model of Alzheimer's disease. Eur J Pharmacol. 2021;910:174499.
3.Dixon SJ, Lemberg KM, Lamprecht MR, Skouta R, Zaitsev EM, Gleason CE, et al. Ferroptosis: an iron-dependent form of nonapoptotic cell death. Cell. 2012;149(5):1060-72.
4.Alim I, Caulfield JT, Chen Y, Swarup V, Geschwind DH, Ivanova E, et al. Selenium Drives a Transcriptional Adaptive Program to Block Ferroptosis and Treat Stroke. Cell. 2019;177(5):1262-79.e25.
5.Yu B, Sun W, Lin J, Fan C, Wang C, Zhang Z, et al. Using Cu-Based Metal-Organic Framework as a Comprehensive and Powerful Antioxidant Nanozyme for Efficient Osteoarthritis Treatment. Adv Sci (Weinh). 2024;11(13):e2307798.
6.Tang W, Zhao K, Li X, Zhou X, Liao P. Bone Marrow Mesenchymal Stem Cell-Derived Exosomes Promote the Recovery of Spinal Cord Injury and Inhibit Ferroptosis by Inactivating IL-17 Pathway. J Mol Neurosci. 2024;74(2):33.
7.Jin LF, Li F, Wang HP, Wei F, Qin P, Du LF. Ultrasound targeted microbubble destruction stimulates cellular endocytosis in facilitation of adeno-associated virus delivery. Int J Mol Sci. 2013;14(5):9737-50.
8.Bai Y, Du Y, Yang Y, Wälchli T, Constanthin PE, Li F. Ultrasound-Targeted Microbubble Destruction Increases BBB Permeability and Promotes Stem Cell-Induced Regeneration of Stroke by Downregulating MMP8. Cell Transplant. 2024;33:9636897231223293.

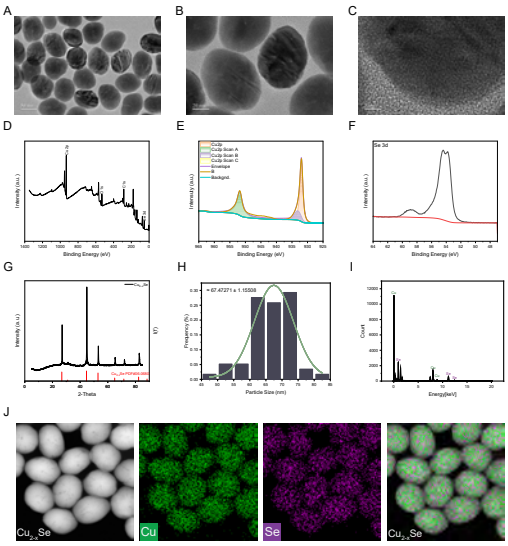

*Fig. 1: Synthesis and functional characterization of ferroptosis-targeting Cu2-xSe nanoparticles (NPs). (A–C) Transmission electron microscopy (TEM) images; (D–F) X-ray photoelectron spectroscopy (XPS); (G) X-ray diffraction (XRD): Peaks indexed to cubic Cu2-xSe (JCPDS 06-0680) phase, with no detectable impurities. (H) Size distribution histogram: Dynamic light scattering (DLS) / TEM-derived average diameter: 67.47 ± 1.16 nm (mean ± SD, *n* = 60). (I) Energy-dispersive X-ray spectroscopy (EDS): Spot analysis verifying Cu:Se atomic ratio (˜2:1) and trace elements. (J) EDS elemental mapping: Homogeneous spatial distribution of Cu (red) and Se (green) in NPs.*

DOI 10.5162/Ultrasonic2025/B1-c3

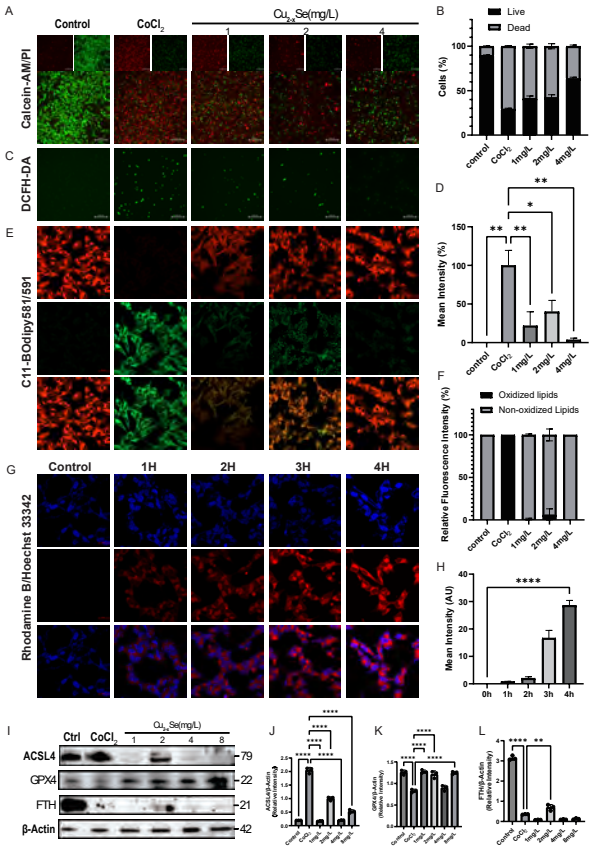

Fig. 2: Cytoprotective effects of Cu2-xSe NPs against CoCl2-induced hypoxia in SH-SY5Y cells (A,B) Cell viability rescue Live/dead staining (AMPI); (C,D) Oxidative stress mitigation; (E,F)Lipid peroxidation (C11-BODIPY); (G,H) Rhodamine B/Hoechst staining; (I-L) Ferroptosis-related protein modulation (Western blot).

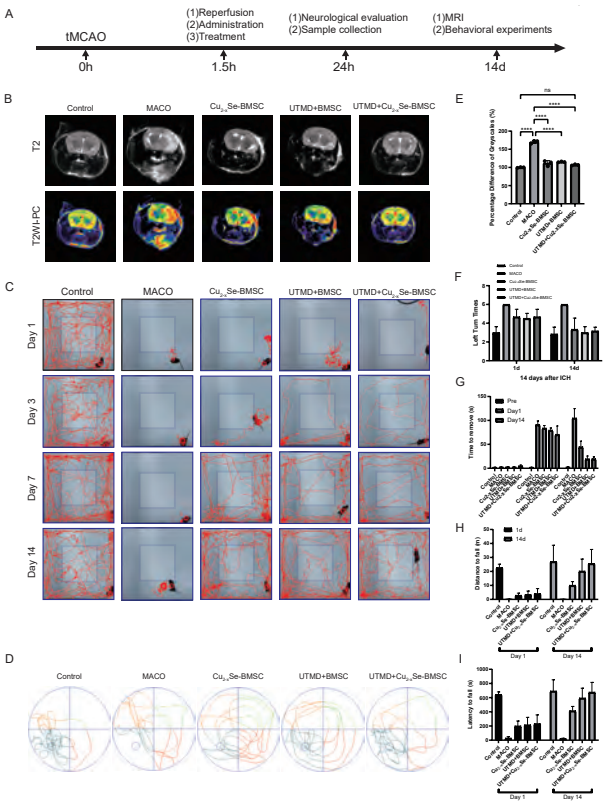

Fig. 3: Therapeutic workflow and functional outcomes of UTMD-enhanced Cu2-xSe NPs-BMSC therapy in tMCAO mice (A) Therapeutic workflow: tMCAO induction: 90-min middle cerebral artery occlusion. Treatment groups: Sham, Model (tMCAO), NPs-BMSC, UTMD-BMSC, UTMD+NPs-BMSC (n=6/group). UTMD delivery: Ultrasound-targeted microbubble destruction (1 MHz, 0.5 W/cm², 30s) to enhance NP-BMSC homing. (B,E) MRI assessment (T2-weighted). (C,F,G,H) Results of Open-Field experiments; (D,I)Results of Water maze experiment.

DOI 10.5162/Ultrasonic2025/B7-a1

Determination of Pulse Wave Velocity in Arteries using High-Frequency and Single-Channel Focused Ultrasound

A.B. Amado-Rey[1,3], L.Elvira[2], C.Duran[2], R. Shaporin[2], J.S. Alarcón[2], and T.Stieglitz[1,3,4]
[1]Laboratory for Biomedical Microtechnology, IMTEK, University of Freiburg, Freiburg, Germany
[2]Instituto de Technologías Físicas y de la Información (ITEFI, CSIC), Madrid, Spain
[3]BrainLinks-BrainTools Center, IMBIT // Neuroprobes, University of Freiburg, Freiburg, Germany
[4]Bernstein Center Freiburg, University of Freiburg, Freiburg, Germany
belen.amado@imtek.uni-freiburg.de

Abstract: Pulse wave velocity (PWV) is a key indicator of our vascular age, a risk predictor of cardiovascular disease. The gold-standard method to measure PWV relies on the measurement of the carotid-femoral arterial distance, and it is not very reliable, due to the changes in the arterial tree. We present in this paper a method to measure local PWV based on high-frequency ultrasound, with a mono channel transducer at 20 MHz, at the arterial site of measurements. We performed in-vitro measurements in a phantom with tubes of 1.5 mm of diameter. Four ultrasound methods to extract PWV based on difference velocity estimation are compared. PWV was validated with pressure sensors and gave a mean error of only 1.1 m/s.

Keywords: High-frequency ultrasound, pulse wave velocity, cardiovascular disease, loop-based methods, medical phantom, blood flow, diameter waveform.

Background, Motivation and Objective

In healthy conditions, our heart pumps 5 litres of blood per minutes through our arteries and veins at rest. Simultaneously, the arteries adapt their diameter to the cardiac output to maintain constant blood pressure. If we measure the movement of the blood in our arterial tree from the aorta to the periphery, we will see a travelling pulse wave. The pulse wave velocity (PWV) depends on the stiffness of our arteries, being increased with our biological age [1] or the hardening of our artery walls, and it is a key indicator of vascular age and a predictor of cardiovascular disease.

The standard PWV measurement is performed at large arteries and over large distances such as the carotid-to-femoral (cfPWV), and it is defined as regional PWV [2]. The gold-standard medical device to measure PWV is the tonometer, which uses two measurement points (at the carotid and femoral artery) to determine the shift in time of the waveforms. The cfPWV is then calculated as the ratio of the distance between those measurement points (ΔD) and the time displacement of the pulse waves (pulse transient time, PTT), as indicated in Eq. (1).

$$cfPWV = \frac{\Delta D}{PTT} \tag{1}$$

cfPWV is given in (m/s), and the mean typicall values for healthy subjects is around 5.8-7.5 m/s for young adults (less than 50 years-old) and of 8.0-8.5 m/s for older adults (more than 50 years-old). Moreover, cfPWV is bigger in males than females. [1]

The main challenge with the cfPWV measurement is the vague estimation of the carotid-femoral distance (ΔD), which is usually done with a ruler externally. Moreover the arterial stiffness is not uniform in all the vessels (change in vessel diameters, wall-thickness and viscoelastic properties), and the global PWV increases distal to the heart and further down to the vascular tree. To solve this problem, local PWV (applied at a single arterial segment and short distances) can be used. Local PWV can assess the arterial heterogeneity and identify early cardiovascular risk at single arterial segments with more precision than global PWV [3].

To measure the PWV at pre-clinical studies in animals, and for microcirculation, high-frequency and high-frame rate ultrasound is required, ensuring accuracy in the detection of the arterial wall movement, and in the measurement of the fast movement of the PWV. Local PWV with ultrasound can be monitored by using dual or multiple ultrasound arrays [4], and applying Eq. (1) as for the global PWV. However, this approach requires synchronization between sensors and also the post-processing of numerous signals.

In this work, we apply the diameter-velocity loop method to determine the local PWV in a customed-made phantom. Velocity and diameter are physiological signals that can be monitored directly with ultrasound using a mono channel-probe, requiring low

DOI 10.5162/Ultrasonic2025/B7-a1

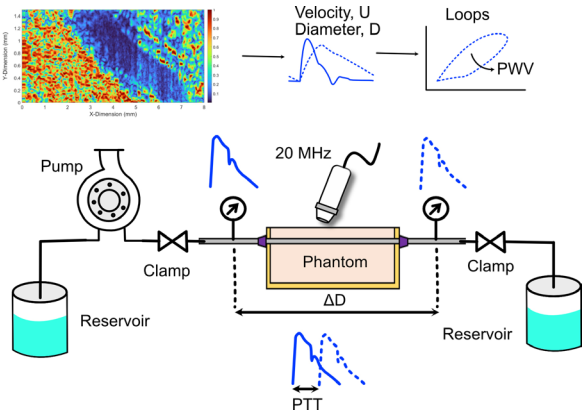

Fig. 1: In-vitro setup for the measurement of the local PWV in the phantom. The PWV is extracted with U and D from the ultrasound acquisition. The measurements are validated with two pressure sensors, after applying Eq. (1)

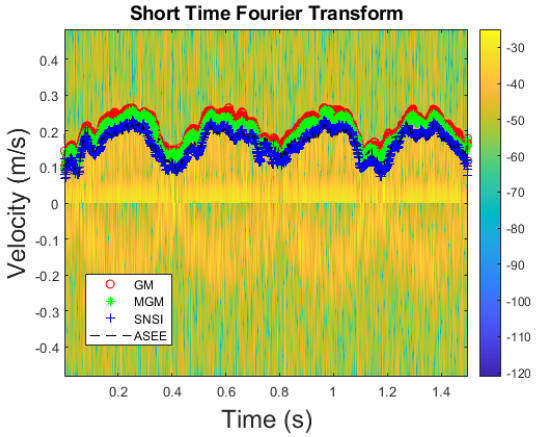

Fig. 2: Velocity curves calculated for the spectrogram of the flow speed in the phantom. The spectral envelope is compared using the geometrical method (GM), modified geometrical method (MGM), signal noise slope intersection (SNSI), and the adaptive spectral envelope estimation (ASEE).

power consumption and also low thermal exposure to the tissue for long-time measurements. The ultrasound device is custom-made, and is mounted in a 3-axis system with motors to obtain B-Mode images. B-mode images provide information of the angle between the liquid flow and the transducer. However, to measure velocity, the probe was operated in a static position, with repeated acquisitions at high pulse repetition frequency (M-mode).

Each line of the M-Mode image is afterwards post-processed. Four different algorithms are applied to extract the ultrasound velocities and the time-of-flight is applied for diameter-wall distension. Validation of the PWV measurements is performed by using commercial pulse pressure sensors.

Ultrasound phantom and in-vitro setup

The measurements and derivation of PWV were performed in an in-vitro setup, as illustrated in Figure 1. The setup consisted on a peristaltic pump (Watson-Marlow) that emulates the heart, silicone tubes, a customized phantom, clamps to change the resistance at the input and ouput of the phantom, and pressure sensors as reference devices for the PWV. The pump delivers the mimicked fluid (that includes *Saccharomyces cerevisiae* yeasts of approximately 7 μm in size to emulate blood cells) from the pump through the phantom.

The phantom is fabricated with polyvinyl alcohol (PVA) at a concentration of 10% by weight (Sigma Mw130000, 99%+ hydrolyzed). Aluminum particles at a concentration of 0.5% by weight and chlorhexidine digluconate as an antiseptic at a concentration of 0.05% by weight (Desinclor, antiseptic solution, chlorhexidine digluconate 1%) are added to PVA. Freeze-thaw cycles are applied to the phantom, which makes the PVA-based mixture form an hydrogel suitable to be used for ultrasound imaging applications. Inside the phantom, a silicone tube with diameter of 1.5 mm, and wall thickness of 0.2 mm is included. The clamps at the inlet and outlet of the phantom help to change the resistance of the setup and maintain a constant pressure inside the phantom.

Two simultaneous measurements were performed: M-Mode ultrasound measurements at one single point, and two pressure measurements with pressure sensors (ABPMANN004BGAA5, Honeywell) for comparison. The probe has a focalized wide-band piezoelectric transducer (Imasonic), with 14 mm curvature radius, 7 mm surface diameter and 20 MHz central frequency. A Difrascope (Dasel Technologies) pulse-echo electronics was used to send and acquire the electric pulses. Pulse repetition rates in the range of 3-20 kHz were applied in this study.

Velocity-Diameter Loop Determination

After monitoring the movement of the particles with the 20 MHz ultrasound probe in the XYZ direction, M-Mode images with the customized setup were acquired. The images at various pump speeds (from 30 RPM till 100 RPM, with steps of 10 RPM) are obtained and save for post-processing. From the M-Mode images, diameter distension and velocity waveforms are derived using MATLAB.

The diameter waveforms are obtained through the application of a band-pass filter, peak detection of the arterial wall for each signal of the M-Mode image (a total of 30.000), and finally the application of the time-

DOI 10.5162/Ultrasonic2025/B7-a1

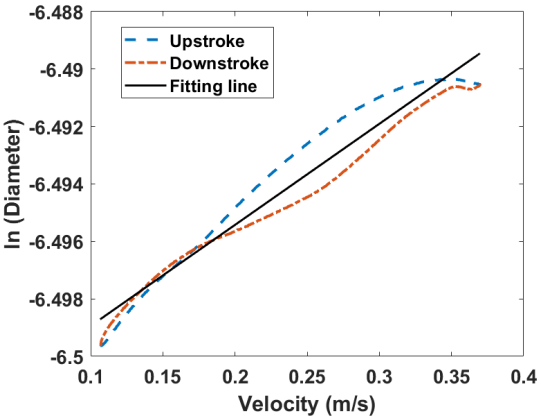

Fig. 3: ln DU-loops measured with ultrasound in the PVA Phantom (for a pump speed of 60 RPM). The upstroke is represented with a discontinued line. The straight line represents the fitting of the loop and provides the value of the slope.

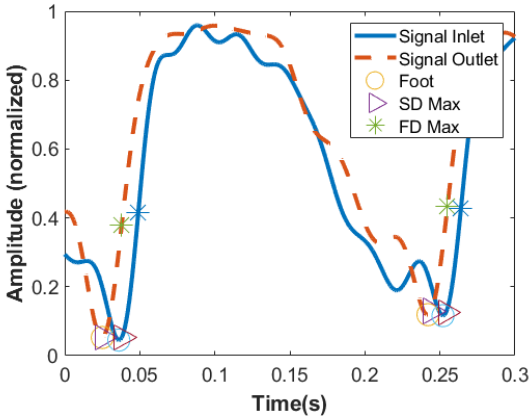

Fig. 4: Waveforms measured with the commercial pressure sensors at the inlet and outlet of the phantom for a pump velocity of 70 RPM. The fiducial points (Foot, FD Max and SD Max) used for the PTT calculation are indicated in the plot with symbols.

of-flight equation. For the velocity, the short-time-fourier-transform provided us with the spectrogram of the ultrasound images. The four algorithms described in [5] are applied into the obtained spectrogram to automatically determine the mean particle velocity in the fluid. An example of the application of the four algorithms to obtain the velocity waveforms is shown in Figure 2.

Velocity-Diameter Loop

Once that the velocity and diameter waveforms for each pump speed are obtained, it is possible to plot the diameter-velocity loops (DU-loops). According to [6], the local wave speed can be determined from the linear relationship between diameter and velocity (when only unidirectional waves are present). That means, if we construct ln DU-loops, the forward wave corresponds to a straight line in the early part of the cycle. After determining the straight line, the wave speed can be estimated as the inverse of the slope of that straight line, following Eq. (2).

$$PWV(US) = \frac{1dU}{2d(lnD)} = \frac{1}{2slope} \qquad (2)$$

The ln DU-loops have been calculated with MATLAB for each of the pump speeds. An example is illustrated in Figure 3. Afterwards linear fitting is applied (in the form of $y = x * slope + b$) to determine the slope of the linear region of the curves. For each Pump speed, the PWV is calculated four times (one for each of the velocity algorithms applied for the velocity spectral estimation).

Validation with two pressure sensors

The PWV obtained with high-frequency ultrasound can be validated by placing two pressure sensors at the inlet and outlet of the phantom. For the determination of the time difference between the two pressure waveforms (PTT), various fiducial points can be used. The most typical one is to use the foot of the waveform. However that point shows non-linear behaviour and reflected waves in some of our measurements. Therefore, apart from the foot, also the peak or maximum of the first derivative (FD Max) and of the maximum of the second derivative (SD Max) are applied as fiducial points for the determination of the PTT.

Figure 4 shows two measured waveforms (at the inlet and the outlet) with the corresponding fiducial points. The PWV is determined dividing the distance between the pressure sensors by the PTT at those fiducial points.

Results

The mean and standard deviation values of the PWV measurements at the different pump speeds (between 30 RPM and 100 RPM) for the pressure sensors is shown in Tab. 1. The PWV determined at the peak of the first derivative provides the highest value, with 12.23 m/s and a standard deviation of 0.61 m/s. When using the foot as the fiducial point the PWV is reduced to 9.23 m/s. However the peak of the second derivative provides a slightly higher PWV (10.06 m/s) with the minimum variation between values (0.39 m/s of standard deviation).

The PWV measured by the ln DU-loops with ultrasound are compared to the PWV measured by the

Tab. 1: Local PWV measurements with the pressure sensors

Fiducial point (Pressure sensors)	PWV average m/s	PWV std m/s
Foot	9.23	1.01
FD Max	12.23	0.61
SD Max	10.06	0.39

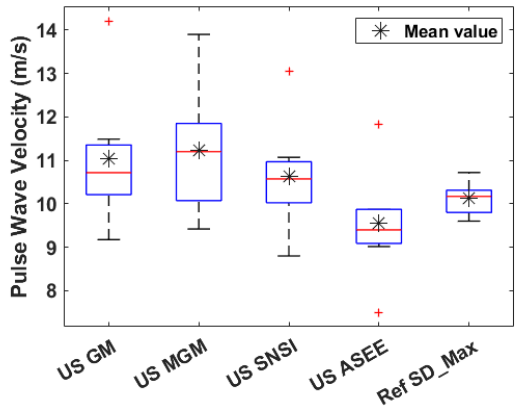

Fig. 5: Box-plots of the PWV measured by ultrasound (In DU-loops) obtained by four ultrasound velocity derivation methods: GM, MGM, SNSI, ASEE. The reference value of PWV measured by the commercial sensors and calculated at the fiducial point SD Max is included for comparison.

pressure sensors in the box-plots of Figure 5. We include only the PWV determined with the SD Max for simplicity in the comparison. The SNSI method in ultrasound provides the lowest PWV error in comparison to the commercial pressure sensors. SNSI achieved a mean PWV of 10.63 m/s and a median PWV of 10.57 m/s. That means, a mean difference with the SD Max of 0.51 m/s (error of 5 %) and a median difference of 0.4 m/s (error of 5.04 %). The ultrasound method with the highest error is the MGM, with a mean error of 1.1 m/s, and a median difference of 1.03 m/s.

Thus, we demonstrate that the custom made high-frequency mono-channel ultrasound can be used to determine the PWV as a potential predictor of atherosclerosis and cardiovascular risks.

Conclusion

In this paper we show and validate a proof-of-concept of a high-frequency monochannel transducer working at 20 MHz for cardiovascular applications. The ultrasound device requires low power, it is non-invasive and low-cost and provides very accurate measurements of PWV in-vitro at single segments of the artery. Through this method the mistakes due to the inhomogeneity of the arterial-tree and the change of PWV through the periphery can be avoided. Thus, high-frequency ultrasound may provide a more patient-specific and more accurate prediction of the vascular age of our microvascular system.

Acknowledgements

The authors would like to thank the department of biomedical microtechnology, for they constant support. This work was supported by the Federal Ministry of Economics, Science and Arts of Baden Wuerttemberg (Margarethe-von-Wrangell Habilitation program) and by the Wissenschaftliche Gesellschaft in Freiburg. This work was funded with 1.026 million € by the Comunidad de Madrid through the LUNABRAIN-CM R&D activities program (TEC-2024/TEC-43), granted by Order 5696/2024; and also by the project PID2022-1380130B-I00 from the Spanish Ministry of Science and Innovation.

References

[1] S. W. A. Diaz M. Tringler et al. "The effects of age on pulse wave velocity in untreated hypertension". In: *J Clin Hypertens (Greenwich)* 20(2) (2018), pp. 258–265. DOI: 10.1111/jch.13167.

[2] P. N. R. Manoj K.V. Raj et al. "Measurement of pressure dependent variations in local pulse wave velocity within a cardiac cycle from forward travelling pulse waves". In: *Sci Rep* 15 (3066) (2025), p. 3066. DOI: 10.1038/s41598-025-87143-z.

[3] E. S. Peper et al. "Regional assessment of carotid artery pulse wave velocity using compressed sensing accelerated high temporal resolution 2D CINE phase contrast cardiovascular magnetic resonance". In: *Journal of Cardiovascular Magnetic Resonance* 20 (2018), pp. 1–12.

[4] C.-J. Tang et al. "Measurement of local pulse wave velocity for carotid artery by using an ultrasound-based method". In: *Ultrasonics* 102 (2020), p. 106064.

[5] A. Kathpalia et al. "Adaptive spectral envelope estimation for Doppler ultrasound". In: *IEEE transactions on ultrasonics, ferroelectrics, and frequency control* 63.11 (2016), pp. 1825–1838.

[6] J. Feng and A. Khir. "Determination of wave speed and wave separation in the arteries using diameter and velocity". In: *Journal of biomechanics* 43.3 (2010), pp. 455–462.

DOI 10.5162/Ultrasonic2025/B7-b3

A 128-channel Ultrasound Imaging System for High Frame Rate Imaging

Xi Zhang[1] *and Jianguo Ma*[1,2]
[1]*School of Instrumentation and Optoelectronics Engineering, Beihang University*
[2] *the Hangzhou International Innovation Institute, Beihang University*
majianguo@buaa.edu.cn

Abstract: Ultrafast ultrasound imaging has opened up new avenues for applications in clinical diagnostics and biomedical research. We developed an open ultrasound platform based on a single FPGA to enable high-frame-rate beamforming. The system comprises a commercial PC for user interaction and an ultrasound acquisition card connected via PCIe 3.0, supporting real-time beamforming and programmable transmission/reception. The parallel delay-and-sum beamformer is implemented using data register shifting technology and can output beamformed images of 128×2048 at a frame rate of 10,557 fps.

Keywords: Beamforming, DAS, FPGA, ultrafast ultrasound, ultrasound system

Introduction

Ultrafast ultrasound technology is increasingly vital for advanced applications like microvascular blood flow imaging and functional ultrasound imaging, fueling the need for higher frame rates in open ultrasound systems [1], [2]. Commercial medical ultrasound systems support various imaging modes but often lack the flexibility needed for research involving custom ultrasound probes. To facilitate advanced ultrasound research, more open and configurable ultrasound platforms are essential. Some commercial open platforms, such as Verasonics, utilize soft beamformers implemented on multi-core CPUs and GPUs[3], [4]. These platforms offer high flexibility and support the development of novel image reconstruction algorithms. Thanks to fully parallel processing, they can even achieve real-time beamforming with frame rates exceeding 1000 fps. However, the performance of soft beamforming is ultimately limited by the data transfer bandwidth of PCI-Express or other high-speed interfaces, as raw RF data must be sent to the host processor for processing.

In contrast, other platforms such as the ULA-OP 256 employ hardware beamformers implemented on field-programmable gate arrays (FPGAs) or application-specific integrated circuits (ASICs)[5]. While hardware beamformers are generally less flexible and harder to modify once deployed, they are capable of much higher frame rates—often surpassing 3000fps—because the FPGA can be directly connected to analog-to-digital converters (ADCs), bypassing the data transfer bottleneck of soft beamforming. Moreover, systems based on FPGA beamforming tend to be smaller, more energy-efficient, and more portable compared to those relying on CPUs and GPUs.

The Delay-and-Sum (DAS) algorithm remains the most widely adopted and straightforward approach for digital beamforming[6]. Although implementing beamforming on a single FPGA simplifies the hardware design of ultrafast ultrasound systems, the need to store a large number of delay values required by the DAS algorithm imposes a considerable burden on FPGA resources. To overcome this limitation, a parallelized FPGA-based DAS architecture has been recently proposed, achieving a beamforming frame rate exceeding 10,000 frames per second for images with a resolution of 128×2048[7].

In this work, we developed a 128-channel ultrafast open ultrasound platform using a single FPGA, and the parallel DAS is implemented in this FPGA. The platform consists of a commercial personal computer (PC) and an ultrasound card, which is connected via PCIe 3.0. The main function of the PC is to interact with users and display information, while the ultrasound card serves as the core component of the platform, enabling beamforming and fully configurable transmission and reception signals. Meanwhile, a sub-aperture 64-channel DAS beamformer is implemented in the FPGA of the ultrasound card. In the beamformer, left and right shifts of the shift register replace the spatial distances between transducer array elements and ultrasound image pixels, enabling parallel DAS beamforming. The beamformer operates at 200 MHz and achieves 10557 frames of image output for 128×2048 images.

Method

Considering a uniform linear array, assuming the pitch of the rectilinear arrays is p, and the total number of array elements is N_X. After beamforming, the image pixel pitch is lp, j is the j-th pixel,and the

DOI 10.5162/Ultrasonic2025/B7-b3

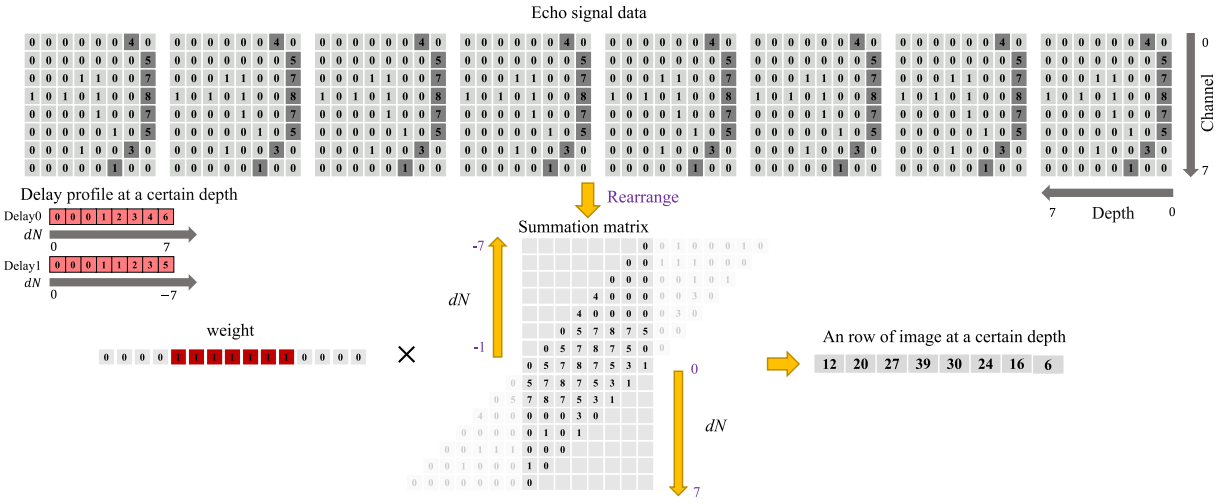

Fig. 1: Schematic diagram of the DAS algorithm for outputting 8 pixels in parallel. Eight copies of the echo signal data sampled from the eight channels are created and stored separately in the memory. Simultaneously, eight delay values at the same depth are read from Delay0 (with positive dN) and Delay1 (with negative dN). Then, the echo signal data are read based on these delay values and shifted left or right according to the corresponding positive or negative dN. Afterward, the processed echo signal data are rearranged in the summation matrix and multiplied by a weight vector related to the sub-aperture. Finally, row summation of the summation matrix is performed to obtain the 8 pixels of the image.

total number of pixels is N_I.The delay value of the parallel DAS with a steering angle θ towards and from a scatterer at (x, z) is written as follows:

$$\tau\left(dN, z, \theta\right) = \left(z * cos\theta + I_p * dN * sin\theta + \sqrt{\left(I_p * dN\right)^2 + z^2}\right)/c \quad (1)$$
$$dN \in \{dN \in \mathbb{Z} | -max(N_X, N_I) \leq dN \leq max(N_X, N_I)\}$$

Where c is the speed of sound. The detailed implementation method of parallel DAS is shown in Fig. 1. It is worth mentioning that the signals are arranged in a summation matrix, and the rows of the summation matrix represent the sub-aperture sizes. Therefore, dynamic aperture can be achieved by multiplying a weight vector representing the aperture with the summation matrix.

Experiments and results

The hardware architecture of the ultrafast open ultrasound platform is shown in Fig.2. The platform comprises a host PC and an ultrasound card, which is inserted into the PCIe slot on the motherboard, similar to a graphics card. The ultrasound card is based on a single Kintex UltraScale FPGA (XCKU060-FFVA1156-2-I; Xilinx Inc., San Jose, CA, USA). This card leverages four three-level pulser transmit/receive switch chips (TX7332, Texas Instruments) to transmit pulses and four analog front-end chips (AFE5832, Texas Instruments) to receive echo signals. The FPGA independently manages eight chips with a serial peripheral interface (SPI) to control 128 probe elements. The flexible printed circuit (FPC) connector interfaces the probe and the system. Meanwhile, the ultrasound card, measuring 12 cm×21 cm and comparable in size to a standard graphics card, is designed to be inserted into the PCIe slot on the PC motherboard, where the raw RF data or beamformed RF data is transferred via the PCIe (PCIe 3.0 x8) interface to a host PC.

The software architecture of the ultrafast open ultrasound platform is illustrated in Fig. 2. The analog echo signals from 128 channels are sampled by AFE chips and transmitted to the FPGA via the LVDS (Low-Voltage Differential Signaling) interface. On the FPGA, the sampled signals are pre-processed by a signal processor to generate raw RF data. This raw RF data is filtered by a first-order high-pass filter, and the filtered signals are then beamformed by a parallelized DAS beamformer to produce beamformed RF data. Subsequently, the beamformed RF data is stored in an 8 GB dynamic random-access memory (DDR) with a data transfer rate of 153.6 Gbps. Finally, the beamformed RF data is transferred to the host PC through PCIe for generating B-mode images for display. The host PC precisely controls the parallel DAS beamformer and ultrasound chip controller by manipulating registers, providing the system with a high degree of flexibility and configurability. In terms

DOI 10.5162/Ultrasonic2025/B7-b3

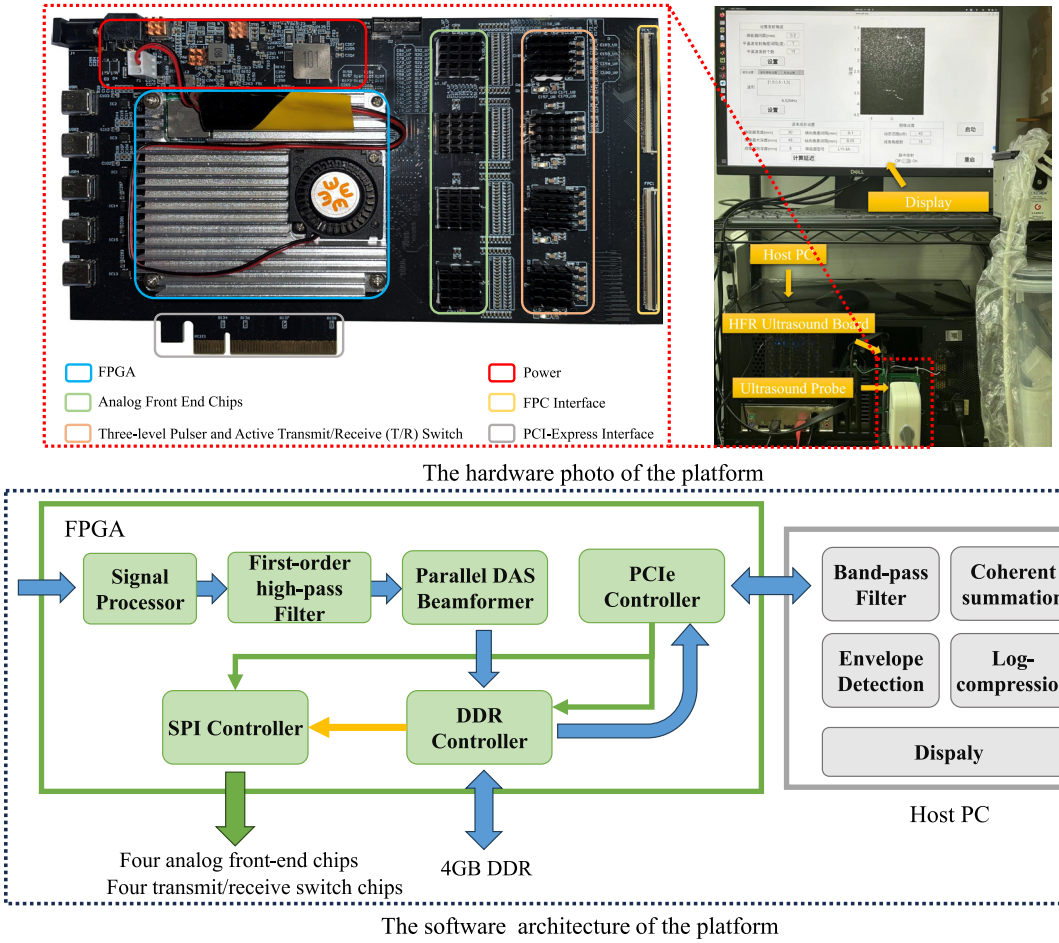

Fig. 2: The hardware and software architecture of the platform

Tab. 1: Main Parameters of the Platform

General Features	128 independent TX/RX channels; Architecture: ultrasound card + host PC; Ultrasound card size: 12 cm × 21 cm; Display frame rate: 15 fps for 15 angles
Transmitter	Three-level adjustable waveform; Output voltages: ±10 Vpp to ±90 Vpp; Minimum pulse width: 10 ns
Receiver	Analog gain: 12 dB to 51 dB; Programmable DTGC; 12-bit @ 40 MSPS ADCs
Beamformer	Configurable based on probe; Operating frequency: 200 MHz; Up to 15 imaging angles 10,557 fps for 128 × 2048 images.
Operating System	Ubuntu 21.04

of FPGA resource consumption, the largest consumption is from LUT and BRAM, accounting for 40.56% and 70.83% of the total usage, respectively. The main parameters of the platform are listed in Tab.1. In order to further verify the effectiveness of the system, experiments based on a phantom were designed and completed. A 128-element, 6.5MHz commercial uniform linear array, L11-3A, was used to acquire a B-mode ultrasound image of commercial small parts phantoms, Sono404(Sun Nuclear, USA). The PRF was set at 5KHz, and the steering angle was applied with angles ranging from -7° to 7° in 1° increments, for a total of 15 angles. And the sample frequency was set at 26.67MHz, the transmit pulse voltage was set to ±60V. First, the raw echo data is acquired using the platform and uploaded to the PC. Then, the MUST beamforming method is applied on the PC to perform DAS beamforming[8]. Subsequently, beamforming is performed using the platform's parallel DAS beamformer, and the resulting data is transferred to the PC for further processing and display. The final ultrasound images of the phantom are shown in Fig. 3.

As shown in Fig. 3, the differences can be observed between the images generated by the platform and those obtained using the MUST method. Visually, the

DOI 10.5162/Ultrasonic2025/B7-b3

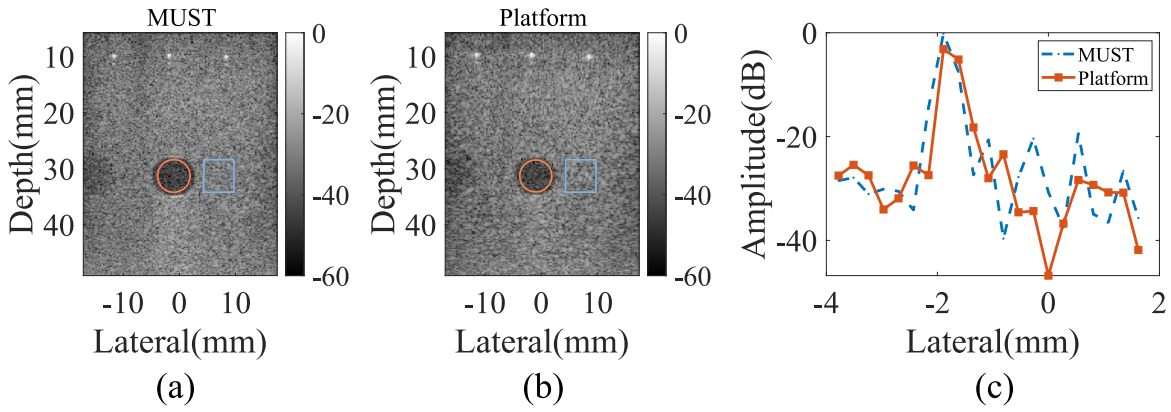

Fig. 3: (a) The results of MUST, (b) results from the platform, (c) the lateral intensity variation of the central strong scatterer.

Tab. 2: The quality of image.

	CR	CNR	FWHM(mm)
MUST	13.77	1.7684	0.3881
Platform	12.00	1.46	0.3375

image quality of the platform output appears somewhat inferior, primarily because the MUST method utilizes full-aperture imaging with floating-point computation, while the platform employs 16-bit fixed-point arithmetic, leading to truncated output values. To further assess image quality, the contrast ratio (CR), contrast-to-noise ratio (CNR), and full width at half maximum (FWHM) are used as evaluation metrics. The region of interest is indicated by a red circle, the background region by a blue rectangle, and the FWHM is calculated based on the central strong scatterer. The results are presented in Tab.2.

Conclusion

In this work, we developed an ultrafast ultrasound imaging platform based on a single FPGA, with a parallel DAS beamformer implemented directly on the hardware. Phantom experiments demonstrate that the image quality of the platform output is somewhat lower than that of the MUST method. However, the platform achieves a significantly higher frame rate. The observed image degradation is acceptable for most applications. Overall, the proposed ultrasound platform is capable of performing ultrafast imaging effectively.

Acknowledgment

This research was funded by the Fundamental Research Funds for the Central Universities (JKF-20240571).

References

[1] J. Bercoff. "Ultrafast ultrasound imaging". In: *Ultrasound imaging-Medical applications* (2011), pp. 3–24.

[2] M. Tanter and M. Fink. "Ultrafast imaging in biomedical ultrasound". In: *IEEE transactions on ultrasonics, ferroelectrics, and frequency control* 61.1 (2014), pp. 102–119.

[3] D. Hyun et al. "An open source GPU-based beamformer for real-time ultrasound imaging and applications". In: *2019 IEEE International Ultrasonics Symposium (IUS)*. IEEE. 2019, pp. 20–23.

[4] B. G. Tomov, R. Daigle, and J. A. Jensen. "Ten-minute continuous acquisitions with the verasonics vantage research scanner". In: *2023 IEEE International Ultrasonics Symposium*. IEEE. 2023.

[5] E. Boni et al. "ULA-OP 256: A 256-channel open scanner for development and real-time implementation of new ultrasound methods". In: *IEEE transactions on ultrasonics, ferroelectrics, and frequency control* 63.10 (2016), pp. 1488–1495.

[6] V. Perrot et al. "So you think you can DAS? A viewpoint on delay-and-sum beamforming". In: *Ultrasonics* 111 (2021), p. 106309.

[7] Z. Kou et al. "High-level synthesis design of scalable ultrafast ultrasound beamformer with single FPGA". In: *IEEE transactions on biomedical circuits and systems* 17.3 (2023), pp. 446–457.

[8] D. Garcia. "SIMUS: An open-source simulator for medical ultrasound imaging. Part I: Theory & examples". In: *Computer Methods and Programs in Biomedicine* 218 (2022), p. 106726.

DOI 10.5162/Ultrasonic2025/B12-a2

Ultrasound Localization of Microbubbles for Active Microrheology of Viscoelastic Media

Anne-Lise DUROY[1], Antoine PENNERON[1], Thomas BRUNET[1], and Diego BARESCH[1]
[1] Univ. Bordeaux, CNRS, Bordeaux INP, I2M, UMR 5295, F-33400, Talence, France
anne-lise.duroy@u-bordeaux.fr, diego.baresch@u-bordeaux.fr

Abstract: Investigating the mechanical properties of biological media over several scales is important for our fundamental understanding of complex biological processes. In this paper, an active microrheology approach for viscoelastic media is proposed, which relies on the use of acoustical tweezers to force individual microbubbles and the ultrasound localization of its induced displacement. Our study shows that a good localization accuracy is achieved and can resolve displacements that are typically observed under acoustic forcing experiments.

Keywords: Microrheology, Ultrasound localization, Acoustical tweezers, Microbubbles, Viscoelasticity

Introduction

From tissues to single cells, investigating the mechanical properties of biological media is essential to study biological processes, and for diagnostic and treatment purposes. It is now known that developing organisms are sensitive to their mechanical environment, and that there is a reciprocal feedback between mechanosensing mechanisms at the cellular scale and the macroscopic properties of tissue [1]. Thus, methods to probe the biomechanical properties of complex systems over several length and time scales are required to provide a finer understanding of the fundamental phenomena involved in the emerging field of mechanobiology.

Several experimental techniques have been developed to actively probe the rheological properties of complex biological systems by manipulating small probe particles *in situ*, and can operate from the subcellular to the multi-cellular tissue scales [2, 3, 4, 5]. For instance, optical tweezers are precise, efficient and versatile tools for manipulation at the sub-cellular scale, but do not easily penetrate into thick, generally opaque-to-light media, and generate weak forces (10-100 pN) despite the high light intensities required, limiting their use at the multi-cellular scale. Magnetic tweezers can generate larger forces (1-100 nN), but they are applied along one direction fixed by the orientation of the magnetic field, making them not well adapted to characterize anisotropic and heterogeneous media. Very recently, acoustic approaches have emerged and highlight the suitability of using the high magnitude radiation forces (1-1000 nN) to probe the rheology of a variety of bulky soft biological materials [6, 7]. In this context, further removing the need for optical imaging methods to track the displacement of the probe particles could open interesting perspectives for the microrheological characterization of a range of currently inaccessible biological systems at the cellular and multi-cellular levels.

In this paper, we propose a proof-of-concept for a method based on the ultrasonic localization of microbubbles displaced by the radiation force generated in acoustical tweezers [7]. Originally developed for vascular imaging, Ultrasound Localization Microscopy (ULM) can provide super-resolution images by tracking the displacement of a large number of microbubbles (MBs) over time using high frame rate ultrasound images [8]. Implementing an ultrasound localization method within the framework of active microrheology could be promising provided the following requirements are met: (i) minute displacements of a MB in response to an applied force are detected, (ii) this detection is obtained with a good spatio-temporal resolution, and (iii) the localization remains robust for MBs embedded in media of increasing complexity. Here, we consider the tracking of an individual MB embedded in a simple viscoelastic media and show that the precision of the localization combined with the good temporal resolution afforded by programmable ultrasonic platforms can allow to assess local rheological properties.

Numerical Method

Several approaches are available to implement ULM methods [8, 9, 10]. Yet, they are all based on detecting and tracking of numerous MBs over time using their characteristic isolated signatures within ultrasound images. In the application proposed here, our focus is on the localization of a single MB whose displacement will be imposed by the local force generated by acoustical tweezers.

Because of their small size ($R_0 \ll \lambda$), where λ is

the imaging wavelength, MBs can be considered as punctual scatterers whose a spherical wave propagating outwards, resulting in a characteristic wavefront (hyperbola) that can be distinguished in raw (or radio-frequency, RF) images [11]. The shape and position of this hyperbola can be described by the time-of-flight (Tof), or the time for the emitted signal to travel through the medium to the MB position (z, x) and back to a transducer element (z_e, x_e). Assuming a constant speed of sound, c_0, and considering an incident plane wave illumination, the Tof equation reads:

$$\tau = \frac{z + \sqrt{(z_e - z)^2 + (x_e - x)^2}}{c_0}. \qquad (1)$$

Thus, a MB can simply be localized within ultrasound images by timing on each element the arrival of the spherical wavefront in the RF image and fitting the experimental hyperbola to the Tof equation, with (z, x) as a couple of adjusting parameters. To obtain the images, numerical simulations are built using the *k-Wave*® open-source toolbox[12]. Space and time are discretized on a regular grid, and the acoustic field is computed at each node of the mesh. To simulate pulse-echo RF images, grid points in the transducer regions are both sources and sensors. More specifically, grid points corresponding to the active elements are modeled as time varying pressure sources, while those within the kerf are left empty. At reception, the signals are averaged over the grid points describing each element, and down-sampled to match a realistic sampling frequency of common ultrasonic imaging platforms. The medium can either be considered homogeneous, with mechanical properties corresponding to water, or contained inhomogeneities by introducing spatial fluctuations of the density and speed of sound values using a normal distribution with standard deviation σ around the properties of water.

Adopting a similar workflow to that described in Ref.[13], the RF images are computed as follows:

1. An incident plane wave is emitted within the medium without considering the MB existence. The pressure field generated by medium inhomogeneities (P_m) is recorded at the transducer positions. Simultaneously, the pressure is computed at the MB positions to estimate the pressure (P_{ac}) experienced by the MB.
2. The MB response to P_{ac} is computed using the nonlinear Marmottant model [14], and the pressure field scattered by the MB (P_s) is determined on the bubble surface and re-injected as a punctual pressure source.
3. The scattered field P_s is finally propagated in the direction of the receivers, and added to the back-scattered field P_m, to form the final RF image.

Consecutive RF images for a moving MB are built by repeating step $2-3$ for the different positions of the MB, and for the different imaging probe parameters presented bellow.

To obtain the hyperbola within RF images, a Hilbert transform is applied to the received signals to extract the pulse envelope. Then, a rectangular region of interest (ROI) containing the MB echo is defined through the normalized cross-correlation between the envelope and that of the emitted signal. Indeed, it is expected that the MB back-scattered pulse will be highly correlated with the emitted signal. The correlation threshold defining the ROI is chosen as a trade-off between a minimal size of the ROI, and a minimal Signal-to-noise ratio (SNR) of the received signals. Finally, we determine the experimental hyperbola by timing the arrival of the maximum of the envelop. Finally, a fit to Eq. (1) using a non-linear regression algorithm provides an estimation of the MB position (z, x).

Results and discussion

Let us first consider a perfectly homogeneous medium imaged with a 5MHz imaging probe (pitch: 600 μm, sampling frequency: $f_s = 25$ MHz), and containing a single MB. The MB is displaced along a two-dimensional path defined by 9 successive positions (Fig. 1-a). The path is located beneath the central element of the imaging probe at a depth of 10 mm. We are interested in the errors, (δ_u,δ_v), inherent to the localization method for the detection of the MB displacement vector (u, v), where $u = z_{i+1} - z_i$ and $v = x_{i+1} - x_i$ are obtained at MB positions i and $i+1$ (Fig. 1-b,c). It is seen that the localized displacement is very close to the ground truth in both directions. The estimated errors are approximately $\delta_u \sim \frac{\lambda}{60}$ and $\delta_v \sim \frac{\lambda}{15}$ in the axial and lateral directions respectively. The better performance in the vertical direction can be ascribed to the good temporal sampling $(1/f_s)$ that allows for a precise timing of the MB back-scattered pulse arrival, whereas the accuracy in the lateral direction is limited by the aperture and the number of transducer elements [11]. Since distant imaging elements can rapidly suffer from a low SNR, a restricted ROI has to be defined as discussed above.

Next we explore the influence of three different parameters on the displacement error estimation: the strength of the medium inhomogeneities (image speckle) in Figure 2-a, the pitch of the imaging probe (aperture) in Figure 2-b, and the central frequency F_0 in Figure 2-c. It can be observed that the displacement precision decreases in both directions with

DOI 10.5162/Ultrasonic2025/B12-a2

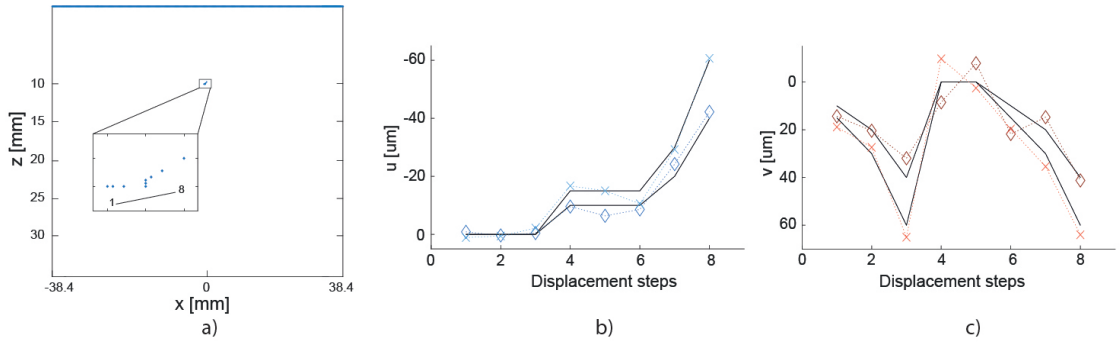

Fig. 1: (a) Scheme of a homogeneous medium imaged using a 600 μm pitch transducer with a central frequency of 5MHz, where each point represents the MB displacement steps. (b) Axial u and (c) lateral v displacement components. The black lines show the ground truth, and the color diamonds the results for different data sets obtained by changing the magnitude of the displacement steps in the initial path.

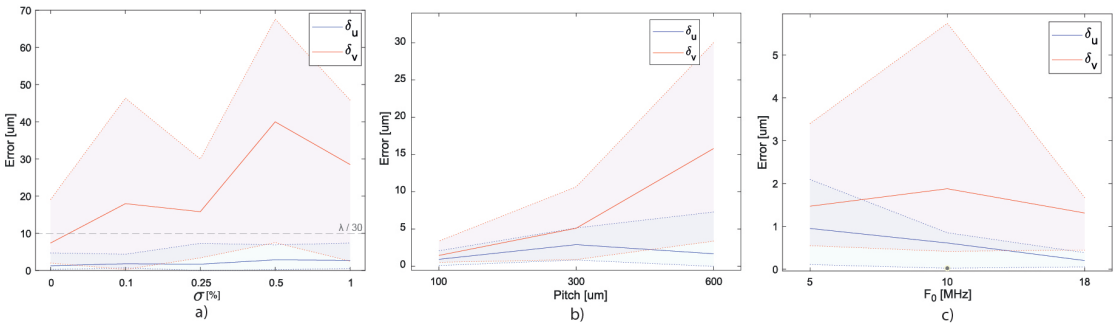

Fig. 2: Estimated axial δ_u (blue) and lateral δ_v (red) displacement errors as a function of: (a) σ (or speckle level in the image), (b) the pitch of the transducer and (c) the central frequency F_0. Solid lines show the median error, and the shaded regions the dispersion of the results.

increasing σ, with a prominent influence on δ_v, because of the degraded SNR. However, the increase of δ_u is very limited, suggesting that the proposed tracking approach will be robust in the axial direction for media of increasing complexity. Regarding the influence of the pitch of the 128-element probe, a net increase in the precision is observed in both directions when the pitch is decreased. This result confirms that the main contribution to the error arises from a degraded SNR on the lateral extremities of the probe. Therefore, it is better to reduce the physical aperture of the probe if the SNR is expected to be poor on the sides and populate this aperture with a maximum number of elements. This result is also suggested in Ref.[11]. Finally, the influence of the central imaging frequency shows that, whereas the error is low for $F_0 = 5$ and 18 MHz, it surprisingly increases for $F_0 = 10$ MHz. This result is possibly due to a decrease in the scattering cross-section of a single MB relatively close but away from the MB resonance, that will then increase again for a higher frequency. This result suggests that properly understanding the physics of the bubble oscillations is important to set the parameter space for future experiments. It's also worth noting that the estimated MB displacement is always more accurate in the axial direction, and is therefore preferred hereafter.

To finish, a proof of concept for the tracking of a single MB in a typical active microrheology experiment performed in a viscoelastic medium having a shear modulus $\mu = 1$ kPa, a viscosity $\eta = 0.1$ Pa.s, and a mild level of inhomogeneities ($\sigma = 0.25$ %) is shown in Figure 3. Using an external force of 50 μN generated by acoustical tweezers [7], a MB (radius $R_0 = 20$ μm) is displaced from its initial position during a 10 ms radiation force pulse in the axial direction of the imaging probe. The theoretical curve is computed using a rheological model [15] and used as the ground truth trajectory. Using a 128-element imaging probe of 18 MHz central frequency and a pitch of 100 μm, we can see that the localization method presented here is able to capture very accurately the trajectory of the displaced MB. Therefore, in a situation where the medium's properties are unknown, the

accurate detection of the MB displacements could provide a micromechanical characterization of the medium using a rheological model.

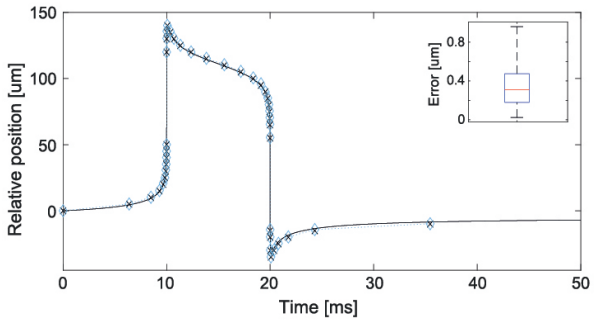

Fig. 3: Typical displacement of a single MB in an active rheology experiment. Solid line show the ground truth, the color diamonds the results, and the box-plot the estimated errors.

Conclusion

In summary, a tracking method for active microrheology experiments with ultrasound was presented. A single MB is forced with acoustical tweezers and the induced displacement is tracked via the sub-wavelength ultrasound localization of the MB. Our results suggest that the good localization precision, especially in the axial direction, of a high frequency imaging probe is well-suited to track complex MB displacements in two-dimensions, showing a promising route for the local micro-mechanical characterization of a variety of complex media, including biological tissues.

References

[1] J. M. Barnes, L. Przybyla and V. M. Weaver, 'Tissue mechanics regulate brain development, homeostasis and disease,' *Journal of Cell Science*, vol. 130, no. 1, pp. 71–82, 2017.

[2] K. Svoboda and S. M. Block, 'Biological applications of optical forces.,' *Annual review of biophysics and biomolecular structure*, vol. 23, pp. 247–85, 1994.

[3] P. Roca-cusachs, V. Conte and X. Trepat, 'Quantifying forces in cell biology,' *Nature Publishing Group*, 2017.

[4] Y. L. Han et al., 'Cell swelling and softening and invasion in a and three-dimensional breast cancer model,' *Nature physics*, vol. 16, pp. 101–108, 2019.

[5] G. Laloy-Borgna et al., 'Magnetic microelastography for evaluation of ultrasound-induced softening of pancreatic cancer spheroids,' *Physical Review Applied*, vol. 22, no. 2, p. 024 024, 2024.

[6] G. Bergamaschi et al., 'Viscoelasticity of diverse biological samples quantified by Acoustic Force Microrheology (AFMR),' *Communications Biology*, vol. 7, no. 1, 2024.

[7] A. Penneron, T. Brunet and D. Baresch, 'Active rheology of soft solids performed with acoustical tweezers,' *Applied Physic Lette*, vol. 126, p. 084 104, 2025.

[8] O. Couture, V. Hingot, B. Heiles, P. Muleki-Seya and M. Tanter, 'Ultrasound localization microscopy and super-resolution: A state of the art,' *IEEE Transactions on Ultrasonics, Ferroelectrics, and Frequency Control*, vol. 65, no. 8, pp. 1304–1320, 2018.

[9] K. Christensen-Jeffries et al., 'Super-resolution ultrasound imaging,' *Ultrasound in Medicine & Biology*, vol. 46, no. 4, pp. 865–891, 2020.

[10] C. Hahne, G. Chabouh, A. Chavignon, O. Couture and R. Sznitman, 'Rf-ulm: Ultrasound and localization microscopy and learned from radio-frequency and wavefronts,' *IEEE Transactions on Medical Imaging*, 2023.

[11] Y. Desailly, J. Pierre, O. Couture and M. Tanter, 'Resolution limits of ultrafast ultrasound localization microscopy,' *Physics in medicine & biology*, vol. 60, pp. 8723–8740, 2015.

[12] B. Treeby, J. Jaros, A. Rendell and B. Cox, 'Modeling nonlinear ultrasound propagation in heterogeneous media with power law absorption using a k-space pseudospectral method,' *Journal of the Acoustical Society of America*, vol. 131, no. 6, pp. 4324–4336, 2012.

[13] J. Brown et al., 'Investigation of microbubble detectionmethods for super-resolution imaging of microvasculature,' *IEEE Transactions on Ultrasonics, Ferroelectrics, and Frequency Control*, vol. 66, no. 4, pp. 676–691, 2019.

[14] P. Marmottant et al., 'A model for large amplitude oscillations of coated bubbles and accounting for buckling and rupture,' *Journal of the Acoustical society of america*, vol. 118, pp. 3499–3505, 2005.

[15] Y. a. Ilinskii, G. D. Meegan, E. a. Zabolotskaya and S. Y. Emelianov, 'Gas bubble and solid sphere motion in elastic media in response to acoustic radiation force,' *The Journal of the Acoustical Society of America*, vol. 117, no. 4, p. 2338, 2005.

DOI 10.5162/Ultrasonic2025/B14-a1

Interfacial State Assessment using Vibration-based Shear Wave Elastography

Naoki Tano[1], Keigo Taniguchi[2], Kousuke Shiwaku[2], Kei Konno[3], Ren Koda[4], Yoshiki Yamakoshi[4], and Marie Tabaru[1]
[1]Institute of Science Tokyo, 4259 Nagatsuta-cho, Midori-ku, Yokohama-shi, Kanagawa
[2]Sapporo Medical University, 17, Minami-1-jonishi, Chuo-ku, Sapporo-shi, Hokkaido
[3]Jichi Medical University, 3311-1, Yakushiji, Shimotsuke-shi, Tochigi
[4]Gunma University, 1-5-1, Tenjin-cho, Kiryu-shi, Gunma
tano.n.d336@m.isct.ac.jp

Abstract: Fascia hydrorelease is an emerging technique aimed at improving gliding around fascial layers. This study investigates how interfacial conditions around fascia affect shear wave propagation. We conducted Finite-Difference Time-Domain simulations and ex-vivo measurements to assess shear wave phase morphology. Both approaches showed that reduced interfacial adhesion leads to measurable phase shifts. These results suggest that shear wave phase analysis may offer a means to assess fascial adhesion.

Keywords: Shear wave elastography, Phase velocity, Fascia, Hydrorelease, Acoustic morphology

Introduction

Fascia is a connective tissue that links muscles to surrounding anatomical structures, forming a continuous, intricate web throughout the entire body [1]. Inflammation and fibrosis cause abnormal fascia to develop, resulting in increased tissue stiffness and restricted range of motion. These conditions can lead to musculoskeletal disorders like frozen shoulder, significantly reducing patients' quality of life [2]. Hydrorelease (HR) has recently gained attention as a therapeutic technique for addressing disorders related to the fascia. HR is performed under ultrasound guidance to deliver saline into the fascial layers, aiming to normalize fascial mobility [3]. A previous biomechanical study has reported reduced gliding resistance following HR [4], suggesting that the procedure may alter interfacial adhesion conditions.

To evaluate such mechanical properties non-invasively, shear wave elastography (SWE) has emerged as a promising modality. Several studies have applied SWE to the myofascial tissue and estimated its elasticity based on the group velocity of shear waves [5, 6]. However, group velocity-based methods assume that the medium is linear, elastic, and locally homogeneous. These assumptions may not hold for myofascial tissue, which typically measures less than 4 mm in thickness [7]. In contrast, phase velocity-based approaches can be better suited for those thin-layered, potentially heterogeneous structures, and are thus considered more appropriate for assessing the mechanical properties of shear waves in fascial tissue. The influence of interfacial conditions on shear wave propagation, however, remains underexplored and is investigated in this study using a phase velocity-based approach. In this research, we conducted Finite-Difference Time-Domain (FDTD) simulations in which interfacial parameters were introduced to model varying adhesion conditions. In addition, ex-vivo experiments were performed using chicken breast, where HR was applied between the pectoralis major and minor muscles to alter fascial adhesion. The resulting morphological characteristics of shear wave phase were visualized using a Doppler-based phase reconstruction method previously developed by the authors [8, 9].

Shear Wave Reconstruction Method

During shear wave propagation, the ultrasound probe detects a Doppler frequency shift, denoted as $\Delta\phi$. The received signal can be expressed as:

$$y(x,z,t) = a \cdot \exp\left(j\left(2\pi f_0 t + \Delta\phi\left(x,z,t\right)\right)\right), \quad (1)$$

where f_0 is the center frequency of the ultrasound probe, and a is the signal amplitude. Through quadrature detection, the complex Doppler component $\exp\left(j\Delta\phi\right)$ can be extracted. The Doppler phase shift can be related to the axial particle displacement as follows:

$$\exp\left(j\Delta\phi\left(x,z,t\right)\right) = \exp\left(j\frac{4\pi f_0}{c} \cdot u_z\left(x,z,t\right)\right). \quad (2)$$

Here, $u_z\left(x,z,t\right)$ represents the displacement of particles along the z-axis. This displacement can be modeled by the following shear wave equation:

$$u_z\left(x,z,t\right) = u_0 \sin\left(2\pi f_s t + \boldsymbol{k}\cdot\boldsymbol{x}\right), \quad (3)$$

DOI 10.5162/Ultrasonic2025/B14-a1

where f_s is the shear wave frequency, u_0 is the displacement amplitude and $\boldsymbol{k}$ is the wavenumber of the shear wave. Accordingly, the spatial phase distribution of the shear wave can be obtained by calculating the argument of the complex Doppler signal.

Simulation

The propagation of shear waves was simulated using the FDTD method. The basic governing equations are derived from the Navier-Stokes equation:

$$\frac{\partial v_x}{\partial t} = \frac{1}{\rho}\frac{\partial \sigma}{\partial z}, \tag{4}$$

$$\frac{\partial v_z}{\partial t} = \frac{1}{\rho}\frac{\partial \sigma}{\partial x}, \tag{5}$$

$$\frac{\partial \sigma}{\partial t} = \mu\left(\frac{\partial v_z}{\partial x} + \frac{\partial v_x}{\partial z}\right) + \eta\left(\frac{\partial \dot{v_z}}{\partial x} + \frac{\partial \dot{v_x}}{\partial z}\right). \tag{6}$$

Here, v_x and v_z represent particle velocity in the x and z directions, respectively. ρ is the density of the medium, σ is the stress, μ is the shear mululus, and η is the viscosity coefficient. HR is known to reduce adhesions between myofascial tissue and surrounding tissues. To model this interfacial effect, we introduced adhesion coefficients α_x and α_z, which modify the interaction across interfaces. The modified set of equations incorporating these coefficients is expressed as:

$$\frac{\partial v_x}{\partial t} = \frac{1}{\rho}\cdot\alpha_z\frac{\partial \sigma}{\partial z}, \tag{7}$$

$$\frac{\partial v_z}{\partial t} = \frac{1}{\rho}\cdot\alpha_x\frac{\partial \sigma}{\partial x}, \tag{8}$$

$$\frac{\partial \sigma}{\partial t} = \mu\left(\alpha_x\frac{\partial v_z}{\partial x} + \alpha_z\frac{\partial v_x}{\partial z}\right) + \eta\left(\alpha_x\frac{\partial \dot{v_z}}{\partial x} + \alpha_z\frac{\partial \dot{v_x}}{\partial z}\right). \tag{9}$$

The adhesion coefficients α_x and α_z range from 0 to 1.0, where $\alpha = 1.0$ represents a fully continuous medium. These coefficients modulate the degree of interfacial continuity in the x and z directions, respectively, by scaling the spatial derivatives $\partial/\partial x$ and $\partial/\partial z$. Values less than 1 indicate a reduction in interfacial adhesion, with lower values corresponding to weaker adhesion across the interface.

The resulting phase distributions from the simulation are shown in Fig. 1. The simulation parameters are summarized in Tab. 1. As shown in Fig. 1-a, when the adhesion coefficient was low ($\alpha = 0.1$), a clear phase shift was observed at the interface located at $z = 10$ mm. In contrast, no significant phase shift was observed when the adhesion coefficient was set to $\alpha = 1.0$, representing a fully adhered interface. Fig. 1-b shows the relationship between the adhesion coefficient and the observed phase shift. As α decreased from 0.5 to 0.1, the phase shift at the interface increased from 0.08 rad to 0.47 rad. These results indicate that weaker interfacial adhesion causes greater discontinuities in shear wave propagation, resulting in a greater phase shift.

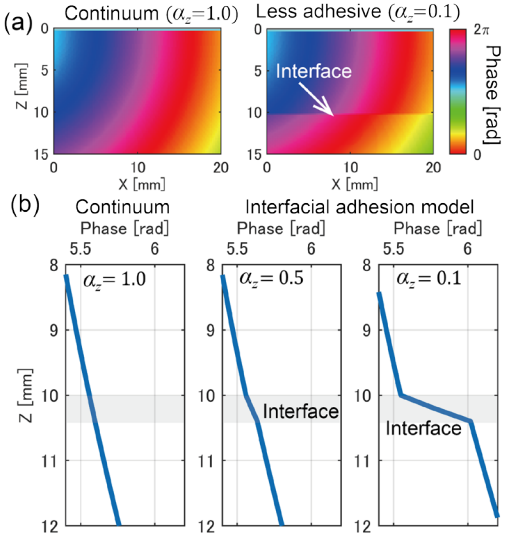

Fig. 1: (a) Phase map from the simulation output at adhesion coefficient $\alpha = 1.0$ (left) and $\alpha = 0.1$ (right). (b) Phase plots at $x = 10$ mm with different adhesion coefficients.

Tab. 1: 2D-FDTD simulation parameters in this study.

Parameter	Value
Model size	50×100 mm
Grid size	0.2 mm
Shear wave frequency	78 Hz (continuous)
Young's modulus	20 kPa
Viscosity η	0.002 Pa·s
Adhesion coefficient α	$0 - 1.0$

Experiments

To experimentally validate the phase shift phenomenon observed in the 2D-FDTD simulation, we conducted an ex-vivo experiment using a commercially available chicken breast tissue. The overall experimental setup is illustrated in Fig. 2-a. Shear wave measurements were performed both before and after the HR procedure to assess changes in interfacial adhesion. The first measurement was taken prior to HR, and the second was acquired 5 minutes after the intervention. The HR procedure was performed using an ultrasound imaging system (Logiq E10, GE Health-

DOI 10.5162/Ultrasonic2025/B14-a1

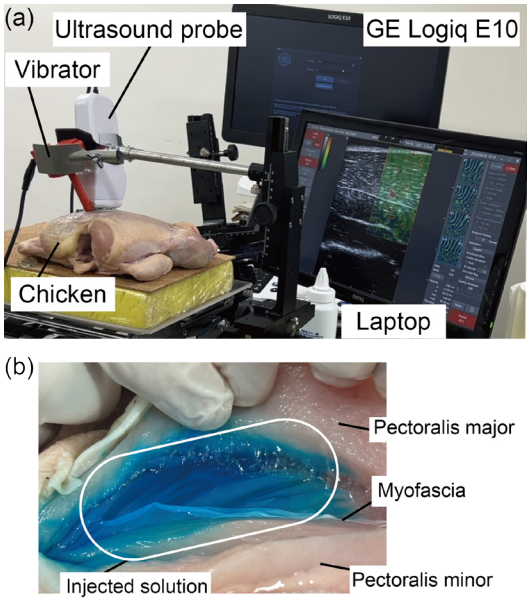

Fig. 2: a) Ex-vivo experimental setup. b) Dissection of chicken breast after HR, validating the successful injection of blue-dyed saline onto the myofascial tissue.

Care, USA) equipped with a linear probe (L2-9VN-D, center frequency: 9 MHz). To alter the degree of adhesion, 2.5 ml of blue-dyed saline solution was injected between the fascia and the overlying pectoralis major muscle. As shown in Fig. 2-b, anatomical dissection confirmed that the solution was correctly delivered into the fascial layer between the pectoralis major and minor muscles. Shear wave measurements were conducted using a separate linear array ultrasound probe (Finggal Link, Japan; 128 active elements, center frequency: 10 MHz). Shear waves were generated using an external mechanical vibrator operating at 78 Hz. The Finggal Link probe was mounted on a 5-axis stage, enabling precise repositioning to the same anatomical location before and after the HR procedure. The shear wave field was reconstructed on a laptop using the Doppler-based phase reconstruction method previously developed by the authors [10].

Results

) The spatial phase distribution of the shear wave is presented as heatmaps in Fig. 3-a. Following HR, a noticeable phase shift was observed, which resembled the simulation results assuming a non-adherent interface. Specifically, a phase shit of 1.2 rad was measured at $x = 4$ mm. As shown in Fig. 3-b, this phase shift extended across 5 mm, indicating a broader spatial spread compared to the sharp transition observed in the FDTD simulation. It is noted that this spread is larger than the fascial thickness observed on the B-mode image, which was approximately 0.5 mm.

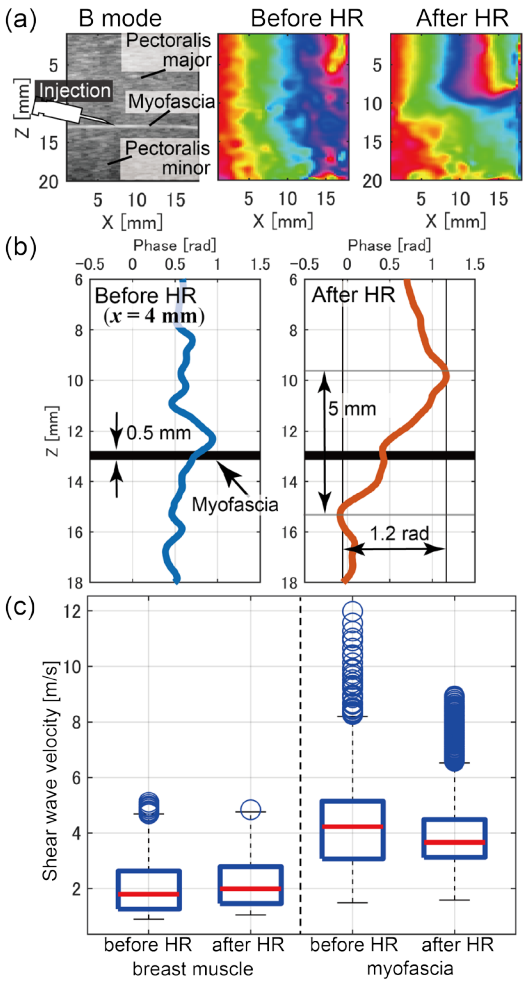

Fig. 3: (a) Resultant B-mode image and shear wave phase map before and after HR. (b) Shear wave phase plot at $x = 4$ mm, before and after HR. (c) Box plots of shear wave velocity within breast muscle and myofascial tissue.

The measured shear wave velocities are summarized as box plots in Fig. 3-c. Within the pectoral muscle, the velocity was 2.02 ± 0.85 m/s, while in the myofascial tissue it increased significantly to 4.35 ± 1.70 m/s. This velocity increase suggests that the fascia possesses higher stiffness than the surrounding muscle tissue, which is consistent with previous elastography studies on fascia [11]. After HR, the shear wave velocity in the myofascial tissue slightly decreased to 4.11 ± 1.60 m/s. This reduction may indicate that the injected saline temporarily decreased fascial elasticity due to the presence of interfacial fluid.

Discussion

Our results indicate that interfacial adhesion between fascia and surrounding tissue affects shear wave phase behavior, with detectable phase shifts observed in

both FDTD simulations and ex-vivo experiments.
However, the observed phase shift in the ex-vivo experiment extended across 5 mm, which is substantially greater than the fascial thickness of about 0.5 mm observed in B-mode imaging. This discrepancy is likely attributed to the limited spatial resolution associated with the relatively low shear wave frequency (78 Hz) used in this study.
Anatomical differences between the chicken breast model and human fascia should also be considered. For instance, the human fascia lata is approximately 1 mm thick [12], notably thicker than the chicken fascia used here. Such structural differences may influence shear wave propagation and affect the applicability of these findings to human tissue.
Furthermore, the shear wave velocity in the myofascial tissue after HR was 4.11 ± 1.60 m/s, consistent with previously reported values (3.8–5.1 m/s) [11]. However, this may have been influenced by the observed phase shifts. Future work should aim to decouple these effects to improve elasticity assessment.
Finally, while the FDTD simulation modeled interfacial adhesion using simplified coefficients α_x and α_z, biological interfaces are more complex. Future simulations should incorporate additional physical parameters, such as friction and interfacial fluid viscosity, to better represent tissue interactions. This may offer deeper insights into how HR improves fascial mobility in clinical contexts.

Conclusion

This study demonstrated that the interfacial adhesion between the fascia and adjacent tissues significantly affects the propagation characteristics of shear waves. Specifically, both FDTD-based numerical simulations and ex-vivo experiments using chicken breast confirmed that reduced interfacial adhesion leads to a distinct phase shift in shear wave propagation. These findings suggest that shear wave elastography has the potential to evaluate fascial adhesion. Future work may focus on both shear wave velocity and waveform morphology to enable a deeper and more comprehensive assessment of tissue characteristics.

Acknowledgements

This work was supported in part by JSPS KAKENHI Grant Number 25K01237, the Cooperative Research Project of Research Center for Biomedical Engineering, JKA's promotion funds from KEIRIN RACE, and a research granted from Murata Science and Education Foundation.

References

[1] D. Marić et al. "FASCIA–THE FORGOTTEN TISSUE". In: *Exercise and quality of life* 6.1 (2014), p. 31.

[2] H. Kanamoto et al. "Effect of Ultrasound-Guided Hydrorelease of the Multifidus Muscle on Acute Low Back Pain". In: *Journal of Ultrasound in Medicine* 40.5 (2021), pp. 981–987.

[3] K. Shiwaku et al. "Fascial Ultrasound-Guided Injection: Where Do We Really Inject?" In: *Cureus* 17.2 (2025).

[4] K. Shiwaku et al. "Biomechanical effects of fascial hydrorelease: a cadaveric study". In: *BMC Musculoskeletal Disorders* 26.1 (2025), p. 306.

[5] L.-R. Liao et al. "Reliability of shear-wave elastography in assessing the stiffness of the nuchal fascia and the thickness of upper cervical muscles". In: *Medical Engineering & Physics* 120 (2023), p. 104039.

[6] T. L.-W. Chen et al. "Ultrasound elastographic assessment of plantar fascia in runners using rearfoot strike and forefoot strike". In: *Journal of Biomechanics* 89 (2019), pp. 65–71.

[7] J. M. Fabrikant and T. S. Park. "Plantar fasciitis (fasciosis) treatment outcome study: plantar fascia thickness measured by ultrasound and correlated with patient self-reported improvement". In: *The Foot* 21.2 (2011), pp. 79–83.

[8] N. Tano et al. "Continuous Shear Wave Elastography for Liver Using Frame-to-Frame Equalization of Complex Amplitude". In: *Ultrasonic Imaging* 46.3 (2024), pp. 197–206.

[9] M. Tabaru et al. "Examination of rapid adjustment system based on screen score obtained using continuous shear wave elastography". In: *Journal of Medical Ultrasonics* 51.3 (2024), pp. 407–418.

[10] R. Koda et al. "Application of continuous shear wave elastography method with multiple frequency selection to liver viscoelasticity measurement". In: *Japanese Journal of Applied Physics* 63.4 (2024), 04SP82.

[11] G. Schillizzi et al. "Evaluation of plantar fasciopathy shear wave elastography: a comparison between patients and healthy subjects". In: *Journal of Ultrasound* 24 (2021), pp. 417–422.

[12] S. Otsuka et al. "Investigation of the association between human fascia lata thickness and its neighboring tissues' morphology and function using B-mode ultrasonography". In: *Journal of Anatomy* 239.5 (2021), pp. 1114–1122.

DOI 10.5162/Ultrasonic2025/B14-a4

Multiple imaging techniques for assessing ocular lesions

N.T. Bui[1], *X. Zhang*[1], *and L. A. Dalvin*[2]
[1]*Department of Radiology, Mayo Clinic, Rochester, MN, USA*
[2]*Department of Ophthalmology, Mayo Clinic, Rochester, MN, USA*
corresponding.authors@zhang.xiaoming@mayo.edu

Abstract: This research is to develop ultrasound vibro-elastography (UVE), Nakagami imaging and power doppler intensity (PDI) image for assessing choroidal nevus and melanoma lesions of human eyes. Significant differences between the ratios of shear wave speed (SWS) between the nevus and melanoma lesions are obtained. Significant differences in contrast to noise ratio of Nakagami-m map are found between the nevus and melanoma lesions. The PDI within the nevus is significantly lower than that of melanoma which corresponds to lower blood volume.

Keywords: Ultrasound vibro-elastography, Nakagami imaging, Microvessel imaging, Melanoma, Nevus.

1. Background, Motivation and Objective

Ocular lesions can only be accurately diagnosed based on tumor biopsy; however, this is an invasive method and is not recommended for use in clinical diagnosis [1, 2, 3, 4]. Therefore, the development of non-invasive imaging tools plays an important role in the diagnosis and monitoring of ocular lesions. Ultrasound is one of the non-invasive methods that plays an important role in the detection and assessment of abnormal eye tumors [1, 5].

Ultrasound elastography is a novel imaging technique for assessing the biomechanical properties of soft tissues. The ultrasound vibro-elastography (UVE) systems use ultrafast frames to capture high-speed images to detect tissue motion. Therefore, using UVE systems to study eye lesions is an effective method and has great potential when applying ultrafast imaging techniques to analyze various components in the lesion including vessel density, back scattering distribution, and biomechanical properties [1, 6, 5].

Quantitative ultrasound (QUS) technique is widely used to analyze tissue characteristics based on the distribution of scattering and reflection amplitudes of radio frequency (RF) signals [7, 8, 9, 10]. QUS images are reconstructed based on tissue microstructure, mechanical properties have demonstrated significant potential in the assessment of abnormal tumors. Shear wave elastography technique is mainly applied to assess the mechanical properties of tissue based on the measurement of shear wave velocity (SWV) in tissue. In addition, Nakagami distribution is a statistical model to use shape parameters to describe the mechanical characteristics of soft tissue by determining the scattering characteristics in tissue [10, 11, 12, 13, 14]. The vessel density is another technique to assess the structure of tissue based on the density of vessels in tumor [5]. All the above techniques have made important contributions to the study of lesion assessment.

For UVE systems, there are 3 basic components in the RF signal: first, the RF signal for reconstructing B-mode image; second, SWV propagating in the tumor; third, the signal for reconstructing the amplitude of SWV in the tumor. To combined with the analysis above, we evaluated the eye lesion based on the analysis of the 3-signal obtained from the UVE system combined with three different imaging techniques.

2. Materials and Methods

2.1 Participants

Ten patients (i.e., 5-melanoma and 5-nevus) were enrolled in this study (i.e., from October 2023 to April 2024) with an institutional review board-approved protocol (IRB: 23-003112, Mayo Clinic, Rochester, MN, USA). Details of the 10 subjects were presented in our previous study and Table 1 below.

2.2 Ultrasound vibro-elastography system

Fig. 1 shows that the UVE system (Vantage-256) was equipped with a linear array transducer (L11-5v, Philips Healthcare, Andover, MA). This UVE system was used for a plane wave imaging sequence with a 0.1second data accumulation (i.e., total of 200 frames with a pulse-repetition-frequency of 2000Hz at 100Hz, 150Hz, and 200Hz with an effective pulse-repetition-frequency (PRF) of 2000Hz). A numerical Butterworth band-pass filter of the fifth order with a cutoff frequency of 50Hz to 250Hz was used to remove tissue signal to give a good tradeoff between motion artifact filtering and microvasculature detection of the radiofrequency (RF) data of ultrasound systems [1, 15].

DOI 10.5162/Ultrasonic2025/B14-a4

Tab 1: Details of 10 subjects [1, 6]

Case	Melanoma (M)					Nevus (N)					*p-value*
	M-1	M-2	M-3	M-4	M-5	N-1	N-2	N-3	N-4	N-5	t-test unpaired, two-tailed
Age (years)	63	40	54	53	56	73	63	85	63	77	0.0098
Sex	M	F	M	F	M	M	F	F	M	F	
Lesion size (mm^2)	34.47	29.17	25.72	18.87	170.27	11.97	14.79	13.00	18.12	12.37	0.1892

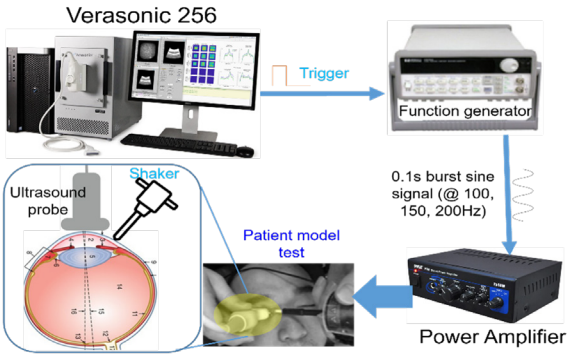

Fig. 1: Enter Caption
Overview of UVE system for eye study.

2.3 Parametric imaging methods

2.3.1 Power doppler intensity image technique

After applying filter autocorrelation to RF data of UVE system, we obtained complex ultrasonic signal s(x, z, t). Then, a power doppler intensity (PDI) image was calculated by estimating the average intensity of each pixel from this filtered data and converted to decibel scale (dB) [15].

$$I = \frac{1}{N}\sum_{k=0}^{N} S_B^2(t_i) \tag{1}$$

where N is the number of samples acquired and S_B the filtered signal. Color flow images were generated by using the 2-D autocorrelation method.

$$f_D = \frac{1}{N}\frac{\int_{-f_{S/2}}^{f_{S/2}} f|S_F^2(f)|df}{\int_{-f_{S/2}}^{f_{S/2}} |S_F^2(f)|df} \tag{2}$$

where S_F is the Fourier transform of the filtered signal (S_B) and f_s is the PRF. We masked the axial velocity image using power Doppler data to keep only the pixels with a sufficient intensity of blood signal.

2.3.2 Nakagami imaging technique

The distribution of the backscattered envelope r under the Nakagami model [6, 12] was calculated as:

$$f(r) = \frac{2m^m r^{2m-1}}{\Gamma(m)\Omega^m} exp(-\frac{m}{\Omega}r^2)U(r) \tag{3}$$

where Γ and U are the gamma and unit step functions, respectively.
The scaling parameter Ω (omega) was calculated as: $E(R^2)$, while the Nakagami parameter m associated with its distribution can be obtained as:

$$\Omega = E(R^2) \tag{4}$$

$$m = \frac{E(R^2)^2}{E(R^2) - E(R^2))^2} \tag{5}$$

where E denotes the statistical mean.

2.3.3 Two-dimensional speed map technique

The in-phase/quadrature (IQ) data consisted of two-dimensional (2D) intensity information for the duration of the vibration excitation. Particle velocity in the axial direction of the ultrasound beam (V) caused by wave propagation was used for wave speed (WS) estimation. V was calculated from IQ data of consecutive frames using an autocorrelation method. Then, Anderssen-Hegland techniques was used to calculate two-dimensional speed map (2D-SM) image value based on shear wave propagation [1, 16]. Details of the processing method for reconstructing 2D-SM were shown in Fig. 2 and our previous studies.

2.3.4 Statistical analysis

Mean values of PDI, contrast-to-noise ratio (CNR) of Nakagami-m, and ratio-WS were compared between N and M using t-test unpaired, two-tails, parametrics. Statistical analysis was performed using GraphPad Prism version 10.0 software [1].

DOI 10.5162/Ultrasonic2025/B14-a4

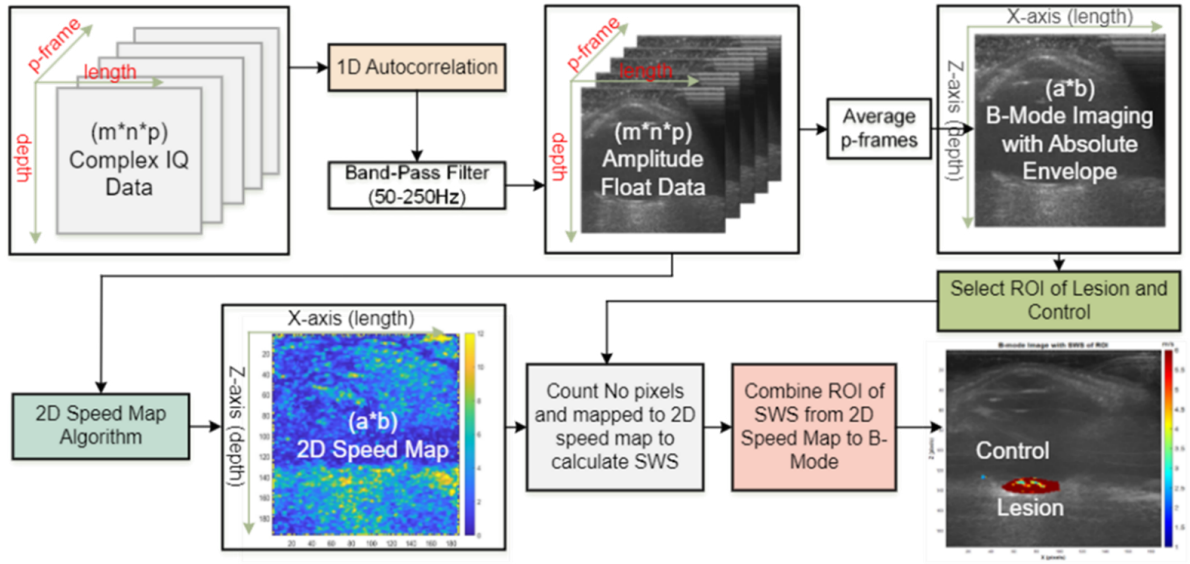

Fig. 2: Overview of reconstruction 2D-SM method from IQ data based on UVE system.

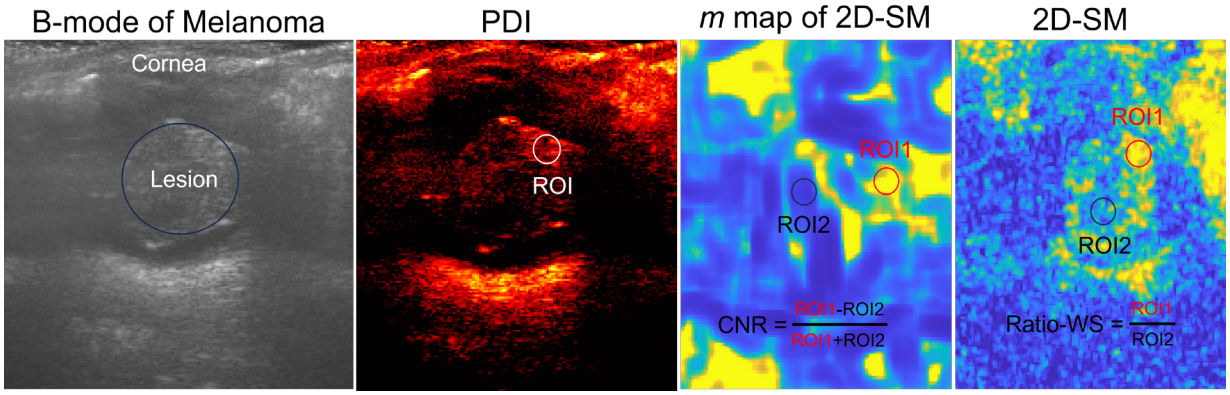

Fig. 3: An example of B-mode image, PDI with ROI, m map with ROI and CNR formular, 2D-SM with ROI and Ratio-WS formular.

3. Results

3.1 Select a region of interest for analysis

Nakagami distribution was used to calculate shape parameter (m) of SWP to create m maps. The 2D-SM and m map image was calculated for all differences frequencies. A region-of-interest (ROI as a circle with diameter of 2mm) was applied to PDI image for calculating PDI in the lesion. Two ROIs were applied to the near surface and central of lesion to calculate ratio-WS (WS of surface/ WS of central lesion). The contrast-to-noise ratio (CNR) of m map was obtained by using two ROIs (i.e., one ROI places inside lesion and another one places at normal tumor close to lesion) [1, 6]. Fig. 3 shows details of these selection.

3.2 Evaluation eye lesion with three different imaging techniques

Fig. 4 shows the comparison of three parametric imaging techniques between N vs. M. The PDI within the nevus was significantly lower than melanoma (N: -68.08 $\pm$ 6.47dB vs. M: -51.33 $\pm$ 8.55dB; $p = 0.0095$) which corresponds to lower blood volume. There were significant differences ($p = 0.0109$) of ratio-WS between N vs. M and significant differences ($p = 0.0086$) in CNR of m map reconstruct from 2D-SM between nevus and melanoma. Details of these results were shown in Table 2.

4. Discussion

The purpose of this study was to investigate effective methods for assessing of choroidal nevus and

Tab 2: Comparison of PDI, CNR of m map image of ROI from 2D-SM, and Ratio-WS.

	Nevus		Melanoma		*p-value*
	mean ± SD	95% CI of mean	mean ± SD	95% CI of mean	
PDI	-51.33 ± 8.55	-57.48 to -45.17	-68.08 ± 6.47	-72.54 to -55.63	0.0095
CNR *of m*	1.32 ± 0.15	1.14 to 1.52	3.94 ± 1.68	1.85 to 6.02	0.0086
Ratio-WS	1.70 ± 0.14	1.52 to 1.88	3.31 ± 1.08	1.96 to 4.64	0.0174

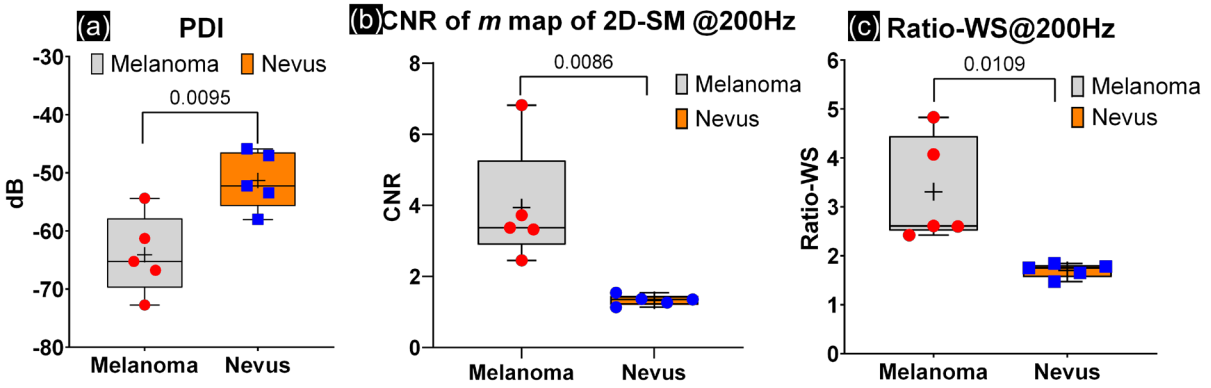

Fig. 4: The comparison of: (a) PDI (n = 5) between N vs. M, (b) CNR of m map with ROI of image reconstructed from 2D speed map (n = 5) between N vs. M, (c) Ratio-WS from 2D-SM (n = 5) between N vs. M with ROI a circle with diameter of 2mm.

melanoma lesions of the human eye based on ultrasound UVE, ultrafast ultrasound microvessel imaging, and parametric imaging techniques. We demonstrated the purposes based on two main objectives: 1) to evaluate data from the UVE system with 3 different imaging techniques including PDI, Nakagami, 2D-SM; 2) to search for biomarkers [9] that can be considered for clinical trials for eye lesions based on the above 3 imaging techniques. In this context, we found that PDI, CNR of Nakagami-m image of 2D-SM, and ratio-WS were statistically significant. These biomarkers have the potential to facilitate the design of smaller, more efficient clinical studies in future studies, thereby reducing the number of subjects exposed to experimental treatments. In addition, we demonstrated lower blood volume with nevus, which suggests a difference between nevus and melanoma patients. These findings are consistent with other studies of nevus vs. melanoma in different regions of the body [2]. Melanoma has a rapid and aggressive growth pattern and therefore requires a larger blood supply than nevus [3].

5. Conclusion

In the present study, we demonstrated three quantitative imaging techniques for assessing choroidal nevus and melanoma lesions of human eyes. Significant differences between the ratios of SWS between the nevus and melanoma lesions are obtained. Significant differences in CNR of m map are found between the nevus and melanoma lesions. The PDI within the nevus is significantly lower than that of melanoma. These techniques provide noninvasive and quantitative measurements for analyzing ocular lesions

References

[1] B. NT et al. "A noninvasive ultrasound vibroelastography technique for assessing ocular lesions". In: *Ultrasonics* 147 (2025), p. 107525. DOI: 10.1016/j.ultras.2024.107525.

[2] K. S, S. CL, and S. JA. "Uveal melanoma: estimating prognosis". In: *Indian J Ophthalmol* 63.2 (2015), pp. 93–102. DOI: 10.4103/0301-4738.154367.

[3] S. AD, T. ME, and T. AK. "Uveal melanoma: trends in incidence, treatment, and survival". In: *Ophthalmology* 118(9) (2011), pp. 1881–5. DOI: doi:10.1038/s41433-020-0885-1..

[4] J. MJ et al. "Uveal melanoma". In: *Nat Rev Dis Primers* 6(1) (2020), p. 24. DOI: 10.1038/s41572-020-0158-0.

[5] B. NT et al. "Analysis wave speed of optic nerve and optic nerve head for assessing normal tension glaucoma by using vibro-elastography technique". In: *Clin Biomech (Bristol)* 124 (2025), p. 106493.

[6] N. T. Bui, L. A. Dalvin, and X. M. Zhang. "Assessment of choroidal melanoma and nevus lesions using ultrasound vibro-elastography and parametric imaging approach". In: *Ultrasonics* 155 (2025). ISSN: 0041-624x. DOI: ARTN10772510.1016/j.ultras.2025.107725.

[7] P. D et al. "Quantitative Ultrasound for Periodontal Soft Tissue Characterization". In: *Ultrasound Med Biol* 51.2 (2025), pp. 288–301. DOI: 10.1016/j.ultrasmedbio.2024.10.003.

[8] L. M et al. "Spectral-based Quantitative Ultrasound Imaging Processing Techniques: Comparisons of RF Versus IQ Approaches". In: *Ultrason Imaging* 46.2 (2024), pp. 75–89. DOI: 10.1177/01617346231226224.

[9] S. K and T. JA. "What are biomarkers?" In: *Curr Opin HIV AIDS* 5.6 (2010), pp. 463–6. DOI: 10.1097/COH.0b013e32833ed177.

[10] Y. G et al. "A Systemic Study on the Performance of Different Quantitative Ultrasound Imaging Techniques for Microwave Ablation Monitoring of Liver". In: *IEEE Transactions on Instrumentation and Measurement* 72 (2023). DOI: 10.1109/TIM.2023.3267375.

[11] M. A, T. PH, and Z. P. "Changes in mechanical properties at the muscle level could be detected by Nakagami imaging during in-vivo fixed-end contractions". In: *PLoS One* 13.19 (2024). DOI: 10.1371/journal.pone.0308177.

[12] T. PH and C. CC. "Imaging local scatterer concentrations by the Nakagami statistical model." In: *Ultrasound Med Biol.* 33.4 (2007), pp. 608–19. DOI: 10.1016/j.ultrasmedbio.2006.10.005.

[13] H. M et al. "Ultrasonic Nakagami imaging for automatically positioning and identifying the treated lesion induced by histotripsy". In: *Ultrason Sonochem* 109 (2024), p. 107002. DOI: 10.1016/j.ultsonch.2024.107002.

[14] Y. G et al. "Multiple ultrasonic parametric imaging for the detection and monitoring of high-intensity focused ultrasound ablation". In: *Ultrasonics* 139 (2024), p. 107274. DOI: 10.1016/j.ultras.2024.107274.

[15] Z. Boran et al. "An Ultrafast Ultrasound Microvessel Imaging Technique for Assessing Patients with Unilateral Papilledema". In: *2018 IEEE International Ultrasonics Symposium (IUS)* (2018), pp. 1–4. DOI: 10.1109/ULTSYM.2018.8580168.

[16] Z. X et al. "Two dimensional penile ultrasound vibro-elastography for measuring penile tissue viscoelasticity: A pilot patient study and its correlation with penile ultrasonography". In: *J Mech Behav Biomed Mater* 103 (2020), p. 103570.

DOI 10.5162/Ultrasonic2025/B15-a1

Laser Micromachining for Fabrication of Low Frequency Single Crystal Piezocomposites

Tönnis Trittler[1], Christan Endisch[2], Sang-Goo Lee[3], Susan Walter[4], Julian Kober[1], Jochen Hampe[1], Henning Heuer[4], and Moritz Herzog[1]
[1] TUD Dresden University of Technology, Else Kröner Fresenius Center for Digital Health, Dresden, Saxony, Germany
[2] SITEC Industrietechnologie GmbH, Chemnitz, Saxony, Germany
[3] iBULe Photonics Co. Ltd, Incheon, Republic of Korea
[4] Fraunhofer Institute for Ceramic Systems and Technologies, Dresden, Saxony, Germany
toennis.trittler@tu-dresden.de

Abstract: This study investigates laser micromachining of the piezoelectric single crystal material PMN-PT for fabrication of piezocomposites below 20 MHz center frequency. Simulation reveals a drop of thickness coupling coefficient for decreasing wall angles, which are to be expected from such a process. However, absolute pressure output and bandwidth increase due to improved impedance matching resulting from a gradient of acoustic impedance. 2-2 piezocomposite samples were micromachined with depths of $130\ \mu\mathrm{m}$ and further processed to functioning piezocomposites with $8.78\ \mathrm{MHz}$ and $10.58\ \mathrm{MHz}$ center frequency.

Keywords: Laser Micromachining, Ultrashort Laser Pulses, Piezocomposite, Single Crystal, PMN-PT, Ultrasonic Transducer

Motivation

Ultrasonic transducers for medical imaging and Non-destructive Testing (NDT) primarily utilize piezocomposites, which combine active piezoelectric phases with passive polymeric phases [1], [2]. Piezocomposites offer advantages over monolithic material such as increased coupling coefficients, decreased dielectric constant, and lower specific acoustic impedance. Single-crystal piezoelectric materials such as PMN-PT (Lead Magnesium Niobate-Lead Titanate) are appealing due to their properties, but their brittleness complicates micromachining. For applications below 20 MHz, dicing saws are commonly used for fabrication of kerfs in the dice-and-fill process. However, the mechanical processing easily leads to the formation of microcracks, which complicates their handling. In the realm of nonmechanical processing methodologies, laser micromachining utilizing ultrashort laser pulses emerges as a compelling alternative. Laser micromachining of single crystal PMN-PT has been investigated for the fabrication of electro-mechanical actuators [3] as well as high frequency piezocomposites [4], [5] for frequencies above 20 MHz. The goal of our work is to investigate laser micromachining for fabrication of piezocomposites below 20 MHz. Given that this approach entails the introduction of a wall angle to the kerfs, the second objective of this study is to investigate the influence of uneven walls on transducer behavior using finite element (FE) simulation.

Simulation Study: Variation of Wall Angle

A FE simulation study was conducted using COMSOL Multiphysics™ Version 6.3 to investigate the influence of varying wall angles on piezocomposite performance. The frequency domain study covers a range from 1 MHz to 20 MHz. The model is based on a 2-2 piezocomposite unit cell configuration (Fig.1a) with the following geometric parameters: Thickness $t = 130\ \mu m$, pitch $p = 50\ \mu m$, kerf width $k = 30\ \mu m$, and pillar width $b = 20\ \mu m$. The wall angle was systematically varied around the middle axis, maintaining a constant piezoelectric material volume fraction of $40\ \%$ across all configurations. Nine distinct wall angles between 82° and 90° were investigated, with 90° representing the ideal reference case. The total aperture of the modeled structure was 5 mm × 5 mm. Two complementary 2D submodels were implemented for the analysis. The first model comprised a unit cell for electrical impedance calculation under mechanical free conditions on the end faces, using [001] PMN-28PT as piezoelectric material. Material parameters for PMN-PT are based on the results from Joh et al. [6]. Epotek 301-2 was used as passive phase with material constants $\rho = 1158\ \mathrm{kg/m^3}$, $v_\mathrm{l} = 2103\ \mathrm{m/s}$, $v_\mathrm{s} = 1082\ \mathrm{m/s}$. The second model adds a backing (Material: Ellsworth EP1121; $\rho = 1127\ \mathrm{kg/m^3}$, $v_\mathrm{l} = 2826\ \mathrm{m/s}$, $v_\mathrm{s} = 1484\ \mathrm{m/s}$; thickness $450\ \mu m$) and water domain for Transmitting Voltage Response (TVR) determination. This comprehensive model incorporates a circular water domain on top of the trans-

DOI 10.5162/Ultrasonic2025/B15-a1

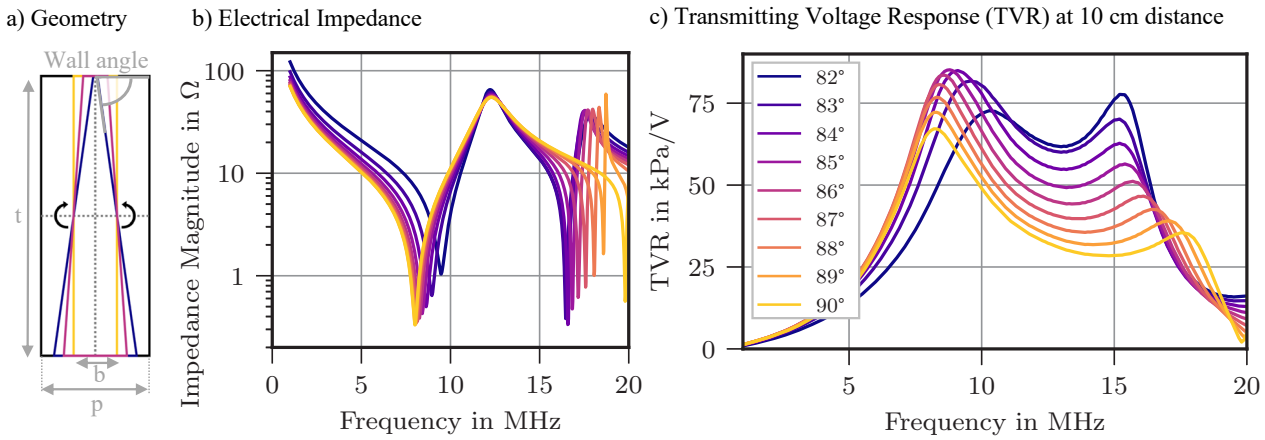

Fig. 1: Simulated unit cell geometry and resulting electrical impedance and transmitting voltage response curves for the simulation study.

ducer with perfectly matched layer and external pressure field calculation at 10 cm distance. The primary transducer characteristics evaluated were the thickness coupling coefficient k_t from electrical impedance data (see (1), according to IEEE standard [7]), center frequency f_c for the main thickness resonance from TVR, and the absolute -3 dB bandwidth from TVR.

$$k_\mathrm{t} = \sqrt{\frac{\pi}{2}\frac{f_\mathrm{r}}{f_\mathrm{a}}\tan\left(\frac{\pi}{2}\frac{f_\mathrm{r}-f_\mathrm{a}}{f_\mathrm{a}}\right)} \qquad (1)$$

The electrical impedance and TVR spectra for different wall angles are presented in Fig.1(b,c), while Fig.2 shows the extracted transducer characteristics.

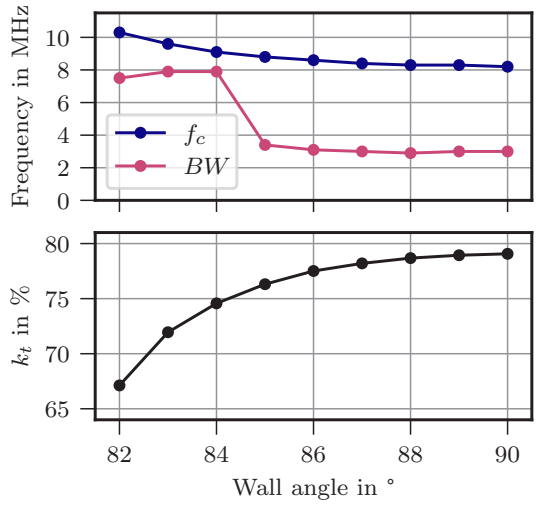

Fig. 2: Center frequency f_c, absolute bandwidth BW (-3 dB) and thickness coupling coefficient k_t.

The electrical impedance analysis reveals that the resonance frequency f_r shifts towards higher frequencies with decreasing wall angles, while the antiresonance frequency f_a remains constant. This behavior results in a decrease of the coupling coefficient k_t. Additionally, the polymer's spurious resonance exhibits a shift from 20 MHz to 17 MHz with decreasing wall angle. The TVR analysis demonstrates that the center frequency f_c shifts from 8.2 MHz to 10.3 MHz, correlating with the f_r shift observed in the electrical impedance data. The maximum TVR value shows an increase from 67.2 kPa/V at 90° to 85.2 kPa/V at 84°, followed by a decrease, though the value at 82° remains above the 90° reference. Concurrent with these changes, the polymer's spurious resonance shifts to lower frequencies with increasing amplitude, eventually exceeding the center resonance at 82°. A significant increase in the -3 dB bandwidth occurs between 84° and 85°. Overall, we observe on the one hand lower k_t with decreasing wall angle, but improved acoustic output in terms of maximum output pressure and bandwidth. This could be attributed to two competing mechanisms affecting transducer performance with decreasing wall angles. The first mechanism manifests as decreased thickness resonance efficiency with lower wall angles due to the changing aspect ratio and therefore increased lateral vibration modes. However, this is counterbalanced by the second mechanism, where improved impedance matching occurs due to lower impedance mismatch at the interface. The data suggests that this gradient of acoustic impedance along the thickness direction benefits transducer performance. The tradeoff between these opposing effects suggests an optimal wall angle range of around 84° for the investigated dimensions, maximizing bandwidth while

DOI 10.5162/Ultrasonic2025/B15-a1

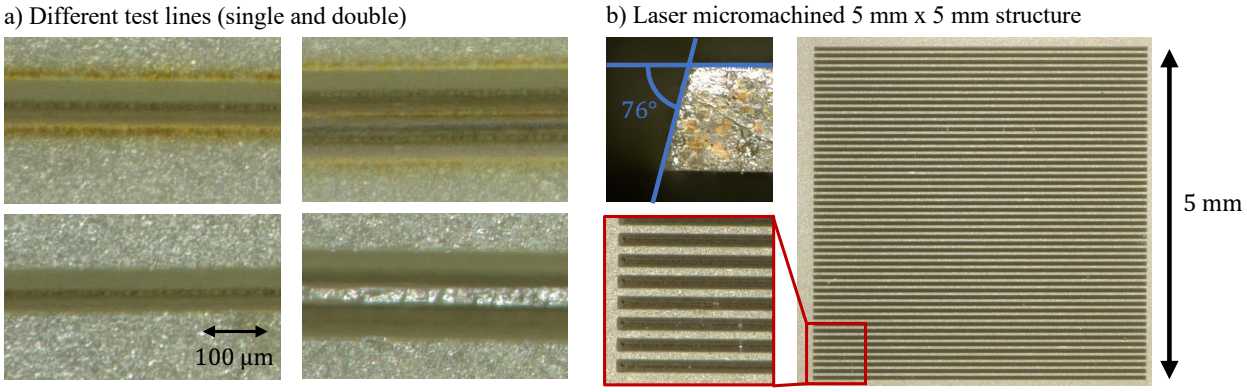

Fig. 3: Microscopy images showing the laser micromachined structures for a) the first ablation tests before and after ultrasonic cleaning and b) the finally produced structures for further piezocomposite fabrication.

maintaining acceptable coupling efficiency.

Laser Micromachining

Micromachining tests were performed using a SITEC Mikrolas machine equipped with a green laser ($\lambda = 514$ nm) operating with femtosecond pulses (Spirit100SHG). The optical setup consisted of a ScanLab intelliSCAN10 optic with 100 mm focal length. The system operated at an average power of 20 W (at 2 MHz) with a spot size of 12 μm.

Preliminary ablation tests were conducted to determine the power threshold and the fluence of the laser pulses for ablation. Based on these results single kerfs were ablated, followed by two parallel kerfs (see Fig. 3). Removal of debris and color changes around the kerfs was tried to remove by ultrasonic cleaning. This lead to breaking off of tips, as can be seen in Fig.3 a (bottom right). Therefore, a cleaning strategy using laser pulses below the ablation threshold was successfully implemented, leading to clean surfaces around the kerfs without breaking of tips. The final process parameters included a laser track spacing of 5 μm, operating frequency of 31.25 kHz, scan speed of 0.156 m/s, and pulse power set to 80%. Due to the heat sensitivity of the PMN-PT, the kerfs were not ablated one after another but layer by layer, quasi-simultaneously to distribute the heating. These parameters enabled the achievement of depths exceeding 120 μm without visible damage to the material.

Based on the test kerf results, a 2-2 piezocomposite structure was fabricated with parallel kerfs in one direction. The structure featured a pitch $p = 100\mu$m, wall angle of $76°$, and approximate depth of 130μm, covering a 5 mm $\times$ 5 mm area in total.

Piezocomposite Fabrication and Characterization

After laser micromachining, the produced samples were further processed into piezocomposites. First, the kerfs were filled with Epotek 301-2. The samples were subsequently lapped to achieve desired thicknesses of 130 μm and 200 μm, followed by chrome-gold metallization through sputtering. Poling was performed at 6 kV/cm, increased from an initial 5 kV/cm due to insufficient poling at lower fields. This could be attributed to non-uniform electrical field distributions due to the wall slope. The resulting structures are shown schematically in Fig. 4a.

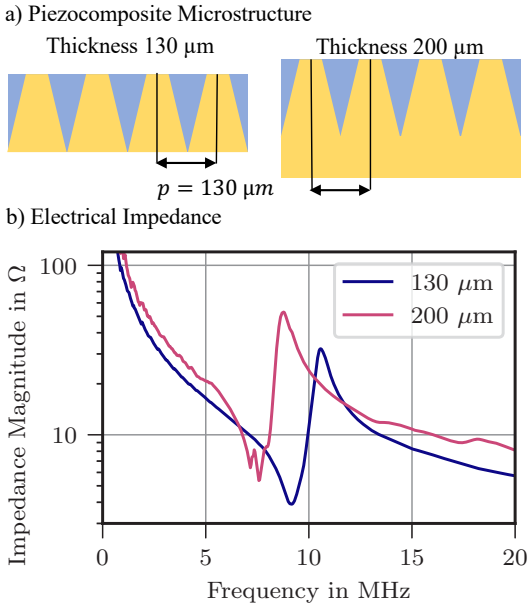

Fig. 4: Geometry (a) and electrical impedance measurement (b) of fabricated piezocomposite samples.

Tab. 1: Derived piezocomposite characteristics.

Thickness	$\varepsilon_{\mathrm{r}}^{\mathrm{T}}$	k_{t}	f_{a}
130 μm	1317	54.0 %	10.58 MHz
200 μm	1927	54.4 %	8.78 MHz

The thinner piezocomposite has kerfs extending to the bottom, whereas for the thicker piezocomposite a bridge of PMN-PT remains. These microstructures correspond to a piezoelectric volume fraction of $67\ \%$ for the thin piezocomposite and $78\ \%$ for the thicker one. Electrical impedance characterization was conducted using an Agilent 4294A impedance analyzer with an Agilent 16334A test fixture. The coupling coefficient k_t was derived according to (1), while the relative permittivity $\varepsilon_{\mathrm{r}}^{\mathrm{T}}$ was calculated from capacitance measurements at $1\ \mathrm{kHz}$. The antiresonance frequency serves as an indication of the center frequency of the piezocomposites. The complete results are summarized in Table 1. For comparison, the monolithic material exhibited a coupling coefficient k_t of $54.2\ \%$ and relative permittivity ϵ_{33} of 4842. The coupling coefficient of the piezocomposites does not exceed the one for pure PMN-PT, but the relative permittivity is significantly smaller.

Conclusion

Our results demonstrate that depths of $130\ \mu\mathrm{m}$ can be achieved with laser micromachining of PMN-PT, making the process suitable for piezocomposites operating at frequencies below 20 MHz. While the piezocomposite manufacturing was successful, the wall angle was limited to $76°$, corresponding to an aspect ratio of approximately 2, which did not yield coupling coefficient advantages over the monolithic material. This is in alignment with the observed drop in coupling coefficients with decreasing wall angle in the simulation results. Nevertheless, other advantages of piezocomposites persist, including lower dielectric constant and reduced specific acoustic impedance. Future improvements to this work will focus on enhancing the wall angle through optimization of the laser process parameters. Additional developments will include extension to 1-3 piezocomposite structures and exploration of different materials, such as [011]-poled material, which is better suited for 2-2 piezocomposites [8]. Furthermore, the fabrication of transducers from the existing samples will enable evaluation of acoustic output characteristics.

Acknowledgment

This research was supported by the European Union and tax revenues on the basis of the budget adopted by the Saxon State Parliament as part of the project HYBRIDECHO under the grant number 100689694. This research was also supported by the Material Technology Development Program (No. 2410004461) through the Korea Evaluation Institute of Industrial Technology (KEIT).

References

[1] P. Kabakov, T. Kim, Z. Cheng, X. Jiang and S. Zhang, 'The versatility of piezoelectric composites,' *Annual Review of Materials Research*, vol. 53, no. 1, pp. 165–193, 3rd Jul. 2023. DOI: 10.1146/annurev-matsci-080921-092839.

[2] T. Herzog, S. Walter, S.-G. Lee, J.-H. Lee, F. Schubert and H. Heuer, 'High-performance ultrasonic transducers based on PMN-PT single crystals fabricated in 1-3 piezo-composite technology,' presented at the 2019 International Congress on Ultrasonics, Bruges, Belgium, 2019, p. 032 007. DOI: 10.1121/2.0001159.

[3] G. Piredda, S. Stroj, D. Ziss *et al.*, 'Micromachining of PMN-PT crystals with ultrashort laser pulses,' *Applied Physics A: Materials Science and Processing*, vol. 125, no. 3, Mar. 2019, Publisher: Springer Verlag, ISSN: 14320630. DOI: 10.1007/s00339-019-2460-9.

[4] Z. Lei, G. Xu, J. Liu, Y. Liu and X. Ji, 'Micromachining of high-quality PMN–PT/epoxy 1–3 composite for high-frequency (30 MHz) ultrasonic transducer applications,' *IEEE Transactions on Ultrasonics, Ferroelectrics, and Frequency Control*, vol. 70, no. 11, pp. 1563–1573, Nov. 2023. DOI: 10.1109/TUFFC.2023.3320652.

[5] Z. Lei, G. Xu, J. Liu and X. Ji, 'Low-stress ultrafast laser micromachining for high-frequency PMN–PT/epoxy composite transducers,' *IEEE Sensors Journal*, vol. 24, no. 5, pp. 5873–5884, 1st Mar. 2024. DOI: 10.1109/JSEN.2023.3347881.

[6] C. Joh, J. Kim and Y. Roh, 'Determination of the complex material constants of PMN–28%PT piezoelectric single crystals,' *Smart Materials and Structures*, vol. 22, no. 12, p. 125 027, 1st Dec. 2013. DOI: 10.1088/0964-1726/22/12/125027.

[7] 'Ieee standard on piezoelectricity,' *ANSI/IEEE Std 176-1987*, 1988. DOI: 10.1109/IEEESTD.1988.79638.

[8] Y. Je, M. Sim, Y. Cho, S.-G. Lee and H.-S. Seo, 'Theoretical and experimental studies on sensitivity and bandwidth of thickness-mode driving hydrophone utilizing a 2-2 piezoelectric single crystal composite,' *Sensors*, vol. 23, no. 7, p. 3445, 24th Mar. 2023. DOI: 10.3390/s23073445.

DOI 10.5162/Ultrasonic2025/B15-a2

Ultrasound Transducer Array with Imaging and Power Output Capabilities for Tumor Perfusion Enhancement

Teng Zhang[1], *Lijun Xu*[1], *and Jianguo Ma*[1]
[1]*School of Instrumentation and Optoelectronics Engineering, Beihang University, Beijing, China*
majianguo@buaa.edu.cn

Abstract: Ultrasound-mediated tumor perfusion enhancement offers a promising strategy to overcome treatment resistance. To enable precise therapy, we developed a dual anti-matching layer transducer array capable of simultaneous imaging and power output. Simulation results show a 31% increase in pulse-echo sensitivity and a reduction in –6 dB bandwidth from 61.9% to 55.5%. The fabricated transducer array achieves a –6 dB bandwidth of 56.5%, close to the simulation, with uniform acoustic output suitable for therapeutic use.

Keywords: Dual anti-matching layers, imaging-guided therapy, transducer design, ultrasound-mediated tumor perfusion enhancement, ultrasound transducer array.

Introduction

Chemotherapy and radiotherapy are currently the main clinical approaches for treating most malignant tumors, while immunotherapy, as an emerging modality, shows promising potential for future development. However, all of these treatment methods often face therapeutic resistance in hypoperfused tumors, which leads to suboptimal efficacy and increased risk of recurrence [1].

In recent years, ultrasound-mediated tumor perfusion enhancement has provided a novel strategy to address this challenge [2, 3]. This technique involves the injection of microbubbles into the bloodstream, followed by ultrasonic stimulation targeted at the tumor region to enhance local perfusion, thereby improving drug delivery and overcoming resistance in hypoperfused tumors [4].

In this approach, the ultrasound transducer must not only deliver sufficient acoustic power to effectively stimulate tissue but also provide real-time imaging capability to ensure treatment precision and safety [5]. If separate transducers are used for imaging and therapy, accurate localization of the therapeutic focus within the image becomes difficult. In contrast, using a single transducer for both functions ensures that the imaging and therapeutic beams share the same path, allowing for direct visualization of the treatment focus in the image and thereby improving targeting accuracy. Therefore, the development of an ultrasound transducer with both imaging and power output capabilities is essential for ultrasound-mediated tumor perfusion enhancement therapy.

However, traditional ultrasound transducers face challenges in meeting this dual-functional requirement. Imaging transducers typically employ a high-acoustic-impedance backing layer behind the piezoelectric element to absorb backward waves and improve axial resolution [6]. However, this design results in 20–30% of the total acoustic energy being converted into heat within the backing layer, reducing transmission efficiency and potentially causing thermal deformation of the backing material, which may damage the transducer. In contrast, therapeutic transducers typically employ an air backing layer with extremely low acoustic impedance to avoid this issue, making them suitable for applications requiring high acoustic power [7], such as high-intensity focused ultrasound (HIFU). However, the air backing layer does not provide mechanical support, and since the piezoelectric array in imaging transducer arrays is relatively fragile, an air backing layer is not suitable for imaging transducers.

To address these challenges, this study developed an ultrasound transducer array incorporating a dual anti-matching layers (AML) structure. By stacking multiple layers of materials to form an equivalent low-impedance backing, this structure provides high acoustic reflectivity and sufficient mechanical support. On one hand, it improves the forward transmission efficiency of the emitted acoustic energy; on the other, it preserves imaging resolution. As such, it enables simultaneous high-performance imaging and high-power delivery, meeting the performance requirements of ultrasound-mediated tumor perfusion enhancement.

Transmission Line Model and Dual Anti-Matching Structure

Traditional ultrasound transducers typically consist of a matching layer, a piezoelectric layer, and a backing layer arranged from front to rear. When electrically excited, the piezoelectric layer emits acoustic waves both forward (toward the matching layer) and back-

DOI 10.5162/Ultrasonic2025/B15-a2

ward (toward the backing layer). To improve reflection of the backward waves, this study introduces two intermediate layers between the piezoelectric layer and the backing layer, referred to as the 1st AM layer and 2nd AM layer (see Fig. 1).

Due to the similarity between the propagation characteristics of acoustic waves in media and electromagnetic waves in transmission lines, microwave transmission line theory is adopted to analyze the energy transfer efficiency of the multi-layer structure [8]. Since the piezoelectric layer is acoustically impedance-matched to the front load via the matching layers, it can be regarded as a pure resistor with an impedance of Z_p in the transmission line model. The backing layer, due to its thickness being much greater than the wavelength, is also treated as a pure resistance Z_b. When the thicknesses of the 1st AM layer and the 2nd AM layer are much smaller than their respective acoustic wavelengths, they can be modeled as transmission line segments with characteristic impedances Z_1 and Z_2, respectively (see Fig. 1).

According to transmission line theory, the acoustic energy transmission efficiency can be calculated as

$$T_I = 1 - |R_p|^2, \tag{1}$$

where R_p is the acoustic pressure reflection coefficient, which can be calculated as

$$R_p = \frac{Z_2 - Z_p^*}{Z_2 + Z_p}, \tag{2}$$

where Z_p^* is the complex conjugate of the impedance Z_p. Z_2 is the equivalent impedance of the dual AML, which is calculated as

$$Z_2 = Z_{a1} \cdot \frac{Z_1 + jZ_{a1}\tan(k_{a1}l_{a1})}{Z_{a1} + jZ_1\tan(k_{a1}l_{a1})}, \tag{3}$$

$$Z_1 = Z_{a2} \cdot \frac{Z_b + jZ_{a2}\tan(k_{a2}l_{a2})}{Z_{a2} + jZ_b\tan(k_{a2}l_{a2})}, \tag{4}$$

As indicated by equations Eq. (1)–(4), when $Z_{a1} < Z_p$, $Z_{a2} > Z_{a1}$, and $Z_b < Z_{a2}$, the structure exhibits high acoustic reflectivity.

In this study, the 1st AM layer is made of epoxy resin (2.7 MRayl), the 2nd AM layer is made of tungsten steel (97.2 MRayl), and the backing layer is made of a mixture of alumina and epoxy resin (5.0 MRayl). The transmission efficiency distribution of the dual AML structure can be calculated based on transmission line theory. Without the dual AML structure, approximately 45% of the backward acoustic energy transmits into the backing layer, with an insertion loss of around –3.5 dB. The dual AML structure exhibits a wideband suppression region, where the strongest suppression occurs when both AML

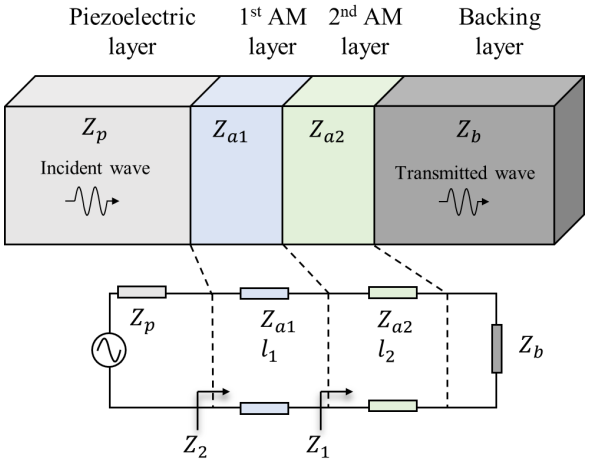

Fig. 1: Schematic view of the equivalent circuits for the dual AML structure.

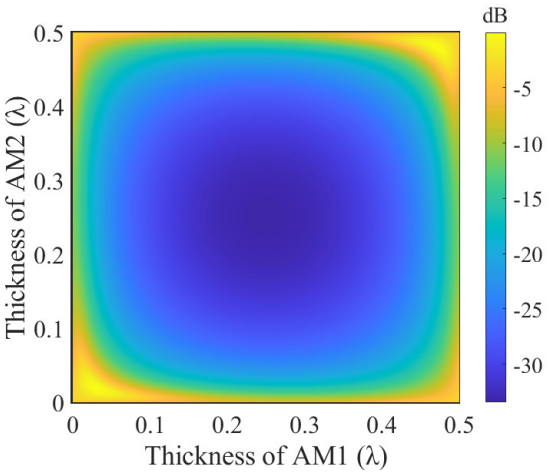

Fig. 2: Insertion loss of double AML structure.

layers are a quarter-wavelength thick. Under this configuration, the insertion loss reaches approximately –33.0 dB, corresponding to a transmission efficiency of only 0.05% (see Fig. 2). This indicates that nearly all the backward-propagating energy is reflected back into the load rather than entering the backing layer, thereby significantly reducing thermal loss and enhancing forward transmission efficiency.

In addition to acoustic performance, the AML structure also provides robust mechanical support, making it suitable for ultrasound transducers that require both high power output and reliable imaging performance.

Transducer Design and Fabrication

In this study, we designed and fabricated an ultrasound transducer array with the dual AML. The transducer consists of 128 elements, with a total array length of approximately 65 mm and a width of 13 mm.

DOI 10.5162/Ultrasonic2025/B15-a2

The design center frequency is 2.8 MHz. The pitch between elements is 0.508 mm, and the kerf width is 0.04 mm.

The backside of the piezoelectric layer is equipped with the dual AML structure (see Fig. 3). The 1st AM layer is composed of epoxy resin, while the 2nd AM layer is made of tungsten steel. Both AM layers have a thickness of one-quarter wavelength at the center frequency to effectively reflect the backward-propagating acoustic waves. Behind the 2nd AM layer, a 10 mm-thick composite backing layer made of alumina and epoxy provides mechanical support.

Although the dual AML structure effectively enhances power output by reflecting backward waves, it also tends to increase pulse duration and reduce bandwidth. For traditional backing layer designs, the primary function is to absorb backward acoustic waves and shorten the pulse duration. The AML structure, equivalent to an extremely low-impedance backing, essentially loses the ability to absorb backward waves, resulting in significantly prolonged pulses. Therefore, precise design of the matching layers is essential to ensure reasonable pulse length and bandwidth for imaging. In this work, a double matching layers structure is employed at the front of the transducer to effectively shorten pulse duration and broaden bandwidth.The detailed structural parameters of each layer are listed in Tab. 1.

The Krimholtz–Leedom–Matthaei (KLM) model was used to simulate the pulse-echo response of the proposed transducer and compare it with that of a traditional backing layer structure. The pulse-echo signals were post-processed by envelope detection. Simulation results show that the proposed transducer achieves a pulse-echo sensitivity of 6.24 mV/V, compared to 4.77 mV/V for the traditional design—an increase of approximately 31%, indicating a significantly stronger output (see Fig. 4). The –6 dB bandwidths of the proposed and traditional transducers are 55.5% and 61.9%, respectively, reflecting a decrease of about 6.4%. These results demonstrate that the proposed design can significantly enhance power output while maintaining comparable imaging performance.

The fabrication process of the proposed transducer is as follows: A PZT-5H piezoelectric ceramic was selected as the base. The dual AML were bonded sequentially to the bottom surface of the piezoelectric ceramic, following the designed thickness. A prefabricated double matching layer was bonded to the top surface. The piezoelectric ceramic was then diced into 128 elements, and the kerfs were filled with epoxy resin. The top electrode of the piezoelectric ceramic was grounded, while signal wires were soldered to the bottom electrodes of each element. Finally, the backing layer was attached behind the 2nd AM layer,

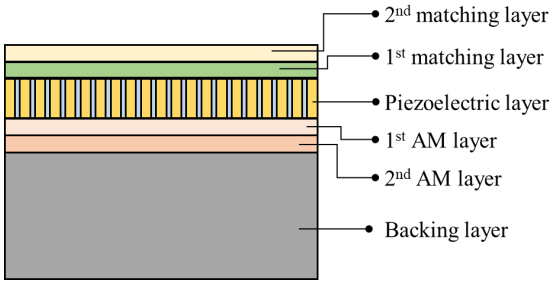

Fig. 3: Structural diagram of the dual AML transducer array.

Tab. 1: Transducer parameters

Structure	Velocity (m/s)	Density (kg/m^3)	Thickness (μm)
2nd matching	2600	1040	214
1st matching	1554	6253	133
Piezoelectric	4400	7500	720
1st AM	2600	1040	232
2nd AM	7200	13500	643
Backing	2307	2180	10000

and the transducer was encapsulated to complete the fabrication.

Transducer Performance

The acoustic performance of the fabricated dual AML transducer array was experimentally evaluated. A pulse-echo test was conducted using an ultrasound pulser/receiver (5073PR, Olympus Corp., USA), which generated excitation pulses with an energy of 8 μJ. The echo signals were captured and recorded using an oscilloscope (MSO54, Tektronix Inc., USA). A reflecting surface was placed in front of the transducer to ensure wave reflection.

The measured pulse-echo peak amplitude was

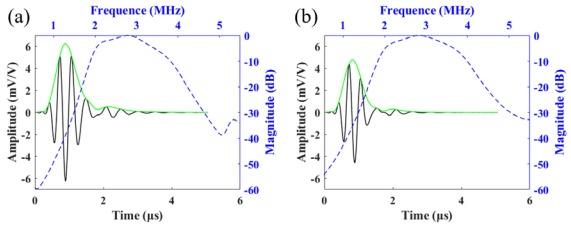

Fig. 4: Pulse-echo waveforms and spectra from KLM simulations of (a) AML and (b) traditional transducers.

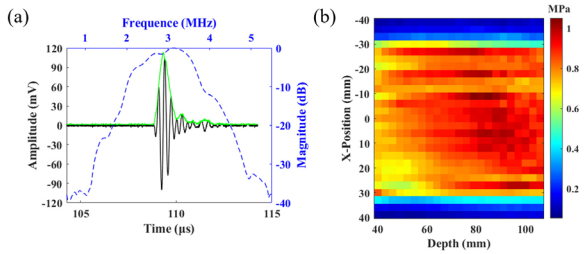

Fig. 5: Measured (a) pulse-echo waveforms and spectra, and (b) acoustic field distribution of the AML transducer array

127.8 mV, and the –6 dB bandwidth was 56.5% (see Fig. 5). The measured bandwidth was slightly higher than the simulation result, which may be attributed to the one-dimensional nature of the KLM model, whereas the actual transducer is a three-dimensional structure—potentially affecting the accuracy of bandwidth prediction.

In addition, the acoustic field of the transducer was scanned using a hydrophone (NH0200, Precision Acoustics Ltd., UK), which was precisely positioned by a three-axis motorized stage. A custom-developed 128-channel ultrasonic driving system was used to excite the transducer with a 2.8 MHz, 5-cycle square wave signal at 20 V. The hydrophone signals were acquired and digitized using an oscilloscope (MSO54, Tektronix Inc., USA).

Experimental results indicate that the transducer maintains good pressure uniformity within a depth range of 40–110 mm, with a lateral –6 dB beamwidth of approximately 60 mm (see Fig. 5). The peak negative pressure in this region exceeds 0.5 MPa, corresponding to a mechanical index (MI) of 0.3, which meets the typical threshold for ultrasound-mediated tumor perfusion enhancement (MI $\approx$ 0.3) [2].

Conclusion

In summary, we developed an ultrasound transducer array with a dual AML structure that enables the integration of imaging and acoustic power output. The proposed design effectively enhances acoustic power transmission through improved reflection of backward waves, while maintaining imaging performance. Both simulation and experimental evaluations demonstrated the transducer's suitability for ultrasound-mediated tumor perfusion enhancement. Overall, this transducer design offers a promising approach for integrating therapeutic ultrasound with real-time imaging, enabling more precise and efficient tumor perfusion enhancement.

Acknowledgment

This research was funded by the Fundamental Research Funds for the Central Universities (JKF-20240571).

References

[1] K. Graham and E. Unger. "Overcoming tumor hypoxia as a barrier to radiotherapy, chemotherapy and immunotherapy in cancer treatment". In: *International Journal of Nanomedicine* 13 (2018), pp. 6049–6058. DOI: 10.2147/IJN.S140462.

[2] Y. Zhang et al. "Effect of diagnostic ultrasound and microbubble-enhanced chemotherapy on metastasis of rabbit VX2 tumor". In: *Medical Physics* 48 (2021), pp. 3927–3935. DOI: 10.1002/mp.14867.

[3] N. Tang et al. "Sononeoperfusion: a new therapeutic effect to enhance tumour blood perfusion using diagnostic ultrasound and microbubbles". In: *Cancer Imaging* 23 (2023), p. 29. DOI: 10.1186/s40644-023-00545-y.

[4] N. Li et al. "Tumor perfusion enhancement by ultrasound stimulated microbubbles potentiates PD-L1 blockade of MC38 colon cancer in mice". In: *Cancer letters* 498 (2021), pp. 121–129. DOI: 10.1016/j.canlet.2020.10.046.

[5] Y. Cai et al. "Ultrasound transducers with both imaging and power output capabilities by anti-matching at backing layers". In: *Applied Physics Letters* 124 (2024), p. 072201. DOI: 10.1063/5.0191191.

[6] Y. Cai et al. "Axial super-resolution ultrasound imaging with quasi-monopolar pulses from a dual-frequency transducer". In: *IEEE Transactions on Instrumentation and Measurement* 72 (2023), p. 9500710. DOI: 10.1109/TIM.2023.3234032.

[7] J. K. Woodacre, T. G. Landry, and J. A. Brown. "Fabrication and characterization of a 5 mm x 5 mm aluminum lens-based histotripsy transducer". In: *IEEE Transactions on Ultrasonics, Ferroelectrics, and Frequency Control* 69 (2022), pp. 1442–1451. DOI: 10.1109/TUFFC.2022.3152174.

[8] M. Huang et al. "Single- and dual-band RF rectifiers with extended input power range using automatic impedance transforming". In: *IEEE Transactions on Microwave Theory and Techniques* 67 (2019), pp. 1974–1984. DOI: 10.1109/TMTT.2019.2901443.

DOI 10.5162/Ultrasonic2025/B15-a6

2025 ICU PADERBORN
INTERNATIONAL CONGRESS ON ULTRASONICS

Wearable Contact Lens Ultrasound Retinal Stimulation for Noninvasive Vision Restoration

Chi-feng Chang[1], *Jie Ji*[1], *Yushun Zeng*[1], *Baoqiang Liu*[2], *Junhang Zhang*[1], *Xin Sun*[1], *Gong Chen*[1], *Hamid Chabok*[3], *and Qifa Zhou*[1,2]

[1]*University of Southern California, Department of Biomedical Engineering, Los Angeles, California, USA*

[2]*University of Southern California, Roski Eye Institute, Keck School of Medicine, Los Angeles, California, USA*

[3]*University of Southern California, Department of Physics and Astronomy, Los Angeles, California, USA*

Abstract: This work presents the first wearable, contact lens-compatible ultrasound neuromodulation device capable of precise retinal stimulation without surgery. A novel wearable contact lens-shaped ultrasound array is designed for potential vision restoration in retinal degenerative diseases through noninvasive neuromodulation. The array is integrated by 64 elements on a biocompatible substrate, aiming for ~100–150 µm resolution. The fabrication process utilizes a 3D-printed mold, silver epoxy, flexible PCB, and Parylene-C coating to create a device operating at 19.5 MHz with over 50% bandwidth. The Field-Programmable Gate Array (FPGA) control supports real-time programmable patterns for high-precision neuromodulation. In contrast to invasive options, this approach minimizes risks and enhances resolution, showing great potential in vision therapy.

Keywords: Retinal stimulation, focused ultrasound, contact lens, vision restoration, noninvasive neuromodulation

Background, Motivation and Objective

Retinal degenerative diseases, including age-related macular degeneration and retinitis pigmentosa, affect over 200 million people globally, causing irreversible blindness due to photoreceptor loss [1-3]. The intact inner retinal circuitry supports prosthetic interventions, yet current solutions like the FDA-approved Argus II rely on invasive electrodes, posing surgical risks and offering limited resolution (~200–300 µm) [1, 4, 5]. Noninvasive neuromodulation, such as transcranial magnetic stimulation, lacks precision, while optogenetics and sonogenetics involve genetic risks [6]. Focused ultrasound (FUS) offers a promising alternative with ~100 µm resolution and minimal thermal effects [2, 3]. Previous studies [2, 5, 7] demonstrated FUS potential in ultrasound neuromodulations, with Lu et al. advancing imaging-guided systems. Despite progress, wearable FUS devices remain limited. We developed a contact lens-shaped transducer with a 64-element PZT array, using a 3D-printed mold, silver epoxy, flexible PCB, and Parylene-C coating for ~100–150 µm resolution and FPGA-controlled patterning [1, 8]. Our goal is to achieve a noninvasive, high-precision, biocompatible vision restoration solution, overcoming implant limitations, with future potential for direct integration into the eye as a wearable contact lens [9].

Method

Design

The contact lens-shaped ultrasound transducer is designed for high-resolution, noninvasive retinal stimulation, featuring a 64-element PZT phased array in a dual-ring configuration: 32 elements in an inner ring (OD 14 mm, ID 12 mm) and 32 in an outer ring (OD 17 mm, ID 15 mm), mounted on a flexible PCB (OD 20 mm, ID 9 mm) with a focal length of 18 mm. The PZT (DL-53) 1-3 composite (DeL Piezo Specialties, LLC), with a longitudinal velocity of ~3087 m/s and impedance of 16–18 MRayl, ensures flexibility and broadband performance, supporting stable operation under extreme conditions. A silver epoxy and Parylene-C matching layers enhance acoustic coupling and biocompatibility, while the design minimizes lens heating (Fig. 1), making it suitable for prolonged ocular use. This configuration is optimized for future direct placement on the eye, mimicking a standard contact lens for seamless wearability.

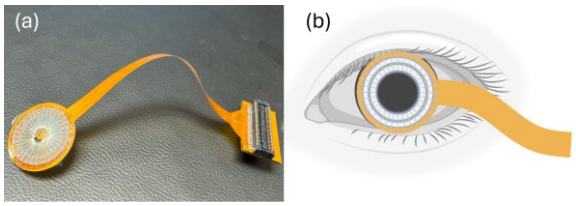

Fig. 1: (a) Contact lens-shaped ultrasound array. (b) Conceptual illustration of the intended wearing method.

Fabrication

A 3D-printed concentric mold (Fig. 2) shapes the dual-ring array, aligning with ocular curvature for a 64-element PZT array (inner ring: OD 14 mm, ID 12 mm; outer ring: OD 17 mm, ID 15 mm) on a PCB (OD 20 mm, ID 9 mm). The PZT (DL-53) 1-3 composite (longitudinal velocity ~3087 m/s, impedance 16–18 MRayl) is placed in the mold, with a silver epoxy matching layer cast on the front and an E-solder backing layer on the rear for connectivity and damping. Segmented fabrication ensures layer uniformity. The PZT is diced into 64 elements at 11.25° spacing rotation, with epoxy-filled gaps for integrity, mounted on the PCB, and fitted with Cr/Au electrodes [10-12]. A Parylene-C coating adds biocompatibility, and epoxy resin fixes the 18 mm focal length for ocular conformity [13]. A single cable connects to the control system, with wireless designs planned. The final fabricated device is a compact, biocompatible contact lens-shaped transducer ready for potential direct ocular integration, as shown in the post-fabrication images (Fig. 2).

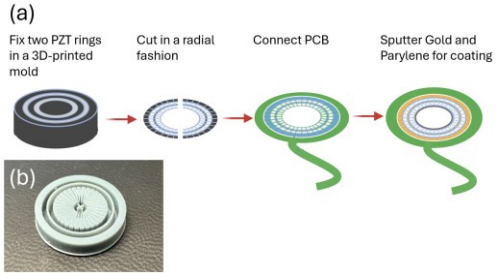

Fig. 2: (a) Completed transducer assembly. (b) 3D-printed mold with radial cutting guides.

Simulation and Control

PiezoCAD (Sonic Concepts, Inc.) was applied to design and optimize the array in a central frequency of 19.5 MHz (PZT thickness ~0.079 mm), -6 dB bandwidth of 81.3%, showcasing the DL-53 1-3 composite's potential in higher stimulation resolution (Fig. 3) [14-16]. The dual-ring design, with a 3087 m/s velocity and ~17 MRayl impedance, optimized focusing for ~100–150 µm resolution. FPGA control enabled real-time beam steering and holography-based patterning, leveraging holographic principles to create complex spatial acoustic patterns by modulating phase and amplitude delays across array elements. This capability supports the future development of direct eye-wearable systems for retinal stimulation.

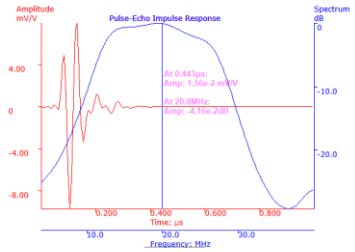

Fig. 3: Pulse-Echo Impulse Response (-6 dB Bandwidth: 81.3%) by simulation.

Wearable 64-Ch Neuromodulation System

The system consists of a 64-channel ultrasound transmitter (TX7364), a low-power FPGA (XC7A100T), and a Wi-Fi module for wireless communication, all powered by a capacitor-based energy storage module (Fig. 4). The high-voltage rail delivers programmable output up to 60 Vpp, enabling the system to drive a 19.5 MHz ring array transducer for targeted therapeutic ultrasound stimulation. The low-voltage rail powers the control logic and communication components. The FPGA offers dynamic and real-time control of individual channel delays, allowing precise adjustment of acoustic focus and stimulation depth. This per-channel programmability enables spatially selective neuromodulation and improves adaptability across anatomical targets. The system supports ultrasound frequencies up to 22 MHz, making it suitable for high-frequency neuromodulation and advanced biomedical research. Wireless communication is supported by a dual-band Wi-Fi module with data transfer rates up to 450 Mbps, ensuring seamless connection to mobile devices or cloud platforms. A 16,000 µF capacitor-based energy storage module ensures stable high-voltage pulse delivery during extended operation, providing both performance and reliability in wearable applications.

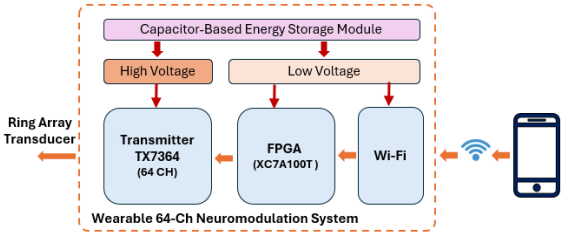

Fig. 4: Block diagram of the wearable 64-channel neuromodulation system.

Experimental Results

Safety Validation

The contact lens-shaped ultrasound transducer underwent a 20-hour safety test, operating continuously at 50 V under extreme conditions, and exhibited reliable thermal and acoustic performance suitable for potential direct ocular integration. All tests were conducted in compliance with FDA

guidelines for ophthalmic ultrasound safety, ensuring the mechanical index (MI) remains below 0.23 [17]. Post-fabrication analysis of the device's thermal behavior, based on the 64-element PZT dual-ring array, reveals a baseline temperature of approximately 20°C prior to stimulation. During maximum stimulation at 50 V, the temperature rises to around 25°C, indicating controlled heat generation within safe limits for prolonged ocular use. Following the 20-hour test, the temperature stabilizes at approximately 22°C (Fig. 5), suggesting effective thermal regulation and confirming the device's biocompatibility.

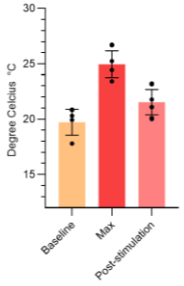

Fig. 5: Thermal Performance Analysis of the Ultrasound Ring Array in a 20-Hour Safety Test.

Acoustic performance under the same 50 V maximum input condition was evaluated, yielding an output voltage of 26.04 mV, a receive-mode sensitivity of 4.26×10^{-8} V/Pa, and a sensitivity of 2.72×10^{-5} V^2cm^2/W. The spatial peak pulse average intensity (I_{sppa}) was measured at 24.92 W/cm^2. The acoustic pressure (P) was calculated as Eq. (1) and determined to be 0.3056 MPa:

$$\boldsymbol{P} = \frac{\boldsymbol{Output}}{\boldsymbol{2 \times Sensitivity\left(\frac{V}{Pa}\right) \times 10^6}} \quad (1)$$

The mechanical index (MI) was calculated using Eq. (2):

$$\boldsymbol{MI} = \frac{\boldsymbol{Pressure\ (MPa)}}{\boldsymbol{\sqrt{Frequency}\ (MHz)}} \quad (2)$$

According to Eq. (2), the MI is 0.068, well below the FDA ophthalmic safety threshold of 0.23. These results support the device's readiness for future in vivo validation and seamless integration as a wearable contact lens under extreme operational conditions

Discussion

This study introduces a contact lens-shaped ultrasound transducer as a noninvasive alternative to retinal prostheses, with a fabrication process emphasizing biocompatibility and ocular conformity for potential direct placement in the eye [18]. The 19.5 MHz frequency, resulting from the combined resonance of the PZT, silver epoxy, and E-solder layers, supports high-resolution (~120 µm) stimulation [2, 7]. Unlike the Argus II's invasive approach, our design eliminates surgical risks and improves biocompatibility [4]. The dual-ring configuration, inspired by Jiang et al.'s F-URSP [7], supports programmable patterns, with FPGA control building on Lu et al.'s imaging-guided systems [5]. The device underwent a 20-hour safety test under extreme conditions with a maximum input voltage of 50 V, demonstrating stable thermal performance with a maximum temperature of 25°C and a post-stimulation stabilization at 22°C, indicating effective thermal regulation for prolonged ocular use. Acoustic performance under the same conditions yielded a mechanical index (MI) of 0.068, well below the FDA ophthalmic safety threshold of 0.23, confirming its safety for neuromodulation. This reliability under high-load conditions underscores the device's potential for future clinical applications.

Future work will address in vivo validation to assess neural responses, long-term biocompatibility to ensure sustained ocular safety, and wireless power challenges to enhance wearability [19]. These advancements could transform vision restoration therapy through a truly wearable, contact lens-integrated device, offering a safe and precise alternative to existing invasive solutions.

Acknowledgements

The project was partially supported by NIH NEI STTR 1R41EY035609-01.

References

[1] C. Xu et al., "Design and Simulation of a Ring Transducer Array for Ultrasound Retinal Stimulation," Micromachines, vol. 13, no. 9, 2022, doi:10.3390/mi13091536.

[2] Q. X et al., "Noninvasive Ultrasound Retinal Stimulation for Vision Restoration at High Spatiotemporal Resolution," BME Frontiers, 2022, doi:10.34133/2022/9829316.

[3] G. Lu et al., "Ultrasound retinal stimulation: a mini-review of recent developments," IEEE Transactions on Ultrasonics, Ferroelectrics, and Frequency Control, vol. 69, no. 12, 2022, doi:10.1109/TUFFC.2022.3220568.

[4] J.-y. Lu, G. Lu, B. B. Thomas, M. S. Humayun, and Q. Zhou, "Ultrasound Concave 2-D Ring Array for Retinal Stimulation," IEEE Transactions on Ultrasonics, Ferroelectrics, and Frequency Control, vol. 70, pp. 1527-1535, 2023, doi:10.36227/techrxiv.22083719.

[5] G. Lu et al., "Noninvasive imaging-guided ultrasonic neurostimulation with arbitrary 2D patterns and its application for high-quality vision restoration," Nature Communications, vol. 15, no. 1, 2024, doi:10.1038/s41467-024-48683-6.

[6] P.-A. Lo et al., "Ultrasonic Retinal Neuromodulation and Acoustic Retinal Prosthesis," Micromachines, vol. 11, no. 10, 2020, doi:10.3390/mi11100929.

[7] L. Jiang et al., "Flexible ultrasound-induced retinal stimulating piezo-arrays for biomimetic visual prostheses," Nature Communications, vol. 13, no. 1, 2022, doi:10.1038/s41467-022-31599-4.
[8] W. Qiu et al., "A novel dual-frequency imaging method for intravascular ultrasound applications," Ultrasonics, vol. 57, 2015, doi:10.1016/j.ultras.2014.10.011.
[9] C. Gong et al., "Non-Invasive Hybrid Ultrasound Stimulation of Visual Cortex In Vivo," Bioengineering, vol. 10, no. 5, 2023, doi:10.3390/bioengineering10050577.
[10] L. B et al., "A Novel Dual-Element Catheter for Improving Non-Uniform Rotational Distortion in Intravascular Ultrasound," IEEE Transactions on Biomedical Engineering, vol. 70, no. 6, 2023, doi:10.1109/TBME.2022.3226955.
[11] B. L. M. S. Z. Z. L. S. Y. Y. W. Qiu, "A Novel Coded Excitation Imaging Platform for Ultra-High Frequency (>100 MHz) Ultrasound Applications," IEEE Transactions on Biomedical Engineering, vol. 72, no. 4, 2025, doi:10.1109/TBME.2024.3496843.
[12] Y. Chen et al., "Focused intravascular ultrasonic probe using dimpled transducer elements," Ultrasonics, vol. 56, 2015, doi:10.1016/j.ultras.2014.07.011.
[13] S. Liang et al., "Evaluation of Blood Induced Influence for High-Definition Intravascular Ultrasound (HD-IVUS)," IEEE Transactions on Ultrasonics, Ferroelectrics, and Frequency Control, vol. 69, no. 1, 2022, doi:10.1109/TUFFC.2021.3108163.
[14] M. Su et al., "High frequency focal transducer with a Fresnel zone plate for intravascular ultrasound," Applied Physics Letters, vol. 119, no. 14, 2021, doi:10.1063/5.0070313.
[15] Z. Y et al., "High-Frequency Wearable Ultrasound Array Belt for Small Animal Echocardiography," IEEE Transactions on Ultrasonics, Ferroelectrics, and Frequency Control, vol. 71, no. 12, 2024, doi:10.1109/TUFFC.2024.3492197.
[16] C. Qiu et al., "Textured-piezoelectric-ceramic-based focused intravascular ultrasonic transducer with improved image quality and uniformity," Applied Physics Letters, vol. 125, no. 23, 2024, doi:10.1063/5.0237897.
[17] FDA, "Marketing Clearance of Diagnostic Ultrasound Systems and Transducers," 2023. Available: https://www.fda.gov/regulatory-information/search-fda-guidance-documents/marketing-clearance-diagnostic-ultrasound-systems-and-transducers.
[18] H. Caffaratti et al., "Neuromodulation with Ultrasound: Hypotheses on the Directionality of Effects and Community Resource," medRxiv, 2025, doi:10.1101/2024.06.14.24308829.
[19] J. Ji et al., "Potential of ultrasound stimulation and sonogenetics in vision restoration: a narrative review," Neural Regeneration Research, vol. 20, no. 12, 2025, doi:10.4103/NRR.NRR-D-24-00841.

DOI 10.5162/Ultrasonic2025/C1-a5

Real-Time Adaptive Ultrasonic Plane Wave Imaging towards Online Automated Curved Structure Inspection

Zhixuan Chang[1,2], Shiwei Wu[1], Keji Yang[1,2], and Haoran Jin[1,2]
[1] Zhejiang University, State Key Laboratory of Fluid Power and Mechatronic Systems, School of Mechanical Engineering, Hangzhou, China
[2] Zhejiang University, The Key Laboratory of Advanced Manufacturing Technology of Zhejiang Province, Hangzhou, China
chang_zhixuan@zju.edu.cn, jinhr@zju.edu.cn

Abstract: Phased array ultrasonic imaging is widely utilized in industrial non-destructive testing and evaluation (NDT&E). With advancements in robotics technology, phased array probes can be mounted on manipulators to autonomously inspect complex curved structures in water-immersed environments, enhancing both inspection capacity and efficiency. Conventional Delay-And-Sum (DAS) based imaging techniques require prior knowledge of the structure's surface geometry and the relative position of the probe. The acoustic path with the shortest time of flight is then determined based on Fermat's principle. However, the inspection Pulse Repetition Frequency (PRF) and the number of pixels are constrained due to the computational cost of the acoustic path searching and DAS operations. Although several optimization methods have been proposed to accelerate or bypass the searching process, inspection performance remains limited by DAS operations. Alternatively, recursive non-stationary phase shift migration based imaging method have been developed to eliminate DAS operations, but their efficiency remains unsatisfactory. In this paper, we propose an adaptive wavenumber domain plane wave imaging method that enables real-time online imaging with fine spatial resolution. Each imaging cycle contains a group of emission events. In the first imaging cycle, conventional wavenumber domain plane wave imaging is employed to reconstruct the surface geometry as an initialization step. From the second imaging cycle onward, the emission focal law is dynamically adjusted based on the reconstructed surface geometry from the latest previous cycle, enabling the generation of steered plane wavefronts beneath the curved couplant-specimen interface. Once the scattering echoes are captured, non-stationary phase shift migration techniques are applied to simultaneously reconstruct both the surface geometry and the scattering wavefield beneath the specimen surface. Finally, the wavenumber domain f-k migration method is utilized to reconstruct inspection images with high computational efficiency. Simulations were conducted to validate the proposed method. The real-time online imaging frame rate exceeds 45 fps, with about 200 thousands pixels in the ROI, demonstrating the potential of the proposed method for automated industrial online NDT&E.

Keywords: Ultrasonic non-destructive testing, Curved structure inspection, Ultrasonic imaging, Adaptive plane wave imaging, High-frame-rate imaging

Introduction

Curved structures are widely deployed in industrial applications, such as pipes, rails, pressure vessel, and so on. It's crucial to detect the internal flaws in such structures as early as possible to ensure the safety. Phased array ultrasonic testing technology is widely utilized due to its environment suitability. The Full Matrix Captured (FMC) based Total Focus Method (TFM) has been widely used for specimen inspection due to its high image quality and precision[1]. However, when inspecting curved structures, determining the focal delay for each pixel requires searching for the minimum acoustic time-of-flight path based on Fermat's principle, introducing heavy computation burden and limiting the imaging frame rate and image resolution [2]. Although sparse matrix operation and Graphic Process Unit (GPU) based methods are utilized to accelerate the computation, the imaging frame rate is still not satisfying especially when the image resolution is large [3]. Plane Wave Imaging (PWI) is an alternative approach to FMC which can reduce emission cycles to generate an inspection image without sacrifice on the image quality [4]. However, these methods requires the prior knowledge of the structure geometry, limiting the implementation of such methods in industrial applications.

DOI 10.5162/Ultrasonic2025/C1-a5

Several dynamic imaging methods has been established to overcome the dependence on the prior knowledge of the structure geometry [5], [6]. The basic idea is measuring the surface geometry online and then calculating focal delay. This further increases the time complexity of the reconstruction process. Another approach is set a group of virtual sources on the boundary of the structure with few emission cycles, and then calculate the focal delay inside the structure [7]. This method avoid the searching process brought by Fermat's principle, but still depends the calculation of focal delay in isotropic medium and DAS algorithm. There are also a kind of method use single emission cycle to generate low quality image at high frame rate, and then use learning based method to improve the image quality [8], but their generalization capacity still needs more verification.

Besides DAS based imaging approaches, wavenumber domain imaging methods are also widely utilized in ultrasonic imaging [9]. These methods convert the scattering wavefield to wavenumber domain with Fourier transform, and then reconstruct wavenumber domain image with a nonlinear mapping, which can realize ultrafast imaging frame rate [10], [11]. These methods have been adapted to curved structure imaging with non-stationary wavefield extrapolation theory [12]. This study presents an adaptive imaging method based on the wavenumber domain non-stationary plane wave imaging method. In each imaging cycle, the surface geometry of the structure is extracted from the reconstructed image, and emission delays are calculated for the next cycle. Simulation based on k-Wave is utilized to validate the proposed method. An real-time imaging frame rate of 45 fps is achieved, highlighting the potential of the proposed method.

Methods

Wavenumber domain cross-correlation imaging condition is utilized to measure the geometry of the wavefield, whose operations share significant overlap with NSPWI method [12].

Considering that the incident wave and received scattering wave are both one-way waves, hence the general analytical forms of incident waves P_i and scattering waves P_s are given by

$$\begin{aligned} P_s(k_x, z, \omega) &= K_2(k_x, \omega) e^{-\imath k_z z}, \\ P_i(k_x, z, \omega) &= K_1(k_x, \omega) e^{\imath k_z z}, \end{aligned} \tag{1}$$

where k_z is the wavenumber along z-axis, which can be calculated by dispersion relation

$$k_z = \operatorname{sgn}(\omega) \sqrt{(\omega/c)^2 - k_x^2}. \tag{2}$$

When $z = 0$, the incident wavefields and scattering wavefield is already known,

$$\begin{aligned} &P_s(k_x, z = 0, \omega) = \iint p_s(x, t) e^{-\imath(k_x x + \omega t)} dx dt, \\ &P_i(k_x, z = 0, \omega) \\ &\quad = \iint S(\omega) A(x) e^{-\imath(k_x x + \omega(t - t_j))} dx dt. \end{aligned} \tag{3}$$

where $S(\omega)$ is the response signal spectrum of an element, $A(x)$ is the apodization function of the array, t_j is the emission delay of the jth element. Hence,

$$\begin{aligned} P_s(k_x, z, \omega) &= P_s(k_x, z = 0, \omega) e^{\imath k_z z}, \\ P_i(k_x, z, \omega) &= P_i(k_x, z = 0, \omega) e^{-\imath k_z z}. \end{aligned} \tag{4}$$

According to the cross-correlation imaging condition, the inspection image in isotropic medium is given by[13]

$$I(x, z) = \iint P_s(k_x, z, \omega) P_i^*(k_x, z, \omega) e^{\imath k_x x} d\omega dx, \tag{5}$$

From the reconstructed image in couplant layer, the acoustic boundary can be extracted by finding pixels with the maximum intensity in each image column,

$$\hat{f}_1(x) = \max_z I(x, z). \tag{6}$$

where $z = f(x)$ is the acoustic boundary curve function. Then the plane wave beamforming algorithm stated in [4] is utilized to calculate the emission delays for next FMC frame. Since the emission delays calculation requires the normal of the acoustic boundary, a cubic smoothing spline $z = \hat{f}_2(x)$ is deployed to reconstruct the directly extracted acoustic boundary with a tolerance of 0.1 mm. The defects consist of a group of Side-Drilled-Holes (SDHs), as illlustrated in Fig. 1.

The imaging scene is illustrated as Fig. 1. Let $p_l(x, t)$ be the scattering wavefield with a steered angle of θ_l, the surface geometry is given as $\hat{f}_2(x)$ from the results of the last imaging cycle. The top and bottom boundaries of the nonstationary interval is the minimum and maximum values of $\hat{f}_2(x)$ respectively

$$h_0 = \min_x \hat{f}_2(x), \quad h_1 = \max_x \hat{f}_2(x). \tag{7}$$

In nonstationary interval, the sound speed is piecewise constant, (4) should be modified to

$$\begin{aligned} &P(k_x, z + \Delta z, \omega) \\ &\quad = \sum_i \left(\alpha_i(k_x, \omega) \mathcal{F}_x W_i\right) \mathcal{F}_{k_x}^{-1} P(k_x, z, \omega), \end{aligned} \tag{8}$$

DOI 10.5162/Ultrasonic2025/C1-a5

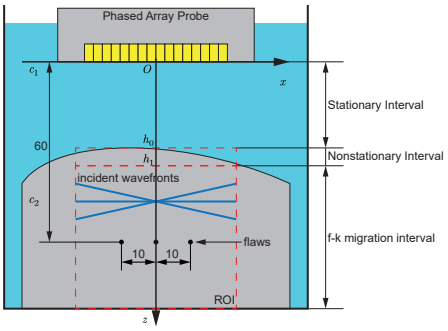

Fig. 1: Imaging scene illustration.

where $\alpha_i(k_x, \omega)$ is the wavefield extrapolation factor in the ith medium

$$\alpha_i(k_x, \omega) = \exp\left(\imath \Delta z \sqrt{(\omega/c_i)^2 - k_x^2}\right). \quad (9)$$

Subsequently, the image within the nonstationary interval can be reconstructed using (5) and (9), yielding $P(k_x, h_1, \omega)$ required by the next f-k migration imaging step. In fact, the scattering wavefield is determined by the scatterers distribution with steered incident wavefronts[12]

$$S_i(k_u(k_x, k_2), k_v(k_x, k_2)) = e^{\imath\omega\sigma_i}\sqrt{k^2 - k_x^2} P\left(k_x(k_u, k_v), z = h_2, k_2(k_u, k_v)\right), \quad (10)$$

where $\boldsymbol{k}_2$ is the wavenumber vector in the second layer medium, and k_u, k_v are given by

$$\begin{aligned} k_x(k_u, k_v) &= k_x - k_2 \sin\theta_i, \\ k_2(k_u, k_v) &= \frac{k_u^2 + k_v^2}{2k_u \sin\theta_i + 2k_z \cos\theta_i}. \end{aligned} \quad (11)$$

Finally, the reconstructed image in f-k migration interval is obtained by

$$I(u, v) = \left| \mathcal{F}^{-1}_{k_u, k_v} \sum_i S_i(k_u, k_v) \right|. \quad (12)$$

Results and Discussion

Simulation is designed to verify the proposed method. The deployed phased array probe has 64 elements with a pitch of 0.6 mm, a width of 0.5 mm. The center frequency of the probe is 5 MHz, and the sampling rate is set to 295 MHz to make sure the CFL of the simulation less than 0.3. In the imaging phase, a 4 subdivision of the sampling rate is used to make the sampling rate more similar to practical configurations. The sound speed of the specimen is set to $c_2 = 5900$ m/s, and that in other area is set to $c_1 = 1483$ m/s. The steered angle of the incident planar wavefronts is set to from -4° to 4° with a step of 1°.

The surface geometry extracted from the image is shown in Fig. 2 (a). The directly detected boundary and smoothed boundary are plotted in black and red lines, respectively. It is obvious that the smoothed boundary has a better precision for normal estimation. The emission delays calculated with the smoothed boundary is shown in Fig. 2 (b). Compared with the exact values obtained from the precise boundary measurements, the error is smaller than 102.4 ns.

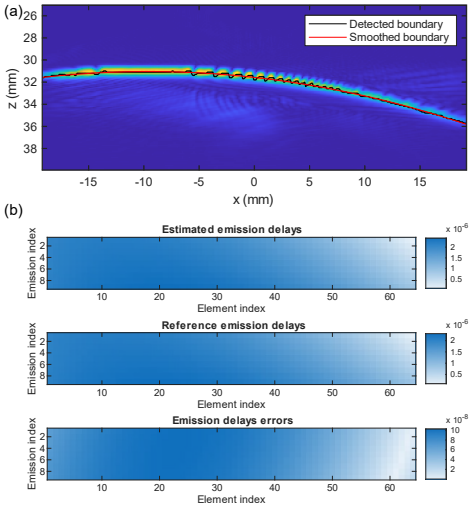

Fig. 2: (a) Extracted boundary and smoothed boundary. (b) Estimated emission delays and estimation error.

Reconstructed image using estimated emission delays are illustrated in Fig. 3 (a). It can be seen that the surface geometry and the SDHs are all identified, although the surface exhibits higher intensity compared to the SDHs due to energy attenuation during wave propagation across the acoustic boundary. The red rectangular area is the ROI which contains flaws. The reconstructed image in ROI is normalized and compressed with log function and plotted in Fig. 3 (b). The exact position of the flaws are plotted with red circles. The maximum intensity projection along depth direction is shown in Fig. 3 (c). The imaging algorithm was implemented using CUDA to accelerate the computation, and a final frame rate of 45 fps is achieved on a commercial computer with a CPU of Core U7 265K ((Intel Corporation, Santa Clara, CA, USA)) and a GPU of RTX 3070Ti (NVIDIA Corporation, Santa Clara, CA, USA).

Conclusion

In this work, we presented an adaptive real-time ultrasonic imaging for curved structure inspection with high frame rate and high image resolution. Wavenumber domain non-stationary wavefield extrapolation and

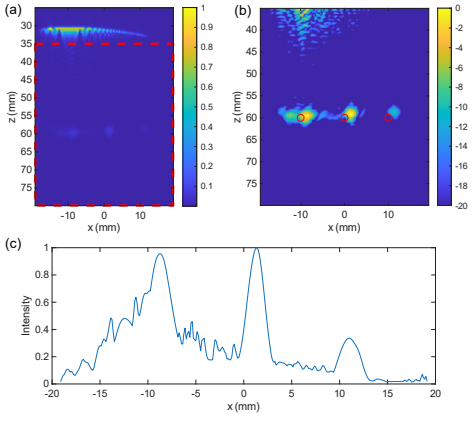

Fig. 3: (a) Reconstructed image. (b) The normalized ROI reconstructed image after log transformation. (c) The maximum intensity projection curve along depth direction.

cross-correlation algorithm were employed to measure the surface geometry during the continuous imaging process. After that the wavenumber domain f-k migration method was applied to reconstruct images with high efficiency. Simulation results showed that the proposed method can achieve high image quality and a frame rate of 45 fps, highlighting the potential of the proposed method for online automated curved structure inspection.

References

[1] C. Holmes, B. W. Drinkwater and P. D. Wilcox, 'Post-processing of the full matrix of ultrasonic transmit–receive array data for non-destructive evaluation,' *NDT & E International*, vol. 38, no. 8, pp. 701–711, 2005.

[2] L. Le Jeune, S. Robert and C. Prada, 'Plane wave imaging for ultrasonic inspection of irregular structures with high frame rates,' in *42ND ANNUAL REVIEW OF PROGRESS IN QUANTITATIVE NONDESTRUCTIVE EVALUATION: Incorporating the 6th European-American Workshop on Reliability of NDE*, Minneapolis, Minnesota, 2016, p. 020 010.

[3] G. Y. Hou et al., 'Sparse Matrix Beamforming and Image Reconstruction for 2-D HIFU Monitoring Using Harmonic Motion Imaging for Focused Ultrasound (HMIFU) With In Vitro Validation,' *IEEE Transactions on Medical Imaging*, vol. 33, no. 11, pp. 2107–2117, 2014.

[4] G. Cosarinsky, J. Fernandez-Cruza and J. Camacho, 'Plane Wave Imaging through Interfaces,' *Sensors*, vol. 21, no. 15, p. 4967, 2021.

[5] L. Le Jeune, S. Robert, P. Dumas, A. Membre and C. Prada, 'Adaptive ultrasonic imaging with the total focusing method for inspection of complex components immersed in water,' in *41ST ANNUAL REVIEW OF PROGRESS IN QUANTITATIVE NONDESTRUCTIVE EVALUATION: Volume 34*, Boise, Idaho, 2015, pp. 1037–1046.

[6] J. Wang, Z. Zhou, Y. Li, G. Yang and W. Zhou, 'A high efficiency adaptive ultrasonic array imaging method with sensitivity correction for curved structures,' *Measurement*, vol. 238, p. 115 322, 2024.

[7] J. F. Cruza and J. Camacho, 'Total Focusing Method With Virtual Sources in the Presence of Unknown Geometry Interfaces,' *IEEE Transactions on Ultrasonics, Ferroelectrics, and Frequency Control*, vol. 63, no. 10, pp. 1581–1592, 2016.

[8] F. Zhang, L. Luo, J. Li, J. Peng, Y. Zhang and X. Gao, 'Ultrasonic adaptive plane wave high-resolution imaging based on convolutional neural network,' *NDT & E International*, vol. 138, p. 102 891, 2023.

[9] M. H. Skjelvareid, T. Olofsson, Y. Birkelund and Y. Larsen, 'Synthetic aperture focusing of ultrasonic data from multilayered media using an omega-K algorithm,' *IEEE Transactions on Ultrasonics, Ferroelectrics and Frequency Control*, vol. 58, no. 5, pp. 1037–1048, 2011.

[10] J.-y. Lu, '2D and 3D High Frame Rate Imaging with Limited Diffraction Beams,' *IEEE Transactions on Ultrasonics, Ferroelectrics and Frequency Control*, vol. 44, no. 4, pp. 838–856, 1997.

[11] Jiqi Cheng and Jian-yu Lu, 'Extended high-frame rate imaging method with limited-diffraction beams,' *IEEE Transactions on Ultrasonics, Ferroelectrics and Frequency Control*, vol. 53, no. 5, pp. 880–899, 2006.

[12] Z. Chang et al., 'An efficient ultrasonic wavenumber-domain plane wave imaging method towards the inspection of curved structures,' *Ultrasonics*, vol. 143, p. 107 416, 2024.

[13] R. Ali, 'Fourier-based Synthetic-aperture Imaging for Arbitrary Transmissions by Cross-correlation of Transmitted and Received Wavefields,' *Ultrasonic Imaging*, vol. 43, no. 5, pp. 282–294, 2021.

DOI 10.5162/Ultrasonic2025/C2-a2

3D imaging with Scanning Acoustic Microscopy – A comparison of the focusing capabilities of array transducers and Synthetic Aperture with highly focused transducers

Mario Wolf[1], *Emanuel Leipner*[1], *Stefan König*[3], *Peter Hoffrogge*[3], *Peter Czurratis*[3], *and Christian Kupsch*[1,2]
[1] *TU Bergakademie Freiberg, Measurement, Sensor and Embedded Systems Lab (MSE Lab), Freiberg, Saxony, Germany*
[2] *TU Bergakademie Freiberg, Center for Efficient High Temperature Processes and Materials Conversion (SN0390002), Freiberg, Saxony, Germany*
[3] *PVA TePla Analytical Systems GmbH, Westhausen, Baden-Württemberg, Germany*
mario.wolf@mse.tu-freiberg.de

Abstract: This paper investigates the potential of Scanning Acoustic Microscopy (SAM) for 3D inspection of modern electronic devices using a single scan. Two complementary approaches to focus on different internal interfaces are examined: the Synthetic Aperture Focusing Technique (SAFT) utilizing a conventional SAM transducer and beaforming applied on an annular array transducer. A detailed comparison of both methods is presented. The image evaluation reveals that the SAFT approach delivers superior performance in terms of resolution and clarity.

Keywords: Scanning Acoustic Microscopy (SAM), 3D inspection of microelectronic devices, Synthetic Aperture Focusing Technique (SAFT), Annular Arrays, Signal processing

Introduction

Scanning Acoustic Microscopy (SAM) is a well-established tool in failure analysis and quality assurance. Traditionally, it has been standard practice to inspect commonly bonded interfaces to detect delaminations or misalignments. Earlier technologies, such as flip-chip packaging, typically required only a two-dimensional evaluation of a single interface. In contrast, modern manufacturing approaches—exemplified by System-in-Package (SiP) designs — necessitate comprehensive three-dimensional inspection. High-Bandwidth Memory (HBM), for instance, consists of a stack of at least eight silicon dies, all of which must be examined. In power electronics, the complexity increases further, with structures such as bond wires routed non-parallel to the surface, posing additional challenges for inspection.

To meet the required detection limits, SAM uses transducers operating within the range of $20\,\mathrm{MHz}$ to $2000\,\mathrm{MHz}$, depending on the specific requirements of the application in consideration. To achieve high resolution, these transducers are characterised by a high degree of focusing, resulting in minimal lateral extension of the focus spot and a correspondingly minimal depth of field. Therefore, it can be concluded that a single scan is capable of producing a sharp image of a single interface with precise focus at the point of interest. However, images of interfaces before or beyond the focus are significantly blurred. For sharp images of all interface several scans need to be performed. Consequently, conventional SAM imaging is forced to compromise between inspection time and the probability of detecting small defects. To overcome this tradeoff, SAFT and annular array focusing can be aplied, allowing focusing in different depths by postprocessing measurement data from a single lateral scan.

The efficacy of the Synthetic Aperture Focusing Technique (SAFT) in enhancing the performance of the inspection process has been demonstrated through its successful implementation [1]. SAFT works by superposing pre-processed signals from multiple measurement positions for each imaging point. This creates a virtual transducer with a synthetic aperture that focuses at a specific depth. SAFT has been demonstrated using laboratory [2] and industrial samples, including an HBM stack [3]. SAFT can be applied with standard single-element SAM transducers.

In other areas of ultrasonic applications, there are many different transducer designs. Phased array probes are a common part of medical ultrasound and low frequency NDT applications. A three-dimensional image can be created by scanning only one line, while focusing in the other two dimensions is achieved through various methods [Huang, 2017]. However, phased arrays consist of 64, 128 or more elements and require advanced technology to manufacture, as well as complex electronics to generate pulses and

DOI 10.5162/Ultrasonic2025/C2-a2

detect signals. Therefore, phased arrays operating at frequencies of $100\,\mathrm{MHz}$ or higher continue to be the focus of theoretical simulation studies.

In contrast, annular arrays consist of several concentric, ring-shaped elements. Typically, only six to ten elements are required to generate a focal spot approximately one wavelength in size, which can be shifted along the acoustic axis. Annular arrays are fabricated using either PVDF [4] or CMUT technology [5] with center frequencies around $50\,\mathrm{MHz}$ are available. As demonstrated in [6], it is well established that thin films of ZnO can be structured accordingly. Therefore, ZnO is a suitable material for the fabrication of annular array structures working above $100\,\mathrm{MHz}$.

The objective of this investigation is to compare the achievable resolutions for different measurement depths from a single lateral scan for three approaches: direct focusing with a single transducer, SAFT reconstruction, and focusing using an annular array. To this end, a customized annular array was designed, taking into account current manufacturing constraints. Sound field simulations were carried out to predict the performance of the proposed design. The evaluation focuses on the detection of delaminations at silicon–copper interfaces for various silicon layer thicknesses.

Methods

Sound field simulation

Sound field calculations are performed using harmonic Green's functions in combination with point source synthesis and a separation approach [7]. The surface of the piezoelectric element is used as the source area, and the stress distribution on the lens surface is computed accordingly. This stress distribution serves as a novel source for calculating the resulting stress distribution on the silicon surface. This approach allows the calculation of the sound field distribution within the silicon sample or on its backside. To obtain time-domain signals, stress components must be calculated for a set of frequencies. Harmonic synthesis is then carried out via the inverse Fourier transform.

SAFT with conventional SAM Transducers

Conventional SAM measurements are performed by scanning an area in the lateral xy-plane. At each scan position, an ultrasonic wave is excited, and the reflected signal is recorded. In the case of C-scan imaging, the maximum amplitude at a defined depth is evaluated and color-coded for each individual pixel. The complete signal is recorded at every position, resulting in a 3D dataset for subsequent processing. For SAFT reconstruction, the phase shift migration (PSM) technique is employed [8]. The 3D dataset is transformed into the frequency domain, multiplied by a phase term, and then transformed back into the time domain. This phase term depends on the sound velocity and the distance between the source and the reconstruction depth.To apply SAFT to SAM data, the transducer's focal point is assumed to act as a virtual point source for the purpose of reconstruction. According to the Near-Field SAFT approach [3], reconstruction can be performed at arbitrary depths—even if the focal point is located beyond the sample.

Beamforming with annular arrays

In most applications involving array transducers, time shifts for beamforming are determined using simple geometric models. Each array element is represented by a discrete attachment point, and the distance from each point to the designated focus position is calculated. Time-of-flight differences are then derived under the assumption of a constant speed of sound in a homogeneous propagation medium.

These time-of-flight differences are used to delay the individual signals prior to their superposition. In the case of the array used in this study, however, the wave propagates from the element through a lens body, is then focused by a spherically shaped calotte, and undergoes refraction as it passes from water into silicon. Due to the complex geometry and the significant refraction at the interface, geometric approximations for the wave propagation prove insufficient in this case. Instead, we make use of simulation data, in which the phase information for each frequency and array element has been precomputed. Beamforming is then achieved by applying phase shifts to the harmonic sound fields, such that all components constructively interfere at the designated focus position.

Generation of simulation data

The 8mm-VHF+ transducer operating at a frequency of $180\,\mathrm{MHz}$ (PVA TePla, Westhausen, Germany) was selected for use as a single-element transducer. A water path of $0.8\,\mathrm{mm}$ was chosen. The amplitude distribution is color-coded in decibels (dB) and normalized to its individual maximum. The sound fields in silicon are calculated for both, the single-element transducer, Fig. 1, and for the six array elements, Fig. 2. The geometry of the array elements is summarized in Tab. 1. The elements are located at the rear side of a lens body, which has a total length of $12\,\mathrm{mm}$ and a spherically shaped calotte with a radius of curvature of $20\,\mathrm{mm}$.

The reflected signal was calculated assuming silicon layers of different thicknesses z, followed by copper, Fig. 3 left. For this purpose, the stress distribution at the corresponding depth was computed. The reflec-

DOI 10.5162/Ultrasonic2025/C2-a2

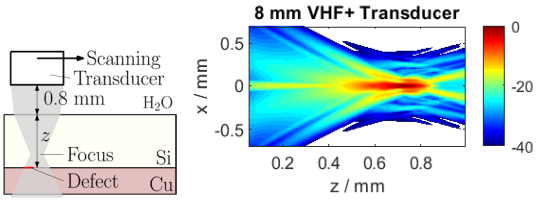

Fig. 1: left: sketch of the simulated setup and right: Sound field of the 8mm-VHF+ Transducer

Tab. 1: Geometry of the annular array with the inner radii r_i and the outer radii r_a of each element

Element	1	2	3	4	5	6
r_i / mm	0	0.72	1.03	1.27	1.48	1.67
r_a / mm	0.68	0.99	1.23	1.44	1.63	1.80

tion coefficient for the defect-free silicon-to-copper interface is 0.39. For a smaller area of $50\,\mu\mathrm{m}$ x $50\,\mu\mathrm{m}$, the reflection coefficient was set to -1, modeling a delamination. The scan data were generated by a 2D convolution of the local reflection coefficients with the signals at the interface. For both transducers, layer thickness z of $0.4\,\mathrm{mm}$, $0.6\,\mathrm{mm}$ and $0.9\,\mathrm{mm}$ were selected. Furthermore, echoes for a layer whose backside is located within the focus of the 8mm-VHF+ transducer at $0.736\,\mathrm{mm}$ were calculated. This reference is used to evaluate image quality. Fig. 3 right illustrates the resulting scan data for the focused scan (top left) and the defocused scans. Additionally, signals obtained from scanning were calculated for all six array elements and all three layer thicknesses.

Results and discussion

Three examples of SAFT reconstructions are shown at the top of Fig. 4. The delamination at $z = 0.6\,\mathrm{mm}$ is reconstructed with greater clarity than at $z = 0.4\,\mathrm{mm}$, which can be attributed to the smaller distance between the defect and the focal point. This observation is consistent with the expected increase in near-field effects at shallower depths (see Fig. 1). In both cases, the structures are surrounded by zones of reduced amplitude. At $z = 0.9\,\mathrm{mm}$, a loss of contrast and an apparent enlargement of the defect are observed. The reduced reconstruction quality results from a significant portion of the reflected wave not returning to the transducer, leading to a loss of signal energy and information. The images obtained using annular array focusing, Fig. 4 bottom, exhibit low contrast and an overestimated defect size. As shown in Fig. 5, the amplitude distribution along a single scan line allows a direct comparison between annular array focusing

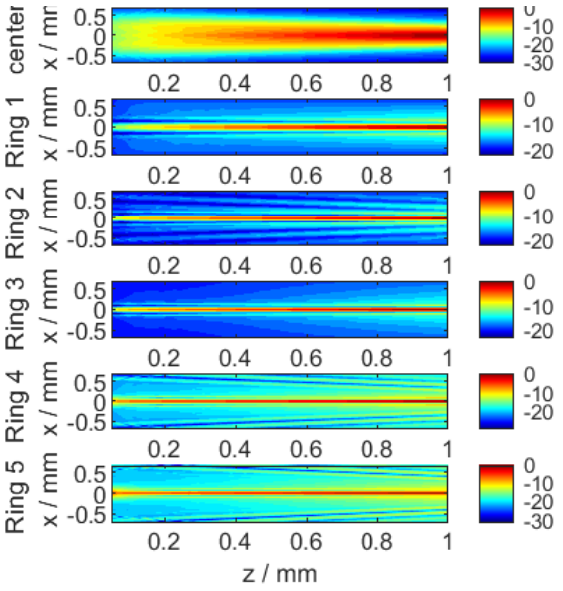

Fig. 2: Sound field of the 6 array elements.

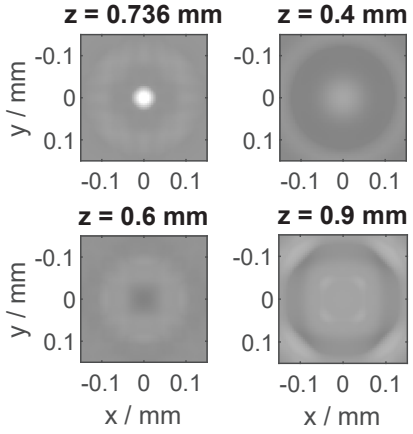

Fig. 3: Scan with 8mm-VHF+ Transducer in focus and for 3 depths out of focus.

(left) and SAFT reconstruction with the 8mm-VHF+ transducer (right). Compared to the amplitude profiles from the directly focused scan (black lines), it becomes clear that only SAFT reconstructions in the near field yield sufficiently accurate results. Even in these cases, a moderate reduction in contrast is observed.It must be noted that the annular array does not meet performance expectations. Despite the high number of degrees of freedom in its design, the array was configured according to established guidelines [4]. All elements have equal surface area to ensure consistent near-field length, and both the lens body length and radius of curvature were selected such that no near-field structures occur within the depth range relevant for the measurements (see Fig. 2). These findings stand in contrast to previous results and applications

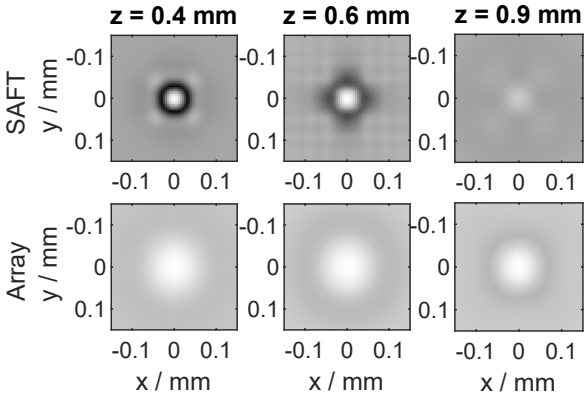

Fig. 4: Calculated images for three different depths; top: SAFT reconstruction with the 8mm-VHF+ Transducer and bottom: focused images obtained with the annular array.

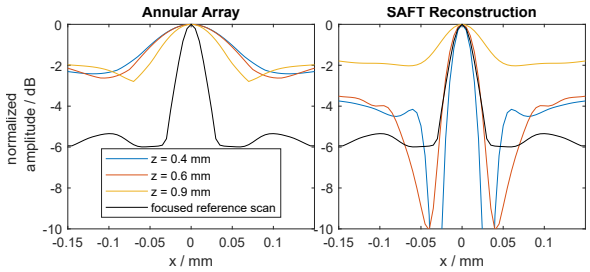

Fig. 5: Comparison of the amplitudes along a line scan; left: focusing with the annular array and right: the SAFT reconstruction.

of annular arrays in fluid environments.

Conclusion

The comparison of reconstruction results demonstrates a clear improvement in performance when applying the Near-Field SAFT algorithm. In contrast, both the far-field SAFT reconstruction (see Fig. 5, yellow line) and the beamforming results obtained with the annular array show reduced contrast and an overestimation of structure size, indicating a loss of resolution. The findings of this study suggest that annular arrays, in their current form, are not well suited for use in SAM. To enable their practical application, the focusing resolution must be significantly improved. This requires a broad parameter space and, consequently, the development of revised design rules. Existing guidelines, derived for configurations with homogeneous sound velocity or simple geometries, appear to be insufficient for more complex cases involving refractive interfaces. It should also be noted that all array designs remain subject to manufacturing constraints. The present design was selected based on current fabrication capabilities, and experimental validation of the simulation results is still pending. Nevertheless, this study provides an initial theoretical assessment of the Near-Field SAFT algorithm's performance. By systematically varying the assumed layer thicknesses, key performance characteristics can be derived, and the applicable limits of the algorithm can be defined.

Acknowledgments

The authors would like to thank the DFG for financial support in the Project 427525397.

References

[1] M. Wolf et al. "Inspection of multilayered electronic devices via scanning acoustic microscopy using synthetic aperture focusing technique". In: *2022 IEEE International Ultrasonics Symposium (IUS)*. IEEE. 2022, pp. 1–4.

[2] C. Kupsch and M. Wolf. "Nonlinear beamforming for Scanning Acoustic Microscopy Imaging through scattering surfaces". In: *2023 IEEE International Ultrasonics Symposium (IUS)*. IEEE. 2023, pp. 1–4.

[3] M. Wolf et al. "Near-Field Synthetic Aperture Focusing Technique to enhance the inspection capability of multi-layer HBM stacks in Scanning Acoustic Microscopy". In: *International Symposium for Testing and Failure Analysis*. Vol. 84741. ASM International. 2023, pp. 448–451.

[4] J. A. Brown, C. E. Demore, and G. R. Lockwood. "Design and fabrication of annular arrays for high-frequency ultrasound". In: *IEEE transactions on ultrasonics, ferroelectrics, and frequency control* 51.8 (2004), pp. 1010–1017.

[5] J. Zahorian and F. L. Degertekin. "Modeling and characterization of thin film coatings for high frequency CMUT annular arrays". In: *2011 IEEE International Ultrasonics Symposium*. IEEE. 2011, pp. 596–599.

[6] A. Kumar et al. "Design, fabrication and reliability study of piezoelectric ZnO based structure for development of MEMS acoustic sensor". In: *Microsystem Technologies* 25.12 (2019), pp. 4517–4528.

[7] E. Kühnicke. "Three-dimensional waves in layered media with nonparallel and curved interfaces: A theoretical approach". In: *The Journal of the Acoustical Society of America* 100.2 (1996), pp. 709–716.

[8] T. Olofsson. "Phase shift migration for imaging layered objects and objects immersed in water". In: *IEEE transactions on ultrasonics, ferroelectrics, and frequency control* 57.11 (2010), pp. 2522–2530.

DOI 10.5162/Ultrasonic2025/C2-a3

S-Parameter based Ultrasonic Transducer Characterization: a case study for high-frequency SAM-Transducers

Emanuel Leipner[1], *Mario Wolf*[1], *Stefan König*[3], *Peter Hoffrogge*[3], *Peter Czurratis*[3], *and Christian Kupsch*[1,2]

[1] *TU Bergakademie Freiberg, Measurement, Sensor and Embedded Systems Lab (MSE Lab), Freiberg, Saxony, Germany*

[2] *TU Bergakademie Freiberg, Center for Efficient High Temperature Processes and Materials Conversion (SN0390002), Freiberg, Saxony, Germany*

[3] *PVA TePla Analytical Systems GmbH, Westhausen, Baden-Württemberg, Germany*

emanuel.leipner@mse.tu-freiberg.de

Abstract: We present a case study applying an S-parameter-based method for characterizing SAM transducers from 20 MHz to 1 GHz. Leveraging the bandwidth and calibration accuracy of vector network analyzers, this approach enables consistent extraction of both electrical impedance and acoustic response. The results demonstrate the method's value in isolating transducer behavior, supporting system-level integration, and facilitating repeatable, high-frequency performance evaluation in scanning acoustic microscopy.

Keywords: Transducer Characterization, transient transducer characterization, Scattering Parameters, time-frequency-analysis, Scanning Acoustic Microscopy (SAM)

Introduction

Scanning Acoustic Microscopy (SAM) is an essential tool in chip manufacturing, providing non-destructive inspection capabilities crucial for quality control and defect detection. The performance of SAM systems heavily relies on the optimization of ultrasonic transducers tailored to specific applications. These transducers operate at high frequencies and employ highly focused ultrasound, covering a wide range of bandwidths from 20 MHz to 1 GHz.

The characterization of SAM transducers is challenging due to the complex interactions between the transducers and the transceiver system. Traditional characterization methods yield system responses that are a convolution of the transceiver and transducer responses, making it difficult to isolate and optimize transducer performance. This issue is exacerbated by the need for different transceivers for various frequency ranges and the coupling of acoustic and electrical domains [1].

To address these challenges, we present a case study demonstrating the application of an S-parameter based characterization method to high-frequency SAM transducers. This method separates the acoustic and electrical domains, providing pure transducer characteristics and enabling optimal system integration and performance enhancement. The case study includes the characterization of transducers with two focusing mechanisms, covering frequencies up to 1 GHz.

By showcasing this method in the field of high-frequency SAM transducer development, we aim to demonstrate its applicability across a wide range of configurations and excitation schemes. Furthermore, this work establishes the S-parameter-based approach as a general and powerful tool for transducer characterization. It allows for precise performance assessment and facilitates the systematic optimization of transducers for integration into advanced SAM systems.

S-Parameter Based Characterization Method

The S-parameter based characterization method offers a novel approach to isolating and optimizing the performance of ultrasonic transducers used in scanning acoustic microscopy (SAM). This method leverages the principles of radio frequency (RF) engineering and the capabilities of Vector Network Analyzers (VNAs) to separate the acoustic and electrical domains, providing pure transducer characteristics. The process involves measuring the S-parameters in the frequency domain, which represent the ratio of the reflected wave to the incident wave at a specific port. By performing calibrations with known standards, the VNA can eliminate the effects of the measurement system, including cables and connectors, and isolate the response of the ultrasonic transducer. The frequency-domain data is then transformed into the time domain using the inverse Fourier transform, allowing for the application of time-domain gating to separate the acoustic and electrical signals. This

approach enables the extraction of both the electrical properties and the acoustic signal of the transducer, providing a comprehensive understanding of its behavior.

Principles of S-Parameter Measurements

Scattering parameters (S-parameters) are used to describe the electrical behavior of electrical n-port networks in radio frequency (RF) engineering. For increased frequency, the typical assumption of concentrated elements in electrical circtuit analyses does not hold and voltages and currents are functions of time and space. Additionally, electrical energy exhibits wave-like propagation behavior, and effects such as reflection at interfaces where impedances change become relevant. A measured voltage at a given moment in time and at a defined point in space would still include the superposition of incident and reflected waves.

To deal with this effect, S-parameters are defined as the ratio of the reflected wave to the incident wave at a specific port - a conceptual interface in an RF network where power flow, voltage, and current are defined and measurable. For an n-port network, the elements $\underline{s}_{ij}$ of the S-parameter matrix $\underline{S}$ (where the underline denotes complex-valued quantities) are given by:

$$\underline{s}_{ij} = \left.\frac{b_j}{a_i}\right|_{a_k=0 \text{ for } k\neq i} \tag{1}$$

where a_i represents the incident wave at port i, b_j represents the reflected wave at port j, and the condition $a_k = 0$ for $k \neq i$ indicates that all other ports are terminated with matched loads.

In the case of ultrasonic transducers, which are typically modeled as 1-port networks, the primary S-parameter of interest is $\underline{s}_{11}$, representing the reflection coefficient at the port. Measuring $\underline{s}_{11}$ over a frequency range provides insights into both the electrical impedance and the acoustic behavior of the transducer.

S-Parameter Measurement - VNA and Calibration

The measurement device used in this method is a Vector Network Analyzer (VNA). To perform the measurement, we must define the reference plane, which is done by calibrating the VNA with known standards. This is done with an 16-term error correction approach measuring the standards Thru, Open, Match, Short (TOMS) and using these measurements to correct for any systematic errors in the measurement system, including the effects of cables and connectors [2].

The calibration process ensures that the measured S-parameters accurately represent the isolated transducer response, including both the electrical and acoustical domains. The result is a set of S-parameters that describe the transducer's behavior over the desired frequency range.

Separation of the Electric and the Acoustic Domains by Time-Domain Gating

To separate the acoustic and electrical domains, time-domain gating [3] is employed. It involves applying a window function to the time-domain impulse response to isolate the electrical signals from the acoustic reflections. Since electrical waves travel at the speed of light and acoustic waves at the much slower speed of sound, their time of flight differs. As a result, the early part of the signal reflects the electrical properties of the transducer, while later components reveal acoustic effects.

The frequency-domain data is transformed into the time-domain using the discrete inverse Fourier transform (iDFT):

$$\underline{x}_{11}(k) = iDFT\left(\underline{s}_{11}(f)\right) \tag{2}$$

where $\underline{s}_{11}(f)$ is the frequency-domain reflection coefficient, and $\underline{x}_{11}(k)$ is the time-domain impulse response.

The gated time-domain response can be expressed as:

$$x_{11,\text{gated}}(k) = x_{11}(k) \cdot w(k) \tag{3}$$

where $w(k)$ is the window function. This window $w(k)$ includes only time samples prior to the arrival of the first acoustic signal component, $k\Delta t < t_{\text{acoustic}}$ where Δt is the time resolution.

After transforming this subset $x_{11,\text{gated}}(k)$ back into the frequency domain by applying the DFT, the result can be used to compute the complex impedance $\underline{z}_{11}$ as follows [4, p. 181]:

$$\underline{s}_{11,\text{gated}}(f) = DFT\left(x_{11,\text{gated}}(k)\right) \tag{4}$$

$$\underline{z}_{11} = Z_0 \frac{1+\underline{s}_{11}}{1-\underline{s}_{11}(t)} \tag{5}$$

To extract the acoustic response and enhance the time resolution, the frequency-domain measurement $\underline{s}_{11}$ is extended to a symmetric vector. This involves synthetically adding the DC point and the complex-conjugated, mirrored copy of the measured N frequency points to create a symmetric spectrum. The iDFT is then calculated to obtain a real-valued time signal.

A time gate is applied to the time signal to extract the remaining part of the time signal $x_{11}(k)$ for

DOI 10.5162/Ultrasonic2025/C2-a3

$k\Delta t > t_{\text{acoustic}}$, which corresponds to the acoustic response of the transducer. This process effectively separates the acoustic and electrical domains, providing a pure acoustic response.

Experimental Setup

The experimental setup for the S-parameter-based characterization method includes a ZNB4 vector network analyzer (Rohde & Schwarz GmbH & Co. KG, Munich, Germany), a ZN-Z135 calibration kit for TOMS-calibration, and a selection of high-frequency SAM transducers (PVA TePla Analytical Systems GmbH, Westhausen, Germany). The transducers under investigation employ two distinct focusing mechanisms: curved piezoelectric elements, where the element itself focuses the wave, and sapphire acoustic lenses, where a planar element generates the wave and a sapphire body shapes it to a focal spot (see Tab. 1).

Tab. 1: Overview of Transducer Specifications [5]

No.	**Name**	**Focusing Mechanism**	**Focus Position**
1	Transducer 30 MHz	curved element	12.7 mm
2	Transducer 150 MHz	sapphire lens	8 mm
3	Rayleigh wave lens 1.000 MHz	sapphire lens	80 µm

The VNA was configured to perform S-parameter measurements in reflection mode. To avoid aliasing in time domain, it is essential to measure low frequency components as these components define the base period of the time signal. Further, to synthetically include the DC point, the lowest measured frequency also defines the frequency step size of the sweep. The maximal frequency must cover the expected frequency range of the transducer and corresponds to the inverse time resolution of the time-domain signal.

Results

Raw Measurement Time Signals and Time Gating

To illustrate the effectiveness of the S-parameter-based characterization, we now present the time-domain signals obtained from the VNA measurements. These were calculated as has been explained in section . The examples highlight how time-domain gating enables separation of electrical and acoustic components for further evaluation. Fig. 1 shows a raw time-signal of the transducer no. 3 and its correspondent time-gate.

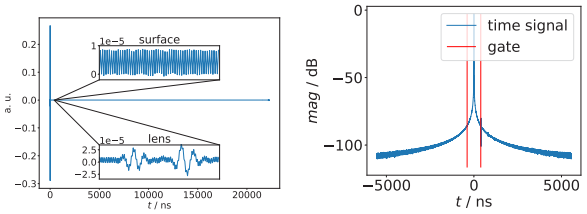

(a) raw time-signal (b) time-domain gating

Fig. 1: Raw magnitude of the S-parameter measurement $\underline{x}(k\Delta t)$ and the corresopndent time-signal and the time-gate applied for transducer no. 3.

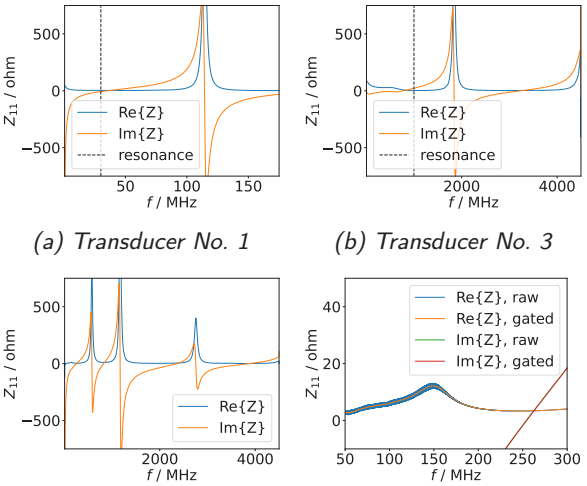

(a) Transducer No. 1 (b) Transducer No. 3

(c) Transducer No. 2 (d) Transducer No. 2, zoom

Fig. 2: Real and imaginary parts of the impedance $\underline{z}_{11}$ for three transducers. Subfigure (d) shows a zoomed view around the resonance of the 150 MHz transducer, comparing raw and gated data.

It is clearly visible that small echo amplitudes are heavily affected by noise, indicating the need for further filtering. The initial portion of the signal contains the electrical reflection, followed by two distinct acoustic pulses corresponding to the interface between the sapphire lens and water. The surface echo is barely distinguishable from the noise floor. A band-pass filtered version of the acoustic signal is shown in Fig. 3c.

Impedance Curves

The frequency-dependent impedance of the ultrasonic transducers is extracted from the S-parameter data, as shown in Fig. 2. These impedance curves provide insight into the electrical behavior of the transducers, including resonance characteristics and coupling efficiency.

Time-domain gating reduces unwanted reflections and system-induced artifacts, resulting in a cleaner

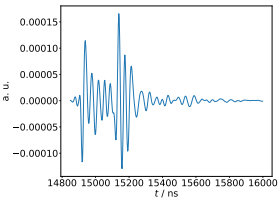

(a) Transducer No. 1

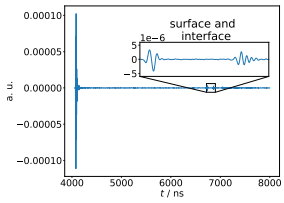

(b) Transducer No. 2

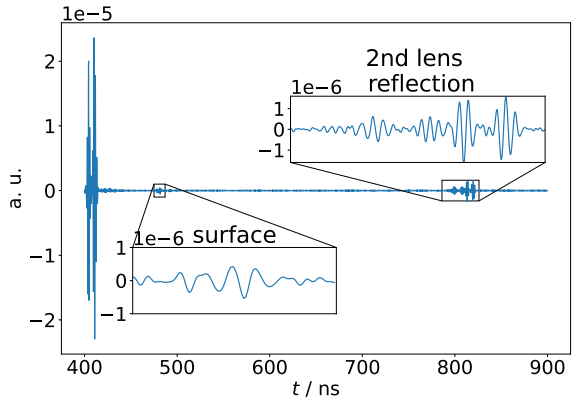

(c) Transducer No. 3

Fig. 3: Bandpass filterd time signals $x_{11}(k\Delta t)$ for three different transducers.

impedance response that more accurately represents the intrinsic behavior of the transducer, as demonstrated in Fig. 2d.

Importantly, the electrical and acoustic resonance frequencies are not aligned, see Fig. 2d. This mismatch indicates an opportunity for optimization: aligning these resonances could improve energy transfer between the electrical and acoustic domains, thereby enhancing transducer efficiency and operational bandwidth.

A-Scan Signals

A-Scan signals are obtained by analyzing the time-domain responses of the transducers, see Fig. 3. These signals represent the amplitude of the reflected ultrasonic waves as a function of time, providing information about the internal structure and defects within the sample. To enhance signal quality, band-pass filtering is applied to reduce the noise floor.

These results demonstrate that a wide range of transducers can be characterized using a single, broadband measurement setup without the need for dedicated transceiver hardware. The method achieves a dynamic range of approximately $88\,\mathrm{dB}$, enabling reliable identification of both strong and weak acoustic echoes. This includes reflections within the lens structure and from sample interfaces, confirming the method's suitability for high-resolution, quantitative A-scan analysis in scanning acoustic microscopy.

This highlights the versatility of the VNA-based method in capturing both weak and strong acoustic features with a single, broadband measurement.

Conclusion

We presented an S-parameter-based method for characterizing ultrasonic transducers in SAM systems. By separating electrical and acoustic domains using VNA measurements and time-domain gating, the method enables accurate impedance and A-scan analysis. It covers the typical $20\,\mathrm{MHz}$ to $1\,\mathrm{GHz}$ frequency range used in SAM applications, supporting efficient transducer evaluation and optimization with a single, broadband setup.

Acknowledgment

The research is funded by German Federal Ministry for Research, Technology and Space (BMFTR) under the reference number 13XP5187F, and by the Deutsche Forschungsgemeinschaft (DFG, German Research Foundation) – Project number 427525397.

References

[1] E. Leipner, M. Wolf, and C. Kupsch. "Characterization of high-frequency ultrasonic transducers using S-parameters: Separation of electrical and acoustic responses". In: *Mechanical Systems and Signal Processing* 238 (2025), p. 113172. ISSN: 0888-3270. DOI: https://doi.org/10.1016/j.ymssp.2025.113172. URL: https://www.sciencedirect.com/science/article/pii/S0888327025008738.

[2] H. Van Hamme and M. Vanden Bossche. "Flexible vector network analyzer calibration with accuracy bounds using an 8-term or a 16-term error correction model". In: *IEEE Transactions on Microwave Theory and Techniques* 42.6 (1994), pp. 976–987. DOI: 10.1109/22.293566.

[3] Z. Chen and Z. Xiong. "Differences of Time Domain Gating Implementions in Vector Network Analyzers". In: *2019 Joint International Symposium on Electromagnetic Compatibility, Sapporo and Asia-Pacific International Symposium on Electromagnetic Compatibility (EMC Sapporo/APEMC)*. 2019, pp. 597–600. DOI: 10.23919/EMCTokyo.2019.8893825.

[4] D. M. Pozar. *Microwave Engineering*. en. 4th ed. Chichester, England: John Wiley & Sons, Nov. 2011.

[5] P. T. A. S. GmbH. *Transducer / Range*. 2025. URL: https://www.pvatepla-sam.com/en/products/transducer/ (visited on 06/23/2025).

DOI 10.5162/Ultrasonic2025/C3-a1

Arbitrary Position and Width Pulses Sequences Excitation for Ultrasound Spectroscopy

Linas Svilainis[1], Alberto Rodriguez-Martinez[2], Muhammad Tayyib[1], Andrius Chaziachmetovas[1], and Juliana Manrique Cordoba[3]
[1]Kaunas University of Technology, Department of Electronics Engineering, Kaunas, Lithuania
[2]University Miguel Hernandez of Elche, Communications Engineering Department, Elche, Spain
[3]University Miguel Hernandez of Elche, Bioengineering Institute, Elche, Spain
linas.svilainiss@ktu.lt

Abstract: Application of spectral losses compensation in thickness resonance ultrasound spectroscopy (TRUS) was investigated. The arbitrary position, and width pulses (APWP) sequences were used to deliver higher energy and bandwidth and results compared to single pulse and chirp excitation in air-coupled and immersion setup.

Keywords: thickness resonance ultrasound spectroscopy, spread spectrum signals, losses compensation.

Introduction

Thickness resonance ultrasound spectroscopy (TRUS) is a tool to simultaneously estimate the sample thickness, density, ultrasound velocity and attenuation [1]. This technique requires wide bandwidth signals. Ultrasonic transducers are not able to provide broadband transduction. Furthermore, usually pulse signals are used for measurements. Pulse duration has to be reduced in order to obtain broadband spectrum. But then energy is reduced leading to SNR reduction. SNR can be improved by using higher excitation amplitude, but there is a limit. Spread spectrum (SS) signals can provide both energy (by increasing the signal duration) and bandwidth. Nonlinear frequency modulation (NLFM) and arbitrary position, and width pulses sequences (APWP) can also provide a programmable spectral content [2]. Then, by pushing the energy of the excitation signal into frequencies where transduction losses are high received signal bandwidth can be improved [3],[4]. This investigation analyses positive effects of spectral losses compensation on TRUS measurements.

Methods

TRUS [1] is exploiting the thickness resonance of the sample and temporal shift when sample is inserted. Its main advantages are that: i) completely overlapping internal reflections and ii) thickness and velocity of the sample are estimated simultaneously along with attenuation and density. When air-coupled ultrasound is used it becomes a non-contact resonant ultrasound spectroscopy (NC-RUS). Yet, it can be used in immersion setup too.

Two transducers (one acting as transmitter and other as receiver) are mounted at some distance, ensuring operation in the near field (flat wavefront). Two measurements (Fig. 1) are taken: i) calibration measurement, when path between transducers is free from obstacles and ii) sample measurement, when sample is inserted between transducers.

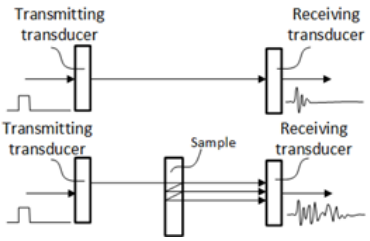

Fig. 1: TRUS measurement: Calibration (top), Reference (bottom) setup.

Calibration measurement is used to simulate the Sample signal by using the transmission model for layered media [5]. Model parameters (sample thickness, density, ultrasound velocity and attenuation) are adjusted until best fit to measured Sample signal is obtained. More details on the algorithm are in [6].

The 2 mm (resonance expected at 560 kHz) polycarbonate (PC) sample was investigated. Measurements were carried out in air-coupled and immersion setup.

Air-coupled setup used a pair of 20 mm diameter wideband 650 kHz center frequency transducers (designed and manufactured by the Spanish National Research Council, CSIC) [7]. Transducers were placed at 32 mm distance. Excitation used a half bridge topology pulser, 10 V bipolar, rectangular chirps (linear frequency modulation, LFM) and APWP [2] sequences. Sensitivity of these transducers is very high, up to 12 Pa/V in transmission, therefore, in order

DOI 10.5162/Ultrasonic2025/C3-a1

to avoid nonlinearity in air and exaggerate noise effects, low excitation voltage was used. Signal from receiving transducer was amplified by a programmable gain preamplifier (0.1-3 MHz bandwidth, 5 kΩ input impedance) [8]. A dedicated ultrasonic signal acquisition system [8] was used to collect data.

The APWP signals were optimised to achieve flat received signal spectrum within predefined frequency range. The 50 µs long bipolar APWP signals were derived using [6], based on 100 kHz-1.5 MHz 100 µs LFM excitation. Two ranges were used: 385 kHz-910 kHz (corresponding to -20 dB-deep losses compensation) and 240 kHz-860 kHz (-6 dB compensation). Additionally, LFM signals of same range were generated for comparison. LFM, APWP and single 100 ns pulse were used in NC-RUS measurements (Fig. 1).

Immersion setup used a pair of 6 mm diameter wideband composite 2 MHz center frequency transducers, placed at 10 mm distance (near field condition is satisfied only beyond 1.5 MHz). No diffraction correction was used. Acqusition used same equipment [2] as in air-coupled setup.

The APWP signals were optimised [3] to achieve flat received signal spectrum witin 740 kHz-3.43 MHz (corresponding to -20 dB-deep losses compensation) and 1.12 MHz-2.34 MHz (-6 dB compensation), basing on 300 kHz-3.9 MHz 50 µs long LFM excitation. Derived 40 µs APWP signals along with same range LFM and 100 ns pulse were used in TRUS [6] immersion measurements.

Results

Spectra of received signals in air-coupled setup for 650 kHz transducer pair are presented in Fig. 2 (compensated for -6 dB bandwidth), and Fig. 3 (-20 dB bandwidth). Results are normalized to excitation voltage, i.e. correspond to excitation using +/-1 V.

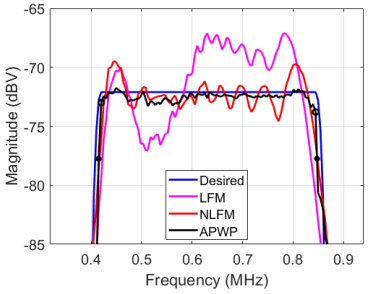

Fig. 2: Received signals spectra for 418 kHz-840 kHz bandwidth in air-coupled setup.

Flat APWP signal spectrum within the optimization range (circles) was achieved in both cases. It must be noted that bandwidth improvement comes at the

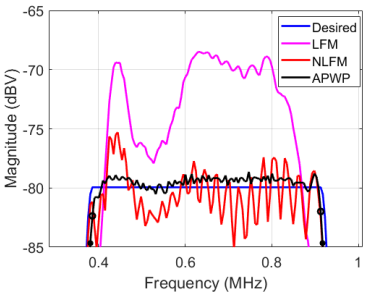

Fig. 3: Received signals spectra for 385 kHz-910 kHz bandwidth in air-coupled setup.

expense of energy loss at center frequency. LFM signal has its excitation spectrum uniformly distributed over desired bandwidth. Therefore, received signal contains losses at the bandpass edges. NLFM signal has broader spectral coverage, comparable to APWP, but its spectrum is nonuniform.

Results of NC-RUS, obtained using signals above are presented in Fig. 4. Frequency range covered by

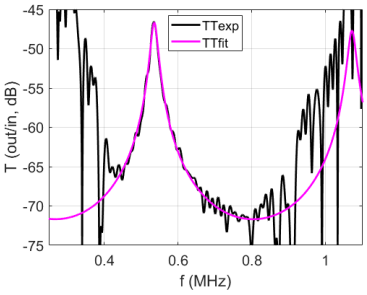

Fig. 4: NC-RUS magnitude for wideband APWP in air-coupled setup.

wideband excitation is sufficient to locate one resonant peak and one valley. NC-RUS inverse solution is close to expected values: thickness *h* is 2028 µm (caliper-measured value is 2050 µm), velocity *v* is 2172 m/s (expected 2222 m/s) density ρ is 1484 kg/m^3 (expected 1193.6 kg/m^3) attenuation α_0 is 29 Np/m at 560kHz (expected 43.5 Np/m) and estimated power law *n* is 0.3 (expected 1). The last two have large deviation form expected, but reason is that wide frequency range is required for these measurements to converge to correct values. Next experiment had much better frequency range coverage.

Results for 2 MHz transducers pair immersion setup when optimization was carried out within transducer -6 dB passband (1.12 MHz-2.34 MHz) are presented in Fig. 5. Results for broader (740 kHz-3.43 MHz), -20 dB passband optimization are presented in Fig. 6. Both have 40 µs length. It must be noted, that reception preamplifier bandwidth was 3 MHz, so compen-

DOI 10.5162/Ultrasonic2025/C3-a1

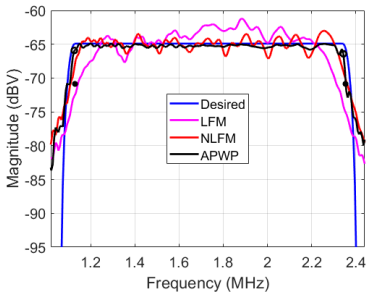

Fig. 5: Received signals at 1.12 MHz-2.34 MHz bandwidth for 2 MHz transducers immersion setup.

sation for preamplifier losses was required in order to attain 3.43 MHz passband. This was done intentionally, to demonstrate the compensation capabilities. Same can be concluded: broader bandwidth requires

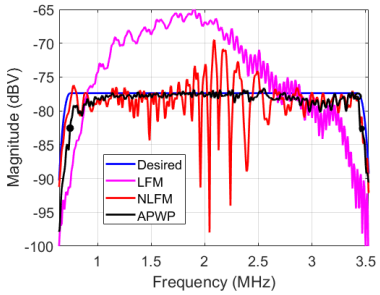

Fig. 6: Received signals at 740 kHz-3.43 MHz bandwidth for 2 MHz transducers immersion setup.

more passband losses, NLFM spectrum is less uniform when more compensation is required. Results of immersion mode TRUS, obtained using signals above are presented in Fig. 7.

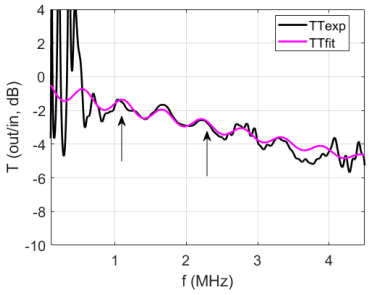

Fig. 7: TRUS magnitude for narrowband APWP signal.

Few conclusions can be drawn: PC impedance is much closer to water than air, therefore signal passing through contains more energy. Also, transduction to water produces much higher pressure. Therefore,

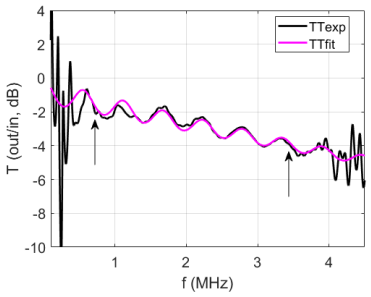

Fig. 8: TRUS magnitude for wideband APWP signal.

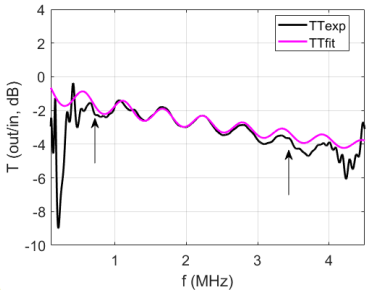

Fig. 9: TRUS magnitude for wideband LFM signal.

SNR is much higher than in previous experiment. Narrowband excitation concentrates more energy into passband, but SNR in the stopband is lower, therefore transmission response beyond the excitation range (indicated by arrows) is distorted. Less energy at high frequencies also means less accuracy in frequency-dependent attenuation estimation (α_0 and n). Wideband LFM signal does not provide enough energy at high frequencies, therefore fitting deviates (compare Fig. 8 and Fig. 9 results).

TRUS results are summarized in Fig. 10.

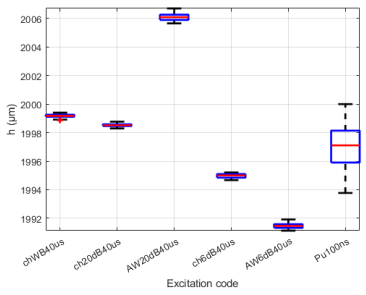

Fig. 10: TRUS results for sample thickness.

It can be noted that only wideband APWP signal (AW20dB40us) is closest to expected thickness h value (2045 µm), yet bias errors for other signals are not large, maximum 0.6 %. Higher bias errors are obtained for narrowband signals. Even pulse bias error

is lower than for narrowband signals. Yet, pulse has low energy therefore random errors are largest here. Same can be found for velocity (Fig. 11).

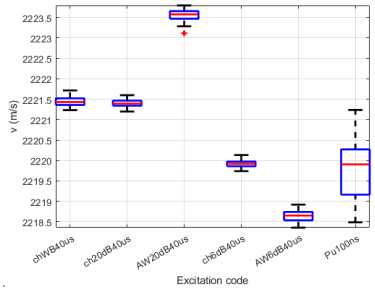

Fig. 11: TRUS results for sample velocity.

Wideband APWP signal is giving 2223 m/s (expected 2222 m/s), lowest bias error. Narrowband (ch6dB40us and AW6dB40us) or even wideband LFM (chWB40us) produce larger errors, yet maximum bias error is 0.2 %. Again, pulse has largest random errors. Similar situation is with density (Fig. 12).

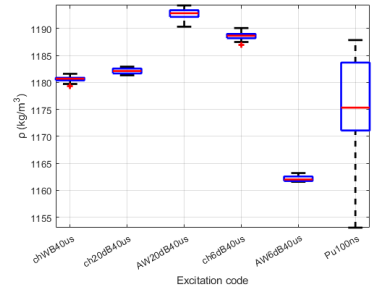

Fig. 12: TRUS results for sample density.

Attenuation was not estimated correctly (expected α_0 is 638 dB/m/MHz, (Fig. 13)), but this can be the case, because transducer diameter was small, for low frequencies wavefront deviates from flat, energy leaks away from beam. This results in artificially reduced attenuation at high frequencies.

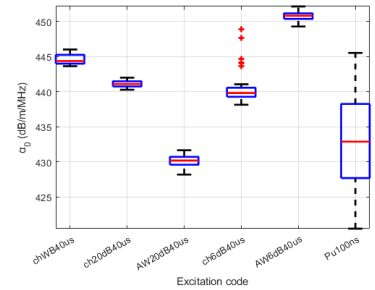

Fig. 13: TRUS results for sample attenuation.

It can be seen that random errors, though extremely small, are higher for APWP signal than its LFM counterpart (refer Fig. 2, Fig. 3, and Fig. 5, Fig. 6 for spectra comparison). This is the toll to be paid for improved bandwidth and reduced bias errors.

Conclusions

APWP signals can be used to broaden the bandwidth. This results in lower bias errors of TRUS if bandwidth is flat. Wideband SS signals, like LFM do not result in flat bandwidth therefore bias errors obtained are higher than for APWP. TRUS random errors are quite small, indicating it as an accurate tool for sample parameters measurement.

Acknowledgment

This research was funded by a Grant No. S-MIP-23-133 from the Research Council of Lithuania, and Project PID2022-138206OB-C32, from the Spanish Government—Agencia Estatal de Investigación (AEI)

References

[1] T. E. G. Álvarez-Arenas. "Simultaneous determination of the ultrasound velocity and the thickness of solid plates from the analysis of thickness resonances using air-coupled ultrasound". In: *Ultrasonics* 50 (2 2010). DOI: 10.1016/j.ultras.2009.09.009.

[2] L. Svilainis and A. Aleksandrovas. "Application of arbitrary pulse width and position trains for the correlation sidelobes reduction for narrowband transducers". In: *Ultrasonics*. Vol. 53. 2013. DOI: 10.1016/j.ultras.2013.04.001.

[3] L. Svilainis et al. "Ultrasound Transmission Spectral Compensation Using Arbitrary Position and Width Pulse Sets". In: *IEEE Transactions on Instrumentation and Measurement* 67 (8 2018), pp. 1778–1785. DOI: 10.1109/TIM.2018.2809838.

[4] M. Tayyib and L. Svilainis. "SNR equalization in non-contact resonant ultrasound spectroscopy measurements". In: *NDT & E International* 154 (2025), p. 103386. DOI: 10.1016/j.ndteint.2025.103386.

[5] L. M. Brekhovskikh and O. A. Godin. *Acoustics of Layered Media I*. Vol. 5. Springer Berlin Heidelberg, 1990. DOI: 10.1007/978-3-642-52369-4.

[6] Ž. Nakutis et al. "Air-Coupled Ultrasound Spectroscopy Air Parameters Compensation Technique". In: *IEEE Sensors Journal* 24 (8 2024), pp. 12667–12675. DOI: 10.1109/JSEN.2024.3369508.

[7] T. G. Alvarez-Arenas. "Air-Coupled Piezoelectric Transducers with Active Polypropylene Foam Matching Layers". In: *Sensors* 13 (5 2013), pp. 5996–6013. DOI: 10.3390/s130505996.

[8] L. Svilainis et al. "Electronics for Ultrasonic Imaging System". In: *Elektronika ir Elektrotechnika* 20 (7 2014). DOI: 10.5755/j01.eee.20.7.8024.

DOI 10.5162/Ultrasonic2025/C3-a2

Investigating the Acoustic Focusing Performance of PDMS Lens for Ultrasound Transducers

Venkata Shanmukha Srivatsav Pakki[1,2], Meghana Vishwanatha[1], Nooshin Saeidi[1,2], Markus Guttman[3,4], Celine Deutschbein[3,4], Karman Selvam[1], Maik Wiemer[1], and Harald Kuhn[1,2]
[1] Fraunhofer ENAS, Chemnitz, Germany
[2] Technische Universität Chemnitz, Chemnitz, Germany
[3] Institute of Microstructure Technology, Eggenstein-Leopoldshafen, Germany
[4] Karlsruhe Institute of Technology, Eggenstein-Leopoldshafen, Germany
venkata.shanmukha.srivatsav.pakki@enas.fraunhofer.de

Abstract: This study investigates acoustic focusing using a PDMS convex lens. The results revealed that the lens caused a shift in the focal region towards the transducer, as observed in experiments and simulations. The lens reduced near-field interference, increased output pressure, and improved beam convergence as indicated by a narrower beam profile. These findings highlight the potential of PDMS lenses for optimizing the performance of ultrasound transducers, including micromachined ultrasound transducers (MUT's), for various applications.

Keywords: Ultrasound transducers, acoustic lens, polydimethylsiloxane (PDMS), acoustic focusing, acoustic beamforming

Introduction

Acoustic focusing allows precise convergence of the ultrasound beam to a specific point enabling effective beam control suitable for applications such as medical imaging [1], particle manipulation and therapy [2]. Three principal strategies are used to create a focal region: geometric focusing of single element transducers, electronic phasing of array of elements, and acoustic lensing. Acoustic lensing will be the primary focus in this paper.

• ***Acoustic Lensing:*** The manipulation of sound waves can be achieved using materials or structures engineered to refract acoustic energy. An acoustic lens, often made of a polymer, alters the propagation of sound wave to create a converging or diverging wavefront.

When an acoustic wave propagates across media with differing acoustic properties (characterized by acoustic impedance Z and speed of sound v), refraction occurs according to Snell's law :

Eq. (1).

$$\frac{\sin(\theta_l)}{V_l} = \frac{\sin(\theta_m)}{V_m} \tag{1}$$

where θ_l and θ_m represent the angles of incidence and refraction, V_l and V_m represent the speed of sound in lens and medium respectively [3].

By carefully selecting lens materials and designing lens geometries, acoustic lenses can effectively control wave propagation. The effectiveness of acoustic lensing is significantly dependent on minimizing reflection losses at interfaces while maximizing transmission efficiency.

The implementations of acoustic lenses often involved solid shaped [4] and liquid-filled structures [5] designed to exploit refractive differences in lens and medium. The primary application of acoustic lensing are as follows:

a. Converging (focusing) lens – A convex lens with $V_l < V_m$ or a concave profile with $V_l > V_m$ causes waves to bend toward the axis, thus shortening the focal distance, increasing the signal to noise ratio (SNR) and on-axis pressure. Converging lenses are mostly used for medical ultrasound imaging [4] applications.

b. Diverging lens – When $V_l > V_m$, a convex profile or a concave profile with $V_l < V_m$ can also achieve divergence. Such designs are often employed to expand the field-of-view in large-area, in flat row–column-addressed (RCA) applications [6].

Polymers are often chosen for lens fabrication due to their suitable range of acoustic impedances such as Poly dimethyl siloxane (PDMS) [4] , Poly Urethane (PU) [7], and Room-temperature-vulcanizing silicone (RTV) [7]. The radius of curvature (R), diameter of transducer (D), thickness of lens (TL) and thickness of collar (TC), and geometrical focal length (F_{geo}) as illustrated in Fig. 1, are critical geometric parameters that influence acoustic focusing. Acoustic lenses are fabricated in various shapes, such as convex [4] and concave [6] geometries. Key goals of lens adaptation, include improving focusing capabilities, adapting the field of view, and achieving optimal resolution at varying depths.

This study investigates the acoustic focusing of ultrasound waves using a PDMS based convex lens.

DOI 10.5162/Ultrasonic2025/C3-a2

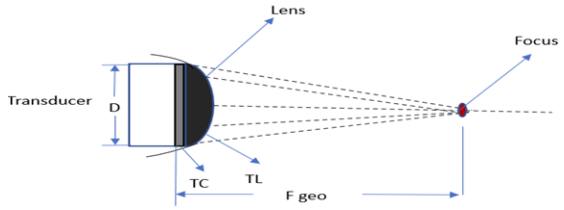

Fig. 1: Schematic of acoustic focusing using convex lens.

Tab. 1: Simulation parameters for acoustic focusing.

Design parameters	Values
Resonant frequency	$2\,\mathrm{MHz}$
Transducer diameter	$10\,\mathrm{mm}$
PDMS (speed of sound)	$970\,\mathrm{m\,s^{-1}}$
PDMS (density)	$1105\,\mathrm{kg\,m^{-3}}$

In this study we simulated, designed, fabricated and tested a convex PDMS lens on a piezo disc ultrasound transducers, operating in an oil medium at ambient temperature.

Method

This research work began with the design and simulation of the lens using k-Wave tool box in MATLAB software to assess its influence on acoustic characteristics. The results from the simulations were used as inputs to model and fabricate the PDMS convex lens. The lens was then characterized experimentally. The detailed methodology is described below.

1. **Design and Simulations:** The system, including the lens, transducer, and coupling medium, was modeled using the k-Wave toolbox in MATLAB to simulate acoustic wave propagation and focusing behavior. Initially, the beam profile of an unfocused ultrasound disc transducer, whose specifications are detailed in i.e. Tab. 1 was simulated in oil medium. The transducer was excited using a 3-cycle of sine wave burst. Simulations were conducted at the transducer's resonant frequency to evaluate their influence on beam profile, beam width, focusing and pressure distribution. To examine the role of lens, subsequent simulations were performed by introducing a convex PDMS lens positioned on top of the transducer. The simulations were performed with varying lens thicknesses(2, 2.5, 3 mm). The resulting variations in the aforementioned parameters were analyzed to gain insight, into the focusing behavior and beam-shaping effects influenced by the lens structure.

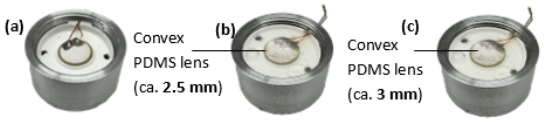

Fig. 2: Pictures of transducer without lens (a), 2.5mm convex lens (b), 3mm convex lens (c).

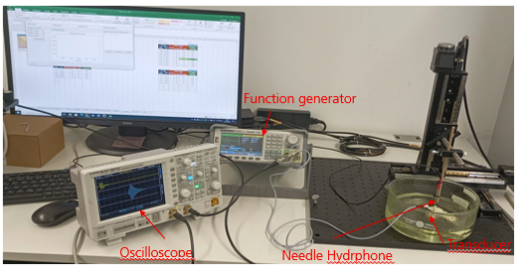

Fig. 3: Experimental setup.

2. **Lens fabrication:**

   The PDMS lens was custom-fabricated in convex shape. Both the transducer holder and the concave lens mold were 3D-printed to match the desired specifications based on simulation parameters. Sylgard 184 polymer was used as the lens material, the elastomer and curing agent were mixed in a 10:1 ratio by weight. The mixture was then degassed under vacuum to eliminate air bubbles, then cast over the disc transducer and into the lens mold. It was subsequently cured at room temperature for 48 hours. The fabricated lens is shown in Fig. 2.

3. **Experimental setup:**

   The fabricated lens was tested experimentally to evaluate the acoustic focusing effect as shown in Fig. 3. A needle hydrophone (Müller Hydrophone, sensitivity - 1.3 mV/bar) was positioned above the transducer using an XYZ translation stage to scan the acoustic field above the transducer. A function generator (Sigilent SDG 2042X Function generator) was used to produce a 3-cycle sine burst excitation signal, and an oscilloscope(Hameg Instruments HM0722, 2 channel, 70MHz digital oscilloscope) was employed to monitor both the input and output signals.

Results

The results are divided into simulations results and experimental results:

1. Simulation results: The simulation results for the unfocused ultrasound transducer revealed complex near field interferences, maximum output pressure of

DOI 10.5162/Ultrasonic2025/C3-a2

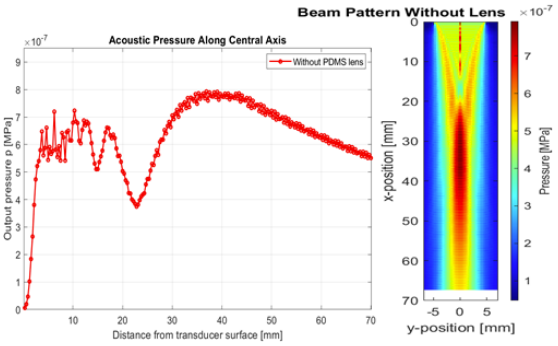

Fig. 4: Simulation results for without lens

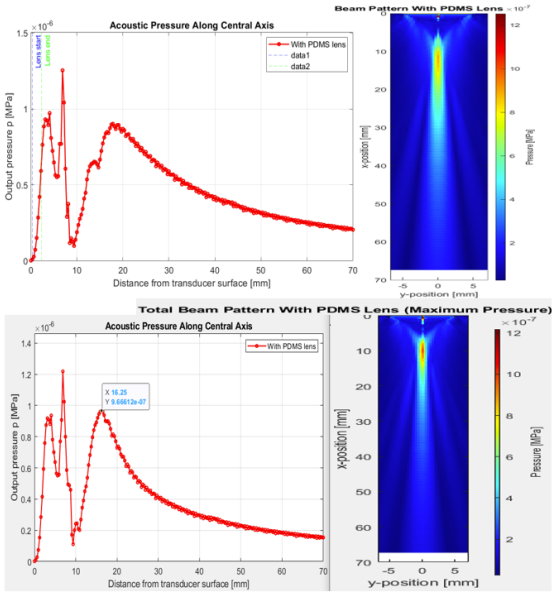

Fig. 5: Simulation results for lens thickness 2 mm(top), 2.5 mm(bottom)

0.8 Pa, focal point at ca. 38 mm and wide (unfocused) beam profile depicted in i.e. Fig. 4 .

The simulation from the 2.0 mm lens, resulted in output pressure of 0.9014 Pa, focal point shifted towards the transducer (to 17.81 mm), a focused (narrower) beam profile was observed as shown in i.e. Fig. 5. Simulation with 2.5 mm lens led to an increased output pressure of 0.9666 Pa, a 7.23% increase relative to the 2.0 mm lens, with the focal point shifting (to 16.25 mm) towards the transducer, and a more narrower beam profile was observed as shown in i.e. Fig. 5). Conversely, the 3.0 mm lens resulted in a decreased output pressure of 0.8775 Pa, a 9.22% reduction compared to the 2.0 mm lens, focal point experienced the largest shift towards the transducer at 13.75 mm, producing the most focused beam profile as shown in i.e. Fig. 6. Based on the simulation results the 2.5

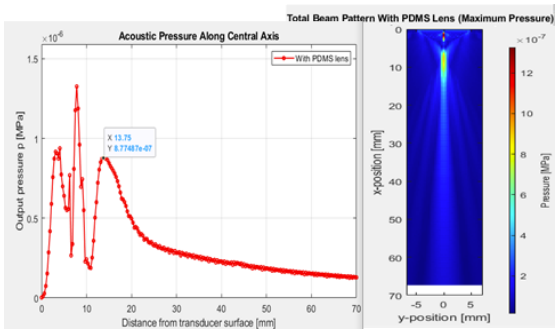

Fig. 6: Simulation results for with 3 mm lens

mm lens yielded the highest output pressure, while the 3.0 mm lens demonstrated superior focusing performance and hence these two thickness were selected for lens fabrication and experimental validation.

2. Experimental results: Initially a frequency sweep was performed to verify whether lens casting and integration affected the transducer's resonance; results showed no change for either the 2.5 mm or 3.0 mm lens. In the next experiment to identify the focal point or region using the XYZ stage, the needle hydrophone was moved with controlled step of 1 mm in Z axis. The focal point of the transducer (without lens) was observed at ca. 16.182 mm and with a peak to peak amplitude of 3.92 V. The results with addition of 2.5 mm lens showed a focal point at 13.746 mm i.e., a shift of 2.736 mm towards the transducer and with a peak to peak amplitude of 7.8 V. The experiment was repeated with a 3 mm lens which showed a focal point at 12.702 mm i.e., a shift of 3.48 mm towards the transducer and with a peak to peak amplitude of 7 V. There is also an decrease in the amplitude maximum at the focal point for 3 mm lens by 11.4% when compared to 2.5 mm thickness lens as shown in i.e. Fig. 7. As shown in Fig. 8, the convex lens significantly enhances the focusing capability of the initially unfocused transducer. Comparing output amplitude values which can be directly correlated to pressure, the trend is in agreement with the simulated results.

To analytically validate the focusing performance of the PDMS lenses, theoretical focal lengths were calculated using the Lens Maker's Equation and compared with values obtained from both simulations and experimental results. For the 3 mm PDMS lens, the theoretical focal length was approximately 11.215 mm, while the experimental value was 12.702 mm and the simulated value was 13.75 mm. Similarly, in the case of the 2.5 mm lens, the theoretical focal length was 12.370 mm, while the experimental and simulated focal lengths were found to be 13.746 mm and 16.25

DOI 10.5162/Ultrasonic2025/C3-a2

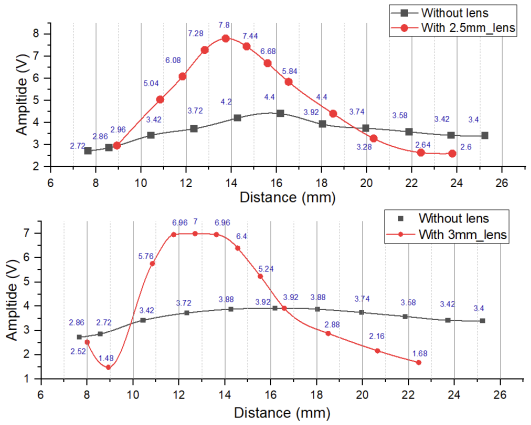

Fig. 7: Experiment results for lenses

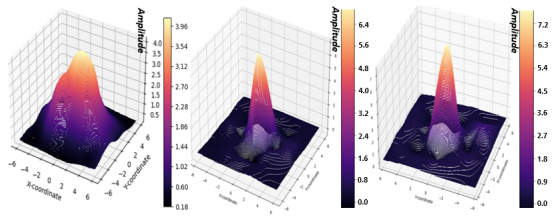

Fig. 8: Visualization of focused acoustic field from experimental measurements of without lens (left), 3mm lens (middle), 2.5mm lens (right)

mm, respectively. These results demonstrate good agreement among theoretical predictions, simulations, and experimental measurements in terms of shift of focal length, thereby validating the lens design and modeling approach. However, the pressure values obtained from simulations do not fully align with those calculated from the experimental amplitude measurements, likely due to factors such as system losses,and calibration differences. While the trends in focusing behavior are consistent, this discrepancy in pressure values highlights the need for careful calibration according to real time setup.

Conclusion

In this study, simulations and experiments were conducted using an ultrasound disc transducer in an oil medium, both without and with a convex shaped encapsulated PDMS lens. The results reveal important trade-offs in transducer design related to lens thickness. While thicker lenses (i.e., 3.0 mm) offer superior beam focusing and focal point closer to the transducer, they didn't yield the highest acoustic output pressure. Conversely, an intermediate thickness (i.e., 2.5 mm) yielded a better balance between acceptable focusing and enhanced pressure output. The discrepancies in output values result from idealized assumptions in the simulations, including the implementation of perfectly matched layers. The selection of an appropriate lens thickness would therefore depend on the specific application requirements or frequency characteristics of the transducer, prioritizing either maximum energy transfer at the focal point or the narrowest possible beam profile with maximum pressure.

Acknowledgment

The authors wish to thank the Center for Microsystems and nano technologies at Technische Universität Chemnitz and Karlsruhe Nano Micro Facility at Karlsruhe Institute of Technology for their valuable support.

References

[1] M. Audoin, A. Salari, B. G. Tomov, K. F. Pedersen, J. A. Jensen and E. V. Thomsen, 'Diverging polymer acoustic lens design for high-resolution row–column array ultrasound transducers,' *IEEE Transactions on Ultrasonics, Ferroelectrics, and Frequency Control*, vol. 14, pp. 202–213, 2024, 10.1109/TUFFC.2023.3327567.

[2] S. Wang, X. Wang, F. You and H. Xiao, 'Review of ultrasonic particle manipulation techniques: Applications and research advances,' *Micromachines*, vol. 14, p. 1487, 2023, 10.3390/mi14081487.

[3] S. H. Øygard, M. Audoin, A. Austeng, E. V. Thomsen, M. B. Stuart and J. A. Jensen, 'Accurate prediction of transmission through a lensed row-column addressed array,' *The Journal of the Acoustical Society of America*, vol. 151, pp. 3207–3218, 2022, 10.1121/10.0010528.

[4] C. Chang et al., 'Acoustic lens for capacitive micromachined ultrasonic transducers,' *Journal of Micromechanics and Microengineering*, vol. 24, p. 085 007, 2014, 10.1088/0960-1317/24/8/085007.

[5] C. Song, L. Xi and H. Jiang, 'Acoustic lens with variable focal length for photoacoustic microscopy,' *Journal of Applied Physics*, vol. 114, p. 194 703, 2013, 10.1063/1.4832757.

[6] H. Bouzari et al., 'Curvilinear 3-d imaging using row–column-addressed 2-d arrays with a diverging lens: Phantom study,' *IEEE Transactions on Ultrasonics, Ferroelectrics, and Frequency Control*, vol. 65, pp. 1182–1192, 2018, 10.1109/TUFFC.2018.2836384.

[7] S. Kim and J. Chang, 'Effect of acoustic properties of lens materials on performance of capacitive micromachined ultrasonic transducers,' *Journal of Medical and Biological Engineering*, vol. 36, pp. 536–544, 2016, 10.1007/s40846-016-0150-z.

DOI 10.5162/Ultrasonic2025/C6-a3

Monitoring the curing process of adhesive bonds using selective excitation of guided ultrasonic waves

Henning Zeipert[1], *Tom Nellius*[1], *Nicolas Schönlau*[1], *Mareen Wippermann*[1], *Leander Claes*[1], *Marcel Nicolai*[2], *Jens Prager*[2], *and Bernd Henning*[1]
[1]*Measurement Engineering Group, Paderborn University, Paderborn, Germany*
[2]*Div. Acoustic and Electromagnetic Methods, Federal Institute for Material Research and Testing, Berlin, Germany*
zeipert@emt.uni-paderborn.de

Abstract: A measurement setup for the selective excitation of guided ultrasonic waves in adhesively bonded plates is introduced. Changes of the dispersive behaviour of the guided waves during the curing process is known to be accompanied by a change in the propagating waves group velocities. The proposed measurement setup is used to monitor that change during the curing process of an aluminium-epoxy-polycarbonate bond.

Keywords: Ultrasonic guided waves, Selective excitation, Non-destructive testing, Adhesive bonding, Condition monitoring

Motivation

Due to their capability of providing very strong and long-lasting material joints as well as their versatility, adhesive bonds are commonly used in a wider range of manufacturing processes. However, the standardised testing methods for adhesive bonds are predominantly destructive. Consequently, those methods can never be applied to the actual joint but only to specially produced test samples. For quality, safety and economic reasons, testing the actual joint is of great interest hence requiring a non-destructive testing (NDT) method. So far, NDT-methods for e.g. flaw detection are well established, but are currently not capable of monitoring the quality of an adhesive bond.

In previous investigations [1], broadband guided ultrasonic waves are utilised to observe the change in dispersive behaviour during the curing of an adhesively bonded aluminium-polycarbonate sample. It is shown that the overall dispersive behaviour of the sample is mainly dominated by the aluminium at the beginning and slowly transitions towards multi-layered behaviour during the curing process. This transition is accompanied by changes in the wave modes group velocities.

Based on those findings, this investigation proposes an approach for the monitoring of adhesive bonds. Utilising an experimental setup for the selective excitation and measurement of guided waves, their group delay and, consequently, their group velocities can be ascertained. The employment of this method during the curing of an epoxy adhesive in an aluminium-polycarbonate structure enables the direct observation of changes in the dispersive behaviour of the system and thus a monitoring method for the curing process.

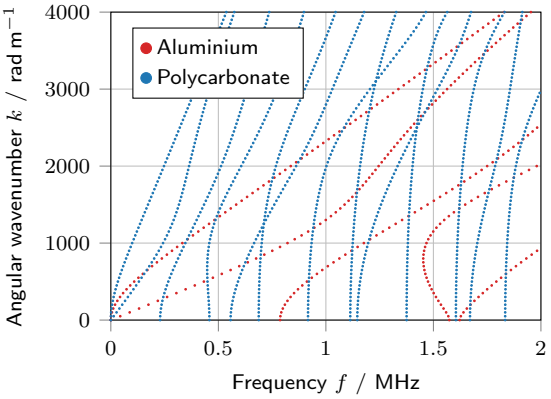

Fig. 1: Dispersion diagrams of an aluminium ● and a polycarbonate ● plate. Both with a thickness of 2 mm.

Guided waves in coupled plate-shaped structures

The properties of guided elastic waves strongly depend on the material as well as the geometric parameters of the waveguide. Fig. 1 shows dispersion diagrams of an aluminium and a polycarbonate plate in frequency-wavenumber-domain. Given that both plates have a thickness of 2 mm and only differ in their respective material parameters the direct comparison emphasises that material dependency. Ultrasonic guided waves are commonly used for NDT-methods due to their high sensitivity to changes of those parameters.

To calculate the dispersion diagrams for given material parameters, the scaled boundary finite element method (SBFEM) [2] can be used. A plate-shaped waveguide is only discretised in its thickness direction, with harmonic, analytical expressions describing the

DOI 10.5162/Ultrasonic2025/C6-a3

Tab. 1: Material parameters of the samples used in this investigation are determined via an inverse measurement procedure.

Material	Long. wave vel. c_L	Trans. wave vel. c_T
Aluminium	$6489\,\mathrm{m\,s^{-1}}$	$3148\,\mathrm{m\,s^{-1}}$
Polycarbonate	$2227\,\mathrm{m\,s^{-1}}$	$917\,\mathrm{m\,s^{-1}}$

waves in their direction of propagation.

In order to carry out precise simulations and thus predict the behaviour of the actual samples in a targeted manner, it is necessary to ascertain the elastic properties of the samples under test. In preparation of further investigations the aluminium and polycarbonate samples behaviour are quantified using an inverse measurement procedure based on the broadband excitation of guided ultrasonic waves [3, 4]. The material parameters of the model are adjusted through this optimisation-based approach, with the objective that the resulting simulations correspond to the measurement based equivalent of their dispersion diagrams. In the context of this study, an isotropic material model is used for the aluminium and polycarbonate layers. This reduces the necessary material parameters to the longitudinal wave velocity c_L as well the transversal wave velocity c_T. The determined parameters, as already used for the underlying simulation of Fig. 1, are provided in Tab. 1.

A spring-based, lumped-element approach is used to represent the adhesive bond between the two layer-materials for further simulations of this study. It can be shown that the transmission of shear movements, i.e. in-plane movement of the plates surface at the interface, shows greater changes during the curing process of the adhesive than normal movements. The model therefore uses separate springs (κ_o, κ_i) for the out-of-plane and in-plane-movements at the material interface [5].

Experimental Setup

A wide range of research on NDT methods is based around broadband guided ultrasonic waves. However, for a considerable number of applications, or at least for their measurement effects, it is not necessary to acquire broadband information of dispersive behaviour of a specimen. On the contrary it is usually beneficial to restrict the excitation to emphasise certain effects. The aim of the experimental procedure presented in the following is to excite a certain mode in the specimen defined by a given frequency f_ex and angular wavenumber k_ex (*selective excitation*). Fig. 2 depicts a schematic representation of the measurement setup used in this investigation. The excitation is done via

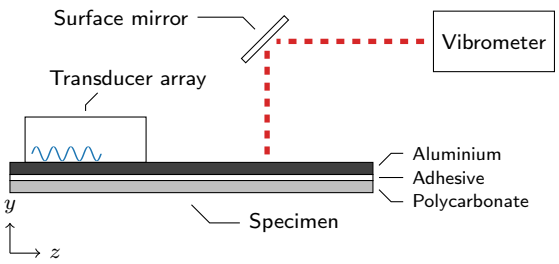

Fig. 2: Measurement setup for the selective excitation of guided ultrasonic waves.

a 64 element transducer array (*Imasonic*), which is directly coupled onto the surface of the specimen using a coupling gel. With the assumption that shifting an oscillation over the array's elements and thereby imprinting a guided wave with the same properties into that specimen, the individual elements are successively excited using the same sinusoidal signal with the selected frequency f_ex. To ensure the imprinted guided waves angular wavenumber matches the expectation, the time shift Δt between the neighbouring elements excitations has to be calculated. Since the elements excitation is pure sinusoidal, the waves group velocity c_gr can directly be calculated from the excitation parameters:

$$c_\mathrm{gr} = \frac{2\pi f_\mathrm{ex}}{k_\mathrm{ex}}$$

To ensure the resulting guided wave propagates with the expected group velocity c_gr, the time delay Δt directly results form the distance between those elements (here $\Delta p = 1\,\mathrm{mm}$):

$$\Delta t = \frac{\Delta p}{c_\mathrm{ph}} = \frac{\Delta p\ k_\mathrm{ex}}{2\pi f_\mathrm{ex}}.$$

The signal generation and setting of the necessary time shift Δt are done via a purpose-build hard- and software-interface developed by Nellius et al. [6].

The detection of the propagating waves are performed using a laser Doppler vibrometer (VibroFlex QTec by *Polytec*). The laser beam is directed on to the specimens surface using a surface mirror. This mirror is mounted onto a linear actuator enabling a precise and reproducible variation of the point of detection.

For an initial proof of concept a $4\,\mathrm{mm}$ aluminium plate is used as a sample. The experiment aims for an excitation of a guided wave with a frequency of $f_\mathrm{ex} = 1.375\,\mathrm{MHz}$ and an angular wavenumber of $k_\mathrm{ex} = 2320\,\mathrm{rad\,m^{-1}}$. Using a Fourier transform on the measurement data enables an initial validation for the excitation of the correct frequency f_ex. For a given frequency, however, multiple modes can propagate in a waveguide (see Fig. 1). But the information

DOI 10.5162/Ultrasonic2025/C6-a3

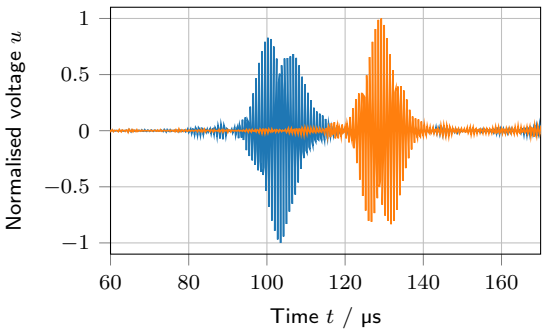

Fig. 3: Measurement signals of selectively excited guided waves ($f_{\mathrm{ex}} = 1.375\,\mathrm{MHz}$, $k_{\mathrm{ex}} = 2320\,\mathrm{rad\,m^{-1}}$). The point of detection is varied by $6.5\,\mathrm{cm}$ between the first ● and the second ● measurement for a determination of the waves group velocity.

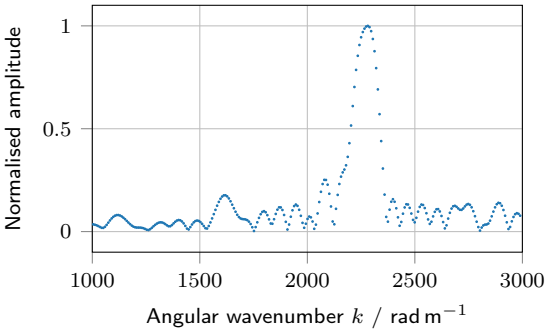

Fig. 4: Angular wavenumber of selectively excited guided waves at the targeted frequency of $f_{\mathrm{ex}} = 1.375\,\mathrm{MHz}$.

regarding the wavenumber can not be extracted directly from the time-resolved measurement data. By varying the point of detection along the direction of propagation (here $\Delta z = 6.5\,\mathrm{cm}$) two different measurements with the same excitation are carried out (see Fig. 3). Based on the time difference between the two measurement signals the group velocity c_{gr} of the waves is obtained. Based on the simulations, the targeted wave is expected to propagate with a group velocity of $c_{\mathrm{gr}} = 2369\,\mathrm{m\,s^{-1}}$. An evaluation of the measurement data yields a group velocity c_{gr} of $2452.8\,\mathrm{m\,s^{-1}}$ and thus deviates $3.5\,\%$ from the prediction.

To investigate the deviation of the group velocities a line scan using the same excitation is carried out: Varying the point of detection with a step size of $\Delta z = 1\,\mathrm{mm}$ and performing a measurement at each position over a length of $8\,\mathrm{cm}$, data in time- and space-domain is acquired. By applying a two-dimensional Fourier transform to that measurement data yields information in frequency- and wavenumber domain. Fig. 4 depicts the angular wavenumber information for the selected frequency of $f_{\mathrm{ex}} = 1.375\,\mathrm{MHz}$. Since the most significant contribution is located close to the desired wavenumber the selective excitation appears successful. It can, however, also be seen that there are a few non-negligible contributions from other wave modes. Since those are notably smaller than the targeted angular wavenumber their impact on the propagating waves are presumed small but may lead to the deviation in the observed group velocity.

Monitoring of an adhesive curing process

In previous studies, the change in the acoustic behaviour of adhesively bonded plates during the process of adhesive curing has been investigated utilising broadband guided ultrasonic waves [1]. It is shown that this change can be observed by determining the group velocity of the propagating modes. Therefore, the presented approach of *selective excitation* is well suited for process monitoring in this application. This approach not only requires less experimental effort, but also provides results in a shorter time. While the previous methods required up to $15\,\mathrm{min}$ per measurement routine, the current setup takes about $50\,\mathrm{s}$ per measurement and could be enhanced further. Especially when observing transient processes, the reduced time is relevant since a single measurement assumes the system to be static and therefore summarises the change happening during a measurement period.

A monitoring of an adhesive curing process is carried out using the specimen configuration as depicted in Fig. 2: A $2\,\mathrm{mm}$ aluminium and a $2\,\mathrm{mm}$ polycarbonate plate are bonded using an epoxy adhesive (see Fig. 2). The parameters for the selective excitation are chosen as $f_{\mathrm{ex}} = 0.65\,\mathrm{MHz}$ and $k_{\mathrm{ex}} = 740\,\mathrm{rad\,m^{-1}}$. Fig. 5 visualise numeric simulations of the selected mode curve for a weakly coupled

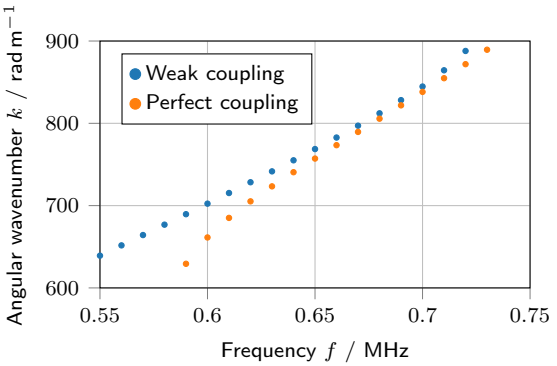

Fig. 5: Computed dispersion curves of a low and high coupled variation of an aluminium-polycarbonate system using a spring-based coupling model.

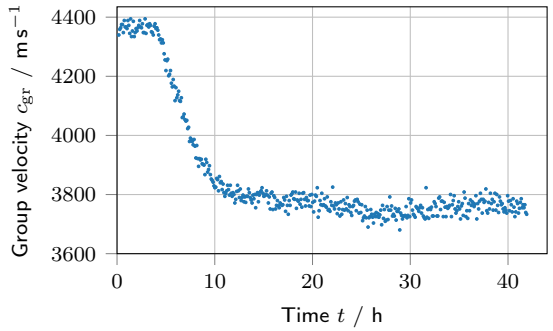

Fig. 6: Change of group velocity of a selectively excited wave mode ($f_{ex} = 0.65\,\mathrm{MHz}$, $k_{ex} = 740\,\mathrm{rad\,m^{-1}}$) during the adhesive curing process of an aluminium-epoxy-polycarbonate bond.

($\kappa_o = 10^{13}$, $\kappa_i = 10^9$) as well as for a perfectly coupled ($\kappa_o = 10^{15}$, $\kappa_i = 10^{15}$) system. The gradient of the mode curve does increase with increasing coupling strength. It is therefore expected to observe a decreasing group velocity during the curing process.

To monitor the curing process a measurement is performed every $5\,\mathrm{min}$. By evaluating the change in runtime of the excited propagating guided waves, their group velocities are determined for each of those measurements. Fig. 6 visualises the change of the waves group velocity c_{gr} in relation to the passing time during the curing process. One can clearly observe the change in the acoustic behaviour of the specimen. While the group velocity does not change much during the initial phase of about $4\,\mathrm{h}$ it decreases significantly over the following time period of about $12\,\mathrm{h}$. The overall behaviour is presumably dominated by the aluminium component at the beginning and changes over time towards the expected multi-layered behaviour. The nearly static value of the group velocity ($c_{gr} \approx 3750\,\mathrm{m\,s^{-1}}$) after the curing process terminates ($t \geq 20\,\mathrm{h}$) is slightly smaller than the simulation based estimation of $3830\,\mathrm{m\,s^{-1}}$. This again may be due to the influence of additionally excited wave components (see Fig. 4).

Conclusion

The investigation at hand introduces and evaluates a measurement setup for the selective excitation of guided ultrasonic waves. This setup is based on the targeted time-delayed excitation of the individual elements of an ultrasonic transducer array. By imprinting a spatiotemporal, sinusoidal wave into plate-like specimens, guided waves with a given frequency and group velocity are excited.

Using this method of selective excitation during the curing process of adhesively bonded aluminium-epoxy-polycarbonate structures, the change in acoustic behaviour can be observed. While the material bond is still dominated by the aluminium behaviour at the beginning, a clear change towards multi-layered behaviour can be observed in the change of the waves group velocity. The method is therefore well suited as a monitoring system for adhesive curing processes.

Nevertheless, evaluations of the measurement method still demonstrated a considerable scope for improvements regarding the selectivity. The bandwidth of the generated guided waves should therefore be further reduced, especially in wavenumber domain. Furthermore, it is important to acknowledge the statistical deviations in the obtained group velocity values, particularly in areas where the specimen under test is expected to exhibit static behaviour. Additional measures will have to be implemented to reduce these deviations further.

Acknowledgements

This research is funded by the Deutsche Forschungsgemeinschaft (DFG, German Research Foundation) – 449607253 (LaWaMoRe II).

References

[1] H. Zeipert et al. "Investigation of change in dispersive behaviour during adhesive curing in multi-layered structures". In: *Fortschritte der Akustik - DAGA 2023*. 2023.

[2] C. Song and J. P. Wolf. "The scaled boundary finite-element method – alias consistent infinitesimal finite-element cell method – for elastodynamics". In: *Computer Methods in Applied Mechanics and Engineering* (1997).

[3] S. Johannesmann et al. "Inverser Ansatz zur akustischen Charakterisierung plattenförmiger Materialproben". In: *Fortschritte der Akustik - DAGA 2017*. 2017.

[4] S. Johannesmann et al. "Lamb wave based approach to the determination of acoustic material parameters". In: *tm - Technisches Messen* (2022). DOI: 10.1515/teme-2021-0134.

[5] M. Nicolai et al. "On the repulsion effect of coupled Lamb waves modes". In: *ICSV30, Annual Congress of International Institute of Acoustics and Vibration (IIAV)*. 2024.

[6] T. Nellius et al. "Ultrasonic phased array interface using programmable I/O and microprocessor clock synchronisation". In: *Sensor and Measurement Science International*. 2025. DOI: 10.5162/smsi2025/a5.4.

DOI 10.5162/Ultrasonic2025/C6-b3

A Holo-array for Enhancement of Ultrasonic Focusing

Yanfeng Lang[1,2], Zhibo Yang[1*], Xuefeng Chen[1], and Zhongqing Su[2**]
[1]Xi'an Jiaotong University, Xian, China
[2]The Hong Kong Polytechnic University, Hong Kong, China, Hong Kong
*phdapple@mail.xjtu.edu.cn **zhongqing.su@polyu.edu.hk

Abstract: Conventional phased arrays are typically used to steer the main lobe under spatial Nyquist constraints. When these constraints are violated, grating lobes emerge. However, in Lamb-wave-based damage identification, side and grating lobes are often overlooked. To address this, a holo-array is proposed in this study. Instead of relying solely on phase control, the phase, frequency, and amplitude of the probe wave are individually tailored for each array element to steer the main lobe, suppress grating lobes, and reduce side lobes. The effectiveness is validated through experiments on an aluminum plate.

Keywords: grating lobe, side lobe, phased array, damage detection,pseudo damage

Introduction

The guided-wave-based phased array (P-array) is a highly effective technique for structural damage detection. Lamb waves, a class of guided waves propagating in plate-like structures, offer distinct advantages such as low attenuation over long distances, rapid propagation velocity, and high sensitivity to various types of damage.

However, the P-array is subject to inherent limitations in its parameter configuration. As reported by Yu et al. [1], with the increase of ratio of element pitch and wavelength of the excitation d/λ, although the beam width is narrower and narrower, which means that the direction precision is improved, more and more sidelobes (with the magnitude lower than the main lobe), even grating lobes (with the magnitude equivalent to the main lobe) appear.

To address this challenge, Antonik [2] introduced the frequency diverse array, which enables dynamic manipulation of the beam pattern in radar systems. In addition to phase and frequency, amplitude serves as a critical parameter in defining signal waveforms and controlling energy distribution within the array.

This study introduces a holo-array approach that leverages the unique dispersive property of Lamb waves. By individually customizing the phase, frequency, and amplitude of the anti-dispersive probe signal for each array element, the holo-array achieves main lobe steering, grating lobe suppression, and sidelobe reduction. The proposed method is experimentally validated on an aluminum plate.

Concept of Holo-array

In the conventional phased array composed of M elements, distinct phase delays are applied to each element to ensure that the emitted signals constructively interfere and become in-phase at the desired focal location. The phase vector can be denoted by $\boldsymbol{\varphi} = [\varphi_1, \varphi_i, ..., \varphi_M]$.

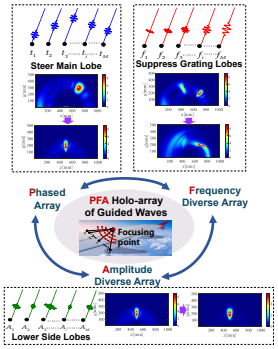

Fig. 1: The concept of PFA holo-array of ultrasonic guided waves

An emitted signal is fundamentally characterized by three parameters: amplitude, frequency, and phase. While conventional phased arrays primarily utilize phase control to achieve constructive interference at a target location, the amplitude and frequency of the array signals can also be tailored to further enhance array performance. The corresponding amplitude vector and frequency vector are denoted by $\boldsymbol{a} = [a_1, a_i, ..., a_M]$ and $\boldsymbol{f} = [f_1, f_i, ..., f_M]$.

With the objective of enhancing array energy at the desired focal point $F(x_0, y_0)$, the phase, frequency, and amplitude of the excitation signals are individually customized according to the following strategy.

The phase for the ith element is calculated by:

$$\varphi_i = k(\omega) r_i^F \tag{1}$$

where r_i^F represents the propagation distance from the ith element to the focusing point $F(x_0, y_0)$

The increasing frequency vector is designed in the work and the frequency for ith element can be calcu-

late by:

$$f_i = f_c + (i - \frac{(M-1)}{2} - 1)\Delta f \tag{2}$$

where f_c is the center frequency and Δf is frequency offset.

The Dolph–Chebyshev synthesis is adopted to construct the array pattern with equiripple sidelobes—i.e., sidelobes of equal amplitude. The amplitude a_i for the ith element of the even-element array and odd-element array can be calculated by Eq. (4) and Eq. (6), respectively.

$$\text{even:} a_i = \sum_{q=i}^{M} (-1)^{M-q} (x_0)^{2q-1} \cdot A \tag{3}$$

$$A = \frac{(q+M-2)!(2M-1)}{(q-i)!(q+i-1)!(M-q)!} \tag{4}$$

$$\text{odd:} a_i = \sum_{q=i}^{M} (-1)^{M-q+1} (x_0)^{2(q-1)} \cdot B \tag{5}$$

$$B = \frac{(q+M-2)!2M}{(q-i)!(q+i-2)!(M-q+1)!} \tag{6}$$

where $x_0 = cosh\left(\frac{cosh^{-1}(10^{-L_s/20})}{M-1}\right)$. L_s is the sidelobe level.

In this study, both amplitude and frequency are incorporated into the array control strategy. Accordingly, we propose a classification scheme for various array configurations. The conventional phased array, in which only phase control is applied, is denoted as the P-array. Arrays that incorporate both phase and amplitude control are referred to as PA-arrays, while those utilizing phase and frequency control are termed PF-arrays. The array configuration that simultaneously manipulates all three parameters is designated as the PFA holo-array.

Anti-dispersion Focusing Strategy

The tone burst signal is commonly-used for Lamb-wave-based damage detection, as shown in Eq. (7).

$$s(t) = w(t) sin(2\pi f_c t) \tag{7}$$

where $w(t)$ denotes the Hann window, which can be expressed as $w(t) = 0.5(H(t) - H(t - \frac{N_c}{f_c}))(1 - cos(\frac{2\pi f_c t}{N_c}))$. $H(\cdot)$ is the Heaviside function .Two parameters need to be determined: the number of cycles N_c and the center frequency f_c.

Lamb waves exhibit dispersive propagation characteristics. The dispersive response under the tone burst excitation at a travailing distance of r can be expressed as:

$$u^{dis}(r,t) = \mathcal{F}^{-1}(S(\omega)\mathrm{e}^{-\mathrm{j}k(\omega)r}) \tag{8}$$

where $\mathcal{F}^{-1}(\cdot)$ represents the inverse Fourier transform; $S(\omega)$ is frequency-domain of the tone burst excitation $s(t)$. Eq. (8) demonstrates that the propagated signal comprises components of varying frequencies, each experiencing a distinct phase shift of $\mathrm{e}^{-\mathrm{j}k(\omega)r}$. This frequency-dependent phase variation is the fundamental characteristic of dispersion.

The redesigned excitation for the ith PZT and the focusing point $F(x_0, y_0)$ can be written as:

$$G_i^F(\omega) = a_i S_i(\omega; f_i)\mathrm{e}^{\mathrm{j}k(\omega)r_i^F} \tag{9}$$

where $S_i(\omega; f_i)$ is the tone burst excitation centered at f_c in frequency domain. By redesigning the excitation signal for each array element and each inspection point, the dispersion compensation strategy and the array focusing mechanism of the holo-array can be simultaneously achieved.

Under the redesigned excitation, the response signal at the inspection point (x, y) can be expressed as:

$$u_i^F(x,y) = \mathcal{F}^{-1}(G_i^F(\omega)\mathrm{e}^{-\mathrm{j}k(\omega)r_i^{xy}}) \tag{10}$$

where r_i^{xy} represents the propagation distance from the ith element to the inspection point (x, y).

Focusing Pattern under Holo-array

The focusing energy pattern of the array under the redesigned anti-dispersive tone burst excitation can be calculated by:

$$E(x,y) = \left| \sum_{i=1}^{M-1} u_i^F(x,y) + \mathrm{j}\mathcal{H}(\sum_{i=1}^{M-1} u_i^F(x,y)) \right|_{t_c}, \tag{11}$$

where $\mathcal{H}(\cdot)$ represents the Hilbert transform and t_c is the focusing moment.

In this study, the uniform linear array with the element pitch of $d = 10$ mm is explored.

Figure 2 and Figure 3 compares the energy pattern focusing at $(500, 300)$ and $(600, 250)$ with various arrays respectively. For the energy pattern of the conventional P-array in Figure 2(a,e) and Figure 3 (a,e), the side lobes always exist. The grating lobes appear at higher frequency at which the Nyquist sampling theory is not satisfied at certain focusing point, as in Figure 3 (e) with the center frequency of $f_c = 120$ kHz and focusing point at $(600, 250)$. Compared with the energy pattern of the P-array, the side lobes are suppressed in the PA-array. But the disadvantage is that the width of the main lobe is expanded, as illustrated in Figure 2(b,f) and Figure 3 (b,f).

For the energy distribution of the conventional P-array shown in Figure 2(a,e) and Figure 3(a,e), sidelobes are consistently present. At higher frequencies, grating lobes emerge due to the violation of the Nyquist sampling criterion at specific focusing points, as illustrated in Figure 3(e), where the center frequency is$f_c = 120$ kHz and the focusing point is

DOI 10.5162/Ultrasonic2025/C6-b3

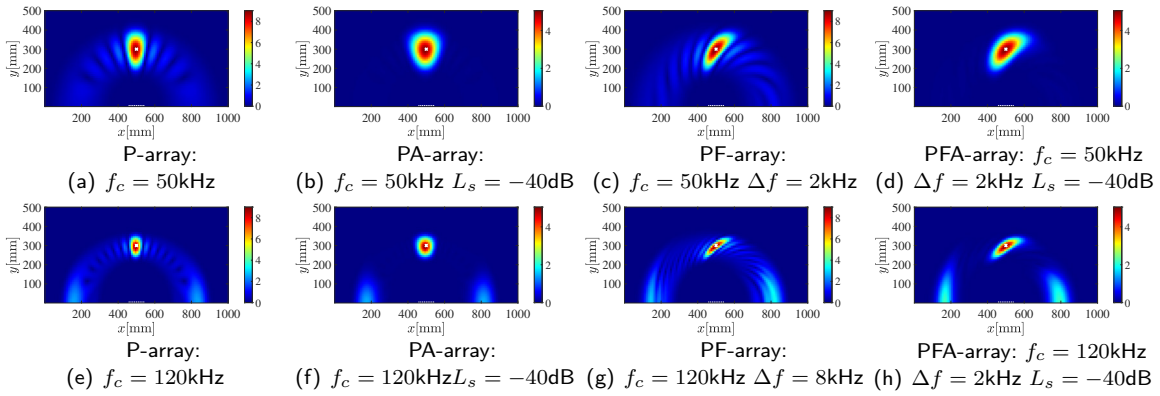

Fig. 2: The energy pattern focusing at (500,300) under 8-cycle tone burst with various arrays.

located at $(600, 250)$. In comparison, the PA-array demonstrates effective sidelobe suppression, as depicted in Figure 2(b,f) and Figure 3(b,f). However, this comes at the cost of an expanded main lobe width and enhanced grating lobe spot, as depicted in Figure 3(f).

For the PF-array, the shape of the focusing point is distorted, transitioning from a droplet-like form in P-array to an arc-like one in PF-array, as in Figure 2(c,g) and Figure 3(c,g). And the grating lobe spot is lowered and distracted, as in Figure 3(g).

The energy distribution for the PFA-array is presented in Figure 2(d,h) and Figure 3(d,h). While the combined control of amplitude and frequency offers enhanced flexibility, it may also introduce conflicting effects. As a result, the PFA-array does not always yield the optimal performance. A trade-off between sidelobe suppression and grating lobe mitigation is therefore necessary to achieve balanced array performance.

Experiments

The experiment is conducted on signal excitation and acquisition system which consists of waveform generator NI PXI-5412, piezo linear amplifier EPA-104, data acquisition card NI PXI-5122 with 8 acquisition channels and the monitor. The specimen is a T6061 aluminum alloy plate with the size of $1000 \times 1000 \times 2$ mm^3. The detailed parameters are listed as: density 2690 kg/m^3, Young's modulus 68.9 GPa and Poisson's ratio 0.33. The uniform linear array consists of 9 elements. The diameter and the thickness of the PZT wafer are 8 mm and 0.5 mm. The diagram of the experimental facilities and the aluminum plate are displayed in the Fig. 4. Two through-hole defects are thrilled at $D_1(500, 300)$,$D_2(600, 250)$ on the plate successively.

Results and Discussions

(1) P-array and PA-array

The excitation is set as the anti-dispersive 8-cycle tone burst centered at $f_c = 80$ kHz. The 6^{th} PZT is the transmitter and the others are receivers. The sidelobe attenuation level of the Chebyshev window is set as -40 in decibels (dB). The damage maps are displayed in the dB range of $[-130]$.

Figure 5 compares the damage from P-array and PA-array. In Fig. 5(a), the map from P-array exhibits several background noise artifacts, primarily caused by the presence of sidelobes. These sidelobes are effectively suppressed in the PA-array, as in Fig. 5(b), which shows a clean image without background noise artifacts. However, a drawback of introducing amplitude control is the broadening of the main lobe.

(2) P-array and PF-array

The excitation is set as the anti-dispersive 8-cycle tone burst. The 4^{th} element is the transmitter. The damage maps are displayed in the dB range of $[-10, 0]$. Figure 6 (a,c) and (b,d) compare the damage maps from P-array and PF-array, respectively.

Figure 6(a,b) show the result from P-array under center frequency $f_c = 50$ kHz and PF-array with the same center frequency and a frequency offset of $\Delta f = 2$ kHz. Compared to the shape of the damage spot in the damage map generated from the P-array in Figure 6(a), the damage spot from the PF-array appears distorted, as shown in Figure 6(b). Figure 6(c,d) compares the damage map under the tone burst excitation centered at $f_c = 120$ kHz with the frequency offset of $\Delta f = 8$ kHz. The damage spot is shrunk as the center frequency increases, as compared in Fig. 6(a,c). However, higher frequencies also increase the likelihood of grating lobe formation, which can introduce pseudo-damage. As shown in Figure 6(c), the P-array produces a pseudo-damage region near coordinates $(270, 160)$, attributed to the presence of a grating lobe. In contrast, Figure 6(d) illustrates that the PF-array effectively eliminates such pseudo-damage, demonstrating the suppression of grating lobes by appending the frequency control.

(3) PFA holo-array

Based on the above, side lobes and grating lobes

DOI 10.5162/Ultrasonic2025/C6-b3

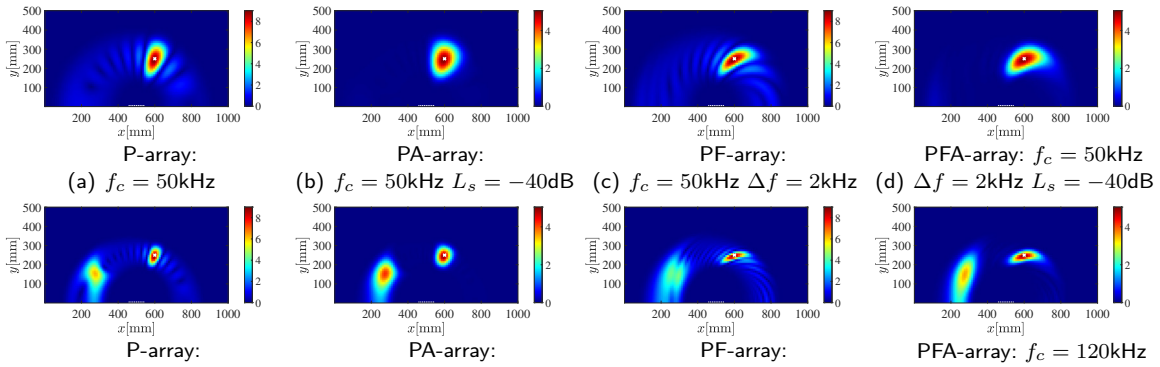

Fig. 3: The focusing energy pattern at (600,250) with the 8-cycle tone burst under various arrays.

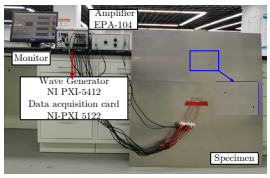

Fig. 4: The diagram of experiment set-up.

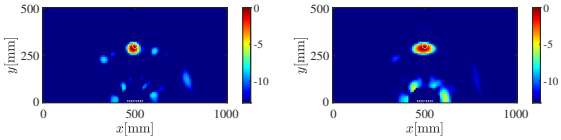

Fig. 5: The comparison of the damage map from (a) P-array and (b) PA-array.

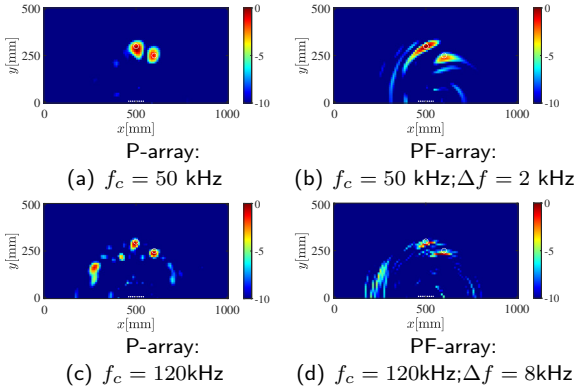

Fig. 6: The comparison of the damage map under (a,c) P-array (b,d) PF-array.

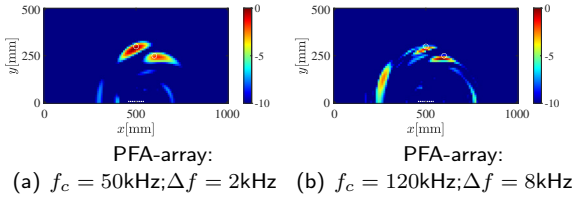

Fig. 7: The damage map under PFA-array under different excitations.

can be effectively suppressed in the PA-array and PF-array, respectively. In this section, damage maps for the PFA holo-array are displayed.

Figure 7 (a) and (b) exhibit the damage map from holo array under various tone burst excitation. It can be concluded that, when there is no grating lobes, the appending of the amplitude control helps to suppress the sides lobes. Compared with the damage map from PF-array in Figure 6(b), the background noise in Figure 7 (a) from the holo-array is reduced, but with the broadened damage spot width.

Nevertheless, in the presence of grating lobes, frequency control contributes to their suppression, whereas amplitude control tends to enhance the grating lobes while simultaneously reducing the side lobes. This behavior is illustrated in Figure 6(d) from PF-array, and in Figure 7(b) from the PFA holo-array.

Conclusions

Building upon the conventional P-array, where phase control is applied to individual array elements, this study further incorporates amplitude and frequency modulation into the array control strategy. Amplitude control effectively suppresses sidelobes but tends to broaden the main lobe and may exacerbate grating lobes. In contrast, frequency control helps reduce grating lobes. Simultaneously achieving a narrow main lobe, low sidelobes, and suppressed grating lobes is challenging; thus, a trade-off among these performance metrics is often required.

References

[1] L. Yu and V. Giurgiutiu. "In-situ optimized PWAS phased arrays for Lamb wave structural health monitoring". In: *Journal of mechanics of materials and structures* 2.3 (2007), pp. 459–487.

[2] P. Antonik et al. "Frequency diverse array radars". In: *2006 IEEE Conference on Radar*. IEEE. 2006, 3–pp.

DOI 10.5162/Ultrasonic2025/C9-a3

Experimental Study of Baker Coded Ultrasonic Signal for Coarse-Grained Material Testing

Yang Mengxin[1,2], *Wang Kun*[1,*], *Zhou Yuxuan*[1], *and Wang Wen*[1]
[1]*Institute of Acoustics, Chinese Academy of Sciences, Beijing, China*
[2]*University of Chinese Academy of Sciences, Beijing, China*
wangkun2018@mail.ioa.ac.cn

Abstract: Ultrasonic testing of coarse-grained materials is affected by scattering noise. We propose a hardware-friendly Barker modulation (0/1 amplitude) that conserves resources. Experiments on the specimens ($1.0\,\mathrm{mm}$ grain size) show that, despite the probe frequency being $500\,\mathrm{kHz}$, the bottom echo signal-to-noise ratio (SNR) reaches its peak at $350\,\mathrm{kHz}$, yielding a $2.53\,\mathrm{dB}$ SNR gain compared to traditional pulse-echo methods; the impact of surface reflections on the filtered signal is negligible. Future work will focus on Golay codes to detect flaws.

Keywords: coarse-grained materials, Barker code, code excitation, ultrasonic testing, phase coding

Introduction

In the industrial field, coarse-grained materials, characterized by large grain size and low grain boundary density, can effectively suppress grain boundary slip and creep failure, making them core materials for high-temperature service components. They are widely used in aerospace, nuclear power, and other fields, such as aero-turbine blades and nuclear reactor pressure vessels. However, their aggravated stress concentration easily initiates microcracks, leading to local damage. Therefore, accurate flaw detection in these materials is of vital importance.

However, severe structural scattering noise and anisotropy seriously reduce the signal-to-noise ratio (SNR) of conventional ultrasonic testing and limit the effective penetration depth. Phase-coding excitation[1] technology provides a promising solution by encoding broadband frequency information into a deterministic signal sequence[2], which can be decoded using a matched filter to suppress random scattering noise[3]. This study employs Barker code encoding excitation with hardware-friendly 0/1 amplitude modulation to simplify excitation circuitry, combined with matched filter compression technology, to improve the SNR.

Existing research shows that phase coding technology can enhance the SNR of ultrasonic testing through pulse compression[4], but most studies focus on non-coarse-grained materials[5]. There remains a gap in coding schemes for coarse-grained materials under the pitch-catch mode. Therefore, this study investigates a rectangular sample ($130 \times 180 \times 330mm$) made of ZG20CrMoV cast steel (with an average grain size of $1.0\,\mathrm{mm}$), prepared by machining. Probes are used and a long Barker code sequence composed of 13-bit codes and 13×5 pulses, with modulation of 0/1 amplitude, is applied to the transmitting probe. Combined with a modulation-matched filter based on probe response, the study investigates the improvement effect on bottom echo SNR, demonstrating significant SNR gain.

Methodology

Barker code, a binary code group with specific regularity, was proposed by R.H. Barker in the early 1950s. It is an aperiodic sequence: a j-bit Barker code $\{X_1, X_2, X_3, \ldots, X_j\}$ consists of elements each taking values of $+1$ or -1, and its autocorrelation function is defined as follows:

$$R(j) = \sum_{i=1}^{N-j} X_i X_{i+j} \tag{1}$$

For $j \neq 1, |R(j)| \leq 1$, confirming that Barker code is the optimal finite binary sequence. Among known Barker codes, the longest one contains 13 bits. The mainlobe-to-sidelobe ratio of its autocorrelation function equals the compression ratio, i.e., the code length j.

To reduce hardware implementation complexity, this study performs a unipolar modification on the traditional bipolar Barker code sequence, adjusting its amplitude range from $[-1, 1]$ to $[0, 1]$. Specifically, a binary amplitude modulation strategy is adopted: zero level (0) represents the -1 polarity in the original sequence, while unit level (1) denotes the $+1$ polarity, with phase modulation of unipolar coding achieved by time-domain flipping operation of the signal. This improvement strategy avoids the need for positive/negative voltage drive circuits in traditional

bipolar excitation, significantly simplifying power amplifier design and enhancing system engineering applicability.

The waveform of the modified 13-bit Barker code sequence is shown in Figure 1, where the coding rule maps "$+1$" in the original sequence to high level (1) and "-1" to low level (0), forming a unipolar pulse sequence.

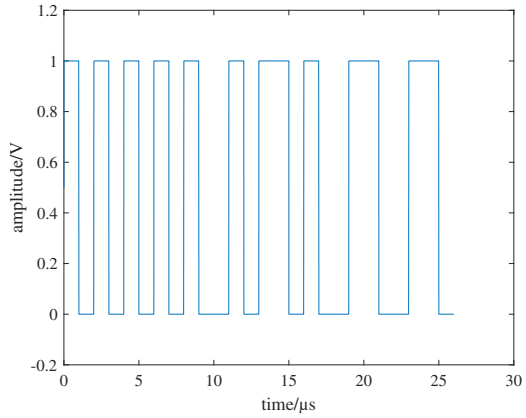

Fig. 1: Modified Barker code sequence waveform

Barker-coded excitation technology achieves pulse compression of detection signals by applying a phase-modulated sequence (e.g., 13-bit binary sequence) at the transmitter and using a matched filter at the receiver. The signal processing flow of the matched filter is shown in Figure 2, whose design principle is derived from the criterion of maximizing the output signal-to-noise ratio (SNR). According to signal detection theory, the output SNR reaches the theoretical maximum when the system satisfies the following conditions:

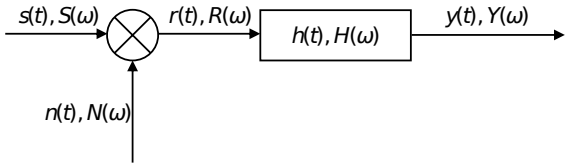

Fig. 2: The model of signal process

SNR optimization model: The system output SNR is given as follows, where E denotes the echo signal energy and n_0 represents the noise power per unit bandwidth.

$$SNR \leq \frac{\int_{-\infty}^{+\infty} |s(\omega)|^2 e^{j\omega t_0{}^2} d\omega}{2\pi \frac{n_0}{2}} \leq \frac{2E}{2} \qquad (2)$$

Frequency-domain matching condition: When the frequency response function $H(\omega)$ of a linear system satisfies the complex conjugate relationship with the input signal $s(t)$, as shown as follows, the system output SNR attains the maximum value. This linear system is defined as a matched filter.

$$H(\omega) = kS^*(\omega) e^{j\omega t_0} \qquad (3)$$

Time-domain response characteristic: The complex conjugate property of the frequency response function corresponds to the time-reversal operation of the signal in the time domain. Given an input signal $s(t)$, the impulse response of the matched filter can be expressed as follows:

$$h(t) = s(T - t) \qquad (4)$$

where T is the duration of the signal.

This characteristic enables the matched filter to achieve pulse compression through correlation operations, effectively suppressing scattering noise. The signal after the matched filter is shown in Figure 3.It demonstrates that although the signal amplitude range is halved, the unipolar Barker code still achieves pulse compression after matched filter processing, verifying the effectiveness of this improvement method in reducing hardware resource requirements while maintaining signal processing performance.

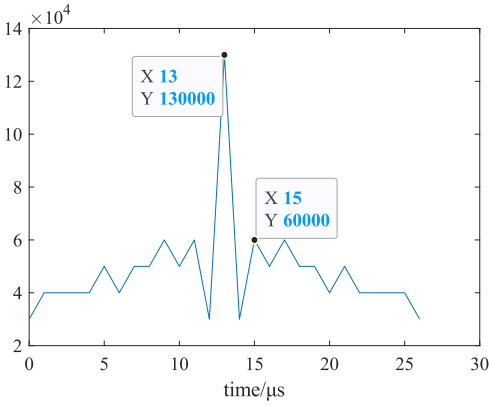

Fig. 3: Modified Barker code matched filtering results

Results

A self-developed 32-channel ultrasound detection system, which integrates signal generation, power amplification and data acquisition, was used for the experiment. The system is connected to two 500 kHz center frequency broadband ultrasound probes ($1inch$ in diameter), which are arranged unilaterally to form a transmitter and a receiver detection mode. The host computer sends control commands to generate a 13-bit unipolar Barker code sequence (0/1 magnitude) to drive the transmitting probes to generate ultrasound

DOI 10.5162/Ultrasonic2025/C9-a3

signals; the acoustic signals acquired by the receiving probes are amplified by the system for quantization; the acquired data are transmitted to the host computer for offline signal processing, including matched filtering and compression, and signal-to-noise ratio calculation. The experimental conditions are shown in Table 1. The object of this experiment is a coarse crystalline material with the dimensions shown in Figure 4, and the speed of sound in the three directions is about $6000m/s$. This experiment is carried out in the direction of the depth of $130mm$.

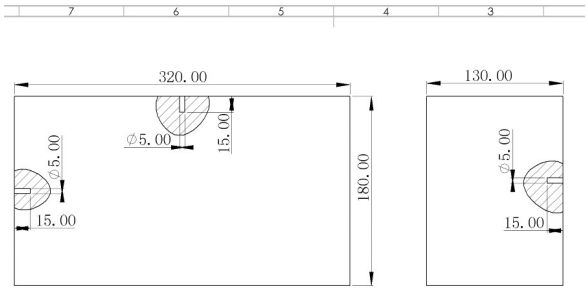

Fig. 4: Dimensional diagram of coarse crystalline material

The host computer sends control commands to generate a 13-bit unipolar Barker code sequence (0/1 magnitude) to drive the transmitting probes to generate ultrasound signals; the acoustic signals acquired by the receiving probes are amplified by the system for quantization; the acquired data are transmitted to the host computer for offline signal processing, including matched filtering and compression, and signal-to-noise ratio calculation. The experimental conditions are shown in Table 1. The object of this experiment is a coarse crystalline material with the dimensions shown in Fig. 6, and the speed of sound in the three directions is about $6000m/s$. This experiment is carried out in the direction of the depth of $130mm$.

Tab. 1: Experimental conditions

condition	Pulse	Barker coded
frequence/kHz	300–500	300–500
Number of pulses	5	13×5=65
excitation voltage/V	200	50
system gain/dB	10	18

Frequency response characteristics: The excitation frequencies are set to $300kHz$, $350kHz$, $400kHz$, $450kHz$ and $500kHz$, and the 65-bit Barker code (13×5 pulse sequence) is used for the excitation.It was found that: When the excitation frequency is $350kHz$, the peak signal-to-noise ratio (SNR) of the bottom echo (13.97dB) is significantly higher than that at $300kHz$ (8.9dB), $400kHz$ (10.57dB), $450kHz$ (6.28 dB), and $500kHz$ (5.90 dB).This phenomenon is attributed to the serious high-frequency attenuation of the ultrasonic signal in the propagation of coarse-crystalline materials, while the frequency of $350kHz$ is the best match for the acoustic scattering of coarse-crystalline materials, which effectively suppresses the incoherent scattering noise at the grain boundaries. The results are shown in Figure.5.

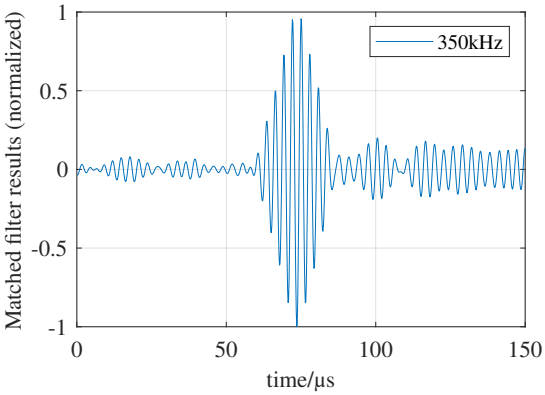

Fig. 5: Bottom surface echo signal at an excitation frequency of 350 kHz

Coding excitation gain comparison: Compared with the traditional single-pulse excitation mode, Barker code at different frequencies achieved SNR improvements, with specific gain values of 1.06dB($300kHz$), 2.53dB($350kHz$), 0.67dB(400kHz), 0.02dB($450kHz$), and -0.99dB($500kHz$), as detailed in Table 2.

Among them, the most prominent signal-to-noise gain is found in the 350kHz band, which is 2.53dB higher than that of the traditional pulse excitation mode, indicating that the Barker code excitation at this frequency matches well with the acoustic properties of the materials to be measured, which effectively suppresses the background noise interference and strengthens the echo signal strength. On the contrary, in the high-frequency bands of $450kHz$ and $500kHz$, the SNR of the signals are relatively low regardless of the impulse method or the Buck Code excitation, which is mainly attributed to the significant enhancement of the influence of the high-frequency acoustic wave by the scattering at the grain boundary, resulting in the decrease in the amplitude of the echo signal and the increase in the relative proportion of noise.In addition, the SNR of the Barker code is lower than that of the pulse method at $500kHz$ frequency, and the reason considered is that it is affected by the

intrinsic characteristics of the Barker code, and the sidelobe structure results in the exacerbation of the aliasing effect of the sidelobe energy with the active signal.

Tab. 2: Comparison of signal-to-noise ratio (SNR) gain between Barker code excitation and traditional single-pulse excitation

Frequency	Pulse	Barker coded
300kHz	7.84	8.9
350kHz	11.44	13.97
400kHz	9.73	10.40
450kHz	6.26	5.90
500kHz	6.89	6.28

Multiple reflection robustness: As shown in Figure 5 ($350\,\mathrm{kHz}$ excitation, Barker code length $185\,\mu\mathrm{s}$), the surface-bottom multiple reflection signals excited by the long code (one echo time of about $45\,\mu\mathrm{s}$) have a significantly reduced impact on the main target echo after matched filtering. The matched filtered output is characterized by a sharp main peak and low side flaps. The analysis shows that: The SNR on the left side of the main peak is about 21dB, which is mainly limited by the intrinsic sidelobe and noise (the theoretical value is 22.3dB). The SNR on the right side of the main peak decreases to about 13.9dB, which is affected by the superposition of the intrinsic flap, noise, attenuation, and residual energy from multiple reflections. Crucially, the multiple reflection energy does not form an interference peak at the main peak location, but is effectively dispersed and suppressed in the sidelobe region by the excellent autocorrelation properties of the Barker code. This proves that the algorithm effectively suppresses the overlapping periodic reflection interference and ensures the reliability of the main target echo detection.

Conclusion

This study systematically investigated the optimization strategy and robustness of the hardware-friendly 0/1 amplitude Barker code modulation excitation technique for noise suppression and signal enhancement in ultrasonic testing of coarse-grained materials. The main conclusions are as follows:

(1) A specific mid-frequency band is identified as the optimal detection band for coarse-grained materials. Experiments show that the bottom echo SNR is significantly enhanced and outperforms other bands under excitation in this band. This band effectively balances high-frequency attenuation and grain boundary scattering noise.

(2) The Barker code excitation with 0/1 amplitude modulation yields significant gains in the dominant band. Compared with traditional pulse excitation, a significant SNR gain (up to 2.53dB) can be achieved, demonstrating the effectiveness of this coded excitation in enhancing target echoes through signal energy accumulation. However, when the frequency increases, the SNR of both excitation modes is low, and the performance of the Barker code may even be lower to the pulse method because of sidelobe aliasing effects.

(3) The algorithm exhibits strong robustness against multiple reflection interference. The matched-filtered output of the long code shows a sharp main peak (left) with a peak sidelobe ratio of 21 dB. Although the SNR on the right side of the main peak is reduced to 13.9 dB due to the superposition of attenuation and residual multiple reflections, the energy from multiple reflections is successfully dispersed and suppressed within the sidelobe regions without interfering with the main peak position. This confirms the algorithm's effectiveness in suppressing overlapping periodic interference.

In summary, the matched filtering scheme based on the hardware-friendly 0/1 amplitude Barker code excitation, achieves dual enhancement of SNR improvement and interference suppression in the detection of coarse-grained materials, releasing hardware resources. It provides an effective technological pathway for reliable extraction of weak echo signals under strong noise backgrounds. Future work will focus on employing complementary sequence (Golay code) techniques to suppress matched filter sidelobes, thereby further enhancing the detection sensitivity for small defects.

References

[1] P. Dycka et al. "Phase-Coded Modulation-Based Time-of-Flight Measurement Improvement for Piezoelectric Ceramic Transducers." In: *IEEE transactions on ultrasonics, ferroelectrics, and frequency control* 68.4 (2021), pp. 1362–1369.

[2] Y. Yang et al. "Rail fracture monitoring based on ultrasonic-guided wave technology with multivariate coded excitation". In: *Ultrasonics* 136.000 (2024), p. 14.

[3] H. Z. Wu et al. "Application of Coded Excitation Signals for Measurement of Rock Ultrasonic Wave Velocity". In: *Pure and Applied Geophysics* 177.3 (2020), pp. 1–10.

[4] M. He et al. "Application of Pulse Compression Technique in High-Temperature Carbon Steel Forgings Crack Detection with Angled SV-Wave EMATs". In: *Sensors (14248220)* 23.5 (2023).

[5] C. Weng, X. Gu, and H. Jin. "Coded Excitation for Ultrasonic Testing: A Review". In: *Sensors (14248220)* 24.7 (2024).

DOI 10.5162/Ultrasonic2025/C9-a4

Exploring the Potential of Plasma Microhollow Cathode Transducers for Air-Coupled Ultrasonic Non-Destructive Testing

Dmitry Solodov[1], Narges Nazari[1], Mate Gaal[1], and Holger Kersten[2]
[1]Bundesanstalt für Materialforschung und -prüfung (BAM)
[2]Christian-Albrechts-Universität zu Kiel (CAU)
dmitry.solodov@bam.de

Abstract: This study examines the feasibility of using Microhollow Cathode (MHC) plasma transducers as contactless, broadband sources for air-coupled ultrasonic nondestructive testing (NDT). To improve the detection of small or weakly bonded defects, the approach integrates Local Defect Resonance (LDR), which amplifies flaw responses at their natural vibrational frequencies.

Keywords: Microhollow cathodes, NDT, LDR, Air-coupled ultrasound

Introduction

Ultrasonic nondestructive testing (NDT) is crucial for assessing material and structural integrity without compromising functionality. It is extensively used in aerospace, civil engineering, and manufacturing, where early defect detection ensures safety and durability. Conventional ultrasonic methods rely on piezoelectric transducers requiring direct contact and coupling media such as water or gel, limiting their application on delicate, rough, or complex surfaces.

To address these limitations, air-coupled ultrasonic techniques have gained interest. Notably, Microhollow Cathode (MHC) plasma transducers offer a novel, compact alternative by generating pressure waves via pulsed plasma discharges in air. This enables high-frequency, broadband excitation without contact or coupling layers [1], making MHCs ideal for inspecting advanced materials like composites, polymers, and 3D-printed structures that are incompatible with traditional methods.

Concurrently, nonlinear ultrasonic techniques have enhanced sensitivity to subtle flaws. Local Defect Resonance (LDR) leverages defects natural vibrational frequencies, producing localized amplified responses detectable with high spatial resolution [2]. This frequency-selective approach improves detection of small defects often missed by conventional reflection-based methods.

This paper presents the integration of MHC plasma transducers and LDR into a fully air-coupled ultrasonic inspection system. Utilizing the broadband MHC emission and LDRs frequency sensitivity, the approach aims to improve flaw detectability while preserving non-contact benefits. The concept is validated through simulations and experimental results on polymer samples measured with laser Doppler vibrometry.

Micro-Hollow Cathode Plasma Transducers

Micro-Hollow Cathode (MHC) plasma transducers operate by initiating a pulsed discharge in a confined gas volume between closely spaced electrodes, typically separated by a gap. When a high-voltage pulse is applied across the gap, a stable glow discharge forms within the microcavity, rapidly heating the surrounding gas and producing ion movement that drives ionic wind, both of which contribute to localized pressure waves. This localized heating results in sudden thermal expansion, generating an acoustic pressure wave that propagates through air as a broadband ultrasonic pulse [1].

The electrical breakdown mechanism responsible for plasma formation is governed by Paschen's Law, which relates the breakdown voltage V_{BD} to the product of the gas pressure p and the gap distance d, i.e., $V_{\mathrm{BD}} = f(pd)$. This empirical relationship assumes a uniform electric field between parallel-plate electrodes and does not explicitly account for electrode geometry.

A commonly used form of Paschen's Law is given by:

$$V_{\mathrm{BD}} = \frac{B \cdot p \cdot d}{\ln(A \cdot p \cdot d) - \ln\left[\ln\left(1 + \frac{1}{\gamma_{\mathrm{se}}}\right)\right]}, \quad (1)$$

where A and B are gas-specific empirical constants, and γ_{se} is the secondary electron emission coefficient. While originally derived for idealized parallel-plate configurations, this expression provides useful insight into breakdown behavior in a variety of geometries. Micro hollow cathode (MHC) designs typically oper-

ate near the Paschen minimum, enabling stable discharge at relatively low voltages [3].
The discharge current within the cavity follows spatial patterns governed by the Helmholtz equation:

$$\nabla^2 j + k^2 j = 0, \tag{2}$$

leading to self-organized current density distributions that resemble acoustic mode shapes. The combined effects of thermal expansion and ionic wind contribute to acoustic emission. The ion velocity, which influences the strength of the acoustic wave, scales with discharge parameters [4] as

$$v_{\mathrm{ion}} \propto A\sqrt{\frac{\varepsilon_0}{\rho_0}} \cdot \frac{U_{\mathrm{HV}}}{d_g}, \tag{3}$$

where ε_0 is the vacuum permittivity, ρ_0 is the gas density, U_{HV} is the applied voltage, and d_g is the gap size.

Concept of Local Defect Resonance (LDR)

Local Defect Resonance (LDR) enhances ultrasonic flaw detection by targeting the natural vibrational frequencies of structural defects. These frequencies emerge due to local variations in stiffness and mass that arise from discontinuities such as voids, delaminations, or inclusions. When the structure is excited near one of these frequencies, the defect responds with significantly amplified, localized vibrations that can be detected remotely [5].
For instance, a cavity embedded in an elastic medium introduces a region of reduced stiffness, causing it to respond more dynamically to external excitation. Planar defects such as delaminations or disk-like cracks exhibit even greater changes in vibrational behavior due to their asymmetry and size. This resonance-based response provides a clear acoustic signature that enhances detectability, especially in composite or layered structures where traditional amplitude-based reflection techniques may fail.
The advantage of LDR lies in its frequency-selective sensitivity. By focusing on the resonant behavior of defects, it offers high contrast between defective and intact regions, improving localization and reducing false positives.

Analytical Modeling of Local Defect Resonance Frequency

To predict the resonance behavior of defects, analytical models based on classical plate theory are employed. A flat-bottom hole (FBH), commonly used as a model defect, is approximated as a circular, clamped thin plate. The natural frequency of this plate-like region can be expressed as:

$$f_{\mathrm{LDR}} = \frac{1}{2\pi}\sqrt{\frac{K_{\mathrm{eff}}}{m_{\mathrm{eff}}}}, \tag{4}$$

where K_{eff} and m_{eff} are the effective stiffness and mass of the defect region. Under idealized conditions, this can be further simplified to:

$$f_{\mathrm{LDR}} = \frac{\alpha}{2\pi}\frac{h}{R^2}\sqrt{\frac{E}{\rho(1-\nu^2)}}, \tag{5}$$

where h is the thickness of the plate, R its radius, E is Young's modulus, ρ the density, ν Poisson's ratio, and α a dimensionless parameter dependent on the boundary conditions [6].
The value of α varies depending on how the edges of the defect are constrained. Clamped edges yield higher frequencies and larger α, while simply supported or free boundaries reduce stiffness and lower the resonant frequency. Real defects seldom conform exactly to those predicted under idealized conditions of a homogeneous, isotropic material. While classical plate theory provides analytical estimates of resonant behavior based on simplified assumptions [7], accurate determination of the resonance parameter α often necessitates numerical modeling or empirical calibration to account for material anisotropy, geometric complexity, and boundary effects.
Despite their simplifications, these models offer valuable insights and enable pre-selection of excitation frequencies for LDR testing. They do, however, neglect damping, material anisotropy, and interaction with surrounding structures, all of which can affect the actual vibrational response. Therefore, analytical predictions are best used in conjunction with experimental or numerical methods.

Conceptual Framework for the Hybrid Technique

The integration of MHC plasma transducers with LDR forms a hybrid ultrasonic inspection method that combines the strengths of both technologies. MHC devices serve as compact, contactless, and broadband acoustic sources capable of exciting a wide range of frequencies. When these frequencies overlap with the natural resonance of a defect, the LDR mechanisms amplify the local response.
This synergy enables air-coupled excitation and the detection of defect-specific vibrations without the need for mechanical coupling, physical contact, or frequency tuning. A single broadband MHC pulse can stimulate multiple vibration modes within the test sample. If a defect resonance lies within the excitation spectrum, it will respond with a measurable increase in vibration amplitude, detectable using non-

DOI 10.5162/Ultrasonic2025/C9-a4

contact sensors like laser Doppler vibrometers or air microphones.
By combining MHCs efficient broadband generation with the frequency-selective sensitivity of LDR, the system offers enhanced detection capabilities for small, subsurface, or weakly bonded defects. It is especially advantageous for inspecting composites or 3D-printed parts where traditional contact-based methods may be impractical.

Results

Three MHC plasma transducers with different geometrical configurations were employed in this study, differing in hollow diameter and electrode gap. For each configuration, the approximate high-voltage level required to ignite the plasma was determined experimentally. An overview of the geometries and corresponding ignition voltages is provided in Tab. 1.

Tab. 1: Geometrical configuration and ignition voltage of the three MHC plasma transducers.

hollow diameter (mm)	electrode gap (mm)	ignition voltage (kV)
1.0	1.6	∼4.2
0.5	1.6	∼7.5–9.0
0.5	1.0	∼4.2

To characterize the acoustic behavior of the MHC-based transducers, a thin membrane was used as the target object, featuring a mass per unit area of 0.0163 $\frac{\mathrm{kg}}{\mathrm{m}^2}$. Plasma-induced pressure waves generated by the MHCs excited mechanical vibrations in the membrane, which were measured using laser Doppler vibrometry (LDV). Surface velocity measurements of the membrane were recorded with a Polytec OFV-505 sensor head combined with an OFV-5000 controller. The schematic measurement setup is shown in Fig. 1.

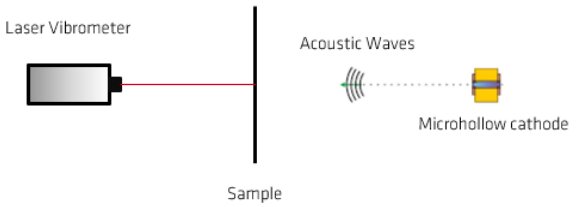

Fig. 1: Schematic setup for LDV-based characterization of MHC transducers.

Fig. 2 presents the membrane velocity signals for one representative MHC transducer. The plot consists of the time-domain response (top) and the corresponding frequency spectrum (bottom). The time-domain plot shows the velocity response of the membrane in $\frac{\mu\mathrm{m}}{\mathrm{s}}$ over time in milliseconds (ms), while the frequency spectrum illustrates the membrane velocity in $\frac{\mu\mathrm{m}}{\mathrm{s}}$ as a function of frequency in kilohertz (kHz). The distance between the membrane and the MHC transducer was 40 mm.

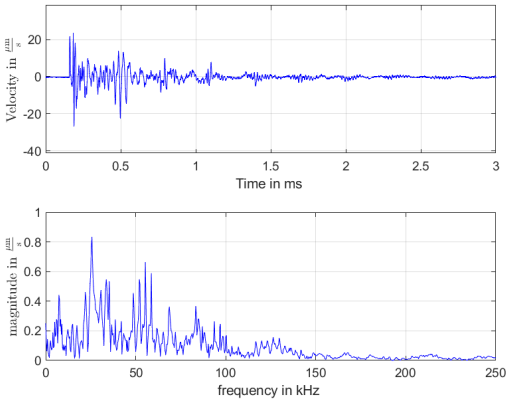

Fig. 2: Membrane response for one representative MHC transducers (1 mm hollow diameter 1.6 mm electrode gap) at 40 mm distance between membrane and transducer.

All transducers demonstrate broadband excitation with spectral content up to approximately 150 kHz.

This section presents an experimental study of a PMMA (polymethyl methacrylate) sample exhibiting a local defect resonance (LDR) near 7.6 kHz. This sample was selected due to its clear resonance behavior observed during preliminary tests.

The study aimed to identify and validate the resonance characteristics of two flat-bottom holes (FBHs) in the PMMA plate measuring $217\,\mathrm{mm} \times 30\,\mathrm{mm} \times 4\,\mathrm{mm}$. Each FBH had a diameter of $20\,\mathrm{mm}$ and a depth of about $3.6\,\mathrm{mm}$. The local defect resonance around 7.6 kHz was the focus.

A MHC transducer with a $1.6\,\mathrm{mm}$ electrode gap and $1\,\mathrm{mm}$ hollow diameter served as the excitation source. To avoid thermal overload during scans longer than five minutes, a transducer with reduced DC power consumption was used.

Initial vibrational responses of both FBHs were recorded using a 1D LDV following the setup shown in Fig. 1. Subsequent 3D scanning vibrometer measurements confirmed these findings. Frequency-domain analysis allowed comparison of resonance frequencies and evaluation of measurement consistency.

DOI 10.5162/Ultrasonic2025/C9-a4

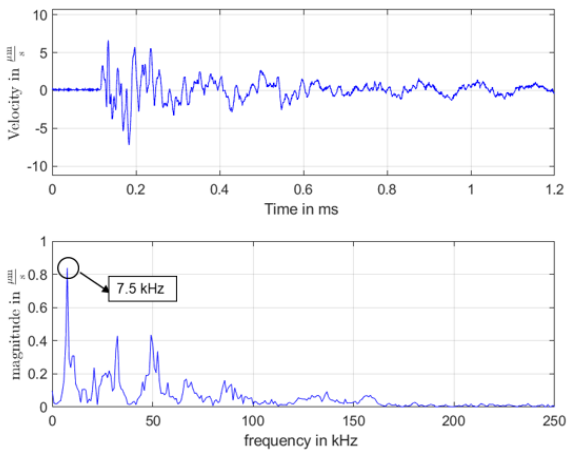

Fig. 3: PMMA sample (7.5 kHz), measurement with 1D laser doppler vibrometer

In both cases, a resonance frequency of 7.5 kHz was identified (see Fig. 3). This result was consistent across the two defects, indicating a reliable and reproducible detection of the LDR.

In order to verify the measurements obtained with the 1D LDV, additional scans were performed using a 3D scanning laser vibrometer. The resonance frequency of one FBH recorded from this method is shown in Fig. 4.

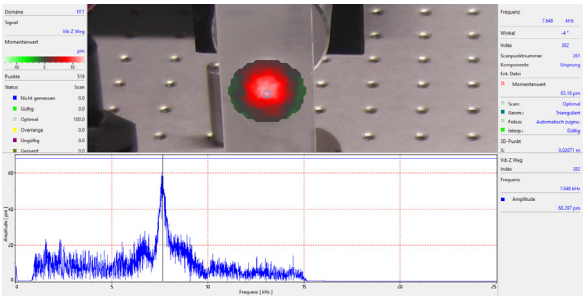

Fig. 4: PMMA sample, first FBH, LDR at 7.648 kHz (3D scanning vibrometer)

A resonance frequency of 7.648 kHz was detected at the first FBH, while the second FBH exhibited a resonance at 7.703 kHz.

Compared to the 1D LDV result (7.5 kHz for both FBHs), the relative deviation is 1.97 % for the first FBH and 2.71 % for the second FBH. These differences are within an acceptable range and confirm the accuracy of the initial 1D LDV measurements. Thus, the 3D vibrometer measurements serve as a supporting validation of the LDR frequency identified using the 1D system.

Conclusions

Experiments on PMMA samples with flat-bottom holes confirmed resonance frequencies near 7.6 kHz using both 1D and 3D laser Doppler vibrometry, closely aligning with analytical predictions. This validates the hybrid method's ability to reliably identify localized defects.

The synergy of MHCs broadband excitation and LDRs frequency-selective sensitivity improves defect detectability and spatial resolution, offering advantages for materials and geometries challenging for conventional contact-based ultrasonics.

Future work will extend this approach to diverse defect types and materials and optimize MHC transducer design for enhanced acoustic output and spectral control.

References

[1] I. Solodov, J. Bai, and G. Busse, Resonant ultrasound spectroscopy of defects: Case study of flat-bottomed holes, *Journal of Applied Physics*, vol. 113, no. 22, p. 223512, 2013. doi: 10.1063/1.4810926.

[2] W. Adebahr, I. Solodov, M. Rahammer, N. Gulnizkij, and M. Kreutzbruck, Local defect resonance for sensitive non-destructive testing, *AIP Conference Proceedings*, vol. 1706, no. 1, p. 050005, 2016. doi: 10.1063/1.4940504.

[3] M. S. Benilov, Comment on Self-organization in cathode boundary layer discharges in xenon and Self-organization in cathode boundary layer microdischarges, *Plasma Sources Science and Technology*, vol. 16, no. 2, p. 422, 2007. doi: 10.1088/0963-0252/16/2/N01.

[4] D. Kotschate, M. Gaal, and H. Kersten, Acoustic emission by self-organising effects of micro-hollow cathode discharges, *Applied Physics Letters*, vol. 112, no. 15, p. 154102, 2018. doi: 10.1063/1.5024459.

[5] I. Solodov, Resonant Acoustic Nonlinearity of Defects for Highly-Efficient Nonlinear NDE, *Journal of Nondestructive Evaluation*, vol. 33, pp. 252–262, 2014. doi: 10.1007/s10921-014-0229-9.

[6] Y. Zhang, L. Liu, Y. Chen, and J. Ouyang, Characteristics of ionic wind in needle-to-ring corona discharge, *Journal of Electrostatics*, vol. 74, pp. 15–20, 2015. doi: 10.1016/j.elstat.2014.12.008.

[7] A. W. Leissa, *Vibration of Plates*, NASA SP-160, U.S. Government Printing Office, Washington, D.C., 1969.

DOI 10.5162/Ultrasonic2025/C9-a5

Optimization of Low-Frequency Shear Wave Transducers for Guided Wave Applications

M.M. Narayanan[1], Marcel Nicolai[1], and Jens Prager[1]
[1]Federal Institute for Material Research and Testing (BAM), Berlin, Germany
narayandae@gmail.com

Abstract: Development of ultrasonic transducers for the excitation of a torsional mode T(0,1) mode in a large pipe of the material typical of actual oil/gas pipelines is discussed. Towards this, 16 ultrasonic transducers are designed and fabricated using shear plates of PIC 255 material, backing mass of tungsten-epoxy composite and brass shims as wear plates. The transducers are qualified using Laser Doppler Vibrometry. Then, the transducers are embedded in a spring-loaded ring and tested on a pipe using a multi-channel ultrasonic system. The results show the successful excitation of T(0,1) mode and it is seen to propagate for distance of 60 m with a good SNR.

Keywords: Ultrasonic guided waves, torsional mode, shear PZT plates, ring array transducer design, pipe testing

Background, Motivation and Objective

The structural integrity of pipelines is critical in oil/gas and chemical industries. A large percentage of world's primary fuels namely, gas and oil are transported by pipelines. Although, the pipes are manufactured and operated in accordance with established standards, they can pose a high risk to human life and environment, in the case of failures, due to the products they carry. Adhering to established standards, good design and construction might mitigate the problems. However, the structural integrity of the pipelines is also threatened by defects (corrosion, erosion, cracks, mechanical damage etc.) that can occur in-service. These service-induced defects are the main cause of failures. This translates to routine non-destructive testing (NDT) and structural health monitoring (SHM) to identify potential defects for safe operation. Traditional ultrasonic bulk-wave methods are reliable due to limited in-sonification and point-by-point screening but are not suitable for inspecting long pipelines, whereas ultrasonic guided-wave (UGW) methods can inspect longer distances but encounter challenges like dispersion and multiple wave modes [1]. Exciting a single, non-dispersive wave mode is essential. Excitation of a non-dispersive mode in a pipe can allow examination of the entire volume of the pipe for many tens of meters (∼100 m) from a single point of excitation, thus paving the way for rapid screening and reducing maintenance costs and inspection time [1]. Usually, UGWs for pipe testing are operated at much lower frequencies (∼kHz) to support propagation over long distances with minimal attenuation [1].

The solutions of Navier's equation dictate that three types of guided waves propagate along a pipe's axial direction: longitudinal L(0,n), torsional T(0,n), and flexural F(m,n) modes [2]. The integer variables, m and n refer to the circumferential variation of the displacement fields and the mode number, respectively. Zeros in L and T indicate no variation of fields around the circumference and hence, L(0,n) and T(0,n) are axisymmetric. F(m,n) modes are non-axi-symmetric in nature. Axisymmetric modes L and T are preferred for long-range inspection and defect detection. The fundamental torsional wave mode, T(0,1), is advantageous due to its completely non-dispersive nature and minimal interaction with low-viscosity fluids due to its shearing nature. There are various transducer solutions to generate T(0,1) mode, which include electromagnetic acoustic transducers (EMATs), magnetostrictive devices, and piezoelectric transduction [3]. EMATs and magnetostrictive devices require a large biasing for good electromechanical coupling and efficiency and are prone to high levels of noise, while piezo-based transduction involves high efficiency, high SNR, high sensitivity, compact size, and ease of fabrication. There are a few commercial portable PZT based guided wave inspection systems available that involve dry coupling by distribution of transducers around a pipe either by clamping mechanism or pneumatics. The technical know-how in the public domain for making one is limited or patented and furthermore, they are prohibitively expensive. PZTs used for T(0,1) mode are usually d15 thickness shear plates with the variation of shear displacements along the thickness of the PZT. Bonding thickness shear PZTs to a pipe can excite T(0,1) mode, but suffers from an inefficient transfer of shear strains to the pipe and in addition, retrieval of PZTs without damage after examination is

also difficult. The generation of T-mode based on d24 and d36 face shear PZTs with d24 generating almost pure T(0,1) mode is reported [3]. However, this study focuses on the development of piezo-based transduction with the use of d15 thickness shear plates of PIC 255, a soft ceramic from PI Ceramic to excite and receive T(0,1) mode. First, individual transducer elements were designed and fabricated in-house, and were embedded in a ring. Secondly, the transducers were spring loaded for dry coupling onto the pipe. Finally, experiments were conducted to check the performance of the proposed transducer ring. The technique employed was the pulse-echo method. The study shows very promising results for SHM of pipelines and the technique is simple to employ at site for operation.

Mode Selection from Dispersion Curves

As mentioned above, T(0,1) mode is the targeted mode for this study. The pipe used was a carbon steel pipe (S235JRH) of outer diameter 88.9 mm and the wall thickness of 3.2 mm. This material is commonly found in oil/gas pipelines with minor variations in alloying elements. To select the range of frequencies, dispersion curves were traced using an in-house developed Scaled Boundary Finite Element Method (SBFEM) code [4]. Figure 1 shows the group velocity dispersion curves. The T(0,1) mode is totally non-dispersive in the frequency range of 0-200 kHz. It can be seen in the figure that T(0,1) mode is surrounded by F(n,1), F(n,2) and F(n,3) modes. The mode shape of F(n,1) mode is similar to that of L(0,1) mode with a small circumferential component. F(n,2) modes are similar to T(0,1) modes and have a large circumferential component with the axial component becoming significant at higher frequencies [3]. F(n,3) modes have significant circumferential and axial displacements at lower frequencies. In the frequency range of 90-150 kHz, the circumferential displacement is significantly lower. Assuming similar excitation efficiencies of F modes and with the aim to suppress their excitation, the number of exciters was chosen to be 16 as a trial.

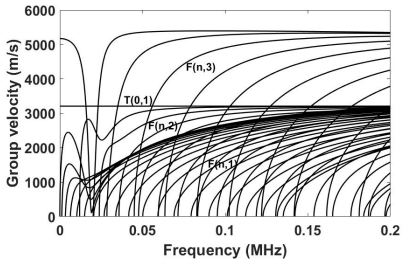

Fig. 1: Group velocity dispersion curves for a carbon steel pipe of outer diameter 88.9 mm and the wall thickness 3.2 mm.

Fabrication of Transducers and a Ring and Experimental setup

PIC 255 shear plates of dimensions 8 mm x 8 mm x 1 mm were used. Each plate has a wrap-around electrode with an electrode-free gap of 0.5 mm. The resonant frequency of the PZT is 890 kHz and the present study involves non-resonant regions of the frequency response of the PZT. Non-resonant regions have relatively flat frequency response leading to uniform excitation. CAD models of enclosures were designed and 3D printed using PLA (polylactide) material. The thickness and height of the enclosure were 1 mm and 20 mm, respectively. The PZT was mounted to the front of the enclosure and glued. A backing mass made of tungsten-epoxy was prepared and cured on the back of the PZT. Towards this, a mixture of tungsten powder of particle size $\sim$10 μm size and epoxy resin (Epotek 301-2) was prepared. The volume fraction of the tungsten powder was approximately 50% in epoxy, which was seen to reduce the ringing significantly. This volume fraction was obtained based on a finite element model developed by us incorporating tungsten-epoxy mixture as inhomogeneous random medium. The results of this are not presented here. The height of the backing was 6 mm, and the remainder of the enclosure was filled with epoxy through which wires from the PZT pass. The enclosure was sealed, and brass sheet of 0.1 mm was glued to the front of the PZT to avoid wear and provide rigidity to the PZT. The performance of the transducers was assessed using a Laser Doppler Vibrometer (LDV) from Polytec. Finally, a ring was prepared using PLA material by 3D printing. The spacing between transducer units was kept at 45°. Each 45° location is flanked by two transducers separated by 5 mm, which makes 16 transducers in total. The transducers were spring loaded, and a screw mechanism was provided to compress the springs onto the transducers. Each spring was calculated to provide 100-150 N force to the transducer. Figure 2 shows the transducer loaded ring mounted close to one end of a 3.0 m long pipe of outer diameter 88.9 mm and 3.2 mm wall thickness. The transducers in the ring were connected to the low-frequency version of Versonics Vantage system, which has the capability of exciting and receiving on 128 channels simultaneously. The system was controlled by a MATLAB loaded computer. The 16 channels were excited in phase and in parallel by 10-cycled windowed tonebursts of frequency 90-150 kHz in the step of 10 kHz and the data were collected in parallel and summed to obtain T(0,1) mode.

Results and Discussion

Figure 3 shows the shear deformation of the PZT plate captured by LDV. Figure 4 shows the average

DOI 10.5162/Ultrasonic2025/C9-a5

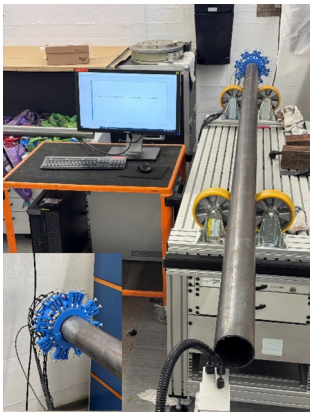

Fig. 2: Experimental setup.

shear displacement (U_x) obtained on the face of the transducer. The transducer was excited with a 50 V Gaussian windowed toneburst of 6 cycles at the center frequency of 110 kHz. The displacement components (U_x, U_y and U_z) were collected from 49 scan points on the face of PZT, as shown in Fig. 3. The signal looks very clean with a good SNR. A minor ringing of 4-5 cycles is also seen to be present in the signal due to minor acoustic impedance mismatch betwen the PZT and the backing mass. The acoustic impedance of the shear plate PZT is approximately 17 MRayl while that of the backing mass may be close to that causing small energy retention within the PZT after the duration of excitation. This could have resulted from a minor deviation in the volume fraction of the tungsten powder in epoxy during its preparation or a minor discrepancy in the modelling of tungsten-epoxy composite as having smoothly distributed properties. However, for practical purposes, the signal appears clean and can be used for conducting experiments. The out-of-plane component (U_z) and the other in-plane component (U_y) have magnitudes of one order lower than that of U_x. Much lower U_y and U_z are desirable as they might suppress the excitation of longitudinal and flexural modes. It was also discovered that these values are tightly tied to the dimensions of the PZT. And this implies the need for finding the optimized size, which is beyond the scope of the paper. Figure 5a shows the experimental time signal generated by the ring transducer, excited by a 40 V peak Hanning windowed toneburst of 10 cycles at the center frequency of 90 kHz in the 3.0 m long pipe of 88.9 mm diameter and 3.2 mm wall thickness. The 40 dB down point bandwidth of the excitation signal is 240 kHz. The signal appears clean with a good SNR of 20 dB. Furthermore, the signal shows 10 end reflections amounting to the propagation distance of 60 m. Each of the end reflected signals maintains almost

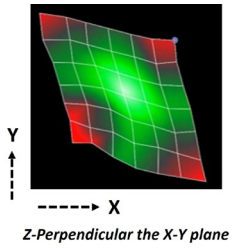

Fig. 3: LDV captured vibration of PZT showing shear deformation.

the same duration indicating that the wavepacket is non-dispersive. There is a gradual fall of the amplitudes due to unavoidable propagation losses. The attenuation of amplitudes turns out to be 0.14 dB/m. The group velocity calculated from the end reflections turns out to be 3200 m/s, which agrees well with the theoretical group velocity of T(0,1) mode of 3206 m/s. This indicates that the mode generated is indeed T(0,1) mode and the ring developed performs well. Furthermore, there are also flexural modes in the signal. However, it is not of serious concern because their amplitudes are extremely small. It can be noticed in the figure that there is a large low frequency portion of the signal at the beginning, which is probably a noise from the receiver amplifier of the system. It can be removed to improve the readability of the signal. Figure 5b is the bandpass filtered version of the signal in Fig. 5a in the range of 40-160 kHz, and it can be seen that the filtering has removed the low-frequency portion of the signal, and the initial zone can now be used for defect detection. However, there is a deadzone of nearly 700 mm, which cannot be avoided. Furthermore, it was also observed that the responses for other frequencies in the range 90-150 kHz were found almost similar. Figure 6 shows the excited amplitudes for various frequencies in the range of 90-150 kHz. The amplitudes are nearly flat indicating similar excitation efficiency of T(0,1) mode in this range validating our assumption. Besides, the signals for higher frequencies in this range also show gradually increasing excitation of flexural modes probably due to the similarity of mode shapes. The SNRs of the signals in the frequency range considered vary from from 20-11 dB with higher SNRs for the lower frequencies.

Conclusions

In this paper, the design and development of a ring with ultrasonic transducers embedded for the excitation of T(0,1) mode in large pipes have been presented. First, ultrasonic transducers with shear plates were fabricated in-house, and the performance was assessed by a Laser Doppler Vibrometer. The transducers were

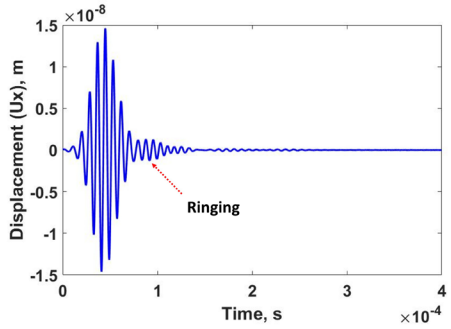

Fig. 4: Average shear displacement (U_x) on the face of the PZT obtained using LDV.

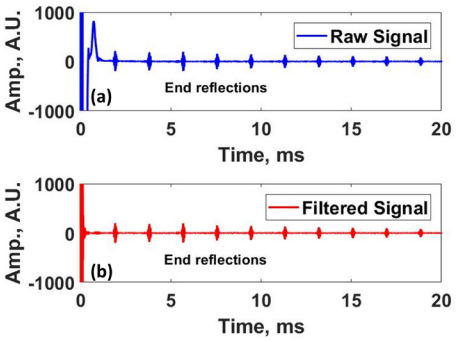

Fig. 5: Experimental signal obtained in a pipe of 88.9 mm OD using a ring of ultrasonic transducers, (a) raw signal and (b) bandpass filtered signal.

found to perform well with a minor ringing. Secondly, a ring was fabricated by 3D printing, and 16 transducers were spring-loaded in the ring, and tested on a pipe. The ring was found to excite the torsional mode T(0,1) successfully, and the mode was found to propagate for a distance of 60 m with reasonable amplitudes. The group velocity obtained experimentally was found to be in good agreement with the theoretical velocity. The mode excited was also found to be very clean. In light of the above promising results, it seems to have a good potential for deployment in actual NDT and SHM for defect detection. Additionally, the use of PIC 255 shear plates and tungsten-epoxy backing demonstrates a cost-effective and efficient approach, offering high SNR for long-range pipeline inspection. The non-dispersive nature of the T(0,1) mode, validated over 60 m, highlights its potential for rapid screening, reducing maintenance costs and inspection time. Future work could focus on optimizing PZT dimensions to further suppress unwanted modes like F(n,1) and F(n,2), enhancing the system's robustness. The spring-loaded ring design proves adaptable for dry coupling, simplifying field deployment. Moreover, the

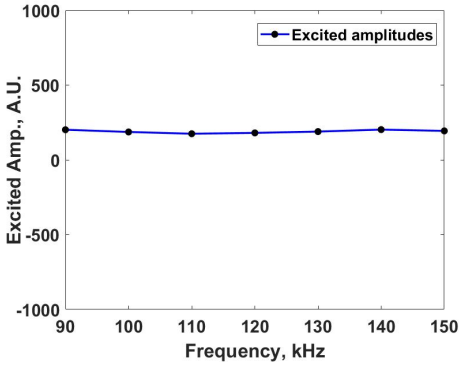

Fig. 6: Excited amplitudes of T(0,1) mode in the frequency range of 90-150 kHz.

minor ringing observed suggests potential improvements in acoustic impedance matching, which could be explored to refine signal quality. This technique's simplicity and scalability make it a viable solution for the oil/gas industry's structural health monitoring needs

References

[1] D.N. Alleyne, T. Vogt and P. Cawley, "The choice of torsional or longitudinal excitation in guided wave pipe inspection". In: Insight - Non-Destructive Testing and Condition Monitoring 51 (2009), pp. 373-377. DOI: 10.1784/insi.2009.51.7.373.

[2] J.L. Rose, Ultrasonic guided waves in solid media, Cambridge University Press, USA (2014).

[3] H. Miao, Q. Huan, Q. Wang and F. Li, "Excitation and reception of single torsional wave T(0,1) mode in pipes using face-shear d24 piezoelectric ring array". In: Smart Materials and Structures 26 (2017), pp. 025021-9. DOI: 10.1088/1361-665X/26/2/025021.

[4] H. Gravenkamp, Numerical methods for the simulation of ultrasonic guided waves, Ph.D. thesis, BAM Dissertation, Berlin (2014).

DOI 10.5162/Ultrasonic2025/C13-a2

Ultrasonic Characterization of Microstructural Inhomogeneity in Additively Manufactured Metals

Junfei Tai[1] *and Zheng Fan*[1]
[1]*School of Mechanical and Aerospace Engineering, Nanyang Technological University, 50 Nanyang Avenue, Singapore*
zfan@ntu.edu.sg

Abstract: Non-destructive evaluation (NDE) of additively manufactured (AM) metals is particularly challenging due to their textured and irregular microstructures, which are intimately linked to their mechanical properties. Ultrasound, with its high sensitivity to microstructural features, offers a powerful non-destructive method for characterizing these materials. While conventional metals typically exhibit a direct, monotonic relationship between ultrasonic scattering and grain size, this correlation becomes ambiguous in AM metals where multiple microstructural features coexist. In this study, we introduce a parameterization approach to quantify microstructural inhomogeneity and examine its correlation with ultrasonic scattering-induced attenuation. Finite element simulations of elastic wave propagation are employed to provide a detailed microscale description of the elastic energy distribution and the degree of microstructural inhomogeneity. Our findings indicate that the proposed parameter effectively captures grain-scale variations, including textures and grain sizes, and demonstrates a monotonic relationship with ultrasonic scattering. Specifically, an increase in microstructural inhomogeneity enhances elastic wave scattering. Moreover, the cumulative effect of scattering leads to ultrasonic attenuation, shows a positive correlation with characteristic length–weighted microstructural inhomogeneity. Importantly, this parameter exhibits a consistent monotonic correlation with ultrasonic attenuation across materials with diverse crystal systems. These results elucidate the fundamental mechanisms linking ultrasonic responses to grain-scale microstructural inhomogeneity and underscore the potential of ultrasound-based NDE for the advanced characterization of AM materials.

Keywords: Ultrasonic scattering, Microstructural inhomogeneity, Additive manufacturing.

Introduction

Additive Manufacturing (AM) has demonstrated great potential for tailoring material microstructures to achieve the mechanical properties required in critical engineering components [1]. As AM technologies continue to advance and find broader application in the fabrication of load-bearing structural parts, ensuring the structural integrity and reliability of these components has become increasingly important. The mechanical performance and ultrasonic response of AM components are primarily governed by their microstructures. Due to the inherently rapid and non-equilibrium solidification processes in AM [2], the resulting microstructures differ significantly from those produced by conventional manufacturing methods. This makes it particularly challenging to apply existing microstructural knowledge to the ultrasonic characterization of AM materials. Given the high-dimensional nature of microstructural parameters in AM, ultrasonic characterization becomes an underdetermined problem, where the coupling effects of multiple features on wave propagation lead to an ill-posed inverse problem.

To address these challenges, this study identifies key microstructural features that influence ultrasonic responses. Special attention is given to grain-scale microstructural inhomogeneity, which strongly affects ultrasonic scattering in the Rayleigh regime. To quantify this effect, a newly formulated microstructural parameter is proposed. A polycrystalline modeling framework incorporating various microstructural features is developed, and the characteristics of the proposed inhomogeneity metric are systematically analyzed. Numerical simulations reveal a monotonic relationship between microstructural inhomogeneity and ultrasonic scattering attenuation. Furthermore, the general applicability of the proposed parameter is validated across multiple materials with different crystallographic systems.

Methodology

To develop a general method for quantitatively characterizing microstructural inhomogeneity across different microstructures, this study first investigates polycrystalline modeling techniques that incorporate a range of microstructural features, particularly grain size and texture intensity. Equiaxed polycrystalline models with

DOI 10.5162/Ultrasonic2025/C13-a2

varying average grain sizes (from 50 to 150 m) are generated using the Neper software package [3], serving as the baseline for constructing additional models. The grain orientations in the Neper-generated microstructures follow a random distribution by default. To systematically vary the texture strength along the $\langle 100 \rangle$ direction, the distribution width of grain Euler angles is adjusted for each model. Thus, texture strength is controlled by the spread of grain orientations. Additionally, elongated grain structures are produced by applying geometric transformations—specifically compression and rotation—on the equiaxed models. Microstructures extracted from Electron Backscatter Diffraction (EBSD) measurements of actual AM samples are also incorporated into the study to enrich the diversity of the dataset. The resulting collection of microstructures, as illustrated in Figure 1, covers a wide range of relevant features for the analysis.

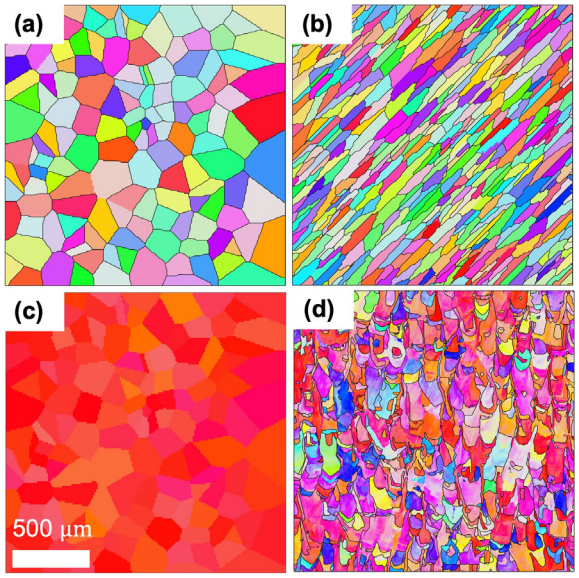

Fig. 1: Illustration of different types of microstructures with various feature.

The inhomogeneity of the microstructure is a key factor causing scattering [4, 5]. The impact of microstructural inhomogeneity at the grain-level leads to uneven distribution of stiffness across the microstructure. This, in turn, results in strain localization under loading, thereby making certain regions of the material more susceptible to the damage initiation. Therefore, an approach to integrate the stiffness inhomogeneity from microstructure features is proposed to correlate the ultrasonic scattering response in this work. In single-phase polycrystalline materials with constant density, the inhomogeneity of the microstructure induced by grains and their orientations leads to variations in the elastic tensors C_{ijkl}, which can be mathematically represented as the perturbation of the local elastic tensors based on the global [5, 6]:

$$C_{ijkl}(x,y) = C^0_{ijkl} + \delta C_{ijkl}(x,y) \tag{1}$$

where $C_{ijkl}(x,y)$ is the fourth rank elastic tensor in the spatial location (x,y). C^0_{ijkl} denotes the expectation of the global elastic tensors with given Euler angles and $\delta C_{ijkl}(x,y)$ signifies the local perturbation of elastic tensors compared with expectation. When Euler angles are assigned globally, the covariance between local elastic tensors and the average of global elastic tensors offers a parametric elucidation of spatial microstructural inhomogeneity.

$$\Xi = \mathbf{E}[C^0_{ijkl} C_{ijkl}(x,y)] - \mathbf{E}[C^0_{ijkl}]\mathbf{E}[C_{ijkl}(x,y)] \tag{2}$$

The scalar Ξ quantifies the deviation of the local elastic tensors within an inhomogeneous microstructure from the global average C^0_{ijkl} with $\mathbf{E}[\cdot]$ denoting averaging over all tensor components. In this work, we apply elastodynamic loading to generate longitudinal wave propagation and tensile loading along the *y*-axis:

$$\Xi_{22} = \mathbf{E}\left[C^0_{22kl} C_{22kl}(x,y)\right] - \mathbf{E}\left[C^0_{22kl}\right]\mathbf{E}\left[C_{22kl}(x,y)\right] \tag{3}$$

The covariance tensor is subsequently normalized by the variance of the expectation to quantitatively define the local deviation of the elastic tensors.

$$\delta(x,y) = \Xi_{22} / (\mathbf{E}\left[(C^0_{22kl})^2\right] - (\mathbf{E}\left[C^0_{22kl}\right])^2) \tag{4}$$

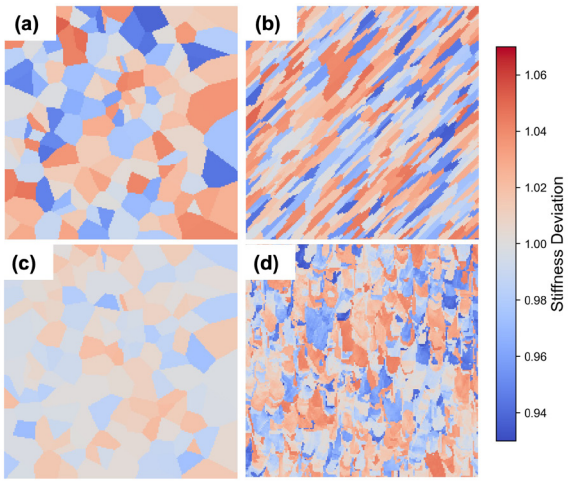

Fig. 2: The stiffness deviation maps of different microstructures.

The transformation of Euler angles into stiffness deviations in the specific dimension effectively preserves crucial spatial information, as demonstrated in Figures 2. Microstructures characterized by random crystalline orientations are observed to exhibit

DOI 10.5162/Ultrasonic2025/C13-a2

notably larger stiffness deviations. We describe the overall microstructural inhomogeneity as the dispersion degree of local stiffness deviations by accurately parameterizing these deviations from the normalized global value.

$$\Delta_A = \frac{1}{A}\iint_A |\delta(x,y) - 1| dxdy \tag{5}$$

where A denotes the area of the two-dimensional microstructure. The microstructural inhomogeneity Δ_A quantifies the average absolute deviation in stiffness relative to the reference plane. Hence, a lower Δ_A value suggests a more homogeneous stiffness space, and vice versa. However, the spatial integration and averaging processes in Eq. ((5)) result in the decoupling of effective grain size. Therefore, the characteristic length is used to assess the cumulative effects of microstructural inhomogeneity, namely the grain projection length L_P, which describes the lengths of the platforms illustrated in Figures 3. The average grain projection length ($\overline{L}_P$) of a specific microstructure can be expressed as:

$$\overline{L}_P = \frac{1}{N}\sum_{i=1}^{N} L_{Pi} \tag{6}$$

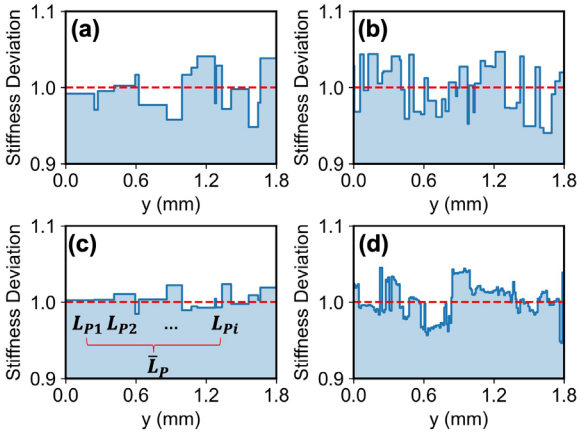

Fig. 3: Cross-sectional profiles of corresponding four types of microstructures.

We employ a series of simulated microstructures with preset grain sizes and texture intensity to investigate the characteristics of the proposed microstructural inhomogeneity. The microstructural inhomogeneity Δ_A along with its product with the average grain projection length $\overline{L}_P$ is calculated and normalized across the dataset of these 50 microstructures, as illustrated in the heat maps in Figures 4(a) and Figures 4(b), respectively. Figures 4(a) supports that Δ_A is independent of the grain size, and it only increases as texture intensity decreases.

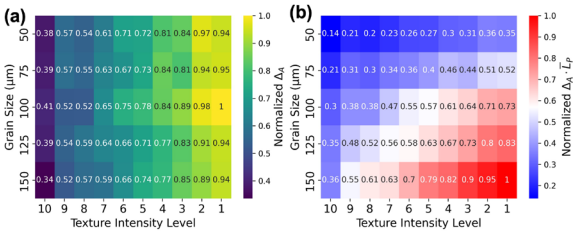

Fig. 4: Heat map of Δ_A and $\Delta_A \cdot \overline{L}_P$ for fifty equiaxed grain models with different grain sizes and texture intensities.

The product of Δ_A and $\overline{L}_P$ mathematically combines the effects of texture intensity and grain size into a single parameter. Physically, this product represents the cumulative effect of texture-induced inhomogeneity over a characteristic length. Specifically, it means that an inhomogeneous event of magnitude Δ_A occurs over the average grain projection length $\overline{L}_P$. As shown in Figures 4(b), a microstructure with strongly textured large grains may have the similar cumulative inhomogeneity effect as a microstructure with weakly textured small grains. This combined metric is capable of indicating the overall influence of these two independent factors derived from the principal characteristics of the microstructure. The proposed parameterization approach to microstructural features offers a valuable perspective for exploring the relationship between microstructural features and ultrasonic responses.

Results

Using the 50 different simulated microstructures and the microstructures obtained from EBSD analysis of LPBF-fabricated SS316L samples, The ultrasound propagation is simulated to investigate the relationship between microstructural inhomogeneity and ultrasonic responses. Their correlation with the proposed parameters $\Delta_A \cdot \overline{L}_P$ is of our interest. In the explicit elastodynamics analysis, a longitudinal plane wave with 10 MHz is applied to the microstructure along the *y*-axis in a through-transmission mode from top surface to the bottom.

The ultrasonic attenuation reflects the cumulative effect of microscale scattering and is typically related to the characteristic length of the microstructure. Figure 5 demonstrates a positive correlation between ultrasonic attenuation and grain projection length-weighted microstructural inhomogeneity ($\Delta_A \cdot \overline{L}_P$). It can be observed that microstructures with different grain sizes and textures follow the same trend in Figure 5, highlighting the ability of proposed parameter to represent diverse microstructural attributes. This indicates that the primary factor influencing ultrasonic

attenuation is the cumulative effect of microstructural inhomogeneity along the grain projection length. This

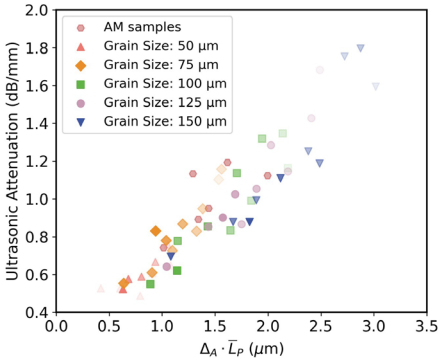

Fig. 5: Correlation between ultrasonic attenuation and $\Delta_A \cdot \overline{L}_P$ at the macroscale.

nearly linear correlation enables the characterization and evaluation of grain projection length-weighted microstructural inhomogeneity using ultrasonic techniques. This implies that the focus of ultrasonic characterization can shift from resolving coupled effects of grain size and texture intensity to characterizing an integrated variable, namely grain projection length-weighted microstructural inhomogeneity. However, further investigation is required to verify the universality of this correlation across different crystal systems.

Explicit elastodynamic simulations and calculations of microstructural inhomogeneity are performed on various materials across different crystal systems. The microstructures used remain consistent with different features, while demonstrate variations in elastic constants corresponding to their distinct crystal systems. As shown in Figure 6, the fitted curves of normalized $\Delta_A \cdot \overline{L}_P$ and ultrasonic attenuation for different materials are plotted together for comparison. The results confirm that the positive correlation holds universally for all crystal systems, though the slope of the correlation differs depending on the anisotropy of each material's elastic tensor. This suggests that the proposed parameterization method has broad applicability, while the quantitative and accurate use for each material requires individual calibration.

Conclusion

This paper examines the challenges and issues associated with ultrasonic characterization of AM materials. The interactions between different microstructural features and their effects on ultrasonic scattering attenuation are mutually coupled, making it a challenging problem with indeterminate solutions. The proposed quantitative parameter of microstructural inhomogeneity from parameterization of microstructural features effectively incorporates grain-level microstructural features into the representation of microstructural inhomogeneity, demonstrating a consistent monotonic relationship with ultrasonic attenuation. This correlation is consistent across all crystal systems, indicating the universality of the proposed parameterization method.

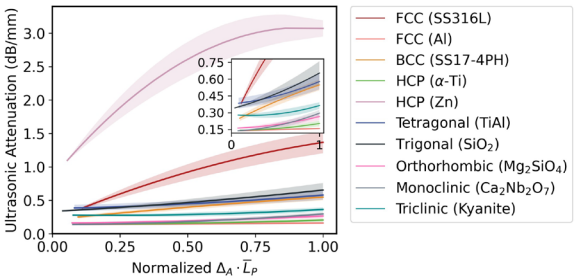

Fig. 6: Correlation between ultrasonic attenuation and $\Delta_A \cdot \overline{L}_P$ applied in multiple materials from different crystal systems.

Acknowledgments

The authors acknowledge support from the Ministry of Education, Singapore, for its Academic Research Fund Tier 1 (RG149/23 and RG69/22).

References

[1] S. Gao et al. "Additive manufacturing of alloys with programmable microstructure and properties". In: *Nature Communications* 14.1 (2023), p. 6752.

[2] M. Qu et al. "Controlling process instability for defect lean metal additive manufacturing". In: *Nature communications* 13.1 (2022), p. 1079.

[3] R. Quey, P. R. Dawson, and F. Barbe. "Large-scale 3D random polycrystals for the finite element method: Generation, meshing and remeshing". In: *Computer Methods in Applied Mechanics and Engineering* 200.17-20 (2011), pp. 1729–1745.

[4] F. E. Stanke and G. S. Kino. "A unified theory for elastic wave propagation in polycrystalline materials". In: *The Journal of the Acoustical Society of America* 75.3 (1984), pp. 665–681.

[5] R. L. Weaver. "Diffusivity of ultrasound in polycrystals". In: *Journal of the Mechanics and Physics of Solids* 38.1 (1990), pp. 55–86.

[6] C. M. Kube and J. A. Turner. "Acoustic attenuation coefficients for polycrystalline materials containing crystallites of any symmetry class". In: *The Journal of the Acoustical Society of America* 137.6 (2015), EL476–EL482.

DOI 10.5162/Ultrasonic2025/C13-a4

Virtual Source Multi-mode Method for Ultra-thick Weld Full-section Inspection

Xinzhi Ma[1,2], Mu Chen[1,2], Keji Yang[1,2], and Haoran Jin[1,2]
[1] Zhejiang University, State Key Laboratory of Fluid Power and Mechatronic Systems, School of Mechanical Engineering, Hangzhou, China
[2] Zhejiang University, The Key Laboratory of Advanced Manufacturing Technology of Zhejiang Province, Hangzhou, China
12325090@zju.edu.cn, jinhr@zju.edu.cn

Abstract: Full-section inspection of ultra-thick welds (UTW) is crucial for the nuclear power industry. The extensive weld section and the nearly vertical groove geometry pose significant challenges for flaw characterization. This paper presents a virtual source multi-mode total focusing method (VSMM-TFM) inspection method. The VS method not only enhances the emission energy but also simplifies multi-mode path calculations. Multi-mode decoupling enables full-section imaging at a single scanning position. Simulation and experiment on a 120-mm workpiece demonstrate that the VSMM-TFM method exhibits significant advantages in terms of inspection sensitivity, data volume, and imaging efficiency.

Keywords: Ultrasonic imaging, Virtual source, Multi-mode, Ultra-thick welds, Full-scetion inspection

Introduction

Ultra-thick narrow-gap weld (UTW) is widely employed in critical components such as pressure vessels that operate under extreme temperature and pressure conditions[1]. The J-shaped groove features a high aspect ratio, with angles typically ranging from 2° to 6°[2]. This type of groove helps reduce filler material consumption and improve production efficiency[3]. However, narrow-gap welding (NGW) is prone to the lack-of-sidewall-fusion (LOSWF) flaws, which are typically oriented nearly perpendicular to the weld surface [4]. Flaws can significantly compromise structural integrity, fatigue resistance, and service life. Therefore, ultrasonic non-destructive testing (NDT) of UTW holds substantial engineering importance.

Phased array ultrasonic testing (PAUT) is widely used for weld inspection and among it, the total focusing method (TFM) achieves point-by-point focusing, significantly enhancing resolution[5]. However, TFM has some limitations in the inspection of UTWs. Firstly, the single-element excitation mode results in low emission power[6]. As illustrated in Fig.1, the interface reflection of the wave caused by the wedge further weakens the energy transmitted into the UTWs. In addition, TFM requires the storage and processing of a large volume of full matrix capture (FMC) data. This challenge will become more pronounced in UTW, where more A-scan sampling points are needed to ensure full-section inspection. In order to improve the emission energy and reduce the time of image reconstruction, Plane Wave Imaging (PWI) has been introduced [7]. However, due to the narrow beam spread of plane waves, multi-angle acquisitions are essential to ensure a good imaging quality[8].

To address this issue, a group of elements can focus the emitted waves on a point, which is known as the Virtual Source (VS) method[9]. VS enables high signal-to-noise ratio (SNR) flaw inspection while reducing the number of emission events[10]. Sumana et al. simulated the inspection of flaws in 200 mm thick components using the VS method, demonstrating its suitability for thick-wall structures[11]. LOSWF flaws are frequently occur at near-vertical angles along the groove, resulting in directional echo patterns. The directional nature of echoes and the extensive weld section necessitate multiple array scanning positions to inspect the entire weld, as shown in Fig.1. Multi-mode TFM is typically employed to inspect such flaws[12]. However, current VS research primarily focuses on direct-mode imaging and has not been extended to multi-mode imaging, particularly involving mode conversion[10]. Therefore, applying the VS approach to the UTWs inspection still presents challenges.

To this end, this study proposes a Virtual Source Multi-Mode TFM (VSMM-TFM) for full-section inspection of UTWs. The VS method is used to enhance emission power and the VS imaging is extended to multi-mode imaging, incorporating back-wall reflections and mode conversions. Various skipping modes of longitudinal and shear waves are decoupled to reconstruct flaws throughout UTWs from top to bottom at a single scanning position. Virtual sources are po-

DOI 10.5162/Ultrasonic2025/C13-a4

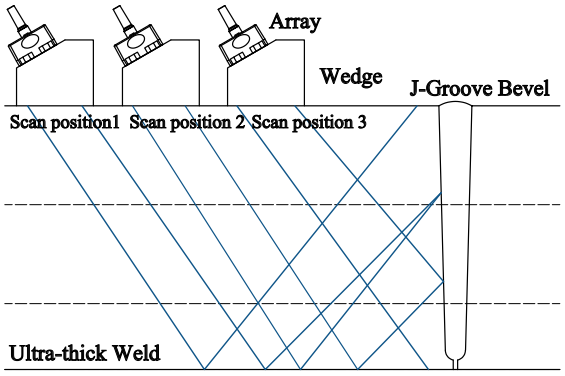

Fig. 1: Schematic diagram of the inspection for ultra-thick welds.

sitioned at the interface between the wedge and the weld surface. Mode conversions are designed to occur during the emission process. Under this configuration, the computational dimensionality of the multi-mode wave propagation model is reduced by one, which significantly improves the efficiency of the time of flight (TOF) calculation. VSMM-TFM achieves flaw imaging with fewer emission events, improving the efficiency.

This paper is structured as follows: Section 2 describes the method, which is validated through the CIVA simulation and experiment in Section 3. Finally conclusion is summarized in Section 4.

VSMM-TFM Inspection Method

A set of sub-elements is excited to generate a virtual source focused at the interface between the wedge and the UTW, as illustrated in Fig.2. The waves propagating into the UTW from P_{VS} can be regarded as a finite extension of the focused waves. Within a certain angular range these waves can be considered as cylindrical waves. For each VS focusing event, data is required by all elements, forming an $M \times N$ FMC dataset, where M and N represent the number of VSs and elements, respectively. The TOF between the imaging point P and elements are calculated for each transmission and reception. All FMC data are then coherently summed to achieve synthetic focusing, yielding the pixel amplitude at point P:

$$I_{VS}(P) = \left| \sum_{i=1}^{M} \sum_{j=1}^{N} \widetilde{s_{ij}}(T_i(P) + T_j(P)) \right| \quad (1)$$

where T_i represents the TOF of the emission process. T_j denotes the travel time of the scattered wave from imaging point to the receiving element. $\widetilde{s}$ is the Hilbert transform of the signals.

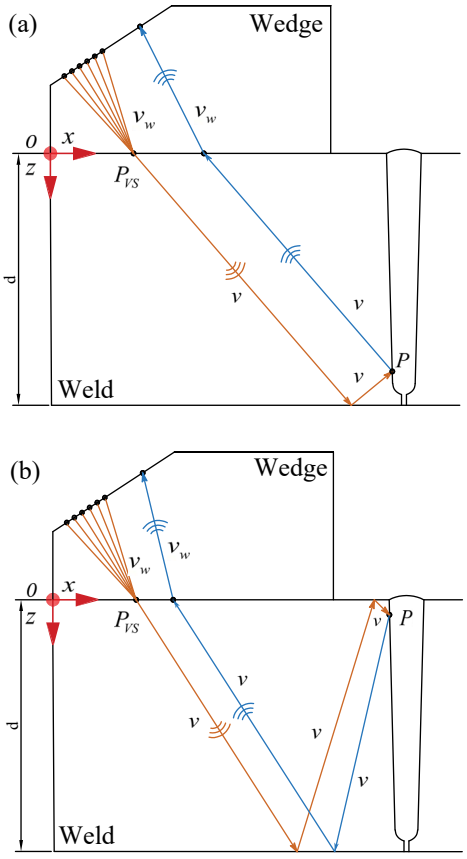

Fig. 2: Virtual source multi-mode TFM ray path: (a) half-skip modes (b) mulit-skip modes.

The TOF in emission can be divided into two parts: the delay from the sub-elements to VS and from VS to imaging point. The TOF in reception can be calculated using the Fermat's principle. In VSMM-TFM, various skipping modes of longitudinal (L) and transverse (T) waves are decoupled to imaging flaws throughout the weld from top to bottom at a single scanning position. Mode conversions are designed to occur during the emission process. Under this case, the computational dimensionality of the multi-mode wave propagation model is simplified, which significantly improves the efficiency of the TOF calculation. The modes employed in inspection are shown in Table 1.

Tab. 1: Inspection modes.

Inspection Region	Inspection Modes
Top	TTT-TT
Middle	TL-L
Bottom	LL-L

DOI 10.5162/Ultrasonic2025/C13-a4

Simulation and Experiment

Simulations were conducted on a 120 mm thick weld using CIVA software to evaluate the method. As shown in Fig.3, notches with a length of 5 mm are machined at three locations on the steel test block. VSMM-TFM inspection was performed using a 5 MHz, 64-element, 0.6 mm pitch linear phased array with a wedge of 16.2°. The element number in VS array is 21, and the pitch is identical to above.The sampling frequency is set to 25 MHz. Additionally, under the same configuration, TFM inspection was also simulated.

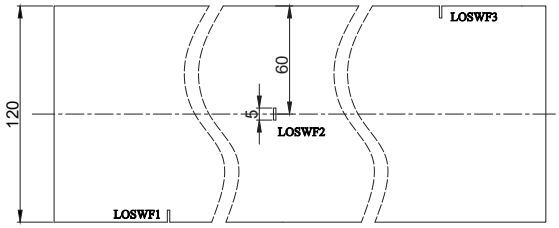

Fig. 3: Schematic diagram of the simulated test block and flaws distribution.

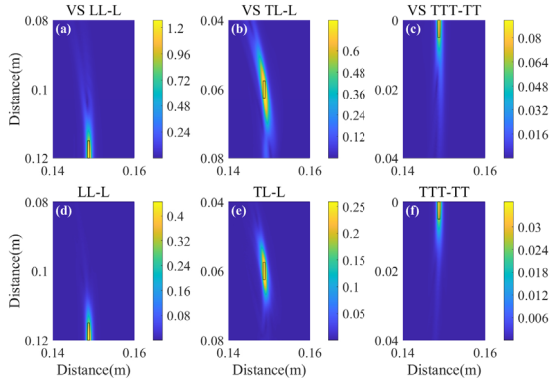

Fig. 4: Flaw reconstruction Results: (a)-(c): VSMM-TFM imaging results; (d)-(f): TFM imaging results.

The comparative results are shown in Fig.4. The results are not normalized, and all images are presented in linear scale. Fig.5 shows the maximum flaw indication amplitudes for each mode under both methods. The inspection sensitivity of VSMM-TFM is significantly higher than that of TFM, increasing by a factor of 2.77 (on average). TFM requires a dataset size of 64 × 64. In contrast, only 21 VSs are configured in VSMM-TFM, resulting in a dataset size of 64 × 21. This represents a 3.05-fold reduction in data volume. On a desktop computer equipped with an Intel Core i7-13700KF CPU and an NVIDIA GeForce RTX 4070 GPU, the computation time for the VSMM-TFM TOF matrix using MATLAB R2021b is 21.80s. Compared to TFM's 655.86s, this represents

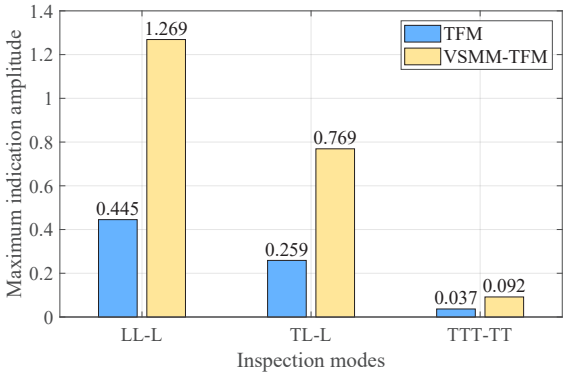

Fig. 5: Comparative inspection sensitivity of two imaging methods for flaws at different parts.

a 30.09-fold speedup (for a pixel grid of 601 × 101). The average imaging time for TFM is 0.56s, while for VSMM-TFM it is only 0.15s, representing a 3.73-fold improvement in efficiency. From the results, VSMM-TFM enables full-section inspection of UTWS at a single scanning position and the flaw indications align perfectly with the actual flaw positions.

Experimental validation was conducted using the same parameters as in the simulation, targeting the LOSWF2 and LOSWF3 (10 mm in length), as shown on the Fig.6. The results are presented on the right side of Fig.6. In both methods, a vector coherence factor was applied to suppress noise. The indication area of the LOSWF2 reconstructed by VSMM-TFM is noticeably larger than that of TFM. VSMM-TFM method achieves a high SNR image of the LOSWF3, which is missed in the TFM image.

These results demonstrate that the VSMM-TFM method is highly suitable for multi-mode imaging of ultra-thick welds, as it enables stronger flaw characterization with higher imaging efficiency.

Conclusions

This paper presents a virtual source multi-mode TFM based full-section inspection method for ultra-thick weld. VSMM-TFM enables stronger flaw characterization in UTWs with higher imaging efficiency. The VS approach not only enhances the emission energy but also simplifies multi-mode path calculations while reducing data volume. Multi-mode decoupling enables full-section imaging at a single scanning position. CIVA simulation and experiment results demonstrate that the VSMM-TFM method exhibits significant advantages over TFM in terms of inspection sensitivity, data volume, and imaging efficiency. In VSMM-TFM images, flaw indications are 2.77 times those of TFM, while the TOF matrix calculation time and imaging time are reduced by 30.09 and 3.73 times respectively. In the experiment, VSMM-TFM successfully inspec-

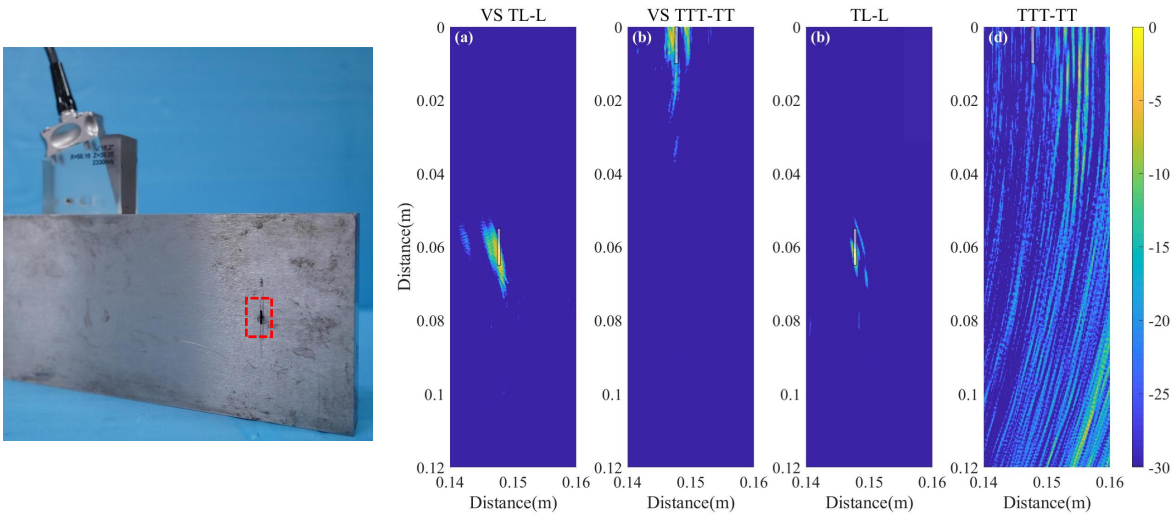

Fig. 6: Experimental setup and test block (left) and corresponding imaging results (right): (a) VSMM-TFM TL-L, (b) VSMM-TFM TTT-TT, (c) TFM TL-L, (d) TFM TTT-TT

ted the top flaw that was missed by TFM. In summary, the VSMM-TFM effectively addresses the insufficient energy issue of conventional TFM in UTW inspection while demonstrating superior inspection efficiency.

References

[1] U. K. Mohanty et al. 'A Resource-Efficient Process Design for Heavy Fabrication: A Case of Single-Pass-per-Layer Narrow Gap Welding'. In: *Sustainable Materials and Technologies* 33 (2022), e00488.

[2] E. Nicolson et al. 'Dual-Tandem Phased Array Method for Imaging of near-Vertical Defects in Narrow-Gap Welds'. In: *NDT & E International* 135 (2023), p. 102808.

[3] H. Xu et al. 'Imaging X70 Weld Cross-Section Using Electromagnetic Testing'. In: *NDT & E International* 98 (2018), pp. 155–160.

[4] E. Nicolson et al. 'Towards an In-Process Ultrasonic Phased Array Inspection Method for Narrow-Gap Welds'. In: *NDT & E International* 144 (2024), p. 103074.

[5] B. W. Drinkwater and P. D. Wilcox. 'Ultrasonic Arrays for Non-Destructive Evaluation: A Review'. In: *NDT & E International* 39.7 (2006), pp. 525–541.

[6] L. Le Jeune et al. 'Plane Wave Imaging for Ultrasonic Non-Destructive Testing: Generalization to Multimodal Imaging'. In: *Ultrasonics* 64 (2016), pp. 128–138.

[7] X. Xu et al. 'Data Fusion of Multi-View Plane Wave Imaging for Nozzle Weld Inspection'. In: *NDT & E International* 141 (2024), p. 102989.

[8] T. Gantala, S. P.L. and K. Balasubramaniam. 'Improved Imaging Technique for Nondestructive Evaluation Using Arbitrary Virtual Array Source Aperture (AVASA)'. In: *NDT & E International* 138 (2023), p. 102869.

[9] E. Hoyle et al. 'Virtual Source Aperture Imaging with Auto-Focusing of Unknown Complex Geometry through Dual Layered Media'. In: *NDT & E International* 98 (2018), pp. 55–62.

[10] J. Wang et al. 'Virtual Source Total Focusing Method for Crack Detection in Complex Curved Structure'. In: *NDT & E International* 140 (2023), p. 102968.

[11] Sumana and A. Kumar. 'Phased Array Ultrasonic Imaging Using Angle Beam Virtual Source Full Matrix Capture-Total Focusing Method'. In: *NDT & E International* 116 (2020), p. 102324.

[12] M. V. Felice and Z. Fan. 'Sizing of Flaws Using Ultrasonic Bulk Wave Testing: A Review'. In: *Ultrasonics* 88 (2018), pp. 26–42.

DOI 10.5162/Ultrasonic2025/C13-b3

Assessment of the influence of curing parameters on fibre reinforced epoxy composite properties using guided ultrasonic waves

Hayrettin Irmak[1], *Leander Claes*[2], *Shuang Wu*[1], *Thorsten Marten*[1], *and Thomas Tröster*[1]
[1]*Chair of Automotive Lightweight Design, Paderborn University, 33098 Paderborn, Germany*
[2]*Measurement Engineering Group, Paderborn University, 33098 Paderborn, Germany*
hayrettin.irmak@uni-paderborn.de

Abstract: The degree of crosslinking in unidirectional prepreg materials was investigated using differential scanning calorimetry to assess their curing behavior and thermal characteristics. To complement these measurements with a non-destructive, in-situ method, the propagation properties of guided acoustic waves in cured carbon fibre-reinforced epoxy plates were analysed. Correlations between the degree of crosslinking and acoustically determined mechanical properties were drawn to enable a future non-destructive evaluation approach.

Keywords: fibre-reinforced polymers, differential scanning calorimetry, degree of crosslinking, guided waves, ultrasound.

Introduction

In the automotive industry, reducing weight through lightweight design is a significant approach for conserving resources and improving vehicle dynamics. In this context, hybrid structures combining metal and fibre-reinforced plastic offer significant potential [1]. Fibre-reinforced polymers (FRP) are widely used in sectors such as automotive and aerospace due to their low mass and high tensile strength [1, 2]. Epoxy-based composites, a common type of FRP, require thermal curing during the manufacturing of components, as process parameters such as curing temperature and duration significantly influence the final component properties. The microscopic and macroscopic properties of these FRP material can be assessed through destructive methods, such as Differential Scanning Calorimetry (DSC). This technique is based on the principle that physical and chemical transformations are associated with changes in heat flow. Investigating the pre-impregnated semi-finished products (prepregs) under DSC provides valuable insights into its curing behavior and offers a fast, reliable method for determining the degree of cure (DOC) [3, 4, 5, 6].

Aiming to complement these measurement with a non-destructive, in-situ method, the properties of guided acoustic waves in cured carbon fibre-reinforced epoxy plates are analysed. Broadband, guided acoustic waves are excited using pulsed laser radiation and detected using a custom piezoelectric transducer. Varying the distance between excitation and detection of the guided waves enables the acquisition of spatiotemporal measurement data, from which the frequencies and wavenumbers of the excited modes can be extracted. These measurement results are matched by the output of a waveguide simulation tool, allowing for the identification of elastic material parameter.

Samples cured under different conditions are analysed with respect to their elastic properties. Similarly, equally conditioned samples are analysed using DSC measurements to infer the degree of crosslinking of the polymers molecules. Relations between the degree of crosslinking and the acoustically determined mechanical properties are draw in an effort to determine the quantity non-destructively in a future measurement procedure.

Material

In this study, the specimens are fabricated from stacked unidirectional (UD) prepreg composed of carbon fibers and the thermosetting matrix resin E320 from SGL Carbon SE, Germany. The matrix content in the current prepreg is approximately $39\,\%$ by weight. The specimens used in this study consist of a single unidirectionally oriented layer with a defined thickness of $0.23\,\mathrm{mm}$. The fibre orientation is aligned along the $0°$ axis, with a fibre volume fraction of $60\,\%$ [7, 8].

DSC cure characterization

DSC measurements were carried out using a DSC 214 (Netzsch, Germany). For each test, approximately $10\,\mathrm{mg}$ of uncured prepreg material was placed into an aluminium crucible with a pierced lid. Dynamic DSC scans were performed at a constant heating rate of $20\,°\mathrm{C\,min^{-1}}$, up to a final temperature of $250\,°\mathrm{C}$. Additionally, isothermal DSC measurements

DOI 10.5162/Ultrasonic2025/C13-b3

were conducted at two curing temperatures T_c of $80\,^{\circ}\mathrm{C}$ and $150\,^{\circ}\mathrm{C}$, under a continuous nitrogen purge.

The objective of these measurements was to evaluate the degree of cure of the prepreg under varying thermal conditions. Upon applying a defined temperature profile, the exothermic curing reaction is triggered. The degree of cure, α, is calculated based on the specific heat released over time, $H(t)$, relative to the total heat of reaction, H, as follows:

$$\alpha = \frac{H(t)}{H} \tag{1}$$

The curing or crosslinking behavior is then described in the form of a rate equation:

$$\frac{d\alpha(t)}{dt} = f(T, \alpha) \tag{2}$$

where $\alpha = 0$ and $\alpha = 1$ represent the uncured and fully cured states, respectively. Fig. 1 and Fig. 2 illustrate the characteristic progression of the degree of cure at $80\,^{\circ}\mathrm{C}$ and $150\,^{\circ}\mathrm{C}$ under isothermal conditions.

The results of the isothermal DSC analysis provide discrete data points of the recorded heat flow at defined intervals (in this case, every six seconds). Based on the respective sample mass, the corresponding specific heat flow values can be calculated. It is important to consider that, in the case of prepreg materials, only the matrix contributes to the reactive portion of the sample, meaning that approximately $40\,\%$ of the total sample mass is involved in the curing reaction. The reaction enthalpy of the curing process is determined by the area between the measured heat flow curve and the corresponding baseline, which is obtained from a second heating run of the fully cured sample. Consequently, the baseline values are subtracted from the measured heat flow. The reaction enthalpy is then calculated by summing and integrating the resulting values over time. Complementary data on temperature, curing time, and degree of cure are provided in Tab. 1. Specifically, at $80\,^{\circ}\mathrm{C}$, $80\,\%$ and complete cure ($100\,\%$) are achieved after $5.3\,\mathrm{h}$ and $10\,\mathrm{h}$, respectively, while at $150\,^{\circ}\mathrm{C}$, the same levels of cure are reached within only $7\,\mathrm{min}$ and $1\,\mathrm{h}$ respectively.

Acoustic material characterisation

In an effort to non-destructively quantify the mechanical behaviour of the samples, the assumption is made that the cured sample constitute acoustic waveguides. Aiming to realise a material characterisation procedure based on the properties of guided waves in the samples, acoustic waves are excited using pulsed laser radiation vie the thermoelastic effect (Fig. 3) [9]. A short pulse duration ($1\,\mathrm{ns}$) and small focus result in excitation of broadband acoustic waves in frequency and wavenumber regime, i.e. spatial and temporal

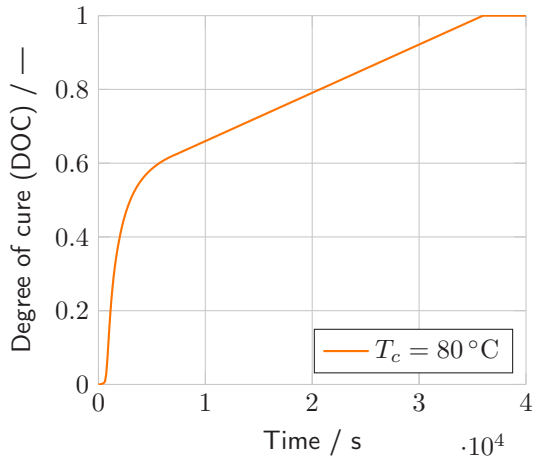

Fig. 1: Progression of the degree of curing of prepreg at $T_c = 80\,^{\circ}\mathrm{C}$ under isothermal curing.

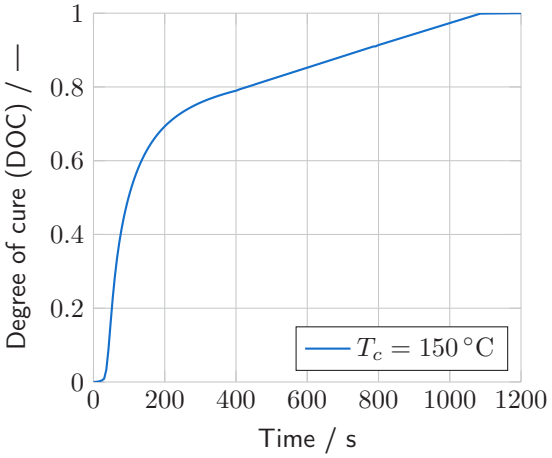

Fig. 2: Progression of the degree of curing of prepreg at $T_c = 150\,^{\circ}\mathrm{C}$ under isothermal curing.

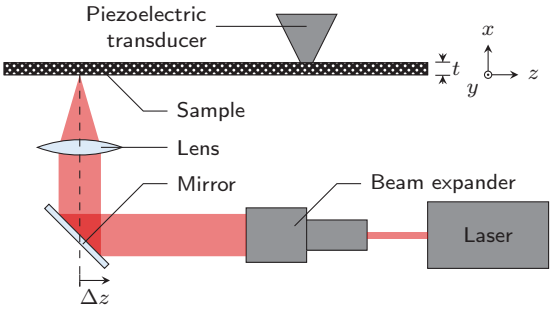

Fig. 3: Experimental setup for the excitation and detection of acoustic waves in plate-like samples with adjustable propagation distance.

DOI 10.5162/Ultrasonic2025/C13-b3

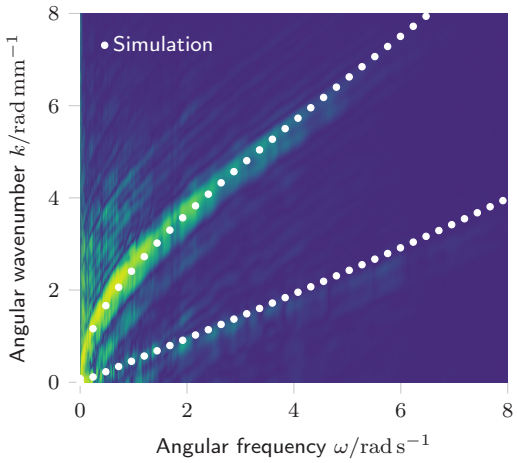

Fig. 4: Processed spectral measurement data for the sample cured at $80\,^{\circ}\mathrm{C}$ for $10\,\mathrm{h}$ superimposed with waveguide simulation data for the determined wave velocities.

frequency. The focus is line-shaped in y-direction for a directed emission of acoustic waves and movable in z-direction. The acoustic waves are detected by an equally broadband piezoelectric transducer with an active area also resembling a line [10].

Measurements are performed moving the excitation position in equidistant steps along the z-direction and recording a signal at each step. The resulting spatio-temporal matrix of measurement data is processed by applying a two-dimensional Fourier transformation, transforming the time to frequency and the spatial axis to wavenumber. In the resulting matrix, modes propagating in the sample and thus present in the measurement data are visible as ridges [11]. In previous work on metallic and homogenous samples [10, 9], large numbers of modes are visible in such depictions. However, due to the complex structure and high absorption of the samples examined in this study, only few rides are pronounced in the data (Fig. 4). These correspond to the basic asymmetric and symmetric modes of the plate.

To identify the an quantitative material model for the samples, the inverse problem of fitting the output of a numerical waveguide model to the measurement data is solved. For this study only the behaviour of the sample perpendicular to the fibre-direction is quantified. Based on the assumption, that the overall material behaviour follows transversely-isotropic symmetry, with the strong axis being aligned with the fibres, the properties of the sample in the observed plane can be assumed isotropic. When parametrising the acoustic behaviour using the longitudinal and transversal wave velocities c_l and c_t only two parameters need to be identified, which greatly simplifies the underlying optimisation problem. This especially advantageous given the limited information carried by the measurement data. The simulation model is based on a semi-analytical finite element method [12], assuming harmonic function in propagation direction z and infinite dimensions in y. For efficiency, a single high-order (16th) element is used, which, due to the assumptions is one-dimensional. Solving for the eigenfrequencies of the system for a given frequency yields the wavenumber of the modes that are able to propagate that frequency.

Tab. 1: Identified acoustic wave velocities for differently processed samples.

Curing			Measurement	
Temp.	Time	DOC	$c_\mathrm{l}/\mathrm{m\,s^{-1}}$	$c_\mathrm{t}/\mathrm{m\,s^{-1}}$
$80\,^{\circ}\mathrm{C}$	$5.3\,\mathrm{h}$	$80\,\%$	5995	1169
$80\,^{\circ}\mathrm{C}$	$10\,\mathrm{h}$	$100\,\%$	6000	1074
$150\,^{\circ}\mathrm{C}$	$7\,\mathrm{min}$	$80\,\%$	6000	1162
$150\,^{\circ}\mathrm{C}$	$1\,\mathrm{h}$	$100\,\%$	6568	1079

The objective function for the subsequent optimisation procedure is formulated by sampling the measurement data at the points yielded by the simulation model. The resulting values are maximised by gradient based optimisation using a trust region algorithm [13], in which the parameters of the simulation model (c_l and c_t) are adapted until measurement and simulation are in agreement. Fig. 4 shows the measurement data for the $80\,^{\circ}\mathrm{C}$ for $10\,\mathrm{h}$ superimposed with the simulation result for the determined wave velocities after the optimisation process showing good agreement. The remaining deviation can be explained by small anisotropic effects still being present, a cause for which may be a possible misalignment between the fibres and the measurement axis.

The results for the wave velocities of the four sample examined in this study are summarised in Tab. 1. The results for the longitudinal wave velocity c_l show now clear indication of influence with respect to the curing parameters. This observation may be due to the fact that the primary sensitivity of the determination of c_l comes from the symmetric mode (the lower wavenumber mode in Fig. 4), which is only present with low intensity in the measurement data. This results in low gradients in the objective function and thus an increased uncertainty of c_l. The determination of the transversal wave velocity c_t, however, is primarily based on the shape of the asymmetric mode, which is more pronounced in the measurement data. Accordingly, the determined transversal wave velocity of the samples show a clear dependence on

the degree of curing, with higher curing degrees yielding lower values for c_t. Within the limited scope of this study, the mode with which the degree of curing is achieved appears to have little influence. The fact that primarily the transverse wave velocity c_t has a high sensitivity with regard to the degree of curing can be considered advantageous for future applications, as acoustic characterisation methods show equally high sensitivity with respect to c_t.

Conclusions

The present study indicates that the degree of cure of epoxy composite can be assessed by the analysis of guided ultrasonic wave properties, in particular the transversal wave velocity c_t perpendicular to the fibre direction. This opens the possibility of a non-destructive testing method, as measurement of c_t are possible excitation of surface acoustic waves. Future research will include the analysis of the complete, anisotropic, viscoelastic material behaviour of the sample, with the aim to find other dependencies between acoustic behaviour and parameters of the curing process, especially the curing time.

References

[1] C. Lauter. *Entwicklung und Herstellung von Hybridbauteilen aus Metallen und Faserverbundkunststoffen für den Leichtbau im Automobil: Zugl.: Paderborn, Univ., Diss., 2014*. Vol. 2014,4. Schriftenreihe / Institut für Leichtbau mit Hybridsystemen. Aachen: Shaker, 2014. ISBN: 978-3-8440-2996-3.

[2] H. Schürmann. *Konstruieren mit Faser-Kunststoff-Verbunden: Mit 39 Tabellen*. 2., bearb. und erw. Aufl. VDI-Buch. Berlin and Heidelberg: Springer, 2007. ISBN: 978-3-540-72189-5.

[3] S. Tinkloh et al. "A micromechanical-based finite element simulation of process-induced residual stresses in metal-CFRP-hybrid structures". In: *Composite Structures* 238 (2020), p. 111926. ISSN: 0263-8223. DOI: 10.1016/j.compstruct.2020.111926.

[4] A. Frick and C. Stern. *DSC-Prüfung in der Anwendung*. 2., aktualisierte und erw. Aufl., [elektronische Ressource]. Hanser eLibrary. München: Carl Hanser Verlag GmbH & Co. KG and Hanser Verlag, 2013. ISBN: 9783446436923. DOI: 10 . 3139 / 9783446436923.

[5] R. Hardis et al. "Cure kinetics characterization and monitoring of an epoxy resin using DSC, Raman spectroscopy, and DEA". In: *Composites Part A: Applied Science and Manufacturing* 49 (2013), pp. 100–108. ISSN: 1359835X. DOI: 10.1016/j.compositesa.2013.01.021.

[6] L. Sun et al. "Characterization of Epoxy Prepreg Curing Process". In: *The Journal of Adhesion* 82.2 (2006), pp. 161–179. ISSN: 0021-8464. DOI: 10.1080/00218460600559573.

[7] SGL CARBON SE. *Harzsysteme E320/E321/E322/E323 - Epoxid-Harzsysteme für SIGRAPREG® Prepregs*. Rev. 01. Technical Datasheet. 2015.

[8] SGL CARBON SE. *Unidirectional epoxy carbon fiber prepreg SIGRAPREG® C U230-0/NF-E320/*$39\,\%$. 2nd ed. Technical Datasheet. 2020.

[9] S. Johannesmann et al. "Lamb wave based approach to the determination of acoustic material parameters". In: *tm - Technisches Messen* 89.7–8 (Mar. 2022), pp. 493–506. DOI: 10.1515/teme-2021-0134.

[10] L. Claes et al. "Determination of the material properties of polymers using laser-generated broadband ultrasound". In: *Journal of Sensors and Sensor Systems* 5.1 (2016), pp. 187–196. ISSN: 2194-878X. DOI: 10.5194/jsss-5-187-2016.

[11] D. Alleyne and P. Cawley. "A 2-dimensional Fourier transform method for the quantitative measurement of Lamb modes". In: *IEEE Symposium on Ultrasonics*. IEEE, 1990. DOI: 10.1109/ultsym.1990.171541.

[12] I. Bartoli et al. "Modeling wave propagation in damped waveguides of arbitrary cross-section". In: *Journal of Sound and Vibration* 295.3 (2006), pp. 685–707. ISSN: 0022-460X. DOI: https://doi.org/10.1016/j.jsv.2006.01.021.

[13] M. A. Branch, T. F. Coleman, and Y. Li. "A Subspace, Interior, and Conjugate Gradient Method for Large-Scale Bound-Constrained Minimization Problems". In: *SIAM Journal on Scientific Computing* 21.1 (Jan. 1999), pp. 1–23. ISSN: 1095-7197. DOI: 10.1137/s1064827595289108.

DOI 10.5162/Ultrasonic2025/C13-b4

Ultrasonic Metrology for the Study of Hydrogen Embrittlement in Steels

Louis Leffray[1], *Guy Feuillard*[1], *Jules Toupin*[1], *Hossep Achdjian*[1], *Julien Bustillo*[1], *and Nicolas Mary*[2]

[1]*GREMAN Laboratory, INSA Centre Val de Loire, UMR CNRS 7347. Université de Tours. 3 rue de la Chocolaterie 41034 Blois Cedex France*

[2]*MATEIS, INSA Lyon, UMR CNRS 5510 Bât. B. Pascal, 4° étage 7, Avenue Jean Capelle 69621 Villeurbanne Cedex France*

guy.feuillard@insa-cvl.fr

Abstract: In this work, we propose the development of an ultrasonic metrology system that allows for real-time measurements of velocity in steels during electrochemical hydrogen charging. This study is coupled with a propagation model in a water-steel-water structure. For 2% variation of the stiffness coefficient when the material is fully charged in hydrogen, we simulate a variation of a few dozen meters per second due to property changes. We report the measurement of velocity variations conducted on a DP800 dual-phase steel. When the effect of the temperature on the velocity measurement is compensated, the standard deviation for the velocity measurement is less than 0.2 $m.s^{-1}$. Experiments were conducted in DP800 dual-phase steel over several tens of hours of electrochemical charging of steel immersed in a hydrogenocarbonate solution on two samples. A hardening of the material is observed, with velocity an increase of 25 $m.s^{-1}$ in one sample and 45 $m.s^{-1}$ in the second one.

Keywords: Ultrasonic metrology system, Hydrogen Embrittlement, velocity measurement.

Introduction

Hydrogen-steel interactions are widely documented in the literature, and regardless of the proposed mechanism, the conclusions remain identical, with the creation of microstructural defects (dislocations, microstructural changes, atomic decohesion) [1]. As a result, the mechanical properties of materials are degraded. The elastic limit of a material is then lowered, leading to premature failure of the structure.Techniques for assessing a steel's sensitivity to hydrogen trapping and diffusion are well known and are largely based on electrochemical charging tests. Although there are only a small number of mechanical tests coupled with electrochemical charging [2], these provide access to the reaction mechanisms involved in hydrogen embrittlement but are not suitable for on-site health monitoring. To achieve this, we need to consider the use of non-destructive testing techniques capable of detecting and quantifying any metallurgical modifications related to the absorption of hydrogen in a metal structure. Among the available methods for characterizing mechanical properties, ultrasonic methods are widely known and used. They can be used in transmission or reflection modes and are based on the analysis of the time arrival and amplitude of the received signal.

In this work, we propose the development of an ultrasonic metrology system that enables real-time measurements of velocity variations in steel samples during hydrogen charging. In the first section, an electroacoustic model is proposed to predict the transmitted pulse response on the receiving transducer. The material and experimental setup are presented, with particular attention given to the description of the ultrasonic setup coupled with electrochemical charging. Finally, we report initial results on velocity variations in two dual-phase steels (DP800).

Modelling

Assuming a plane ultrasonic wave, the propagation in a multilayer structure can be described by a transfer matrix formalism. Considering a structure consisting of n layers, each layer, i, is described by a transfer matrix given by Eq. (1)

$$[M_i] = \begin{bmatrix} \cos(k_i L_i) & -jZ_i \sin(k_i L_i) \\ -\frac{j}{Z_i}\sin(k_i L_i) & \cos(k_i L_i) \end{bmatrix} \quad (1)$$

Where Z_i is the acoustic impedance of the medium given by the product of the density by the ultrasonic phase velocity, k_i is the wave number, L_i is the thickness of the layer, and j is the complex number.

The total transfer matrix system is given by the product of the matrices Eq. (2)

DOI 10.5162/Ultrasonic2025/C13-b4

$$[M_{\text{tot}}] = \prod_{i=1}^{n} [M_i] \tag{2}$$

This multilayer structure is excited by a pressure source P_1, giving rise to particle velocity v_1 from a transducer of internal acoustic impedance Z_t. The multilayer is closed on the acoustic impedance of the receiving transducer Z_s (Fig. 1). P_e is the excitation pressure, P_2, v_2 the pressure and the particle velocity at reception.

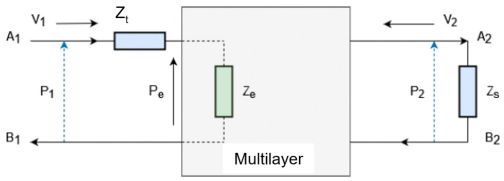

Fig. 1: Equivalent scheme for transfer function calculation.

Denoting A, B, C, D the components of $[M_{\text{tot}}]$ we have Eq. (3).

$$\begin{pmatrix} P_e \\ V_1 \end{pmatrix} = \begin{bmatrix} A & B \\ C & D \end{bmatrix} \begin{pmatrix} P_2 \\ -V_2 \end{pmatrix} \tag{3}$$

Knowing that $V_2 = P_2/Z_s$, the transmission transfer function is given by Eq. (4)

$$H_t(f) = \frac{P_2}{P_e} = \frac{1}{A - \dfrac{B}{Z_s}} \tag{4}$$

For a given excitation signal, $x(t)$, the frequency transmitted pulse response is obtained by multiplying the transfer function $H_t(f)$ by the spectrum of the excitation signal. The time response then is obtained by taking the inverse Fourier transform. For all the simulations, we have chosen a Gaussian excitation signal centered on the transducer's center frequency.

Experimental set-up

In our study, a commercial $DP800$ dual $-$ phase steel was used. $DP800$ is mainly made of ferrite and martensite steel with a lower content of bainite. Typical value reported in literature [3] for the volume fraction of each component is 69% of ferrite 30% of martensite and less than 1% of bainite. Samples used for the experiment were $1\ mm$ thick with lateral dimensions of $50 \times 30\ mm^2$.

The experimental set-up is shown in Fig. 2. Hydrogen charging was performed by an electrochemical technique using a three-electrode configuration. Steel samples (i.e., the working electrode) were connected to a potentiostat (*Biologic, MPG2, Seyssinet-Pariset, France*). The counter electrode was a Platinum plate, and the reference electrode was an $Ag/AgCl$ secondary reference electrode ($E = +237mV/ESH$). The charging electrolyte was a solution of $NaHCO_3$ with a concentration of $0.5M$ at room temperature. To control the physico-chemical state of the surface before charging, a surface conditioning step was used. During experiments, a potential scan until –1.2 V vs Ag/AgCl at a scan rate of $100mV/s$ is applied. Finally, the charging potential was maintained at –1.2 V vs Ag/AgCl for several tens of hours.

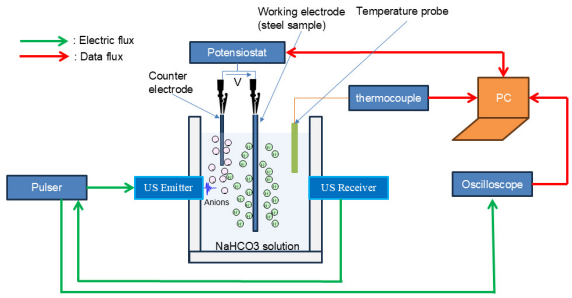

Fig. 2: Experimental setup diagram.

The ultrasonic measurements were carried out in normal incidence. The setup consists of two $50\ MHz$ ultrasonic transducers (*Olympus Panametrics - NDT* $V358\ 50MHz/0.25$), one used as an emitter and the second one as a receiver. Electrical excitation was provided by a Panametrics Model $5601A/TT$ pulser receiver. The received signals were acquired by a digital oscilloscope (Rohde $\&$ Schwarz $RTB2004$, Munich, Germany) at a sampling frequency of $2.5\ GHz$, with an averaging over 1024 acquisitions and then transferred to a computer for processing on Matlab. Simultaneously with hydrogen charging and ultrasonic measurements, the temperature was measured using a $Pt100$ temperature probe connected to its conditioner and transferred to the computer. A typical transmitted signal is presented in the red curve Fig. 3. The first echo corresponds to the ballistic pulse, i.e., the direct transmission, and the following successive echoes correspond to the round-trip into the steel sample. During hydrogen charging, both changes in velocity and attenuation are expected. However, due to the presence of hydrogen bubbles in the medium, only velocity measurements were carried out. The ultrasonic longitudinal wave velocity in steel (Eq. (5)), v, is related to the Time Of Flight (TOF) between two echoes Δt and the thickness, e, of the sample.

$$v = 2\frac{e}{\Delta t} \tag{5}$$

During experiments, a good signal-to-noise ratio is observed, and the TOF is then determined by tak-

DOI 10.5162/Ultrasonic2025/C13-b4

ing the average TOF between two successive echoes determined by cross-correlation until the tenth echo. With a sampling frequency of $2.5\ GHz$, a sample thickness of $0.95\ mm$, and an ultrasonic longitudinal wave velocity of $6000\ m.s^{-1}$ in the material (which is typical for steel materials), the induced error on the velocity measurement due to a mislocation of the maximum of cross-correlation is approximately $\pm 7\ m.s^{-1}$ per time sample. This error is too large for accurate monitoring of the ultrasonic velocity in the sample, where variations of about $20\ m.s^{-1}$ are expected. To improve time-of-flight estimation accuracy, the signal is oversampled by a factor of 100 using the *Makima* interpolation method in MATLAB.

Results and discussions

Fig. 3 shows the comparison between experiments and simulations for an uncharged $DP800$ sample. For the simulations, the properties are given in Tab. 1 for steel.

Tab. 1: Simulation parameters.

Gaussian Signal		
A_0	σ	f_c
1	2.10^{-8}	$50\ MHz$
Material properties		
	Velocity	Acoustic impedance
Water	$1500\ m.s^{-1}$	$1.5\ MRayl$
DP 800	$6062\ m.s^{-1}$	$47.59\ MRayl$

The positions of the echoes within the sample are accurately predicted; however, the amplitudes differ, as the attenuation of the ultrasonic waves in the steel was not precisely taken into account in the model. Additionally, the shape of the simulated echoes differs from that of the experimental ones. This discrepancy is attributed to the use of a Gaussian waveform in the simulations. Hydrogen charging results in a hardening of the material. For DP800 steel, the literature reports an increase in the stiffness coefficient of a few percent, corresponding to a similar change in ultrasonic velocity [4]. In this study, we considered a 2% increase in the stiffness coefficient for a fully hydrogen-charged steel. This variation leads to a velocity increase of approximately $16 m.s^{-1}$, which is well within the resolution achievable with the algorithm used for velocity measurements.

Electrochemical hydrogen charging of steels is a diffusion-driven process with kinetics that can span several days. It is therefore essential to control the temperature and assess its impact on the measurements. To this end, we conducted an initial experiment in which we measured the ultrasonic wave velocity in the steel as a function of time and temperature,

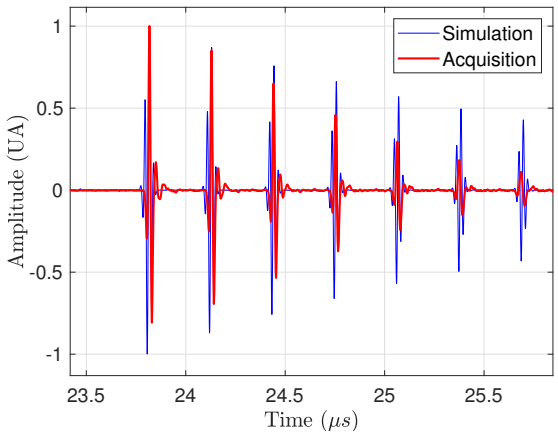

Fig. 3: Experimental and simulated transmitted signal through uncharged DP800 steel.

without hydrogen charging. Fig. 4 shows the evolution of velocity as a function of temperature in steel over a 48-hour measurement period. During this period, the temperature varied between 21 and $25°C$, and we observed a linear dependence of the velocity on this temperature. The temperature coefficient is $0.68 m.(s.°C)^{-1}$, consistent with what is reported in the literature for steels [4]. When the temperature is compensated over the given period (Fig. 4), the variance on the measurement of the velocity is $0.13\ m.s^{-1}$, which should allow for monitoring the hydrogen charging.

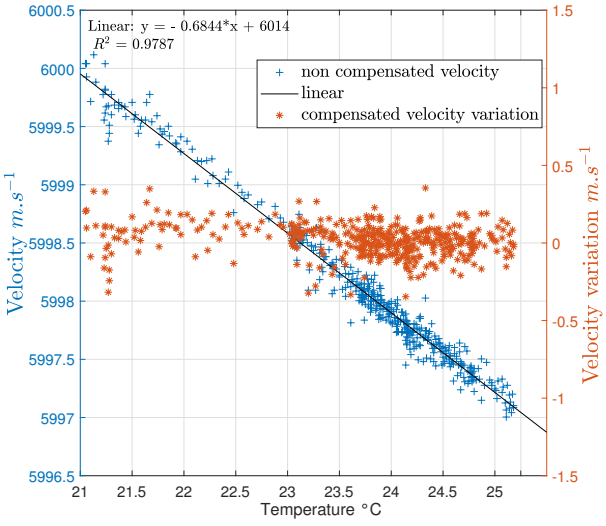

Fig. 4: Ultrasonic wave velocity in the DP 800 steel sample as a function of temperature and temperature-compensated velocity variations.

Fig. 5-a and Fig. 5-b show the temperature-compensated variations in velocity observed during

hydrogen charging on two DP800 samples. We also show the evolution of the current in the solution. For these measurements, the reference velocity was determined after $60\ mn$, after the temperature and the short-time current began to stabilize in the measurement cell. Hydrogen charging times are 120 hours for the first measure and 55 hours for the second. During the experiments, it was necessary to periodically refill the measurement cell with water due to significant water evaporation over time, which led to current fluctuations during the second measurement. However, it is important to note that the electrochemical potential remained below the threshold required for hydrogen charging. Current fluctuations are attributed to the formation of gas bubbles on the surface of the counter-electrode and to the evaporation of water, which alters the immersed surface area of the counter-electrode. These phenomena explain the noise observed in the current curves. For the first measurement, we observed an increase in velocity variation of $25\ m.s^{-1}$ with a plateau appearing after 50 hours of experiment. This plateau corresponds to a stabilization of the current at $-10\ mA$ that seems to indicate that the charging in this sample is complete. It should be noted that this sample had previously been used for electrochemical hydrogen charging tests, and we cannot guarantee that it is completely blank. As reported in the literature, we observed an increase in the ultrasonic velocity and a stiffening of the steel. For the second measurement, we worked on a blank sample and observed a $40\ m.s^{-1}$ velocity variation. However, we did not observe a plateau at the end of the 50-hour experiment. For this sample, the relative velocity variation is around 0.7%, corresponding to a relative increase of the stiffness coefficient of 1.4%.

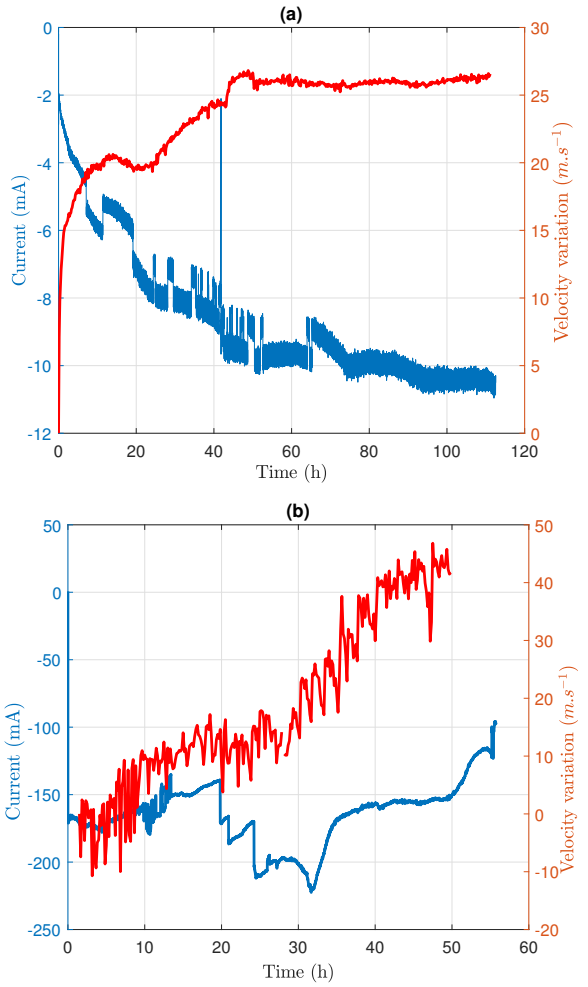

Fig. 5: Velocity variation in DP 800 steel and current into the electrochemical bath for the two samples.

Conclusion

In this study, we have demonstrated that ultrasonic measurements represent a promising non-destructive technique for monitoring hydrogen uptake in steel by observing variations in ultrasonic velocity during hydrogen diffusion. We report maximum velocity variations of 25 $m.s^{-1}$ and 45 $m.s^{-1}$. Given the precision achieved through temperature compensation, these changes can be attributed to hydrogen migration within the steel samples rather than to temperature fluctuations. To date, the experiments have been limited to a single steel grade. Literature suggests that the response to hydrogen charging may vary depending on the steel composition. Further investigations are warranted to generalize these findings.

References

[1] S. Lynch. "Hydrogen embrittlement phenomena and mechanisms". In: *Corrosion reviews* 30.3-4 (2012), pp. 105–123. DOI: 10.1533/9780857093769.1.90.

[2] D. Mallick et al. "Study of diffusible behavior of hydrogen in first generation advanced high strength steels". In: *Metals* 11.5 (2021), p. 782. DOI: doi.org/10.3390/met11050782.

[3] R. O. Santos et al. "Damage identification parameters of dual-phase 600–800 steels based on experimental void analysis and finite element simulations". In: *Journal of Materials Research and Technology* 8.1 (2019), pp. 644–659. DOI: 10.1016/j.jmrt.2018.04.017.

[4] A. Kumar and S. K. Paul. "Local strain evolution and microstructural characterisation of hydrogen-induced damage at different strain rates in dual phase (DP 780) steel". In: *Forces in Mechanics* 13 (2023), p. 100237. ISSN: 2666-3597. DOI: https://doi.org/10.1016/j.finmec.2023.100237.

DOI 10.5162/Ultrasonic2025/C13-c1

Inversion of the corrugation parameters of a double corrugated liquid/solid interface from the diffraction of homogeneous plane waves with the Ultrasonic Polar Scan

Emil Aleksiewicz-Drab[1], Mathias Kersemans[2,3], and Koen Van Den Abeele[1]
[1]KU Leuven Campus Kulak, Dept. of Physics, Belgium
[2] Ghent University, Dept. of Materials, Textiles and Chemical Eng., Ghent, Belgium
[3]Flanders Make, FlandersMake@UGent, Corelab MIRO, Lommel, Belgium
emil.aleksiewicz-drab@kuleuven.be

Abstract: This study focuses on inverting the geometrical characteristics of the surface of corrugated interfaces from ultrasonic polar scan data. Based on an analytical model to predict the reflection and transmission of homogeneous plane waves on a 2D periodically corrugated surface, and in combination with numerical calculations and machine learning, we were able to inversely estimate the corrugation parameters (the periodicity, shape and height) from the reflected ultrasonic polar scan landscape.

Keywords: Ultrasonic Polar Scan, Periodically corrugated surface, Corrugation height, Non-destructive characterization, 2-D corrugated surface.

Introduction

In the past, several studies of acoustic waves interacting with corrugated materials have been reported, for both 1-D [1–5] and 2-D [6] surface corrugations due to its potential use in material characterization and non-destructive testing (NDT). These studies investigated the interaction of homogeneous as well as inhomogeneous plane waves, and showed that the geometrical parameters which describe the corrugation, such as the corrugation period Λ, the height h and the shape S, significantly influence the scattering characteristics of particular modes in reflection or transmission [3].On the other hand, to our knowledge, only one study so far has been dedicated to the inverse estimation of the underlying interface properties themselves [7]. This experimental work, be it quite limited, showed interesting potential for further exploration of the inverse problem with the help of theoretical models as a guideline for the inversion of the corrugation characteristics. In addition, ongoing development of a novel phased array (PA)-based Ultrasonic Polar Scan (UPS) [8–10] device should be able to facilitate a more comprehensive means for accelerated experimental measurements and verification.

In the current paper, we first reintroduce the state-of-the-art theoretical framework. Next, we show how specific corrugation parameters can be estimated using numerical calculation and machine learning, keeping in mind the possibilities and limitations of future experimental validation. Finally, we discuss the inversion results and the validity of this approach, which points to potential limitations and the need for a next generation experimental measurement campaign.

Mathematical framework for the forward model

We consider a doubly corrugated surface at a single liquid-solid boundary given by:

$$g(x,y,z) = f(x,y) - z = f_x(x) + f_y(y) - z = 0 \quad (1)$$

with

$$f_x\left(x+\Lambda_x\right) = f_x(x),\ f_y\left(y+\Lambda_y\right) = f_y(y) \quad (2)$$

An incident homogeneous plane wave $\mathbf{N}^{inc}$, with a complex wave vector $\mathbf{k}^{inc}$, interacts with the corrugated interface and is scattered into multiple wave fields in reflection and transmission. The wavefield contributions of the incident wave (*inc*), the reflected longitudinal in the liquid (*r*), and the transmitted dilatational (*d*) and shear components (s) in the solid), representing the solutions to the time-independent wave equation as infinite series, can be written as

$$N^{inc} = A^{inc}\phi^{inc}(ik_x^{inc}e_x + ik_y^{inc}e_y + ik_z^{inc}e_z) \quad (3)$$

$$N^r = \sum_{m,n} R^{m,n}\phi^{m,n,r}\left(ik_x^{m,n,r}e_x + ik_y^{m,n,r}e_y + ik_z^{m,n,r}e_z\right) \quad (4)$$

$$N^d = \sum_{m,n} A^{m,n,d}\phi^{m,n,d}\left(ik_x^{m,n,d}e_x + ik_y^{m,n,d}e_y + ik_z^{m,n,d}e_z\right) \quad (5)$$

$$N^s = \sum_{m,n} A^{m,n,s}\phi^{m,n,s}P^{m,n,s} \quad (6)$$

with A^{inc} the amplitude of the incident wave, and $R^{m,n}$, $A^{m,n,d}$, $A^{m,n,s}$ the complex valued amplitudes of the reflected longitudinal, transmitted dilatational and transmitted shear of order m, n respectively, which are directly proportional to A^{inc}. Further, the acoustic potentials can be expressed as $\phi^{\zeta} = e^{i(k^{\zeta} \cdot r)}$ for $\zeta \in \{(m,n,r);\ (m,n,d);\ (m,n,s)\}$, and

$$k_x^{m,n,s} P_x^{m,n,s}, k_y^{m,n,s} P_y^{m,n,s} + k_z^{m,n,s} P_z^{m,n,s} = 0 \tag{7}$$

where $\mathbf{P}^{m,n,s}$ is the polarization vector.

The displacement components Eq. (3) – Eq. (6) have to obey the continuity conditions at the boundary $z = f(x,y)$[11], consisting of the continuity of the normal displacement across the interface:

$$\begin{aligned} \left(N^{inc} + N^{r}\right) \cdot \nabla g = \left(N^{d} + N^{s}\right) \cdot \nabla g \\ \text{on } g(x,y,z) = 0 \end{aligned} \tag{8}$$

and the continuity of the normal and tangential stresses below (1) and above (2) the boundary

$$\sum_j T_{ij}^1 (\nabla g)_j = \sum_j T_{ij}^2 (\nabla g)_j,\ i,j = x,y,z \tag{9}$$

$$\begin{aligned} \left(A_{mn}^s P_x^{m,n,s} k_x^{m,n,s} + A_{mn}^s P_y^{m,n,s} k_y^{m,n,s} \right. \\ \left. + A_{mn}^s P_z^{m,n,s} k_z^{m,n,s}\right) \phi^{m,n,s} = 0 \end{aligned} \tag{10}$$

The established conditions Eq. (8) – Eq. (10) lead to five equations that are periodic in x and y, where a sufficient condition for the solution is to demand that the Fourier coefficients are equal over the intervals $[0,\ \Lambda_x] \times [0,\ \Lambda_y]$, resulting in a linear system of equations in the unknown coefficients $R^{m,n}$, $A^{m,n,d}$, $A^{m,n,s}$. The whole system is however too large to enclose in this paper. Included in the system are wavenumbers, $k_\gamma^\eta = k_\gamma^{inc} + \eta \frac{2\pi}{\Lambda_\gamma}$ with $\eta \in \{m,n\}$ and $\gamma \in \{x,y\}$, denoting the wave-vector components in the γ direction of the η-th order scattered waves which are projected on the surface, and which obey the generalized Snell's law for periodic gratings [6].

Note that this quasi-analytical description of the scattered ultrasonic field is only valid for small roughness [12], i.e. $\Lambda_x, \Lambda_y \approx \lambda$ and $h \ll \lambda$, where λ is the wavelength of the incident wave, and h is the height of the corrugation.

Numerical calculations

Although the linear system of equations is infinite by construction, the infinite summation may be truncated based on an intuitively decreasing amplitude with mode number. Assuming a maximum mode value N_γ, the dimension of the linear system to be solved is (5 (2N_x+1) (2N_y+1) by 5 (2N_x+1) (2N_y+1)).

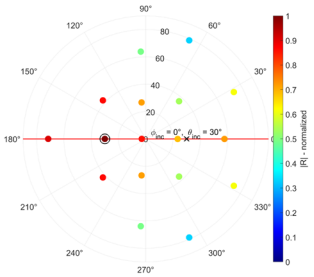

(a) $h = 50\,\mu m, \quad \Lambda = 1.1\,mm$

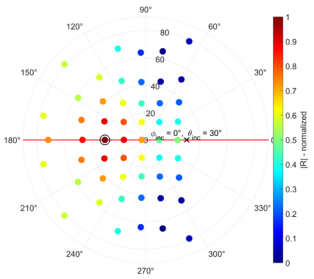

(b) $h = 100\,\mu m, \quad \Lambda = 2.2\,mm$

Fig. 1: Reflection landscape in a polar plot representation for two different corrugation periodicities Λ and two different corrugation heights h

Throughout this paper, a symmetric doubly corrugated surface between water and brass will be considered, and $N_x = N_y = 4$ is taken for both scattering directions. Further, we assume: density $\rho_w = 1000\ \mathrm{kg/m^3}$ for water and $\rho_b = 8100\ \mathrm{kg/m^3}$ for brass; dilatational wave speed $v_w = 1480\ \mathrm{m/s}$ for water and $v_{bd} = 4840\ \mathrm{m/s}$ for brass; shear wave speed for brass is $v_{bs} = 2270\ \mathrm{m/s}$. ; attenuation $\alpha_{wd}\omega^2 = 4 \times 10^{-8}\ \frac{\mathrm{Np}}{\mathrm{mm}}$ at $1\,\mathrm{MHz}$ for water, while $\alpha_{bd}\omega^2 = 4 \times 10^{-6}\ \frac{\mathrm{Np}}{\mathrm{mm}}$ and $\alpha_{bs}\omega^2 = 2 \times 10^{-5}\ \frac{\mathrm{Np}}{\mathrm{mm}}$ at $1\,\mathrm{MHz}$ for brass. In terms of 2D corrugation, we consider three basic shapes: a sinusoidal corrugation, a triangular corrugation and a square corrugation. As an example, Fig. 1 shows the reflection landscape in a polar plot representation for an homogeneous incident plane wave at $\Psi^{inc} = \left[\theta^{inc} = 30°,\ \varphi^{inc} = 0°\right]$ from a 2D sawtooth corrugated interface between water and brass for different corrugation periodicities and different heights. The dots represent the polar position of the modes in reflection, while the colour of the dots is linked to the mode's amplitude.

Inverse estimation of corrugation characteristics

For practical NDT applications, the ultimate goal is to estimate the values of the corrugation parameters Λ_x, Λ_y, h, S from observable experimental data,

DOI 10.5162/Ultrasonic2025/C13-c1

i.e. while having access only to the reflection angles for different modes, being a combination of θ_r^{mn} and φ_r^{mn}, and the magnitude of the reflection coefficient $R^{m,n}$ of these modes as input values to perform the inversion. Calculation of Λ_x, Λ_y is relatively simple and comes from Snell's law for periodic gratings [6].

$$k_x^m = k_x^{inc} + m\frac{2\pi}{\Lambda_x},\ k_y^n = k_y^{inc} + n\frac{2\pi}{\Lambda_y} \tag{11}$$

These equations allow to express the angles of the reflected mode '*m,n*' as a combination of a polar φ_r^{mn} and reflection θ_r^{mn} angle in the following way:

$$\varphi_r^{mn} = \tan^{-1}\left(\frac{k^{inc}\sin\theta^{inc}\sin\varphi^{inc} + n\frac{2\pi}{\Lambda_y}}{k^{inc}\sin\theta^{inc}\cos\varphi^{inc} + m\frac{2\pi}{\Lambda_x}}\right) \tag{12}$$

$$\theta_r^{mn} = \sin^{-1}\left(\frac{1}{k_r^{mn}}\sqrt{\begin{aligned}&\left(k^{inc}\sin\theta^{inc}\right)^2 \\ &+4\pi k^{inc}\sin\theta^{inc} \\ &\times\left(\frac{m}{\Lambda_x}\cos\varphi^{inc} + \frac{n}{\Lambda_y}\sin\varphi^{inc}\right) \\ &+4\pi^2\left(\left(\frac{m}{\Lambda_x}\right)^2 + \left(\frac{n}{\Lambda_y}\right)^2\right)\end{aligned}}\right) \tag{13}$$

Assuming $\theta^{inc} = 0$, corresponding to normal incidence, those expressions can be largely simplified, and lead, after straightforward calculations, to potential expressions for the corrugation periods Λ_x and Λ_y;

$$\Lambda_y = \left|\frac{2\pi n\sqrt{1+\tan^2\varphi_r^{mn}}}{k_r^{mn}\sin\theta_r^{mn}\tan\varphi_r^{mn}}\right|,\ \Lambda_x = \left|\frac{m\Lambda_y\tan\varphi_r^{mn}}{n}\right| \tag{14}$$

Thanks to the fact that the new UPS device that we intend to develop in the future using phased array technology will be able to gather reflected signals at multiple angles at once, one experimental measurement at one incidence angle should in theory be sufficient to determine both lengths.

The inversion of the corrugation height h and the shape S is far more complicated, because there is no a-priori simple relation to the input parameters $R^{m,n}$. Since the forward model is computationally inexpensive, a data-driven approach is proposed to estimate these two parameters. The database was created by varying the input parameters θ^{inc}, φ^{inc}, f, h, S, resulting in nearly 3.5 million unique combination, for which a set of reflection coefficients was obtained. The proposed inversion approach is a two-step method, where first the shape S is determined, followed by an estimation of the corrugation height h. This approach is a result of preliminary testing which showed that knowing the shape beforehand massively improves the accuracy of the height estimation. Both approaches rely on supervised machine learning but use different techniques.

For the shape estimation, we considered four different shapes: two variations of a rectangular corrugation with a duty cycle of 90% (S_{R90}) and 75% (S_{R75}) respectively, a symmetrical triangular corrugation(S_T) and a sinusoidal corrugation(S_S). Wide Neural Network was used in this classifier [13, 14], with 100 neurons fully connected to the first layer. The costs of misclassification were set to 0 when the predicted shape matches the true one, and 1 otherwise. The data was split into 80/20 for training/validation and testing. The predictors were provided in the following form: $(\theta^{inc},\ \varphi^{inc},\ |R^{m,n}(f)|)$, where $m, n \in \{-1, 0, 1\}$ and f being 25 different frequencies ranging from 500 kHz to 2.5 MHz, essentially meaning that we provide the values of the first nine modes of the reflection coefficient as a function of frequency, on a grid of polar and azimuthal incident angles. Even though the height h is also varied between 10 to 90 μm in the database, it is not provided as one of the predictors, since in an experimental setting with an unknown sample, this parameter would a priori be unknown. Because the model is trained with purely synthetic data, k-fold cross validation was used to ensure some degree of robustness, as well as 5% Gaussian noise to all of the $R^{m,n}$ modes used, simulating a realistic measurement uncertainty in an experimental condition. The performance of the classifier is presented in Fig. 2 in the form of a confusion matrix which shows the correctness of the assignments in terms of percentages for each shape. The labels from 1 to 4 correspond to S_{R90}, S_{R75}, S_T and S_S respectively.

While the average accuracy of the model is 93%, the quality of the assignments is different for S_{R90} and S_S when compared to S_{R75} and S_T, with the former being significantly better, which can be attributed to the fact that these modes are more distinguishable when compared to the other two based on the features for classification used here. The addition of noise heavily impacted the accuracy of the model, as the tests without it showed a performance of 99.5% instead.

The performance of the classifier was then propagated further into a regression model used to estimate the height. The regression model was a bagged decision tree ensemble [15]. This method combines multiple decision trees to improve prediction accuracy and reduce overfitting. The model was structured in such a way, that the minimum leaf size was 5, with 40 learners in total. The input array for the predictors

DOI 10.5162/Ultrasonic2025/C13-c1

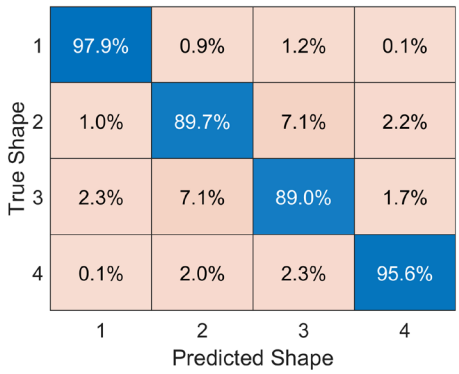

Fig. 2: Confusion matrix for 4 different shapes obtained after testing the neural network model.

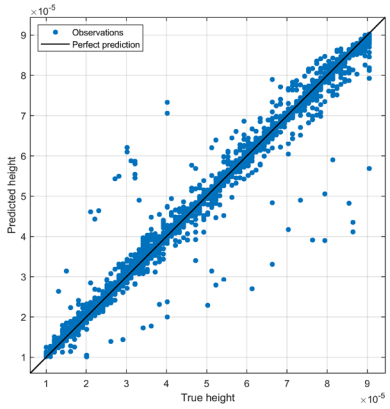

Fig. 3: Predicted vs true height plot obtained using the bagged tree ensemble model.

was almost the same as in the case of the classifier, however the shapes are now assumed to be known along with the classifier's performance.

To incorporate that information, each of the shapes was weighted using the probability distribution obtained from the confusion matrix, e.g. for S_S 95.6% of the inputs were labelled as S_s, 0.1% as S_{R90}, 2% as S_{R75} and 2.3% as S_T respectively. To avoid the model being overly optimistic, 25 frequencies were used for the predictors which were different than the ones used for the classifier. The performance of the model was assessed using common metrics and a 'predicted vs actual' plot is shown in Fig. 3, where the blue dots represent individual estimated height values, and the black straight line denotes the perfect prediction.

The Mean Average Error (MAE) is $0.789\ \mu m$, whereas the Root Meas Square Error (RMSE) is $2.51\ \mu m$. This means that, while the average error is relatively small taking into account the range of corrugation heights used for training, there are large outliers as indicated by the RMSE, which can most probably be attributed to a misclassification of the shapes in the earlier stage. This also implies that the shape influences the value of $|R^{m,n}|$ independently of the height.

Concluding remarks

A hybrid analytical-numerical model to study the impact of different geometries of doubly periodic corrugated interfaces on the reflection landscape of an incident ultrasonic plane wave was used as the basis to develop methods allowing an estimation of the corrugation parameters: the corrugation period Λ, the height h and the shape S. Using a data-driven machine learning approach, it was shown that for relatively small h, it is possible to estimate these geometric parameters for an unknown sample. Although the precision to which this method is able to estimate the height is lower than a regular profilometer, it can still provide globally useful information for some applications. Despite the method's inherent limitations, it can serve as a good starting point for further research. Firstly, the procedure should be validated with a series of experiments. This could be performed as part of a novel use-case for a new UPS design with phased array emission and reception in reflection, which is currently under development. In addition, an extension to a plate corrugated on one/two sides can be considered and studied in detail to eventually define inversion strategies in a similar way as was suggested in this paper.

Acknowledgements

Research funded by the KUL C2 project [C24_21_22].

References

[1] Mampaert and Leroy. J. Acoustical Society of America, 83(4):pp. 1390–1398.
[2] Claeys et al. Journal of Applied Physics, 54(10):pp. 5657–5662.
[3] V. D. Abeele. et al. J. Acoustical Society of America, 99(5):pp. 2883–2897.
[4] Briers and Leroy. SPIE, 1844:pp. 196–205.
[5] Briers et al. J. Acoustical Society of America, 106(2):pp. 682–687.
[6] Declercq. et al. Ultrasonics, 43(8):pp. 605–618.
[7] Liu and Declercq. Ultrscs, 53(4):pp. 853–861.
[8] Daemen. PhD Thesis KU Lueven. 2020.
[9] Martens. PhD Thesis KU Lueven. 2020.
[10] Kersemans. PhD Thesis UGent. 2014.
[11] Charlier and Crowet. J Acoust Soc Am, 79(4):pp. 895–900.
[12] Lippmann. JOSA, 43(5):pp. 408–408.
[13] Radhakrishnan et al. Proc of the National Academy of Sciences, 120(14).
[14] Anders and Korn. Neural Networks, 12(2):pp. 309–323.
[15] Breiman. Mach Learn, 24(2):pp. 123–140.

DOI 10.5162/Ultrasonic2025/C13-d2

Ultrasonic Imaging for Archaeological Metal Artefacts

Siwei Zhang[1,2], *Ajit Kumar Maddheshiya*[1,3], *Dicky Silitonga*[3], *Pooja Dubey*[1,2], *Phool Singh Yadav*[2], *Raja Ram Yadav*[2], *and Nico F. Declercq*[1,2]

[1] *IRL 2958 Georgia Tech – CNRS, 2 Rue Marconi, 57070 Metz, France*

[2] *George Woodruff School of Mechanical Engineering, Georgia Institute of Technology, Atlanta, GA 30332, United States*

[3] *Department of Physics, Faculty of Science, The University of Allahabad, Prayagraj, Uttar Pradesh 211002, India*

[4] *Arts et Métiers de Metz - LEM3 – UMR CNRS 7239, 4 rue Augustin Fresnel, 57070 Metz, France*

declercq@gatech.edu

Abstract: We assess ultrasound as a noninvasive, low-cost complement for subsurface imaging of metallic archaeological artifacts, addressing the depth limits of optical and spectral methods by applying transmission and reflection modes to minted samples and analyzing peak-to-peak amplitude and time-of-flight. Multiple transducer frequencies and scanning geometries were tested, and reflection-coefficient contrasts confirmed multi-metallic structure. Results show ultrasound's clear potential to extend archaeological analysis at depth.

Keywords: Minted metals, Ultrasound imaging, Archaeology, Surface characterization

Background and Introduction

For over two millennia, minted metals have circulated in commerce and reflect regional cultural–historical dynamics. Beyond their economic role, they serve as archaeological markers, frequently recovered in funerary contexts to help identify tomb owners and periods. Traditional imaging in cultural heritage, such as Hyperspectral Imaging [1] and Polynomial Texture Mapping [2], enhances surface detail but lacks penetration for subsurface characterization. Radiographic methods [3] provide depth but entail high costs and strict radiation controls. This study evaluates ultrasound as a cost-effective, complementary tool for nondestructive subsurface imaging in archaeology. We tested various Euro coins and metallic samples, systematically assessing imaging quality, transducer frequency selection, and feature detection. Higher frequencies improved resolution, and combining transmission and reflection modes enabled estimation of acoustic properties. The results reveal internal structures often missed by conventional imaging and support broader integration of ultrasonics into heritage science, with potential to refine historical interpretation of ancient coins.

Samples

In this study, three samples are investigated: One euro coin (2002) of 2.3 mm thickness with a cupronickel inner core and a nickel-brass outer ring (Figure 1); Two euro coin (2002) of 2.2 mm thickness featuring a nickel-brass center and a copper-nickel outer ring (Figure 2); the trimetallic souvenir badge of 2.2 mm thickness from the Georgia Tech Woodruff School of Mechanical Engineering, showing the steel core with selective nickel, gold, and black nickel (a sulfurized nickel alloy) plating (Figure 2). All of these samples are associated with changes in material properties across different regions, which uncovers the potential for imaging using acoustic characteristics against optical approaches.

Fig. 1: Obv. (left) and rev. (right), 2002 1 Euro coin.

Fig. 2: Obv. views of 2 Euros coin (left) and of trimetallic Georgia Tech souvenir badge (right).

DOI 10.5162/Ultrasonic2025/C13-d2

Experimental setup

Figure 3 shows the experimental setup in transmission configuration with immersion transducer as emitter, needle hydrophone of 0.5 mm diameter as receiver and water-coupled sample coaxially aligned and all immersed in water tank. Samples were steadily held in between the transmitter and the receiver by precision arms of C-Scanner. The samples were positioned such that the hydrophone tip received maximum amplitude along the ultrasonic beam. The scans were obtained by moving the precision arm at the controlled pace while keeping the emitter and receiver fixed. Fixation of samples was first ensured by hot gluing in a preliminary study and further iterated by FDM-printed holders which stabilized the sample and minimized spatial misalignment during scans while facilitating sample replacement in-between. The signal generator, connected to the emitter, produced 2–4 μs pulses in the 1–10 MHz frequency range. The ultrasonic pulse propagated through the medium, interacts with the metal sample, and was captured by the receiving needle. The received signal was then processed and digitized using a high-speed oscilloscope with a fixed sampling rate of 100 MHz. In reflection setup, a single focus-type immersion transducer was used in a pulse-echo configuration. The samples were positioned horizontally on a flat acrylic carrier sheet to ensure that the transducer operated near its focal distance of 10% tolerance to achieve maximum signal strength. The zero reference was taken when the transmitter was in contact with the reference acrylic. During acquisition, the transducer was translated parallel to the sample surface and placed perpendicular to the emission axis. The sample and the transducer were kept immersed in water. A focused-type transducer was selected to eliminate the need for post-processing with beam reconstruction techniques, as suggested in existing literature.([4]). Reflected pulses of 0.1–0.5 μs in the 30–100 MHz frequency range were received and analyzed to identify internal boundaries and qualify surface degradation. No rectification technique was applied, but signal amplification at 12–20 dB was selected depending on the sample surface quality to achieve the clearest results. The pulse-echo reflection setup in Figure 4 was illustrated using a single transducer with water coupling. Care was taken to eliminate air bubbles on the surface of the transducer and the specimen to prevent spurious reflections, and then scanning was carried out in the scan plane formed by the X and Y axes, or respectively scan and index axes as shown in Figure 3 and Figure 4, with resolution determined by incremental step sizes. From optimization of emitter frequency, image quality and data acquisition time, resolution of 0.1 mm was widely applied to most of the scans, except the ones obtained from preliminary study using 0.2 mm resolution (Figures 6a and 6b). Scan speed was selected empirically at 1.2 mm/s for 0.1 mm resolution. A signal averaging count of 180 acquisitions was applied for all scans in both transmission and reflection modes to improve the signal-to-noise ratio.

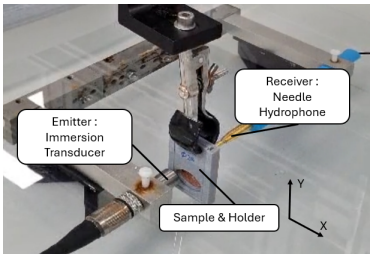

Fig. 3: Transmission-mode Ultrasound Setup.

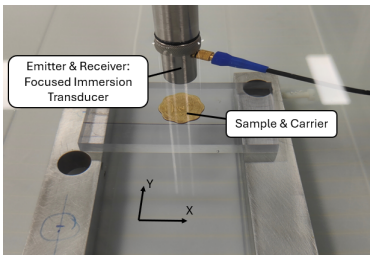

Fig. 4: Reflection-mode Ultrasound Setup.

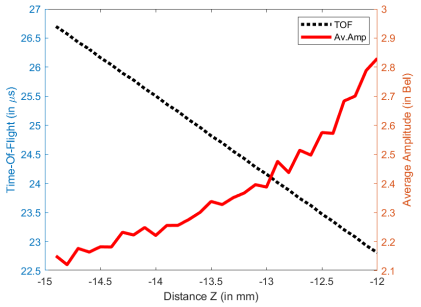

Fig. 5: Graph of variation of peak-to-peak amplitude and time-of-flight averages as a function of distance from focus transducer to reference acrylic in reflection configuration.

Processing method

For each measurement, the maximum peak-to-peak amplitude was extracted from the time-domain signal of each pixel in the C-scan, and the time-of-flight (TOF) was determined as the temporal position corresponding to this maximum amplitude. For transmission mode results, only the amplitude plots are

shown since the TOF plots did not yield significant color contrast revealing coin features. However, an estimation of the speed of sound in metal can be made by measuring sample thickness through calipers and calculating the average TOF over the field region of the sample. For reflection mode results, both the amplitude plots and the TOF plots were obtained and combined to study. The amplitude plots for each of the results are represented on a logarithmic scale to enhance the visualization of signal variations, whereas the TOF value was kept in linear scale. A reference signal from water at the same depth level is obtained to compensate for the effects of acoustic damping in water, the converging nature of the emission beam, and reflections from the acrylic surface. This correction is essential for accurately extracting the longitudinal speed and acoustic impedance of metallic samples using reflection coefficients. As shown in Figure 5, the variation of averaged amplitude and TOF versus distance between the immersion transducer and reference along the vertical Z axis was plotted. The working distance for 100 MHz transducer was fixed at -15 mm, and the samples had a thickness in the range of 1.0-2.5 mm, hence the range of -15 to -12 mm was plotted to calibrate the effects of sample thickness to amplitude. The dashed line in Figure 5 follows a linear trend and its slope corresponds to the longitudinal velocity of 1492 m/s. For a flat transducer with only attenuation in water being considered, the amplitude trend should ideally follow a linear pattern according to the Beer-Lambert law. However, the amplitude profile in the results does not appear to be linear over the entire distance range, due to the focused nature of the transducer. The jagged noise linked to interference artifacts has been reduced by taking an average over 60 pixels, and the averaging is increased until the curve is monotonic and smooth. By averaging amplitude and time-of-flight (TOF) values across the inner and outer ring regions as well as the water background, several (acoustic) properties of the sample can be determined. In reflection mode, TOF plots enable precise estimation of sample thickness. In transmission mode, the longitudinal speed of sound can be derived from TOF measurements. The relative reflection coefficient is obtained by normalizing the amplitude values against a water-based reference, which further allows calculation of the acoustic impedance. Due to the difficulty in decoupling transmission coefficients from attenuation effects in transmission amplitude plots, transmission coefficients were not quantified in this study.

Results

Figures 6a and 6b present the amplitude plots of the 1 Euro sample in transmission mode, highlighting the effects of varying the emitter frequency. It is observed, with an increase in emitter frequency, that the color contrast across different regions was amplified and more pronounced. More relief details with thin thickness and tiny dimension were also revealed at higher frequencies, which can be explained by the interaction of ultrasonic wavelength and the size of design elements. Higher frequency sheds light on more details, but yields stronger attenuation and needs higher amplification. The optimized frequency for the transmission mode is 20 MHz, and the one for the reflection mode is 100 MHz, for instance. The results showing amplitude and TOF of one euro sample are shown in Figure 7a and Figure 7b, respectively. Although the obtained amplitude plots are affected by interference artifacts, they demonstrate higher sensitivity to structural interfaces, clearly revealing the junction in bimetallic regions. In contrast, TOF plots provide clearer representation of overall contrast distribution but exhibit limited sensitivity to fine structural features. Notably, variations in color contrast within the EU territory element are only visible in the amplitude plots, indicating their greater sensitivity to surface roughness. TOF plots, on the other hand, primarily outline the boundaries of different material regions without capturing surface texture. This behavior is consistently observed across other specimens, particularly those with corroded surfaces. The precise thickness of the sample, longitudinal speed of sound, relative reflection or transmission coefficients, absolute coefficients, acoustic impedance and mass density can then be calculated by utilizing both the amplitude and TOF plots in transmission and reflection modes. For the one euro sample in Figure 7a, its field thickness was calculated as 2.25 mm. The relative reflection coefficient of the inner ring with respect to the outer one is 95.1%. For the two euros sample in Figure 8, the field thickness is estimated as 2.14 mm and a relative reflection coefficient of 96.0% is found from the outer region with respect to the inner. The consistency on a slightly higher reflection capability of nickel-brass alloy against copper-nickel

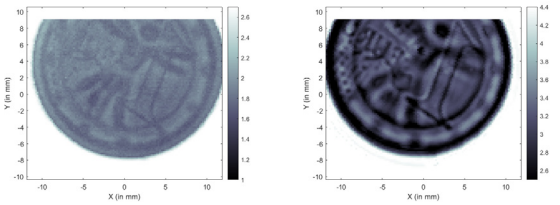

(a) 1 MHz *(b) 5 MHz*

Fig. 6: Transmission amplitude at 1 MHz (left) and 5 MHz (right) for one euro.

alloy is demonstrated by having similar relative reflection coefficient results under a position switch of inner and outer rings in both euro samples. The relative reflection coefficient of black nickel plating with respect to gold plating is 40.4%, which implicitly shows the effects of microstructure and chemical composition on acoustic impedance. One key limitation encountered is the inability to accurately calculate the speed of sound without reliable transmission data, which remains highly susceptible to noise and numerical instability. Similarly, estimating the acoustic impedance requires knowledge of the absolute reflection coefficient, which was not obtained in this study. These challenges highlight the need for improved measurement techniques and calibration strategies. Ongoing efforts are focused on developing refined methods to overcome these issues and enhance the accuracy of ultrasonic property extraction in metallic artifacts.

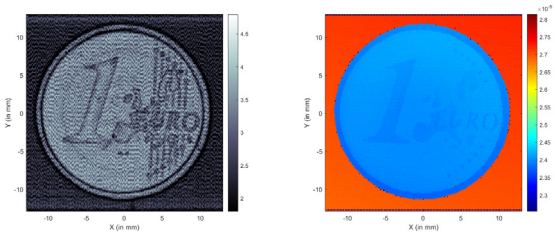

(a) Amplitude *(b) TOF*

Fig. 7: Reflection amplitude (left) and TOF (right), 100 MHz, 1 euro obv.

Conclusion

The experimental results, as proof-of-concept, demonstrate that both transmission and reflection ultrasound techniques are effective in assessing surface conditions and compositional variations in metallic samples. Higher-frequency emissions enhance spatial resolution, revealing finer details, but are more prone to attenuation. Time-of-flight (TOF) plots in reflection mode enable estimation of local thickness, while

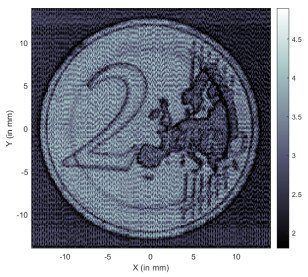

Fig. 8: Reflection amp., 100 MHz, 2 euros obv. face.

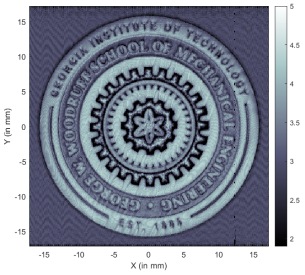

Fig. 9: Reflection amp., 100 MHz, souvenir badge.

amplitude plots provide insights into reflection coefficients and acoustic impedance. In transmission mode, TOF plots allow for calculation of the longitudinal speed of sound, and amplitude plots offer qualitative information on attenuation characteristics. As a low-cost and non-ionizing alternative to X-ray imaging, these approaches provide distinct advantages in detecting acoustic contrasts and material defects which are often invisible under optical inspection alone.

Acknowledgements

Supported by the IMPACT project LUE "I-META," part of the French PIA project "Lorraine Université d'Excellence," reference ANR-15-IDEX-04-LUE.

References

[1] C. Fischer and I. Kakoulli. "Hyperspectral Imaging for Pigment Mapping". In: *Studies in Conservation* 59 (2014), S177–S187. DOI: 10.1179/204705814X13975704318930.

[2] M. Mudge, T. Malzbender, and C. Schroer. "Reflectance Transformation Imaging". In: *VAST: International Symposium on Virtual Reality, Archaeology and Cultural Heritage*. Eurographics. 2006, pp. 145–152.

[3] M. Eveno and A. Duran. "X-ray Tomography of Corroded Coins". In: *Analytical Chemistry* 86.21 (2014), pp. 10849–10855. DOI: 10.1021/ac503075k.

[4] C. W. Yao. "An ultrasonic method for 3D reconstruction of surface topography". In: *Journal of Physics Communications* 2.5 (May 2018), p. 055034. DOI: 10.1088/2399-6528/aac691. URL: https://dx.doi.org/10.1088/2399-6528/aac691.

DOI 10.5162/Ultrasonic2025/C13-d5

Sensitivity Analysis of Piezoelectric Material Parameters Using Sobol Indices

Franziska Anderl[1] and Michael Mayle[1]
[1] Technische Hochschule Nürnberg Georg Simon Ohm, Faculty of Applied Mathematics, Physics and Humanities, Keßlerplatz 12, 90489 Nürnberg, Germany
michael.mayle@th-nuernberg.de

Abstract: This computational study examines the sensitivity of the vibrational eigenmodes of a block-shaped piezoelectric test specimen upon variation of the underlying material parameters. The method of Sobol is employed with the calculated resonance positions and their respective electrical impedance as quantity of interest. For this purpose, the FEM-Software COMSOL Multiphysics®in combination with MATLAB® is used to calculate the resonance frequencies and impedance values as well as a mode shape analysis for eigenmode identification.

Keywords: Sobol Indices, Piezoelectric Material Parameters, Mode Selection, COMSOL Multiphysics, MATLAB

Introduction

For finite-element simulations of piezoelectric devices, material parameters are crucial for accurate results. Several methods have been developed to determine these parameters. Traditionally, the IEEE standard [1] suggests using at least four test specimens with isolated vibrations for parameter extraction via impedance measurements, which can be expensive and susceptible to errors [2]. An alternative inverse method, using just two specimens and optimization to match simulated and measured impedance curves, reduces the effort but requires knowledge of material parameter sensitivity. Sobol indices are a common way to quantify this sensitivity [3, 4]. In Ref. [5] the authors examined the applicability of the method of Sobol to the non-smooth, resonant behavior of a vibrational eigenmode of a piezoelectric material for the first time. This work extends the previous study to overlapping resonances. Introducing a mode shape analysis for resonance identification, the Sobol indices are calculated for the specifically selected eigenmodes. The resonance position and its electrical impedance value are considered as sensitivity objective.

Piezoelectric Materials

The effect that occurs in piezoelectric materials can be described by two coupled state equations for the dielectric displacement (D_m) and the mechanical stress (T_{ij}), known as the stress-charge form,

$$D_m = e_{mkl} S_{kl} + \epsilon^S_{mn} E_n, \tag{1}$$

$$T_{ij} = c^E_{ijkl} S_{kl} - e_{ijn} E_n, \tag{2}$$

where E_n is the electric field and S_{kl} the mechanical strain [2]. The material parameters ϵ^S_{mn} (electric permittivity at constant strain), c^E_{ijkl} (elastic stiffness at constant electric field), and e_{ijn} (the piezoelectric stress tensor) are tensor quantities. Symmetries of the crystalline structure reduce the number of independent tensor components which leads (for a crystall class 6mm) to a reduced set of matieral parameters, namely $c^E_{11}, c^E_{12}, c^E_{13}, c^E_{33}, c^E_{44}, c^E_{66}, e_{31}, e_{33}, e_{15}, \epsilon^S_{11}$ and ϵ^S_{33}. Note that the indices are given in the Voigt notation. Which parameters are truly relevant depends on the excited mode shape and/or geometry of the used specimen. When considering the impedance curve of a specimen, it can be observed that resonance frequencies (minima) are not always nicely separated from others. In this work, the so called T1-L-mode and the T1-W-modes of a block shaped sample from [2] are examined. While the T1-L mode shows a nicely isolated frequency, the resonances of the T1-W mode are close together, making them difficult to distinguish when the material parameters are varied [5].

The Method of Sobol

Sensitivity analyses assess how variations in model parameters influence outputs, thereby identifying influential and insignificant parameters. Local methods examine output changes due to small parameter changes in proximity to a fixed value, while global approaches consider the entire parameter space, often using sampling techniques like Latin Hypercube Sampling (LHS) [6]. Sobol indices are commonly employed in global sensitivity analysis to quantify the contribution of each input parameter to the output variance. In this study, the resonance frequency and its associated impedance value, respectively, serve as the model output $y[\mathbf{x}]$ and are calculated upon variation of the

DOI 10.5162/Ultrasonic2025/C13-d5

model parameters $\mathbf{x} = x_1, ..., x_n$, namely the piezoelectric material parameters. The resulting variance is decomposed into the contributions attributable to the individual input parameters.

The first order Sobol index (the so-called main effect) of parameter x_i is defined as [7, 3]

$$S_i = \frac{\mathcal{V}_{x_i}\left[E_{\mathbf{x}_{\sim i}}\left[y|x_i\right]\right]}{\mathcal{V}_{\mathbf{x}}\left[y\right]} \in [0,1], \tag{3}$$

where $\mathcal{V}_{x_i}[y]$ is the total variance of the model $y[\mathbf{x}]$ over all input parameters and $E_{\mathbf{x}_{\sim i}}[y|x_i]$ is the mean value of y with given parameter x_i [8]; the indices x_i and $\mathbf{x}_{\sim i}$ denote which parameters ought to be varied, the latter meaning all but the ith one. With the first order Sobol index, the influence on the variance by one parameter alone can be accessed. To calculate second or higher order interactions S_{ij}, $S_{ijk}, \ldots$, one would have to calculate the resulting model variance when two or more input parameters are varied and subtract the variance of each parameter alone. This procedure is very time consuming, therefore the total Sobol index, which is defined as

$$S_i^T = \frac{E_{\mathbf{x}_{\sim i}}[\mathcal{V}_{\mathbf{x}_{\sim i}}[y|\mathbf{x}_{\sim i}]]}{\mathcal{V}_{\mathbf{x}}[y]} \in [0,1], \tag{4}$$

is often used [7, 3]. The total Sobol index S_i^T is calculated using the variance of x_i including all higher order interactions that involve x_i. If the first order Sobol index equals the total Sobol index, then no interactions exist between the specified material parameters. The direct calculation of the Sobol indices by solving the variance integral is not feasible. Instead, the integrals are approximated by estimators using a statistical approach with only $m \cdot (n+2)$ model evaluations [3]. Here, m denotes the sample size while n is the number of parameters. With the Latin Hypercube Sampling (LHS) two $m \times n$ matrices A and B containing independent samples are generated. These matrices are rearranged into cross matrices AB_i by inserting the ith column of matrix B at the position of the ith column of matrix A. In this way, the dependencies among individual variables are represented.

Simulation Model and Methods

This study focuses on the vibrational eigenmodes of block-shaped piezoelectric specimens, characterized by an increased vibration at resonance. In this work, the eigenfrequencies are calculated using the eigenfrequency study in COMSOL followed by a frequency domain study to calculate the associated impedance values. This approach combines the computationally cheap eigenfrequency study with the costly frequency domain study, which itself is only executed for the identified eigenfrequencies.

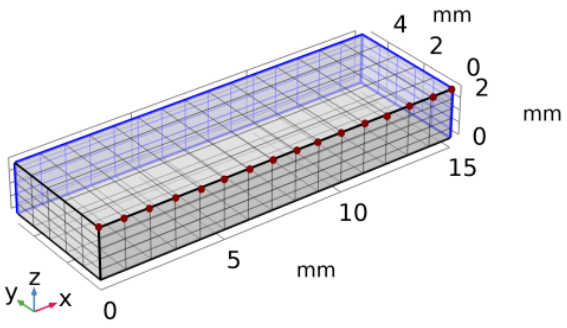

Fig. 1: Model geometry and mesh of the block-shaped test specimen considered in this work. Highlighted are the symmetry planes used to reduce the model size and the evaluation points for the displacement.

For our analysis, a block of length 30 mm, width 10 mm, and thickness 2 mm from [2] is used. The block is polarized in the thickness (z-)direction and made of the material PIC255 for which optimized material parameters can be found in Ref. [2]. Furthermore, as a loss and damping model, the loss factor damping is used, for which the tensors ϵ^S and c^E from Eq. (1) and Eq. (2) are supplemented with an imaginary part, that represents a loss or damping factor.

In COMSOL Multiphysics®, piezoelectricity is modelled using the Solid Mechanics and Electrostatics interfaces coupled via the Piezoelectricity interface. A 1 V voltage boundary condition is applied to the top surface, with the bottom grounded. Two symmetry planes are used to reduce computational cost (see Figure 1). The mesh consists of 15 x 5 x 5 cubic elements. The frequency domain study is configured to search for eigenfrequencies whose real part is larger than a specified value, 40 kHz for the T1-L-mode and 130 kHz for the T1-W-mode. For the last mentioned mode, a difficulty arises, as two resonances very close in frequency exist. Therefore, seven eigenfrequencies are identified followed by a post processing step, where the eigenfrequencies are matched using their mode shape. This is necessary as the eigenfrequencies shift with varying material parameters. For this purpose, a reference mode (with fixed material parameters) that shows the desired eigenfrequencies and has well distinguishable mode shapes is used to calculate the correlation

$$r_{xy} = \frac{\frac{1}{n}\sum_{i=1}^{n} x_i y_i - \overline{xy}}{\sqrt{\left(\frac{1}{n}\sum_{i=1}^{n} x_i^2 - \bar{x}^2\right)\left(\frac{1}{n}\sum_{i=1}^{n} y_i^2 - \bar{y}^2\right)}}. \tag{5}$$

The correlation of two variables $\mathbf{x}$ und $\mathbf{y}$ is limited

DOI 10.5162/Ultrasonic2025/C13-d5

between -1 and 1 with -1 indicating a negative linear, 1 a positive linear and 0 no relationship. It is evaluated for every reference mode paired with every calculated mode, which leads to a matrix of 7x7 entries, similar to a correlation matrix. Then, using the exclusion principle, the modes are matched according to the highest correlation. Fig. 3a shows the reference modes, the desired modes are highlighted. In this case, the mode shape was evaluated using the absolute displacement of the test specimen along an edge in x-direction. The evaluation points are marked in Fig. 1.

To check that the right eigenfrequencies are identified, two visualizations are utilized. The histogram in Figure 2 shows the distributions of the distance between the 1^{st} and 2^{nd} eigenfrequencies of the T1-W mode; it has a continuous behavior and is always positive - as it should be. Similarily, the mode shapes themselves, cf. Figures 3b and 3c, form only one family of curves for each mode with no outliers.

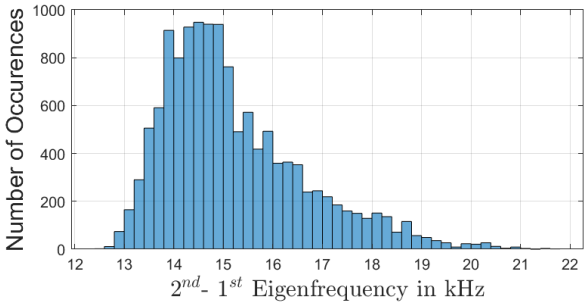

Fig. 2: Histogram of the distance between the 1^{st} and 2^{nd} eigenfrequencies.

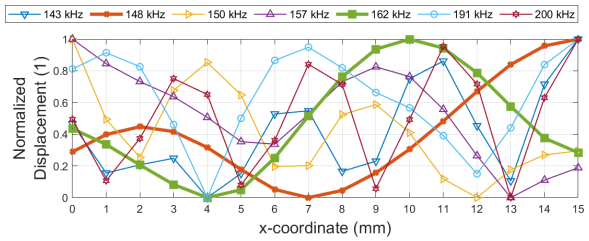

(a) Computed Eigenfrequencies. The desired eigenfrequencies at $148\mathrm{kHz}$ and $162\mathrm{kHz}$ are highlighted as bold lines.

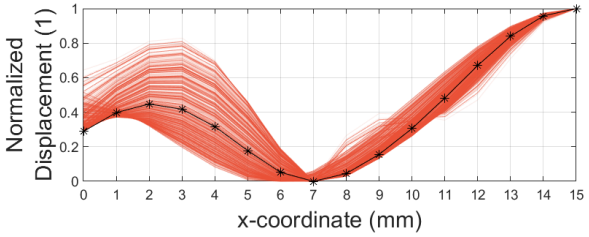

(b) 1^{st} Eigenfrequency

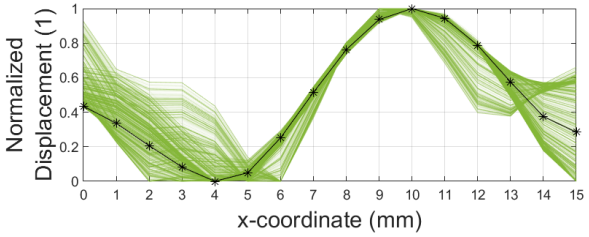

(c) 2^{nd} Eigenfrequency

Fig. 3: (a) Min-Max-normalized displacement along an edge of the block shaped sample. (b, c) Family of mode shapes of identified eigenfrequencies for a sample size of $m = 100$.

Computational Approach

The LHS sampling and COMSOL model creation are performed using MATLAB® and the COMSOL LiveLink™ for MATLAB®, followed by simulations in COMSOL Multiphysics®. Post-processing and statistical analysis are conducted in MATLAB®.

Material parameters are sampled in 5 % intervals from literature values using MATLAB's lhsdesign() function, with sample sizes up to $m = 5000$. Additionally, a statistical approach is implemented to calculate the mean Sobol indices over a sampling using different random seeds. Details of this approach can be found in [5]. It is important to calculate different sample sizes to access the convergence of the mean Sobol indices. In the following, the converged values with a sample size of $m = 5000$ are considered.

Results

Figures 4a to 4d show the first order and total Sobol indices for the eigenfrequency and the associated impedance value. Only material parameters identified as important are considered. The remaining Sobol indices are close to zero. Different Sobol indices can be observed for the eigenfrequency and impedance values, indicating that the same material parameter can exert a different degree of influence on the eigenfrequency and the associated impedance. When comparing the first-order and total Sobol indices, it is evident that the values are within the same range for the eigenfrequencies, indicating minimal interaction with other material parameters. Conversely, the total Sobol indices are bigger for the impedance, meaning that there are more interactions.

Conclusion and Outlook

In this work, the first order and total Sobol indices were calculated for two modes, one showing two eigenfrequencies. A method for identifying the wanted eigenmodes from the multitude of computed eigenfrequencies was implemented using their mode shape. In conclusion, the results indicate, that the same material parameter can have more influence on the resonance

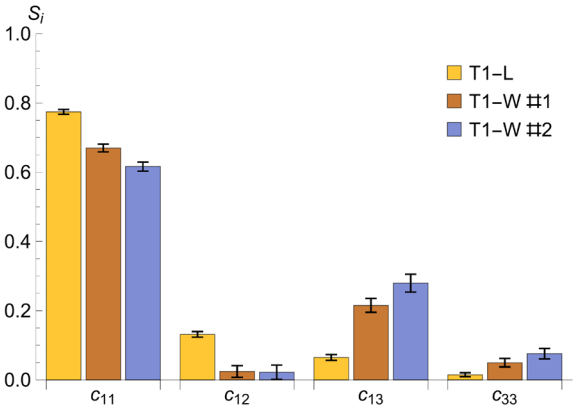

(a) 1^{st} order Sobol index for the eigenfrequency.

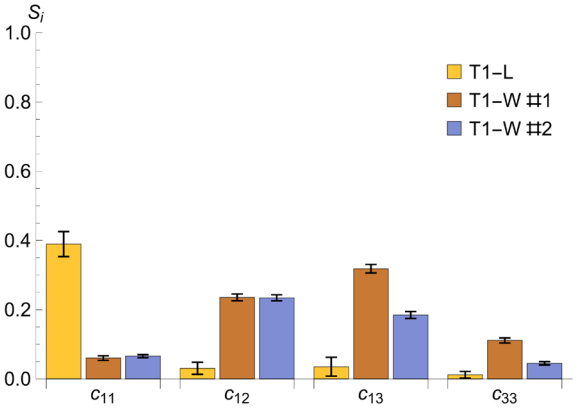

(b) 1^{st} order Sobol index for the impedance.

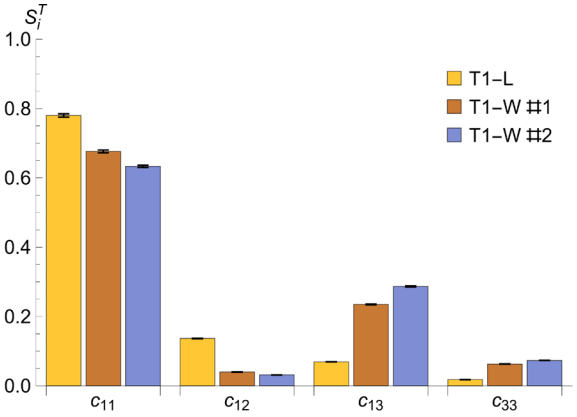

(c) Total Sobol index for the eigenfrequency.

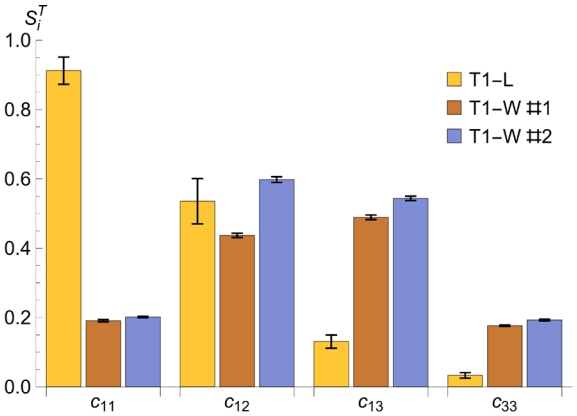

(d) Total Sobol index for the impedance.

Fig. 4: Mean values and 95 % confidence intervals of first order and total Sobol indices for selected material parameters.

frequency than on the impedance and vice versa, as well as interactions with other material parameters can appear for the impedance value alone. This warrants further investigation in future works.

References

[1] "Publication and Proposed Revision of ANSI/IEEE Standard 176-1987 "ANSI/IEEE Standard on Piezoelectricity"". In: *IEEE Transactions on Ultrasonics, Ferroelectrics, and Frequency Control* 43.5 (Sept. 1996). Conference Name: IEEE Transactions on Ultrasonics, Ferroelectrics, and Frequency Control, pp. 717–. ISSN: 1525-8955.

[2] S. J. Rupitsch. *Piezoelectric Sensors and Actuators: Fundamentals and Applications*. Topics in Mining, Metallurgy and Materials Engineering. Berlin, Heidelberg: Springer, 2019. ISBN: 978-3-662-57532-1.

[3] C. Prieur and S. Tarantola. "Variance-Based Sensitivity Analysis: Theory and Estimation Algorithms". en. In: *Handbook of Uncertainty Quantification*. Ed. by R. Ghanem, D. Higdon, and H. Owhadi. Cham: Springer International Publishing, 2016, pp. 1–23. ISBN: 978-3-319-11259-6.

[4] B. Iooss and A. Saltelli. "Introduction to Sensitivity Analysis". en. In: *Handbook of Uncertainty Quantification*. Ed. by R. Ghanem, D. Higdon, and H. Owhadi. Cham: Springer International Publishing, 2016, pp. 1–20. ISBN: 978-3-319-11259-6.

[5] F. Anderl and M. Mayle. "Sensitivity analysis of piezoelectric material parameters using Sobol indices". In: *tm - Technisches Messen* 92.6 (2025), pp. 234–242.

[6] M. D. McKay, R. J. Beckman, and W. J. Conover. "A comparison of three methods for selecting values of input variables in the analysis of output from a computer code". In: *Technometrics. A Journal of Statistics for the Physical, Chemical and Engineering Sciences* 21.2 (1979), pp. 239–245. ISSN: 0040-1706,1537-2723.

[7] I. M. Sobol. "Global sensitivity indices for nonlinear mathematical models and their Monte Carlo estimates". In: *Mathematics and Computers in Simulation*. The Second IMACS Seminar on Monte Carlo Methods 55.1 (Feb. 2001), pp. 271–280. ISSN: 0378-4754.

[8] A. Saltelli et al. "Variance based sensitivity analysis of model output. Design and estimator for the total sensitivity index". en. In: *Computer Physics Communications* 181.2 (Feb. 2010), pp. 259–270. ISSN: 00104655.

DOI 10.5162/Ultrasonic2025/D3-a2

Automated Implementation of Selective Matrix Capture using Laser-Induced Phased Arrays for Large Area Inspection

Don Pieris[1], *Panagiotis Kamintzis*[1], *Peter Lukacs*[1], *Geo Davis*[1], *and Theodosia Stratoudaki*[1]
[1]*Department of Electronic and Electrical Engineering, University of Strathclyde, UK*
don.pieris@strath.ac.uk

Abstract: In-process non-destructive evaluation (NDE) is critical for the widespread adoption of additive manufacturing (AM) in high-value industries. Existing inspection methods struggle to cope with the high deposition rates and complex geometries from processes such as wire arc additive manufacturing (WAAM). Laser-induced phased arrays (LIPA) offer a remote, couplant-free ultrasonic inspection technique capable of imaging subsurface features in optically opaque components. While full matrix capture (FMC) has previously been used for data acquisition, its reliance on a large number of array elements results in prohibitively long inspection times. Selective matrix capture (SMC) is a novel data acquisition method designed to enhance inspection efficiency [1]. This paper presents the automation of SMC, a two-stage process that first locates the presence of a defect using a sparse array, then uses an optimised array to image and classify the defect.

Keywords: Selective Matrix Capture, Laser-Induced Phased Arrays, Non-Destructive Evaluation, Additive Manufacturing, Automated Inspection

Background

Ultrasonic testing (UT) is widely adopted across industries such as aerospace, civil engineering, and renewable energy for non-destructive evaluation [2]. It enables real-time, non-invasive imaging of internal structures, making it particularly valuable in safety-critical applications. With the advancement of manufacturing technologies, such as additive manufacturing (AM), there is a demand for high-resolution, in-process inspections [3]. Laser ultrasound (LU) has been identified as a technology that can address the requirements for in-process inspection because it is a remote, couplant-free technique suitable for extreme heat and restrictive access environments of manufacturing processes [4]. Laser-induced phased arrays (LIPAs) have a strong potential to address the shortcomings of conventional ultrasonic transducer arrays in such extreme environments, because they offer high-quality ultrasonic imaging.

LIPAs are based on the principle of laser ultrasonics, where the excitation and detection of ultrasound is done using lasers. The ultrasonic excitation beam from a pulsed laser generates ultrasound, and the ultrasonic detection beam of a continuous wave laser detects it. The two lasers are scanned on the surface of the inspected component, acquiring data in a series of positions, synthesising an array where the array generation and detection elements are the corresponding laser positions. Full-matrix capture (FMC) is a data acquisition methodology where ultrasonic signals from all possible combinations of generation and detection elements are captured. The FMC data are then used with a variety of imaging algorithms, including the total focusing method (TFM), which yields high-quality ultrasonic imaging, and this has been demonstrated with LIPAs [5]. The mechanical scanning of the laser beams introduces a long data acquisition time, which compromises the implementation of LIPAs for in-process inspection.

Lukacs et al. have proposed a novel data acquisition method referred to as selective matrix capture (SMC) [1]. SMC is an adaptive methodology based on the concept that not all signals from FMC are information-rich, making it ineffective to acquire signals uniformly across the inspected region. Instead, SMC aims to capture only information-rich signals, without compromising ultrasonic imaging quality using a two-stage data acquisition process. The first stage is the agnostic stage, where the location or absence of any region of interest (ROI) is unknown. A sparse LIPA is synthesised with the minimum amount of array elements required to provide a reliable answer to the following two questions: a) Is there an ROI? and if the answer is "yes", then b) where is the ROI? The first stage yields a series of low-resolution ultrasonic images, and if an ROI has not been identified, the scanning process ends. If an ROI is identified, then SMC enters the second stage: the optimisation stage.

During the second stage, the information for the location of the ROI is used to synthesise a new LIPA with optimum element configuration (array element number, distribution and aperture) to inspect the ROI. Two array optimisation strategies have already been suggested in the literature [1].

SMC has been shown to reduce the time for data acquisition by an order of magnitude [1]. The SMC with LIPAs is well suited for automation and consequently for large area inspection: the lasers can be mounted onto robotic platforms and inspection can be achieved through automated scanning of fibre-coupled beams. For full automation, a robust criterion is needed to translate the inspection from the first to the second stage of the SMC, and one such criterion has been proposed to be the pixel intensity distribution of the low-resolution ultrasonic images resulting from the first stage of FMC. Previously, this criterion was used while the sparsity of the synthesised LIPA was iteratively decreased, until an ROI was found. Therefore, the criterion was designed to signal the presence of an ROI, but was not able to declare a region defect-free. It is important for a fully automated SMC-based system that the methodology is developed to ensure reliability that the region is defect-free when sparse arrays are used for imaging. The present paper addresses this point by introducing a pre-inspection study of the probability of detection (POD) and the false positive rate (FPR) to identify a suitable degree of array sparsity for a reliable threshold for the shift of the pixel intensity distribution that would signal a ROI. This study is based on the worst-case scenario for defect detection, identifying the minimum defect size expected at the largest depth required for inspection. These parameters are dependent on the NDE application and can be adapted accordingly.

SMC Methodology

The SMC data acquisition methodology has been described in the literature [1]. This section presents: a) the pixel intensity distribution as a criterion for transitioning to the second stage of the SMC; b) the pre-inspection study, to identify the parameters for automated implementation of the SMC.

Pixel intensity distribution criterion

The pixel intensity distribution criterion is based on the assumption that the TFM image of an area in the absence of any defects will have a certain pixel intensity distribution, which is due to incoherent noise only (e.g. due to electric or instrumentation noise). When the imaged data has coherent signals from a defect, above the noise floor, then these signals will correspond to TFM pixels with intensity higher than the noise pixel intensity distribution. Therefore, these pixels will cause a shift in the characteristic pixel intensity distribution of the noise floor. Identifying the location of the pixels that cause the shift leads to the identification of the ROI. On the contrary, if no defect is present (and there is no other source of coherent noise, such as artefacts from reflections or undesired ultrasonic modes), there will not be a shift of the characteristic pixel intensity distribution of the noise floor. The peak of the pixel intensity distribution is a convenient point of reference to measure this shift. If this peak shifts beyond a predefined threshold, then it signals the presence of an ROI. Otherwise, the area is considered defect-free. The following study was conducted to identify this threshold.

Pre-inspection study

The pre-inspection study was based on a worst-case NDE inspection scenario: the minimum size of defect expected to be reliably detected was set to be a 1 mm diameter side drilled hole (SDH), which is an omnidirectional scatterer, optimal for detection with a 1D LIPA. The inspected component was a rectangular aluminium sample with a total thickness/depth of 38 mm. The SDH was located at the maximum targeted depth of 13 mm below the surface. A total of 123 LIPAs with 64 elements and 0.4 mm pitch were synthesised across the sample surface, and the full matrix was captured. The aperture (25.6 mm) of each 64-element LIPA was shifted relative to the next by 0.4 mm (with a 98.4% overlap), and the total area covered by LIPA was 74.4 mm. The SDH was located at the centre of this scanned region. These data sets were then undersampled and used to synthesise LIPAs of 32, 16 and 8 elements of the same aperture (25.6 mm) and pitch of 0.8 mm, 1.2 mm and 1.6 mm, respectively, to identify the minimum number of array elements for a sparse LIPA, suitable for the first stage of the SMC. TFM images using the shear-shear wave mode arrival, with a digital filter centred at 4 MHz and a bandwidth of 100%, were produced from each dataset [4]. The shift of the pixel intensity distributions of the TFM images was analysed with respect to the ground truth (presence or absence of the SDH) as shown in Fig. 1. Then, the POD and FPR were calculated using the method shown in the literature [6], and the results are shown in Tab. 1 and Tab. 2.

Discussion

The presence of the SDH (ground truth) is expected in TFM images from arrays No. 61-123. Fig. 1 shows that the peak of the noise intensity distribution for arrays No. 61-123, with 64 and 32 elements, is at <-24 dB, but the peak in the noise remains >-24 dB for all arrays with 16 and 8 elements. The peak of

DOI 10.5162/Ultrasonic2025/D3-a2

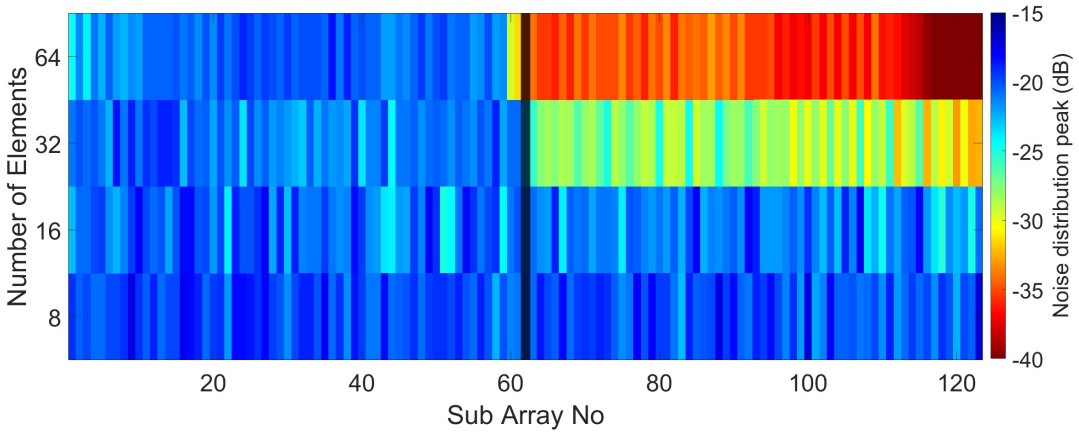

Fig. 1: Noise distribution from 123 arrays with an increasing number of elements. The defect is known to be present in all TFM images from arrays No. 61-123 (to the right of the black vertical line)

the noise distribution does not demonstrate a shift for the arrays No. 1-60, with 64, 32, 16 and 8 elements, in agreement with the ground truth, as the SDH is absent in these TFM images.

The results in Tab. 1 and Tab. 2, show how a 32-element array and a threshold of -24 dB correspond to a POD of 97% and FPR of 2%. These were seen to be the optimal parameters and were used in the automated first stage of the SMC.

Tab. 1: Experimentally obtained, FPR calculated for a range of thresholds. The highlighted value was chosen for 1st stage of SMC.

Threshold	Number of Elements			
	8	16	32	64
-16	100%	100%	100%	100%
-18	93%	95%	100%	100%
-20	40%	60%	80%	72%
-22	2%	20%	18%	8%
-24	0%	7%	2%	3%
-26	0%	0%	0%	2%
-28	0%	0%	0%	2%
-30	0%	0%	0%	0%

Automated implementation of SMC

Using the parameters identified, five sparse 32-element LIPAs with an aperture of 25.6 mm, pitch of 0.8 mm and overlap of 2.3% (0.6 mm) were synthesised across the surface of the sample as shown in Fig. 2. A total surface area of 125 mm was scanned. A known defect of 1 mm diameter SDH was located at the centre of the scanned area, 13 mm below the surface. In accordance with the ground truth, the pixel intensity distribution of LIPA No. 3 crossed the pre-determined

Tab. 2: Experimentally obtained POD calculated for a range of thresholds. The highlighted value was chosen for 1st stage of SMC.

Threshold	Number of Elements			
	8	16	32	64
-16	100%	100%	100%	100%
-18	90%	94%	100%	100%
-20	51%	86%	100%	100%
-22	5%	24%	98%	100%
-24	0%	8%	97%	100%
-26	0%	0%	86%	100%
-28	0%	0%	54%	100%
-30	0%	0%	14%	100%

-24 dB threshold, indicating the presence of a ROI, while LIPAs 1,2,4 and 5 did not present a sufficient shift in the pixel intensity distribution as shown in Fig. 3, indicating defect-free regions. In addition, the location of the ROI was successfully localised based on the corresponding TFM pixel presenting the maximum pixel intensity in the distribution.

Conclusion

This study demonstrated a data-driven approach for calibrating sparse LIPAs as part of the first stage of SMC. An automated methodology was developed and validated through a pre-inspection study, identifying the minimum array configuration required to reliably detect a 1 mm SDH at a depth of up to 13 mm in aluminium. A 32-element sparse array with a -24 dB threshold was used for the automated first stage of the SMC. This threshold enabled the system to distinguish between defect-present and defect-free regions. The use of five, sparse 32-element LIPAs in the large area

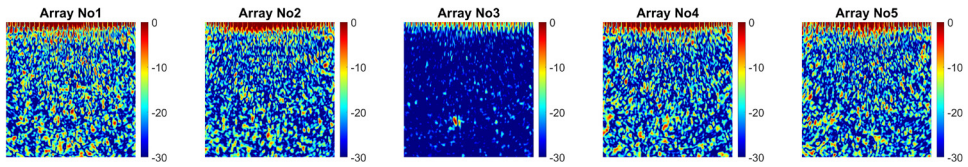

Fig. 2: Five TFM images obtained using 32-element arrays, showing how no ROI were present in Arrays No. 1,2,4 and 5. Array No. 3 shows the presence of a small ROI at the bottom left corner.

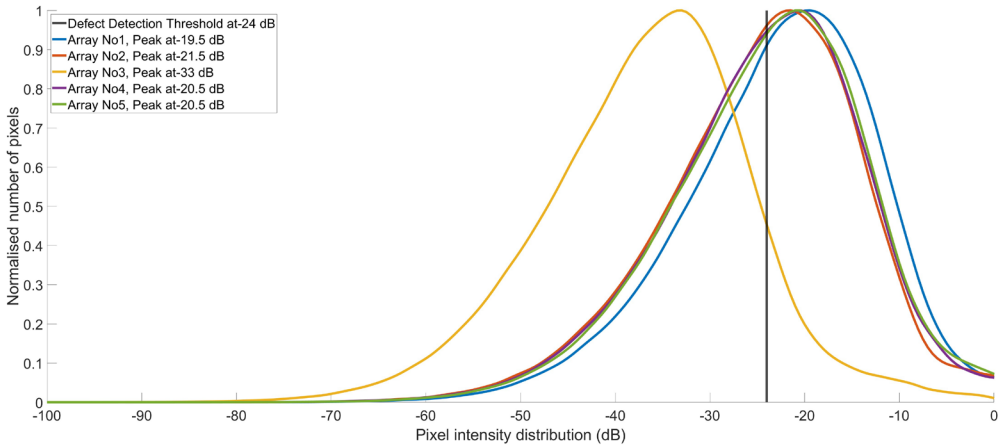

Fig. 3: Graphs showing the pixel intensity distributions for the five arrays. Array No. 3 crosses the pre-determined threshold of -24 dB.

inspection corresponded to a data acquisition time of 15 minutes, compared to a data acquisition time of just over an hour for five, dense 64-element LIPAs, corresponding to 75% faster data acquisition. The resulting ROI can then be used to guide the design of optimised stage-two arrays, forming the basis for a fully automated SMC workflow.

References

[1] P. Lukacs et al. "Online evolution of a phased array for ultrasonic imaging by a novel adaptive data acquisition method". In: *Scientific Reports* 14.1 (Dec. 2024), p. 8541. DOI: 10.1038/S41598-024-59099-Z.

[2] C. Payan, O. Abraham, and V. Garnier. "Ultrasonic Methods". In: *Non-destructive Testing and Evaluation of Civil Engineering Structures*. Jan. 2018, pp. 21–85. DOI: 10.1016/B978-1-78548-229-8.50002-9.

[3] D. Pieris et al. "Laser Induced Phased Arrays (LIPA) to detect nested features in additively manufactured components". In: *Materials & Design* 187 (Feb. 2020). DOI: 10.1016/j.matdes.2019.108412.

[4] T. Stratoudaki, M. Clark, and P. Wilcox. "Laser induced ultrasonic phased array using Full Matrix Capture data acquisition and Total Focusing Method". In: *Optics Express* (Sept. 2017). DOI: 10.1364/oe.24.021921.

[5] T. Stratoudaki, M. Clark, and P. D. Wilcox. "Adapting the full matrix capture and the total focusing method to laser ultrasonics for remote non destructive testing". In: *2017 IEEE International Ultrasonics Symposium (IUS)*. IEEE, Sept. 2017, pp. 1–4. DOI: 10.1109/ULTSYM.2017.8092864.

[6] P. D. Wilcox et al. "Fusion of multi-view ultrasonic data for increased detection performance in non-destructive evaluation". In: *Proceedings of the Royal Society A* 476.2243 (Nov. 2020). DOI: 10.1098/RSPA.2020.0086.

This work was supported by the EPSRC funded Royce Industrial Collaboration Program (ICP) and the UK Research Center in Non-Destructive Evaluation Engineering (RCNDE).

DOI 10.5162/Ultrasonic2025/D3-a4

Robotic Implementation of Laser-Induced Phased Arrays for Complex Geometries Towards Industrial Deployment

Don Pieris[1], *Panagiotis Kamintzis*[1], *Peter Lukacs*[1], *Matthew Riding*[1], *Charalampos Loukas*[1], *Charles MacLeod*[1], *Gareth Pierce*[1], *and Theodosia Stratoudaki*[1]
[1]*Department of Electronic and Electrical Engineering, University of Strathclyde, UK*
don.pieris@strath.ac.uk

Abstract: This study presents a robotic implementation of laser-induced phased arrays (LIPA). The system is targeted towards addressing the challenge of in situ inspection of complex geometries, such as additively manufactured components, curved surfaces and pipes. This Robotic LIPA system aims to combine the non-destructive and non-contact nature of laser ultrasound with the flexibility and adaptability of a robotic inspection to overcome the challenges faced by conventional ultrasound when inspecting complex industrially relevant components.

Keywords: Robo-LIPA, Non-Contact Inspection, Additive Manufacturing, Non-Destructive Evaluation, In-process Inspection

Background

Non-contact, non-destructive evaluation (NDE) techniques are increasingly important across industries such as nuclear energy, aerospace, and advanced manufacturing, where component integrity must be verified without disrupting operations or compromising safety [1]. Traditional ultrasonic inspection methods typically rely on mechanical coupling and direct probe access, limiting their applicability in high-temperature, radioactive, or geometrically complex environments. Laser-Induced Phased Arrays (LIPAs) offer a promising alternative by enabling fully remote, high-resolution ultrasonic imaging without the need for physical contact or couplant [2]. Industrial robots have already been demonstrated in the literature as effective platforms for deploying various NDE techniques, including conventional phased arrays and eddy current testing [3]. This establishes a strong foundation for extending robotic deployment to LIPAs, enabling flexible, automated, and contact-free inspection.

Motivation

In additive manufacturing (AM), in-process inspection is vital for detecting defects as they form, yet the part geometry and enclosed build environments hinder access. Similarly, the inspection of internal components in nuclear facilities is limited by safety risks and restricted physical access. These challenges underscore the need for a compact, modular LIPA platform that combines laser ultrasonic capabilities with robotic actuation to enable autonomous inspection across complex or confined surfaces [4].

A robotic LIPA system has the potential to extend non-contact ultrasonic imaging into environments previously considered inaccessible, supporting quality assurance in safety-critical applications and advancing LIPA technology towards operational readiness.

Objective

This work aims to develop a modular, robotically deployable LIPA system for non-contact, high-resolution ultrasonic inspection in access-limited industrial environments.

The optical system was designed to reduce physical footprint and optical complexity while maintaining the imaging resolution required to detect subsurface defects. A key objective was to ensure seamless integration with existing robotic platforms, allowing for fully automated inspection workflows. The resulting system not only increases inspection flexibility and accessibility but also supports scalable implementation across advanced manufacturing settings.

Method

To transition LIPA technology toward industrial deployment, the optical and mechanical architecture of the previous LIPA system presented in the litrature was redesigned [5]. A single robotic arm was used for global positioning, complemented by linear translation stages for the detection laser and a galvo mirror for local steering of the generation laser. This configuration significantly reduced system complexity while enhancing precision and ease of deployment.

An additional refinement was the optical coupling of the generation and detection lasers via a dichroic mirror. This allowed both beams to share a common optical path while retaining independent control, reducing system size and enabling a wider, more symmetric scanning field for the generation beam. These innovations collectively support a compact, modular

DOI 10.5162/Ultrasonic2025/D3-a4

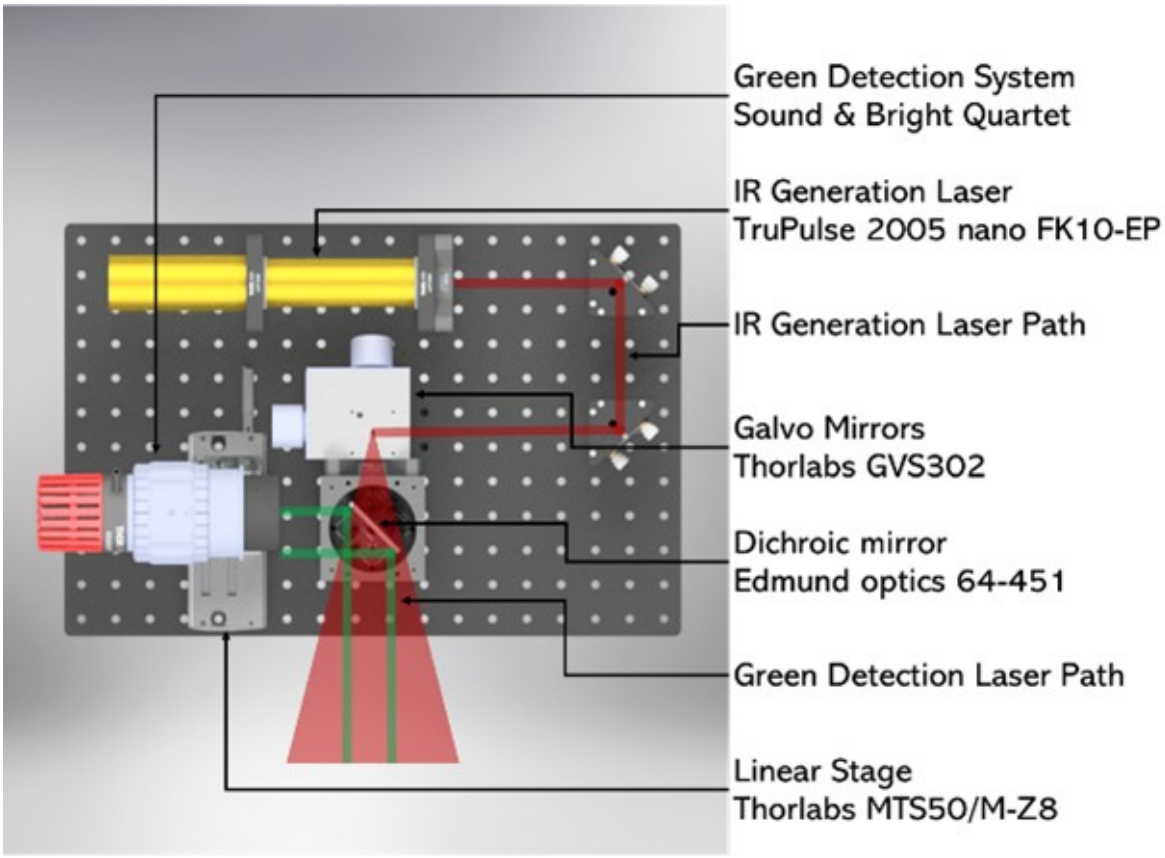

Fig. 1: Experimental schematic of the compact LIPA system mounted on the robotic arm.

LIPA system capable of integration into existing industrial inspection processes, bringing the technology closer to real-world application.

The KUKA KR10 industrial robot was selected for this initial trial due to its compact size and sufficient payload capacity. Despite its smaller form factor, the KR10 could support the 15 kg weight of the prototype LIPA system, making it a practical choice for early-stage development and integration.

The developed LIPA system performs Full Matrix Capture (FMC) by sequentially scanning both generation and detection lasers across discrete spatial positions to acquire ultrasonic signals from all transmit–receive combinations, forming a complete N×M dataset. This dataset is processed using the Total Focusing Method (TFM), a synthetic focusing algorithm that applies time-delay corrections across all element pairs to achieve focusing at every pixel in the ultrasonic image. The resulting TFM image provides high-resolution imaging without requiring surface contact or coupling.

In addition to its mechanical suitability, the KR10's compact footprint offered significant advantages in terms of laser safety. As the system employs two Class 4 lasers, the ability to enclose the entire robotic LIPA

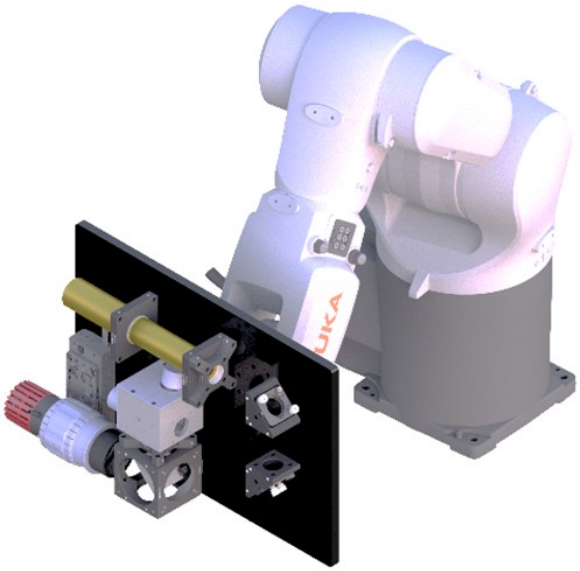

Fig. 2: 3D rendered image of the combined Robo LIPA system using a KUKA KR10 Industrial Robot.

DOI 10.5162/Ultrasonic2025/D3-a4

setup within a relatively small, self-contained safety enclosure was a key consideration. This configuration supports the development of future Robo-LIPA systems as Class 1 laser-safe units, enabling safe operation within mixed-use laboratories or workshop environments without the need for dedicated laser facilities.

Results - WAAM

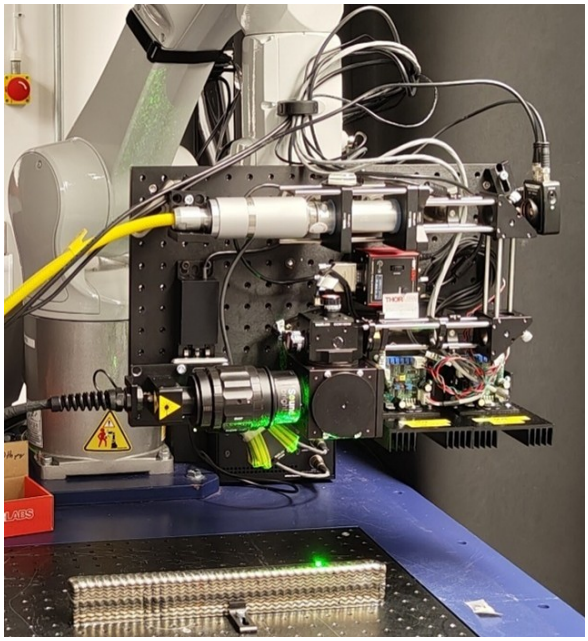

Fig. 3: Image of the Robo LIPA system inspecting a WAAM wall section.

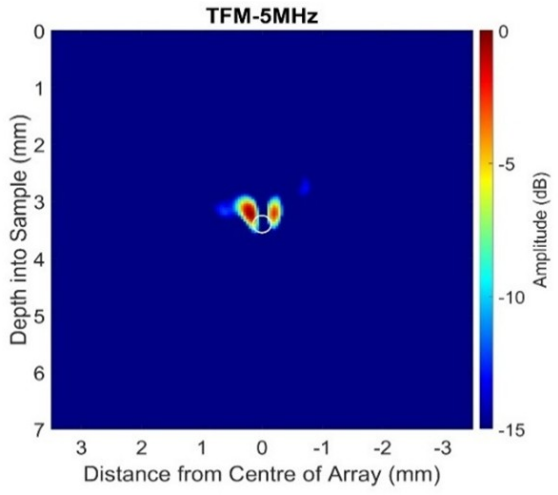

Fig. 4: TFM image from the as-deposited surface of a Ti64 WAAM component, showing two indications about 3 mm below the surface.

The first inspection scenario involved an additively manufactured Ti-64 WAAM wall section containing a 3 mm diameter side-drilled hole located approximately 3 mm below the surface.

Fig. 3 shows the system inspecting a WAAM wall section at a standoff distance of about 150 mm. This marked the first robotic implementation of a LIPA system where the sample remained static while the optical system was moved relative to it.

The TFM image in Fig. 4 demonstrates how the side-drilled hole was imaged as two distinct indications.

Results - Pipe

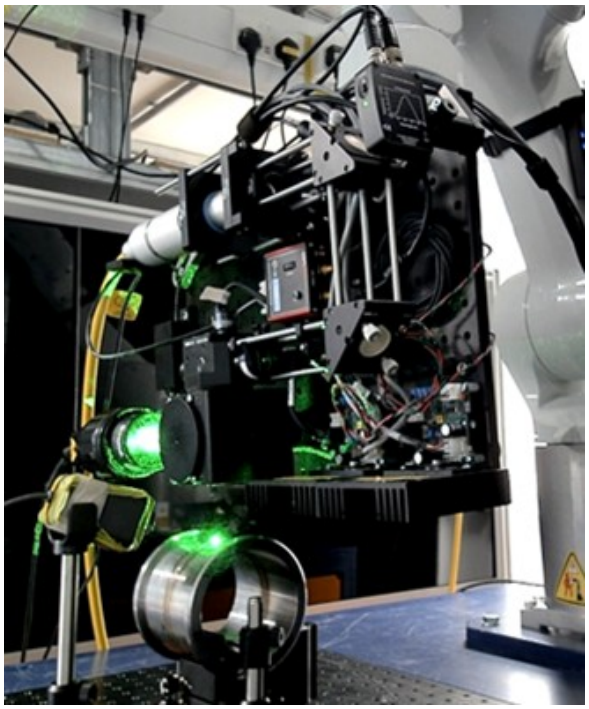

Fig. 5: Image of the Robo LIPA system inspecting the pipe section.

The second inspection scenario involved a laser-welded P91 pipe section. The pipe was positioned horizontally, and the LIPA system was rotated around its central axis, as shown in Fig. 5. This allowed multiple FMC datasets to be acquired from the pipe's outer surface, enabling TFM imaging through its wall thickness.

The LIPA was synthesised on the outside of the cylinder and off-centre to the weld, resulting in the TFM image shown in Fig. 6, where there is a clear indication at the weld root (bottom left).

The flexibility of the robotic LIPA system was used to collect seven TFM images by moving the LIPA system using the robotic arm around the central axis

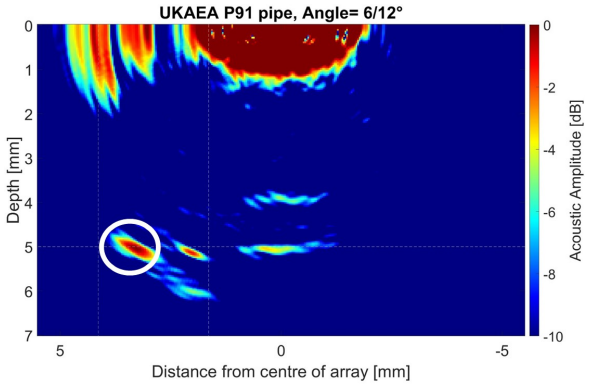

Fig. 6: TFM image, with the array positioned off-centre to the weld (dotted lines), showing an indication at the weld root (white circle). The flexibility.

of the pipe. This data was used to plot the 2.5D image by stacking the individual 2D TFM images taken from the 1D LIPAs scanned parallel to each other [5]. The resulting TFM image can be seen in Fig. 7.

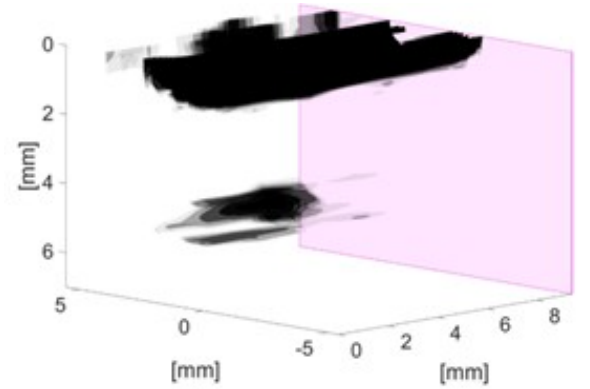

Fig. 7: 2.5D image created by stacking 7 separate 2D TFM images showing an indication of the internal weld defect as the black region at the bottom.

Discussion

The results from both the WAAM wall and the pipe section illustrate the expanded capabilities enabled by a robotically deployed LIPA system. These demonstrations highlight the shift from previous setups—where components had to be brought to a fixed system—to one where the LIPA system can be manoeuvred around the component itself.

This initial robotic LIPA implementation provides a solid foundation for future developments, offering a flexible and mobile platform with the potential to meet the demands of complex, real-world inspection scenarios.

Conclusion

This study has demonstrated the feasibility of integrating LIPAs with industrial robotics to enable non-contact ultrasonic inspection of complex and access-limited components. By combining the optical system and an industrial robot, the developed robotic LIPA system successfully imaged subsurface features in both additively manufactured and welded components. Although operating as an early-stage prototype, the system's modular design and mobility offer a promising route toward in situ ultrasonic inspection in high-value manufacturing and a wide range of other industrial applications.

Future developments will focus on improving SNR, enhancing system robustness, and supporting fully automated inspection workflows.

References

[1] M. E. Torbali, A. Zolotas, and N. P. Avdelidis. "A State-of-the-Art Review of Non-Destructive Testing Image Fusion and Critical Insights on the Inspection of Aerospace Composites towards Sustainable Maintenance Repair Operations". In: *Applied Sciences* 13.4 (Feb. 2023), p. 2732. DOI: 10.3390/APP13042732.

[2] T. Stratoudaki, M. Clark, and P. Wilcox. "Laser induced ultrasonic phased array using Full Matrix Capture data acquisition and Total Focusing Method". In: *Optics Express* (Sept. 2017). DOI: 10.1364/oe.24.021921.

[3] R. Zimermann et al. "Multi-layer ultrasonic imaging of as-built Wire + Arc Additive Manufactured components". In: *Additive Manufacturing* 48 (Dec. 2021), p. 102398. DOI: 10.1016/J.ADDMA.2021.102398.

[4] D. Pieris et al. "Laser Induced Phased Arrays (LIPA) to detect nested features in additively manufactured components". In: *Materials & Design* 187 (Feb. 2020). DOI: 10.1016/j.matdes.2019.108412.

[5] P. Lukacs et al. "2D Laser Induced Phased Arrays for Remote Volumetric Ultrasonic Imaging". In: *IEEE Transactions on Ultrasonics, Ferroelectrics, and Frequency Control* (2025). DOI: 10.1109/TUFFC.2025.3580168.

This work was supported by the EPSRC funded Royce Industrial Collaboration Programme (ICP) and the UK Research Centre in Non Destructive Evaluation Engineering (RCNDE).

DOI 10.5162/Ultrasonic2025/D3-a5

Non-Destructive Evaluation and Defect Characterization of Ceramic Matrix Composites Using Laser Ultrasonics

Ruben Burger[1,2], *Datong Wu*[1], *and Christian U. Grosse*[2]
[1] *Munich University of Applied Sciences HM, Lothstr. 34, 80335 München, Germany*
[2] *Technical University of Munich - Chair of Nondestructive Testing, Lichtenbergstr. 2, 85748 Garching bei München, Germany*
ruben.burger0@hm.edu, datong.wu@hm.edu

Abstract: Laser ultrasonic non-destructive testing was applied for the first time to oxide–oxide ceramic matrix composites. A fully optical setup generated and detected broadband ultrasound in both transmission and reflection modes. The measured shear wave velocity matched predictions within $5\,\%$, confirming reliable wave generation in the highly porous material. Although the current signal-to-noise ratio is modest, simple hardware upgrades could raise performance, positioning LU as a practical inline, non-contact quality-control tool for oxide–oxide CMCs.

Keywords: Ceramic Matrix Composites, Laser Ultrasonics, Non-Destructive Testing, Laser Doppler Vibrometer, Guided Waves

Introduction

Ceramic Matrix Composites (CMCs) are high-performance materials developed for use in environments demanding exceptional thermal and mechanical properties, such as those found in aerospace, energy, and defense industries [1, 2]. Unlike monolithic ceramics, which are characterized by brittleness and susceptibility to catastrophic failure, CMCs combine ceramic matrices with reinforcing fibers, resulting in enhanced toughness, damage tolerance, and resistance to thermal shocks [3].

CMCs are generally classified into Oxide-Oxide (Ox-Ox) and Non-Oxide systems. Ox-Ox CMCs typically consist of alumina (Al_2O_3) matrices reinforced with fibers such as alumina or mullite, providing excellent oxidation resistance but generally limited to lower-temperature applications compared to Non-Oxide systems [4]. In contrast, Silicon Carbide (SiC)-based CMCs, particularly SiC/SiC composites, exhibit superior high-temperature mechanical properties albeit with reduced oxidation resistance requiring protective coatings for certain applications [5].

However, the complex microstructure, inherent porosity, and anisotropic properties of CMCs create significant challenges for non-destructive evaluation (NDE). Various NDE techniques have been investigated for evaluating CMCs, each with distinct advantages and limitations. X-ray Computed Tomography (CT) offers high-resolution imaging and deep penetration capabilities, ideal for detecting internal porosity and cracks, but it is limited by high costs, long scan times, and requirements for specialized facilities [6].

Active Infrared Thermography (IRT) has demonstrated rapid, large-area inspection capabilities and effective detection of subsurface defects through thermal contrast, particularly beneficial for monitoring damage progression in CMCs under mechanical stress [7]. However, IRT's utility is limited by shallow penetration depth, sensitivity to surface emissivity variations, and thermal diffusion-induced image blurring, complicating accurate defect characterization.

Terahertz Time-Domain Spectroscopy (THz-TDS) has emerged as another non-destructive method, capable of detecting internal porosity, delaminations, and moisture ingress, with the advantage of higher resolution than microwaves and better penetration than IR techniques. The technique was applied by the authors to Ox-Ox CMC successfully [8]. Nonetheless, its widespread application is limited by significant signal attenuation in ceramics, slow data acquisition rates, and the high cost of equipment [9].

Conventional pulse-echo or immersion contact based ultrasonic testing remains the industrial baseline for CMC inspection [6]. It can detect delaminations and bulk porosity when adequate acoustic coupling is achieved. However, the open porosity and rough surfaces typical of Ox-Ox CMCs cause strong scattering and attenuation of high-frequency waves; furthermore, liquid couplants can infiltrate the pore network, complicating processing.

Air-coupled ultrasound (ACU) avoids the problems with liquid couplants by using impedance-matched membrane or capacitive transducers to transmit and receive sound through air. Vasechko et al. [10] demonstrated through-transmission ACU C-scans on porous alumina-fibre CMCs up to $16\,\mathrm{mm}$ thick, accurately mapping delaminations and high-porosity regions in agreement with CT data. Owing to the large

DOI 10.5162/Ultrasonic2025/D3-a5

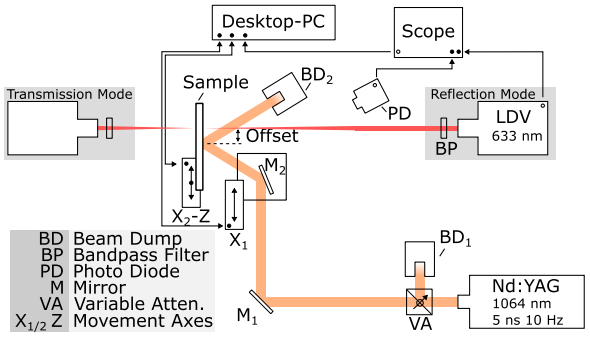

Fig. 1: Laser ultrasonic measurement setup. Sample can be moved in horizontally and vertically and the distance between excitation and measurement spots horizontally. Both transmission and reflection mode is possible with repositioning of the LDV. See details in text.

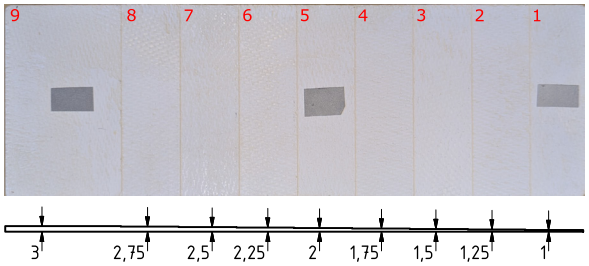

Fig. 2: Top: photograph of the front surface with three strips of reflective tape that serve as LDV targets in transmission. Red numerals label the individual steps and are used as identifiers in the text. Bottom: schematic of the stepped thickness profile.

air-to-ceramic impedance mismatch, ACU is most effective in transmission mode and typically employs narrow-band signals below $300\,\mathrm{kHz}$ which lengthens scan times.

Laser ultrasonics (LU) is a fully non-contact NDE technique in which a short-pulse laser excites broadband ultrasonic waves, while surface displacements are monitored remotely with a laser interferometer [11]. Quintero et al. [12] demonstrated that LU in through transmission geometry can visualize impact damage and delaminations in turbine-grade SiC/SiC (non-oxide) panels with image quality comparable to immersion C-scans. Ox-Ox CMCs exhibit markedly higher open porosity and acoustic attenuation due to scattering, factors that complicate wave propagation and have so far precluded LU studies.

To the authors' knowledge, the work reported here is the first systematic investigation of LU inspection for oxide–oxide CMCs, evaluating its feasibility in both through-transmission and single-surface reflection geometries.

Methods

The fully optical laser–ultrasonic setup illustrated in Figure 1 and provides a standoff distance of over $50\,\mathrm{cm}$ for both ultrasonic generation and detection. Broadband ultrasonic waves are generated by photoelastic excitation using a Q–switched Nd:YAG laser (InnoLas Spitlight 200, $1064\,\mathrm{nm}$ wavelength, $5\,\mathrm{ns}$ pulse width, $10\,\mathrm{Hz}$ repetition rate). The pulse energy, adjusted with a variable attenuator (VA), is fixed at $50\,\mathrm{mJ}$. The unfocused beam is routed to the CMC-sample via mirrors ($\mathrm{M}_{1/2}$), producing a Gaussian spot with a $5\,\mathrm{mm}$ $1/e^2$ diameter on the sample surface. The resulting fluence of $130\,\mathrm{mJ\,cm^{-2}}$ is well below the damage threshold of the Ox-Ox CMC.

The excitation spot can be translated over $50\,\mathrm{mm}$ along the x-axis (stage X_1) using a motorized linear stage. An angle of incidence of $45°$ leaves the normal direction unobstructed for detection; the reflected pump beam is absorbed by a beam dump (BD2).

The sample is mounted on a custom 3D printed mount that offers travel of $50\,\mathrm{mm}$ in both horizontal and vertical directions.

Surface vibration is monitored with a heterodyne laser Doppler vibrometer (Polytec OFV-505, $633\,\mathrm{nm}$ wavelength, $25\,\mathrm{MHz}$ $3\,\mathrm{dB}$ bandwidth, $1\,\mathrm{mW}$ output power). A $5\,\mathrm{nm}$ bandpass filter centered at $633\,\mathrm{nm}$ suppresses optical crosstalk from the pump laser. The analog LDV signal is digitized at $2.5\,\mathrm{GS\,s^{-1}}$ with a Rohde&Schwarz RTA4000 oscilloscope, triggered by a fast photodiode that monitors the pump pulse.

Stage motion, trigger synchronization, LDV autofocus, and data acquisition are controlled by a custom `.NET` application. By repositioning the LDV head, the setup supports both reflection and transmission geometries without altering the pump-beam optics (cf. Fig.1).

The $\mathrm{Al_2O_3}$ Ox-Ox CMC sample (cf. Fig.1) investigated in this work is a $300\,\mathrm{mm}$ by $100\,\mathrm{mm}$ step wedge with variation in thickness ($1\,\mathrm{mm}$ to $3\,\mathrm{mm}$ with steps of $0.25\,\mathrm{mm}$). The steps are numbered sequentially with increasing thickness. It was previously investigated using THz-TDS in reflection mode [8]. Artificial damage was not introduced. The surface is not coated or modified to increase excitation laser absorption and is also not smoothed to improve LDV signal. At $\approx 30\,\%$ porosity, the material exhibits strong attenuation for elastic waves in the MHz range. The elastic modulus of the material normal to the fiber orientation is considerably lower, leading to low wave velocities in the range of $2600\,\mathrm{m\,s^{-1}}$ ($1500\,\mathrm{m\,s^{-1}}$) for the longitudinal (shear) mode. In the photoelastic range, the excitation is dominated by the shear mode. The excited area is large relative to the thickness

DOI 10.5162/Ultrasonic2025/D3-a5

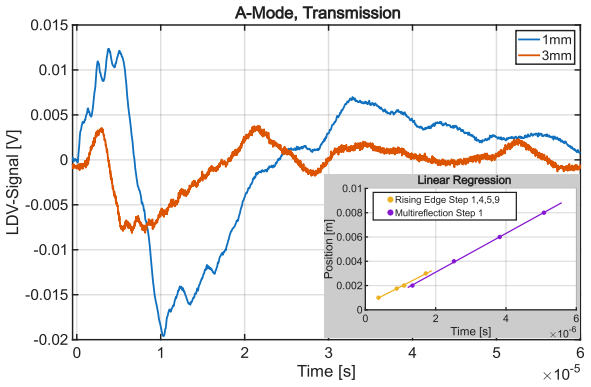

Fig. 3: A-mode signal of the thickest and the thinnest part of the sample. First peaks correspond to the arrival of the shear mode. For the thinnest areas, multiple reflections of the shear mode can be observed. Inset show linear regression for the arrival times using two method (c.f. main text).

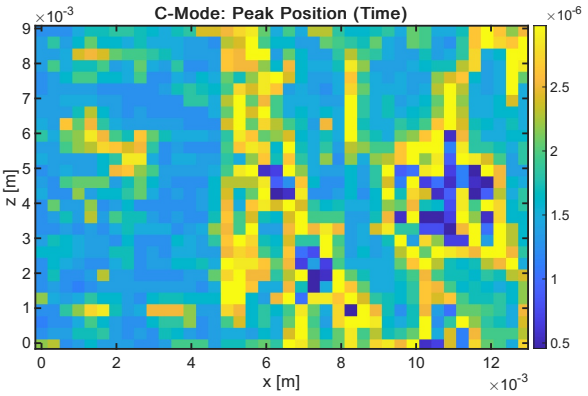

Fig. 4: C-mode image of transmission measurement across step 8 to 9. The colormap corresponds to the position in time of the first positive peak. The step is located at around $x = 5\,\mathrm{mm}$. The pattern corresponds to the varying coupling of the reflective tape due to changing surface quality between steps.

to reduce beam directivity [11, 12]. In transmission mode, reflective tape was applied to the measurement spots to increase the signal-to-noise ratio (SNR) and protect the LDV from partial transmission of the excitation pulse through the sample. This is especially important for the thinner section, where even the LDV laser shines through the sample. With reflective tape, the signal was averaged 10 times for all positions. The excitation and measurement spots were aligned for central overlap using the X_1-stage. C-Scan data was collected on a 30 by 40 grid (steps: $0.33\,\mathrm{mm}$) by moving both sample stages (X_2,Z). In reflection mode, linear scans with increasing distance between excitation and measurement were performed to track guided wave propagation, starting from direct overlap (allowing for impulse echo measurements) to a distance of $2\,\mathrm{mm}$ in steps of $0.25\,\mathrm{mm}$. Since no reflective tape was used in this measurement mode, the number of averages was set to 50 to compensate for the high measurement noise. Due to the long measurement times, no C-Scans were performed in this mode. For both measurements, at each position the LDV was refocused by the measurement application to achieve better signal quality on the rough surface of the sample.

Results and Discussion

The results of the transmission measurements are shown in Figs. 3 and 4. The received signal has a bandwidth of approximately $1\,\mathrm{MHz}$, considerably lower than the $5\,\mathrm{ns}$ excitation pulse would generates. The signals in Figure 3 are the average of a 3 by 3 pixel area with good coupling between the sample and the reflective tape. To validate the origin of the first peaks, two methods are used: tracking the rising edge of the signal across four thicknesses and tracking multiple reflections of the pulse for the thinnest step. Both regression results are shown in the inset of Figure 3. The calculated velocity is $v = 1484(220)\,\mathrm{m\,s^{-1}}$ and $v = 1587(98)\,\mathrm{m\,s^{-1}}$, respectively, confirming the origin of the signal as the shear mode. Longitudinal mode signals could not be detected in any of the measurements. The observed voltage amplitudes correspond to surface displacements of around $0.5\,\mathrm{nm}$. The C-mode image in Figure 4 shows the peak position in time of the first positive peak between steps 8 and 9. The edge is located around $x = 5\,\mathrm{mm}$ and can be clearly identified in the data. The observed pattern corresponds to the surface quality of the scan area: On the left, the surface is smooth and thus shows good coupling to the reflective tape. On the right, the ceramic fibers are bare, leading to very uneven coupling.

An example of the reflection mode measurements is shown in Figure 5. The characteristic dispersive A_0 Lamb mode can be clearly identified for the full scan range. Further modes could not be detected due to low SNR. The inset of Figure 5 shows the impulse-echo signal at overlap between excitation and detection. The peak position is in agreement with the shear velocities observed in transmission mode.

This study confirms that LU NDT is a promising tool for Ox-Ox CMC inspection. The measured wave speeds align with the expected shear-wave velocity of the composite, validating both the optical generation scheme and the material model. Reflection-mode data show clear elastic arrivals, indicating that LU can be adapted for in-service inspections where only a single surface is accessible.

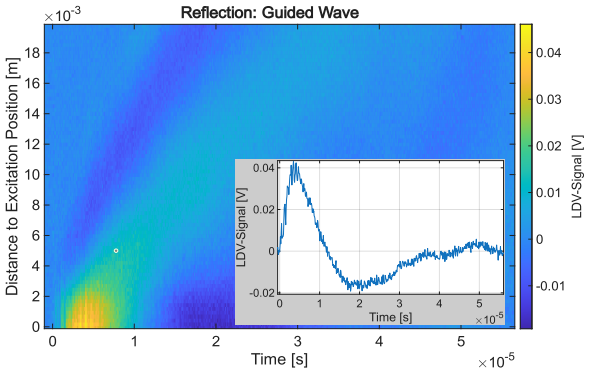

Fig. 5: Linear Scan in reflection mode (time vs. excitation distance) at step 7. Dispersive guided wave mode (A0 Lamb) is clearly visible. Inset shows impulse echo signal at overlap.

Although the current signal-to-noise ratio is modest, several straightforward upgrades are available:

1. *Excitation.* Switching to ultraviolet pulses with slightly longer durations could increase surface absorption and preferentially excite the sub-$1\,\mathrm{MHz}$ bandwidth that propagates efficiently in porous media.

2. *Detection.* Modern LDVs featuring active speckle tracking will better accommodate surface roughness and deliver higher amplitude fidelity.

3. *Scanning speed.* Replacing mechanical stages with galvanometric or MEMS mirrors will cut acquisition time by an order of magnitude.

Future work should focus on these hardware improvements and extend the study to production-grade components with complex geometries. Collectively, these efforts will advance LU-NDT toward a robust, shop-floor-ready technology for the quality assurance of Ox-Ox CMC structures.

References

[1] R. Naslain. "Design, preparation and properties of non-oxide CMCs for application in engines and nuclear reactors: an overview". In: *Composites Science and Technology* 64.2 (2004), pp. 155–170.

[2] W. Krenkel. *Ceramic matrix composites: fiber reinforced ceramics and their applications*. John Wiley & Sons, 2008.

[3] A. Evans and D. Marshall. "Overview no. 85 The mechanical behavior of ceramic matrix composites". In: *Acta Metallurgica* 37.10 (1989), pp. 2567–2583. DOI: 10.1016/0001-6160(89)90291-5.

[4] C. G. Levi et al. "Processing and performance of an all-oxide ceramic composite". In: *Journal of the American Ceramic Society* 81.8 (1998), pp. 2077–2086.

[5] R. Naslain et al. "Oxidation mechanisms and kinetics of SiC-matrix composites and their constituents". In: *Journal of materials science* 39 (2004), pp. 7303–7316.

[6] N. Ida and N. Meyendorf. *Handbook of advanced nondestructive evaluation*. Vol. 10. Springer International Publishing Cham, Switzerland, 2019.

[7] K. G. Dassios et al. "Nondestructive Damage Evaluation in Ceramic Matrix Composites for Aerospace Applications". In: *The Scientific World Journal* 2013.1 (2013), p. 715945. DOI: 10.1155/2013/715945.

[8] D. Wu et al. "Application of terahertz time domain spectroscopy for NDT of oxide-oxide ceramic matrix composites". In: *Infrared Physics & Technology* 102 (2019), p. 102995. DOI: 10.1016/j.infrared.2019.102995.

[9] F. Ellrich et al. "Terahertz quality inspection for automotive and aviation industries". In: *Journal of Infrared, Millimeter, and Terahertz Waves* 41 (2020), pp. 470–489.

[10] V. Vasechko et al. "Air-coupled ultrasonic inspection technique as NDT tool for evaluation of porous wound oxide/oxide composite ceramics". In: *Proceedings of the 19th World Conference of Non-Destructive Testing, Munich, Germany*. 2016, pp. 13–17.

[11] C. Scruby and L. Drain. *Laser Ultrasonics Techniques and Applications*. CRC Press, 1990.

[12] R. Quintero et al. "Noncontact laser ultrasonic inspection of Ceramic Matrix Composites (CMCs)". In: *NDT & E International* 88 (2017), pp. 8–16. DOI: 10.1016/j.ndteint.2017.02.008.

DOI 10.5162/Ultrasonic2025/D3-a6

Exploring Laser-Induced Ultrasound for Fruit Quality: Multi-Fruit Validation and Avocado Ripening Studies

J. L. Castaño[1] and J. L. Ealo[2]
[1]Universidad del Valle, Mechanical Engineering School, Cali, Colombia
[2]Universidad del Valle, Centre for Bioinformatics and Photonics (CIBioFi), Cali, Colombia
jose.luis.castano@correounivalle.edu.co

Abstract: We evaluate a laser-generated ultrasound method for non-destructive fruit assessment. Unlike prior full-contour studies, this paper provides a non-destructive method for determining phase velocity and attenuation over a short linear segment of the surface. Trials on kiwi, banana, and avocado revealed strong attenuation sensitivity to viscoelastic differences. In avocados, postharvest monitoring showed measurable attenuation drops with ripening, while phase velocity remained stable. The method detected structural changes before visible softening and may support early pest damage detection and automated quality grading.

Keywords: Fruit, Laser ultrasonics, attenuation, phase velocity, Non destructive monitoring

Introduction

Non-invasive techniques have emerged as effective alternatives for characterizing internal properties of fruits without compromising their integrity. Among these, optical methods such as hyperspectral imaging and near-infrared spectroscopy (NIR) have gained prominence due to their capacity to detect internal bruises and monitor chemical composition. However, these optical methods face limitations when applied to thick-skinned fruits due to reduced light penetration and sensitivity to surface heterogeneity. These constraints hinder their effectiveness in assessing mechanical properties during postharvest changes such as ripening.

Laser-induced ultrasound (LIUS) offers a compelling solution by combining deep tissue penetration with high spatial and temporal resolution [1]. This approach enables the remote generation and detection of elastic waves, allowing the measurement of mechanical parameters, such as wave attenuation and velocity, in fruits that evolve during ripening. Measurements have shown a close relationship with structural changes in apples [2, 3], kiwifruit [4], and mangoes [5] during post-harvest periods. While LIUS offers promising capabilities, its application in tropical and structurally complex fruits remains underexplored.

This study proposes and validates a non-contact optoacoustic method to characterize the elastic behavior of fruit tissues, focusing on a spatial profile of 10 mm linear scan. A pulsed laser generates surface-guided waves on the fruit exocarp, while a laser Doppler vibrometer captures the dynamic response. Initial experiments on bananas (*Musa acuminata*), kiwis (*Actinidia deliciosa*), and avocados (*Persea americana*, cv. Fuerte) demonstrated the feasibility of generating and processing spatiotemporal wavefields. Avocados were further selected for postharvest ripening analysis.

The mechanical evolution of avocado tissue was evaluated by extracting attenuation coefficients and phase velocity dispersion curves across multiple days. Signals were processed using dynamic time warping (DTW) in the time domain and slant-stacking in the frequency domain, enabling a comparative analysis throughout ripening stages.

The experimental configuration and signal processing methods are described, followed by results on attenuation and phase velocity in the three fruits. The study examines their evolution during avocado ripening and summarizes the main conclusions and future perspectives.

Methodology

Fig. 1 illustrates the optoacoustic implementation used. A Nd:YAG laser (532 nm, <10 ns, 20 Hz, 2 mJ, 1 mm spot) generated elastic waves on the exocarp of the fruits. The laser energy was adjusted to maintain operation within the thermoelastic regime, avoiding tissue damage. The mechanical response was captured by a laser Doppler vibrometer (LDV) (Polytec OFV-505, 10 mm/s/V sensitivity, up to 250 kHz bandwidth). Beam delivery used collimating optics and galvanometric scanning for linear surface profiling under non-contact excitation. Signals were acquired with an oscilloscope (Rigol DS6104) and transferred to a computer for digital processing. To improve the signal-to-noise ratio, a thin layer of white ink was applied to the linear profile.

Riped kiwi (*Actinidia deliciosa*), banana (*Musa acuminata* cv. Cavendish), and avocado (*Persea americana*, cv. Fuerte) were tested under 20 ± 1 C and

DOI 10.5162/Ultrasonic2025/D3-a6

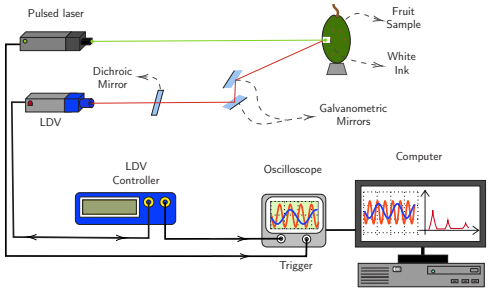

Fig. 1: Experimental scheme for laser-induced ultrasound mapping over a short linear segment of fruit surface.

$70 \pm 5\%$ RH. Avocado was monitored daily over 7 days of ripening. The LDV scanning range was $[-5, +5]$ mm and a distance interval of 0.2 mm for banana. The range for avocado and kiwi was $[-10, +10]$ mm with 0.1 mm intervals. All waveforms were zero-padded and low-pass filtered (250 kHz cutoff).

After preprocessing, attenuation and phase velocity estimations were performed. Wave attenuation was assessed with an exponential model $A(x) = A_0 e^{-\mu x}$, where A_0 is the amplitude at $x = 0$, $A(x)$ at position x, and μ the linear attenuation coefficient. The μ values were selected based on the fit yielding the highest coefficient of determination (R^2). Attenuation in dB/mm was obtained via $\alpha = 8.686 \cdot \mu$.

Main phase-front velocities in the time domain were estimated using the Dynamic Time Warping (DTW) algorithm [6, 7, 8]. The reference was typically the closest trace to the laser impact; if inadequate, a nearby high-quality trace within ± 0.4 mm was used. Time-of-flight Δt was extracted, and velocity was estimated via linear fits of the predominant wave phase front.

To extract dispersion curves, slant-stacking and phase-shift methods were applied [9, 10, 11, 12, 13]. Each signal was Fourier transformed, normalized, and phase-corrected using trial velocities. The corrected spectra were coherently summed to form a spectral coherence matrix S(f,c), from which the dominant phase velocities were identified. Amplitude maxima in S(f,c) were semi-automatically selected by visual inspection and localized peak detection across frequency bands.

Results and discussion

In order to compare the responses between fruits, Fig. 2 shows attenuation (α) for kiwi, avocado, and banana.

Within 25–100 kHz, kiwi exhibits the highest attenuation, avocado intermediate, and banana the lowest. Kiwi rises from 0.22 dB/mm to 1.0 dB/mm; avocado from 0.18 to 0.75 dB/mm; and banana from 0.14 to

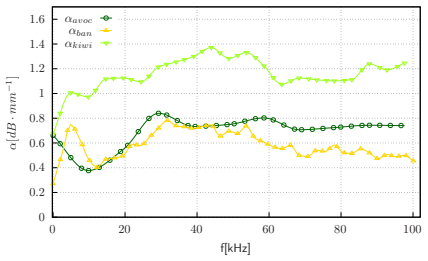

(a) α vs f

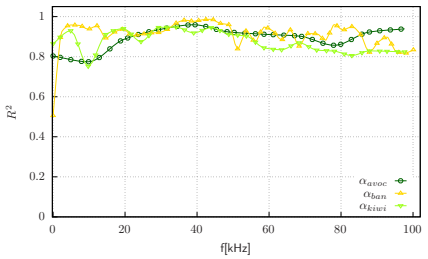

(b) R^2 vs f

Fig. 2: (a) Attenuation coefficient (α) for kiwi (light-green), avocado (dark-green), and banana (yellow) as a function of frequency, obtained from exponential fits of the amplitude-decay model. (b) Goodness–of-fit (R^2) for attenuation linear fits, which confirmed the reliability of the extracted α values in the 0–100 kHz band.

0.60 dB/mm. This reflects the higher viscoelasticity and reduced exocarp thickness of kiwi. Kiwi's steeper curve slope indicates stronger frequency-dependent dissipation, consistent with its high water content. All fits showed R^2>0.8, confirming model reliability (Fig. 2b). Differences in attenuation reflect variations in tissue stiffness, layered structure and moisture content among fruits.

Fig. 3 shows space-time wavefields for each fruit. Orange $\times$ markers indicate DTW-aligned time-of-flights; red lines show linear fits. The estimated velocities were 48.96 $\pm$ 2.7 m/s (banana), 82.29 $\pm$ 7.59 m/s (kiwi), and 78.41 $\pm$ 14.95 m/s (avocado) in each predominant wave phase front. These values reflect the stiffness and hydration levels of each fruit: kiwi exhibited the fastest propagation due to its compliant and water-rich structure, followed by avocado with a stiff exocarp, while banana, with its thicker and high fiber-content, supported the slowest surface wave speed.

Dispersion curves in Fig. 4 confirm the velocity trends observed in time-domain wavefields. Banana exhibits the lowest phase velocities, ranging from 46.8 to 68.7 m/s, limited above 75 kHz due to signal attenuation. Kiwi shows higher velocities ranging from 89.7 to 130.4 m/s, with avocado presenting intermediate

DOI 10.5162/Ultrasonic2025/D3-a6

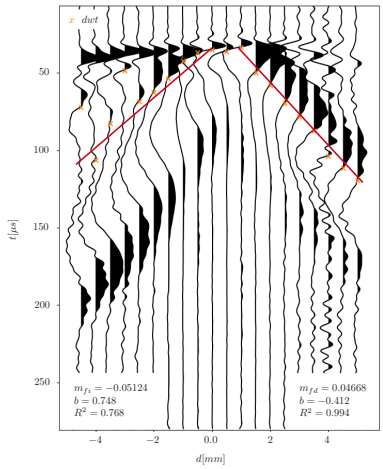

(a) Wavefield banana

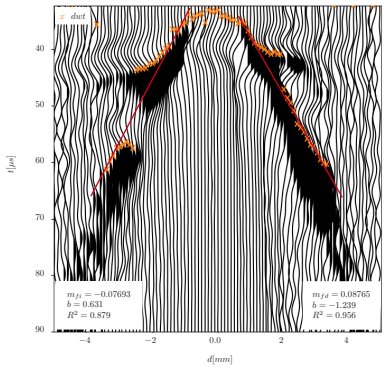

(b) Wavefield kiwi

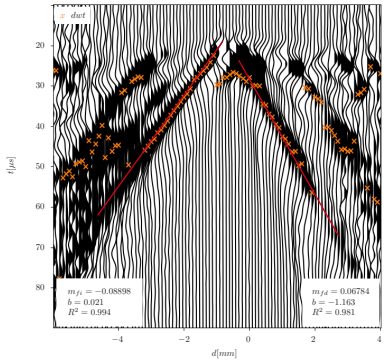

(c) Wavefield avocado

Fig. 3: Time-domain wavefields along the laser-scan line for (a) banana, (b) kiwi, and (c) avocado. Black traces plot the out-of-plane surface velocity; orange $\times$ marks show the DTW-derived time-of-flight Δt for each trace. Red lines represent linear fits whose slopes (m_{fd}, m_{fi} in mm/μs) appear at the lower corners of every plot.

values. The relative increases in phase velocity across the frequency range were 71% (kiwi), 78% (avocado), and 47% (banana). These results indicate that the

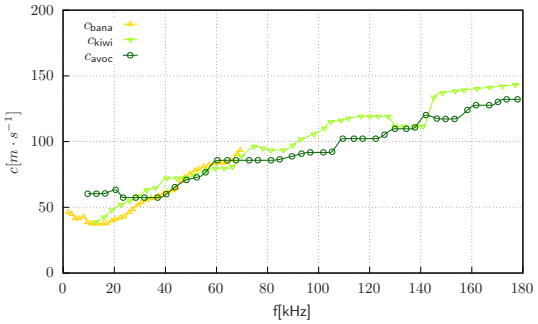

Fig. 4: Dispersion curves for banana, kiwi, and avocado: phase velocity as a function of frequency.

LIUS technique is sensitive to variations in fiber composition, moisture content, and structural differences at the exocarp–mesocarp interface.

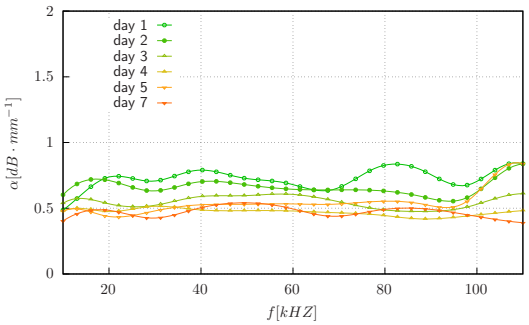

Fig. 5: Attenuation curves (α) of avocado tissue measured from day 0 to day 7 of postharvest ripening. Each curve corresponds to a distinct stage in the maturation process. All exponential fits showed correlation coefficients above $R^2 > 0.8$.

The results on avocado attenuation (Fig. 5) decreased from day 0 to day 3 (1.2 to <0.8 dB/mm at 100 kHz), with average values falling from 0.705 to 0.472 dB/mm. By day 7, it rose slightly to 0.481 dB/mm. This correlates with ripening-induced lignification [14], which increases fiber rigidity and reduces wave attenuation. Structural changes likely drive the observed attenuation trends; future work will research additional biochemical factors affecting wave propagation.

Fig. 6 confirms stable propagation during ripening. Phase velocities ranged from 77.6–81.6 m/s (low band), 111.5–124.2 m/s (mid), and 134.4–143.7 m/s (high). This suggests that attenuation is a more sensitive indicator of tissue changes than phase velocity in the linear profile measured and in the energy regime used in the pulsed laser.

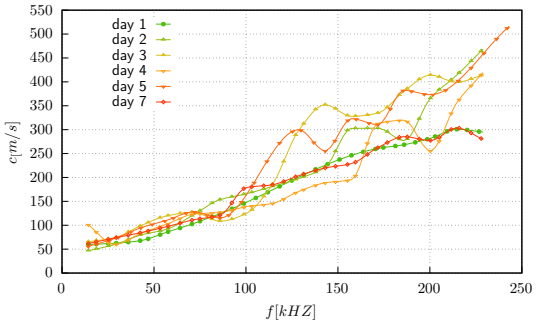

Fig. 6: Phase velocity curves for avocado samples from day 0 to day 7 of ripening.

Conclusions

The optoacoustic evaluation revealed that attenuation and phase velocity effectively reflect structural differences and ripening stages. Kiwi exhibited the highest attenuation and phase velocity, avocado showed intermediate values, and banana presented the lowest, consistent with differences in tissue hydration and stiffness. During avocado ripening, attenuation decreased markedly in early stages due to structural transformations like exocarp lignification, increasing rigidity and altering tissue contrast, thereby affecting attenuation. Phase velocity remained stable, indicating lower sensitivity to early physiological changes. These findings highlight laser ultrasound as a promising tool for potential practical applications such as automated sorting, early damage detection, storage optimization, and rapid pest infestation screening.

Acknowledgments

The authors would like to thank postdoctoral researcher Evert Duran and Professor Kasper van Wijk for their support and assistance during their doctoral internship at the University of Auckland.

References

[1] C. Scruby and L. Drain. *Laser Ultrasonics: Techniques and Applications*. First. New York: Taylor & Francis Group, 1990.

[2] S. Hitchman, K. van Wijk, and Z. Davidson. "Monitoring attenuation and the elastic properties of an apple with laser ultrasound". In: *Postharvest Biology and Technology* 121 (2016), pp. 71–77.

[3] N. Hosoya et al. "Non-destructive firmness assessment of apples using a non-contact laser excitation system based on a laser-induced plasma shock wave". In: *Postharvest Biology and Technology* 128 (2017), pp. 11–17.

[4] L. A. Cobus and K. van Wijk. "Non-contact acoustic method to measure depth-dependent elastic properties of a kiwifruit". In: *Wave Motion* 119 (2023), p. 103126.

[5] N. Arai et al. "Soft Mango Firmness Assessment Based on Rayleigh Waves Generated by a Laser-Induced Plasma Shock Wave Technique". In: *Foods* 10.2 (2021).

[6] E. L. Durán, L. Adam, and I. C. Wallis. "A robust methodology for time picking and error analysis of ultrasonic waveforms and rock densities in the laboratory". In: *Geophysics* 84.2 (2019), MR85–MR97.

[7] C. Bishop. *Pattern Recognition and Machine Learning*. Springer, Jan. 2006.

[8] H. Sakoe and S. Chiba. "Dynamic programming algorithm optimization for spoken word recognition". In: *IEEE transactions on acoustics, speech, and signal processing* 26.1 (1978), pp. 43–49.

[9] E. A. Olafsdottir, S. Erlingsson, and B. Bessason. "Tool for analysis of multichannel analysis of surface waves (MASW) field data and evaluation of shear wave velocity profiles of soils". In: *Canadian Geotechnical Journal* 55.2 (2018), pp. 217–233.

[10] E. Á. Ólafsdóttir. "Multichannel analysis of surface waves for assessing soil stiffness". MA thesis. University of Iceland, 2016.

[11] J. Taipodia, A. Dey, and D. Baglari. "Influence of data acquisition and signal preprocessing parameters on the resolution of dispersion image from active MASW survey". In: *Journal of Geophysics and Engineering* 15.4 (2018), pp. 1310–1326.

[12] B. R. Cox and D. P. Teague. "Layering ratios: a systematic approach to the inversion of surface wave data in the absence of a priori information". In: *Geophysical Journal International* 207.1 (2016), pp. 422–438.

[13] C. B. Park, R. D. Miller, and J. Xia. "Imaging dispersion curves of surface waves on multichannel record". In: *SEG technical program expanded abstracts 1998*. Society of Exploration Geophysicists, 1998, pp. 1377–1380.

[14] R. Espinosa-Velázquez et al. "Morphostructural description of unripe and ripe avocado pericarp (Persea americana Mill var. drymifolia) descripción". In: *Revista Mexicana de Ingeniería Química* 15.2 (2016), pp. 469–480.

DOI 10.5162/Ultrasonic2025/D6-a2

Non-intrusive power ultrasonic approach for calcium carbonate scale reduction in industrial pipelines

J. H. Lopes[1], *J. G. B. Cavalcante*[1], *R. Calheiros*[2], *M. Calheiros*[2], *M. S. G. Tsuzuki*[3], *and J. P. Leão-Neto*[1]
[1]*Federal University of Alagoas, Campus Arapiraca, Arapiraca, Brazil*
[2]*2Solve Engineering and Technology, Vitória, Brazil*
[3]*University of São Paulo, Escola Politécnica, São Paulo, Brazil*
jose.andrade@arapiraca.ufal.br

Abstract: This study investigates the use of ultrasound to mitigate scale formation in pipelines within the iron ore filtration process. The formation of calcium carbonate scale, caused by the addition of lime and carbon dioxide, results in blockages, increased pressure, and equipment wear. Experimental tests for characterize and reduce the fouling were performed. The results suggest that while ultrasound may not be feasible for large-scale removal, it holds promise for scale prevention in mining pipelines.

Keywords: Calcium carbonate, Langevin transducer, acoustic cavitation, pipeline fouling, scale formation.

Background, Motivation and Objective

Fouling in pipelines is a critical operational challenge in mineral processing plants, especially during the filtration stage of iron ore slurries [1, 2, 3, 4]. The use of chemical additives like calcium oxide (CaO) facilitates the process, but also leads to the formation of calcium carbonate ($CaCO_3$) as a by-product of subsequent pH control with CO_2. The deposition of $CaCO_3$ scales along the inner surfaces of pipes and equipment can cause significant disruptions, including reduced flow rates and increased pressure drops. Recent studies have explored non-invasive techniques such as high-power ultrasound to mitigate these issues [5, 6, 7]. Ultrasonic waves, when applied via transducers like those of the Langevin type, induce cavitation and microstreaming, which can weaken or dislodge scale layers, potentially reducing the rate of fouling without the need for harsh chemicals or frequent mechanical interventions. Recent studies have demonstrated the feasibility and effectiveness of inducing cavitation using high-power ultrasonic transducers in pressurized environments, such as vessels and pipelines [8]. Cavitation effects are known to enhance scale removal particularly at rough interfaces, as demonstrated for $CaCO_3$-coated metallic surfaces under ultrasonic exposure [9].

In this study, the application of high-power ultrasound transducers as an alternative strategy to reduce pipeline fouling in real iron ore filtration processes is investigated. Furthermore, the fouling samples were acoustically characterized. Propagation velocity, density, attenuation, porosity and acoustic impedance were measured. By introducing ultrasonic waves into critical segments of the pipeline system, we aim to disrupt the early formation of $CaCO_3$ deposits through mechanisms such as acoustic cavitation and surface vibration. The study is conducted under representative operating conditions of an industrial mineral processing unit, enabling a realistic evaluation of ultrasound's potential to reduce maintenance demands, improve process stability, and lower chemical consumption. The findings may contribute to more efficient, safer, and environmentally friendly scale control strategies in large-scale ore beneficiation operations.

Methodology

The ultrasonic system employed in this study was initially designed, fabricated, and experimentally characterized to ensure its applicability for fouling control in iron ore filtration pipelines. The design process focused on developing a high-power Langevin-type transducer to operate at a nominal frequency of 21 kHz.

The transducer design was carried out using finite element analysis (FEA) with the COMSOL Multiphysics software. A 2D axisymmetric geometry was employed to model the transducer configuration. The Solid Mechanics and Electrostatics modules were coupled and solved in the frequency domain, allowing the prediction of the electrical impedance response of the device.

Following the simulation model, the individual mechanical components of the transducer were machined based on the optimized geometry obtained from the numerical model. To validate the numerical model, the electrical impedance spectrum of the constructed transducer was measured using an impedance ana-

DOI 10.5162/Ultrasonic2025/D6-a2

lyzer. Figure 1 presents a photograph of the built transducers.

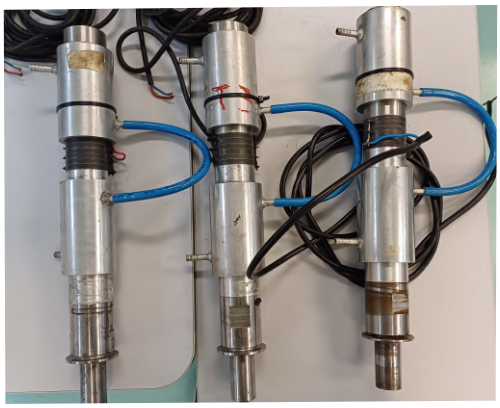

Fig. 1: Photograph of the build transducers.

The characterization of the fouling samples was carried out by means of transmission-reception tests in water. Two 1 MHz narrowband transducers were used for signal transmission and reception. By means of the acoustic signals that pass through the sample, it is possible to obtain important quantities such as sound propagation speed, attenuation, and acoustic impedance. Measurements of the density of the samples, as well as the level of porosity, were also carried out. These quantities are essential to understand the propagation of sound as it passes through the samples and thus design the appropriate ultrasound reduction system.

To validate the analysis regarding the effectiveness of ultrasound in reducing calcium carbonate ($CaCO_3$) fouling in pipelines, a closed-loop experimental circuit was constructed incorporating a 500 mm long section of 12-inch diameter carbon steel pipe. The pipe segment was sourced directly from an operational mineral processing plant. The pipeline was modified by welding two flanges to its ends. This allowed the system to be sealed using 12 mm thick acrylic covers, bolted to the flanges with screws and nuts. Additionally, five threaded studs were installed along the length of the pipeline to allow for the mounting of the ultrasonic transducers.

Five Langevin-type ultrasonic transducers were strategically mounted onto the pipe via custom-designed fixation points to ensure optimal acoustic coupling and spatial coverage of the inner wall. This setup was integrated into a recirculating fluid loop equipped with a centrifugal pump to maintain continuous flow, as illustrated in Figure 2. To prevent thermal degradation and ensure operational stability of the transducers during prolonged use, an individual heat exchanger was implemented for each unit, enabling effective thermal management throughout the experiments.

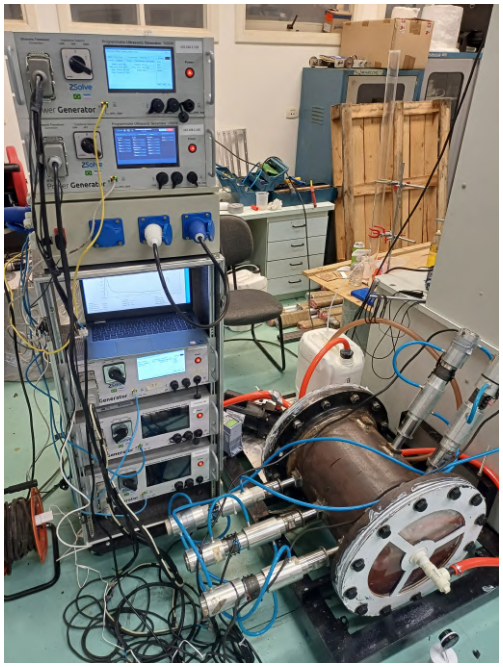

Fig. 2: Photograph of the experimental setup.

The fouling reduction laboratory experiments were conducted in four main steps to evaluate the effectiveness of power ultrasound in reducing mineral scale deposits in iron ore filtration pipelines sample. Initially, hot water circulation tests were performed, followed by tests using a 5% acetic acid solution and in both cases tests were performed with and without ultrasound. In the first step, only hot water at approximately $50\,^{\circ}\mathrm{C}$ was circulated through the encrusted pipeline for 3 hours without the application of ultrasound. In the second step, the procedure of the first step was repeated, with the addition of ultrasound effects. The five transducers were powered with an average power of 250 W. In the third step, a 5% acetic acid solution was used as the circulating fluid for a period of 180 min without the use of ultrasound, and in the last step, ultrasound effects were added together with the acid solution.

Results

Before conducting the scale reduction experiments using ultrasound high-power transducers, the fouling material inside the pipeline was characterized. Since the sample was collected from a real iron ore filtration plant, the incrustation contained not only calcium carbonate but also impurities such as iron oxide. To this end, fragments of the incrustation were carefully removed and subjected to ultrasonic characterization

DOI 10.5162/Ultrasonic2025/D6-a2

using the pulse-transmission technique. The setup employed two 1 MHz ultrasonic transducers. A total of five physical quantities were measured. Table 1 presents all quantities that were ultrasonically characterized.

Tab. 1: Ultrasonic characterization of incrustation material

Measurements	Values
Density [g/cm^3]	1.71
Speed of sound [m/s]	1022
Attenuation [dB/cm]	27.85
Impedance [MRayl]	2
Porosity [%]	13
Dry mass [g]	11.6
1 hour Wet mass [g]	13.8

Figure 3 presents the ultrasonic signals obtained during the characterization tests using the pulse-transmission setup with 1 MHz transducers. The graph shows two waveforms: one acquired with the incrustation sample positioned between the transducers, and another acquired in the absence of the sample, representing the reference signal. A significant reduction in amplitude and a delay in the arrival time can be observed in the presence of the fouling material.

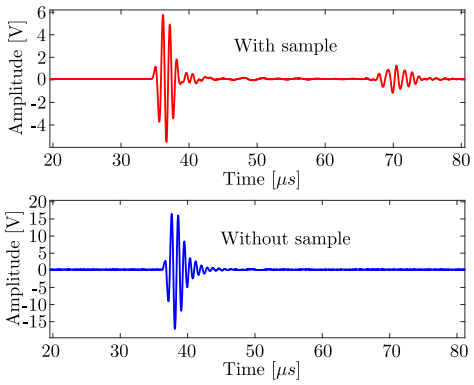

Fig. 3: Ultrasonic signals recorded during the pulse-transmission test with and without the incrustation sample between the transducers.

Following sample characterization, the fouling reduction experiments were conducted. Initially, hot water at $50\,^{\circ}\mathrm{C}$ was circulated through the system for a period of 180 minutes without the use of ultrasound. This process resulted in the removal of 11 g of scale. Next, five Langevin-type transducers (each operating at approximately 200 W) were activated, and hot water was recirculated for the same duration of 180 minutes. A slightly higher amount of residue (19 g) was collected. However, the overall removal efficiency with hot water alone remained low, suggesting limited physical disaggregation of the deposits by ultrasound under these conditions. This behavior aligns with results from FEM-assisted ultrasonic descaling tests in industrial pipelines, which showed modest removal efficiency in the absence of chemical assistance [10].

The 5% acetic acid solution was prepared by mixing 1L of 100% acetic acid with 19L of pre-heated water at $50\,^{\circ}\mathrm{C}$. Each test lasted 40 minutes. As with the tests using water, the first experiment involved circulating only the acid solution without ultrasound activation, resulting in the extraction of 140 g of solid residue.

Subsequent tests were performed with ultrasound applied during the acid circulation. For this condition, three independent test batches were carried out, each lasting 40 minutes. The amounts of residue removed in these tests were 227 g, 169 g, and 175 g, respectively. All solid residues collected from each experiment were separated by decantation, dried, and weighed, confirming that the use of ultrasound significantly enhanced the descaling efficiency of the acid solution. Similar enhancement effects have been reported in other contexts, such as the ultrasonic cleaning of compact heat exchanger surfaces using high-power transducers [11].

Table 2 summarizes the amount of residue collected in each experimental test. The results indicate that the experiments using ultrasound were more effective than those performed with circulating acid alone. At the end of the test campaign, a total of 741.86 g of detached scale was collected. Compared to the estimated total mass of encrusted material prior to the tests (55 kg), the amount of residue removed corresponds to approximately 0.02% for the test with heated water alone, 0.034% for water with ultrasound, 0.22% for the test using acetic acid without ultrasound, and approximately 0.37% for each test using acetic acid combined with ultrasound.

Tab. 2: Mass of scale removed in each experimental test

Tests	Time	Reduction [g]
Water	180	11
Water and ultrasound	180	19
Acetic acid (AA)	40	140
AA and ultrasound	40	227
AA and ultrasound	40	169
AA and ultrasound	40	175

Additionally, visual inspection revealed further reduction of incrustation due to the chemical reaction of acetic acid with calcium carbonate, which produces CO_2 and facilitates scale dissolution. Notably, increased degradation was observed in the region aligned with the position of the ultrasonic transducers. Figure 4 presents photographic records of the inner surface of the pipeline: (a) before the treatment, (b) a magnified view of the encrusted region, and (c) after ultrasonic application. A clear degradation of the scale layer is visible within the red dashed rectangle, which corresponds to the area directly aligned with the transducer installation.

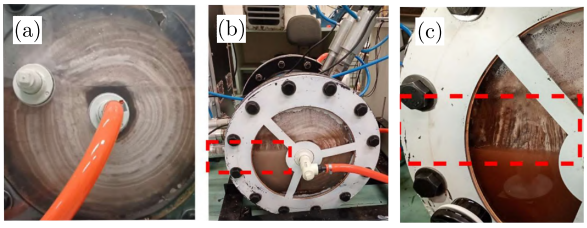

Fig. 4: Photographs of the pipeline's internal surface before and after ultrasonic treatment: (a) fouling surface before ultrasonic treatment, (b) a general view of the structure after the treatment, and (c) surface condition after ultrasonic application. The red dashed rectangle highlights the region aligned with the ultrasonic transducer, where more pronounced degradation of the scale was observed.

Conclusion and perspective

A detailed characterization of scale samples collected from the filtration process of an iron ore processing plant was conducted. The incrustation material exhibited high acoustic attenuation, which significantly limits the penetration of ultrasonic waves and prevents the occurrence of acoustic cavitation within the interior of the pipeline. As a result, the effective reduction of scale through ultrasonic treatment is severely hindered. Despite the modest descaling performance observed using power ultrasound, particularly in the removal of calcium carbonate deposits from the pipeline walls, the proposed system demonstrates potential as a preventive solution. Its application in continuous operation could inhibit early-stage scale formation, thereby reducing the frequency and intensity of required chemical or mechanical cleaning interventions.

References

[1] Z. Qu et al. "Influence of water flow velocity on fouling removal for pipeline based on eco-friendly ultrasonic guided wave technology". In: *Journal of Cleaner Production* 240 (2019), p. 118173.

[2] W. Ma et al. "Study on fouling characteristics of $CaCO_3$ at low reynolds number". In: *Environ Prog Sustainable Energy* 38 (2019), p. 13163.

[3] L. Zhang et al. "Corrosion-induced $CaCO_3$ fouling in steel tube of oilfield wastewater treatment and the interfacial bonding mechanism: An experimental and theoretical investigation". In: *Journal of Petroleum Science and Engineering* 205 (2021).

[4] J. B. R. Loureiro et al. "Large-Scale Pipe Flow Experiments for the Evaluation of Nonchemical Solutions for Calcium Carbonate Scaling Inhibition and Control". In: *SPE Journal* 28 (2023), pp. 201–214.

[5] Z. Qu et al. "Methodology for removing fouling within liquid-filled pipelines based on ultrasonic guided waves cavitation effect". In: *Applied Acoustics* 157 (2020).

[6] N. Kamar. "Scaling control by using ultrasonic guided waves". In: *Chemical Engineering and Processing - Process Intensification* 176 (2022).

[7] C. E. T. da Silva et al. "A New Ultrasonic Reactor for $CaCO_3$ Antiscaling in Pipelines and Equipment". In: *SPE Journaul* 28 (2023), pp. 215–225.

[8] N. Tanabi et al. "Fluid Cavitation Analysis in Pressurized Vessels Using High-Power Ultrasonic Transducers". In: *Proceedings of the 2024 IEEE UFFC Latin America Ultrasonics Symposium (LAUS)*. Montevideo, Uruguay: IEEE, 2024, p. 1.

[9] B. Pečnik et al. "Scale deposit removal by means of ultrasonic cavitation". In: *Ultrasonics Sonochemistry* 45 (2018), pp. 28–36.

[10] A. Mohammadi et al. "Improving the Descaling Rate of an In-Situ Ultrasonic Fouling Removal Method for Industrial Water-Filled Pipelines". In: *Preprint* (2023). arXiv/Research Square preprint. DOI: 10.21203/rs.3.rs-3281577/v1.

[11] H. Nasiri et al. "Cleaning of Printed Circuit Heat Exchangers (PCHE) Using High-Power Ultrasonic Transducers". In: *Proceedings of the 2024 IEEE UFFC Latin America Ultrasonics Symposium (LAUS)*. Montevideo, Uruguay: IEEE, 2024, p. 1.

DOI 10.5162/Ultrasonic2025/D6-a4

High-power ultrasound transducer for mitigating biofouling in subaquatic structures from the oil and gas industry

J. H. Lopes[1], E. K. Ueda[2], F. O. Matos[3], F. Buiochi[2], and M. S. G. Tsuzuki[2]
[1]Federal University of Alagoas, Campus Arapiraca, Arapiraca, Brazil
[2]Escola Politécnica da Universidade de São Paulo, Brazil
[3]PETROBRAS/CENPES, Av. Horácio Macedo 950, Ilha do Fundão, Rio de Janeiro, Brazil
jose.andrade@arapiraca.ufal.br

Abstract: Biofouling, the accumulation of aquatic organisms on submerged structures, poses significant challenges to offshore operations by obstructing water flow and accelerating corrosion. Traditional mitigation methods are often environmentally harmful and demand frequent maintenance. This study explores the use of high-power ultrasound transducers as an eco-friendly solution for biofouling prevention in sea subaquatic structures. Numerical simulations and field experimental tests were performed. Results showed effective biofouling mitigation through ultrasonic pressure and microvibrations on the sea chest structures.

Keywords: Ultrasonic transducers, biofouling, acoustic cavitation, subaquatic structures

Introduction

Biological fouling, or biofouling, refers to the undesirable accumulation of organisms on artificial surfaces and structures immersed in water. This phenomenon poses a significant challenge to the marine industry, resulting in billions of dollars in annual maintenance costs and causing severe environmental impacts [1, 2]. This research and development project focuses on the study of biofouling on specific submerged marine structures, including sea chests and bell mouths.

In sea chests, the accumulation of fouling organisms can obstruct visibility and impede class inspection, requiring periodic cleaning by divers to allow proper access and evaluation. In bell mouths, biofouling, particularly the growth of barnacles on movable coupling components, can prevent the successful execution of riser pull-in operations, thereby compromising the interconnection between risers and the production unit. Consequently, pre-cleaning by divers becomes essential before such mechanical operations. Notably, no specific studies have been found addressing the growth dynamics of biofouling on these types of submerged structures.

Among the various fouling organisms, barnacles are of particular concern due to their size and tendency to colonize submerged surfaces in gregarious clusters. The barnacle life cycle includes six planktotrophic nauplius stages, a non-feeding cyprid larval stage, and a sessile adult stage. The cyprid stage is considered the most critical for biofouling control, as cyprids explore submerged surfaces to select settlement sites where metamorphosed barnacles will grow. Thus, deterring or inhibiting cyprid settlement is a key strategy for barnacle biofouling prevention.

While biocidal antifouling coatings can be effective, their application is increasingly restricted or banned due to environmental concerns. One promising antifouling alternative is the use of ultrasound to prevent biofouling. The propagation of high-power ultrasonic waves in liquids and biological tissues can induce biological changes through thermal and non-thermal effects. In this study, thermal effects were not considered, as no temperature increase was detected during the experiments. Non-thermal effects are primarily attributed to ultrasonic pressure waves, acoustic cavitation, or a combination of both [3, 4].

Ultrasonic cavitation involves the formation, growth, and collapse of vapor or gas bubbles, which can be either stable or transient [2, 5]. In the context of biofouling, cavitation has been reported as the primary mechanism responsible for inhibiting bacterial growth, removing algae, and disrupting biofilms [3, 6, 7]. However, cavitation is influenced by several factors, including dissolved gas content, hydrostatic pressure, ambient temperature, liquid viscosity, ultrasound frequency, and acoustic intensity. Cavitation only occurs when the threshold energy level is reached, and studies have shown that degassed conditions require higher ultrasonic energy to initiate cavitation.

The use of ultrasonic waves has demonstrated promising results for the control of marine biofouling, particularly that induced by barnacles. For instance, [8] used ultrasound-induced cavitation to eliminate barnacle nauplii during ballast water treatment, while [9] re-

DOI 10.5162/Ultrasonic2025/D6-a4

ported the inhibition of cyprid settlement, alterations in exploratory behavior, and reduced size of newly metamorphosed barnacles under ultrasonic exposure.

This work combined numerical simulations and experimental field tests to investigate a biocide-free strategy for the prevention of marine biofouling. To validate our work, a sea chest miniature structure was constructed to allow the coupling of Langevin-type ultrasonic transducers for the generation of acoustic cavitation. Field experiments were conducted in a seawater environment at Ubatuba Beach, Brazil, where the structures were deployed under real marine conditions. The preliminary results indicate that the ultrasonic system is capable of effectively preventing biofouling, particularly by barnacles, during 30 days of exposure. These findings suggest that ultrasonic cavitation may offer a promising approach for short-term biofouling mitigation on submerged structures.

Methodology

This study was divided into two main stages: numerical simulations, in which the entire ultrasonic system was designed, and field experiments, which involved the construction of sample structures, deployment at experimental sites, and evaluation of the effectiveness of ultrasound in preventing biofouling.

The design of the ultrasonic transducers was carried out through numerical simulations using the COMSOL Multiphysics software. Each transducer consists of four PZT-8 piezoelectric ceramic discs sandwiched between two metallic masses made of 7075 aluminum alloy, and mechanically clamped using a high-strength central bolt. These transducers operate as half-wavelength resonators, meaning that the overall length of the device is determined based on the acoustic wavelength in aluminum at the operating frequency. For the intended frequency, the wavelength in aluminum is approximately 300 mm, which was used as a reference for estimating the transducer's dimensions.

The numerical modeling was performed using a 2D axisymmetric geometry, employing the solid mechanics and electrostatics modules. The analyses were conducted in the frequency domain to identify the resonance frequency of the transducer assembly. To characterize the vibrational behavior of the device, simulations were used to generate electrical impedance and mechanical displacement plots. After the simulation and analysis of the transducer's resonance, a detailed technical drawing of each component was prepared to guide the fabrication of the parts. Fig. **??** shows a schematic representation of the transducer model and a photograph of the built transducers.

The field experiments were conducted at the Oceanographic Institute of the University of São Paulo, located in Ubatuba. In Ubatuba, electrical and structural installations were carried out to support the experiments, which involved the submersion of sea chest models equipped with ultrasonic transducers beneath a floating pier.

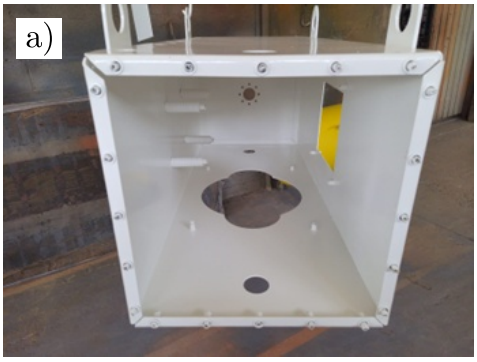

Fig. 1: Illustration of the fabricated sea chest used in the experimental field tests.

Scaled-down model of the sea chest structure was fabricated and deployed under real marine conditions. A scaled-down model of the sea chest structure was fabricated, as illustrated in Fig. 1. Two units were fabricated: one to serve as the control (without ultrasound), and the other equipped with the ultrasonic system. The coating process for these marine structures was carried out on both sides of the steel plate using abrasive blasting to near-white metal, in accordance with the ISO 8501-1 standard, achieving an anchor profile between $80\,\mu\mathrm{m}$ and $100\,\mu\mathrm{m}$. Next, the protective coating was applied to both sides of the plate. The procedure consisted of two coats of PETROBRAS N-2680 paint, with a minimum dry film thickness (DFT) of $150\,\mu\mathrm{m}$, followed by a single coat of PETROBRAS N-2677, with a minimum DFT of $70\,\mu\mathrm{m}$.

After assembly, the sea chest structures were transported to the pier, where the installation of the ultrasonic transducers and functionality tests were initiated. Eight holes were drilled on the face of each sea chest to accommodate the transducers, resulting in the installation of eight transducer units per structure. The transducers were designed and constructed to operate at a frequency of 21 kHz, and each unit was supplied with an electrical power of approximately 250 W. The structures were submerged in the sea at a depth of approximately 1 meter, with the grated face oriented toward the sunrise. Fig. 2 shows an image of the transducer installation process on the sea chest structures.

DOI 10.5162/Ultrasonic2025/D6-a4

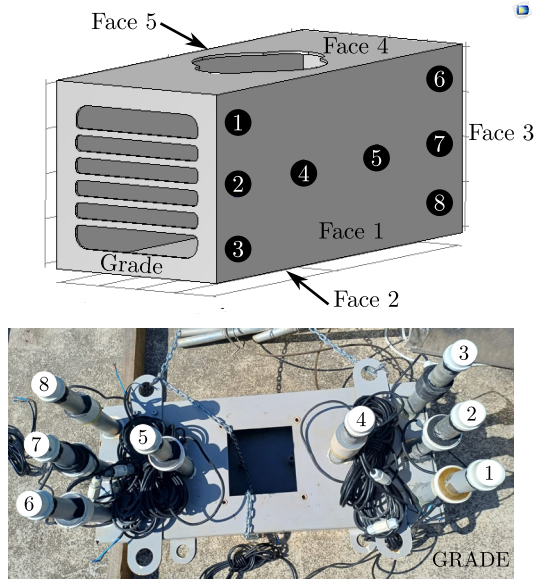

Fig. 2: Installation process of ultrasonic transducers in the sea chest structure, illustrating the transducer arrangement.

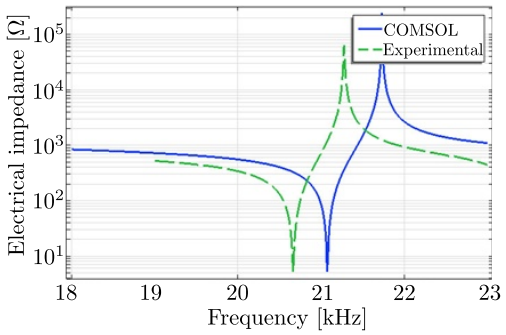

Fig. 3: Comparison between simulated and experimentally measured electrical impedance curves for the ultrasonic transducer.

Results

Before conducting the biofouling prevention tests on the sea chest structures, it was necessary to experimentally characterize the transducer designed through numerical simulations. The transducers were assembled, and their electrical impedance curves were measured under laboratory conditions. The experimental results were compared to the simulated impedance curves to validate the numerical model. Fig. 3 presents this comparison, showing good agreement between the numerical and experimental results. The minor discrepancies observed between the curves are attributed to variations in material properties used in the simulation model.

After the transducers were characterized, tests were initiated to evaluate the use of ultrasound for biofouling prevention in the sea chest structure. Although eight transducers were mounted, only four units were excited during the experiment, each powered at an average electrical power of 250 W. The remaining transducers were installed as backups, intended to replace any units that might become damaged or non-functional during testing. For this experimental campaign, transducers 1, 2, 3, and 7 were activated.

Position	Signal	Pressure
Grade	10 Vpp	380 kPa
Face 1	20 Vpp	760 kPa
Face 2	8 Vpp	304 kPa
Face 3	12 Vpp	456 kPa
Face 4	15 Vpp	570 kPa
Face 5	5 Vpp	190 kPa

Tab. 1: Acoustic measurement data at different positions inside the sea chest.

The acoustic pressure inside the sea chest was measured using a calibrated hydrophone (model: Brüel & Kjær). Table 1 presents the pressure values measured at a central point on each internal face of the structure, representing an average position within the volume.

The field experiments were conducted through daily monitoring, using photographic records of each internal face of the submerged sea chests with and without ultrasonic treatment. The ultrasonic system was programmed to operate in cycles, activating the transducers for 10 minutes followed by 15 minutes off, continuously over a 30-day period. All regions on the inner surfaces of both the ultrasound-treated and control sea chests were selected to monitor biofouling development.

Figure 4 presents the evolution of biofouling on Face 3, located at the end of the sea chest, for both the control (without ultrasound) and the ultrasound-treated structure. After 30 days of submersion, the sea chest equipped with the ultrasonic system exhibited only a small amount of algal fouling, with no significant colonization by macrofouling organisms. In contrast, the control structure showed visible colonization by various microorganisms, including bryozoans and barnacles. The appearance of barnacle fouling was first observed on day 17, indicating the settlement phase of these organisms on the untreated surface. A similar pattern was observed on Face 5, as shown in Fig. 5.

Conclusion

The study demonstrated the feasibility and effectiveness of using high-power ultrasonic transducers to mitigate biofouling in subaquatic structures commonly

DOI 10.5162/Ultrasonic2025/D6-a4

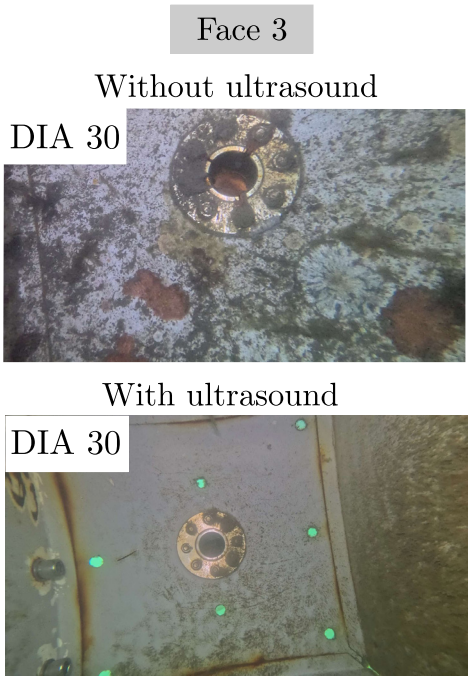

Fig. 4: Photographic comparison of biofouling evolution on Face 3 of the sea chest after 30 days of submersion, with (right) and without (left) ultrasound application

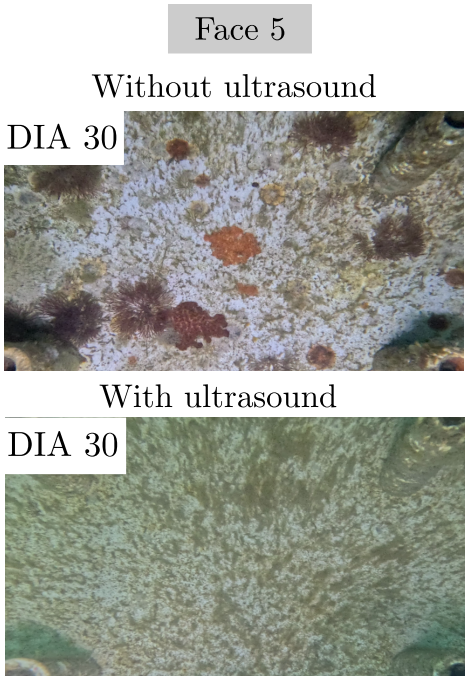

Fig. 5: Biofouling development on Face 5 of the sea chest under control conditions (without ultrasound) after 30 days, highlighting the presence of barnacles and bryozoans.

employed in the oil and gas industry, such as sea chests. Numerical simulations guided the design of half-wavelength Langevin transducers, which were validated experimentally through electrical impedance measurements. Field experiments conducted in a natural seawater environment revealed that the application of ultrasound significantly reduced biofouling, particularly the settlement of barnacles, when compared to control structures. After 30 days of exposure, the ultrasound-treated surfaces exhibited only minimal algal colonization, while control surfaces showed substantial fouling by macroorganisms

References

[1] N. Aldred et al. "The effects of a serine protease, Alcalase, on the adhesives of barnacle cyprids (Balanus amphitrite)." In: *Biofouling* 24 (2 2008).

[2] D. M. Yebra, S. Kiil, and K. Dam-Johansen. *Antifouling technology - Past, present and future steps towards efficient and environmentally friendly antifouling coatings*. 2004.

[3] R. E. Apfel. "Sonic effervescence: A tutorial on acoustic cavitation". In: *The Journal of the Acoustical Society of America* 101 (3 1997).

[4] J. Frohly et al. "Ultrasonic cavitation monitoring by acoustic noise power measurement". In: *The Journal of the Acoustical Society of America* 108 (5 2000).

[5] J. E. Gittens et al. "Current and emerging environmentally-friendly systems for fouling control in the marine environment". In: *Biotechnology Advances* 31 (8 2013).

[6] N. Oulahal-Lagsir et al. "The development of an ultrasonic apparatus for the noninvasive and repeatable removal of fouling in food processing equipment". In: *Letters in applied microbiology* 30 (1 2000), pp. 47–52.

[7] Z. Liang et al. "Study of low-frequency ultrasonic cavitation fields based on spectral analysis technique". In: *Ultrasonics* 44 (1 2006).

[8] N. Seth et al. "Quantification of the energy required for the destruction of Balanus amphitrite larva by ultrasonic treatment". In: *Journal of the Marine Biological Association of the United Kingdom* 90 (7 2010).

[9] S. Guo et al. "Effect of ultrasound on cyprids and juvenile barnacles". In: *Biofouling* 27 (2 2011).

DOI 10.5162/Ultrasonic2025/D6-b2

Phase-controlled array of ultrasonic transducers for active focusing of waves in air. Applied to foam abatement

R. Galleguillos-Silva[1], *C. Leon-Montalva*[1], *E. Cancino-Jaque*[2], *J. Meneses-Diaz*[2], *M. Carrion-Acuña*[2], *Y. Vargas-Hernandez*[2], *and L. Gaete-Garreton*[2]
[1] *Universidad Finis Terrae, Av. Pedro de Valdivia 1509, Providencia, Chile*
[2] *Universidad de Santiago de Chile, Av. Libertador Bernardo Ohiggins 3363, Estacion Central, Chile*
rgalleguillos@uft.cl

Abstract: This work presents the development and experimental validation of an annular array of 56 ultrasonic transducers operating at $25\,\mathrm{kHz}$ for contactless industrial foam abatement. Through phase control algorithms, the system achieves acoustic focusing in air, generating pressure levels exceeding $150\,\mathrm{dB}$ SPL at the focal point. Experimental results demonstrate successful foam disruption capabilities, and the scalability was also validated through numerical simulations in COMSOL Multiphysics and laboratory testing.

Keywords: Airborne ultrasound, phased array, acoustic focusing, industrial foam abatement, piezoelectric transducers.

Background, Motivation, and Objective

Industrial foam elimination has been a persistent challenge in numerous sectors, including food processing, pharmaceuticals, petroleum refining, and pulp manufacturing [1, 2]. Foam formation can lead to product losses, reduced equipment efficiency, and operational failures [3]. Traditional defoaming methods are based on chemical additives or mechanical approaches, which can introduce contamination risks or require significant maintenance [4].

Ultrasonic technology offers a promising non-invasive alternative for foam control. Although extensively studied in liquid and solid media for degassing and bubble disruption [5], airborne ultrasound applications face significant challenges due to high acoustic impedance mismatch and transmission losses in air [6]. Recent advances in phased array systems have demonstrated the feasibility of generating high intensity focused ultrasound (HIFU) in air through constructive interference [7].

Annular array configurations are particularly advantageous for acoustic focusing due to their radial symmetry, which enables efficient energy concentration along the central axis [8]. This geometry facilitates the generation of symmetric focal patterns essential for precise targeting applications. In this paper, the development of an active control system using airborne ultrasound specifically designed for contactless industrial foam abatement is presented. The primary objective is to verify whether a low-frequency ultrasonic annular array can generate sufficient acoustic intensities in air to destabilize industrial foam without physical contact or chemical additives.

Prototype Design and Construction

An annular phased array prototype was designed comprising 56 piezoelectric ultrasonic transducers with a nominal frequency of $25\,\mathrm{kHz}$ and a diameter of $16\,\mathrm{mm}$. The transducers were mounted on a rigid $140 \times 140\,\mathrm{mm}$ PCB, arranged in eight concentric rings with radial symmetry to promote acoustic focus along the central axis.

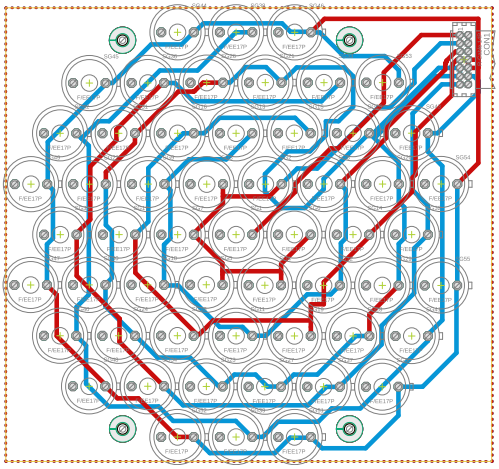

Fig. 1: PCB layout of the ultrasonic transducers developed for this research. Each transducer can be identified, arranged in a hexagonal array, which achieves the highest spatial density.

The geometric configuration formed by eight groups of transducers, each one is separated $18\,\mathrm{mm}$ from its neighbors, following a hexagonal pattern, Fig. 1. Each concentric group was powered by individual electronic

DOI 10.5162/Ultrasonic2025/D6-b2

stages capable of applying to each group of concentric transducer specific the phase delays. The delays were calculated for each radial group of transducers, considering their position with respect to the desired focal point. In this opportunity, the focal point was located $95\,\mathrm{mm}$ above the array center. Phase delays were determined using spherical wave propagation models in air, considering a propagation velocity of $343\,\mathrm{m/s}$, and rounding the values to integers of microseconds, which is the resolution of the developed electronic system.

Transducer excitation was achieved through H-bridge amplifiers optimized for proper impedance matching between signal sources and transducers. Control and synchronization were implemented using a Teensy 4.0 microcontroller programmed via Arduino IDE with custom libraries for precision timing control.

Numerical Simulation

A three-dimensional numerical model was developed in COMSOL Multiphysics using the Pressure Acoustics Module to predict the acoustic field produced by the device and compare this prediction with the experimental results. The model represents the whole system geometry: an air volume of $150 \times 80 \times 80\,\mathrm{mm}$ above the array plane with transducers arranged in concentric rings, replicating prototype dimensions and pressure scanning zone.

To optimize computational time, quarter of the transducers were included in the simulation. This simplification was justified by the radial symmetry of the array. The air domain was modeled as compressible medium with density $\rho = 1.22\,\mathrm{kg/m^3}$ and sound velocity $c = 343\,\mathrm{m/s}$. Operating frequency was set at $25\,\mathrm{kHz}$, corresponding to the used transducer.

Each transducer was modeled as a normalized pressure source with specific phase delays according to radial position for focusing energy at $95\,\mathrm{mm}$ height above array center. Open radiation boundary conditions were imposed on lateral and upper walls to prevent unwanted reflections.

Experimental Characterization

Because the acoustic field is axially symmetric, two-dimensional acoustic field measurements were enough to its characterization. The measurements were performed using a 1/8" condenser microphone (B&K Type 4138) mounted on a motorized XZ positioning system. The scanning system moved in $2.5\,\mathrm{mm}$ steps along both the X and Z axes over a two-dimensional grid. In the Fig. 2 the transducer array mounted in its scanning system can be appreciated. During the scanning, at each measuring point, acoustic pressure amplitudes were recorded, enabling reconstruction of the spatial pressure field profile generated by the array,

Fig. 2: Acoustic field characterization setup, showing an array of ultrasonic transducers. On the left edge of the array, the tip of the microphone waveguide can be distinguished, which is arranged horizontally and attached to the two-dimensional scanning system.

assuming rotational symmetry in the acoustic field. In this way, measurements were made to characterize the acoustic pressure in the perpendicular plane centered on the central axis of the array. This allowed quantification of system performance with all transducers emitting waves with phase delays calculated for focus the acoustic field at the desired position.

Results

COMSOL Multiphysics simulation revealed an acoustic pressure distribution in the XZ plane, clearly showing constructive interference patterns converging at a focal axis approximately $95\,\mathrm{mm}$ from the emitter plane (Fig. 3). The maximum amplitude reached values around 1 normalized unit of pressure, confirming the formation of a high-pressure focused lobe. This behavior validates the design parameters calculations for concentrating acoustic energy at a specific point in airspace for interaction with sensitive materials such as industrial foams.

Measurements

The acoustic field, measured with the two-dimensional scanning system, reveals an acoustic field consistent with the desired characteristics. In fact, the acoustic field reproduced expected behavior with a well-defined focal axis and maximum pressure exceeding $800\,\mathrm{Pa}$ (Fig. 4), corresponding to sound pressure levels above $145\,\mathrm{dB}$ SPL at the focal point. These measurements experimentally validate the constructive interference principle induced by phase control applied to the annular array. The spatial distribution obtained confirms the capability of the system to concentrate acoustic energy at predetermined locations with intensities

DOI 10.5162/Ultrasonic2025/D6-b2

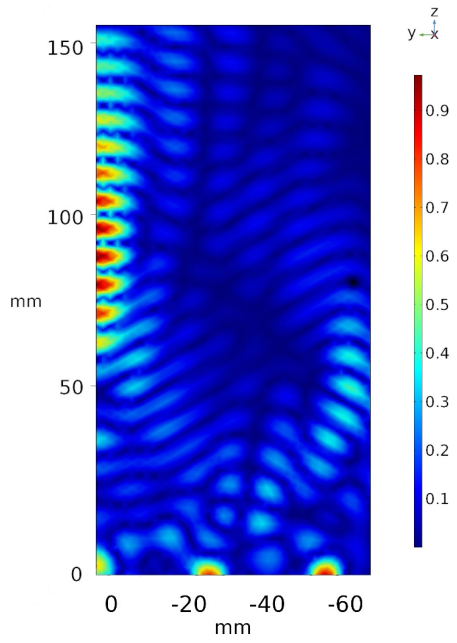

Fig. 3: Result of the acoustic field simulation. In the lower left corner is the central transducer, just above which is the line of maximum expected pressure, the focusing axis. The pressure is normalized, so the scale in the graph is relative as long as the linearity of the medium is maintained.

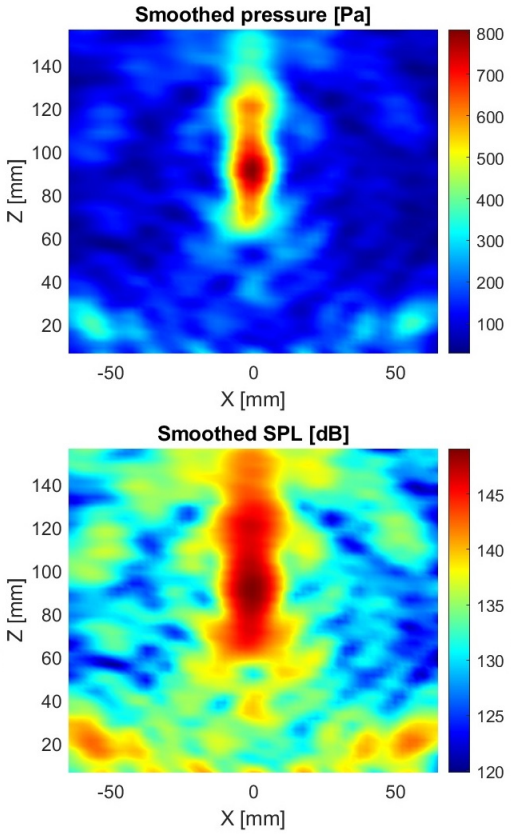

Fig. 4: Result of the acoustic pressure scan based on the X and Z coordinates, in the vertical plane of the array. The maximum pressure obtained under these excitation conditions is over $800\ \mathrm{Pa}$ *and* $145\ \mathrm{dB}$ *SPL.*

high enough for defoaming processes. These results are particularly promising in applications where chemical additives or physical contact are undesirable.

Due to the encouraging results obtained in the first field measurements, we are looking for the limits of the developed system. The power limitation of the generator was established in terms of the maximum feed current allowable without achieving system saturation. This current turned out to be approximately $250\,\mathrm{mA}$. Because the system is operating in its linear regime, the current fits the displacement of the transducers and also the acoustic pressure generated. The maximum acoustic pressure capability performed, based on the excitation current consumed by the array, turned out to be the power limitation of the generator was established in terms of the maximum feed current allowable without achieving system saturation. This current turned out to be approximately $250\,\mathrm{mA}$ of about $1000\,\mathrm{Pa}$ and $150\,\mathrm{dB}$ SPL, as shown in Fig. 5.

Foam Disruption Validation

Practical system effectiveness was evaluated by foam breaking tests in an experimental tank. Results demonstrated a clearly delimited opening in the foam. Because the very poor contrast between the foam and the surrounding space, to facilitate the observation of foam breaking the acoustic field was applied in an edge of a borosilicate container. According to predict results a zone, corresponding to the focal axis shows clearly, a foam disruption process. These findings indicate the system's capability to concentrate acoustic energy at specific points with relevant intensity enough to initiate foam destabilization processes. Fig. 6 shows the foam breakup after $0.6\,\mathrm{s}$ of exposure.

Analysis suggests that scaling up the number of transducers or redesigning electronic stages could substantially increase achievable acoustic intensity, approaching levels required for industrial environments.

Conclusions

Results confirm the hypothesis that an annular array of small ultrasonic transducers with phase control can generate effective airborne wave focusing, producing acoustic pressure levels relevant for foam elimination applications. Simulations and experiments validate system capability to concentrate energy at desired points, opening possibilities for scaling this technology toward industrial applications.

DOI 10.5162/Ultrasonic2025/D6-b2

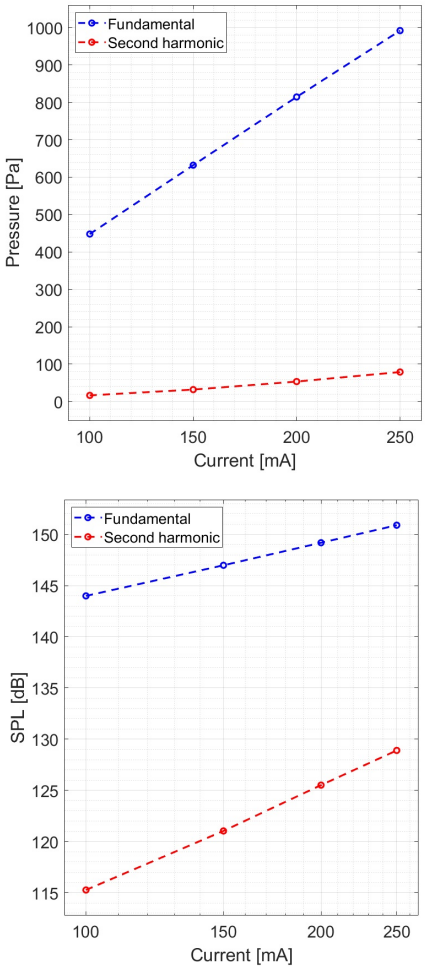

Fig. 5: Acoustic pressure curve as a function of the current consumed by the array, for the fundamental frequency and the second harmonic. It is necessary to remember that the excitation signal is square, so it was necessary to characterize the second harmonic in addition to the fundamental frequency.

Although achieved levels remain below those used in robust industrial systems, the proposed system's simplicity, energy efficiency, and scalability potential make it a viable alternative for environments requiring non-invasive, chemical-free solutions with low maintenance requirements. The natural next step involves scale up and experimental validation with actual foam under applied conditions to directly evaluate effectiveness in real-world scenarios.

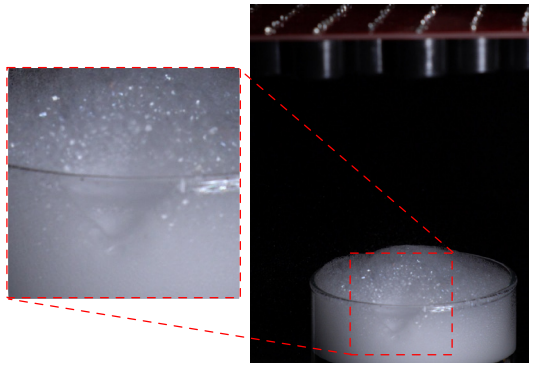

Fig. 6: Photograph of the effects of high-intensity radiation applied to soap foam generated by pressurized air injection. The exposure time required to generate this effect is only $0.6\,\mathrm{s}$. The developed array of ultrasonic transducers can be seen above.

References

[1] M. J. Owen. "Antifoaming Agents". In: *Encyclopedia of Polymer Science and Technology*. John Wiley Sons, Ltd, 2001. ISBN: 9780471440260.

[2] R. J. Pugh. *Bubble and Foam Chemistry*. Cambridge University Press, 2016.

[3] C. M. Charoux et al. "Applications of airborne ultrasonic technology in the food industry". In: *Journal of Food Engineering* 208 (2017), pp. 28–36.

[4] J. M. S.M. Deotale S. Dutta. "Foaming and defoaming–concepts and their significance in food and allied industries: a review". In: *Discover Chemical Engineering* 3 (2023).

[5] J. A. Gallego-Juarez. "High-power ultrasonic processing: Recent developments and prospective advances". In: *Physics Procedia* 3.1 (2010). International Congress on Ultrasonics, Santiago de Chile, January 2009, pp. 35–47. ISSN: 1875-3892.

[6] A. Marzo et al. "Holographic acoustic elements for manipulation of levitated objects". In: *Nature Communications* (2015).

[7] T. Fushimi et al. "Acoustophoretic volumetric displays using a fast-moving levitated particle". In: *Applied Physics Letters* 115.6 (2019).

[8] J. W. Hand et al. "A random phased array device for delivery of high intensity focused ultrasound". In: *Physics in Medicine Biology* 54.19 (Sept. 2009), p. 5675.

DOI 10.5162/Ultrasonic2025/E2-a1

Coupling of elastic waves and voltage waveforms in monopole ALWD: role of piezoelectricity and acoustic propagation

Chao Zhang[1], *Zihao Chen*[1], *and Wei Guan*[1]
[1]*Harbin Institude of Technology, Academy of Astronautics, Harbin, China*
corresponding.guanw@hit.edu.cn

Abstract: Acoustic Logging While Drilling (ALWD) acoustic measurement, characterized by combining drilling and logging operations, is widely used to obtain elastic parameters of formation surrounding the borehole. Most published simulated monopole acoustic LWD waveforms are typically represented by acoustic pressure. However, these pressure waveforms do not match the voltage waveforms recorded experimentally. To investigate this discrepancy, we employed the finite element method to comprehensively calculate both the piezoelectric effects of transducers and acoustic wave propagation, obtaining voltage waveforms and mechanical waveforms. Quantitative comparisons between mechanical and voltage waveforms reveal that the output voltage does not represent pressure signals alone but rather constitutes a combination of multiple mechanical signals. Based on piezoelectric equations and the structure of piezoelectric transducers used in this study, we systematically investigated the coupled effects of four mechanical quantities on output voltage: radial strain and axial stress (reflecting formation information), as well as acoustic pressure and radial displacement in borehole fluid (indicating interference effects from measurement tools). Further analysis explores the respective contributions of these four mechanical quantities to different wave groups. This research provides valuable insights for understanding the coupling mechanisms between elastic waves in logging applications.

Keywords: Acoustic logging while drilling (LWD), boundary condition, piezoelectric effect, elastic waves, voltage waveforms

Methods

To better understand the relationship between mechanical quantities and the voltage received by the transducer, we've built a FEM model that combines the piezoelectric effect and acoustic wave propagation [**Zhang 2021**]. This integrated approach covers the entire process from voltage signal generation to acoustic wave propagation and back to voltage signal reception. In the radial direction, the FEM model is divided into four parts: the fluid inside the collar, the collar itself, the fluid outside the collar, and the formation.

The acoustic LWD tool includes a transmitting transducer and a receiving transducer placed 3 m apart. Both transducers, with identical geometric structures and surrounded by epoxy seals, are shallowly embedded in the outer surface of the drill collar. These tubular piezoelectric transducers are radially polarized. The inner wall of the piezoelectric ceramic tube is grounded, while the outer wall is connected to the excitation voltage.

In our multiphysics coupling model, we simultaneously simulate the acoustic field within the borehole fluid, the elastic field in solid materials, and the coupled mechanical and electrostatic fields in the piezoelectric ceramic tube.For boundary conditions, the fluid's far-field boundary employs a plane-wave-radiation condition [**Givoli 2004**] and the solid's far-field boundary uses a low-reflecting condition [**Lalanne 2000**]Both designs aim to minimize boundary reflections that could interfere with the simulation results. The mesh utilizes a free quadrilateral pattern. The maximum element size is determined by $v/(6f_0)$, where v represents the minimum wave velocity among all model materials, and f_0 denotes the center frequency of the excitation voltage. Model parameters and material properties are detailed in Tab. 1.

Fig. 1 presents the process of acoustic wave generation, propagation, and reception. When an excitation voltage signal is applied to the transmitter's outer electrode, the transmitter utilizes the inverse piezoelectric effect to convert the input voltage signal into various mechanical signals like strain $\boldsymbol{\varepsilon}$, stress $\boldsymbol{\sigma}$, displacement $\boldsymbol{u}$, particle velocity $\boldsymbol{v}$, and particle acceleration $\boldsymbol{a}$. The generated acoustic waves then propagate through the borehole and formations to reach the receiver. At the receiver, these mechanical

DOI 10.5162/Ultrasonic2025/E2-a1

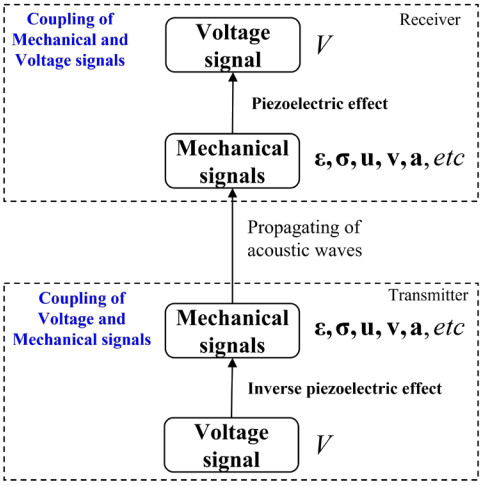

Fig. 1: The coupling process of excitation, propagation, and reception.

signals, which contain information about the borehole and formations, are transformed back into voltage signals via the piezoelectric effect and then outputted. Both the transmitter and receiver involve the coupling of elastic and voltage waveforms.

Tab. 1: Materials and geometric parameters of fluid, drill collar, piezoelectric transducer and formation

Component	ρ (kg/m^3)	v_p (m/s)	v_s (m/s)	Thickness (m)	Height (m)
Inner fluid	1000	1470	–	0.027	$+\infty$
Drill collar	7800	5860	3131	0.063	$+\infty$
PZT-5H	7500	4118	1751(SV) 1770(SH)	0.006	0.088
Epoxy	1500	3089	1589	0.010	0.120
Outer fluid	1000	1470	–	0.027	$+\infty$
Formation	2320	3970	2455	$+\infty$	$+\infty$

Waveforms difference between mechanical quantities and voltage

This section calculates the pressure, radial displacement, and voltage waveforms, considering the transducer's piezoelectric effect and acoustic wave propagation. To explore their differences and similarities, we set up three models:

$\boldsymbol{Model\ 1}$: The tube transducer is slightly indented 0.063 m from the collar's external surface, with the collar in infinite fluid.

$\boldsymbol{Model\ 2}$: The tube transducer is slightly indented 0.063 m from the collar's external surface, with the collar in a borehole.

$\boldsymbol{Model\ 3}$: The tube transducer is slightly indented 0.050 m from the collar's external surface, with the collar in a borehole.

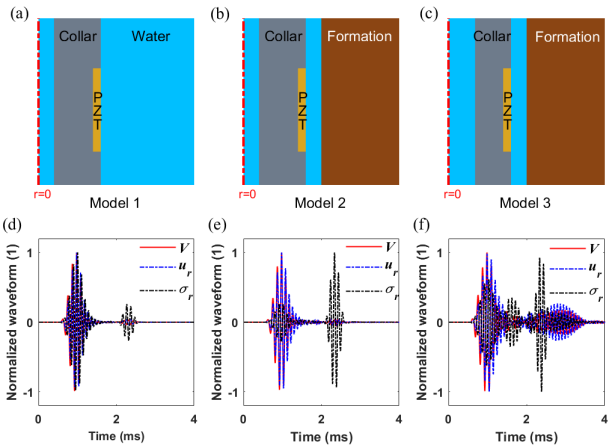

Fig. 2: The schematics of the three models show the voltage, radial displacement, and radial stress (negative pressure) waveforms. Figures (a) and (d) depict collars with a thickness of 0.063 m in infinite fluid. Figures (b) and (e) show collars with a thickness of 0.063 m in infinite boreholes. Figures (c) and (f) illustrate collars with a thickness of 0.050 m in boreholes. The voltage source has a center frequency of 10 kHz.

The voltage source used for the transmitting transducer is a cosine envelope pulse centered at 10 kHz. At the outer surface center of the receiver, the normalized waveforms of voltage, radial stress (negative pressure), and radial displacement were calculated. Fig. 2 presents the schematics of the three models and their corresponding normalized waveforms. Each waveform clearly shows two distinct waves: the collar wave and the Stoneley wave, ordered by their arrival time. In all three FEM models, the voltage waveforms exhibit similar characteristics, with a strong collar wave followed by a weak Stoneley wave. This pattern aligns with the voltage waveform characteristics observed in experimental recordings [**Zhu 2008**].

In Fig. 2d, with the collar in infinite fluid, both the pressure and radial displacement waveforms display a dominant collar wave and a minor Stoneley wave, mirroring the voltage waveform. In Fig. 2e, when the collar is positioned in a borehole, the radial displacement waveform continues to show a strong collar wave and a weak Stoneley wave, aligning with the voltage waveform. However, the pressure waveform in this case exhibits a weak collar wave and a strong Stoneley wave, conflicting with the voltage waveform. Comparing Fig. 2d and Fig. 2e reveals that the disparity between the voltage and pressure waveforms increases when a formation is present, primarily reflected in the relative amplitude of the collar wave. In Fig. 2f, a thinner collar in the borehole produces waveforms similar to those in Fig. 2e. The comparison

DOI 10.5162/Ultrasonic2025/E2-a1

between Fig. 2e and Fig. 2f shows that even with a reduced collar thickness, the voltage and pressure waveforms still exhibit significant differences, mainly in the relative amplitude of the collar wave.

Relation between four mechanical quantities and voltage

As established in the previous section, voltage is more likely to be generated from a combination of multiple mechanical quantities rather than a single one. This raises two key questions: which specific mechanical quantities are involved in this conversion, and what are the respective weights of these quantities? To address these questions, this section delves into the piezoelectric equations for an in-depth exploration.

$$\begin{cases} \varepsilon_\theta = s_{11}^E \sigma_\theta + s_{12}^E \sigma_z + s_{13}^E \sigma_r + d_{31} E_r \\ \varepsilon_z = s_{12}^E \sigma_\theta + s_{11}^E \sigma_z + s_{13}^E \sigma_r + d_{31} E_r \\ \varepsilon_r = s_{13}^E \sigma_\theta + s_{13}^E \sigma_z + s_{33}^E \sigma_r + d_{33} E_r \end{cases} \tag{1}$$

Here, $s_{1i}, i = 1, 2, 3$, and $d_{3j}, j = 1, 2, 3$, represent the compliance coefficient and piezoelectric constant of the piezoelectric ceramic tube, respectively. E_r denotes the radial electric field intensity, ε represents strain, and σ indicates stress. The subscripts r, z, and θ correspond to the radial, axial, and circumferential components, respectively.

For a radially polarized thin tube piezoelectric transducer,

$$V = \delta E_r \tag{2}$$

$$\varepsilon_\theta = \frac{u_r}{r} \tag{3}$$

Here, δ denotes the thickness of the piezoelectric ceramic, and r represents the distance between the outer wall of the transducer and the borehole axis.

Thus, the voltage V can be expressed in terms of four mechanical quantities selected from u_r, ε_z, ε_r, σ_θ, σ_z, and σ_r. Note that these mechanical quantities pertain to the piezoelectric ceramics in the transducer. However, in acoustic LWD, the transducer is intended to sense the mechanical quantities of the borehole fluid. According to the boundary conditions, radial displacement u_r and radial stress σ_r are continuous between the transducer and the borehole fluid, making them representative of the borehole fluid's mechanical quantities. Additionally, radial strain ε_r and axial strain ε_z have shown high similarity to voltage waveforms, making them preferable candidates. Consequently, u_r, σ_r, ε_r, and ε_z are chosen to represent the voltage, and the expression for V is obtained as follows:

$$V = V_1 + V_2 + V_3 + V_4 \tag{4}$$

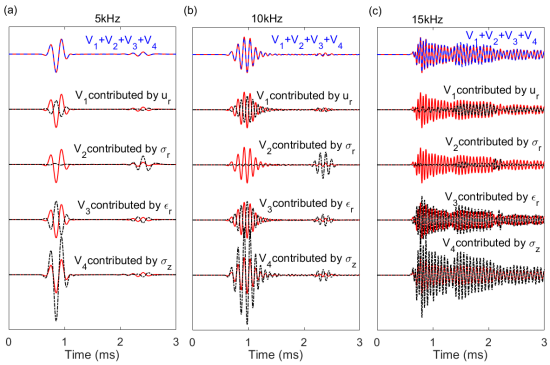

Fig. 3: The contributions of u_r, σ_r, ε_r, and σ_z to voltage V at three distinct center frequencies: (a) 5 kHz, (b) 10 kHz, and (c) 15 kHz, are analyzed. The black dotted lines denote the voltage components V_1, V_2, V_3, and V_4, which are contributed by u_r, σ_r, ε_r, and σ_z, respectively. The blue dashed lines illustrate the combined sum of these four voltage components. For comparison, the red solid lines indicate the actual voltage V recorded by the transducer.

with,

$$\begin{aligned} V_1 &= \frac{s_{13}\delta}{r\left(s_{13}d_{31} - s_{11}d_{33}\right)} u_r \\ V_2 &= -\frac{\left({s_{13}}^2 - s_{11}s_{33}\right)\delta}{s_{13}d_{31} - s_{11}d_{33}} \sigma_r \\ V_3 &= -\frac{s_{11}\delta}{\left(s_{13}d_{31} - s_{11}d_{33}\right)} \varepsilon_r \\ V_4 &= -\frac{s_{13}\left(s_{12} - s_{11}\right)\delta}{s_{13}d_{31} - s_{11}d_{33}} \sigma_z \end{aligned} \tag{5}$$

Eq. (4) presents the voltage V obtained by substituting Eq. (1) and Eq. (3) into Eq. (2). Eq. (5) depicts the voltage components associated with the four mechanical quantities illustrated in Fig. 3. For a transducer with a known material composition and dimensions, the weight coefficients of these mechanical quantities in the voltage components are well - defined. At the boundary between the transducer and the borehole fluid, the radial displacement of the transducer equals that of the fluid, and the transducer's negative radial stress corresponds to the fluid's acoustic pressure. Hence, the first two voltage components in Eq. (4) represent the weighted radial displacement and acoustic pressure of the borehole fluid, offering insights into borehole and formation characteristics. Conversely, the last two components reflect the transducer's radial strain and axial stress, which indicate tool-related interference. To enhance formation information and mitigate tool interference, the material properties and dimensions of the transducer can be optimized. This optimization aims to increase the

weighting of the first two voltage components while reducing the weighting of the last two in Eq. (4).

Eq. (5) presents how u_r, σ_r, ε_r, and ε_z contribute to the voltage. We computed the waveforms of these four voltage components under different voltage excitation center frequencies, results shown in Fig. 3. The figure includes the waveforms of the four mechanical quantities and voltage. The black dash - dotted lines indicate the voltage components V_1, V_2, V_3, and V_4 from u_r, σ_r, ε_r, and ε_z, calculated by weighting the mechanical quantity waveform data per Eq. (5). The blue dashed line shows the sum of the four voltage components ($V_1 + V_2 + V_3 + V_4$), and the red solid line represents the voltage waveform V from the finite element model.

From the top waveforms (red and blue lines) in each subplot of Fig. 3, it is evident that the voltage waveform V at different frequencies aligns with the waveform of the total four voltage components. This matches the result in Eq. (4). Comparing the amplitudes of the voltage waveform and the four voltage component waveforms (red line vs. black lines) shows that u_r, ε_r, and σ_z significantly contribute to the drill collar wave and are key for studying its characteristics. Meanwhile, σ_r has a smaller contribution to the drill collar wave but a larger one to the Stoneley wave. This might relate to using the Stoneley wave to invert formation permeability.

Conclusions

By considering both the piezoelectric effect of the transducer and the propagation of the acoustic wave, we simulate the mechanical responses and output voltage in monopole acoustic LWD. The main conclusions include the following:

The output voltage recorded by the transducer results from an acoustic-voltage coupling process, jointly contributed by multiple mechanical quantities via the piezoelectric effect rather than a single physical parameter. Borehole fluid radial displacement and radial stress carry formation information, while transducer radial strain and axial stress reflect tool interference. This coupling mechanism necessitates receiver designs that amplify the weighting factors of formation-information carriers (radial displacement/stress) during electroacoustic transduction, while suppressing the coupled influence of tool-interference terms (radial strain/axial stress) to effectively extract target formation signals.

Decoupling the contributions of individual mechanical quantities to the output voltage waveform reveals that the acoustic-voltage coupling selectively reconstructs waveform features. The collar wave is dominated by strong coupling pathways from borehole fluid radial displacement, transducer radial strain, and axial stress, whereas the Stoneley wave is primarily governed by a specific coupling channel from borehole fluid radial stress. This demonstrates how differential coupling intensities of mechanical quantities during electromechanical conversion directly shape the voltage waveform's characteristic amplification of collar waves and suppression of Stoneley waves.

Acknowledgments

This work was supported in part by the National Key R&D Program of China under Grant 2023YFF0720700, and in part by the National Natural Science Foundation of China under Grants 42404125 and 42474141.

References

[1] D. Givoli and B. Neta. "High-order Non-reflecting Boundary Scheme for Time-dependent Waves". In: *Journal of Computational Physics* 86(2004), pp.24–46. DOI: 10.1016/S0021-9991(03)00005-6

[2] B. Lalanne and M. Touratier. "Aeroelastic Vibrations and Stability in Cyclic Symmetric Domains". In: *International Journal of Rotating Machinery* 6(2000), pp.445–452. DOI: 10.1155/S1023621X00000403

[3] C. Zhang, D. Chen, and H. Hu. "The mechanical responses in monopole acoustic LWD and their relation with the output voltage waveform". In: *Journal of Geophysics and Engineering* 18(2021), pp.712–724.

[4] Z. Zhu, M. N. Toksöz, and R. Rao, et al. "Experimental studies of monopole, dipole, and quadrupole acoustic logging while drilling (LWD) with scaled borehole models". In: *Geophysics* 73(2008), pp.E133-E143. DOI: 10.1190/1.2919827.

DOI 10.5162/Ultrasonic2025/E2-a2

Neural network method for inversion of S-wave velocity in soft formation from monopole acoustic logging signals

Wanting Lin[1] *and Hengshan Hu*[1]
[1]*Harbin Institute of Technology, Harbin, Heilongjiang, China*
hhs@hit.edu.cn

Abstract: It is generally believed that the monopole acoustic logging cannot be used to invert the S-wave velocity in a soft formation. However, the theoretically synthesized pressure waveform of monopole acoustic logging changes obviously with S-wave velocity, indicating a correlation between the two. This paper uses one-dimensional convolution neural network to invert the S-wave velocity. In the absence of dipole S-wave logging data, S-wave velocity is inverted with less than 2% error through the full waveform of monopole acoustic logging.

Keywords: neural network, S-wave velocity, soft formation, monopole acoustic logging, borehole.

Introduction

S-wave velocity serves as an important basis for calculating rock mechanics parameters, stress parameters, and formation anisotropy. It is still necessary to predict S-wave velocity using monopole logging data [1]. Although dipole acoustic logging is currently employed, a large amount of existing old data only contains monopole logging data. Hence, accurately obtaining S-wave velocity is of crucial importance. It is generally believed that the critically refracted S-wave arrivals cannot be received in boreholes within soft formations. Although it has been proven that critically refracted S-waves can exist in boreholes within soft formations [2], such inhomogeneous waves attenuate rapidly as they move away from the borehole wall, making them difficult to be detected by receivers located on the borehole axis. Wu [3] used the low - frequency approximate formula of Stoneley wave velocity obtained under different formation medium models and logging sonde configurations to invert the formation S-wave velocity. However, when the source frequency is higher than 5 kHz or in the case of a harder formation, this approximate formula cannot effectively reflect the relationship between the Stoneley wave velocity and the S-wave velocity. Cheng [4] proposed a method for obtaining S-wave velocity from critically refracted P-waves in acoustic logging within formations where critically refracted S-waves or pseudo-Rayleigh waves do not exist. However, when there are errors in the input parameters when the input parameters of the inversion algorithm (such as P-wave velocity and formation density) are not accurate enough, the accuracy of the inverted S-wave velocity will also decrease. The works documented in references [3][4] represent efforts to invert for S-wave velocity in scenarios where independent S-waves or pseudo-Rayleigh waves are unavailable. However, relying solely on individual characteristics of the full waveform makes it challenging to achieve S-wave velocity inversion with sufficient accuracy, as the one-to-one correspondence between these individual full-waveform features and S-wave velocity remains unclear. For this reason, this paper avoids individual characteristics of the waveform and attempts to invert the S-wave velocity from the entire wave train itself.

This paper leverages a one-dimensional convolutional neural network (1D-CNN) [5] to address the issue of S-wave velocity inversion in monopole acoustic logging. Given the close interrelationship among P-wave velocity, density, and S-wave velocity [6], we opt to invert these three parameters simultaneously to enhance the stability and accuracy of the inversion algorithm. First, we analyze the feasibility of S-wave velocity inversion in soft formations. Next, we employ an analytical algorithm to synthesize full-waveform curves and construct a dataset. Ultimately, we develop a 1D-CNN to achieve the inversion of formation P-wave velocity, S-wave velocity, and density.

Feasibility Analysis of Inversion for S-wave Velocity

Fig. 1 illustrates a monopole acoustic logging model. In this model, the cylinder represents the well hole. The transmitter located at the origin serves as a point-expanding acoustic source. The dashed lines in the figure depict the propagation paths of the head waves that first arrive at the receivers. The acoustic pressure expression at the borehole axis is given as

DOI 10.5162/Ultrasonic2025/E2-a2

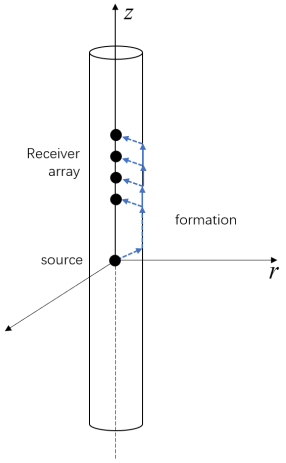

Fig. 1: Monopole acoustic logging model

follows [7],

$$p(z,t) = \frac{1}{2\pi^2}\int_{-\infty}^{\infty}\left[\frac{e^{ik_z z}}{z} + \frac{1}{\pi}\int_{-\infty}^{\infty} A(k_z,\omega)\, e^{ik_z z} dk_z\right] \times X(\omega)\, e^{-i\omega t} d\omega. \tag{1}$$

Among them, p represents the acoustic pressure at the well axis, $X(\omega)$ represents the frequency spectrum of the time function of the acoustic source, and $A(k_z,\omega)$ is the reflection coefficient of the wellbore wall. The expressions for S-wave velocity and P - wave velocity are respectively as follows,

$$v_s = \sqrt{G/\rho}, \tag{2}$$

$$v_p = \sqrt{(\lambda + 2G)/\rho}. \tag{3}$$

The low-frequency approximation formula for the phase velocity of Stoneley waves in the elastic formation surrounding the wellbore is presented as follows [8],

$$v_t{}^2 = \frac{v_f{}^2}{1 + \frac{\lambda+2G}{G}}. \tag{4}$$

Here, v_s represents the S-wave velocity of the formation outside the borehole, v_p is the P-wave velocity of the formation outside the borehole, v_f denotes the velocity of the fluid inside the borehole, v_t stands for the Stoneley wave velocity, G is the shear modulus of the formation, λ is the Lamé parameter of the formation, and ρ is the density of the formation. The shear modulus appears not only in the expression for S-wave velocity but also in those for P-wave and Stoneley-wave velocities. From the expression for S-wave velocity, it can be seen that when the density is fixed, the S-wave velocity varies with the shear modulus. Consequently, it can be inferred that the waveforms of both P-waves and Stoneley waves contain information related to the formation shear modulus.

Tab. 1: Wellbore fluid and formation parameters

	ρ (kg/m^3)	v_p (m/s)	v_s (m/s)
Wellbore fluid	1000	1500	–
Formation 1	2000	2300	900
Formation 2	2000	2300	1100

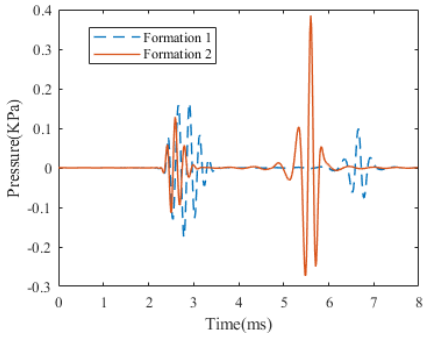

Fig. 2: Comparison of full-wave curves in soft formation

Then, the full-waveform curves of the acoustic pressure received at the well axis under two different soft formation conditions were calculated using the real-axis integration method [9]. The only difference between formation 1 and formation 2 is the S-wave velocity. The parameters of the fluid within the wellbore and the formations surrounding the wellbore are presented in Tab. 1. The radius of the wellbore is 0.1 m. The acoustic source is a cosine envelope pulse with a center frequency of 6 kHz and a half bandwidth of 4 kHz. The acoustic pressure amplitude at a distance of 0.01 m from the acoustic source was set to 100 kPa. In Fig. 2, the solid line represents the full acoustic pressure wave waveform curve received when the formation surrounding the borehole is Formation 2. As shown in Fig. 2, the first arrival is the critically refracted P-wave, followed by the Stoneley wave. In contrast, the dashed line depicts the acoustic pressure waveform corresponding to Formation 1. It can be seen that there is no S-wave waveform in Fig. 2. However, when the S-wave velocity is reduced from 1100 m/s to 900 m/s while keeping the other parameters of the formation unchanged, the amplitude of the P-wave increases and its duration becomes longer, while the amplitude of the Stoneley wave decreases and its arrival time becomes earlier. Clearly, both the P-wave and the Stoneley wave are related to the S-wave velocity. Some scholars have attempted to invert the S-wave velocity of the formation from the characteristics of the P-wave and the Stoneley wave. For example, Zhou [10] used the amplitude of the P-wave to solve for the S-wave velocity in the formation.

DOI 10.5162/Ultrasonic2025/E2-a2

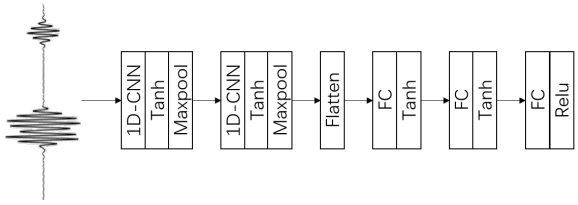

Fig. 3: 1D-CNN model

Wu [3] inverted the S-wave velocity of the formation using the low-frequency approximation formula of the Stoneley wave velocity obtained under different formation medium models and logging acoustic systems.

Although variations in S-wave velocity can induce changes in the full - waveform curve, the relationship between them is difficult to represent using a single characteristic of the wave. Therefore, we establish the relationship between the full - waveform curve and S-wave velocity with the aid of a one - dimensional Convolutional Neural Network (1D-CNN). Even when the receiver in a soft formation fails to detect a separate S wave, it is expected to invert the S-wave velocity from the waveforms of P-waves and Stoneley waves by 1D-CNN.

1D-CNN for Formation Parameters Inversion

This paper, based on the monopole acoustic logging model shown in Fig. 1, employs the real-axis integration method to compute multiple full-waveform curves using P-wave velocity, S-wave velocity, density, and other borehole parameters. In the dataset, we calculated full-waveform curves not only in soft formations but also in hard formations, with the expectation that the 1D-CNN could simultaneously invert the P-wave and S-wave velocities as well as the density of both soft and hard formations. These curves are then consolidated into a dataset comprising a total of 24,754 entries. During neural network training, 80% of the data from the dataset is randomly selected as the training set, 10% as the validation set, and the remaining 10% as the test set.

The one-dimensional convolutional neural network (1D-CNN) constructed in this paper is illustrated in Fig. 3. In the 1D-CNN, the input size is set to 1024*1, where 1024 represents the length of the input full-waveform curve. The output size is 3*1, corresponding to a set of values for P-wave velocity, S-wave velocity, and density. In Fig. 3, the first convolutional layer employs 64 convolutional kernels of size 16*1 to extract features from the full-waveform curve, yielding feature maps without additional padding. The second convolutional layer, also with 64 convolutional kernels of size 16*1, is connected to the pooled output of the first convolutional layer, again without additional padding. The first fully connected layer consists of 32 neurons and takes the flattened features from the last convolutional layer as input. The second fully connected layer has 16 neurons. The third fully connected layer, with 3 neurons, outputs the P-wave velocity, S-wave velocity, and density in the form of a 3*1 vector. The stride for convolution in all convolutional layers is set to 1. Max-pooling is employed in all pooling layers, with a kernel size of 8*1 and a stride of 4. The activation functions in the first to fourth activation function layers are the tanh function, $\tanh(x) = \frac{e^x - e^{-x}}{e^x + e^{-x}}$. The activation function in the fifth activation function layer is the ReLU function, with the expression $f(x) = \max(0, x)$. The loss function is as follows:

$$L = (L_s + L_p + L_\rho)/3 \tag{5}$$

where

$$\begin{aligned} L_s &= \frac{1}{N}\sum_{i=1}^{N}\left(S_i - \hat{S}_i\right)^2 \\ L_p &= \frac{1}{N}\sum_{i=1}^{N}\left(P_i - \hat{P}_i\right)^2 \\ L_\rho &= \frac{1}{N}\sum_{i=1}^{N}\left(\rho_i - \hat{\rho}_i\right)^2 \end{aligned} \tag{6}$$

Here, L represents the loss function. L_s, L_p, and L_ρ denote the mean squared errors of S-wave velocity, P-wave velocity, and density, respectively. S_i and $\hat{S}_i$ represent the actual and predicted values of S-wave velocity, respectively. P_i and $\hat{P}_i$ represent the actual and predicted values of P-wave velocity, respectively. ρ_i and $\hat{\rho}_i$ represent the actual and predicted values of density, respectively. During network training, the number of training epochs is set to 150, and the batch size is 128. The Adam optimizer [11] is selected to optimize the network weights in order to minimize the loss function. The initial learning rate is 0.001. If the loss function on the validation set does not decrease for 5 consecutive training epochs, the learning rate is halved.

Results

After training, the 1D-CNN has learned the relationships between the full-waveform curves and the P-wave velocity, S-wave velocity, and density. When performing formation velocity inversion, 1D-CNN do not require pre - processing of the full - waveform curve. Running on a processor (i7-8700) and a graphics card (GeForce GTX 1050 Ti), the 1D-CNN takes only 3 milliseconds to predict a set of P-wave velocity, S-wave velocity, and density values. We use the relative error for evaluation, and its formula is $\delta = \left|y_i - \widehat{y_i}\right| / y_i \times 100\%$, y_i represents the actual value, and $\widehat{y_i}$ represents the predicted value. On the

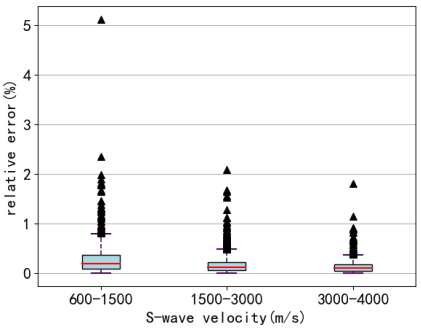

Fig. 4: Box plot of relative error in S-wave velocity

test set, the average relative errors of the S-wave velocity, P-wave velocity, and density predicted by the 1D-CNN are 0.187%, 0.122%, and 0.265%, respectively. The box plot of the relative errors in the inverted S-wave velocities is presented in Fig. 4. The triangles in the graph represent outliers within the relative error data. In soft formations, only three outliers exceeded 2%. In the box plot, the red line represents the median of the relative error. Softer formations exhibit larger relative errors and more outliers compared to harder formations. Nevertheless, the average relative error in the inverted S-wave velocity for soft formations is still very small (0.335%), with 99.4% of the S-wave velocities having relative errors within 2%, indicating that the inverted values are very close to the actual values. The 1D-CNN demonstrates high accuracy in inverting S-wave velocities, with errors fluctuating within a narrow range.

Conclusion

This paper employs a 1D-CNN to simultaneously invert the formation's P-wave velocity, S-wave velocity, and density from the full-waveform curves of monopole acoustic logging. The trained 1D-CNN achieves average relative errors of 0.187%, 0.122%, and 0.265% for S-wave velocity, P-wave velocity, and density, respectively, on the test set. It demonstrates high accuracy with errors fluctuating within a narrow range. The average relative error in the inverted S-wave velocity for soft formations is very small (0.335%), with 99.4% of the S-wave velocities having relative errors within 2%. When the formation is soft, even if the receiver on the borehole axis cannot receive the S-wave, the 1D-CNN can still effectively invert the formation's S-wave velocity from the acoustic pressure full-waveform curves.

Acknowledgments

We acknowledge the financial support by the National Science Foundation of China (NSFC-12472087 and NSFC-12272107).

References

[1] Z. Ma and J. Xie. "Study on the Relationship Between Longitudinal Wave Velocity, Shear Wave Velocity, and Density of Rocks". In: *Progress in Geophysics* 20.4 (2005), pp. 905–910.

[2] K. Wang, Z. Cui, R. Song, et al. "Theoretical Proof That the First Arrival of Shear Wave in Acoustic Logging of Soft Formations Is an Evanescent Wave". In: *Proceedings of the Chinese Geophysical Society*. 2009, p. 126.

[3] X. Wu, S. Yu, and K. Wang. "Method and Application Research on Inversion of Formation Shear Wave Velocity Using Stoneley Wave Velocity". In: *Chinese Journal of Geophysics* 38.S1 (1995), pp. 216–223.

[4] C. H. Cheng. "Full waveform inversion of P waves for Vs and Qp". In: *Journal of Geophysical Research* 94.B11 (1989), pp. 15619–15625.

[5] I. Goodfellow, Y. Bengio, and A. Courville. *Deep Learning*. MIT Press, 2016. ISBN: 978-0262035613.

[6] Q. Li. "The Relationship Between Longitudinal Wave Velocity and Shear Wave Velocity of Rocks". In: *Geophysical Prospecting for Petroleum* 27.1 (1992), pp. 1–12+154.

[7] L. Tsang. "Numerical Evaluation of Transient Acoustic Waveform Due to a Point Source in a Fluid-Filled Borehole". In: *Geophysics* 44 (1979), pp. 1706–1727. DOI: 10.1190/1.1441020.

[8] M. A. Biot. "Propagation of Elastic Waves in a Cylindrical Bore Containing a Fluid". In: *Journal of Applied Physics* 23.9 (1952), pp. 997–1005. DOI: 10.1063/1.1702365.

[9] J. E. White and R. E. Zechman. "Computed Response of an Acoustic Logging Tool". In: *Geophysics* 33.2 (1968), pp. 302–310. DOI: 10.1190/1.1439927.

[10] S. Zhou, K. Wang, J. Ma, et al. "Application Research of Generalized Linear Inversion Method for Obtaining V_S and Q_P Values Using Borehole First Arrival Waves". In: *Chinese Journal of Geophysics* 38 (1995). suppl., pp. 242–252.

[11] D. P. Kingma and J. Ba. "Adam: A Method for Stochastic Optimization". In: *International Conference on Learning Representations*. 2014.

DOI 10.5162/Ultrasonic2025/E4-a1

RG-UNet: Automated Muscle Ultrasound Segmentation Using the U-Net Architecture Augmented with Monogenic Phase Asymmetry Maps

Pascal Engl[1], *Hossein S. Aghamiry*[2], *Johannes Schwerdt*[1], *and Klaus-Vitold Jenderka*[1]
[1] *University of Applied Sciences Merseburg, Eberhard-Leibnitz-Str. 2, 06217 Merseburg, Germany*
[2] *Department of Radiology, Charité-Universitätsmedizin Berlin, Charitéplatz 1, 10117 Berlin, Germany*
pascal.engl@hs-merseburg.de

Abstract: This study presents a novel deep learning approach for automated image segmentation of dynamic ultrasound images of the *vastus lateralis* muscle, which addresses key challenges like data availability and image variability. The proposed RG-UNet augments a standard lightweight U-Net architecture with a secondary input channel derived from monogenic phase asymmetry analysis, providing the network with intensity-invariant structural information for tissue boundaries and muscle fascicles and by this achieving superior segmentation performance.

Keywords: automated image segmentation, U-Net architecture, musculoskeletal ultrasound, monogenic signal, deep learning

Introduction

In medical diagnostics, ultrasound applications often require the identification and characterization of specific regions of interest (ROIs) within B-mode images. To effectively analyze large sets of images and their corresponding ROIs in real-time, automated image segmentation (IS) is essential. IS not only facilitates the detection of abnormalities but also allows for a systematic quantitative examination of ROIs for their diagnostic relevance, for example, using specialized quantitative ultrasound algorithms.

Over the past decade, artificial intelligence has significantly advanced automated medical image analysis [1], and deep learning (DL) models have substantially improved accuracy for image segmentation tasks. For the latter, a widely used DL architecture is the U-Net, which is built on convolutional neural networks and is characterized by its name-giving encoder-decoder shape [2]. The U-Net is capable of effectively capturing contextual features while preserving spatial information, even with relatively small datasets. It was originally developed for biomedical image segmentation by Ronneberger et al. in 2015 [3] and has since been adapted and refined by many research groups across different fields [2], [4].

In this study, we employ deep neural networks with a U-Net architecture for the segmentation of B-mode ultrasound images of the *vastus lateralis* muscle. A dataset of 130 images from 10 subjects with corresponding ground-truth segmentation masks was constructed. To address the challenges of low-data availability and image variability, we hypothesize that providing a deep learning model with an explicit, intensity-invariant feature map can serve as a powerful inductive bias. We engineer such a feature using monogenic phase asymmetry, which is designed to highlight anatomical structures like tissue boundaries, muscle fibers, and fascia, regardless of image contrast. We posit that this feature-augmented, lightweight model can outperform larger, more complex architectures that rely solely on representation learning from limited data. For benchmarking the performance of our models, the popular state-of-the-art U-Net implementation nnU-Net v2 from MIC-DKFZ was used [4].

Material and Methods

Data Acquisition and Preparation: Time-resolved ultrasound echo data (RF data) of the *vastus lateralis* muscle of ten healthy male volunteers were recorded with a 5 –11 MHz linear array transducer from Telemed (LF11-5H60-A3). The field of view of the resulting B-Mode images is approximately 44x40 mm^2 (see Fig. 1 for the measurement setup and top left of Fig. 2 for an example B-Mode image). Three of the ten volunteers were measured twice, resulting in a total of 13 measurements. During each dynamic measurement, the subjects tensed their thigh muscles to 20 % of their predetermined maximum voluntary contraction (MVC), following a trapezoidal MVC curve (see Fig. 1). Each measurement lasted 40 s and the RF data was recorded at a frame rate of 100 Hz. The tensioning of the muscle visibly changes muscle boundaries and muscle fascicles configuration.

DOI 10.5162/Ultrasonic2025/E4-a1

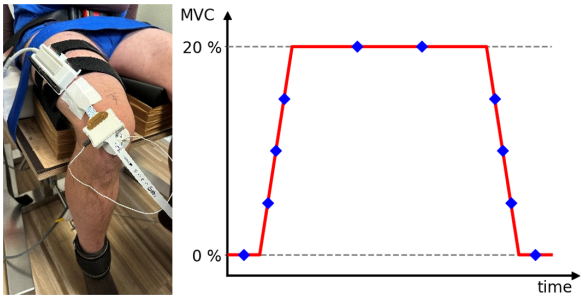

Fig. 1: Left: subject on a measurement seat with an ultrasound transducer strapped around the upper thigh and a force sensor around the ankle. Right: MVC curve which the subject follows during the measurement. Blue diamonds indicate the 10 points in time where the images were taken for the dataset.

For the training and test dataset, 10 frames were extracted from each measurement at points in time where the most variance between these frames is expected (see Fig. 1). In total, this resulted in 130 images, which were manually labeled with polygon-shaped binary segmentation masks (for examples, see Fig. 4). A set of 30 instances from 3 individual subjects was held out for final model evaluation.

U-Net Model Architecture: The deep neural networks were developed using Python 3.11, TensorFlow 2.18, and Keras 3.8. The U-Net architecture features a distinctive U-shaped encoder-decoder structure. The encoder extracts spatial features through convolutional blocks, while the decoder translates these into binary segmentation masks using 2D Up-Convolution and skip connections to preserve spatial information (see [3] for more details). As larger images did not significantly enhance model performance, the images were scaled down to 128x128 pixels to increase training speed. The most relevant hyperparameters were optimized through grid search, resulting in a network depth of 4, initial number of filters of 8, a dropout rate of 0.3 between network layers, and swish activation. In total, our model has approximately 390,000 trainable parameters, which is very few in the context of deep learning, making it lightweight and suitable for real-time applications. For training, a batch size of 1, the Dice loss, and the Adam optimizer with a learning rate of 0.001 were used.

Feature Engineering with Monogenic Phase Asymmetry: To provide the segmentation model with an explicit representation of structural information that is robust to intensity variations, we employed a feature engineering pipeline based on the monogenic signal. The monogenic signal, as introduced by Felsberg & Sommer [5], is a powerful mathematical framework for analyzing multidimensional signals such as images. It serves as a 2D generalization of the 1D analytic signal, a concept widely used in signal processing. The monogenic signal replaces the 1D Hilbert transform with the Riesz transform constructing a 3-component signal, combining the original image with the two components of its Riesz transform. This signal decomposes the image at each point into three fundamental, locally-defined properties: local amplitude (representing energy), local phase (representing structure), and local orientation (representing geometry) [6].

A key property of this decomposition is the *split of identity*, where local phase is invariant to changes in the signal's energy (i.e., image brightness and contrast), while the local amplitude is directly representative of that energy [5]. This characteristic makes phase-based features exceptionally well-suited for analyzing medical images like ultrasound, where absolute intensity values can be unreliable due to operator-dependent settings and physical artifacts, but the underlying anatomical structures remain consistent. The local phase effectively highlights line-like structures and edges, which correspond directly to the muscle fascicles and fascial planes that are critical for accurate segmentation. Notably, this approach is conceptually consistent with the formation of B-mode images themselves, which rely on the 1D analytic signal to demodulate the RF data and extract the signal envelope [6], [7].

From the local phase information, a more specialized feature known as phase asymmetry can be derived, which acts as a highly robust detector for edges and lines, particularly in low-contrast areas [8]. In the context of muscle ultrasound, this means it generates a map that sharply accentuates the muscle boundaries (aponeuroses) and the internal linear texture of the muscle fibers (fascicles). For this study, the phase asymmetry map was generated from the envelope of the original RF data for each corresponding B-mode image. This map, containing explicit and intensity-invariant structural information, was then used as the second input channel for the U-Net. This was implemented by setting the B-mode image and the corresponding phase asymmetry map to the red and green channels of an image, respectively, and feeding this red-green (RG) image into the U-Net, as shown in Fig. 2. In the following, we refer to this extension as the RG-UNet.

Benchmarking with nnU-Net and Evaluation Metrics: In order to have a benchmark for the performance of our models, we trained the popular self-configuring U-Net implementation nnU-Net v2 from the Division of Medical Image Computing of the German Cancer Research Center (MIC-DKFZ), which is publicly available on GitHub [4]. For the training with our dataset, the standard self-configuration was used.

DOI 10.5162/Ultrasonic2025/E4-a1

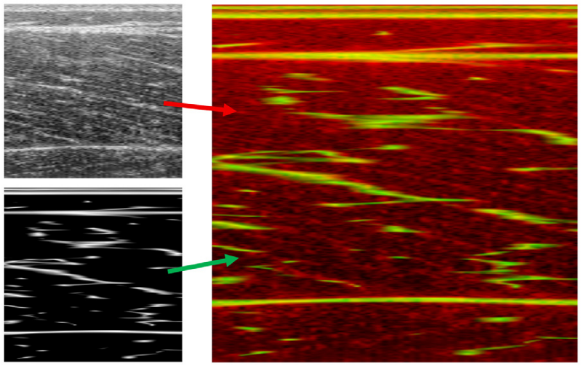

Fig. 2: The B-mode image (upper left) and its corresponding monogenic phase asymmetry map (lower left) are assigned to the red and green channels, respectively, of the resulting RG input image (right).

For the evaluation of segmentation algorithms, two standard metrics are most commonly used: Intersection over Union (IoU) and the Dice coefficient (DC). Both metrics measure the similarity between ground truth and predicted binary segmentation masks, ranging from 0 (no similarity) to 1 (identity).

Results

The U-Net, RG-UNet, and the nnU-Net were evaluated on the holdout test dataset of 30 images from 3 subjects. The resulting DC and IoU values along with their standard deviations are given in Tab. 1. The test scores are further illustrated in a boxplot in Fig. 3, and Fig. 4 provides a qualitative comparison of the predicted segmentation masks of all three models for 4 test instances.

Tab. 1: IoU and DC test scores with corresponding standard deviations for the three models.

Model	IoU	DC
nnU-Net	0.77 ± 0.15	0.86 ± 0.10
U-Net	0.89 ± 0.06	0.94 ± 0.04
RG-UNet	0.93 ± 0.06	0.96 ± 0.04

Both the U-Net and RG-UNet perform very well on the test dataset compared to the nnU-Net, where the RG-UNet exhibits the highest median and mean scores, and the U-Net has the most uniform distribution of test scores without any outliers. The nnU-Net is usually trained with much larger datasets and more often used in the context of MRI and CT imaging, so the comparison here is biased. In our configuration, it had around two orders of magnitude more trainable parameters than our U-Nets (∼45,000,000 vs. ∼390,000), making it more prone to overfitting, especially with a small training dataset. More fundamentally, its performance decline highlights the challenge of pure representation learning when data is scarce. Without a sufficient number of examples, the model struggles to learn the necessary invariances to contrast and texture.

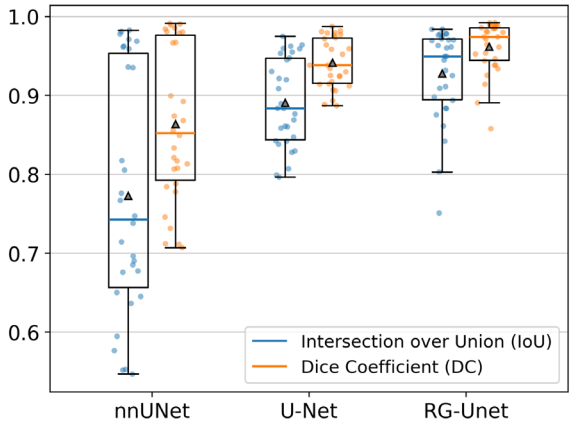

Fig. 3: Boxplot comparing the IoU and DC scores of the three evaluated models for the 30 test instances. Median values are shown as colored lines, mean values as black triangles.

In contrast, our RG-UNet is provided with a powerful, domain-relevant inductive bias through the phase asymmetry channel. This pre-engineered feature explicitly encodes the structural information, guiding the lightweight network to a more robust and generalizable solution in a data-efficient manner. From Fig. 3 and Fig. 4, it can be seen that for test images from one subject, the nnU-Net performed as well as and even better than the other two models, but it could not generalize nearly as well to the images of the other two subjects.

Overall, for test instances with clear muscle-skin separation, the U-Net and RG-UNet models consistently achieved IoU scores well above 0.9 (third row in Fig. 4). However, in cases with unclear separations, low signal-to-noise ratio, or bright echoes in the skin fat layer, some predicted masks showed significant artifacts such as holes and bulges (first, second, and fourth row in Fig. 4). In most of these challenging cases, the RG-UNet excelled over the standard U-Net.

Conclusion and Outlook

The U-Net demonstrated itself to be a lightweight, efficient, and highly capable deep learning model for segmenting muscle ultrasound B-mode images, even with a relatively small dataset. Incorporating monogenic phase asymmetry maps into the U-Net architecture as an additional input channel further improved

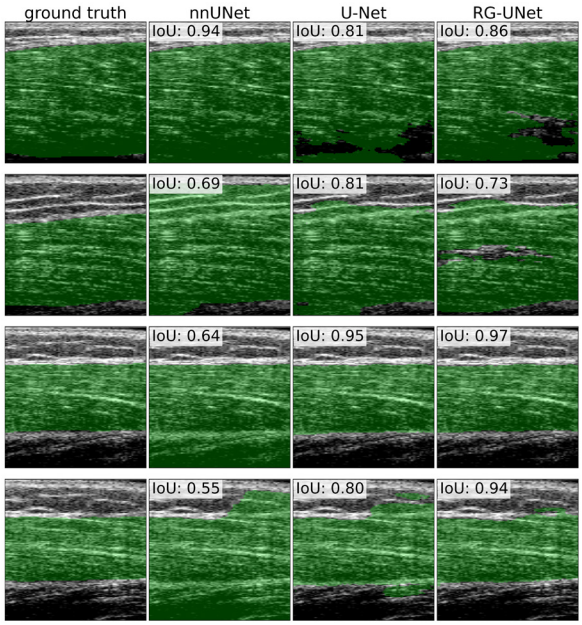

Fig. 4: Qualitative comparison of the predicted segmentation masks (green overlays) produced by the three models for 4 test instances.

its performance, underscoring the value of integrating engineered features that provide a strong inductive bias.

A larger and more diverse dataset could unlock the full potential of the nnU-Net, which will be explored in future studies. Additional measurements involving more subjects are already planned. Furthermore, individual frames from a single dynamic ultrasound measurement show a high degree of temporal correlation. Modifying the U-Net architecture to process time-resolved images could further enhance its generalizability. Here, the nnU-Net may perform significantly better, as it can be natively fed with 3D input data and is also able to handle sparse and so-called scribble annotations [9].

Looking forward, while this study demonstrates the profound impact of a fixed, engineered feature, a promising avenue for future research lies in learning these features end-to-end. Recent advancements in trainable monogenic layers allow for the optimization of filter parameters, such as scale and bandwidth, directly within the deep learning framework [10]. Integrating such a trainable layer could further enhance model performance and generalization by automatically adapting the feature extraction process to the specific characteristics of the dataset, representing a logical next step that builds upon the foundational findings presented here.

References

[1] L. Pinto-Coelho, 'How artificial intelligence is shaping medical imaging technology: A survey of innovations and applications,' *Bioengineering*, vol. 10, no. 12, p. 1435, 18th Dec. 2023. DOI: 10.3390/bioengineering10121435.

[2] R. Azad *et al.*, 'Medical image segmentation review: The success of u-net,' *IEEE Transactions on Pattern Analysis and Machine Intelligence*, vol. 46, no. 12, pp. 10 076–10 095, Dec. 2024. DOI: 10.1109/TPAMI.2024.3435571.

[3] O. Ronneberger, P. Fischer and T. Brox, 'U-net: Convolutional networks for biomedical image segmentation,' in *Medical Image Computing and Computer-Assisted Intervention – MICCAI 2015*, N. Navab, J. Hornegger, W. M. Wells and A. F. Frangi, Eds., vol. 9351, Series Title: Lecture Notes in Computer Science, Cham: Springer International Publishing, 2015, pp. 234–241. DOI: 10.1007/978-3-319-24574-4_28.

[4] F. Isensee, P. F. Jaeger, S. A. A. Kohl, J. Petersen and K. H. Maier-Hein, 'nnU-net: A self-configuring method for deep learning-based biomedical image segmentation,' *Nature Methods*, vol. 18, no. 2, pp. 203–211, Feb. 2021. DOI: 10.1038/s41592-020-01008-z.

[5] M. Felsberg and G. Sommer, 'The monogenic signal,' *IEEE transactions on signal processing*, vol. 49, no. 12, pp. 3136–3144, 2002.

[6] C. Wachinger, T. Klein and N. Navab, 'The 2d analytic signal for envelope detection and feature extraction on ultrasound images,' *Medical image analysis*, vol. 16, no. 6, pp. 1073–1084, 2012.

[7] C. P. Bridge, 'Introduction to the monogenic signal,' *arXiv preprint arXiv:1703.09199*, 2017.

[8] K. Mei, B. Hu, B. Fei and B. Qin, 'Phase asymmetry ultrasound despeckling with fractional anisotropic diffusion and total variation,' *IEEE Transactions on Image Processing*, vol. 29, pp. 2845–2859, 2019.

[9] K. Gotkowski *et al.*, *Embarrassingly simple scribble supervision for 3d medical segmentation*, 2024. arXiv: 2403.12834.

[10] A. Kimbowa, A. Parmar, M. Badii, D. Liu, M. Harkey and I. Hacihaliloglu, 'Mono2d: A trainable monogenic layer for robust knee cartilage segmentation on out-of-distribution 2d ultrasound data,' *arXiv preprint arXiv:2503.09050*, 2025.

DOI 10.5162/Ultrasonic2025/E4-a3

Investigation of a Deep Learning Methodology for Automatic Detection and Characterization of Crack-Type Defects in Ultrasonic Non-Destructive Testing

Patrick Scott Sheehan[1], Roberto Miorelli[1], Sébastien Robert[1], Sylvain Chatillon[2], and Bastien Chapuis[1]
[1]Université Paris-Saclay, CEA, List, 91191 Gif-sur-Yvette, France
[2]EDF, Direction Qualité Industrielle (DQI), 93206 Saint-Denis, France
roberto.miorelli@cea.fr

Abstract: The paper introduces a supervised simulation-based deep-learning pipeline for characterising welding defects with ultrasonic arrays in Non-Destructive Testing and Evaluation. Synthetic, multimodal TFM images generated with CIVA form the training and validation sets. The pipeline trains several state-of-the-art models using automated hyperparameter optimization. The trained models are then applied to experimental data collected under conditions mirroring the simulations. We compare regression performance and outline future directions.

Keywords: Ultrasonic testing, Deep-learning, Total Focusing Method, Simulation, Defect characterisation

Introduction

Within the ultrasonic Non-Destructive Testing and Evaluation (NDT&E) community, experimental datasets containing defects are limited since real defects in critical infrastructures are rare and most inspection results remain confidential. This scarcity hinders the effectiveness of Machine-Learning (ML) models, which rely on large and representative datasets to achieve reliable predictions.

This work employs images reconstructed by the Total Focusing Method (TFM) [1], one of today's most widely used ultrasonic imaging techniques in NDT&E. The TFM images are generated from Full Matrix Capture (FMC) data where each element in the phased-array probe is pulsed sequentially, launching an ultrasonic wave that propagates through the solid specimen. Echoes from internal reflectors are recorded simultaneously by every element of the array, yielding the complete transmit-receive data matrix needed for TFM reconstruction. Each reflection within the solid produces compressional/Longitudinal (L) and Shear/Transverse (T) waves, which propagate at different velocities and along distinct trajectories. To obtain multiple acoustic signatures of the same internal defect and enhance the information content of each sample of our training data, we employ multimodal TFM (M-TFM) reconstruction. It considers both direct and indirect propagation paths as well as mode conversions between wave types. While this approach enhances image richness, it also increases complexity for manual interpretation. With recent advances in ML demonstrating human-level or superior performance in various domains, there is growing interest in applying Deep-Leaning (DL) to automate defect characterisation in NDT&E when dealing with vast amounts of data. However, applying simulation-trained DL models to experimental conditions introduces specific challenges [2].

In this work we deploy an Automated Machine-Learning (AutoML) [3] pipeline to train and tune several regression models on CIVA-simulated M-TFM data, then evaluate their performance and robustness on independent experimental data to analyse environmental and operational uncertainties.

The remainder of this paper is organised as follows. First, we describe the experimental setup and the datasets generated from it. Next, we present the DL pipeline and report the corresponding results. Finally, we draw our conclusions and outline directions for future work.

Experimental Setup

The experimental specimen is a ferritic-steel mock-up that replicates the geometry of a butt-weld joint as used in [4]. Its back wall is deliberately complex where two planar facets meet at the weld root and slope in opposite directions (view Fig. 1). Four artificial notches have been machined into the chamfer to represent surface-breaking cracks. Each notch is 0.2 mm wide and 20 mm long. Their heights alternate between 3 mm and 10 mm, with the first two oriented vertically and the last two tilted 14° from the vertical axis. The inspection is carried out by coupling a 64-element, 5 MHz linear array (0.6 mm pitch) through a 15 mm-high Rexolite wedge set at

DOI 10.5162/Ultrasonic2025/E4-a3

37° in contact to the specimen, which refracts the beam to roughly 55° inside the steel. The material is treated as isotropic, with longitudinal and shear-wave velocities of 5 920 m/s and 3 230 m/s, respectively. This arrangement provides a realistic weld-inspection scenario in which direct, mode-converted, and back-wall-reflected paths all interact with the sloping rear surface and the surface-breaking cracks. The Panthere acquisition system from Eddyfi Technologies has been used to excite the piezoelectric elements of the probe using a sampling frequency of 50 MHz.

Previous Work

Four experimental acquisitions were performed, each centered on a different notch, with the wedge's back side positioned at X_0 = 30 mm from the specimen edge, as illustrated in Fig. 1. To model operational uncertainties representative of real inspections, we reconstructed altered TFM images from the same FMC data using nine combinations of T-wave velocity and back-wall slope within the specimen's tolerance range. The simulated dataset is composed of parameter variations close to the real mock-up settings, resulting in 6000 training, 550 validation, and 900 test samples. Inputs to the machine learning models are nine M-TFM reconstructions (TT, TTT, TTL, TLT, TLL, TTTT, TLLT, TTLT, MAX – pixel-wise maximum of the first eight modes). The training labels used for the supervised regression task consist of four parameters (Flaw height, Flaw tilt, Backwall slope, Celerity T-waves) directly derived from the specimen's characteristics sensed by the FMC acquisitions (FMC parameters), and two parameters (Backwall slope, Celerity T-waves) associated with the reconstruction settings of the TFM imaging algorithm (TFM parameters). In total, we obtain six different parameters to predict as shown in Table 1. The FMC parameters correspond to physical alterations of the model specimen chosen to be similar to the experimental mock-up, whereas the TFM parameters are obtained by perturbing the reconstruction settings to model plausible environmental uncertainties.

Recent Work

This work aims to extend the previous experimental campaign by collecting newly acquired experimental data to study the effects of both environmental and operational conditions. Four lateral scans of the probe along the butt-weld were performed, each acquiring one FMC every 2 mm. Between each scan, the probe was incrementally moved 2 mm closer to the weld to analyze the effect of positional uncertainty relative to the butt-weld. In the simulated training dataset, the probe was positioned at a fixed distance (X_0=30 mm). By progressively decreasing the distance between the

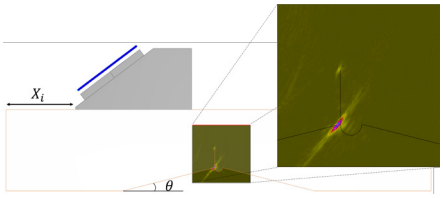

Fig. 1: Plane view of the mock-up showing the ultrasonic probe mounted on a wedge in contact with the specimen. The reference position is set at X_0 = 30 mm, which places the probe's front edge 20 mm from the weld root. The backwall slope is at an angle θ=14°. The TT-mode TFM reconstruction is displayed, revealing the 10 mm vertical defect located at the weld root.

probe and the weld in the experimental acquisitions to imitate operational uncertainties, we aim to assess the impact of these variations on TFM reconstructions and prediction performance. Furthermore, we repeated the acquisitions while introducing 0°, 1°, 2°, and 3° of skew to the probe to evaluate the model's regression performance under angular positioning errors, as may occur in real inspection scenarios. In all cases, we preserved the same input/output data structure as previously.

Deep-Learning Pipeline

To streamline and automate the training of machine learning models across different mock-up datasets, we developed a pipeline that combines state-of-the-art (SOTA) model backbones with an AutoML-based backend to optimize their fully connected layers. Specifically, the deep learning pipeline handles model selection, hyperparameter tuning, and full training of the most promising architectures. In our case, four model backbones (i.e., ResNet-50, DeiT, EfficientNet-B3 and VGG-16) implemented via the PyTorch Image Models (timm) library [5] are adapted for regression by replacing their classification heads with a fully connected block, whose depth (1–3 layers) and width (128, 256, 512, or 1024 neurons per layer) are determined through AutoML. We use Ray Tune [6] to perform randomized hyperparameter search, varying additional factors such as the learning rate (10^{-4} to 10^{-2}, log-uniform distribution), batch size (32 or 64), dropout rate (0 to 0.5, uniform distribution), and whether batch normalization is activated. Each trial runs for a few epochs on the simulated training set, with validation mean-squared error as the objective loss type in order to determine the promising model variants. Once the training procedure is ended, the top-K models are chosen and retrained from scratch for a higher number of epochs, using

DOI 10.5162/Ultrasonic2025/E4-a3

Tab. 1: Parameters Used to Simulate and Reconstruct Data for Training

Parameters	Range of Variation acquisition parameters (FMC)	Range of Variation reconstruction parameters (TFM)
Flaw height [mm]	[2.0, 12.0]	NA
Flaw tilt [deg]	[-20, 0]	NA
Backwall slope [deg]	[10, 18]	[10, 18]
Celerity T-waves [m/s]	[3030, 3380]	[3030, 3380]

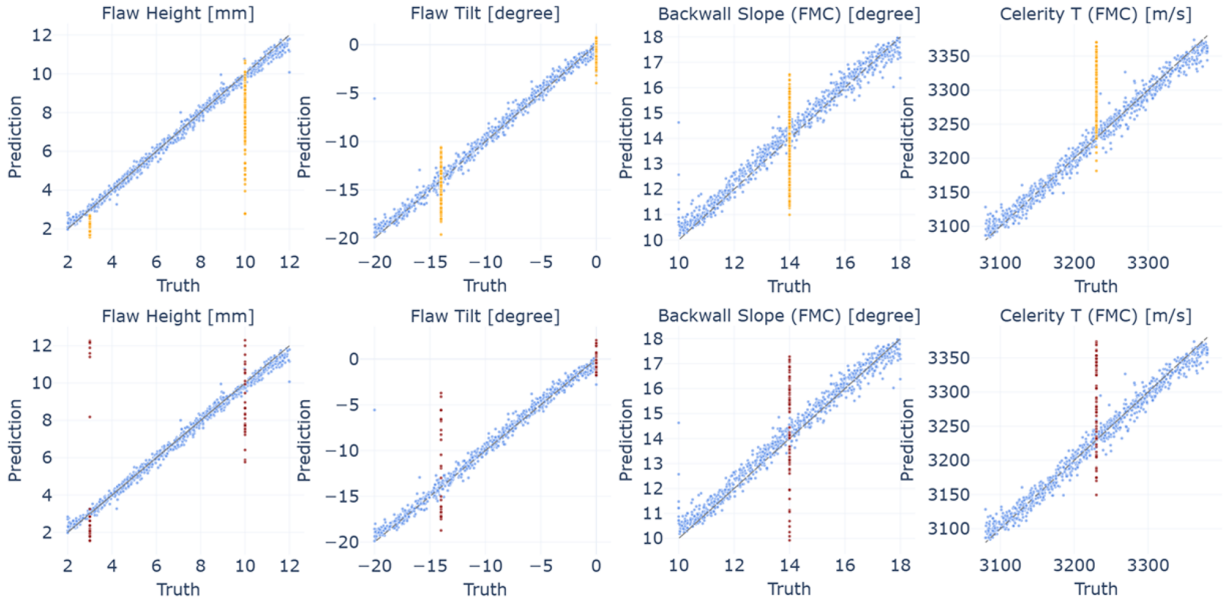

Fig. 2: True vs predicted plots comparing model outputs to ground truth values for flaw height, flaw tilt, back-wall slope, and T-wave celerity. Blue points correspond to simulated data, yellow points (top row) to experimental data with environmental uncertainties, and red points (bottom row) to experimental data with operational uncertainties. The grey dashed diagonal represents perfect prediction ($y = x$), with deviations indicating prediction errors.

early stopping with a patience threshold of 20% to prevent overfitting. Once trained, the models are frozen and evaluated on the experimental dataset. Model performance is reported using the mean absolute error (MAE), which represents the average absolute difference between predicted and true values: $\mathrm{MAE} = \frac{1}{n}\sum_{i=1}^{n}|y_i - \hat{y}_i|$ and the coefficient of determination (R^2), which reflects how well the predictions approximate the true values: $R^2 = 1 - \frac{\sum_{i=1}^{n}(y_i-\hat{y}_i)^2}{\sum_{i=1}^{n}(y_i-\bar{y})^2}$. All training procedures use the Adam optimizer.

Model customization

To maintain a general-purpose pipeline, we included only a minimal set of preprocessing layers. First, a normalization layer independently adjusts each TFM image, giving the model resilience to gain variations introduced by the operator or acquisition system. Second, a global max-pooling layer is appended to the end of the backbone, enabling the model to handle varying image resolutions seamlessly. These modifications are common in the machine learning community and preserve the generality of our pipeline, making it applicable to other related inspection problems.

Results analysis

In this work, we compare two data acquisition scenarios in Fig. 2. The first involves previously acquired data with a single FMC acquisition per flaw, where only TFM reconstruction uncertainties are considered, specifically variations in T-wave celerity and backwall slope, representing environmental conditions. The second scenario, based on newly acquired data, introduces operational uncertainties such as probe skew and varying the probe's distance from the butt-weld. Each flaw is scanned at four probe distances (0, 2, 4, and 6 mm) as shown in Fig. 1 and four skew angles (0°, 1°, 2°, and 3°). For each of the 16

DOI 10.5162/Ultrasonic2025/E4-a3

Tab. 2: MAE and R^2 metrics for flaw height and tilt versus probe skew and position increment

	Flaw tilt								**Flaw height**							
	MAE [deg]				R^2 [a.u.]				MAE [mm]				R^2 [a.u.]			
Skew variations [deg]	0	1	2	3	0	1	2	3	0	1	2	3	0	1	2	3
Increment 0 mm	3.92	4.06	4.65	4.97	0.49	0.46	0.25	0.21	2.16	2.14	3.80	3.36	0.54	0.49	−0.88	−0.89
Increment 2 mm	1.18	1.69	3.01	3.13	0.96	0.92	0.67	0.65	1.46	1.28	3.23	3.26	0.81	0.84	−0.68	−0.87
Increment 4 mm	1.77	1.83	1.72	1.52	0.91	0.91	0.91	0.92	1.40	1.00	1.07	3.58	0.81	0.87	0.86	−0.92
Increment 6 mm	2.27	2.37	2.13	2.32	0.88	0.87	0.89	0.85	1.29	1.14	1.82	2.90	0.80	0.84	0.41	−0.68

distance–angle scan configurations, we performed an independent FMC acquisition on the center of each of the four flaws, yielding $16 \times 4 = 64$ samples (red points in Fig. 2). This setup allows us to evaluate the impact of variable operational conditions on regression performance.

We trained 100 models per architecture on simulated data and selected the top performer for further evaluation. During the hyperparameter search phase, we used RayTune [6] with randomized sampling to explore configurations across all four architectures. In our experiments, VGG-16 achieved the best overall predictive performance, closely followed by the others. Fig. 2 illustrates its results: The simulated set, generated from randomized variations, is visualized as blue points aligning closely with the theoretical diagonal, demonstrating high prediction accuracy. For the previously acquired experimental data containing environmental uncertainties, TFM reconstructions were generated for each of the four flaws by combining nine TFM variations for both the backwall slope and the T-wave celerity, using the same FMC acquisition, resulting in 324 $(4 \times 9 \times 9)$ prediction samples. The gap in predictive performance on experimental data stems both from the lack of varying increment and skew effects in the training set and from discrepancies between simulated and real ultrasonic images, and it is supposed that these discrepancies migth be properly addressed by employing fully numerical (i.e., finite element method) solvers. In Fig. 2, we further evaluated the same model on a second experimental dataset, which included variations in probe distance from the butt-weld and different skew angles. In contrast, varying the probe's increment for the experimental acquisitions produced only marginal changes in performance. In Table 2 we can see the performance drop depending on the probe increment and skew variations, where the latter seems to have a higher impact on the prediction results.

Conclusion

Multiple directions emerge from this study. First, we showed that a machine learning model trained solely on simulated data can achieve reasonable performance on experimental data for regression-based inversion problems using readily available SOTA backbones without extensive model optimization. Second, our AutoML pipeline successfully trained multiple state-of-the-art models tailored to the task, with performance on both simulated and experimental data comparable to previous work. Despite lower accuracy on experimental data due to domain differences and real-world uncertainties, the pipeline is easy to implement and was evaluated under environmental and operational conditions representative of on-site inspections. Future work will focus on developing DL strategies to leverage a subset of acquisitions, integrating simulations that account for operational conditions, and improving the model's experimental performance through the established pipeline.

References

[1] C. Holmes, B. W. Drinkwater, and P. D. Wilcox. "Post-processing of the full matrix of ultrasonic transmit–receive array data for non-destructive evaluation". In: *NDT & E International* (2005).

[2] G. E. Granados et al. "Generative domain-adapted adversarial auto-encoder model for enhanced ultrasonic imaging applications". In: *NDT & E International* (2024).

[3] M. Baratchi et al. "Automated machine learning: past, present and future". In: *Artificial Intelligence Review* (2024).

[4] R. Miorelli et al. "Use of deep learning and data augmentation by physics-based modelling for crack characterisation from multimodal ultrasonic TFM images". In: *Nondestructive Testing and Evaluation* (2024).

[5] R. Wightman. *PyTorch Image Models (timm)*. 2019. URL: https://github.com/huggingface/pytorch-image-models.

[6] R. Liaw et al. "Tune: A Research Platform for Distributed Model Selection and Training". In: *arXiv preprint arXiv:1807.05118* (2018).

DOI 10.5162/Ultrasonic2025/E5-a2

Elliptical polarization and irrotational characteristics of inhomogeneous plane elastic longitudinal waves

Hengshan Hu[1], *Tian Lin*[1], *and Wei Guan*[1]
[1]*Harbin Institute of Technology, Harbin, Heilongjiang, China*
hhs@hit.edu.cn

Abstract: When a homogeneous plane longitudinal or P-wave in a fluid is incident on a fluid-solid interface at a supercritical angle, it generates an inhomogeneous refracted P-wave in the elastic solid. In this study an inhomogeneous elastic P-wave is demonstrated to have components parallel to and perpendicular to the direction of propagation, exhibiting elliptical polarization characteristics. While the wavefield remains irrotational, the traveling velocity along the propagation direction is slightly less than that of a homogeneous P-wave.

Keywords: longitudinal wave, inhomogeneous wave, polarization, elastic medium, borehole.

Introduction

When discussing P-waves, the common perception is that particle displacement aligns with the propagation direction—a characteristic indeed true for homogeneous plane P-waves. However, inhomogeneous P-waves propagating along elastic medium interfaces (or surfaces) exhibit nonuniform amplitude distribution across wavefronts, with amplitudes decaying as distance from the interface/surface increases [1]. This raises the question: Does particle displacement in inhomogeneous elastic P-waves remain parallel to the propagation direction?

In elastic media, inhomogeneous waves are often termed evanescent, decaying, or vanishing waves. Inhomogeneous plane P-waves commonly occur near interfaces or surfaces, such as "glide" P-waves in acoustic logging [2] and P-head waves at the seafloor in marine exploration [3]. The P- and S-waves measured in acoustic logging propagate axially along the borehole wall before returning to the wellbore, traveling at speeds close to those of body waves in homogeneous media. Some scholars refer to them as "glide P-wave" and "glide S-wave" [4]. The glide P-wave is also known as primary head wave, while the glide S-wave is known as secondary head wave. Chen et al. [5] observed that glide P-waves possess both axial and radial displacement components.

These studies indicate that the borehole P-wave differs significantly from the homogeneous P-wave in a unbounded medium. Here we focus our attention on the properties of the refracted inhomogeneous P-wave generated at fluid-solid interface.

Inhomogeneous Refracted P-Waves at a Fluid-Solid Interface

Consider a homogeneous plane P-wave obliquely incident from a fluid half-space to a solid half-space

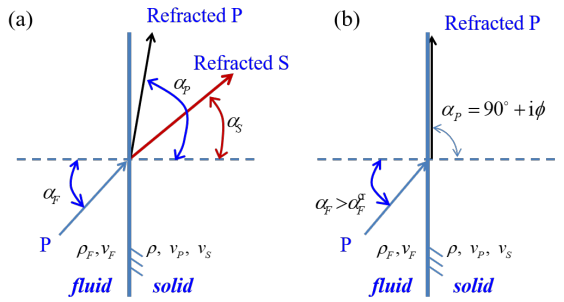

Fig. 1: Schematic of refraction on a fluid-solid boundary. (a) at small incident angle, (b) at supercritical incident angle.

(Fig. 1a). Here both the fluid and the solid are assumed to be perfectly elastic.

Wave conversions on the boundary obey Snell's law

$$\frac{\sin\alpha_P}{v_P} = \frac{\sin\alpha_F}{v_F}, \tag{1}$$

where v_F is P wave velocity in the fluid, v_P and v_S are P and S wave velocities in the solid. α_F is the incident angle in the fluid side. α_P and α_S are respectively the angles of refraction P and S waves. It is assumed that $v_P > v_F$, so that $\alpha_P > \alpha_F$. When $\alpha_P = 90°$, the P wave in the solid is critically refracted and travels along the boundary. In that case, the incident angle is

$$\alpha_F^{\rm cr} = \sin^{-1}\frac{v_F}{v_P}. \tag{2}$$

When the incidence angle becomes larger than the critically incidence angle, as in Fig. 1b, Eq. (1) remains valid and

$$\sin\alpha_P = \frac{v_P}{v_F}\sin\alpha_F > \frac{v_P}{v_F}\sin\alpha_F^{\rm cr} = 1. \tag{3}$$

DOI 10.5162/Ultrasonic2025/E5-a2

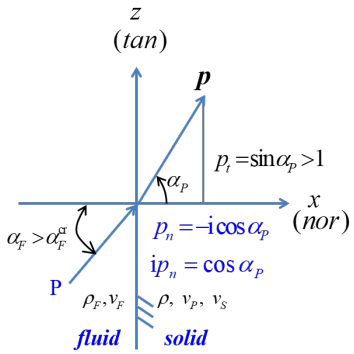

Fig. 2: The complex refraction angle and the complex propagation vector

The angle of the refracted P wave, α_P, must be a complex number, with the real part being $\pi/2$, i.e.,

$$\alpha_P = 90^\circ + \mathrm{i}\phi. \tag{4}$$

Now $\cos\alpha_P$ is a pure imaginary number because

$$\cos\alpha_P = \sqrt{1-\sin^2\alpha_F} = \mathrm{i}\sqrt{\sin^2\alpha_F - 1}. \tag{5}$$

The sign of square root is so chosen that the wave amplitude decreases with the depth into the solid, as will be seen in the next section. As depicted in Fig. 2, the propagation vector $\boldsymbol{p}$ has a tangential component p_t of real value and a normal component $\mathrm{i}p_\mathrm{n} = \mathrm{i}\sqrt{\sin^2\alpha_F - 1}$, with

$$p_\mathrm{t} = \sin\alpha_P > 1, \tag{6}$$

$$p_\mathrm{n} = -\mathrm{i}\cos\alpha_P = \sqrt{\sin^2\alpha_P - 1} > 0, \tag{7}$$

so that

$$\boldsymbol{p} = \boldsymbol{e}_t \sin\alpha_p + \boldsymbol{e}_n \cos\alpha_p = p_t\boldsymbol{e}_t + \mathrm{i}p_n\boldsymbol{e}_n. \tag{8}$$

Expressing in the form of plane harmonic wave, the displacement is

$$\begin{aligned}\boldsymbol{u} &= A\boldsymbol{d}\exp\left[\mathrm{i}k(\boldsymbol{p}\cdot\boldsymbol{x} - v_p t)\right] \\ &= A\boldsymbol{d}\exp\left[\mathrm{i}k(p_t z + \mathrm{i}p_n x - v_p t)\right] \\ &= A\boldsymbol{d}\exp\left(-kp_n x\right)\cdot\exp\left[\mathrm{i}k(p_t z - v_p t)\right],\end{aligned} \tag{9}$$

where A is the amplitude factor, k is the wavenumber. From Eq. (9) it is clear that the displacement decays exponentially with the depth x normal to the interface, the refracted P-wave is thus called inhomogeneous. It propagates with a tangential velocity

$$v_\mathrm{t} = \frac{dz}{dt} = \frac{v_P}{p_\mathrm{t}} = \frac{v_P}{\sin\alpha_P} < v_P, \tag{10}$$

in which Eq. (6) is used. Eq. (10) tells us that the tangential phase velocity v_t is less than the homogeneous P-wave velocity.

When a homogeneous P-wave in a fluid is obliquely incident on the fluid-solid interface with the incidence angle larger than critical incidence angle, the angle of refraction will be a complex value, and the refracted wave in the elastic sold half-space travels with a tangential velocity less than the P-wave velocity in the medium, and with an amplitude decreasing with the depth normal to the interface.

Polarization feature of the refracted inhomogeneous P-waves

In this section, we discuss particle displacement pattern in the refracted inhomogeneous P-wave field. Achenbach [1] proved that a plane wave in the time domain expressed by Eq. (11)

$$\boldsymbol{u} = \boldsymbol{d}f(\boldsymbol{p}\cdot\boldsymbol{x} - ct) \tag{11}$$

is irrotational as long as

$$\boldsymbol{d} = \boldsymbol{p} \tag{12}$$

and

$$\boldsymbol{p}\cdot\boldsymbol{p} = 1 \tag{13}$$

Here, we point out that Eq. (13) does not require the a complex propagation vector $\boldsymbol{p}$ is of unit length. In fact, when $\boldsymbol{p} = \boldsymbol{p}_R + \mathrm{i}\boldsymbol{p}_I$, Eq. (13) leads to

$$\boldsymbol{p}_R\cdot\boldsymbol{p}_I = 0, \tag{14}$$

$$\boldsymbol{p}_R\cdot\boldsymbol{p}_R - \boldsymbol{p}_I\cdot\boldsymbol{p}_I = 1, \tag{15}$$

in which $\boldsymbol{p}_R$ and $\boldsymbol{p}_I$ are respectively real and imaginary parts of the propagation vector. In our expression for super-refracted P wave, the propagation vector described by Eq. (8) satisfies Eq. (13), with $\boldsymbol{p}_R = \boldsymbol{e}_t p_t = \boldsymbol{e}_t\sin\alpha_p$, $\boldsymbol{p}_I = \boldsymbol{e}_n p_n = \boldsymbol{e}_n\sqrt{\sin^2\alpha_p - 1}$, and $p_t^2 - p_n^2 = 1$. The super-refracted P wave is irrotational as long as $\boldsymbol{d} = \boldsymbol{p}$.

Rewriting Eq. (9) as

$$\begin{aligned}\boldsymbol{u} &= A(\boldsymbol{p}_R + \mathrm{i}\boldsymbol{p}_I)\exp(-kp_n x)\cdot\exp\left[\mathrm{i}k(p_t z - v_p t)\right] \\ &= A(\boldsymbol{e}_t p_t + \mathrm{i}\boldsymbol{e}_n p_n)\exp(-kp_n x)\cdot\exp\left[\mathrm{i}k(p_t z - v_p t)\right].\end{aligned} \tag{16}$$

The tangential and normal components are respectively

$$u_t = Ap_t\exp(-kp_n x)\cdot\exp\left[\mathrm{i}k(p_t z - v_p t)\right], \tag{17}$$

$$u_n = \mathrm{i}Ap_n\exp(-kp_n x)\cdot\exp\left[\mathrm{i}k(p_t z - v_p t)\right]. \tag{18}$$

Their real parts are

$$\mathrm{Re}(u_t) = Ap_t\exp(-kp_n x)\cdot\cos\left[k(p_t z - v_p t)\right], \tag{19}$$

$$\mathrm{Re}(u_n) = -Ap_n\exp(-kp_n x)\cdot\sin\left[k(p_t z - v_p t)\right]. \tag{20}$$

DOI 10.5162/Ultrasonic2025/E5-a2

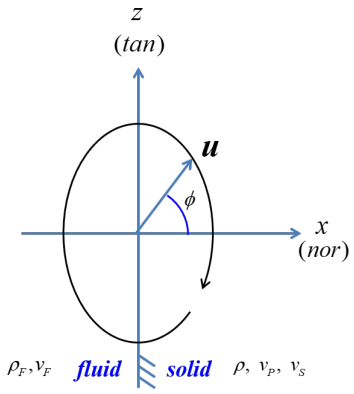

Fig. 3: The trajectory of refracted P-wave displacement at $z = 0$ on the boundary.

It is obvious that

$$\frac{[\mathrm{Re}(u_t)]^2}{[Ap_t \exp(-kp_n x)]^2} + \frac{[\mathrm{Re}(u_n)]^2}{[Ap_n \exp(-kp_n x)]^2} = 1. \tag{21}$$

Because $p_t > 1$ and $p_n = \sqrt{\sin^2 \alpha_p - 1} < p_t$, the trajectory of the displacement of a particle on the boundary is elliptic, with the long axis being in the tangential direction. Specifically, the trajectory shape changes with the incidence angle α_F, so that

$$\frac{[\mathrm{Re}(u_t)]^2}{A^2 \left(\frac{v_p}{v_F}\right)^2 \sin^2 \alpha_F \mathrm{e}^{-2kp_n x}} + \frac{[\mathrm{Re}(u_n)]^2}{A^2 \left(\left(\frac{v_p}{v_F}\right)^2 \sin^2 \alpha_F - 1\right) \mathrm{e}^{-2kp_n x}} = 1, \tag{22}$$

in which p_n also depends on α_F because $p_n = \sqrt{\left(\frac{v_P}{v_F}\right)^2 \sin^2 \alpha_F - 1}$. The displacement vector of a particle on the boundary goes clockwise as shown in Fig. 3.

The trajectory is similar to the Rayleigh wave on the surface of an elastic half-space. The Rayleigh wave is well known as a combination of an inhomogeneous P wave and an inhomogenous S wave. It travels with a velocity less than that of the shear wave in the medium. Now we see that the displacement of a homogenous P-wave itself goes with an elliptic trajectory, with the long axis in the tangential direction, and the short axis normal to the interface.

Discussions

The super-refracted P-wave has a tangential velocity smaller than the P-wave velocity of the formation. The recorded P-wave in acoustic logging is composed of inhomogeneous P-wave generated when the incident angle exceeds the critical incidence angle. Although critical refraction does occur at exact critical incidence angle, the acoustic energy associated with a cone of the zero thickness might be negligible. It is reasonable to conclude that the observable P-wave is inherently associated with inhomogeneous P-wave, so that the picked up velocity by commonly used slowness-time coherence method [6] will inevitably be slower than the real P-wave velocity of the formation. We suggest a correction scheme be provided after careful investigation.

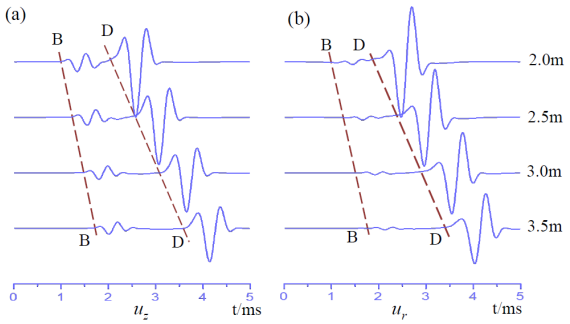

Fig. 4: Waveforms of displacement components at the borehole wall in a slow formation

We would like to point out that the Snell's law is in fact a part of the conclusions drawn from boundary conditions. It is the incident wave and all outgoing waves combining together that satisfies the boundary conditions. The refracted S-wave is among the outgoing waves as long as the incidence angle is nonzero.

When investigating waves excited by an acoustic monopole source in a borehole, Hu [7] calculated the z-axial and radial components of the displacement on the borehole wall in a slow formation with $v_P = 2331\,\mathrm{m/s}$, $v_S = 1083\,\mathrm{m/s}$, $\rho = 2259\,\mathrm{kg/m^3}$. The density and acoustic velocity in the fluid are respectively $\rho_F = 1000\,\mathrm{kg/m^3}$ and $v_F = 1500\,\mathrm{m/s}$. In his result, both the radial displacement and the axial displacement exhibit a disturbance with the P-wave velocity, as in Fig. 4.

Two facts can be used to explain the waveform of u_r in Fig. 4b. The normal displacement waveform exhibits a disturbance with an approximate P-wave velocity because the glide P-wave is actually elliptically polarized, with a normal displacement component as well as a tangential one. Besides, refracted S-wave is generated whenever the incidence angle is nonzero.

Similarly, refraction S-wave will have a complex angle when the incidence angle in the fluid is greater than the second critical incidence angle. The super-refracted S-wave is also inhomogeneous and has a tangential velocity smaller that the S-wave velocity of the formation. It causes tangential displacement as

well as normal displacement. The displacement trajectory can be similarly analyzed. The displacement of a inhomogeneous S-wave goes along an elliptic trajectory, with the short axis in the tangential direction, and the long axis normal to the interface.

Conclusion

Inhomogeneous refracted P-wave is generated in the formation when the incidence angle in the fluid is larger than critical incidence angle. While it remains an irrotational wave, it travels along the interface with a velocity slower than that of P-wave in a unbounded medium. Its displacement has a normal component as well as a tangential displacement. For a particle on the interface, the displacement vector of the inhomogeneous refracted P wave goes clockwise along an elliptic trajectory, with the long axis being in the tangential direction. Different than the Rayleigh wave, the inhomogeneous P wave has a traveling velocity slightly lower than that in a unbounded medium.

Discussed here is about waves in perfect elastic medium. The conclusions here can be drawn from the more general theory on inhomogeneous waves in viscoelastic media as expounded by Borcherdt [8] in 2009. In spite of being so, our presentation on inhomogeneous waves in perfect elastic medium is easier to understand. We expect it to be beneficial to borehole geophysicists for understanding the wave mechanism of the glide P and S waves on a borehole wall.

Acknowledgments

We acknowledge the financial support by the National Science Foundation of China (NSFC-12472087 and NSFC-12272107).

References

[1] J. D. Achenbach. *Wave Propagation in Elastic Solids*. Amsterdam/New York: North - Holland Publishing Company/American Elsevier, 1973.

[2] Q. Dong, K. Wang, C. Luo, et al. "Resonance and attenuation of the head wave in a fluid - filled borehole". In: *Chinese Journal of Geophysics* 34.02 (1991), pp. 228–239.

[3] J. M. Carcione. *Wave fields in real media: wave propagation in anisotropic, anelastic, porous and electromagnetic media*. 3nd. Amsterdam/New York: Elsevier Science, 2011.

[4] J. Zhang. "Detection depth of acoustic velocity logging". In: *Well Logging Technology* 5.06 (1981), pp. 64–67.

[5] W. Chen, Z. Chu, S. Wang, et al. "Theoretical and Experimental Study on Acoustic Frequency Spectrum Log in a Well Model". In: *Well Logging Technology* 22.06 (1998), pp. 3–11.

[6] C. Kimball and T. Marzetta. "Semblance processing of borehole acoustic array data". In: *Geophysics* 49.3 (1986), pp. 274–281.

[7] H. Hu. "Acoustic head wave on the borehole wall in a porous formation and the causes for its accompanying electromagnetic field". In: *Acta Physica Sinica* 52.8 (2003), pp. 1954–1959.

[8] R. Borcherdt. *Viscoelastic Waves in Layered Media*. New York: Cambridge University Press, 2009.

DOI 10.5162/Ultrasonic2025/E5-b3

Reflection and Attenuation Analysis of Ultrasonic Pitch-Catch Measurement in Oil Wells with Casing Irregularity

Feng Cheng[1], *Xuelian Chen*[1*], *Jinlin Pan*[1], *Xihao Gu*[1], *Yali Zhou*[1], *and Xiaoming Tang*[1]
[1]*China University of Petroleum (East China), School of Geosciences, Qingdao, China*
B24010036@s.upc.edu.cn

Abstract: In cement-bonding evaluation, ultrasonic Lamb waves have been widely studied and applied in regular casing wells. However, its feasibility in irregular casing wells remains unknown. The relationship between ultrasonic Lamb waves and casing irregularity based on finite element time-domain simulation was investigated. According to the Lamb wave propagation, irregularity interfaces were determined by the Lamb wave attenuation and reflection wave amplitude changes. We propose a novel measurement method to detect surface unevenness of housings. This study assists in irregular casing cement-bonding evaluation.

Keywords: cementing quality evaluation, leaky lamb wave, attenuation, reflection

Introduction

The quality of cement bonding is crucial to ensure zonal isolation and well integrity. Traditional sonic logging assesses the quality of cement bonding using the amplitude of the casing wave throughout the life cycle of hydrocarbon wells. In recent years, the evaluation of ultrasonic cement has advanced significantly.

Zeroug and Froelich (2003) proposed integrating ultrasonic pulse-echo and pitch-catch measurements to distinguish gas, liquid, and cement behind the casing[1]. Viggen et al. (2016) employed the finite element method to simulate ultrasonic pitch-catch measurements, investigating the attenuation characteristics of through-tubing logging[2]. Brill and Klieber (2016) demonstrated that ultrasonic Lamb waves scatter and undergo mode conversion at discontinuous interfaces of layered structures[3]. Song et al. (2019) examined the effects of partial cement loss on ultrasonic pitch-catch logging[4]. This study investigates the scattering and mode conversion of ultrasonic Lamb waves at irregular interfaces in the casing caused by corrosion or perforation, focusing on variations in the amplitude, phase, and attenuation of the received waves. Based on the analysis results, a novel measurement and analysis method is proposed to detect casing nonuniformity.

Theory and Methods of Lamb Wave Simulation

The Lamb wave modes propagating in the casing are divided into two types. For the symmetric mode, the in-plane displacement(u) is symmetric as Eq. (1) , while the out-of-plane displacement(w) is antisymmetric as Eq. (2).The antisymmetric mode exhibits the opposite behavior.

Symmetric modes

$$u = u_1 = \mathrm{i}kA_2 \cos(px_3) + qB_1 \cos(qx_3) \quad (1)$$

$$w = u_3 = -pA_2 \sin(px_3) - \mathrm{i}kB_1 \sin(qx_3) \quad (2)$$

Antisymmetric modes

$$u = u_1 = \mathrm{i}kA_1 \sin(px_3) - qB_2 \sin(qx_3) \quad (3)$$

$$w = u_3 = pA_1 \cos(px_3) - \mathrm{i}kB_2 \cos(qx_3) \quad (4)$$

Selective excitation of specific Lamb wave modes can be achieved through controlled boundary conditions based on the constitutive relationship of displacement fields. To investigate the scattering and mode conversion of Lamb waves at irregular interfaces, specific mode Lamb wave excitation is preferable. Mode conversion is directly confirmed when a distinct mode emerges at irregular interfaces. It is difficult for the oblique incidence method to excite specific mode Lamb waves, making it unclear whether other modes resulted from the discontinuity.

We apply antisymmetric and symmetric out-of-plane displacement boundary conditions on the outer side of the casing to generate pure symmetric and antisymmetric Lamb waves, respectively. The simulation results are illustrated in Fig. 1, with highly magnified images showing the distribution of the displacement vector field and its impact on the shape of the casing. The arrows in the figure indicate the vector representation of the particle displacement. The symmetric mode should not be considered merely as a type of in-plane vibration. As one moves along the mode, the ratio of in-plane to out-of-plane displacement changes. Particularly noteworthy are the changes observed on the outer surface of the structure. In the

DOI 10.5162/Ultrasonic2025/E5-b3

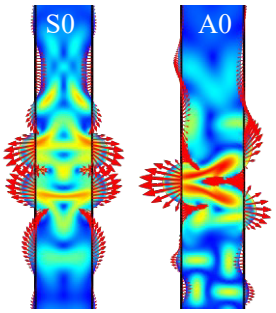

Fig. 1: S0 and A0 mode Lamb wave displacement field snapshot.

same way, antisymmetric modes cannot be considered as modes with only out-of-plane displacement values. The displacement associated with the S0 mode exhibits symmetry on both sides of the casing and appears as a compression wave. In contrast, the displacement corresponding to the A0 mode is identical on both sides of the casing and is characterized by a flexural waveform.

Fig. 2 shows the wave structures of the two modes along the thickness of the casing. For the symmetric mode, the in-plane displacement (u)is axially symmetric about the center of the casing thickness, while the out-of-plane displacement(w)is centrally symmetric about the center of the casing thickness(see 2a). For the antisymmetric mode, the in-plane displacement(u)is centrally symmetric about the center of the casing thickness, and the out-of-plane displacement(w)is axially symmetric about the center of the casing thickness(see 2b).

Leaky Lamb Wave Simulation in Irregular Casing

To simulate the effects of corrosion, the thickness of the upper casing was adjusted. Using the simulation method described above, S0-mode Lamb waves were excited in the casing. Fig. 3 illustrates the snapshots of the acoustic pressure field captured in the simulation model. At 60 μs, the in-phase pressure field in the casing indicates the exclusive presence of the S0 mode. At 100 μs, after passing through the irregular interface, the downward reflected wave is generated. At 140 μs, the out-of-phase pressure field in the casing indicates A0 mode. The array receivers were placed symmetrically on both sides of the casing in the model. The labels on the inside of the casing are RA and RA', while those on the outside are designated as RB and RB'. The resulting waveforms are presented in Fig. 4. As depicted in 4a, the waveform received at the source distance of 31 cm has already

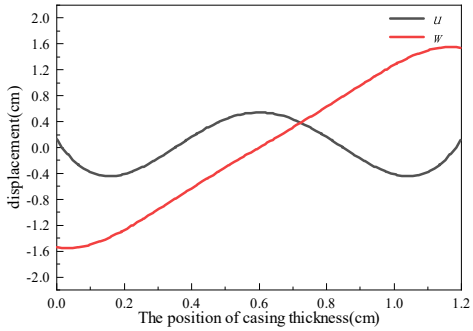

(a)

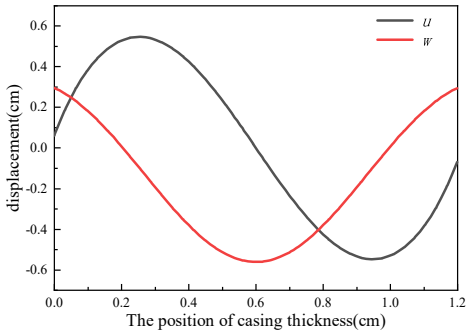

(b)

Fig. 2: Wave structure (a) S0 mode. (b)A0 mode.

been influenced by scattered waves. For the receiver at the source distance of 35 cm, the waveform displays an antisymmetric mode after 140 μs. In 4b, the reflected wave has been converted to the A0 mode. The results indicate that the irregular interface not only induces reflection and transmission phenomena but also causes mode conversion within the casing.

In pitch-catch logging, attenuation is calculated to assess the medium phase state behind the casing[5]. Irregular interfaces, such as those caused by casing corrosion, induce alterations in the waveforms of the two receivers. Moreover, reflections at these irregular interfaces cause significant attenuation. Attenuation increases with the degree of corrosion. Therefore, casing inhomogeneity leads to the scattering of Lamb waves. Placing receivers beyond the irregular results in a diminished amplitude and increased attenuation of the direct wave[6]. This increase in attenuation is independent of the medium behind the casing and the bonding condition. In addition to casing corrosion, perforation holes also generate irregular casing interfaces, which can also result in increased attenuation. Attenuation is maximized as the receivers span these perforations. Consequently, in pitch-catch logging results, perforation locations can be identified by analyzing local maxima in attenuation.

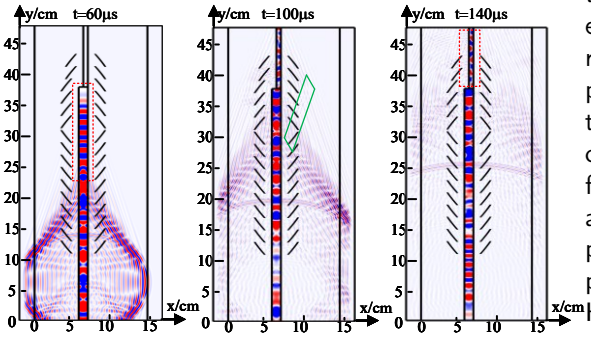

Fig. 3: Acoustic pressure field.

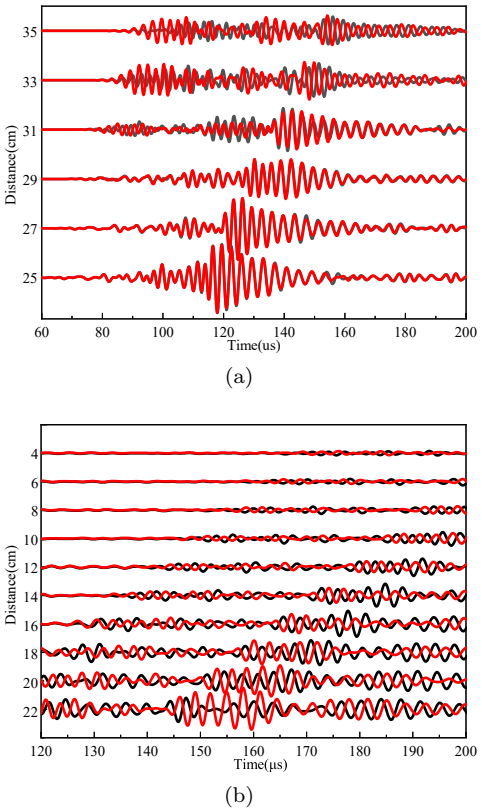

Fig. 4: (a)Transmission wave. (b) Reflection wave.

Application to Field Data

Fig. 5 compares the ultrasonic Lamb wave logging waveform and interpretation results for well X before and after perforation. The first trace represents depth (Depth). The second and third traces represent waveforms measured by the far receivers (Non-per F8; Per F8). The fourth and fifth traces represent the impedance behind the casing, both pre-and post-perforation (Non-per Im; Per Im). The sixth and seventh traces represent the attenuation calculated from the receiver waveforms (Non-per Att; Per Att). The eighth and ninth traces represent the medium states resulting from the ultrasonic pitch-catch logging data processing (Non-per SLG; Per SLG). Compared with the pre-perforation state, two significant changes were observed: firstly, the waveform amplitude in the perforation section was notably reduced; secondly, the attenuation result exhibited a "blocky" pattern after perforation. This "blocky" pattern indicated a good perforation condition from 1431.5 m to 1437.5 m. However, from 1437.5 m to 1441 m, the "blocky" pattern became less pronounced, indicating an ineffective perforation result.

Conclusion

In field production wells, inhomogeneous casing is common, leading to scattering and mode conversion at irregular interfaces during ultrasonic pitch-catch logging. The amplitude of the reflected wave serves as a reliable indicator for assessing the degree of non-uniformity in the casing. The transmitter can also function as a receiver, capturing reflected waves from irregular interfaces in the casing. Consequently, ultrasonic pitch-catch logging data from wells with non-uniform casings can be utilized to evaluate the degree of casing corrosion and estimate the non-leakage attenuation.

Acknowledgment

The authors express their gratitude to COSL for providing the field data used in this study. Furthermore, this work is supported by the National Natural Science Foundation of China (grant no. 42374156 and no. 41774141).

References

[1] S. Zeroug and B. Froelich. "Ultrasonic leaky-lamb wave imaging through a highly contrasting layer". In: *IEEE Symposium on Ultrasonics, 2003.* Vol. 1. 2003, 794–798 Vol.1. DOI: 10.1109/ULTSYM.2003.1293520.

[2] E. M. Viggen, T. F. Johansen, and I.-A. Merciu. "Simulation and modeling of ultrasonic pitch-catch through-tubing logging". In: *Geophysics* 81.4 (2016), pp. D383–D393.

[3] S. Zeroug et al. "Sonic and ultrasonic measurement applications for cased oil wells". In: *Insight-Non-Destructive Testing and Condition Monitoring* 58.8 (2016), pp. 423–430.

[4] R. Song, H. Dong, and X. Bao. "Numerical study of the effect of cement defects on flexural-wave logging". In: *Geophysics* 84.4 (2019), pp. D171–D177.

DOI 10.5162/Ultrasonic2025/E5-b3

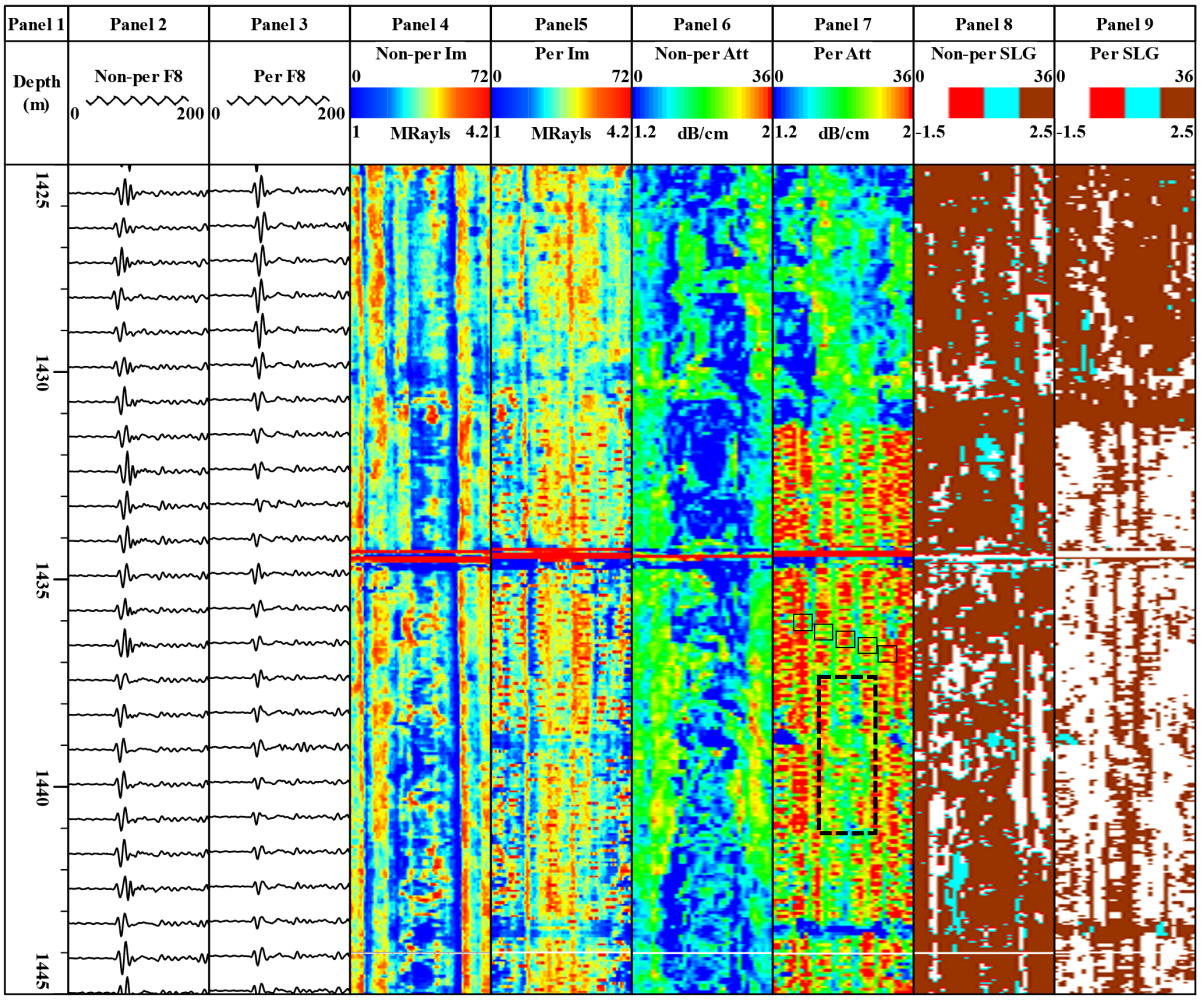

Fig. 5: Results of ultrasonic pitch-catch logging data processing before and after perforation in X casing well.

[5] S. Thierry et al. "Ultrasonic cement logging: Expanding the operating envelope and efficiency". In: *SPWLA Annual Logging Symposium*. SPWLA. 2017, D053S016R006.

[6] D. N. Alleyne and P. Cawley. "The interaction of Lamb waves with defects". In: *IEEE transactions on ultrasonics, ferroelectrics, and frequency control* 39.3 (1992), pp. 381–397.

DOI 10.5162/Ultrasonic2025/P1.2

Quantitative Ultrasonic Multilayer Characterization for Integration Monitoring of Hip Implants

J. Lützelberger[1] *and K.S. Drese*[1]
[1] *Coburg University of Applied Sciences and Arts, ISAT - Institute of Sensor and Actuator Technology, Coburg, Bavaria, Germany*
jan.luetzelberger@hs-coburg.de

Abstract: New quantitative data processing methods could enable ultrasound as a potential diagnostic method for hip implant integration monitoring. For development of such methods, suitable acoustic simulation tools are essential. In this work, a novel 1D FDTD simulation tool for multilayer structures, considering frequency-dependent properties, is introduced, particularly meeting the special needs of this application. Simulation results show excellent agreement with experimental data, confirming accurate prediction of wave propagation in multilayer systems.

Keywords: Ultrasound simulation, Finite-Difference Time Domain (FDTD) simulation, Quantitative Ultrasound (QUS), Hip prostheses, Multilayer systems

Introduction

Model-based ultrasonic methods for characterizing multilayer structures with thin interlayers are well-known in industrial applications, such as non-destructive testing of adhesive bonds [1]. In medicine, quantitative ultrasonic (QUS) methods for tissue characterization are gaining importance too [2]. However, many anatomical structures are multilayer systems, leading to multiple transmission and reflection effects. This complicates understanding sound propagation and developing suitable data processing methods for analyzing such structures. One example is the multilayer-like structure in the thigh of patients with hip prostheses, consisting of soft tissue, bone, a mm- to sub-mm-thin bone-implant interlayer, and the implant [3]. Determining thicknesses and material properties of these layers could enable a quantitative implant integration monitoring and early detection of pathological changes like implant loosening [4, 5].
The properties of each layer which are relevant for implant integration quality (thicknesses, sound velocity, sound impedances, attenuation coefficients) can vary in large ranges [6], so it is not possible to capture all configurations within experiments. Simulation studies are therefore essential to identify the relevant configurations for experimental evaluation of new data processing algorithms. Furthermore, they enable visualization and therefore deeper understanding of sound propagation within the layered system itself, while, in experimental analysis, ultrasonic transducers can only detect signals at the outer layers of the system. Consequently, they play an important role in the actual development of new data processing methods too.
A suitable simulation tool for modeling longitudinal ultrasound propagation in complex multilayer structures has to fulfill several requirements: the possibility to model any desired multilayer system (various thicknesses and acoustic properties per layer), support of any number of layers, representation of frequency-dependent attenuation, inclusion of multiple reflection and transmission processes at each layer boundary, support of any excitation pulse frequency and shape and visualization of the resulting wave field at any time and location within the simulation area.
Well-known acoustic simulation tools for industrial and medical purposes mainly include Field II [7], SimSonic [8], k-Wave [9] and COMSOL Multiphysics [10]. While Field II does not support multiple layers with different properties, SimSonic fails to model more complex attenuation patterns. MATLAB-based k-Wave and COMSOL Multiphysics meet these requirements but rely on commercial licenses.
This publication now introduces a novel, Python-based and therefore completely open-source simulation tool for ultrasonic propagation through multilayer structures, particularly addressing the special requirements stated above. It currently works for one dimension and parallel layers, but can potentially be extended to more spatial dimensions. The basic principles of the simulation tool are described as well as results from a comparison with experimental data.
While this paper focuses on this new simulation tool enabling the development of new multilayer characterization methods, novel data processing procedures themselves will be presented in future publications.

Materials and Methods

The presented simulation tool is based on a Finite-Difference Time Domain (FDTD) approximation of the linear transport equations in $-x$- and $+x$-

DOI 10.5162/Ultrasonic2025/P1.2

direction, respectively,

$$\frac{\partial \sigma}{\partial x} = \pm \frac{1}{c} \frac{\partial \sigma}{\partial t} \tag{1}$$

where σ represents the propagating sound field quantity (e. g. mechanical stress) propagating in $\mp x$-direction through time t with sound velocity c. By using two linear transport equations instead of one wave equation which combines both of them, sound propagation in each direction can be visualized separately, enhancing clarity of the simulation results. Within one layer, the transport equations are discretized using explicit Lax-Wendroff method

$$\frac{\sigma_r^{p+1} - \sigma_r^p}{\delta t} = \pm c \frac{\sigma\,{}^{p+1/2}_{r+1/2} - \sigma\,{}^{p+1/2}_{r-1/2}}{\delta x} \tag{2}$$

of $\mathcal{O}(\delta x^2, \delta t^2)$ to reduce numerical dissipation and enhance accuracy. At the layer boundaries, Upwind discretization with

$$\frac{\sigma_r^{p+1} - \sigma_r^p}{\delta t} = \pm c \frac{\sigma\,{}^{p}_{r+1} - \sigma\,{}^{p}_{r}}{\delta x} \tag{3}$$

was used to calculate the wave field σ_r^{p+1} at the next time step t_{p+1}. r and p indicate the current space and time step x_r and t_p, while δx and δt represent the space and time increments. Given one of them, the other one results from the well-known CFL condition by taking the system's highest sound velocity.
Fig. 1 illustrates how the simulation area is built by

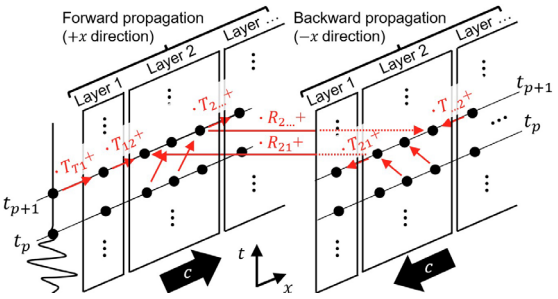

Fig. 1: Schematic drawing of the simulation area and the principle of calculating the next time step t_{p+1}.

one matrix per layer and propagation direction. Using Eq. (2), σ_r^{p+1} is computed for each point inside a layer. Correct reflection and transmission behavior is applied by first calculating the wave field at each boundary point using Eq. (3) and then multiplying with the associated reflection or transmission coefficient calculated from the respective acoustic impedances by

$$R_{ij} = \frac{Z_j - Z_i}{Z_i + Z_j}; \quad T_{ij} = \frac{2\,Z_j}{Z_i + Z_j} \tag{4}$$

as Fig. 1 shows too. i and j indicate the previous and next layer according to the propagation direction.

Frequency-dependent attenuation is modeled by a Fourier decomposition of the excitation signal as shown in Fig. 2. After decomposition, one simulation with the associated monofrequent oscillation (see Fig. 2) for each Fourier coefficient as input signal is performed. In every time step, the resulting deflection is reduced by the attenuation value for this specified frequency. Finally, a summation of simulated wave fields for all frequencies gives the wave field for the actual broadband excitation signal.

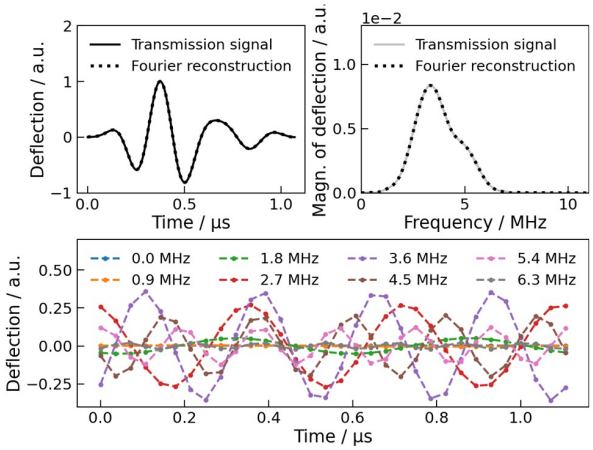

Fig. 2: Spectral decomposition by Fourier expansion for exemplary excitation signal.

As input parameters, the simulation tool needs thickness, sound velocity, acoustic impedance, attenuation coefficient and attenuation exponent for each layer as well as the desired spatial increment, total simulation time and excitation signal.

Results

Tab. 1 shows the relevant properties of an exemplary multilayer system consisting of a flexible acoustic coupling mat (layer 1), a cortical bone plate (layer 2), a water gap of variable thickness (layer 3) and a titanium plate (layer 4). The attenuation exponent was

Tab. 1: Properties of each layer of the exemplary multilayer system the simulation tool was tested with.

Layer	Thickness mm	Sound velocity m/s	Acoustic impedance MNs/m³	Attenuation coefficient dB/(cm MHz)
1	8.5	1465	1.230	0.530
2	4.2	3376	6.840	3.960
3	–	1483	1.479	0.002
4	21	6112	26.97	0.246

DOI 10.5162/Ultrasonic2025/P1.2

set to 1 for all layers. The acoustic properties of these materials were determined by puls-echo measurements and evaluation of the multiple reflections within the material probes in time and frequency domain using an immersion transducer (C384-SU, Evident Corporation, Tokyo, Japan). This multilayer system artificially represents the acoustic path at a thigh with hip prosthesis. As different thicknesses of the water interlayer represent different prosthesis integration or loosening states, evaluation of those plays an important role for implant integration monitoring.

Fig. 3 now shows the simulated wave field at different

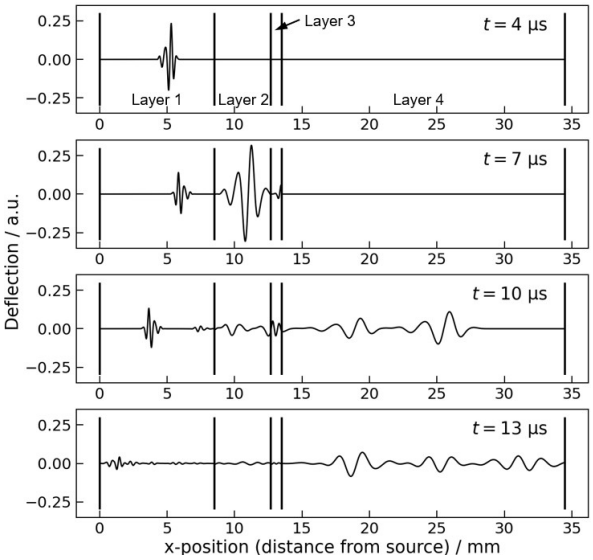

Fig. 3: Simulated wave fields at different points in time after excitation for a multilayer system with properties listed in Tab. 1, water gap thickness of $h_3 = 800\,\mu m$ and $\delta x = 5\,\mu m$. Each vertical line represents a layer boundary.

times for this multilayer system using an excitation signal as produced by the C384-SU transducer and already shown in Fig. 2. Several transmission and reflection effects are visible, including amplitude changes and different wavelengths across the various layers.

For evaluating the accuracy of the simulation tool by comparing with experimental data, a similar measurement setup as in [5] with the same measurement devices including the C384-SU transducer in pulse-echo mode but with the layer materials stated above was used. Fig. 4 shows the simulated wave field at $x = 0\,\mu m$, i. e. the received signal in pulse-echo mode, and the experimentally determined signal as well. Both signals show good agreement in shapes and amplitudes, except for the parts marked with numbers.

The signal range where the interlayer reflections occur is marked with a rectangular box as it contains the most relevant information for implant integration monitoring. For this signal part, Fig. 5 directly compares

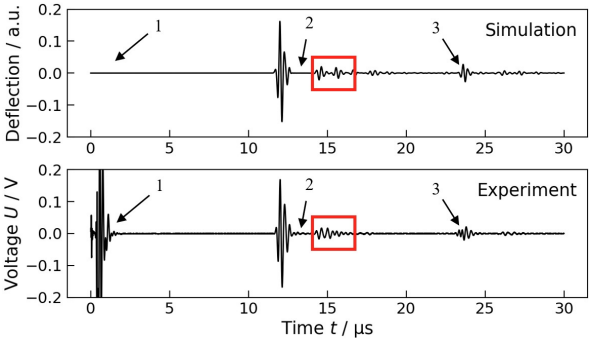

Fig. 4: Simulated and measured received signals for the same multilayer system as in Fig. 3 at $x = 0\,\mu m$. Deviating signal effects are marked by numbers.

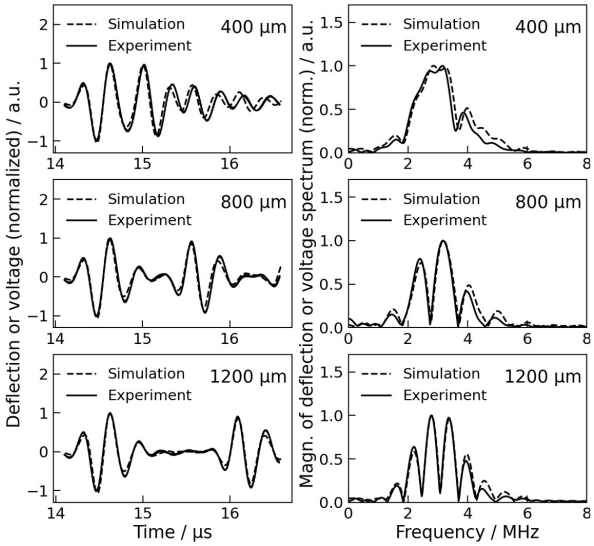

Fig. 5: Comparison of simulated and measured received signal within the interlayer reflection range (rectangular box in Fig. 4) for three different water gap thicknesses in time and frequency domain.

simulated and measured reflection signals for three different water gap thicknesses in time and frequency domain. The latter is shown because the frequency domain is especially suitable for determining small interlayer thicknesses [5]. For all three thicknesses, simulation and experiment agree almost completely, with slight deviations especially a higher frequencies.

Discussion

The comparison of the resulting wave fields from the presented simulation tool with experimental data shows a very good overall agreement, both for the total received signal and the interlayer reflection interval as the main region of interest.

Within the total received signal (see Fig. 4), the experimental effect at marking 1 is related to electrical crosstalk due to the electrical switch used to perform transmission and reception with one and the same transducer. The small oscillations in the experimental signal at marking 2 point to scattering within the bone plate which is not captured by the simulation tool. Finally, the additional reflection effect in the experimental signal at marking 3 is caused be multiple reflections inside the transducer's matching layer which is also not part of the simulation model.
For the interlayer reflection interval (see Fig. 5), the small deviations in time and frequency domain may result from scattering effects that are not included in the simulation model and overlay with the reflections at the interlayer boundaries or deviations in the actual water gap thickness within the experimental setup caused by not exactly plane-parallel surfaces.
Overall, the developed simulation tool fully meets the initially stated requirements and is therefore suitable for assisting in developing new ultrasonic data processing algorithms for an hip implant integration monitoring. Nevertheless, it does not address several sound propagation aspects that could also be relevant for the actual application, like curved surfaces with refraction, heterogeneous and porous structures with anisotropic and scattering effects or the sound field geometry of real ultrasonic transducers. For such simulation tasks, one has to use more complex simulation tools like FEM-based COMSOL Multiphysics or k-Wave which is based on a pseudo-spectral method.

Conclusion

A novel FDTD simulation tool for 1D wave propagation in multilayer systems was introduced. It especially takes account for frequency-dependent attenuation and arbitrary properties of any number of layers. A comparison with pulse-echo data from an experimental multilayer system showed very good agreement and high accuracy of the simulation results. Next steps include expanding the tool to two spatial dimensions and including other propagation effects like refraction, scattering and anisotropic material properties.

Acknowledgments

The authors especially thank Sandra Ebert and Siegfried Vorister for their technical support of the experiments and B. Braun SE as well as Forschungszentrum Ultraschall gGmbH for providing additional materials supporting the experimental work.
This research was funded by the German Federal Ministry of Research, Technology and Space (BMFTR) as part of DATIpilot program (03DPS1094), Technologieallianz Oberfranken (TAO) and the The Bavarian State Ministry of Science and the Arts (BMWK) within Bayerisches Wissenschaftsforum (BayWISS).

References

[1] F. Chang et al. "Principles and Application of Ultrasonic Spectroscopy in NDE of Adhesive Bonds". In: *IEEE Transactions on Sonics and Ultrasonics* 23.5 (1976), pp. 334–338. DOI: 10.1109/T-SU.1976.30887.

[2] C.-C. Glüer. "Quantitative Ultrasound - It is time to focus research efforts". In: *Bone* 40.1 (2007), pp. 9–13. DOI: 10.1016/j.bone.2006.07.014.

[3] L. Weiser et al. "The role of inter-prosthetic distance, cortical thickness and bone mineral density in the development of inter-prosthetic fractures of the femur: A biomedical cadaver study". In: *The Bone and Joint Journal* 96.2 (2014), pp. 1378–1384. DOI: 10.1302/0301-620X.96B10.33461.

[4] J. H. Cachão et al. "Altering the Course of Technologies to Monitor Loosening States of Endoprosthetic Implants". In: *Sensors* 20.1 (2019), p. 104. DOI: 10.3390/s20010104.

[5] J. Lützelberger et al. "Ultrasonic Interferometric Procedure for Quantifying the Bone–Implant Interface". In: *Sensors* 23.13 (2023), p. 5942. DOI: 10.3390/s23135942.

[6] M. O. Culjat et al. "A Review of Tissue Substitutes for Ultrasound Imaging". In: *Ultrasound in Medicine & Biology* 36.6 (2010), pp. 861–873. DOI: 10.1016/j.ultrasmedbio.2010.02.012.

[7] J. Jensen. "Simulation of advanced ultrasound systems using Field II". In: *2004 2nd IEEE International Symposium on Biomedical Imaging: Macro to Nano (IEEE Cat No. 04EX821)*. Vol. 2. IEEE, 2004, pp. 636–639. DOI: 10.1109/isbi.2004.1398618.

[8] F. Padilla et al. "Numerical simulation of wave propagation in cancellous bone". In: *Ultrasonics* 44 (2006), e239–e243. DOI: 10.1016/j.ultras.2006.06.042.

[9] E. Martin, J. Jaros, and B. E. Treeby. "Experimental Validation of k-Wave: Nonlinear Wave Propagation in Layered, Absorbing Fluid Media". In: *IEEE Transactions on Ultrasonics, Ferroelectrics, and Frequency Control* 67.1 (2020), pp. 81–91. DOI: 10.1109/tuffc.2019.2941795.

[10] A.-M. Zelenyak, N. Schorer, and M. G. Sause. "Modeling of ultrasonic wave propagation in composite laminates with realistic discontinuity representation". In: *Ultrasonics* 83 (2018), pp. 103–113. DOI: 10.1016/j.ultras.2017.06.014.

DOI 10.5162/Ultrasonic2025/P1.4

Non-Invasive Ultrasonic Measurement of Piston Position in High-Pressure Hydraulic Cylinders

J. Elsner[1] *and K.S. Drese*[1]
[1] *Coburg University of Applied Sciences and Arts, ISAT – Institute of Sensor and Actuator Technology, Coburg, Bavaria, Germany*
jakob.elsner@hs-coburg.de

Abstract: This work introduces a non-invasive ultrasonic method for accurate piston position measurement in high-pressure hydraulic cylinders. By analyzing time-of-flight shifts using externally mounted transducers, it enables precise tracking without coming into contact with the pressurized fluid. This prevents sealing issues, minimizes contamination risks, and reduces maintenance effort. The method achieves sub-millimeter accuracy over an 80 mm stroke. Experiments confirm its robustness and industrial applicability.

Keywords: ultrasonic position sensing, piston position measurement, high-pressure hydraulic cylinders, non-invasive monitoring, time-of-flight analysis

Introduction

High-pressure hydraulic cylinders are critical components in industrial automation, especially in systems requiring reliable control and high-precision motion feedback. In many applications, such as automated cable cutting, piston position must be determined with high accuracy and robustness to ensure safety and process quality. Conventional position measurement techniques, such as magnetic field sensors or magneto-inductive methods [1], [2], often require significant changes to the cylinder design and may be susceptible to electromagnetic interference. Optical distance sensors [3], though externally mountable, are sensitive to contamination and reflective disturbances, limiting their suitability in harsh environments. Existing ultrasonic methods [4]–[6], while promising, typically rely on structural modifications such as windows or recesses in the cylinder wall, which are unsuitable for high-pressure applications.

To address these limitations, we present a novel non-invasive ultrasonic method for real-time piston position tracking that eliminates the need to access the hydraulic fluid directly. The approach relies on externally mounted piezoelectric transducers that generate and detect ultrasonic waves propagating through the piston rod and cylinder structure. This method requires no modifications to the pressure chamber, enabling easy integration into existing hydraulic systems while withstanding variable pressure and temperature conditions common in industrial environments. A robust algorithm and a stand-alone hardware enable real-time measurement and end-position detection of the hydraulic cylinder, offering a promising alternative to traditional invasive and non-invasive measurement techniques.

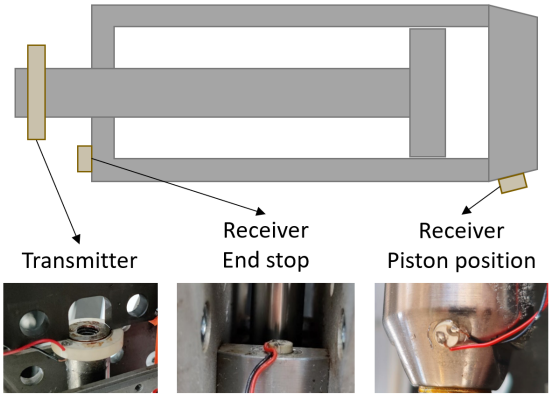

Fig. 1: Schematic representation of the experimental setup of the piston, including the positions of the three acoustic transducers.

The main objectives of this work are:

- To achieve real-time, sub-millimeter accurate piston tracking over the full stroke.
- To enable robust mechanical end-stop detection under varying environmental conditions.

Materials and Methods

The method employs piezoelectric ultrasonic transducers arranged on the exterior of the piston rod and the cylinder, as shown in Fig. 1. Two transducers are used in a transmitter-receiver configuration. The ultrasonic wave generated by the first transducer travels along the piston rod, propagates through the seal region, and is partially transmitted to the piston head, which guides the wave toward the second transducer. As the piston moves, the acoustic path length changes,

DOI 10.5162/Ultrasonic2025/P1.4

resulting in a measurable shift in the time-of-flight (ToF) of the received signal. The piston position can be calculated based on this shift.

Due to hardware constraints of the final stand-alone electronics, the transmitted signal was designed as a sequence of five rectangular pulses at a center frequency of 330 kHz. This frequency was chosen because it yielded the highest signal amplitude during preliminary testing, resulting in an optimal signal-to-noise ratio. However, other tested frequencies within the range of 100 kHz to 500 kHz showed comparable performances.

The spectral components outside the central frequency - particularly low- and high-frequency components introduced by the rectangular pulses - were subsequently filtered from the received signal using a Butterworth band-pass filter centered around 330 kHz.

The transmission was performed using a function generator (Agilent 33521A) with an amplitude of 20 V_{pp}. The received signals were first amplified by 20 dB and then recorded using an oscilloscope (LeCroy HDO6034).

Data acquisition was carried out at intervals of 25 ms, resulting in 800 individual measurements over a total duration of 20 s. During this period, the piston advanced, pressure was built up to its maximum value, and the piston subsequently retracted.

The reference measurement of the piston position was taken using a linear potentiometer, which was measured synchronously with the ultrasonic data.

An example of the measured time-domain signal is shown in Fig. 2a. The eight zero-crossings used to determine the time-of-flight shift are marked. As shown in Fig. 2b, there is an approximately linear relationship between the actual piston position and the measured ToF shift.

Temperature also influences the speed of sound, and therefore affects the signal's time-of-flight. In the temperature range considered here (-5° C to 50 °C), the effect can also be approximated as linear. Based on this, the following linear model is used to estimate piston position from the ToF shift:

$$x_{lin}(t_0, ..., t_7) = \frac{1}{\gamma_t} \cdot \tau_{mean}$$

$$\text{with } \tau_{mean} = \frac{1}{8}\sum_{i=0}^{7} t_i - \frac{i}{f} - \alpha_T \cdot T - t_{0,0°C}$$

Here, t_i denotes the position of the i-th zero-crossing. The ToF gradient $\gamma_t = 0.39\,\frac{\mu s}{mm}$, the temperature correction coefficient $\alpha_T = 0.014\,\frac{\mu s}{°C}$, and the zero-crossing position $t_{0,0°C} = 57.1\,\mu s$ at 0 °C were determined from experimental data using a least-squares fit. The parameters were optimized for the extending stroke of the piston, as this part is the more

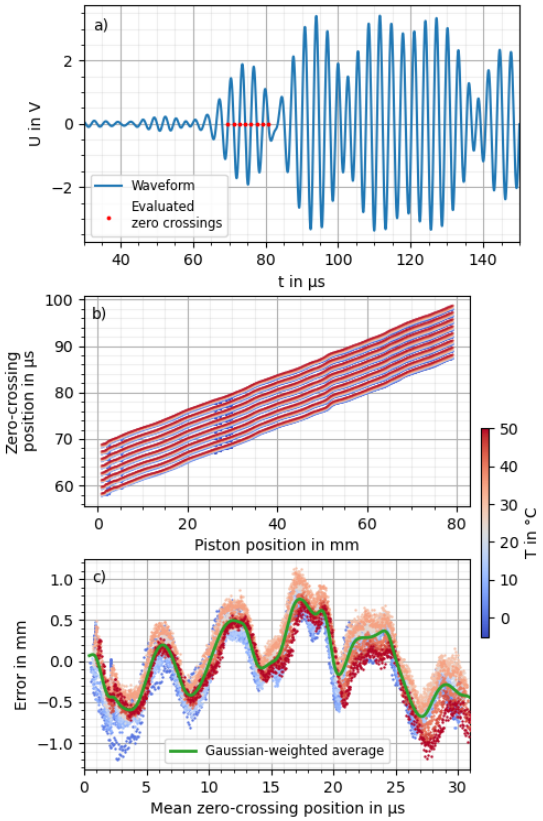

Fig. 2: a) Representative measurement signal used to determine the piston position, with indicated zero-crossings utilized for evaluation. b) Position of the evaluated zero-crossings as a function of piston position and temperature. c) Error of the linear model for piston position estimation as a function of zero-crossing displacement and temperature, including the Gaussian-weighted average of this error.

safety-critical motion. For the excitation frequency f, a value of 330 kHz was used, corresponding to the signal frequency applied during transmission. The resulting coefficient of determination, $R^2 = 0.9997$, indicates excellent agreement between the model and the observed measurements, showing that piston position can already be predicted with high accuracy.

The residuals of this linear model are shown in Fig. 2c. It can be seen that the residuals are nearly independent of temperature, which confirms that the linear temperature correction generalizes well. However, the residuals are not randomly distributed but follow a wave-like pattern. This trend is also visible in the oscillations of the ToF shift in Fig. 2b.

To improve prediction accuracy, the linear model was extended by adding a nonlinear component $K(\tau_{mean})$, resulting in a hybrid model. To estimate the nonlinear part, a weighted moving average of the

DOI 10.5162/Ultrasonic2025/P1.4

residuals was calculated for each piston position using a Gaussian kernel with a standard deviation of 0.3 µs. This correction term is shown in green in Fig. 2c and is added to the linear model.

The final hybrid model is thus defined as:

$$x_{hyb}(t_0, ..., t_7) = x_{lin}(t_0, ..., t_7) + K(\tau_{mean})$$

The prediction accuracy of this model is analyzed in more detail in the following section.

A third transducer was added near the mechanical end-stop of the piston stroke for clear identification of the piston reaching its limit position. The detection of the mechanical end stop using the third ultrasonic transducer proved to be more reliable than estimating it indirectly through the piston position. Position-based detection is always subject to some measurement uncertainty, which makes it difficult to clearly distinguish between a position close to the end stop and the actual contact.

The end stop is detected by analyzing the root mean square (RMS) of the received signal, representing the signal energy. When the piston hits the end stop, additional acoustic paths are created on the rear side of the piston, in addition to the existing sound transmission through the piston seal. These additional paths increase the acoustic excitation of the cylinder, which results in a noticeable increase in the measured signal energy and the system can reliably detect the end-of-stroke condition, which is crucial in safety-critical processes such as cable cutting.

The selected time window of the ultrasound signal was optimized to meet two criteria: first, to maximize the difference in RMS values between the two states to be distinguished, and second, to make the window as large as possible to improve robustness against noise. Both conditions are best fulfilled with a time window ranging from 0 to 80 µs.

Results

The dual-transducer setup, combined with optimized signal processing and the hybrid model, demonstrated high accuracy and repeatability. Within the tested stroke range of 80 mm, the final model achieved a maximum absolute error of 0.78 mm and a standard deviation of 0.18 mm during the extending stroke.

As the model was optimized for the piston's extending stroke, slightly higher deviations were observed during the return stroke. The maximum absolute error in this case was 1.04 mm, with a standard deviation of 0.23 mm. These error distributions are shown in Fig. 3a. Additionally, the return stroke error distribution exhibits an offset of approximately 0.22 mm. This hysteresis-like behavior can also be observed in the position-dependent model error illustrated in Fig. 3b and 3c.

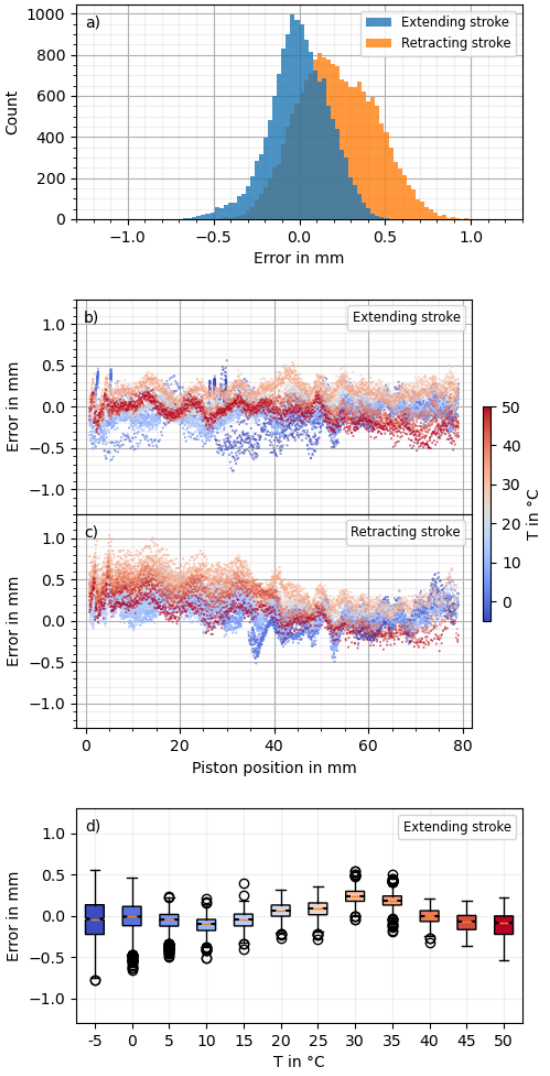

Fig. 3: a) Error distribution of the piston position predicted by the hybrid model for the extending and retracting stroke. b) & c) Error distribution of the predicted piston position as a function of the actual piston position and temperature for the extending (b) and retracting stroke (c). d) Boxplot of the prediction error of the hybrid model during the extending stroke as a function of temperature.

This is likely caused by mechanical play or slight deformation of the piston seal due to the direction of motion. This leads to a minor offset in the signal response for identical piston positions, depending on the motion direction.

As shown in the temperature-dependent error distribution in Fig. 3d, the model performs best at typical ambient temperatures around 20 °C, where a standard deviation of 0.09 mm and a maximum absolute

DOI 10.5162/Ultrasonic2025/P1.4

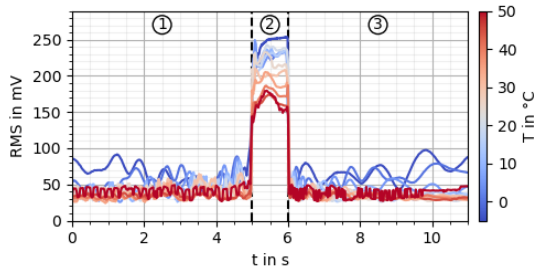

Fig. 4: RMS value of the end-stop receiver as a function of time and temperature. Three phases are highlighted: (1) Initial piston position and extending stroke, (2) Reaching the end-stop and pressure buildup in the piston, (3) Retracting stroke of the piston with partial return to the initial position.

error of 0.32 mm were observed. At the temperature extremes of -5 °C and 50 °C, the prediction accuracy decreases slightly, with standard deviations of 0.24 mm and 0.11 mm, and maximum absolute errors of 0.78 mm and 0.54 mm, respectively. Therefore, for most practical applications, the actual accuracy is even better than the overall error values reported above.

Incorporating temperature as an additional input to the nonlinear error correction term $K(\tau_{mean}, T)$ could potentially improve performance at the extremes. However, a temperature-independent correction was chosen to simplify calibration and implementation.

The detection of the mechanical end-stop was based on RMS signal energy, which increased significantly when the piston made contact with the cylinder boundary. As shown in Fig. 4, the difference in RMS levels between contact and non-contact states was pronounced and consistent across all tested temperatures.

However, the absolute RMS values decreased with rising temperature. To maintain detection reliability, a temperature-dependent threshold was implemented, which dynamically adjusts the RMS threshold RMS_{thr} based on real-time temperature.

$$RMS_{thr} = 157\,\mathrm{mV} - 1\,\frac{\mathrm{mV}}{^{\circ}\mathrm{C}} \cdot T$$

This approach enabled a highly reliable binary classification of end-stop states over the full tested temperature range from -5 to 50 °C.

Conclusion

This work presents a fully non-invasive ultrasonic measurement system capable of accurately determining the position of a piston in a high-pressure hydraulic cylinder. The method, based on externally mounted bulk wave transducers, avoids fluid contact and eliminates the need for structural modifications.

The key contributions of this work are:

- A dual-sensor ToF-based measurement approach with sub-millimeter accuracy.
- A temperature-compensated hybrid model for improved accuracy.
- Reliable end-stop detection through RMS signal energy analysis and dynamic thresholding.

The system was experimentally validated under variable thermal conditions and demonstrated excellent reliability, paving the way for industrial application in safety-critical systems. Its low maintenance, high accuracy, and modularity make it particularly attractive for retrofitting existing hydraulic systems without requiring structural changes.

Acknowledgement

This research was funded by the German Federal Ministry of Economic Affairs and Energy (BMWE) within the programme "Zentrales Innovationsprogramm Mittelstand (ZIM)" under grant number KK5048306SN3.

References

[1] S. Taghvaeeyan, R. Rajamani and Z. Sun, 'Non-intrusive piston position measurement system using magnetic field measurements,' *IEEE Sensors Journal*, vol. 13, no. 8, pp. 3106–3114, 2013.

[2] M. Jagiella, S. Fericean, R. Droxler and R. Dorneich, 'New magneto-inductive sensing principle and its implementation in sensors for industrial applications,' in *Proceedings of IEEE Sensors*, Austria: IEEE, 2004, pp. 1020–1023.

[3] A. R. Ali, M. Tarek, M. Lokma, N. Eid and T. S. Eldin, 'High sensitive measurement sensor for industrial hydraulic cylinder stroke based on fabry-pérot optical interferometer,' in *2023 International Microwave and Antenna Symposium (IMAS)*, Cairo, Egypt: IEEE, 2023, pp. 207–210.

[4] P. K. Chande and P. C. Sharma, 'A fully compensated digital ultrasonic sensor for distance measurement,' *IEEE Transactions on Instrumentation and Measurement*, vol. 33, no. 2, pp. 128–129, 1984.

[5] K. Nagai, 'Position detector for fluid cylinder,' U.S. Patent 6267042B1, 5th Aug. 1999.

[6] K.-Y. Lee, C.-F. Huang, S.-S. Huang, K.-N. Huang and M.-S. Young, 'A high-resolution ultrasonic distance measurement system using vernier caliper phase meter,' *IEEE Transactions on Instrumentation and Measurement*, vol. 61, no. 11, pp. 2924–2931, 2012.

DOI 10.5162/Ultrasonic2025/P1.6

Optimization Design of Basic Structure of Dry Coupling Shear Wave Probe Based on Piezoelectric Double-laminated Vibrator

Yonghao Lu[1,2], *Yinqiu Zhou*[1,2], *Chenhui Zhu*[1], *Xueshen Cao*[1], *Hao Chen*[1,2], *Dehua Chen*[1,2], *and Zhixiang Sun*[1,2]
[1]*Institute of Acoustics, Chinese Academy of Sciences, Beijing 100190, China*
[2]*University of Chinese Academy of Sciences, Beijing 100049, China*
zhouyinqiu@mail.ioa.ac.cn

Abstract: Conventional surface-coupled probes require good contact surface flatness and efficient coupling agents, while the absence of these conditions is often encountered in field tests. In this paper, we propose a dry coupling shear wave probe based on the double-laminated vibrator. The resonant frequencies calculated by two beam theories are compared with the simulation values, and the importance of selecting the appropriate theoretical model for optimization is discussed. Simultaneously, we discuss the backing layer suitable for the small-sized low-frequency probe in this paper. Instead of the solid-state backing, we select the high-viscosity liquid damping and preliminarily verify its effect through the testing.

Keywords: double-laminated, dry coupling, backing layer, shear horizontal wave.

Introduction

The ultrasonic pulse echo technique is a prevalent method in exploration engineering, valued for its simple testing procedure, cost-effectiveness, and straightforward interpretation of its results. Within this technology, shear waves have shorter wavelengths thus higher resolution than longitudinal waves at a given frequency, making them particularly effective for larger-scale structure detections. The SH0 wave mode is especially advantageous, as it is non-dispersive in the isotropic medium. Because its particle vibration is perpendicular to the wavefront, the propagation of the SH0 wave is less affected by the surrounding media [1]. Furthermore, there is less mode conversion when the SH0 wave encounters defects or boundaries [2]. These characteristics of the SH0 wave can reduce the complexity of recorded signals and can facilitate the interpretation of results.

Conventional ultrasonic testing probes are primarily surface-coupled with large flat surfaces. However, materials such as rocks and concrete often have uneven and rough surfaces, so they require complicated processes such as grinding and polishing contact surfaces before testing. Furthermore, an appropriate coupling agent must be applied to fill air gaps between the probe and the material, thereby minimizing signal loss. In some cases, surface cleanliness must be considered, and the prolonged use of numerous coupling agents is cumbersome and inconvenient. In certain scenarios, the use of liquid coupling agents is entirely prohibited. Especially for shear wave probes, high-viscosity coupling agents have the potential to make test signals unstable, easily resulting in signal loss [3]. In consequence, to address these challenges, a dry coupling technique is required for materials such as rock and concrete.

This paper focuses on a dry coupling shear wave probe designed with a piezoelectric double-laminated vibrator and a point contact structure. The vibrator is composed of two identical piezoelectric ceramic plates in a laminated structure. The flexural vibration of this double-laminated vibrator can be used to excite low-frequency shear waves within a small size of the probe for crack detection. The hemispherical shape of the dry coupling head provides point contact, which improves the ability of the probe to couple with different complex surfaces.

Theoretical Analysis and Simulations of the Piezoelectric Double-laminated Vibrator

For porous materials such as rock and concrete, the low-frequency shear wave is the optimal detection method due to its lower acoustic attenuation. Furthermore, to enable subsequent crack detection with array imaging, it also requires a compact probe design to allow the array integration. Flexural vibration occurs at a significantly lower resonant frequency than either longitudinal vibration or thickness vibration at the same geometry, which is the most appropriate method to generate the low-frequency shear wave for these situations. The operating principle of the double-laminated vibrator is that when an electric field is applied, one piezoelectric layer extends while

DOI 10.5162/Ultrasonic2025/P1.6

the other contracts. This opposing action causes the entire rectangular structure to produce a flexural vibration.

To get the first-order flexural vibration resonant frequency of the double-laminated vibrator, we use two distinct beam theories: the Euler-Bernoulli theory and the Timoshenko theory. The Euler-Bernoulli theory is predicated on two fundamental assumptions: (1) the cross-section remains planar post-deformation, and (2) the cross-section remains normal to the beam's axis post-deformation. This framework is primarily applicable to thin beams, with its characteristic equation for the first-order resonant frequency presented as Equation 1 [4],

$$cos(\beta L)cosh(\beta L) - 1 = 0 \tag{1}$$

where $\beta^4 = \rho S\omega^2/YI$, ρ is the density of the piezoelectric ceramic, S is the cross sectional area, ω is the angular frequency, Y is the elastic compliance constants of the piezoelectric material, $I = SH^2/12$ is the inertia moment, and L is the vibrator length.

On the other hand, the Timoshenko beam theory [5]incorporates shear strain by changing the second assumption, positing that the cross-section is no longer perpendicular to the axis after deformation, which makes it suitable for moderately thick beams. The characteristic equation of its resonance frequency is shown in Equation 2,

$$\left(\rho^2 SI\right)\omega^4 - \left[YI\rho S\beta^2 + k_s SG\left(\rho S + \rho I\beta^2\right)\right]\omega^2 + YIk_s SG\beta^4 = 0 \tag{2}$$

where $G = Y/2(1+\upsilon)$ is the shear modulus, υ is is the Poisson's ratio, $k_s \approx 5/6$ is the correction factor [6].

By solving both characteristic equations, we obtain sets of resonant frequencies with different lengths and thicknesses. Concurrently, we develop a 3D model of the piezoelectric double-laminated vibrator using finite element analysis software to calculate the resonant frequency of the first-order flexural vibration, comparing the simulated results with the analytical values. Fig. 1 illustrates the differences between the theoretical values derived from the Euler-Bernoulli theory and the simulation results, presenting their relative errors. Similarly, Fig. 2 displays the differences with their relative errors between the Timoshenko theoretical values from the simulations. The comparison revealed that for a small length-to-thickness ratio (L/H), the first-order resonant frequencies calculated by the Euler-Bernoulli theory are significantly higher than the simulation values, while the Timoshenko theory corrects this discrepancy effectively, with calculated frequencies closely matching the simulation

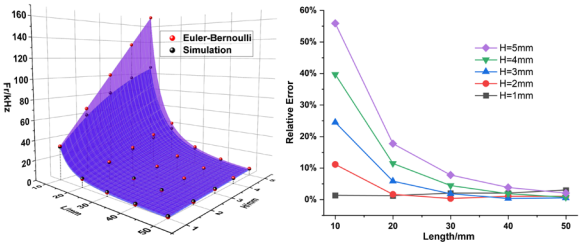

Fig. 1: Comparison of the Euler-Bernoulli theoretical values and simulation results.

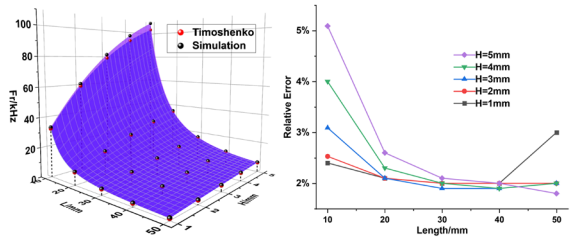

Fig. 2: Comparison of the Timoshenko theoretical values and simulation results.

values with minimal errors. Conversely, for a large L/H ratio, both theoretical results are in close agreement with simulation values; however, the Euler-Bernoulli theory has smaller errors under this condition. Notably, in Fig. 2 the simulated values are consistently higher than the theoretical values because the width is taken into consideration in the finite element software. During flexural vibration, the width is influenced by the mode shape, which provides additional stiffness to the whole structure and results in a higher simulated resonant frequency.

Most piezoelectric double-laminated vibrators are designed with a high length-to-thickness ratio (L/H > 10), and for such configurations, the Euler-Bernoulli beam theory is better suitable for guiding the optimal design as it provides a simpler analytical form for resonant frequencies. However, considering the subsequent array imaging application, we require both to minimize the probe's size and to ensure the probe resolution as high as possible within a low-frequency range. Therefore, we select the operating frequency approaching 100 kHz, which corresponds to short, thick beam models. As the comparison of Fig. 1 and Fig. 2 clearly shows, we have to use the Timoshenko theory to guide our optimization in this paper and ultimately chose a model with H=4mm and L=10mm

DOI 10.5162/Ultrasonic2025/P1.6

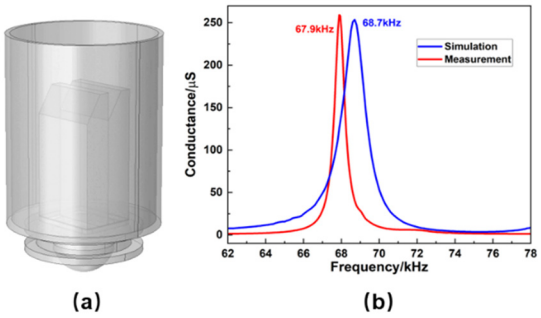

Fig. 3: The probe basic structure with air backing. (a)physical model, (b) comparison of simulated and measured conductance.

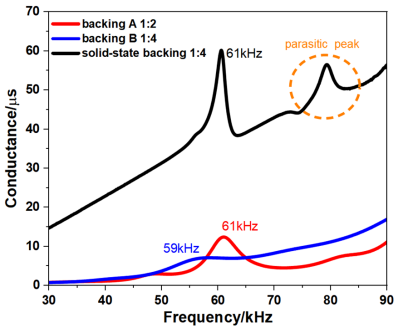

Fig. 4: Admittance curves under different backing layers.

as the low-frequency shear wave source, operating at approximately 97 kHz.

In addition, the general rule of the resonant frequency changing with three-dimensional sizes has been discussed in the previous study [7], where we also studied the elastic wave field generated by the double-laminated vibrator and determined that this structure has a high ratio of shear wave to longitudinal wave with the omnidirectional SH-waves. Besides, we analyzed the effect of the dry coupling head on probe energy loss.

Backing Layer Experimental Test

After confirming that the operating frequency of the piezoelectric vibrator is consistent with the simulation result, which is the most important part of the probe, we proceed to consider other structures. This involves bonding a wear-resistant ceramic tip to the vibrator to serve as a dry coupling head and adding a backing layer between the vibrator and the probe shell. Firstly, we calculate the admittance curve of this basic structure without a backing layer, that is, the air backing condition, and compare it with the measured result. Furthermore, the basic structure of the probe, including the optimized piezoelectric vibrator, probe shell, and the dry coupling head, is constructed using finite element simulation software. The resonant frequencies obtained from the simulation are compared with the experimentally measured frequencies in Fig. 3b, which are in close agreement. The operating frequency is changed to 68 kHz as a result of the added mass and stiffness introduced by the dry coupling head and the shell.

Since the size of the vibrator is only 10mm in length and the diameter of the basic structure of the probe is only about 15mm, the wavelength is close to or even higher than the geometric size. In this case, the backing layer is too small to effectively attenuate the sound wave by internal propagation. Furthermore, a conventional solid backing made of the epoxy-tungsten powder composite not only provides insufficient damping, but its added mass and stiffness can also disrupt the vibrator's natural resonance, which may lead to the parasitic resonance peak near the primary ones. For this reason, we consider using a liquid-state epoxy-tungsten powder mixture as a high-efficiency viscous damping system with the weak stiffness effect but the prominent viscous energy consumption, which facilitates the rapid attenuation of the vibration.

Therefore, we prepare three different backing layer samples. The backing A is formulated with a 1:2 mass ratio of epoxy resin to tungsten powder while the backing B uses a 1:4 ratio. Both are prepared without the curing agent and finally presented as a highly viscous liquid state. For comparison, a solid-state backing is created using the same formulation as Backing B but with the curing agent added.

The admittance curves in Fig. 4 clearly show the parasitic resonance peaks caused by the solid backing, while the two liquid-state backings demonstrate the ability to effectively suppress this parasitic peak. Due to the influence of additional mass, the heavier backing B has a lower resonant frequency than the backing A, which are respectively 59 kHz and 61 kHz. The solid-state backing is affected by both additional mass and stiffness, and the main resonance peak is located at 61 kHz. To analyze the damping effect of the backing, the time-domain pulse signals of the vibrator under different backings are shown in Fig. 5. The signal of the probe with backing B, which has a higher damping, attenuates faster than that with backing A. Also, the signal of the probe with solid-state backing attenuates less than the liquid-state backing under the same mass ratio as expected.

Conclusion and Discussion

Based on rectangular piezoelectric double-laminated models, finite element simulations are conducted to optimize the size and shape of the vibrator. The gen-

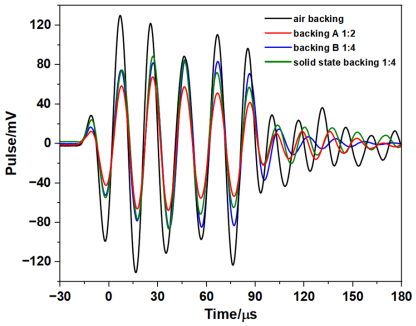

Fig. 5: Pulse ringing attenuation under different backing layers.

eral rule is that the resonant frequency of flexural vibration has a negative correlation with the length, while it has a positive correlation with the thickness of the vibrator. For structures of varying dimensions, the selection between the Euler-Bernoulli and Timoshenko theories should be predicated on the length-to-thickness ratio (L/H) to calculate the analytical solution for flexural vibration. Through design optimization, we eventually determine the appropriate structure and dimensions of the double-laminated vibrator. The basic structure prepared based on optimization results shows excellent agreement with simulations in both its admittance curve and resonant frequency. Moreover, after the theoretical analysis of the backing layer of the small-sized probe, we propose the structure of liquid damping and verify that is better than the solid backing in this probe after the preliminary test. With the study proceeding, we will study further and optimize the design of backing layer, ultimately completing the experimental verification of the probe.

Acknowledgment

This work is supported by the National Natural Science Foundation of China (Grant Nos. 42127807,12274432, 52227901).

References

[1] M. Nilsson, P. Ulriksen, and N. Rydén. "Ultrasonic imaging of concrete-embedded corroded steel liners using linear and nonlinear evaluation". In: *Nondestructive Testing and Evaluation* 40.8 (2025), pp. 3464–3492.

[2] L. Godinho et al. "Numerical study towards the use of a SH wave ultrasonic-based strategy for crack detection in concrete structures". In: *Engineering structures* 49 (2013), pp. 782–791.

[3] W.-p. SI et al. "Experimental analysis of the influence of coupling methods on rock samples acoustic velocity measurement". In: *Progress in Geophysics* 33.5 (2018), pp. 1951–1955.

[4] R. S. Woollett. *The flexural bar transducer*. Naval Underwater Systems Center, 1986.

[5] S. P. Timoshenko. "LXVI. On the correction for shear of the differential equation for transverse vibrations of prismatic bars". In: *The London, Edinburgh, and Dublin Philosophical Magazine and Journal of Science* 41.245 (1921), pp. 744–746.

[6] G. Cowper. "The shear coefficient in Timoshenko's beam theory". In: *Journal of applied mechanics* 33.2 (1966), pp. 335–340.

[7] Y. Lu et al. "Optimized Design of the Basic Structure of Dry-Coupled Shear Wave Probe for Ultrasonic Testing of Rock and Concrete". In: *Sensors* 25.9 (2025), p. 2660.

DOI 10.5162/Ultrasonic2025/P1.9

Spectral Content Improvement by Spread Spectrum Excitation for Air-Coupled Ultrasound

Linas Svilainis[1], *Andrius Chaziachmetovas*[1], *Alberto Rodriguez-Martinez*[3], *Valdas Eidukynas*[2], *and Muhammad Tayyib*[1]
[1]*Kaunas University of Technology, Department of Electronics Engineering, Kaunas, Lithuania*
[2]*Kaunas University of Technology, Department of Mechanical Engineering, Kaunas, Lithuania*
[3]*University Miguel Hernandez of Elche, Communications Engineering Department, Elche, Spain*
andrius.chaziachmetovas@ktu.lt

Abstract: Analysis how spectral content of the air-coupled signals can be improved, by using the spread spectrum (SS) signals is presented. Three air-coupled transducers were used to compare the obtained bandwidth, SNR and spectral flatness, when excited using conventional signals and programmable spectrum signals.

Keywords: air-coupled ultrasound, spread spectrum signals, losses compensation.

Introduction

Air-coupled ultrasound is offering the advantage of non-contact measurements. However, the impedance mismatch between the piezoelement and the air objects efficient transduction. Using quarter wavelength matching layers improve transduction but transmission is still relatively narrowband [1]. Other transduction techniques, like capacitive are able of broader bandwidth, but suffer sensitivity [2]. Use of higher excitation amplitude voltage can increase the signal SNR, but there is a limit (breakdown voltage, electronics capabilities [3]). Also, if narrower pulse is used aiming the bandwidth, excitation energy is lower. Spread spectrum (SS) signals offer bandwidth which does not depend on signal duration. It was already demonstrated that SS signals, like nonlinear frequency modulation (NLFM), arbitrary position, and width pulses sequences (APWP) enable to control the spectral content [4]. Then spectral losses in transduction can be compensated, broadening the transmitted bandwidth [5], [6]. This investigation analyses how spectral content of the air-coupled signals can be improved, by using the SS signals.

Methods

Three pairs of air-coupled transducers were used in investigation: i) quarter-wavelength layers-matched PZT with center frequency 650 kHz, ii) quarter wavelength layers-matched PZT with center frequency 1 MHz and iii) capacitive (electrostatic) transducer. The quarter-wavelength layers-matched PZT transducers (designed and manufactured by the Spanish National Research Council, CSIC) had a 20 mm diameter piezoelement [7]. Capacitive transducer was made by placing a 12 μm metalized (300 nm Al) PET film on FR4 PCB with 20 mm diameter copper electrode on it. A pair of same transducers, one transmitting, other receiving was used. Transducers were placed at 20 mm distance, were excited by a half bridge topology pulser (SE-TX01-02) [3], using bipolar, rectangular chirps (linear frequency modulation, LFM, 0.1-1.5 MHz 100 μs long). The $\lambda/4$ matched PZT 650 kHz and 1 MHz center frequency transducers were excited by 10 V amplitude, capacitive transducer was excited by 50 V. The capacitive transducer had 300 V bias. Receiving transducer signal was amplified by a programmable gain preamplifier SE-RX02-00 (0.1-3 MHz bandwidth, 1kΩ input impedance) [8]. A dedicated ultrasonic signal acquisition system [8] was used. Signals acquired were used to derive the 100 μs long bipolar APWP signals using technique described in [5]. Optimization of APWP signals aimed to get a flat spectrum within same frequency range. Tukey window with 0.1 transition rate was used with flat portion of the window corresponding to the desired frequency range. This type of signals is useful is application requiring flat and broad spectrum: non-contact resonant spectroscopy, imaging, ranging applications requiring axial resolution. Narrow correlation peak is obtained after pulse compression thanks to wider bandwidth. As an intermediate results NLFM signals were derived. Additionally, preamplifier output noise was measured when loaded by transducer and was converted to input-referenced noise using technique [9].

All signals used for excitation were rectangular, bipolar counterparts of the respective versions of the signals used. These signals then were used to excite the same transducer pairs and results stored for further processing. Signals, received using LFM and APWP signals were transferred into frequency domain and results were compared in a sense of obtained bandwidth, SNR and spectral flatness.

DOI 10.5162/Ultrasonic2025/P1.9

Results

The transmission response of the whole system can be obtained by taking the ratio of the received signal spectrum to the spectrum of code transmitted. Transmission response of the $\lambda/4$ matched PZT 650 kHz center frequency transducer is presented in Fig. 1.

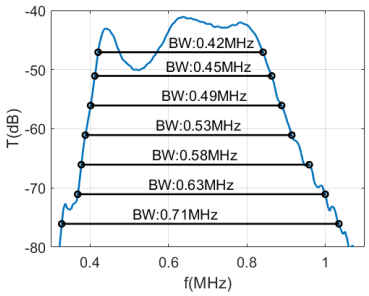

Fig. 1: System transmission when $\lambda/4$ matched PZT 650 kHz center frequency transducers.

Note the transmission bandwidth of the system at -6, -10, -15, -20, -25, -30 and -35 dB. Same for 1 MHz center frequency $\lambda/4$ matched PZT transducer is presented in Fig. 2.

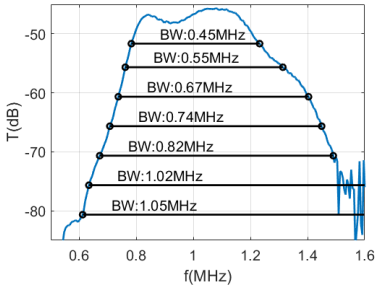

Fig. 2: System transmission response in case $\lambda/4$ matched PZT 1 MHz frequency transducers.

It can be noted that bandwidth is broader than 650 kHz case: at -20 dB bandwidth is 0.74 MHz vs. 0.53 MHz. Sensitivity is slightly lower therefore -30 dB and -35 dB bandwidth estimation is unreliable due to noise presence. Estimated passband frequencies were used as a range for NLFM and APWP derivation. Results for capacitive transducers pair are presented in Fig. 3. Despite lower resonance frequency, -20 dB bandwidth is 1.32 MHz, almost twice compared to PZT transducers. Capacitive transducers had lower sensitivity, therefore bandwidth estimation below -20 dB is not reliable. Capacitive transducers had lower sensitivity (compare -80 dB transmission at peak vs. -40 dB and -45 dB for PZT), therefore bandwidth estimation below -20 dB is not reliable.

Spectra of received signal for 650 kHz transducer

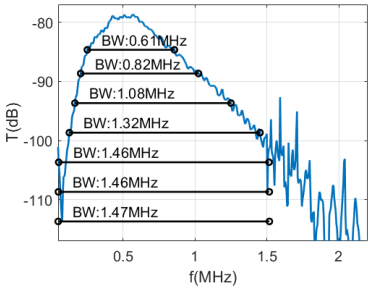

Fig. 3: System transmission of capacitive transducers.

pair when spectral losses are compensated are presented in Fig. 4 (-20 dB). Results are normalized to excitation voltage, i.e. excitation using +/-1 V.

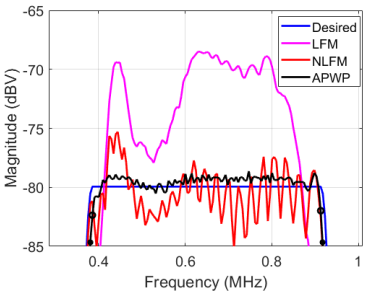

Fig. 4: Received optimized signals spectra for -20 dB (Fig. 1) bandwidth for PZT 650 kHz transducers.

Flat spectrum within the optimization range (circles) was achieved in both cases. More nonuniformity can be noted in NLFM signals when more compensation is required.

Two essential differences can be noted: i) broader compensation bandwidth requires more passband losses (compare -72 dBV vs. -85 dBV in passband, a 13 dB drop in signal level) and ii) spectrum is less uniform when more compensation is required. Results for 1 MHz transducers pair is presented in Fig. 5 (-30 dB).

Same can be concluded: broader bandwidth requires more passband losses (-75 dBV vs. -95 dBV in passband, a 20 dB drop), spectrum is less uniform when more compensation is required. Results for capacitive transducers pair is presented in Fig. 6 (-20 dB).

One more important aspect should be accounted: usually noise spectral density is nonuniform, see Fig. 7 for 1 MHz transducer.

Resulting SNR for 650 kHz transducer is presented in Fig. 8 and Fig. 9. It must be noted that results are for +/-1 V excitation voltage. Therefore, SNR reported has to be scaled by actual excitation voltage. Since excitation voltage in air-coupled measurements

DOI 10.5162/Ultrasonic2025/P1.9

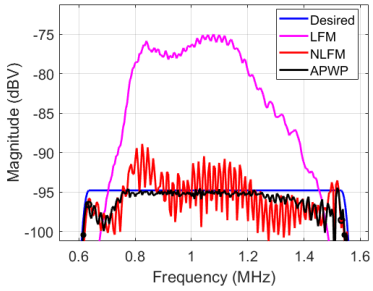

Fig. 5: Received optimized signals spectra for -30 dB (Fig. 2) bandwidth for PZT 1 MHz transducers.

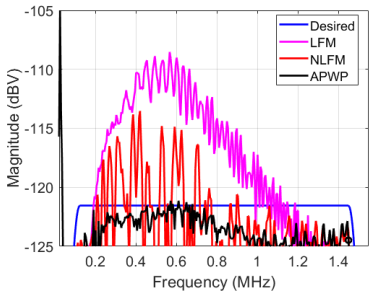

Fig. 6: Received optimized signals spectra for -20 dB (Fig. 3) bandwidth for capacitive transducers.

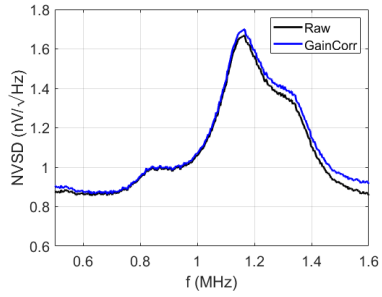

Fig. 7: Input-referenced noise of PZT 1 MHz.

usually is hundreds or even thousands of volts, much larger SNR can be expected in actual measurements.

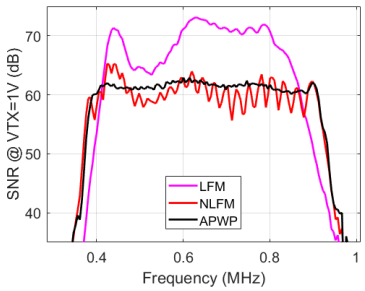

Fig. 8: SNR of PZT 650 kHz at -20 dB comp.

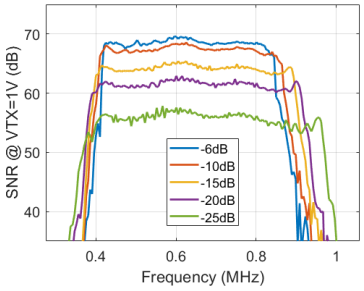

Fig. 9: All cases SNR of PZT 650 kHz transducers.

It can be noted that SNR spectrum is not as uniform as signal received, though smoother than in case of LFM or NLFM signals. The resulting SNR for 1 MHz transducers pair is presented in Fig. 10 and Fig. 11.

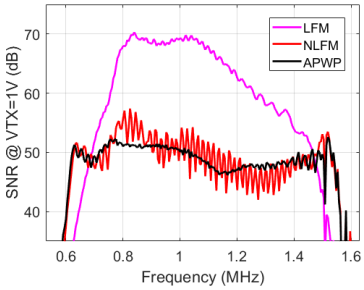

Fig. 10: SNR of PZT 1 MHz at -30 dB compensation.

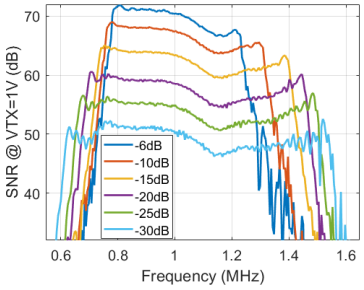

Fig. 11: All cases SNR of PZT 1 MHz transducers.

SNR for the capacitive transducers pair is presented in Fig. 12 and Fig. 13, in -6, -10, -15, -20 dB cases. Note: SNR evaluation results are for +/-1 V excitation voltage. Therefore, actual SNR, if higher excitation voltage is used, will be higher.

If normalized to the same excitation voltage, PZT-based $\lambda/4$-matched transducers deliver much higher SNR than capacitive transducers. Yet, capacitive transducers have more uniform AC response, therefore broader bandwidth can be obtained after compensation (Fig. 14).

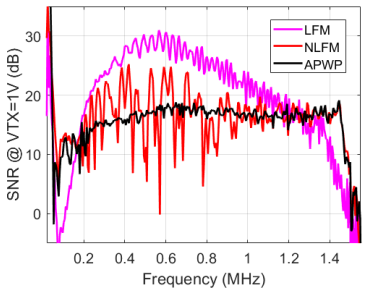

Fig. 12: Capacitive transducer SNR, -20 dB comp.

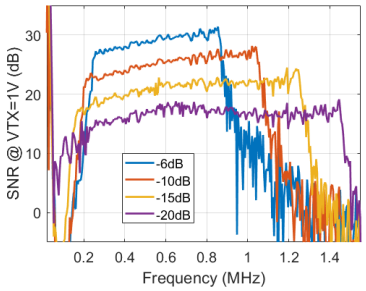

Fig. 13: All cases SNR of capacitive transducers.

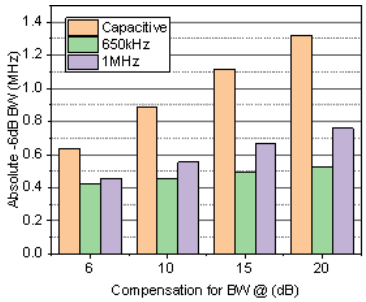

Fig. 14: Attainable -6 dB bandwidth.

It can be concluded that efficiency of the bandwidth improvement depends on transition band roll-off rate: the less steep is the transition band roll-off the better results can be obtained after spectral losses compensation.

Conclusions

APWP signals can be used to broaden the bandwidth of the received signal if excitation signal spectrum is programmed to compensate the spectral losses. Compensation is achieved by pushing the energy of the excitation signal into transition band. As a consequence, SNR is reduced. For instance, 650 kHz PZT-based transducer bandwidth can be improved from 420 kHz to 570 kHz at the expense of SNR reduction from 72 dB to 62 dB (at 1 V excitation). Bandwidth of 1 MHz PZT-based transducer can be widened from 450 kHz to 760 kHz but SNR is reduced from 72 dB to 62 dB. Capacitive transducer bandwidth can be improved from 570 kHz to 1320 kHz at the expense of SNR reduction from 30 dB to 18 dB.

Acknowledgements

This research was funded by a Grant No. S-MIP-23-133 from the Research Council of Lithuania.

References

[1] V. T. Rathod. "A review of acoustic impedance matching techniques for piezoelectric sensors and transducers". In: *Sensors* 20 (14 2020). DOI: 10.3390/s20144051.

[2] D. Hutchins, T. Robertson, and D. Billson. "New designs of focused air-coupled ultrasonic transducer". In: *Revista de Acustica* 33 (2002), p. 3.

[3] L. Svilainis, V. Dumbrava, and A. Chaziachmetovas. "Investigation of the half bridge and transformer push-pull pulser topologies for ultrasonic transducer excitation". In: *Journal of Circuits, Systems and Computers* 24 (5 2015). DOI: 10.1142/S0218126615500620.

[4] L. Svilainis and A. Aleksandrovas. "Application of arbitrary pulse width and position trains for the correlation sidelobes reduction for narrowband transducers". In: *Ultrasonics*. Vol. 53. 2013. DOI: 10.1016/j.ultras.2013.04.001.

[5] L. Svilainis et al. "Ultrasound Transmission Spectral Compensation Using Arbitrary Position and Width Pulse Sets". In: *IEEE Transactions on Instrumentation and Measurement* 67 (8 2018), pp. 1778–1785. DOI: 10.1109/TIM.2018.2809838.

[6] M. Tayyib and L. Svilainis. "SNR equalization in non-contact resonant ultrasound spectroscopy measurements". In: *NDT & E International* 154 (2025), p. 103386. DOI: 10.1016/j.ndteint.2025.103386.

[7] T. G. Alvarez-Arenas. "Air-Coupled Piezoelectric Transducers with Active Polypropylene Foam Matching Layers". In: *Sensors* 13 (5 2013), pp. 5996–6013. DOI: 10.3390/s130505996.

[8] L. Svilainis et al. "Electronics for Ultrasonic Imaging System". In: *Elektronika ir Elektrotechnika* 20 (7 2014). DOI: 10.5755/j01.eee.20.7.8024.

[9] L. Svilainis, V. Dumbrava, and D. Kybartas. "Evaluation of the ultrasonic preamplifier noise voltage density". In: *Journal of Circuits, Systems and Computers* 23 (1 2014). DOI: 10.1142/S0218126614500078.

DOI 10.5162/Ultrasonic2025/P1.10

Study on the Wetting Catalytic Mechanism of Acoustic-Driven Flow in Granular Medias

Xinyu Qi[1] *and Li-Yun Fu*[1,2]
[1]*State Key Laboratory of Deep Oil and Gas, China University of Petroleum (East China), Qingdao, China*
[2]*Laboratory for Marine Mineral Resources, Qingdao Marine Science and Technology Center, Qingdao, China*
lfu@upc.edu.cn

Abstract: Vibration-triggered granular flow phenomena are widespread in nature. However, their influencing factors, triggering mechanisms, and flow characteristics remain incompletely elucidated. This study focuses on the triggering effect of near-static-threshold vibrations on shear instability in granular layers under different wettability conditions. The research reveals that under varying wetting conditions, vibrations with specific amplitudes and frequencies can induce system instability, leading to self-accelerating inertial flow or creep flow in the granular layer.

Keywords: vibration, granular, wettability, self-accelerating inertial flow, creep flow

Introduction

Recent studies indicate that the transition of granular media from a jammed (solid) to a flowing (liquid) state represents a subcritical bifurcation process [1][2][3][4][5]. This dynamic behavior closely resembles the multi-interface solid friction behavior [6]. Based on the rate-and-state constitutive law, commonly referred to as the Dieterich-Rice-Ruina model [7][8], the ratio of shear stress τ to normal stress σ_n, denoted as $\mu = \tau/\sigma_n = F_t/F_n$, exhibits a nonlinear evolution characterized by velocity V or shear rate $\dot{\gamma}$. Engineering and geophysical observations indicate that vibrations can induce fluidization by altering the topological structure of particle contact force chains, yet the underlying physical mechanism remains unresolved. Existing studies primarily characterize vibration intensity through the following dimensionless parameters. The first is the peak acceleration ratio, $\Gamma = a/g = (2\pi f)^2 U_0/g$ (U_0 is the displacement amplitude)[9]. The second is the square of vibration velocity $v_a = (2\pi f)U_0$, which drives nonequilibrium transitions through granular temperature $T_g \sim (1/2)mv_a^2$(m is particle mass)[10]. Additionally, collision-like pressure $p_c \sim (1/2)\rho v_a^2$, describes stress transfer in inertia-dominated regimes ($\dot{\gamma} < \dot{\gamma}_0$)[11][12]. Although extensive experimental and theoretical studies have been devoted to analyzing its influencing factors, experimental research on vibration-triggered granular flow mechanisms under different wettability conditions remains absent.

This study investigates the coupling effects of particle system wettability and vibration parameters. Previous studies have shown that shear lubrication can reduce the local threshold friction at particle contacts[13]. We demonstrate that, depending on the interplay between wettability, vibration amplitude, and driving force, the granular layer can exhibit three states: jammed solid, slow creep flow, and fast inertial flow. Experimental results are analyzed within the framework of velocity-weakening friction models.

Experiments

The experiments employed a high-performance vibration testing system comprising a computer, vibration controller, power amplifier, and shaker, with a frequency range of $2-7000$ Hz, a maximum amplitude of 6.5 mm, and the capability to generate high-precision longitudinal sinusoidal waveforms.The shaker surface was coated with uniform glass beads to ensure controlled friction characteristics at the particle-substrate interface. A fixed-volume sample cell ($40mm*40mm*6mm$) was filled with a specific mass of glass microspheres (1 mm diameter). The pore volume $V_{Pore} = V_{Box} - M/\rho$ was calculated, and water was injected to adjust the pore water saturation $S = V_{water}/V_{Pore}$. The granular layer formed a 6 mm thick uniform layer via gravitational sedimentation. After 5 minutes of rest to eliminate aging effects, the platform tilt angle was adjusted until continuous stable flow occurred, with the angle recorded as the maximum static angle θ_m. For constant particle diameter, θ_m is determined by substrate roughness, granular layer thickness, and water saturation. Longitudinal sinusoidal vibrations ($f = 2000/5000$ Hz, amplitude $0.00005-0.00020$ mm) were applied to study granular layer behavior under initial jammed

DOI 10.5162/Ultrasonic2025/P1.10

conditions ($\theta < \theta_r$).

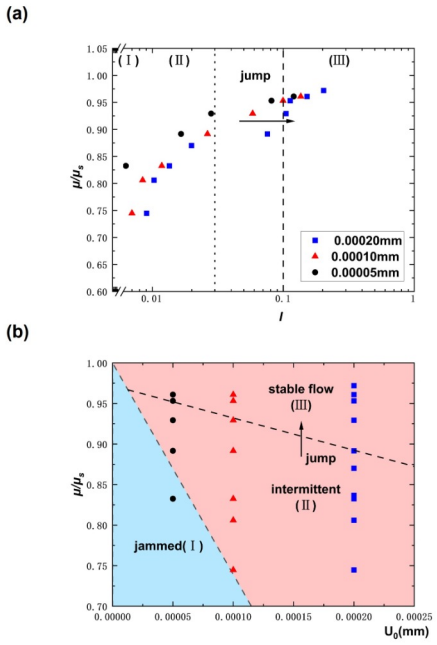

Fig. 1: (a) Evolution of normalized friction coefficient μ/μ_s versus inertial number $I = \dot{\gamma}d\sqrt{\rho/p}$ for a granular layer with thickness $h/d = 6(d = 1\ mm)$ and $f = 2000\ Hz$, under controlled contact roughness. Flow is driven by vibration amplitudes U_0 =0.00005, 0.00010 and 0.00020 mm (black circles, red triangles, and blue squares, respectively). (b) Phase diagram constructed by replotting μ/μ_s from (a) as a function of U_0, illustrating the systems different states.

The vibration amplitude was gradually increased until particle motion was detected, and particle positions were recorded via high-speed imaging. Particle tracking velocimetry (PTV) was used to calculate flow velocity. Fig. 1(a) illustrates the relationship between the normalized friction coefficient ($\mu/\mu_s = tan\theta/tan\theta_m$) and the inertial number $I = \dot{\gamma}d\sqrt{\rho/p}$ (characterizing flow rate)[14] under identical roughness conditions. This curve reflects three dynamic states of the granular layer under vibrational excitation, determined by the systems proximity to the yield threshold (μ/μ_s) and the coupling between vibrational energy and shear stress. In the jammed solid state (Region I), the system is near static yield conditions ($\mu/\mu_s \ll 1$), and the granular layer remains nearly stationary, consistent with the Coulomb jammed state, where weak vibrations fail to destabilize the contact network. In the slow creep flow (Region II), when $\mu/\mu_s \approx 0.9$, the system undergoes a rapid transition from intermittent creep to faster continuous inertial flow near $I \approx 3 \times 10^{-2}$ (Fig. 1(a) dashed line). In the fast inertial flow (Region III), where $I > 10^{-1}$, the flow velocity rivals natural avalanches, driven by inertial stresses and collisional momentum transfer. Here, the system becomes insensitive to vibrational input, indicating that gravity dominates over vibrational forcing near the yield threshold.

Results

Fig. 1(b) constructs a phase diagram of jammed (I), creep (II), and inertial (III) states by replotting μ/μ_s versus amplitude U_0. The non-monotonic transition paths in the $(\mu/\mu_s, U_0)$ plane reveal synergistic coupling between shear stress and vibrational energy: at low μ/μ_s, vibrations dominate flow initiation, with U_0 determining transitions from creep to inertial flow; at high μ/μ_s, shear stress governs dynamics, reducing the critical amplitude U_0. Within the dynamic transition zone (II - III), the inertial number (flow rate) is highly sensitive to U_0 at fixed μ/μ_s. For example, at $\mu/\mu_s = 0.90$, increasing U_0 from 0.00005 mm to 0.00020 mm raises I by approximately 0.06. Fig. 2 systematically quantifies the unlocking threshold $\mu_s{}^*$ of the static granular layer($d = 1\ mm, h = 6\ mm$)as a function of U_0, confirming that vibrational excitation and static shear stress perturbations play complementary roles in triggering.

Discussion

To qualitatively understand the vibration-triggered flow states (Fig. 1), we refer to the heuristic friction model developed by Jaeger et al[15]. In this model, the friction coefficient μ comprises a static component (velocity-weakening term) and a dynamic component (velocity-strengthening term). Vibration-induced shear lubrication reduces μ_s, with pore water saturation SS influencing the system:

$$\mu = \frac{\mu_s(S)}{1 + \alpha_1(S)\widetilde{\dot{\gamma}}^2} + [\beta_0 + \beta_1\eta(S)]\,\widetilde{\dot{\gamma}}^2 \qquad (1)$$

Where, $\mu(\widetilde{\dot{\gamma}})$ is the normalized shear defined above, $\widetilde{\dot{\gamma}} = \dot{\gamma}\sqrt{d/g_\perp}$ (d is the size of the particles) is the dimensionless flow (shear) rate, $\dot{\gamma}$ would scale with V_{flow}/h(h is related to the thickness of the granular layer). $\mu_s(S)$ is the static friction coefficient of particles under different pore water contents, depending on interparticle friction and water content. Pore water content manifests as capillary forces and lubrication effects in the system, regulating the friction coefficient through competition:

$$\mu_s(S) = \mu_{s0}\,[1 + k_1 S(1 - S/S_c) - k_2(S/S_c)^n] \qquad (2)$$

Here, μ_{s0} is the friction coefficient between particles in dry conditions, S is the pore water content, S_c

DOI 10.5162/Ultrasonic2025/P1.10

is the critical pore water content balancing capillary and lubrication effects, k_1 is the capillary force enhancement coefficient related to particle surface hydrophilicity, and k_2 is the lubrication effect parameter controlling the rate of friction coefficient decrease at high water contents.

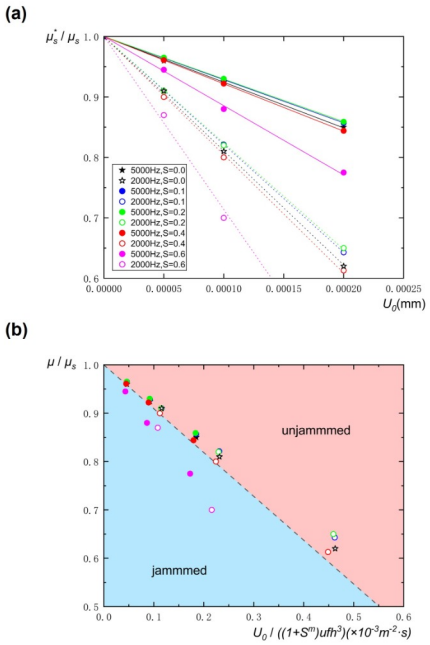

Fig. 2: (a) For a granular layer with thickness $h/d = 6(d = 1\ mm)$, the variation of the normalized static friction coefficient (threshold) μ_s^*/μ_s with vibration amplitude U_0 under different pore water saturations S and vibration frequencies f.Solid symbols correspond to $f = 5000\ Hz$, hollow symbols to $f = 2000\ Hz$. Black, blue, green, red, and pink symbols represent pore water saturations S =0.0, 0.1, 0.2, 0.4 and 0.6, respectively. Lines are fitted using Eq. (3). (b) Data from (a) replotted via Eq. (3), showing the jammed (I) and unjammed (II/III) states of the system, corresponding to the lines in Fig. 1(b).

In Eq.(1) $\alpha_1(S)$ and $\beta_0 + \beta_1\eta(S)$ describe particle geometry and energy loss during collisions, including the coefficient of restitution. $\alpha_1(S)$ and $\beta_1\eta(S)$ describe the contribution of liquids to the velocity-weakening and velocity-strengthening parts, respectively. The black solid line in Fig.3.(a) shows the $\mu(\widetilde{\dot{\gamma}})$ classic curve obtained using Eq.(1) and parameters from reference[15].In this case, spontaneous stable flow occurs only when the initial flow rate is greater than $\widetilde{\dot{\gamma}}^*$ corresponding to the initial angle μ_n, which is reflected in the jump region of Fig. 1(a). The black, blue, green, red, and pink curves in Fig.3.(a) correspond to S = 0.0, 0.1, 0.2 , 0.4 and 0.6, with the friction coefficient between particles first increasing and then decreasing as pore water content rises, dominated by capillary adhesion below the critical point and lubrication above. Now, let us consider the effects of vibration on these two distinct flow regimes in granular layers. As discussed in Ref.[16], vibration can induce frictional slip at particle contacts, leading to frictional dissipation and reduced shear contact stiffness, thereby decreasing the macroscopic modulus of the granular medium. Additionally, previous studies on single sphere-plane contact configurations have demonstrated that oscillatory sliding reduces the static threshold from μ_s to μ_s^*[13]. This threshold reduction modifies the friction model, as shown in Fig. 3(b), where the reference black solid line for μ_s shifts downward to the black dashed line ($\mu_s^* < \mu_s$). Consequently, whenever the system is loaded, vibration triggers avalanches when $\mu > \mu_s^*$ Specifically, we propose the following scenarios for two distinct applied shear forces: (i) near-threshold shear ($\mu = \mu_1$), satisfying $\mu\left(\widetilde{\dot{\gamma}}_0\right) < \mu_1 \leq \mu_s$, and (ii) sub-threshold shear $\mu = \mu_2 < \mu_d$. For $\mu_1 \leq \mu_s$, flow initiates from a metastable state and persists after vibration ceases, as the system reverts to its initial state (black solid line). The system is driven into the inertial flow regime (III), governed by the term $[\beta_0 + \beta_1\eta(S)]\,\widetilde{\dot{\gamma}}^2$ in Eq. (1). In contrast, for $\mu_2 < \mu_d$ (minimum in the black solid line), the granular system halts flow without vibration and returns to the initial jammed state (I) at $\widetilde{\dot{\gamma}}_0 = 0$. Notably, systems with low pore water saturation (S) exhibit greater vibration-induced lubrication (larger friction reduction), though their initial friction coefficients are higher. As previously noted, in confined granular materials, vibration reduces shear contact stiffness via micro-slip at particle contacts, inducing frictional dissipation and material softening[16][17][18].According to the Mindlin friction model, the reduction in shear contact stiffness $\Delta k_t/k_t$[16] and interparticle friction coefficient $\Delta\mu_p/\mu_p$[13] scales with $-f_t/(\mu_p f_n)$, where f_t is the oscillatory tangential force and f_n is the static normal force per contact. This scaling $(-F_{ac}/(\mu_p W))$ extends to effective shear contact stiffness at multi-contact interfaces[19], shear modulus[17] and yield stress[20] in vibrated granular media, where polydisperse contact roughness is replaced by particle contacts and inertial effects are negligible. Here, F_{ac} is the macroscopic oscillatory shear force, W is the normal load, and μ is the (average) effective interparticle friction coefficient. Thus, we adopt this scaling to describe the reduction in $\Delta\mu_p/\mu_p \sim -F_{ac}/(\mu_p W)$, implying $\mu_s^*/\mu_s \sim 1 - F_{ac}/(\mu_s W)$. For the granular layer, the shear vibration force is expressed as $F_{ac} = \hat{k}\hat{U}$, where $\hat{k}$ is the effective stiffness of the

layer, and $\hat{U}$ is the average displacement amplitude over the layer thickness $h\,(=6\ mm)$. To estimate $\hat{U}$, we assume the amplitude at distance z from the vibration table follows $U(z)\sim U_0\exp(-z/\delta)$, where U_0 is the source amplitude and $\delta\,(\sim\lambda=c/f)$ is the attenuation length dominated by wave scattering[2].

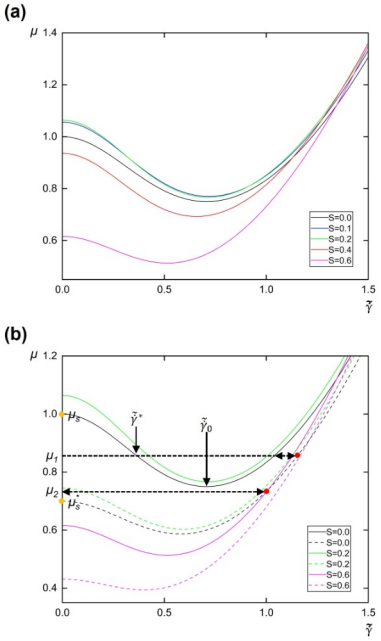

Fig. 3: (a) The effective friction coefficient μ versus flow velocity $\widetilde{\dot{\gamma}}$, as described by Eq. (1) (black solid line), illustrating velocity-weakening behavior for $0<\widetilde{\dot{\gamma}}<\widetilde{\dot{\gamma}}_0$. The minimum shear occurs at $\widetilde{\dot{\gamma}}_0=0.7$, where $\mu_d=0.75$. As pore water saturation increases, the interparticle friction coefficient first rises, then declines beyond a critical saturation. (b)Vibration reduces the interparticle friction coefficient, lowering the yield threshold from $\mu_s=1$ (black solid line) to $\mu_s=0.7$ (black dashed line). The yield criticality also decreases for different pore water content conditions (solid line before applying vibration, dashed line after applying vibration), which triggers the particle flow explained in this paper (red dots).

Thus $\widehat{U}=(1/h)\int_0^h U_0\exp(-z/\delta)dz=(\delta/h)U_0[1-\exp(-h/\delta)]$. In experiments, $\delta\ll h$, so $\hat{U}\sim(\delta/h)U_0\sim(c/fh)U_0$[1]. Using $W\sim(\rho gh)L^2$ and wave speed $c=(G/\rho)^{1/2}$, and introducing a water-dependent attenuation factor $\left[\frac{1}{1+\alpha_2 S^m}\right]$ to account for nonlinear liquid effects, we derive:

$$\frac{\mu_s^*}{\mu_s(S)}\sim 1-\frac{c^3}{g}\cdot\frac{U_0}{\mu_s(S)fh^3}\cdot\left[\frac{1}{1+\alpha_2 S^m}\right] \quad (3)$$

Eq. (3) captures key dependencies, enabling rescaling of experimental data for varying layer thicknesses, pore water saturations, vibration amplitudes, and frequencies (Fig. 2(b)). This scaling aligns with observations in Fig. 2(a), where larger U_0 is required to unjam systems with $S<S_c$. However, residual data scatter after rescaling highlights the need for further studies to quantify layer thickness and frequency effects, improving understanding of transitions between jammed (I) and unjammed (II/III) states.

Conclusion

In summary, we investigated vibration-triggered granular flow under varying wettability. Near the repose angle, reduced μ_p lowers particle threshold μ_s, the mean velocity of the triggered flow increases with vibration amplitude, and this peristaltic flow can only be sustained under prolonged excitation of the vibration and stagnates under excitation shutdown. Near the maximum avalanche angle (θ_m), rapid inertial avalanches occur, dominated by self-driven dynamics. Meanwhile the particle threshold μ_s first rises with the increase of particle pore water content and then rapidly decreases after exceeding the critical water content. We believe that this work provides a unified framework for understanding the behaviour of vibration-triggered granular material flow. Multiscale analyses will contribute to a better understanding of local and remote dynamic triggering of landslides and earthquakes by seismic waves (including aftershocks)[5][21].

References

[1] J. Léopoldès et al. "Triggering granular avalanches with ultrasound". In: *Physical Review E* 102.4 (2020), p. 042901.

[2] X. Jia, C. Caroli, and B. Velicky. "Ultrasound propagation in externally stressed granular media". In: *Physical Review Letters* 82.9 (1999), p. 1863.

[3] C.-h. Liu and S. R. Nagel. "Sound in sand". In: *Physical review letters* 68.15 (1992), p. 2301.

[4] V. Durand et al. "On the link between external forcings and slope instabilities in the Piton de la Fournaise Summit Crater, Reunion Island". In: *Journal of Geophysical Research: Earth Surface* 123.10 (2018), pp. 2422–2442.

[5] C. H. Scholz. *The mechanics of earthquakes and faulting*. Cambridge university press, 2019.

[6] H. A. Makse et al. "Granular packings: Nonlinear elasticity, sound propagation, and collective relaxation dynamics". In: *Physical Review E-Statistical, Nonlinear, and Soft Matter Physics* 70.6 (2004), p. 061302.

[7] E. T. Owens and K. E. Daniels. "Sound propagation and force chains in granular materials". In: *Europhysics Letters* 94.5 (2011), p. 54005.

[8] P. A. Johnson and X. Jia. "Nonlinear dynamics, granular media and dynamic earthquake triggering". In: *Nature* 437.7060 (2005), pp. 871–874.

[9] J. A. Dijksman et al. "Jamming, yielding, and rheology of weakly vibrated granular media". In: *Physical review letters* 107.10 (2011), p. 108303.

[10] A. Daerr and S. Douady. "Two types of avalanche behaviour in granular media". In: *Nature* 399.6733 (1999), pp. 241–243.

[11] P. Coussot et al. "Avalanche behavior in yield stress fluids". In: *Physical review letters* 88.17 (2002), p. 175501.

[12] M. Wyart. "On the dependence of the avalanche angle on the granular layer thickness". In: *Europhysics Letters* 85.2 (2009), p. 24003.

[13] J. Léopoldès, G. Conrad, and X. Jia. "Onset of sliding in amorphous films triggered by high-frequency oscillatory shear". In: *Physical Review Letters* 110.24 (2013), p. 248301.

[14] A. H. Clark et al. "Frictional weakening of vibrated granular flows". In: *Physical Review Letters* 130.11 (2023), p. 118201.

[15] H. Jaeger et al. "Friction in granular flows". In: *Europhysics Letters* 11.7 (1990), p. 619.

[16] X. Jia, T. Brunet, and J. Laurent. "Elastic weakening of a dense granular pack by acoustic fluidization: Slipping, compaction, and aging". In: *Physical Review EStatistical, Nonlinear, and Soft Matter Physics* 84.2 (2011), p. 020301.

[17] J. Brum et al. "Drastic slowdown of the Rayleigh-like wave in unjammed granular suspensions". In: *Physical Review E* 99.4 (2019), p. 042902.

[18] S. Van den Wildenberg, M. van Hecke, and X. Jia. "Evolution of granular packings by nonlinear acoustic waves". In: *Europhysics Letters* 101.1 (2013), p. 14004.

[19] L. Bureau, C. Caroli, and T. Baumberger. "Elasticity and onset of frictional dissipation at a non–sliding multi–contact interface". In: *Proceedings of the Royal Society of London. Series A: Mathematical, Physical and Engineering Sciences* 459.2039 (2003), pp. 2787–2805.

[20] S. van den Wildenberg et al. "Ultrasonic tracking of a sinking ball in a vibrated dense granular suspension". In: *Scientific Reports* 9.1 (2019), p. 5460.

[21] R. Burridge and L. Knopoff. "Model and theoretical seismicity". In: *Bulletin of the seismological society of america* 57.3 (1967), pp. 341–371.

DOI 10.5162/Ultrasonic2025/P1.11

High frequency ultrasound platform for non-invasive online monitoring of 3D cell cultures

Ruslan Shaporin[1], *Carmen Durán*[1], *Jorge Huecas*[1], *Óscar Martínez-Graullera*[1], *Alberto Ibáñez*[1], *Monserrat Parrilla*[1], *and Luis Elvira*[1]
[1]*Instituto de Tecnologías Físicas y de la Información, CSIC, Serrano 144, Madrid 28006, Spain*
luis.elvira@csic.es

Abstract: A high-frequency (10-70MHz) ultrasound platform was developed for the study of 3D cellular cultures. The system provides ultrasound images through a continuous monitoring automatically controlled. The experimental methodology proposed is compatible with the sterility and thermal conditions required for cellular studies. This work was focused on the monitorization of S.cerevisiae 3D cultures in a solid agar matrix. Results show how the availability of nutrients and medium inhomogeneities influence the morphological structure and size of the 3D cell colony.

Keywords: Non invasive monitorizacion of cells, high frequency ultrasound, 3D cellular structures.

Introduction

3D cellular cultures have gained significant interest in recent years due to their improved ability to replicate *in vitro* the *in vivo* conditions of tissues and organs, being referred as organoids. Their growing relevance lies, among others, in their potential for drug testing and the development of personalized medicine, as they can be derived from a patient's own cells. [1]. Experimental configurations comprise suspension-based systems, where cells are cultured in Matrigel —a gel that mimics the extracellular matrix by providing structural, biochemical, and biomechanical support- or Organ-on-a-Chip (OoC), which incorporates microfluidic channels to simulate the microenvironment and key functional aspects of living organs at a microscale. More recently, bioprinting has emerged as a promising technique that employs biomaterials such as collagen, Matrigel, and cells to fabricate biological structures for tissue and organ engineering [2]. Despite the advantages of 3D cultures over conventional 2D cultures and animal models, they still have some limitations, such as challenges in recreating the biochemical and physical microenvironment of the human body, lack of innervation, immune cells, and tumor stroma, as well as insufficient vascularization.

In this scenario there is a need to implement monitoring techniques that support controlled growth. Currently, the primary monitoring methods are optical and fluorescence-based techniques, which include conventional optical microscopies such as Widefield Fluorescence Microscopy, Confocal Laser Scanning Microscopy, and Multiphoton Microscopy; as well as super-resolution microscopies such as Stimulated Emission Depletion Microscopy, Single-Molecule Localization Microscopy, and Structured Illumination Microscopy [3]. Other non-fluorescence-based optical techniques are also employed, such as Optical Coherence Tomography (Full-Field OCT, Spectral Domain OCT, and Ultraviolet OCT), as well as Raman spectroscopy and microscopy [4]. Although these techniques are non-invasive, they can be destructive due to prolonged light exposure, leading to progressive fluorescence loss (photobleaching) and cellular damage (phototoxicity). Tissue penetration may also be an issue for some of them.

High frequency ultrasound imaging emerges as another monitoring approach, offering the advantage of continuous, real-time monitoring throughout the growth process without damaging cell arrangements. It enables the study of structural features, morphological changes, mechanical properties such as elasticity, and vascularization at various depths —on the order of millimeters— which is sufficient for the typical dimensions of 3D cultures [5]. Furthermore, ultrasound devices can penetrate opaque materials and have moderate cost, though image analysis requires prior expertise for accurate interpretation.

To explore the potential contributions of ultrasound to this field, a preliminary monitoring study was conducted on a 3D culture of *S. cerevisiae* yeast embedded in a solid agar matrix. The goal of this study is to pave the way for future investigations involving more complex cellular structures, such as the aforementioned organoids.

DOI 10.5162/Ultrasonic2025/P1.11

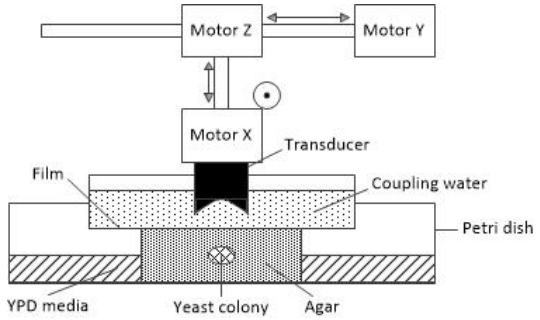

Fig. 1: Detail of the ultrasound probe and coupling with the agar containiong cells.

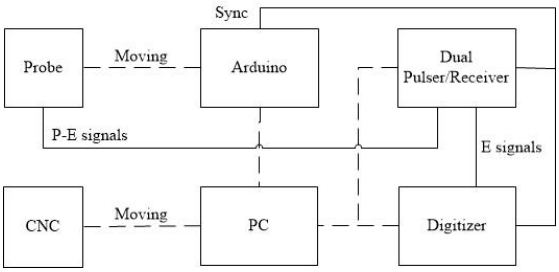

Fig. 2: Block diagram and connections of electronics.

Experimental methodology

A comercial bakery strain of *Sacharomyces cerevisiae* yeast was used for culturing. A small amount of them mixed with 100ml of YPD culture medium (2% glucose, 1% yeast extract and 2% peptone diluted in water) and placed into a culture chamber at 37 °C for 24 hours. From this liquid culture, a small volume was removed with the inoculation loop and gently dabbed on different places on the surface of a Petri dish containing YDP medium with 2% agar concentration, so new yeast colonies grew separately from each other over the agar for several days.

For the ultrasound monitoring assay, a new culture should be grown inside an agar matrix. For this purpose, a new agar with a 0.7% agar content was made under sterile conditions in a laminar flow chamber. Two differents YDP culture media were used for making this agar, once like the previous YPD described above and another using a glucose concentration of 0.3% instead of the usual 2%. The mixture YPD plus agar was heated above 90 °C to make it liquid and then, poured into a polystyrene box with a volume of 7.4 ml. After some minutes, the gel temperature falls down and the viscosity of the agar increases. When its temperature approaches 37 °C, a small yeast colony, 1–2 mm diameter, and about 1 μl volume, was placed inside the gelifying agar using tweezers to push it down until it is 3 mm below the surface. This colony was taken from the Petri dish containing the yeast colonies mentioned at the last paragraph.

Once the new agar is solidified and reached an ambient temperature close to 25 °C, it is removed from the polystyrene box and placed at the center of a new empty Petri dish. Some more YDP medium is added to ensure continuous hydration. Then a sterilyzed transparent plastic film is placed over the agar. This film separates the culture from the water used for coupling the ultrasonic transducer with the cell culture. A wide band (10-70MHz) focalized transducer, from S-Sharp was mounted in a probe able to perform linear scans through a step micromotor (X movement) at 8mm/s speed. The transducer has 10mm curvature radius and 6mm diameter. All the arrangement, ultrasound probe and culture medium (see Fig. 1) was placed over a 3D motorized and thermostatized platform (CNC VEVOR-3018-Pro) which was controlled by a PC and was used for moving the probe in Y and Z directions for getting the 3D dataset. The temperature of the platform was set to 33.5 °C to have 30 °C inside the Petri plate.

Regarding the electronics (Fig. 2), electric wideband pulsed were generated by a dual pulser-receiver (DPR-500, JSR instruments) to excite the ultrasound emission in pulse-echo configuration. Received echoes were sent to a digitizer (Picoscope-6400C), working at 313MHz sampling frequency, which finally transferred data to the control PC. An Arduino Uno microprocessor was used to generate square pulses to drive the internal motor of the probe which makes 8mm length linear scans. This pulses were synchronized with the pulser emission and the digitizer acquisition. Each B-scan was made with 10 μm lateral resolution displacements and an axiallength of 50 μm. To increase tha axial field of view, successive movements in the Z dimension provided a total field depth of 4.5mm in the experiments presented in this work. Finally, Y movements of 50μm were used to register different image slices with a total lateral displacement of 6 mm. This way, the total volume scanned was 8mm x 6mm x 4.5mm, with 1.2pl voxels (0.01mm x 0.05mm x 0.024mm), which is equal to 1.2 pl. 1 hour was needed to acquire a complete image of this volume. Four experiments were made (2 repetitions using 2% glucose medium and other 2 repetitions with 0.3% glucose medium), each lasting 120 hours.

Results

Fig. 3 and Fig. 4 shows 3D and 2D representations respectively, of the evolution of a yeast culture over time. In particular, these images belong to the first culture developed with a glucose content 2% in the agar. The 3D representation provides information about the growth towards different directions while 2D b-

DOI 10.5162/Ultrasonic2025/P1.11

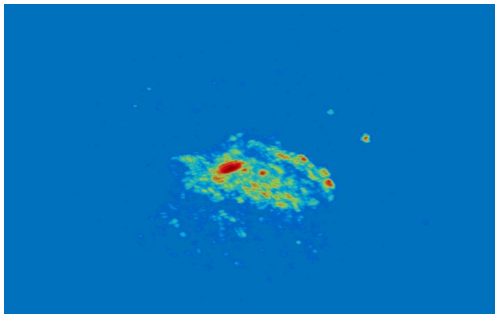

(a) Culture time: 1 hour

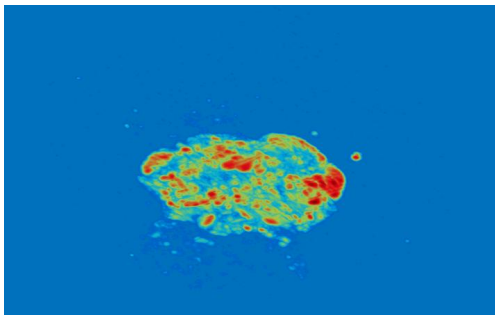

(b) Culture time: 35 hours

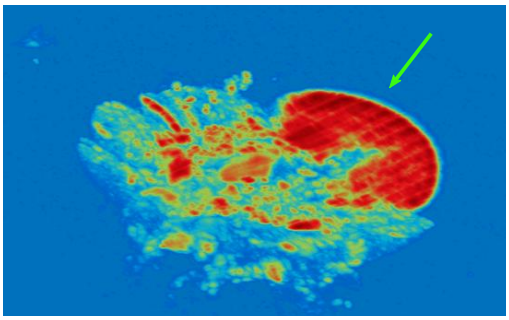

(c) Culture time: 131 hours

Fig. 3: 3D plot of the yeast colony at different culturing times. The green arrow in (c) marks an apparent crack in the medium.

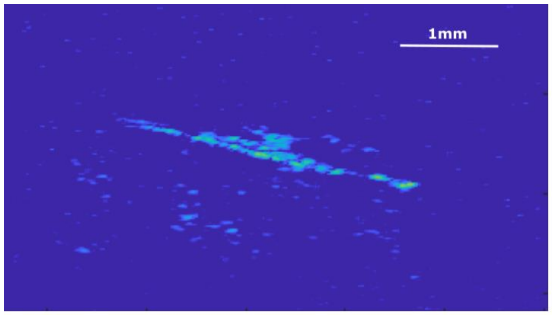

(a) Culture time: 1 hour

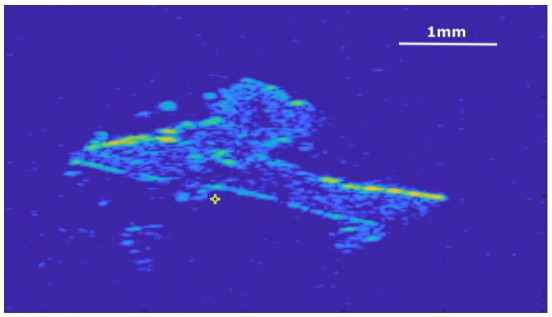

(b) Culture time: 35 hours

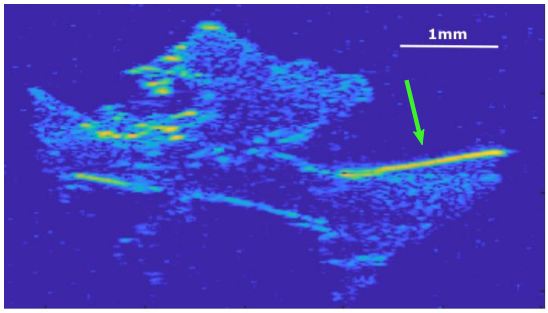

(c) Culture time: 131 hours

Fig. 4: 2D section of the yeast colony at different culturing times with scale dimensions. The green arrow in (c) marks an apparent crack in the medium.

scans complete this information by showing the echoic features of the inner parts of the colony.

In the figures presented, the volume occupied by cells increases over time. Growth is limited by the semi-solid nature of the agar and the lack of mobility in yeast cells. However, as new cells emerge by gemation, they occupy new regions of agar while seeking nutrients. This causes colony expansion in multiple directions, with irregularities in geometry that vary across the different growths monitored. These deviations from ideal globular growth may stem from local variability in nutrient distribution, statistical differences among individual cells, or mechanical variability in the gel matrix, which may experience linking failures or crack formation. This phenomenon is evident in Fig. 4, where a highly echoic line marked with an arrow (seen as a plane in Fig. 3) breaks the colony's globular structure. This echo could indicate a crack caused by internal pressure from yeast anabolism increasing biomass and/or yeast catabolism producing carbon dioxide that may form bubbles. Further studies are needed to determine the exact origin of these echoes.

Quantifying the echogeneity of the colony may help to evaluate its growth. A common way to measure microorganism concentration in liquid media is by using a spectrophotometer to assess light absorption, which correlates with cell density. Growth curves often begin with a lag phase, where cells adapt to new conditions. If conditions are similar to the previous environment, this phase may be absent (as in our case).

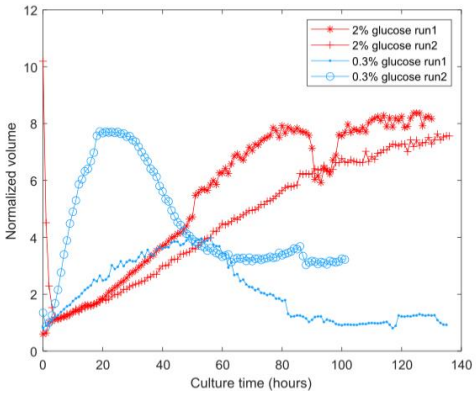

Fig. 5: Evolution of the yeast colony volume along time for 0.3% and 2% glucose content in the culture medium. The volume of the colony is normalized to the initial volume of the colony.

Then, exponential growth occurs as cells replicate, until nutrients decline, slowing growth and leading to a plateau when cell death equals cell formation.

In a parallel way, it is proposed in this work to evaluate the number voxels reaching a given intensity threshold. This number multiplied by the volume of each voxel (1.2 pl) provides the volume of the colony above such amplitude threshold. For this purpose, envelope data were referenced to the maximum and converted to dB. Fig. 5 represent the evolution of the volume of the colony above -30dB, for the two repetitions of the experiment (run 1 and run 2) made for each glucose concentration of the agar (0.3% and 2%). As the volume of the colony was sligthly different at the beggining of each experiment, this volume was normalized by the initial volume of the culture to make the volume increasing comparable between experiments. An initial growth phase was found to be even faster when the amount of glucose was lower. This probably is due to the fact that the starting colonies, which were taken from another agar plate which was cultured along several days, were also adpated to a low glucose availability. However, after some days of growth those colonies growing in the medium with a lower glucose amount exhibit a reflectivity loose between the second and the third growing day. On the contrary, those colonies growing in the medium with 2% glucose concentration did not reach this decaying stage, at least before reaching 130 culturing hours, showing a behavior similar to that described for light absorption in liquid media. The decreasing of reflectivity found for the lower glucose concentration experiments may be a result of four different processes: cell deaths exceeding cell production when the glucose availability is suddenly reduced; a fast carbon dioxide production giving rise to wave reflection (first reflectivity increment) which, afterwards, is slowly dispersed in the medium (reflectivity decreasing); a high local concentration of cells which is followed by a stage of cell spreading in the medium which made many cells not able to produce an echo level reaching the threshold for quantification, and/or a change in the cellular state and physical properties as a result of nutrient depletion: yeast may form spores with a significant smaller size than yeast cells. Further studies should clarify the most determinant yeast processes under the reflectivity evolution registered.

Conclusions

The high frequency ultrasound imaging system proposed was able to monitor 3D yeast growing arrangements in a semi-solid matrix, providing information of structures developed inside such formations. This opens the possibility of using such technology to monitor other 3D cellular arrangements (tissues, organoids...) providing insights about their structural and mechanical features.

Acknowledgements

Work funded by PID2022 -138013OB -I00 /MCIN /AEI /10.13039/ 501100011033/ FEDER, UE and by the project UCRAN20017 (CSIC funds). Jorge Huecas was hired under the Generation D initiative, promoted by Red.es, an organisation attached to the Ministry for Digital Transformation and the Civil Service, for the attraction and retention of talent through grants and training contracts, financed by the Recovery, Transformation and Resilience Plan through the European Union's Next Generation funds (European Commission – NextGenerationEU, through Momentum CSIC Programme: Develop Your Digital Talent).

References

[1] Z. Zhao et al. "Organoids". In: *Nature Reviews Methods Primers* 2.1 (2022), p. 94.

[2] E. Garreta et al. "Rethinking organoid technology through bioengineering". In: *Nature materials* 20.2 (2021), pp. 145–155.

[3] W. Mao et al. "Spectroscopic techniques for monitoring stem cell and organoid proliferation in 3D environments for therapeutic development". In: *Advanced Drug Delivery Reviews* 201 (2023), p. 115074.

[4] B. Sarri et al. "In vivo organoid growth monitoring by stimulated raman histology". In: *npj Imaging* 2.1 (2024), p. 18.

[5] S. Y. Nam et al. "Ultrasound and photoacoustic imaging to monitor vascular growth in tissue engineered constructs". In: *Optics in Tissue Engineering and Regenerative Medicine III*. Vol. 7179. SPIE. 2009, pp. 104–110.

DOI 10.5162/Ultrasonic2025/P1.15

Data-Driven Frequency-Domain Full Waveform Inversion for Ultrasonic Breast Imaging

Mengting Qin[1], *Yue Zhao*[1], *and Hanlong Yin*[1]
[1]*Control Theory and Engineering, School of Astronautics, Harbin Institute of Technology,Harbin, China*
yue.zhao@hit.edu.cn

Abstract: Frequency-domain full waveform inversion is a high-resolution ultrasound method. It shows potential for breast imaging. However, it requires heavy computation and storage. These limitations restrict clinical use. We propose an end-to-end deep learning framework. This framework is constructed upon the encoder-decoder architecture of convolutional neural networks (CNNs) and is capable of directly mapping ultrasonic field data to the corresponding sound velocity distribution. Numerical simulations verify its effectiveness and efficiency.

Keywords: full waveform inversion, frequency-domain, deep learning, ultrasound tomography, breast imaging

Introduction

Ultrasound Computed Tomography (UCT) is an emerging imaging modality that employs ultrasonic transducers to emit ultrasound waves and capture interaction data with internal tissues. This enables the reconstruction of cross-sectional quantitative parameter distributions—such as sound speed and acoustic attenuation—within target tissues [1], [2]. UCT demonstrates significant potential in breast imaging by providing high-resolution images of acoustic properties within breast tissue [3].

Full Waveform Inversion (FWI), a high-resolution imaging technique originating in seismic exploration, achieves precise subsurface modeling through the utilization of full wavefield information [4]. Compared to conventional geometric reconstruction methods used in UCT, FWI establishes physics-based models grounded in wave theory equations and reconstructs tissue distributions using complete acoustic pressure data, yielding superior resolution [5]–[7]. However, FWI's high-precision imaging capability comes at the cost of substantial computational resources and storage requirements for repeated wave equation solutions, hindering its clinical adoption [8].

To mitigate computational demands, most clinical UCT implementations employ frequency-domain FWI [9], [10]. By eliminating temporal parameters and utilizing selected frequency components, frequency-domain FWI significantly reduces computational load while preserving high imaging accuracy. Nevertheless, even frequency-domain FWI necessitates iterative solutions of Helmholtz equations, resulting in prolonged computation times and high algorithmic complexity.

Recent advances in deep learning have demonstrated the capability of neural networks to approximate nonlinear operators [11], [12]. Current research focuses on leveraging neural networks to accelerate time-domain FWI reconstruction [13]–[15]. Inspired by these developments, this work proposes a deep learning-based image reconstruction method that achieves end-to-end sound speed reconstruction via frequency-domain FWI using tri-frequency breast simulation data. While conventional numerical FWI reconstruction with only three frequency bands typically fails to produce high-resolution images, our proposed network maintains satisfactory reconstruction quality while significantly reducing both input frequency requirements and computation time. Comparative studies with traditional reconstruction methods validate the effectiveness of deep neural networks in accelerating frequency-domain FWI image reconstruction.

Theory and Methods

The frequency-domain FWI imaging method is based on the frequency-domain acoustic wave equation, i.e., the Helmholtz equation. Following discretization of the imaging domain, the method establishes the functional relationship between the acoustic source s, angular frequency ω (where $\omega = 2\pi f$), velocity distribution c, and the resulting wavefield u as:

$$\left(\nabla^2 + \left(\frac{\omega}{c(\boldsymbol{r})}\right)^2\right) u(\boldsymbol{r},\omega) = -s(\boldsymbol{r},\omega) \quad (1)$$

where $\boldsymbol{r} \in \mathbb{R}^2$ is the position vector in the imaging domain, and ∇ represents the second-order spatial differential operator acting on the relevant field.

Traditional FWI imaging requires repeated solutions of the Helmholtz equation, where solving these second-order differential equations demands substantial computational resources and time. To accelerate

DOI 10.5162/Ultrasonic2025/P1.15

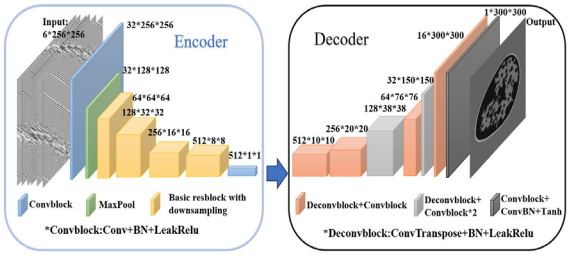

Fig. 1: The encoder-decoder framework based on CNNs.

computations, this study employs a data-driven approach to establish a direct mapping from observed wavefield data to velocity distribution.

Model: The proposed convolutional neural network (CNN) adopts an encoder-decoder architecture designed to capture complex input-output relationships, enabling direct transformation from the wavefield domain to the velocity domain (Fig. 1).

Using the encoder, high-dimensional input data undergoes feature extraction and dimensionality reduction. The encoder architecture incorporates pooling layers and diverse convolutional modules, which ultimately transform the extracted features into multi-channel unit vectors. Correspondingly, the decoder receives these high-dimensional unit vectors and reconstructs the features through a deconvolution module, mapping them back to the sound velocity field.

The model input consists of tri-frequency breast wavefield observation data. Each dataset contains wavefield measurements acquired through a circumferential array of 256 equally spaced transducers functioning simultaneously as transmitters and receivers. During data acquisition, each transmitter undergoes sequential excitation while all receivers concurrently record the resulting wavefields. The output is a reconstructed sound velocity distribution map of the breast.

Loss function: The neural network's loss function integrates composite L1 and L2 norms comparing predicted and true sound velocity distributions in breast tissue, formally expressed as

$$L_\phi = L_1\left(\phi\left(u_{obs}\right) - c_{real}\right) + L_2\left(\phi\left(u_{obs}\right) - c_{real}\right) \tag{2}$$

where c_{real} denotes the true sound velocity distribution within the breast tissue and u_{obs} represents the tri-frequency wavefield measurement data. While the L2 norm constitutes the predominant objective function in FWI methodologies, it exhibits significant noise sensitivity. Conversely, the L1 norm demonstrates relative noise insensitivity. To leverage these complementary properties, this work employs a composite objective function integrating both norms.

Numerical Simulation

The breast sound velocity and wavefield observation data utilized in this study originate from the "Reconstruction of Wave Velocity in Ultrasonic Computed Tomography" competition within the AI4S Cup. The dataset comprises 7,200 paired instances of breast wavefield observations and corresponding sound velocity distributions.

The wavefield observations contain tri-frequency measurements at 0.3 MHz, 0.4 MHz, and 0.5 MHz. For each frequency, data acquisition involves sequential acoustic emission from individual transducers within a 256-element circumferential array, with all elements simultaneously functioning as receivers. Consequently, each frequency band contains 256 $\times$ 256 complex-valued measurements. To prepare these complex wavefield data for network input, real and imaginary components are separated into distinct channels. The complete breast observation dataset thus forms 6 $\times$ 256 $\times$ 256 tensors (three frequencies $\times$ two components). To mitigate near-field interference artifacts, measurements from transducers adjacent to the active emitter are nullified.

Sound velocity distributions are represented as 480 $\times$ 480 real-valued matrices. During training, only the clinically relevant central region [90:390, 90:390] (300 $\times$ 300 matrix) is retained as model output. Given the distinct characteristics of complex-valued inputs versus positive-real outputs, separate normalization schemes are applied: input data are scaled to [-1, 1], while output velocities are normalized to [0, 1]. This differentiated preprocessing is critical for optimizing imaging performance.

Numerical breast phantoms (N = 7,200) were partitioned into training (80 percent) and testing sets (20 percent). Reconstruction quality was quantified using Structural Similarity Index Measure (SSIM) and Root Mean Square Error (RMSE). Training employed 300 epochs with batch size 16, using the Adam optimizer (initial learning rate 0.001).

For traditional method comparison, benchmark FWI reconstructions were performed using competition-provided velocity phantoms. Simulations featured a 256-element transducer array (radius 3.225 cm) imaging a 480 $\times$ 480 grid (pixel size 0.15 mm). Frequency-domain FWI utilized 20 frequencies from 0.3-1.25 MHz (50 kHz increments) with 3 iterations per frequency.

Results

The quantification results of the test set subsequent to being processed by the network are presented in Tab. 1. Quantitative analysis yielded mean SSIM and RMSE

DOI 10.5162/Ultrasonic2025/P1.15

Tab. 1: Quantitative assessment results.

Quantitative Evaluation	Mean	Range
SSIM	0.88	$(0.70, 0.94)$
RMSE	9.58	$(4.60, 41.05)$

values of 0.88 and 9.58. For most test images, reconstructed SSIM exceeds 0.8 while RMSE predominantly resides within [5, 20]. Evaluation metrics reveal limited cases where predicted sound velocity distributions significantly deviate from ground truth—an inherent limitation of data-driven approaches. This method lackes explicit physical constraints and cannot achieve perfect mapping, resulting in challenging mappings from wavefield observations to velocity distributions for certain samples.

Fig. 2 comparatively demonstrates reconstruction outcomes between deep learning and conventional methods. Traditional FWI yields clearer internal tissue boundaries but suffers from circular boundary artifacts and internal artifacts caused by suboptimal sound velocity initialization or phase mismatch. Conversely, the deep learning approach produces smoother velocity distributions at the cost of some internal boundary detail. Despite localized inaccuracies, deep learning reconstructions exhibit superior image resolution.The cross-sectional sound velocity comparison reveals that the deep learning method produces a smoother velocity profile with minimal fluctuations across the continuous range, potentially limiting its ability to resolve subtle variations. Nevertheless, its overall trend closely corresponds with the true sound velocity. In contrast, the traditional inversion method can generally match the actual trend of sound velocity changes, although the reconstructed sound velocity values are not completely accurate.The root cause of this phenomenon likely stems from the network's inability to effectively incorporate frequency-related information present in the input data. This limitation hinders the network's capacity to capture the characteristic dependencies between the observed data and its frequency components. As a result, significant detail loss occurs during image reconstruction. This is particularly notable given that traditional methods typically require approximately 7-fold more observed data input than deep learning approaches.

When achieving accurate velocity mapping, the deep learning approach attains reconstruction quality comparable to conventional FWI. Notably, our method requires only three frequency observations versus twenty for traditional FWI. Crucially, the data-driven approach reconstructs breast sound velocity maps in less than 1 second versus almost 3 hours for

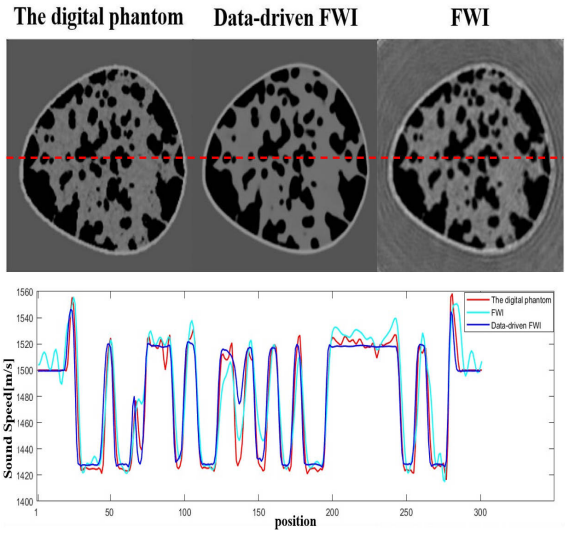

Fig. 2: Comparison of data-driven methods and traditional methods in imaging.

conventional methods. This demonstrates deep learning's potential to accelerate computationally intensive FWI techniques, suggesting trained neural networks could facilitate clinical translation of time-intensive wave velocity reconstruction.

Conclusion

This study demonstrates a data-driven FWI methodology for ultrasound breast image reconstruction. The proposed neural network employs an encoder-decoder architecture to establish direct mapping from tri-frequency wavefield observations to breast sound velocity distributions. Numerical experiments confirm the method's efficacy, with the trained network achieving high reconstruction metrics (mean SSIM: 0.88, RMSE: 9.58). Crucially, the data-driven approach generates artifact-free images comparable to conventional frequency-domain FWI results in less than 1 second versus about 3 hours. However, owing to the absence of explicit physical interpretation, deep learning methods are unable to guarantee fully accurate predictions. While deep learning reconstructions exhibit marginally reduced detail fidelity compared to traditional methods, the substantial acceleration presents a clinically viable pathway for real-time ultrasound reconstruction - particularly when balancing diagnostic utility against computational demands in clinical deployment.

ACKNOWLEDGMENT

This study was partially funded by the Natural Science Foundation of Heilongjiang province under Grant No. YQ2022F010, by the Natural Science Foundation of China (62173116, 62473108) and the postdoctoral

initial funding of Heilongjiang Province (No. LBH-Q21097).

References

[1] N. Duric, P. Littrup and C. Kuzmiak, 'Breast ultrasound tomography,' *Breast Imaging*, vol. 6, 2018.

[2] C. Li, N. Duric, P. Littrup and L. Huang, 'In vivo breast sound-speed imaging with ultrasound tomography,' *Ultrasound in medicine & biology*, vol. 35, no. 10, pp. 1615–1628, 2009.

[3] N. Duric, P. Littrup, C. Li *et al.*, 'Detection and characterization of breast masses with ultrasound tomography: Clinical results,' in *Medical Imaging 2009: Ultrasonic Imaging and Signal Processing*, SPIE, vol. 7265, 2009, pp. 457–464.

[4] A. Tarantola, 'Inversion of seismic reflection data in the acoustic approximation,' *Geophysics*, vol. 49, no. 8, pp. 1259–1266, 1984.

[5] L. Guasch, O. Calderón Agudo, M.-X. Tang, P. Nachev and M. Warner, 'Full-waveform inversion imaging of the human brain,' *NPJ digital medicine*, vol. 3, no. 1, p. 28, 2020.

[6] F. Lucka, M. Pérez-Liva, B. E. Treeby and B. T. Cox, 'High resolution 3d ultrasonic breast imaging by time-domain full waveform inversion,' *Inverse Problems*, vol. 38, no. 2, p. 025 008, 2021.

[7] N. Zhang, Y. Zhao, Y. Yuan, Y. Xiao, M. Qin and Y. Shen, 'Cross-correlation adjustment full-waveform inversion with source encoding in ultrasound computed tomography,' *Ultrasonics*, vol. 142, p. 107 392, 2024.

[8] K. Wang, T. Matthews, F. Anis, C. Li, N. Duric and M. A. Anastasio, 'Waveform inversion with source encoding for breast sound speed reconstruction in ultrasound computed tomography,' *IEEE transactions on ultrasonics, ferroelectrics, and frequency control*, vol. 62, no. 3, pp. 475–493, 2015.

[9] R. Ali, T. M. Mitcham, T. Brevett *et al.*, '2-d slicewise waveform inversion of sound speed and acoustic attenuation for ring array ultrasound tomography based on a block lu solver,' *IEEE transactions on medical imaging*, 2024.

[10] C. Zhou, K. Xu and D. Ta, 'Frequency-domain full-waveform inversion-based musculoskeletal ultrasound computed tomography,' *The Journal of the Acoustical Society of America*, vol. 154, no. 1, pp. 279–294, 2023.

[11] G. Wang, J. C. Ye and B. De Man, 'Deep learning for tomographic image reconstruction,' *Nature machine intelligence*, vol. 2, no. 12, pp. 737–748, 2020.

[12] L. Lozenski, H. Wang, F. Li *et al.*, 'Learned full waveform inversion incorporating task information for ultrasound computed tomography,' *IEEE transactions on computational imaging*, vol. 10, pp. 69–82, 2024.

[13] W. Zhang and J. Gao, 'Deep-learning full-waveform inversion using seismic migration images,' *IEEE Transactions on Geoscience and Remote Sensing*, vol. 60, pp. 1–18, 2021.

[14] Y. Wu and Y. Lin, 'Inversionnet: An efficient and accurate data-driven full waveform inversion,' *IEEE Transactions on Computational Imaging*, vol. 6, pp. 419–433, 2019.

[15] T. Robins, J. Camacho, O. C. Agudo, J. L. Herraiz and L. Guasch, 'Deep-learning-driven full-waveform inversion for ultrasound breast imaging,' *Sensors*, vol. 21, no. 13, p. 4570, 2021.

DOI 10.5162/Ultrasonic2025/P1.16

Construction of a high-frequency ultrasonic flow-through chamber for emulsion and suspension separation

E.J Ramírez González[1], C.M Giraldo Atehortua [1], T.F. de Oliveira [1], L.O V. Pereira [2], J. H. Lopes[3], M. S.G. Tsuzuki[1], and F. Buiochi[1]
[1]Universidade de São Paulo, Department of Mechatronics Engineering Escola Politécnica, São Paulo, Brazil
[2] Petrobras, CENPES, Rio de Janeiro, Brazil
[2]Universidade Federal de Alagoas, Campus Arapiraca, Maceió, Brazil
eduardo1@usp.br

Abstract: High-frequency standing field can use the produced acoustic radiation force to separate and/or manipulate droplets and/or particles in liquids. While recent research has focused on microfluidics, there still remains a gap regarding the design parameters and characterization of large-scale, flow-through acoustic separation devices. Experimental validation demonstrated the formation of ultrasonic standing wave bands and the separation of oil-in-water emulsions. Simulation and experimental results showed consistent similarities.

Keywords: High-frequency ultrasound, acoustic separation, chamber design, oil-in-water emulsion, cornstarch suspension.

Introduction

Ultrasonic standing waves have been widely studied for particle manipulation and emulsion/suspension separation in microfluidic acoustophoresis and macroscale chambers [1]. High-frequency stationary ultrasonic fields generate acoustic radiation forces [2], which drive particles in liquids toward pressure nodal or antinodal planes. These forces enhance phase separation in acoustic chambers containing emulsions and suspensions [3]. Using ultrasound in the high kilohertz to low megahertz range is appealing due to its ability to control particles with minimal deformation and lower energy consumption compared to other methods [4]. Although recent studies have explored the fundamentals of acoustic standing waves in microfluidic systems, gaps remain in the design and characterization of large-scale, flow-through acoustic separators. Promising applications include the food, petrochemical, pharmaceutical, and biomedical sectors [5].

The resonating chamber design is critical for ultrasonic separators. Large chambers produce parallel nodal planes using a piezoelectric element bonded to a carrier layer. This assembly emits sound into a liquid-holding cavity, or active volume, which is bounded by a reflector. The cavity's resonant frequency depends on the sound speed in the active volume, which is temperature-dependent [6].

The present work presents the design of a high-frequency flow-through chamber for emulsion and suspension separation with six ultrasonic transducers of 1MHz. Working in the resonant frequencies of the cavity is crucial to maintain the standing wave inside the chamber, which may be altered by temperature or other parameters [6], therefore, a frequency tracking strategy was implemented to overcome the sound speed variation inside the active volume due to its temperature variation [7] .

Theory

Sound is an oscillating pressure wave that propagates through a medium with a specific frequency. When an ultrasound field is applied to a fluid containing suspended particles, they are influenced by the acoustic radiation force generated by wave scattering on the particles [8]. A standing wave forms from the reflection of a sound wave off a wall or a second transducer, resulting from the superposition of two propagating waves. This creates constructive interference, producing regions of maximum pressure amplitude (antinodes) and regions of zero pressure (nodes) [5].

Acoustic radiation force is categorized into primary and secondary components. The primary force acts along the wave propagation direction and drives particles toward nodes or antinodes of a standing wave. The secondary force clusters particles and helps maintain their positions. The primary radiation force (PRF) is given by [9]

$$F_r = -\left(\frac{\pi p_0^2 V_c}{2\lambda\rho_0 c_0^2}\right)\phi\sin(2kx). \qquad (1)$$

This force is proportional to the square of the acoustic pressure amplitude p_0^2 and the particle volume V_c. Here, x is the droplet position relative to a pressure node, λ the acoustic wavelength, k the wavenumber,

DOI 10.5162/Ultrasonic2025/P1.16

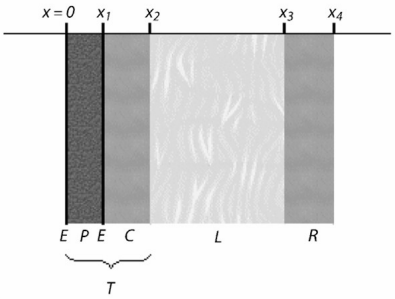

Fig. 1: Layered resonator and parts [6].

and c_0 the speed of sound in the fluid. The force strongly depends on particle size. Note also that pressure amplitude scales with applied voltage in piezoceramics. The acoustic contrast factor ϕ is defined as [9]

$$\phi = \frac{5\rho_d - 2\rho_0}{2\rho_d + \rho_0} - \frac{\rho_0 c_0^2}{\rho c_d^2}, \tag{2}$$

where ρ_d and c_d are the droplet's density and sound speed, respectively. The sign of ϕ—determined by the relative densities and sound speeds of the droplet and fluid—dictates force direction: droplets with positive ϕ migrate to pressure nodes, while those with negative ϕ move to antinodes.

The goal in designing and assembling the chamber is to efficiently transfer acoustic energy into the fluid. Fig. 1 shows a simple stack of plane-parallel layers: a piezoelectric element (P) bonded to a carrier layer (C). Together, they form the transducer (T), which emits an acoustic signal into the cavity containing the suspension liquid (L), also called the active volume (AV). This volume is bounded by a reflector (R) on the opposite side, which must remain parallel to the carrier to generate a standing wave [6].

PZT (lead-zirconate-titanate) ceramics, especially "hard" types, are commonly used as piezoelectric elements due to their strong ultrasonic output and high electro-mechanical coupling, particularly when the plate thickness is near multiples of a half wavelength. The reflector layer typically has high acoustic impedance (i.e., hard and dense), and its thickness should also be a multiple of $\lambda/2$ [10]. The active volume length is usually a multiple of $\lambda/2$ [11]. In multi-wavelength resonators, maintaining the driving frequency is essential, as temperature changes alter the speed of sound and thus the wavelength [12]. Turbulence, the main mechanism for flow across nodal planes, becomes more likely as dimensions increase [6].

Method and materials

A 136 cm^3 active volume chamber with six 1 MHz PZT piezoceramic plates (40×20×2 mm) was built,

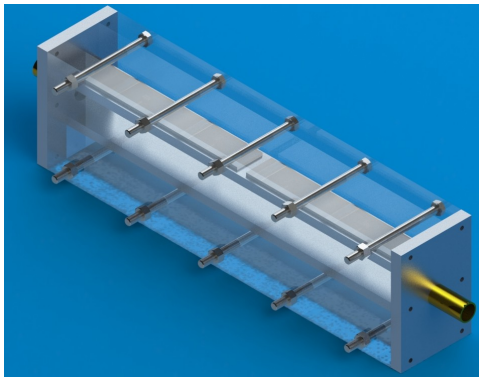

Fig. 2: Render of ultrasonic separation chamber.

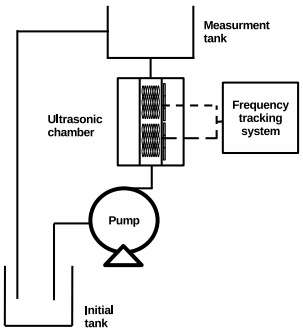

Fig. 3: Experimental circuit.

as illustrated in Fig. 2. The PZTs were bonded with conductive epoxy (EPO-TEK H20E) to a 6.4 mm aluminum coupling layer (approximatelly 2×λ/2) to generate standing waves in a 20 mm cavity, bounded by a parallel aluminum reflector of equal thickness. Acrylic plates allowed sample visualization, and both ends were sealed with aluminum plates featuring 9.2 mm inlet and outlet ports. To verify resonance, the chamber was characterized using an impedance analyzer (E5061 Keysight). Acoustic pressure simulations with water were performed in COMSOL Multiphysics 6.2, modeling piezoelectric, electric, and acoustic coupling.

Flow-through acoustic separation tests were conducted using a cornstarch suspension (9 g in 1800 cm^3 water) and a synthetic oil-in-water microemulsion with 3000 ppm oil (10 g petroleum, 9 g surfactant, 3000 cm^3 water at 80°C). Oil content was measured with an HD-1000 oil-in-water analyzer. Both tests ran at 40 W, 100 mL/min flow rate, and 30 minutes of ultrasound exposure. A resonance tracking system compensated for frequency shifts from temperature-induced sound speed variations. The experimental circuit diagram is shown in Fig. 3.

DOI 10.5162/Ultrasonic2025/P1.16

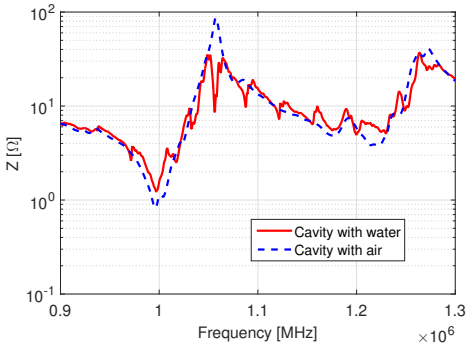

Fig. 4: Impedance of ultrasonic separation chamber.

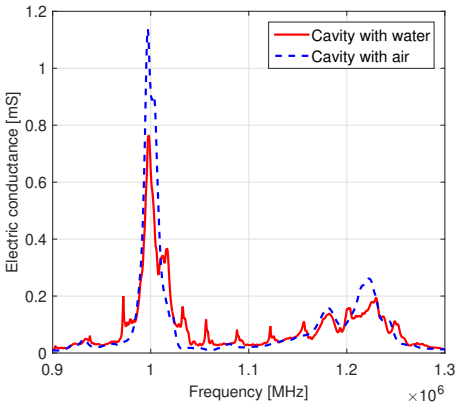

Fig. 5: Conductance of ultrasonic separation chamber.

Results and discussion

The constructed chamber was characterized by measuring impedance and conductance with and without water, as shown in Fig. 4 and Fig. 5. The piezoceramic resonance appears near 1MHz—as a low-impedance peak in Fig. 4 and a conductance peak in Fig. 5. The small peaks are attributed to the cavity. The presence of fluid introduces additional peaks from standing wave resonances, which shift with temperature.

A 2D COMSOL simulation was used to analyze standing wave pressure distribution across frequencies. Materials included aluminum, water, and PZT-4. Interfaces applied were pressure acoustics, frequency domain, solid mechanics, and electrostatics, with couplings for acoustic-structure boundary and piezoelectric effect. The fluid domain was meshed at $\lambda/8$ and given 0.2dB/m attenuation; the piezoelectric damping factor was set to 1×10^{-8}. Simulated impedance is shown in Fig. 6 alongside the experimental curve.

Fig. 6 shows that most resonance peaks align in frequency between simulation and experiment, though simulated amplitudes are higher—likely due to unmodeled attenuation in the experimental setup. The first flow-through acoustic separation test used the corn-

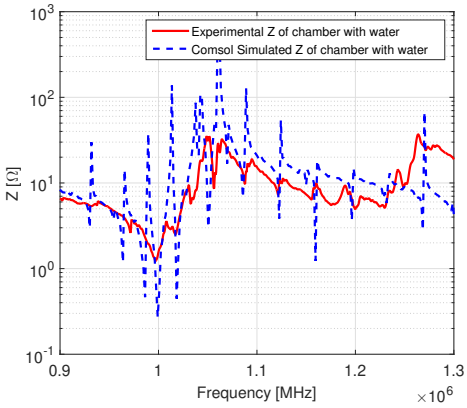

Fig. 6: Impedance of the ultrasonic chamber.

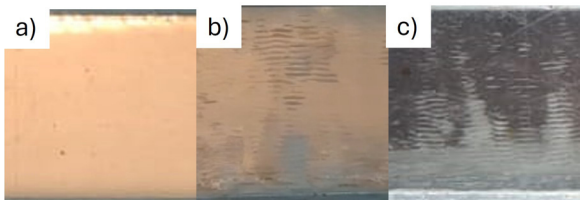

Fig. 7: Cornstrach separation test. a) Ultrasound OFF, b) Ultrasound ON, c) Treated water.

starch suspension. Upon ultrasound activation, particles rapidly agglomerated in a pattern that matched the simulations. Over time, cornstarch settled at the cavity bottom, leaving visibly clearer water (see Fig. 7). Although the operation remained stable, turbulence near the fluid inlet increased at flow rates of 500–1000 cm^3/min, which hindered particle agglomeration. Simulated and experimental standing wave patterns are shown in Fig. 8. A second experiment used a 3000 ppm synthetic oil-in-water microemulsion, with six tests—three with 30-minute ultrasound exposure and three without. Results are shown in Fig. 9 and Tab. 1.

Since the microemulsion was initially at approximately 55°C, early measurements were taken in a stirred tank since the pump operates below 45°C. Once cooled, measurements continued at the ultrasonic chamber outlet. Despite similar trends (Fig. 9), results show that ultrasonic treatment achieves faster

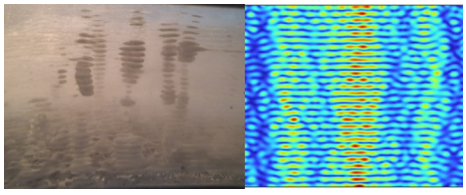

Fig. 8: Pressure pattern inside cavity.

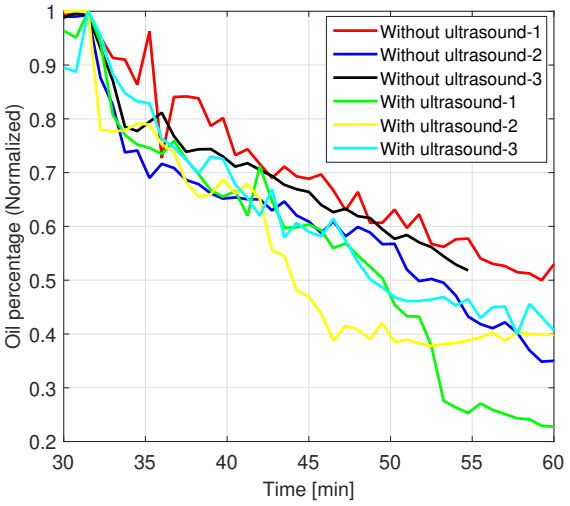

Fig. 9: Oil separation over time.

Tab. 1: Oil separation efficiency

Ultrasound	Ini. (PPM)	Fin.(PPM)	Separ (%)
Off 1	2354	1448	38%
Off 2	2053	1378	33%
Off 3	2067	1378	33%
On 1	2080	709.7	66%
On 2	2339	1133	52%
On 3	2650	1358	49%

and higher separation efficiency.

The results shown in Tab. 1 were obtained by measuring the petroleum content before and after a 20-minute acoustic treatment. In the absence of ultrasound, the average separation was 35%, in contrast, ultrasound application increased the average separation to 55%, with a maximum value of 66%. This corresponds to an improvement of approximately 36% relative to the condition without ultrasound.

Conclusions

A high-frequency ultrasonic flow-through chamber was designed, built, characterized, and tested for emulsion and suspension separation. Ultrasound effectively enhanced separation, as validated by simulations and impedance measurements. In oil-in-water emulsions, separation improved by approximatelly 36% over baseline. However, high inlet flow rates caused turbulence, reducing efficiency by disrupting droplet clustering—emphasizing the need to optimize both flow and acoustic conditions. Future studies will explore flow rate and power variations to identify optimal settings. Overall, results confirm ultrasound as a scalable method for improving separation in flow-through systems, with applications in wastewater treatment and oil recovery.

Acknowledgements

The authors acknowledge Petrobras/ANP (grants 5850.0109314.18.9 and 5850.0108871.18.9), CAPES, and CNPq (grants 306.123/2022-3 and 312.126/2021-2) for their financial support to this research.

References

[1] F. J. Trujillo et al. "Separation of suspensions and emulsions via ultrasonic standing waves - A review". In: *Ultrason Sonochem*. Vol. 21. 2014, pp. 2151–2164.

[2] X. Luo et al. "Phase separation technology based on ultrasonic standing waves: A review". In: *Ultrason Sonoch* 48 (2018), pp. 287–298.

[3] G. D. Pangu and D. L. Feke. "Acoustically aided separation of oil droplets from aqueous emulsions". In: *Chem Eng Sci* 59 (15 2004), pp. 3183–3193.

[4] J. Mierez et al. "Recent advances of ultrasound applications in the oil and gas industry". In: *Ultrason Sonochem* 103 (2024).

[5] T. Leong et al. "Ultrasonic separation of particulate fluids in small and large scale systems: A review". In: *Ind Eng Chemistry Research* 52 (47 2013), pp. 16555–16576.

[6] J. J. Hawkes and S. Radel. "Acoustofluidics 22: Multi-wavelength resonators, applications and considerations". In: *Lab Chip* 13 (4 Feb. 2013), pp. 610–627. ISSN: 14730189. DOI: 10.1039/c2lc41206c.

[7] C. M. G. Atehortúa et al. "Design and Implementation of the Frequency Control in an Ultrasonic Break Water-in-Oil Emulsion Chamber". In: *Physics Proc* 70 (2015). 2015 ICU, pp. 42–45.

[8] H. Bruus. "Acoustofluidics 7: The acoustic radiation force on small particles". In: *Lab Chip* 12 (6 2012), pp. 1014–1021.

[9] T. Laurell, F. Petersson, and A. Nilsson. "Chip integrated strategies for acoustic separation and manipulation of cells and particles". In: *Chem Soc Rev* 36 (3 2007), pp. 492–506.

[10] L. Kinsler et al. *Fundamentals of Acoustics*. Wiley, 2000. ISBN: 9780471847892.

[11] A. Lenshof et al. "Acoustofluidics 5: Building microfluidic acoustic resonators". In: *Lab Chip* 12 (4 2012), pp. 684–695.

[12] M. Greenspan and C. E. Tschiegg. "Tables of the Speed of Sound in Water". In: *J Acoust Soc Am* 31 (1).

DOI 10.5162/Ultrasonic2025/P1.17

Separation of crude oil from wastewater using high-frequency ultrasound

Carlos Mario Giraldo Atehortua[1], *Agesinaldo Matos Silva Jr*[1], *Flávio Buiochi*[1], *Luiz Octávio Vieira Pereira*[2], *José Henrique Araujo Lopes de Andrade*[3], *and Marcos Sales Guerra Tsuzuki*[1]
[1]*Department of Mechatronics Engineering, Escola Politécnica da Universidade de São Paulo, Brazil*
[2]*PETROBRAS/CENPES, Av. Horácio Macedo 950, Ilha do Fundão, Rio de Janeiro, Brazil*
[3]*Grupo de Acústica e Aplicações (GAAP), Núcleo de Ciências Exatas (NCEX), Universidade Federal de Alagoas, Campus Arapiraca, Alagoas, Brazil*
carlosmgiraldo@usp.br

Abstract: Crude-oil and gas production always generates a large amount of stable oily wastewater. An alternative treatment involves the use of high-frequency ultrasound to induce oil separation. A controlled 1 MHz ultrasonic chamber was used to separate a 2500ppm (g_{oil}/g_{water}) synthetic Brazilian crude-oil-in-water emulsions without the use of chemical additives. An oil separation efficiency of about 70% was achieved with a power input of around 40 W applied for 2 minutes. In contrast, the non-acoustic reference resulted in an oil separation of only around 3.6%.

Keywords: High-frequency ultrasound, acoustic radiation force, resonance control, oil-in-water emulsion, emulsion separation.

Introduction

A large amount of oily wastewater is constantly generated during the crude-oil and gas production [1]. The wastewater can be considered a crude-oil-in-water microemulsion, with oil concentrations varying up to 5000 ppm, which must be treated before being discarded or reused following strict environmental regulations and oil industry specifications [2]. Such microemulsions remain a challenge for the oil industry due to their high stability, which makes them difficult to separate and recover [3]. Their treatment is commonly performed using the following processes: gravity separators and bed coalescers [4] that are essentially large settling tanks for water and settleable solids, hydrocyclones [5] in which the oily water is forced through a conical spiral that accelerates and displaces it along the internal walls, and the oil droplets tend to be displaced towards the central part of the spiral, facilitating their extraction, gas flotation [6] injection of dissolved or induced gas is a technique used to increase the difference in density between water and oil droplets to promote separation, and chemical additives [7] that usually are water-soluble and aid the flocculation process in which particles are aggregated together.

An alternative treatment involves the use of the acoustic radiation force, generated by high-frequency ultrasound, to induce oil separation. Although this technique is being applied in industries such as chemical, food processing, and medicine, its application for separating crude-oil from wastewater is still under development [8]. In the ultrasonic technique for treating oily wastewater, an acoustic chamber is used to produce high-frequency ultrasound that promotes oil separation by inducing the agglomeration and/or coalescence of oil droplets [9]. This process increases the size of the droplets and their buoyant capability, consequently enhancing the separation process.

A dual closed-loop control system was implemented in the ultrasonic chamber to maintain consistent resonance and stable delivery of acoustic energy. This setup actively monitors the resonance frequency and modulates input power through proportional-integral and proportional controllers. Similar feedback mechanisms have been successfully employed to enhance acoustic control and precision in treatments such as selective cell trapping and resonator-based bulk mode acoustophoresis [10, 11]. These methodologies offer reliability despite varying loads and temperatures, making them ideal for intricate emulsified systems.

Acoustic separation

An acoustic chamber vibrates at its resonance frequency driven by a piezoelectric transducer, which generates the so-called acoustic radiation force within a sample cavity of the chamber. In oily wastewater, the collision of emulsified oil droplets can be improved by this force, which can induce coalescence between droplets and aid in their separation [12].

The acoustic contrast factor is a characteristic value that defines the direction and magnitude of the acoustic force. This parameter contains the relative physical

DOI 10.5162/Ultrasonic2025/P1.17

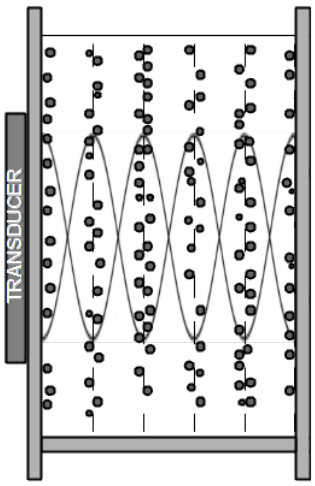

Fig. 1: Representation of High-frequency ultrasound agglomerating oil droplets in water at the antinodes.

properties of the fluid, or continuous phase, and the emulsified droplets or diluted particles [13]. For an oil-in-water emulsion, the factor indicates the oil droplets motion due to the acoustic standing wave field generated inside a chamber. The differences in density and compressibility between the continuous phase and the droplet, or particles, define the acoustic contrast factor ϕ_{ac} as follows:

$$\phi_{ac} = (5\rho_{dr} - 2\rho_F)/(\rho_{dr} + \rho_F) - \beta_{dr}/\beta_F, \quad (1)$$

in Eq. (1), ρ_F and ρ_{dr} are the densities of the fluid medium and emulsified droplet, respectively, β_F and β_{dr} are the compressibilities of the fluid and the droplet, respectively. The acoustic contrast factor is negative for oil-in-water emulsions, indicating that the oil droplets will be pushed toward the antinodes of the acoustic standing wave field by the acoustic radiation force.

Fig. 1 presents a schematic representation of the action of high-frequency ultrasound on crude-oil droplets emulsified in water, in which gray circles represent oil droplets emulsified in water, two sinusoidal lines represent the acoustic standing wave field created by a piezoelectric transducer, and the vertical dashed lines indicate the positions of the antinodes. In the figure, the oil droplets are driven toward the pressure antinodes of the standing acoustic wave, which promotes droplet agglomeration and increases the separation potential.

Materials and Methods

A high-frequency acoustic chamber is a resonant device with a piezoelectric transducer that is electrically excited by a sinusoidal voltage signal at a frequency of around $1\,\mathrm{MHz}$. The transducer causes the entire chamber to resonate, and the vibration produced is transmitted to any sample inside the device. Two parallel aluminum plates, spaced 20mm apart by an acrylic "U" shaped component, create cavity in the chamber. The first plate acts as a coupling layer, and the second serves as a reflecting element. The acoustic standing wave field was generated between the aluminum plates by four $1\,\mathrm{MHz}$ square PZT-4 piezoceramic plates. Their positive electrodes were bonded to the $6.4\,\mathrm{mm}$ thick coupling layer. The resonance frequency of the chamber depends primarily on the dimensions of the chamber cavity, the properties of the emulsion, and the process temperature.

Tab. 1: Table synthetic wastewater components.

Component	Quantity
Deionized water	200 g
Surfactant	300 mg
Crude-oil	500 mg $(+15\%)$

For the optimal operation of the acoustic chamber, a dual closed-loop control system is implemented. This system ensures that the driving frequency remains aligned with the resonance of the chamber and accurately regulates the acoustic power delivered to the ultrasonic device. The electrical power is continuously monitored and modulated, taking into account the effects of electrical noise, fluctuations in amplifier gain, and the acoustic characteristics of the sample, as detailed in [14]

The control system utilizes a proportional-integral (PI) controller to minimize tracking deviations in the resonance frequency caused by temperature variations. Another simpler proportional controller is used to maintain the acoustic power at a predetermined level, as determined by previous empirical findings, by modulating the input voltage. This robust system achieves resonance, thereby maintaining both resonance stability and power delivery throughout the treatment period. These measures ensure the consistency of experimental conditions and enable the comparison of outcomes with those from non-acoustic treatments.

A synthetic wastewater containing approximately 2,500 ppm of oil (g_{oil}/g_{water}) was used to simulate microemulsions typical in the oil industry. The preparation of the samples involved the dissolution of the surfactant, the surfactant was dissolved in deionized water at $80\,^{\circ}\mathrm{C}$, the Brazilian petroleum (approximately 24 °API) was added at room temperature (including a 15% increase due to preparation losses). The quantities used are presented in Tab. 1.

DOI 10.5162/Ultrasonic2025/P1.17

Tab. 2: Liquids properties.

Component	Property	Quantity
Water	Dens. ρ_F $[kg/m^3]$	998
	Comp. β_F $[m^2/s]$	4.51×10^{-10}
Crude-oil	Dens. ρ_{dr} $[kg/m^3]$	909.2
	Comp. β_{dr} $[m^2/s]$	5.53×10^{-10}

An UltraTurrax ICA T25 homogenizer was used to initially mix the components at 10,000 rpm for 3 minutes to ensure full incorporation, followed by emulsification at 15,000 rpm for 30 minutes. Synthetic wastewater presented an oil content decrease of about $4\,\%$ in one hour.

Results

A controlled 1 MHz acoustic chamber was used to separate synthetic Brazilian crude-oil-in-water microemulsions. No chemical additives were used to help the separation process. The ultrasonic test at high frequency followed this procedure: the oil concentration in the synthetic wastewater was initially measured for a period of 10 minutes. Subsequently, a power of around 40 W ($\approx 0.42 W/cm^2$) was applied to the chamber, with a sonication duration of 2 minutes. Lastly, the oil measurement was conducted for approximately 35 minutes. Both continuous lines in Fig. 2, referred to as *emulsion treatment*, represent the oil content variation during the ultrasonic test. In this figure, a reference test is also presented, indicated by a dotted line. The oil separation efficiency was determined using measurements from an oil-in-water content analyzer (HD-100, Advanced Sensors).

Fig. 2 shows that the acoustic field was switched on after approximately 10 min, as indicated by the label in the plot. Shortly after the onset of sonication (2 min), the oil content of the emulsion (solid line) drops rapidly, whereas the reference test (dotted line) exhibits only minor fluctuations around its initial value.

Before ultrasound ($t < 10$ min), both curves overlapped at $\approx 2,590$ ppm (g_{oil}/g_{water}), confirming negligible gravity-driven separation on the time scale investigated. Upon sonication, the treated synthetic wastewater sample dropped by $\approx 27\,\%$ within 5 min (time required to stop the oil content analyzer, perform the ultrasonic treatment, and restart the analyzer), and stabilized near 660 ppm (g_{oil}/g_{water}) after 35 min. It can also be observed in Fig. 2 that once the chamber reached its resonant condition and the ultrasound was applied, the oil concentration in the treated sample decreased significantly. These results

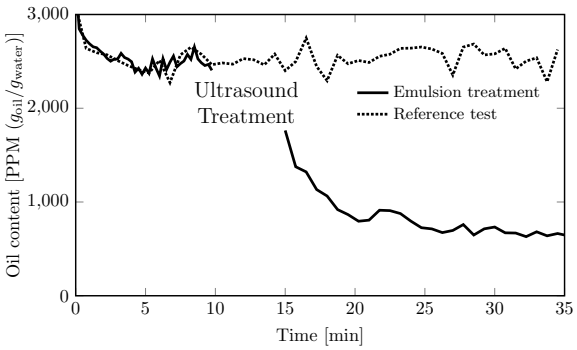

Fig. 2: Oil content variation.

are summarized in Tab. 3.

The separation process, therefore, removed almost 70 % of the initial oil content. In contrast, the reference remained between 2,400 and 2,600 ppm (g_{oil}/g_{water}). The findings confirm that radiation forces agglomerate droplets and accelerate buoyancy, delivering enhanced separation without the need for chemical additives or mechanical filters. As previously mentioned, the acoustic radiation force pushes the oil droplets emulsified in water toward the antinodes of the standing wave. This behavior is consistent with expectations, as the acoustic contrast factor ϕ_{ac} of the synthetic wastewater is negative, $\approx$ -0.32, this value can be calculated with the parameters listed in Tab. 2 and using Eq. (1).

The controlled application of high-frequency ultrasound successfully separated oil from a Brazilian crude-oil-in-water microemulsion with an initial concentration of about 2,500 ppm (g_{oil}/g_{water}) without using chemical additives. The results demonstrated oil separation efficiency slightly above 70%, achieved with a power input of around 40 W ($\approx 0.42 W/cm^2$) applied for 2 minutes. In contrast, the reference test (non-acoustic) yielded an oil separation of only approximately 3.6%.

Highlights

The controlled application of high-frequency ultrasound significantly improved the oil separation compared to the non-acoustic separation. These results suggest that ultrasound constitutes a promising tech-

Tab. 3: Oil separation test

Test	Inicial PPM $[g_{oil}/g_{water}]$	Final PPM $[g_{oil}/g_{water}]$
Ultrasound	$2595.2(\pm 77.4)$	$665.5(\pm 33.6)$
Reference	$2474.6(\pm 103.2)$	$2536(\pm 124.8)$

nique for crude-oil separation. To validate the findings presented, additional tests of the unconsidered conditions will be required for further confirmation. However, high-frequency ultrasound can be regarded as an environmentally friendly alternative as it eliminates the need for the use of chemical additives to induce oil separation. As outlined in Tab. 3, the application of ultrasound reduced the oil content from approximately 2,595 to 665 ppm (g_{oil}/g_{water}), while the control sample remained almost the same.

Acknowledgement

The research team acknowledges Petrobras/ANP (grants 5850.0109314.18.9 and 5850.0108871.18.9), CAPES, and CNPq (grants 306.123/2022-3 and 312.126/2021-2) for their financial support to this research.

References

[1] J. M. Dickhout et al. "Produced water treatment by membranes: A review from a colloidal perspective". In: *Journal of colloid and interface science* 487 (2017), pp. 523–534.

[2] M. A. Al-Ghouti et al. "Produced water characteristics, treatment and reuse: A review". In: *Journal of Water Process Engineering* 28 (2019), pp. 222–239.

[3] M. Fingas and B. Fieldhouse. "Water-in-oil emulsions: Formation and prediction". In: *Handbook of Oil Spill Science and Technology* (2014), pp. 225–270.

[4] F. B. P. da Silva Almeida et al. "Coalescence process to treat produced water: an updated overview and environmental outlook". In: *Environmental Science and Pollution Research* 26 (2019), pp. 28668–28688.

[5] O. M. Ekechukwu, T. Asim, and H. K. Hawez. "Recent Developments in Hydrocyclone Technology for Oil-in-Water Separation from Produced Water". In: *Energies* 17.13 (2024), p. 3181.

[6] M. Piccioli et al. "Gas flotation of petroleum produced water: a review on status, fundamental aspects, and perspectives". In: *Energy & Fuels* 34.12 (2020), pp. 15579–15592.

[7] A. S. Santos et al. "Evaluation of the efficiency of polyethylenimine as flocculants in the removal of oil present in produced water". In: *Colloids and Surfaces A: Physicochemical and Engineering Aspects* 558 (2018), pp. 200–210.

[8] I. Adeyemi, M. Meribout, and L. Khezzar. "Recent developments, challenges, and prospects of ultrasound-assisted oil technologies". In: *Ultrasonics Sonochemistry* 82 (2022), p. 105902.

[9] G. D. Pangu and D. L. Feke. "Acoustically aided separation of oil droplets from aqueous emulsions". In: *Chem Eng Sci* 59.15 (2004), pp. 3183–3193.

[10] V. Farmehini et al. "Real-Time Detection and Control of Microchannel Resonance Frequency in Acoustic Trapping Systems by Monitoring Amplifier Supply Currents". In: *ACS Sensors* 6.10 (2021), pp. 3765–3772.

[11] V. Vitali et al. "Differential impedance spectra analysis reveals optimal actuation frequency in bulk mode acoustophoresis". In: *Scientific Reports* 9.1 (2019), pp. 1–10.

[12] G. D. Pangu and D. L. Feke. "Droplet transport and coalescence kinetics in emulsions subjected to acoustic fields". In: *Ultrasonics* 46.4 (2007), pp. 289–302.

[13] T. Laurell, F. Petersson, and A. Nilsson. "Chip integrated strategies for acoustic separation and manipulation of cells and particles". In: *Chemical Society Reviews* 36.3 (2007), pp. 492–506.

[14] C. M. G. Atehortua et al. "Resonance Frequency Tracking and Power Supply Adjusting Control for a High Frequency Ultrasonic Device Used to Oil-in-Water Microemulsion (Wastewater) Separation". In: *2024 IEEE UFFC Latin America Ultrasonics Symposium (LAUS)*. Montevideo, 2024, p. 1.

DOI 10.5162/Ultrasonic2025/P1.18

Preliminary Study on Muscular Tissue Characterization Using Continuous Shear Wave Elastography

Marie Tabaru[1], Naoki Tano[1], Toru Ogawa[2], Ren Koda[3], and Yoshiki Yamakoshi[3]
[1] Institute of Science Tokyo, 4259 Nagatsuta-cho, Midori-ku, Yokohama, Kanagawa, 226-8503, Japan
[2] Tohoku University Hospital, 1-1 Seiryo-machi, Aoba-ku, Sendai, Miyagi, 980-8574, Japan
[2] Gunma University, 1-5-1 Tenjin-cho, Kiryu, Gunma, 376-0052, Japan
tabaru.m.ab@m.titech.ac.jp

Abstract: There is a need for methods to assess muscle elasticity considering tissue inhomogeneity and heterogeneity. This study investigated shear wave morphology in muscle tissue during continuous shear wave elastography. Shear wave velocity, direction, and attenuation were measured in beef, pork, and chicken. Even when velocities were similar, attenuation and direction differed with fat and fibrotic content. These results support the feasibility of using this technique to assess muscle elasticity considering tissue inhomogeneity and heterogeneity.

Keywords: shear wave elastography, muscular characterization, heterogeneity, inhomogeneity, acoustic morphology

Introduction

In muscle tissue diagnosis using ultrasound elastography, there is a need for evaluation criteria that take into account the inhomogeneity and heterogeneity of muscle tissue [1, 2, 3]. For example, localized stiffness in the masseter muscle is a characteristic symptom of temporomandibular joint disorder. Since the internal structure of the masseter is more complex compared to other muscles, in clinical practice, palpation is used to assess tenderness related to stiffness, often employing the nine-part method [4]. Although there are studies on stiffness evaluation of the masseter muscle [5], the mechanism of its pathogenesis remains unclear. Drakonaki *et al.* reported that muscle elasticity images (i.e., color images) show the normal relaxed muscle as an inhomogeneous mosaic of intermediate stiffness. However, they do not yet understand what the color variation depends upon, and whether the color patterns are reproducible between different muscles and different individuals.

Meanwhile, continuous shear wave elastography (C-SWE), developed by the authors, utilizes an external mechanical vibrator to generate shear waves within biological tissue [6, 7, 8]. This vibrator induces microscale displacements in the tissue. The C-SWE technique reconstructs the excited shear waves, allowing for the visualization and assessment of muscle elasticity [9]. This study focused on observing the propagation characteristics of shear waves excited in C-SWE, investigating the inhomogeneity and heterogeneity of the muscle tissue. While morphological features in conventional ultrasound images have been widely used for disease diagnosis [10], here, we evaluate muscle tissue based on the morphological characteristics observed in shear wave imaging.

Measurement Method

In this study, five types of samples were prepared: chicken breast (CB), pork belly (PB), beef round (BR), pork tenderloin (PT), and beef tenderloin (BT), all purchased from a supermarket. Fig. 1(a) illustrates the experimental system setup to measure shear waves. An external mechanical vibrator was put on the surface of each sample, and shear waves were generated using the vibrator operating at 78 Hz. Shear wave measurements were conducted using a separate linear array ultrasound probe (Finggal Link, Japan; 128 active elements, frequency: 10 MHz) and a C-SWE system installed on a laptop computer [8]. B-mode image data and the real (I) and the imaginary (Q) signals (i.e., IQ signals) of the ROI (16×26 mm) were acquired by the C-SWE system.

Reconstruction Method of Shear Wave

Here, the reconstruction method of shear wave is described. The acquired IQ signals correspond to the Doppler signal, s, which is expressed as Eq. (1).

$$s = y_0 \exp(j\Delta\omega t), \tag{1}$$

where y_0 is the amplitude of the IQ signals. $\Delta\omega t$ is the phase component of the IQ signals. The Doppler phase shift is related to the displacement of the scatterer. Accordingly, the following relationship can be derived:

$$\Delta\omega t \propto u_0 \sin(2\pi f_s t + \Phi) \tag{2}$$

Here, u_0 is the amplitude of shear wave, f_s is the shear wave frequency, and Φ is the phase of shear

DOI 10.5162/Ultrasonic2025/P1.18

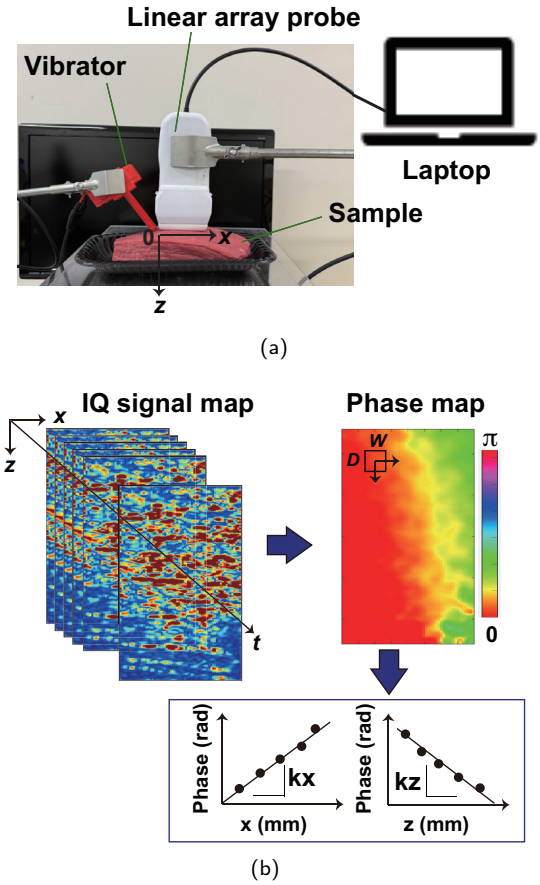

Fig. 1: (a) C-SWE experimental system and (b) flowchart of signal processing for shear wave reconstruction.

wave. Therefore, by extracting the phase component of the IQ signals, the phase of shear wave is obtained. The wavenumbers, the shear wave velocity, and the shear wave propagation direction are calculated from Φ, which which is expressed as Eq. (3).

$$\Phi = k_x x + k_z z, \tag{3}$$

where k_x and k_z are the wavenumbers in the x and z directions, respectively. The wavenumbers of shear wave, the shear wave velocity, and shear wave propagation direction were calculated from Φ. k_x and k_z were calculated by Eqs. (4) and (5).

$$k_x = \frac{\partial \Phi}{\partial x} \tag{4}$$

$$k_z = \frac{\partial \Phi}{\partial z} \tag{5}$$

The shear wave velocity, v, was calculated by Eq. (6).

$$v = \frac{2\pi f_s}{\sqrt{k_x^2 + k_z^2}} \tag{6}$$

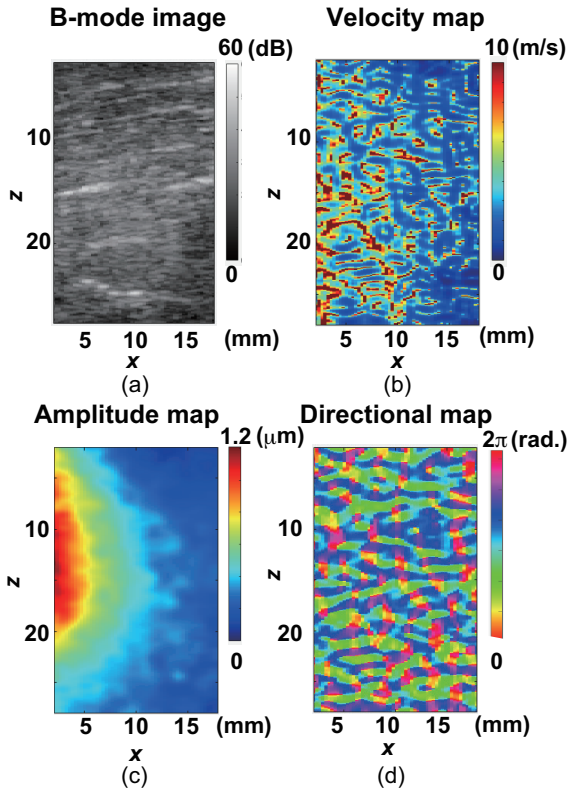

Fig. 2: Resultant images of BR sample. (a) B-mode image. (b) Velocity map. (c) Amplitude map. (d) Directional map.

The shear wave propagation direction, dir, was calculated by Eq. (7).

$$dir = \arctan\left(\frac{k_x}{k_z}\right) \tag{7}$$

The amplitude of shear wave was also calculated from $|\Delta\omega t|$.

Fig. 1(b) illustrates the flowchart to calculate Φ and wavenumbers from IQ signals. In the experiment, a Φ was reconstructed by a signal processing method developed by the authors [8]. The phase signals inside the ROIs were divided into multiple sub-ROIs (D: 1.2 mm, W: 1.2 mm) and linear regression was performed to calculate the biaxial phase gradients in the sub-ROIs.

Results

Fig. 2 shows the B-mode image, the shear wave velocity map, the shear wave amplitude map, and the directional map of the BR sample. The vibration point is located approximately at $x = 0$ mm and shear wave propagates in the direction of $+x$. The resulting morphological characteristics of phase, velocity, amplitude, and direction reflect the properties of the muscle tissue. To evaluate the shear wave characteristics, we

DOI 10.5162/Ultrasonic2025/P1.18

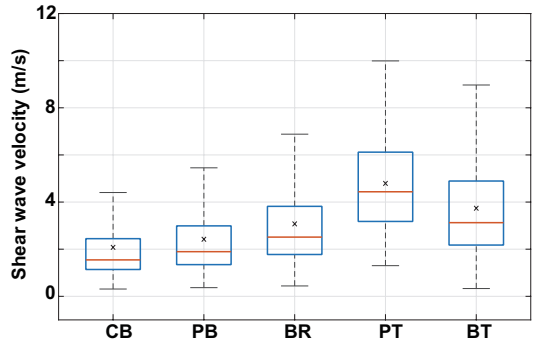

Fig. 3: Box plots of shear wave velocities. The 'x' symbol represents average values.

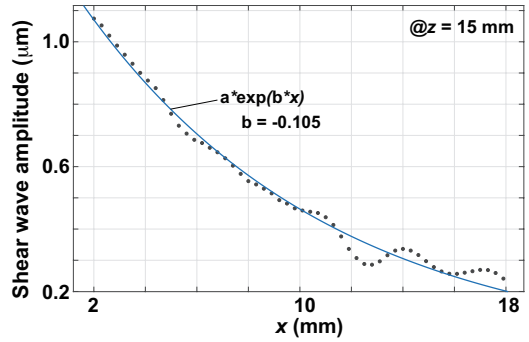

Fig. 4: Shear wave amplitude plot at $z = 15$ mm of BR sample and curve approximated by curve fitting method.

first consider the shear wave velocities. The calculated box plots are shown in Fig. 3. Here, velocities greater than 10 m/s were considered outliers. The velocities were 2.04 ± 1.52, 2.45 ± 1.67, 3.03 ± 1.84, 4.82 ± 2.04, and 3.45 ± 2.15 m/s for CB, PB, BR, PT, and BT, respectively. The velocities were within the range of the reference values [11]. CB and PB can be classified as samples with relatively slow shear wave velocities. On the other hand, PT and BT can be classified as samples with relatively fast shear wave velocities.

Second, the attenuation characteristics were investigated. As shown in Fig. 2 (c), the shear wave amplitude decreased as shear wave propagated. The attenuation coefficient, b, was calculated from the amplitude curve as shown in Fig. 4. Function, $a * \exp(b * x)$ is fitted to the attenuation curve by using Curve Fitting Toolbox (Matlab2025, MathWorks), where a is a real number. The b of BR was -0.105 (1/mm). The curve fit showed a high coefficient of determination of 0.98. Attenuation coefficients of CB, PB, BR, PT, and BT were -0.093, -0.170, -0.105, -0.065, and -0.064 (1/mm), respectively. The attenuation coefficient of pork belly was the highest. This is considered to be due to the high-fat content in pork belly.

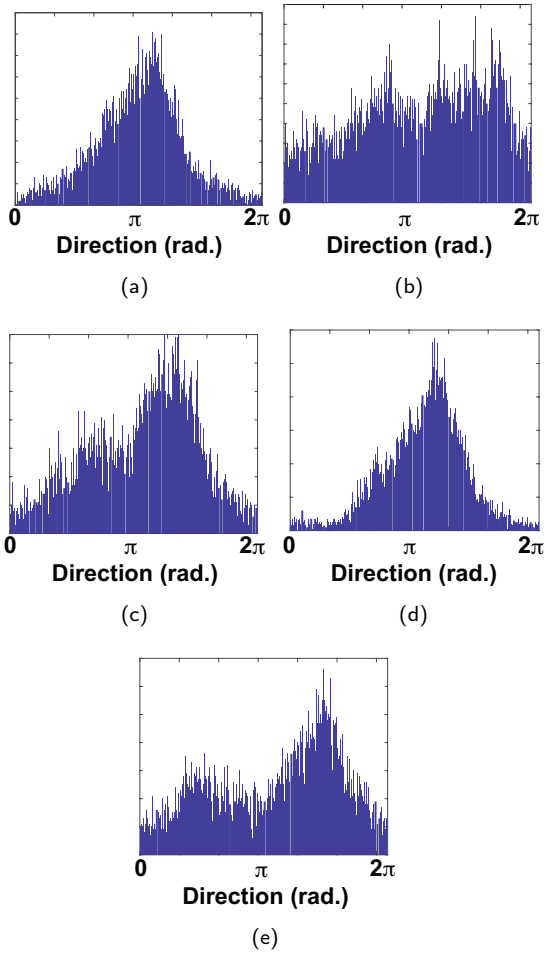

Fig. 5: Histogram of shear wave direction. π indicates that the propagation direction is horizontal. (a)CB. (b)PB. (c)BR. (d)PT. (e)BT.

Third, we investigate the propagation directions of shear wave. Fig. 5 shows the histograms of the directional maps. The directions of CB and PT are concentrated around π. This indicates that shear waves are propagating in the $+x$ direction. This observation indicates a high degree of structural homogeneity and alignment of the muscle fibers within the CB and PT regions. The directional variability observed in the PB region is presumably due to its heterogeneous structure, comprising both muscular and fat components. The wave propagation in the BR and BT regions exhibits components along the $+z$ axis, with a smaller proportion also oriented in the -z direction. This phenomenon is likely attributable to the inherent inhomogeneity in muscle structure and fiber orientation within the bovine tissue.

Discussion

First, we discuss the propagation direction of shear waves within muscle tissue. The variability in shear

wave direction is considered to be influenced by reflections occurring at muscle fibers, fat tissue, and fascial structures. This suggests that, in the future, directional variability of shear waves may enable the visualization of fibrosis — one of the parameters representing muscle inhomogeneity. However, further investigation using a physical simulation model is required. Next, we discuss the inhomogeneity and heterogeneity of muscle tissue. Skeletal muscle is composed of muscular tissue, fat components, and fibrous structures. In this study, an ex vivo feasibility study was conducted to explore the potential for evaluating tissue inhomogeneity and heterogeneity based on the direction and amplitude distribution of shear waves. In the future, quantitative evaluation using inhomogeneous or heterogeneous phantoms—with controlled fiber layering, density, and fiber orientation—along with the development of a corresponding physical model, will be necessary.

Conclusion

In this study, the inhomogeneity and heterogeneity of muscle tissue were evaluated based on the morphological characteristics observed in shear wave imaging. Shear wave velocity, propagation direction, and attenuation coefficient were measured in beef, pork, and chicken samples. Although the shear wave velocities were similar across samples, attenuation and directional characteristics varied depending on tissue composition, such as fat and fibrotic structures. These findings support the feasibility of using continuous shear wave elastography to assess muscle elasticity while accounting for tissue inhomogeneity and heterogeneity. As a future work, the evaluation of inhomogeneity and heterogeneity will be conducted using phantoms and simulations.

Acknowledgments

This work was supported in part by JSPS KAKENHI Grant Number 25K01237, the Cooperative Research Project of Research Center for Biomedical Engineering, and JKA's promotion funds from KEIRIN RACE.

References

[1] E. Drakonaki, G. Allen, and D. Wilson. "Ultrasound Elastography for Musculoskeletal Applications". In: *The British Journal of Radiology* 85.1019 (2012), pp. 1435–1445. DOI: 10.1259/bjr/93042867.

[2] D. Turo et al. "Novel Use of Ultrasound Elastography to Quantify Muscle Tissue Changes After Dry Needling of Myofascial Trigger Points in Patients With Chronic Myofascial Pain". In: *Journal of Ultrasound in Medicine* 34.12 (2015), pp. 2149–2161. DOI: 10.7863/ultra.14.08033.

[3] R. Sigrist et al. "Elastography: Review of Techniques and Clinical Applications". In: *Theranostics* 7.5 (2017), pp. 1303–1329. DOI: 10.7150/thno.18650.

[4] S. Beaumont et al. "Temporomandibular Disorder: a practical guide for dental practitioners in diagnosis and management". In: *Australian Dental Journal* 65.3 (2020), pp. 172–180. DOI: 10.1111/adj.12785.

[5] M. Takashima et al. "Quantitative Evaluation of Masseter Muscle Stiffness in Patients with Temporomandibular Disorders using Shear Wave Elastography". In: *Journal of Prosthodontic Research* 64.4 (2017), pp. 432–438. DOI: 10.1016/j.jpor.2017.01.003.

[6] Y. Yamakoshi et al. "Shear Wave Imaging of Breast Tissue by Color Doppler Shear Wave Elastography". In: *IEEE Transactions on Ultrasonics, Ferroelectrics, and Frequency Control* 64.2 (2017), pp. 340–348. DOI: 10.1109/TUFFC.2016.2626359.

[7] N. Tano et al. "Continuous Shear Wave Elastography for Liver Using Frame-to-Frame Equalization of Complex Amplitude". In: *Ultrasonic Imaging* 46.3 (2024), pp. 197–206. DOI: 10.1177/01617346241247127.

[8] R. Koda et al. "Application of Continuous Shear Wave Elastography Method with Multiple Frequency Selection to Liver Viscoelasticity Measurement". In: *Japanese Journal of Applied Physics* 63.4 (2024), 04SP82. DOI: 10.35848/1347-4065/ad3ae4.

[9] M. Tabaru et al. "Examination of Rapid Adjustment System Based on Screen Score Obtained using Continuous Shear Wave Elastography". In: *Journal of Medical Ultrasonics* 51.3 (2024), pp. 407–418. DOI: 10.1007/s10396-024-01439-7.

[10] S. Otsuka et al. "Investigation of the Association between Human Fascia Lata Thickness and its Neighboring Tissues' Morphology and Function using B-mode Ultrasonography". In: *Journal of anatomy* 239.5 (2021), pp. 1114–1122. DOI: 10.1111/joa.13505.

[11] L. S. Mikaela, A. M. Seyed, and A. M. Agur. "Measuring Shear Wave Velocity in Adult Skeletal Muscle with Ultrasound 2-D Shear Wave Elastography: A Scoping Review". In: *Ultrasound in Medicine & Biology* 49.6 (2023), pp. 1353–1362. DOI: 10.1016/j.ultrasmedbio.2023.02.005.

DOI 10.5162/Ultrasonic2025/P1.19

Applications of Ultrasonic Actuators for Electrochemical Deposition Processes

Johannes Landskron[1], Conrad R. Wolf[1], Gerhard Fischerauer[2], and Klaus-Stefan Drese [1]
[1]Institute for Sensor and Actuator Technology, Coburg University of Applied Science, 96450 Coburg, Germany
[2]Chair of Measurement and Control Systems, Bayreuth University, 95447 Bayreuth, Germany
Johannes.Landskron@hs-coburg.de, Klaus.Drese@hs-coburg.de

Abstract: Ultrasound has been used in various actuator applications, including mixing, phase separation, and enhancing chemical reactions. Moreover, electrochemical processes have been identified as an application for acoustic actuators. Ultrasound has been demonstrated to target the depletion layer directly, thereby improving mass transport and enhancing the process. This results in a reduction of processing time, a decrease in energy consumption, and an enhancement of material properties such as hardness and surface roughness.

Keywords: Guided Acoustic Waves, Electrochemical Deposition, Acoustic Streaming, Acoustic Actuator, Sonoelectrochemistry

Introduction

Ultrasound has been used for versatile actuator technologies to assist in a wide variety of pharmaceutical or chemical processes for a long time [1, 2]. Common applications are lab-on-a-chip devices for the manipulation of liquids or particles. Typically, ultrasonic waves have been used to mix reactants or to separate different phases, but also to accelerate chemical reactions. A less commonly known but equally promising application for ultrasound are electrodeposition processes such as electroplating or electropolishing [3].
Despite the paucity of established industrial applications in this domain, it has been recognized that ultrasound can provide a beneficial effect on these processes. A review of the extant literature indicates that the predominant utilization of acoustic waves in this context is of an inefficient diffuse nature, emanated by sonotrodes [4]. However, guided acoustic waves (GAW) hold particular promise in ensuring precise mixing at the interface between the surface and the electrolyte [5].
Consequently, this study proposes a multi-stage methodology for modeling such electrochemical interface processes, utilizing the example of copper electropolishing. In addition, the impact of ultrasonic technology on electrochemical processes in experimental settings is demonstrated.

Methods and Results

Generally, gradients in ion concentration at electrochemical interface processes are known to have a negative impact on the processes [6]. In this context, the basic idea behind ultrasound technology using GAW is to overcome concentration-based limitations by utilizing acoustically induced streaming right on the interface. To understand the processes behind this, a multi-step simulation model was developed. This model was based on a simple electropolishing process of a copper electrode in a phosphoric acid electrolyte. The first step was to calculate all relevant combinations of GAW modes and the corresponding pressure fields in the electrolyte for this setup. To achieve this, a section of the electrode in contact with the electrolyte was modeled in an eigenfrequency study based on a unit cell approach [7]. The simulation provided the local plate displacement u and the electrolyte pressure field p for the existing GAW mode shapes. A standing Quasi-Scholte-platemode (QSP) with an evanescent pressure field was selected as the starting point for the next simulation step (Fig. 1a). This mode carries the sound wave's energy directly on the interface, preventing it from being lost by any decoupling parts.
In the next step, the acoustically induced flows were calculated for the corresponding modes using a perturbation approach [8]. Fig. 1b shows the resulting vortex flows, with four alternatively rotating flows per wavelength. In the final step, ion transport in the electrolyte and charge exchange at the surface were considered. The charge exchange depends on the ion concentration at the surface and can be calculated using the Butler–Volmer equation [9]. Ion transport in the electrolyte occurs via diffusion or forced streaming. In addition to other mixing methods, the acoustically induced streaming vortexes from the previous step were considered. Fig. 1c shows the concentration profile at the deformed electrode due to acoustic streaming. This acoustic-based mixing

DOI 10.5162/Ultrasonic2025/P1.19

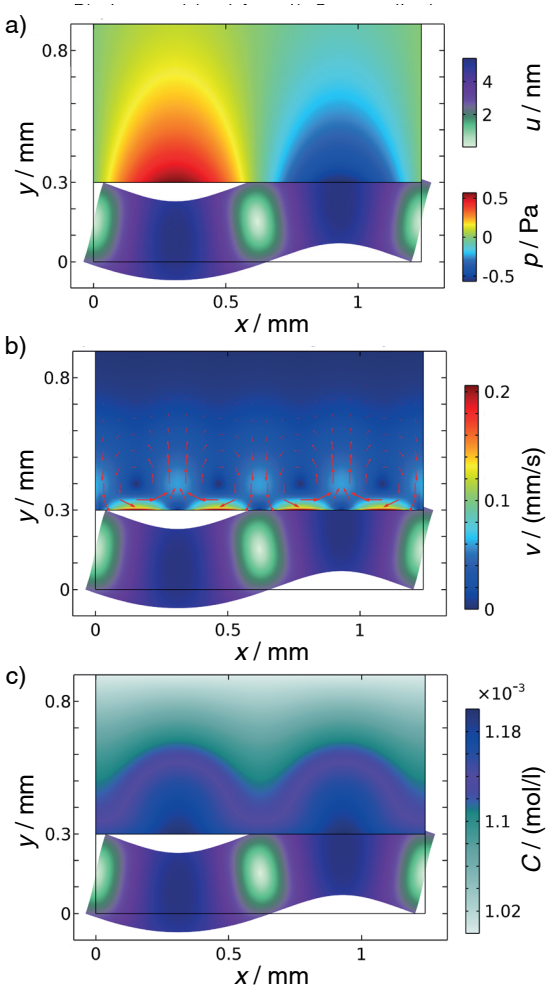

Fig. 1: Multi-stage simulation for the evaluation of different relevant aspects of electrochemical processes with GAW-based enhancement: (a) sound field, (b) streaming profile and (c) ion concentration distribution.

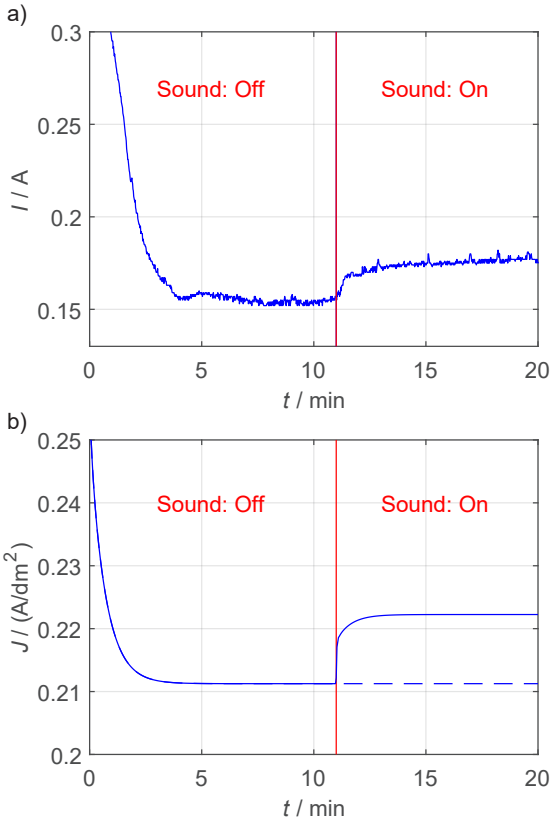

Fig. 2: Current profiles for an electro-polishing process of a copper plate in phosphoric acid with temporary GAW-based enhancement: (a) experimental data and (b) transient simulation.

ensured that fresh electrolyte was transported to the electrode while exhausted electrolyte was removed. Comparative calculations have shown reduced processing time using ultrasonic technology.

In order to evaluate the multi-step model, the data from an experiment was compared with the simulations. In the experiment, a copper plate was subjected to potentiostatic polishing for a duration of 20 minutes in two phases. The initial phase was performed without acoustic enhancement. In the second phase ($t > 11$ min) the acoustic excitation was activated. The measured current profile is shown in Fig. 2a. At the beginning of the experiment, the polishing current exhibits an initial high value. This phenomenon can be attributed to the fact that, at this particular stage, fresh electrolyte is present at the surface. During the initial phase of the polishing process an inhibition layer was formed gradually as a result of the progressive presence of dissolved copper ions. The trend of the curves shows that, after a period of $t > 4$ min, a state of equilibrium was achieved. Here, only the amount of copper is dissolved which can be removed by diffusion and convection effects. In the second phase of the experiment, the polishing current was raised to a higher level by switching on the GAWs. This level was kept until the end of the experiment. So, the corresponding process efficiency was increased by 10 % to 20 %. The corresponding transient simulation of the polishing process is shown in Fig. 2b. It is evident that the two processes were performing highly analogous. The findings from simulation and experiment have demonstrated the initial formation of an inhibitory diffusion layer, in addition to the subsequent escalation of the polishing current attributable to acoustically induced mixing.

It is evident that the model presented is capable of being readily transferred from anodic to cathodic

DOI 10.5162/Ultrasonic2025/P1.19

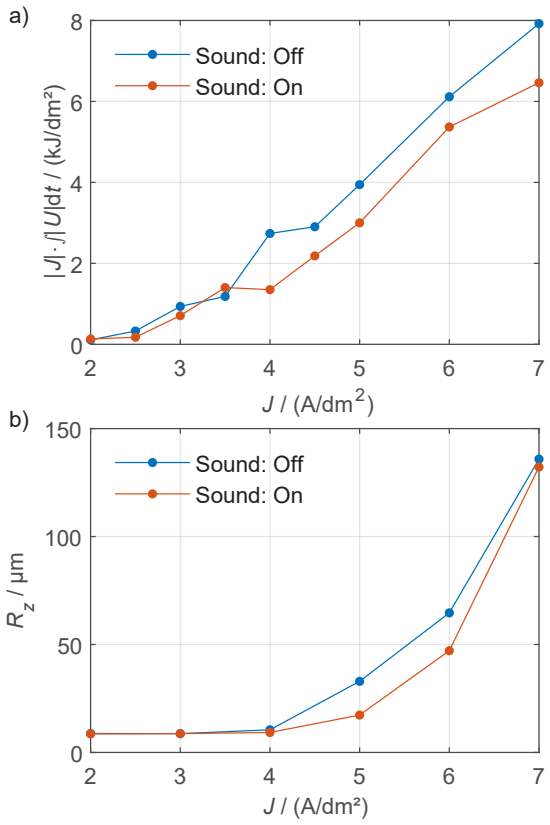

Fig. 3: Influence of ultrasound on the (a) energy efficiency of the plating process and (b) the resulting surface roughness for a additive-free Cu-Eletrolyte.

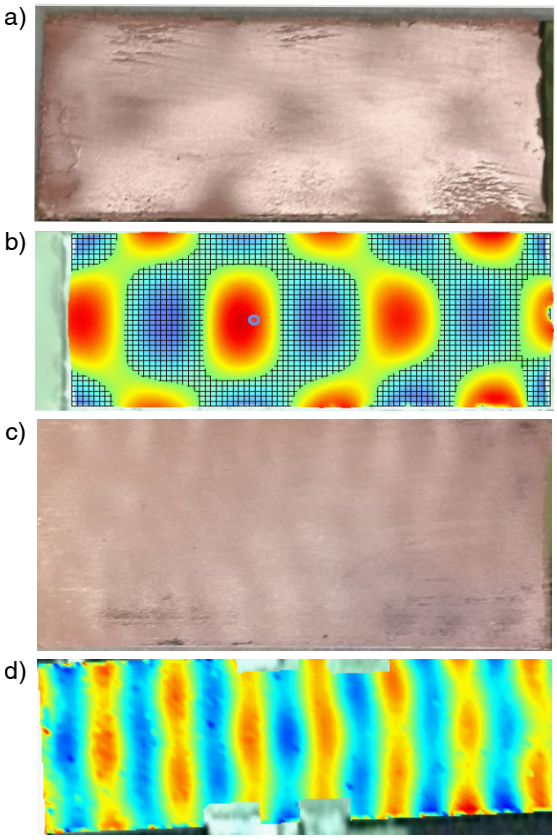

Fig. 4: Probes show a visible pattern on the sample surface (a,c) after acoustic enhanced plating. This pattern matches the related standing waves visualized by LDV measurements (b,d).

processes. For typical coating process, the electrolyte generally contains a higher concentration of dissolved ions from the outset. It is imperative to ensure the availability of sufficient free ions at the component surface throughout the process. Consequently, the occurrence of depletion effects would be able to inhibit the process.

For industrial applications, often mechanically generated flows are employed for active mixing. Therefore, nozzles or continuous sample movement are typically used for such applications. However, most of the circulation occurs far away from the component with minimal impact on the boundary layer close to the surface. This is equally applicable to sonotrode-based acoustic applications. In this instance, too, there is a lack of power in the areas where it is required. In addition, chemical additives are frequently used to ensure the uniform distribution of layers or to produce glossy surfaces. These substances frequently require analytical monitoring and online dosing. To this end, the potential of ultrasound technology in this field was investigated.

In order to address this topic, experiments were carried out with an industrial electrolyte free of additives. The samples were subjected to galvanostatic plating at varying current densities. In all cases, one sample was coated with sound, while a reference sample was coated without sound. The evaluation process involved the calculation of the energy requirements for each sample, which are displayed in Fig. 3a. As demonstrated in Fig. 3a, the two curves match within the low current density range up to $J \leq 3.5\text{A/dm}^2$. This is also specified in the datasheet as the normal operating range. In contrast, the two curves exhibit a divergence at this point. Thereby, the ultrasonic curve is consistently lower than the other curve. This phenomenon can be attributed to the active reduction of inhibitions by ultrasonic technology, thereby decreasing bath resistance. In addition, the roughness values on the coated samples were determined (Fig. 3b). Here, the values for low current densities are also congruent. Beyond the conventional operational parameters, there is a pronounced increase in surface

roughness, which can be considered as a reduction in surface quality. Again, the values with sound perform out those without.

In experiments in which samples were subjected to high acoustic amplitudes during the plating process, irregularities were observed on the surface of the resulting coating. Fig. 4a,c illustrates two examples. The observation of these patterns clearly shows the impact of ultrasonic excitation on the process. These phenomena bear a striking resemblance to wave patterns, particularly standing waves, which are known to occur on finite samples. One sample displays a "checkerboard pattern" (Fig. 4a), while the other exhibits a "parallel waves" (Fig. 4c) configuration. A subsequent analysis of the excited oscillations using laser Doppler vibrometry (LDV) corroborates this initial supposition (Fig. 4b,d) [10]. In both specimens, there is an observable congruence between the surface pattern and the oscillation pattern. The distinction between the various types can be attributed to the utilization of varying frequencies in combination with different piezoelectric transducers used for the GAW excitation. Consequently, such patterns can also be avoided by slightly varying the frequencies during the plating process.

Discussion and Outlook

In summary, the ultrasonic technology based on GAWs promises to enhance the efficiency of electrochemical processes. The results presented demonstrate that processes can be accelerated, inhibitions reduced, the range of applications extended, and material properties improved. The imprinted wave patterns further substantiate the hypothesis that the crystal structure is influenced by the GAWs. Our preliminary research on electroplated nickel coatings has yielded initial evidence suggesting that ultrasonic waves may enhance the hardness of the coatings. This phenomenon is further substantiated by the observations made by the use of a scanning electron microscope. The images reveal a more sophisticated columnar growth in the presence of sonication as compared to its absence. These observations must be further investigated and confirmed in future experiments.

Funding

This research was funded by: Technologie Allianz Oberfranken TAO; Bayerisches Staatsministerium für Wirtschaft, Landsentwicklung und Energie; Bayerisches Staatsministerium für Wissenschaft und Kunst; Bundesministerium für Bildung und Forschung and Gemeinsame Wissenschaftskonferenz GWK

References

[1] J. Gao et al. "Lab-on-a-chip for high frequency acoustic characterization". In: *Sensors and Actuators B: Chemical* 177 (Feb. 2013), pp. 753–760. DOI: 10.1016/j.snb.2012.11.037.

[2] A. Agarwal et al. "Design and development of an efficient fluid mixing for 3D printed lab-on-a-chip". In: *Microsystem Technologies* 26.8 (Aug. 2020), pp. 2465–2477. DOI: 10.1007/s00542-020-04787-9.

[3] J. G. Kaufmann et al. "Megasonic agitation for enhanced electrodeposition of copper". In: *Microsystem Technologies* 15.8 (Aug. 2009), pp. 1245–1254. DOI: 10.1007/s00542-009-0886-2.

[4] S. Coleman and S. Roy. "Effect of ultrasound on mass transfer during electrodeposition for electrodes separated by a narrow gap". In: *Chemical Engineering Science* 113 (July 2014), pp. 35–44. DOI: 10.1016/j.ces.2014.03.026.

[5] J. Wu. "Acoustic Streaming and Its Applications". In: *Fluids* 3.4 (Dec. 18, 2018), p. 108. DOI: 10.3390/fluids3040108.

[6] H. J. Lewerenz. "On the Structure of the Helmholtz Layer and its Implications on Electrode Kinetics". In: *ECS Transactions* 50.52 (Apr. 1, 2013), pp. 3–20. DOI: 10.1149/05052.0003ecst.

[7] S. Van Den Boom, F. Van Keulen, and A. Aragón. "Fully decoupling geometry from discretization in the Bloch–Floquet finite element analysis of phononic crystals". In: *Computer Methods in Applied Mechanics and Engineering* 382 (Aug. 2021), p. 113848. DOI: 10.1016/j.cma.2021.113848.

[8] P. B. Muller et al. "A numerical study of microparticle acoustophoresis driven by acoustic radiation forces and streaming-induced drag forces". In: *Lab on a Chip* 12.22 (2012), p. 4617. DOI: 10.1039/c2lc40612h.

[9] I. Kovácsovics et al. "Numerical Simulation of Copper Deposition in the Hull Cell Based on Butler-Volmer Kinetics". In: *Journal of The Electrochemical Society* 167.12 (Sept. 1, 2020). Publisher: The Electrochemical Society, p. 122506. DOI: 10.1149/1945-7111/abb1d5.

[10] S. Rothberg et al. "An international review of laser Doppler vibrometry: Making light work of vibration measurement". In: *Optics and Lasers in Engineering* 99 (Dec. 2017), pp. 11–22. DOI: 10.1016/j.optlaseng.2016.10.023.

DOI 10.5162/Ultrasonic2025/P1.20

A Deep Learning Segmentation Approach for Lung Ultrasound Scoring Classification

M. Muñoz[1,2], X. Han[3], L. Demi[3], T. Perrone[4], A. Smargiassi[5], R. Inchingolo[5], Y. Tung Chen[6], A. Trueba Vicente[7], and J. Camacho[1]

[1]Institute for Physical and Information Technologies, Spanish National Research Council, Madrid, Spain

[2]Electronic Department,Universidad de Alcalá, Madrid,Spain

[3]Department of Information Engineering and Computer Science, University of Trento, Trento, Italy

[4]Department of Internal Medicine, IRCCS San Matteo, Pavia, Italy

[5]UOC Pneumologia, Dipartimento Neuroscienze, Organi di Senso e Torace, Fondazione Policlinico Universitario Agostino Gemelli IRCCS, Rome, Italy

[6]Department of Internal Medicine, Hospital Universitario La Paz, Madrid, Spain

[7]Department of Internal Medicine, Hospital de Emergencias Enfermera Isabel Zendal, Madrid, Spain

mario.munoz.prieto@csic.es

Abstract: This work presents a Deep Learning method to automate the interpretation of lung ultrasound (LUS), aiming to reduce diagnostic subjectivity. A segmentation model was developed to first identify key artifacts, such as vertical artifacts or consolidations, and then calculate a corresponding severity score. Its performance was benchmarked against a classification model across two video datasets. The segmentation model achieved comparable accuracy to the traditional classification method. Furthermore, the approach proved robust to variations in the ultrasound probe's orientation.

Keywords: Lung Ultrasound (LUS), Deep Learning, Image Segmentation, Computer-aided diagnosis, Automated Scoring.

Introduction

Lung ultrasound (LUS) has rapidly evolved into an essential, non-invasive imaging tool for assessing a variety of pulmonary conditions. Its interpretation, however, is not based on a direct anatomical view but on sonographic artifacts that arise from the interaction between ultrasound waves and the lung parenchyma. These artifacts include horizontal A-lines, which are reverberations of the pleura indicative of a normal lung, and vertical B-lines, which appear when alveolar air is displaced by fluid, suggesting pathological conditions like pneumonia. As a disease progresses, tissue can solidify, appearing as hypoechoic consolidations. The correct identification of these patterns requires significant expertise and is susceptible to inter-observer variability, which limits the broader clinical application of the technique.

To address these challenges, Artificial Intelligence (AI) has emerged as a powerful tool to aid diagnosis by helping less experieced clinicians and reducing subjectivity. In clinical practice, physicians quantify lung involvement using a scoring system based on the presence and extent of key sonographic artifacts. This study adopts the 4-level scoring criteria proposed by Soldati et al. [1]:

- **Score 0 (Normal):** Characterized by a continuous, regular pleural line with the presence of horizontal A-line artifacts.
- **Score 1 (Mild):** Defined by the presence of vertical artifacts (B-lines) while the pleural line remains intact and unbroken.
- **Score 2 (Moderate):** Corresponds to a broken or irregular pleural line with confluent vertical artifacts affecting less than 50% of its length. Small consolidations may also be present.
- **Score 3 (Severe):** Indicates severe abnormalities, characterized by widespread, confluent vertical artifacts affecting more than 50% of the visible pleura, which may be accompanied by extensive consolidations.

Automating this process with AI has primarily followed two real-time paradigms:

classification models (CM), which are trained to directly predict a severity score from an image, and segmentation models (SM), which first delineate the

DOI 10.5162/Ultrasonic2025/P1.20

artifacts themselves and then, calculates the score based on these findings. In this work, we propose and validate a novel workflow that translates the rich output of an artifact segmentation model into a clinical severity score. The performance of this segmentation-to-score approach is evaluated against expert clinician annotations and benchmarked against a classification model trained specifically for the scoring task on a multi-center, multi-scanner dataset.

Datasets and Acquisition Protocols

This international, multi-center study was a collaborative effort analyzing a general dataset of 2219 LUS videos from COVID-19 patients in Italy and Spain. All data was acquired in accordance with the Declaration of Helsinki and approved by the respective institutional ethical committees. The analysis was performed on two distinct datasets:

- **Dataset-1:** This dataset comprises 1530 videos from 83 patients, following a 14-region acquisition protocol [2]. The data was acquired using three different ultrasound scanners (Esaote Mylab50, Philips IU22, CerberoATL) with varying imaging configurations, including frequencies from 2.5 to 10 MHz and both convex and linear probes depending on the patient as ins explained in [3].
- **Dataset-2:** This dataset consists of 689 videos from 30 patients, following a 12-region acquisition protocol [4]. All acquisitions were performed with a single scanner (UltraCOV) using a 3.5 MHz convex probe and a standardized scanning criteria to minimize variability [5]. For each patient, examinations included both longitudinal and transversal probe orientations (337 and 352 videos, respectively).

AI Models and Scoring Methodology

Two deep learning models were evaluated.

Classification Model (CM). The classification model (CM) utilizes a ResNet18 architecture [6], a convolutional neural network known for its effectiveness in image classification. It was pre-trained on a large dataset of 58,924 LUS images acquired from the same scanner models present in Dataset-1 [7]. The model is designed to classify LUS images directly into the 4-level severity score (0-3)

Segmentation Model (SM). The segmentation model (SM) approach is a complete workflow that translates segmented artifacts into a clinical score (Fig. 1). It consists of the following steps:

- *Input Data & Model Architecture:* The model uses an Attention U-Net architecture [8] which was trained on 9,159 LUS images contained in Dataset-2. A key methodological choice was to use B-scan images (raw data of 128×256 pixels) as input instead of conventional sector images (Pre-processing block in Fig. 1), making the model more robust to scanner-specific geometries.
- *From Segmentation to Score:* The workflow translates the SM output into a score by mimicking clinical reasoning. First, the SM delineates the pleural line. Then, a post-processing algorithm calculates the percentage of the pleura affected by B-lines, by dividing the number of scan lines where B-lines are detected by the total number of scan lines where the pleura is visible [9]. Finally, this metric is mapped to the 4-level clinical severity score based on established guidelines avobe mentioned.

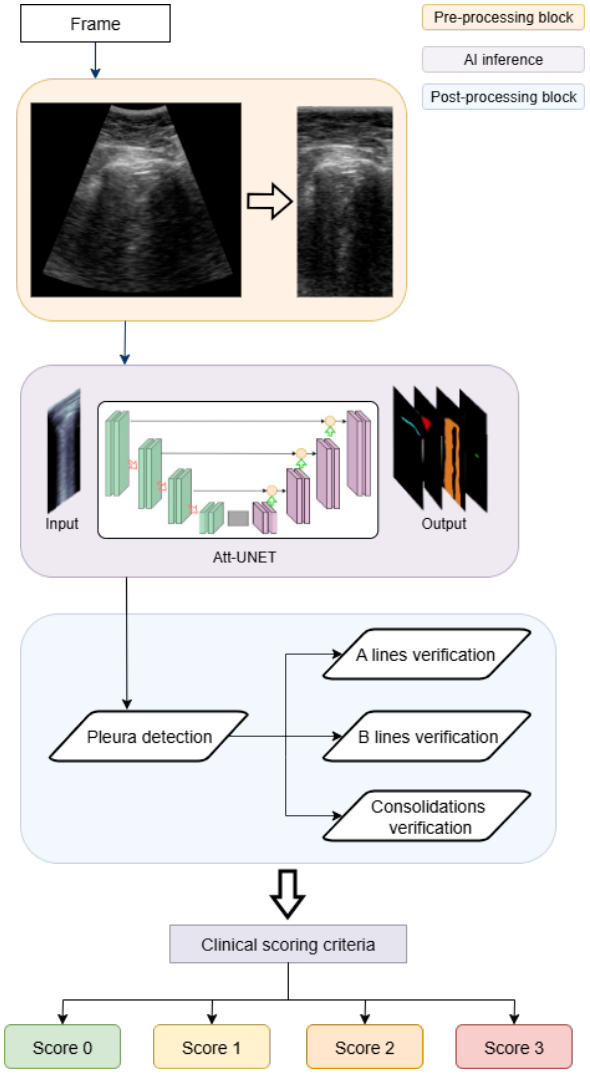

Fig. 1: From segmentation to score workflow.

DOI 10.5162/Ultrasonic2025/P1.20

Tab. 1: Video-level performance comparison of CM and SM methods. For Dataset-2, overall results are presented alongside a breakdown by probe orientation (longitudinal and transversal).

	Dataset-1		Dataset-2					
			CM			SM		
Metric	**CM**	**SM**	**General**	**Long**	**Trans**	**General**	**Long**	**Trans**
Accuracy	0.53	0.46	0.55	0.56	0.54	0.71	0.72	0.70
Accuracy ($\pm$1 tol.)	0.86	0.87	0.88	0.89	0.88	0.92	0.91	0.93
Cohen's Kappa (K_{qwc})	0.63	0.58	0.66	0.70	0.63	0.79	0.78	0.81

Experimental Setup and Evaluation Metrics

To assign a single score to each video, a 1% thresholding technique was employed [10]. This method identifies the highest severity score present in at least 1% of the video frames and assigns it to the entire video. The analysis was conducted at video level using as primary metric for assessing agreement with expert clinicians the Quadratic Weighted Cohen's Kappa (K_{qwc}), which measures inter-rater agreement while accounting for chance [11]. Also 1 error tolerance accuracy is performed to account for potential inter-observer variability in the annotations.

Results

The video-level performance of the Classification Model (CM) and Segmentation Model (SM) method are summarized in Table 1. Both method demonstrated good performance on the standardized Dataset-2, achieving substantial agreement than the CM, particularly in transversal acquisitions. A key finding is the robustness of both models to probe orientation, with performance on longitudinal and transversal views being highly comparable, confirming the method's flexibility in a clinical setting.

Discussion

The primary finding of this study is that the segmentation-based workflow (SM) demonstrates a prognostic capability comparable to a dedicated classification model (CM) in both datasets. The significance of this result lies in the inherent interpretability of the SM approach. Different from a "black box" classification model, the SM workflow provides a severity score based on quantifiable metrics, such as the percentage of the pleura affected by B-lines, which directly mimics the diagnostic reasoning a clinician would apply. Furthermore, the equivalent performance of both models on longitudinal and transversal acquisitions indicates a successful generalization of the problem, confirming that the AI is robust to this key acquisition variable. This would have positive implications for clinical practice, offering greater flexibility during the examination.

A key finfing from our analysis is the fundamental impact of data acquisition standardization on AI performance. A clear contrast in results was observed between the heterogeneous, multi-scanner Dataset-1 and the standardized, single-scanner Dataset-2. Although the CM was trained on a dataset with same scanners to those in Dataset-1, its significant performance improvement on Dataset-2 strongly suggests that variations in image quality, likely caused by different hardware and post-processing filters, are significant barriers to generalizability. This leads to the conclusion that standardizing image acquisition protocols may be as crucial as the AI architecture itself for achieving reliable and clinically translatable results.

Despite these promising findings, several limitations of this study must be acknowledged. Its retrospective nature means we could not control for potential selection bias. Another significant methodological limitation is the potential for data leakage in the SM results on Dataset-2, as the segmentation model was trained on images from 27 of the 30 patients that comprise this dataset, however, these results are presented to ensure a comprehensive study that includes all possible model and dataset combinations despite this known constraint.

Conclusions

This study demonstrates that a segmentation-based workflow can be effectively repurposed for severity scoring in lung ultrasound, achieving a prognostic accuracy comparable to that of a model trained specifically for classification. Furthermore, the results indicate that while these AI algorithms are robust to variations in probe orientation, their reliable performance is fundamentally dependent on high-quality, standardized image acquisition. This underscores that the successful clinical translation of AI-assisted diagnosis in LUS depends not only on algorithmic innovation, but also on the promotion of consistent clinical protocols.

References

[1] G. Soldati, A. Smargiassi, R. Inchingolo, et al. "Proposal for International Standardization of the Use of Lung Ultrasound for Patients With COVID-19: A Simple, Quantitative, Reproducible Method". In: *Journal of Ultrasound in Medicine* 39.7 (2020), pp. 1413–1419. DOI: 10.1002/jum.15285.

[2] L. Demi, F. Mento, A. Di Sabatino, et al. "Lung Ultrasound in COVID-19 and Post-COVID-19 Patients, an Evidence-Based Approach". In: *Journal of Ultrasound in Medicine* 41.9 (2022), pp. 2203–2215. DOI: 10.1002/jum.15902.

[3] L. Demi et al. "Lung Ultrasound in COVID-19 and Post-COVID-19 Patients, an Evidence-Based Approach". In: *Journal of Ultrasound in Medicine* 41.9 (Sept. 2022), pp. 2203–2215. DOI: 10.1002/jum.15902.

[4] Y. Tung-Chen, S. Ossaba-Vélez, K. S. Acosta Velásquez, et al. "The Impact of Different Lung Ultrasound Protocols in the Assessment of Lung Lesions in COVID-19 Patients: Is There an Ideal Lung Ultrasound Protocol?" In: *Journal of Ultrasound* 25.4 (2022), pp. 483–491. DOI: 10.1007/s40477-021-00610-x.

[5] J. Camacho, M. Muñoz, V. Genovés, et al. "Artificial Intelligence and Democratization of the Use of Lung Ultrasound in COVID-19: On the Feasibility of Automatic Calculation of Lung Ultrasound Score". In: *International Journal of Translational Medicine* 2.1 (2022), pp. 17–25. DOI: 10.3390/ijtm2010002.

[6] K. He et al. "Deep Residual Learning for Image Recognition". In: *Proceedings of the 2016 IEEE Conference on Computer Vision and Pattern Recognition (CVPR)*. 2016, pp. 770–778. DOI: 10.1109/CVPR.2016.90.

[7] U. Khan, S. Afrakhteh, F. Mento, et al. "Benchmark methodological approach for the application of artificial intelligence to lung ultrasound data from COVID-19 patients: From frame to prognostic-level". In: *Ultrasonics* 132 (2023), p. 106994. DOI: 10.1016/j.ultras.2023.106994.

[8] O. Oktay et al. "Attention U-Net: Learning Where to Look for the Pancreas". In: *arXiv preprint arXiv:1804.03999* (2018).

[9] M. Muñoz et al. "Deep Learning-Based Algorithms for Real-Time Lung Ultrasound Assisted Diagnosis". In: *Applied Sciences* 14.24 (2024), p. 11930. DOI: 10.3390/app142411930.

[10] F. Mento et al. "Deep learning applied to lung ultrasound videos for scoring COVID-19 patients: A multicenter study". In: *The Journal of the Acoustical Society of America* 149.5 (2021), p. 3626. DOI: 10.1121/10.0004855.

[11] J. Cohen. "Weighted kappa: Nominal scale agreement provision for scaled disagreement or partial credit". In: *Psychological Bulletin* 70.4 (1968), pp. 213–220. DOI: 10.1037/h0026256.

DOI 10.5162/Ultrasonic2025/P1.21

Characterization of defects in aluminum plates using acoustic impedance analysis of piezoelectric ceramic discs

Mário Kyohi Takahasi[1], *Joaquim Miguel Maia*[1,2,3], *Wilson José da Silva*[1,3], *Amauri Amorin Assef*[1,4], *Rosalba da Costa*[4], *Sergio Francisco Pichorim*[1,3], *and Eduardo Tavares Costa*[5]
[1] *Graduate School of Electrical Engineering and Applied Computer Sciences (CPGEI), Federal University of Technology–Paraná (UTFPR), Curitiba, Brazil*
[2] *Graduate Program in Biomedical Engineering (PPGEB)*
[3] *Academic Department of Electronics Engineering (DAELN), UTFPR, Curitiba, Brazil*
[4] *Academic Department of Electrical Engineering (DAELT), UTFPR, Curitiba, Brazil*
[5] *Department of Electronics and Biomedical Engineering (DEEB), & Biomedical Engineering Centre (CEB), State University of Campinas (UNICAMP), Campinas, Brazil*
joaquim@utfpr.edu.br

Abstract: This work aimed to identify defects in aluminum plates by analyzing the module and phase angle of the electrical impedance of piezoelectric ceramics. Five aluminum plates with three centrally aligned holes in the center of the plate, and one reference plate (without holes) were used. Four ceramic discs were fixed to each of the six plates, and the impedances were compared using the root mean square deviation index (RMSD). The results showed that the method can be used for material characterization using the vibration modes of the ceramics.

Keywords: Piezoelectric ceramics, aluminum plates, electrical impedance, RMSD, material characterization.

Background, Motivation, and Objective

Piezoelectric ceramics coupled with different materials for defect evaluation offer a low-cost alternative for performing non-destructive tests (NDT) and material characterization to be applied in various areas, including biomedicine, the construction industry, naval, aeronautics, mechanical, physics, and others [1]–[7].

These kinds of NDT have been used for a long time and can still be innovative today. Some applications use the electrical impedance of piezoelectric ceramics [1]–[4]; the propagation of Lamb waves through the materials [8]–[10]; the instantaneous phase, attenuation, and speed of ultrasound waves measured using the pulse-echo or the transmission-reception methods [2], [5]–[7], [11], [12]; 2D and 3D images acquired using the B-mode scan; among others [7].

This work aimed to identify defects in aluminum square plates by analyzing the electrical impedance of piezoelectric ceramics coupled in different positions of these plates.

Materials and Methods

Six aluminum plates measuring 500 × 500 × 5 mm³ were used, one of which, without holes, was the reference plate. The others had three holes of the same diameter, aligned in the center of the plate, 250 mm from each side where the ceramics were placed and 125, 250, and 375 mm from the edges where there were no ceramics, simulating defects with 2, 4, 6, 8, and 10 mm in diameter. Four piezoelectric ceramic discs of APC 855 type (12.7 mm diameter and 2.0 mm thickness) were fixed to each of the six plates using conductive silver-based glue. The ceramics were all placed on the same side of the plate, one close to the bottom edge (centered at 250 mm – PR), and three close to the top edge (centered at 125 mm – P1, 250 mm – P2, and 375 mm – P3), as shown in Fig. 1(a). The module and phase angle of electrical impedance were measured in each ceramic disc on all the sample plates using an impedance analyzer (model 4294A, Agilent Technologies). Fig. 1(b) presents the block diagram of the setup used to measure the electrical impedance of each ceramic disc coupled to the sample plates.

The impedances were compared in three ranges (40 kHz to 1.3 MHz – all vibration modes, 150 kHz to 200 kHz – radial vibration mode, and 950 kHz to 1.3 MHz – axial vibration mode) using the root mean square deviation index (RMSD), as in Eq. (1) [4], where Zn,r is the impedance module in the reference plate, Zn,s is for the sample plate containing defects, n corresponds to the measurement obtained, and p (801 points) is the total number of measurements comprising the range of frequencies used in the impedance analyzer.

$$\mathrm{RMSD} = \sqrt{\frac{\sum_n^p (Z_{n,s} - Z_{n,r})^2}{\sum_n^p Z_{n,r}^2}} \qquad (1)$$

DOI 10.5162/Ultrasonic2025/P1.21

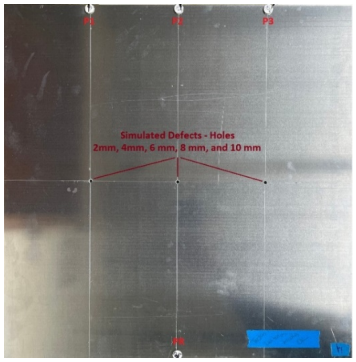

(a)

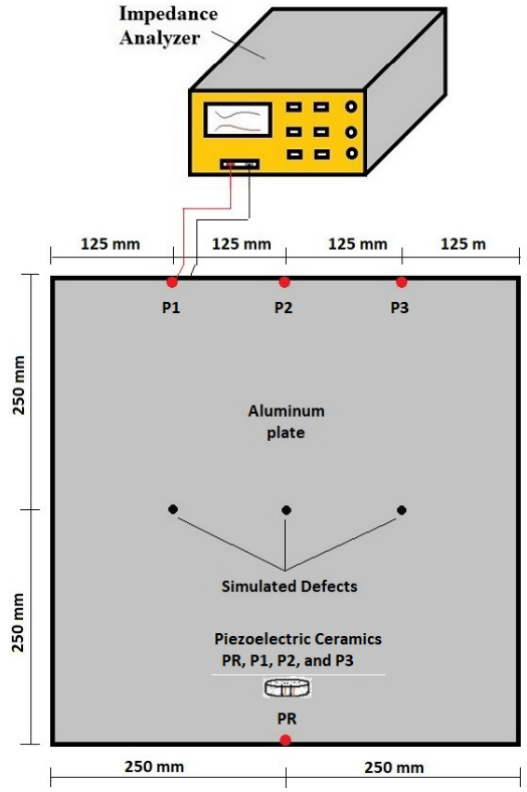

(b)

Fig. 1: (a) Sample plate with the ceramic discs APC 855 (12.7 mm × 2.0 mm) fixed using conductive silver-based glue; (b) Block diagram of the system used to measure the electrical impedance of the piezoelectric discs coupled to each of the six sample plates.

Results and Discussion

The module and phase angle of the electrical impedance obtained for a free APC 855 ceramic disc are shown in Fig. 2(a). It is possible to see all vibration modes in the frequency range of 40 kHz to 1.3 MHz. Fig. 2(b) shows the impedance modules for the six free ceramics before they were fixed in the position PR, see Fig. 1(b), of the aluminum plates, showing a similar module for all of them.

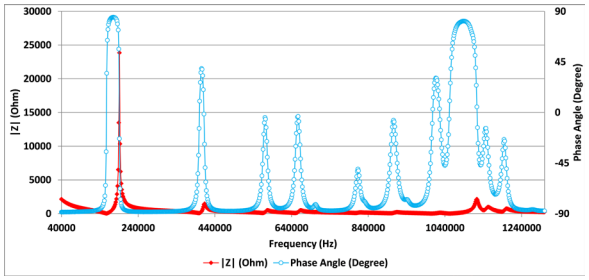

(a)

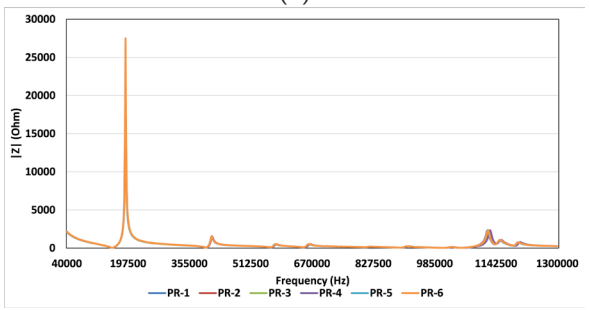

(b)

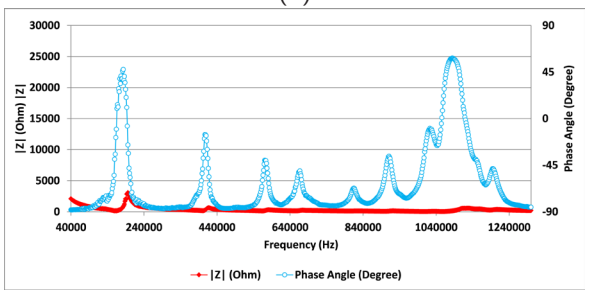

(c)

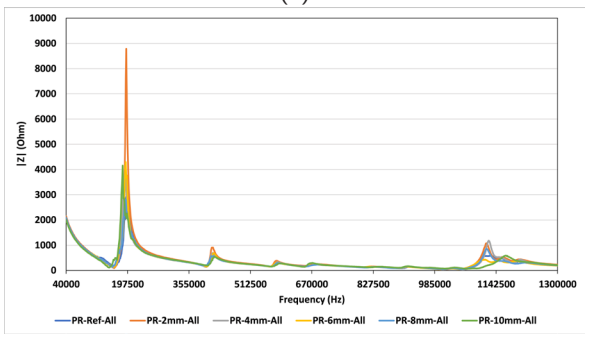

(d)

Fig. 2: (a) Electrical impedance for a free ceramic disc APC 855 showing a frequency range (40 kHz – 1.3 MHz) that includes all vibration modes; (b) Module of the impedance for all six free ceramics before they were fixed in the position PR of the six plates; (c) Electrical impedance for a fixed ceramic disc in the position PR, see Fig. 1(b), of the reference plate, showing the changes in the vibration mode when compared with the results shown in (a); (d) Impedance module for the six ceramics fixed in the six plates (the reference plate, and those with holes of 2, 4, 6, 8, and 10 mm).

DOI 10.5162/Ultrasonic2025/P1.21

When one of the ceramics was fixed in the position PR of the reference plate, changes in the vibration modes were observed, as shown in Fig. 2(c). Fig. 2(d) shows the changes for the impedance module after the six ceramics were coupled to the six aluminum plates (the reference plate and those with holes of 2, 4, 6, 8, and 10 mm). These kinds of changes were also observed in other studies [1]–[4].

Fig. 3(a) presents the impedance modules for the ceramics coupled to the six aluminum plates for the radial vibration mode (frequency range of 150 kHz – 200 kHz), and Fig. 3(b) presents the curves for the axial vibration mode (frequency range of 950 kHz – 1.3 MHz).

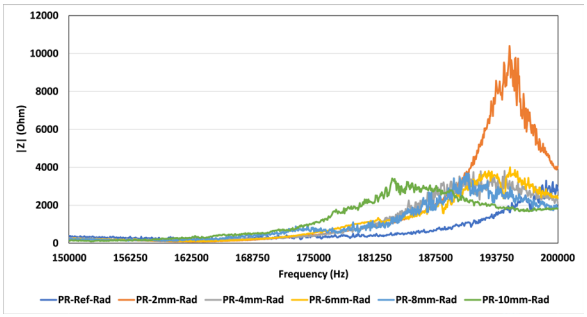

(a)

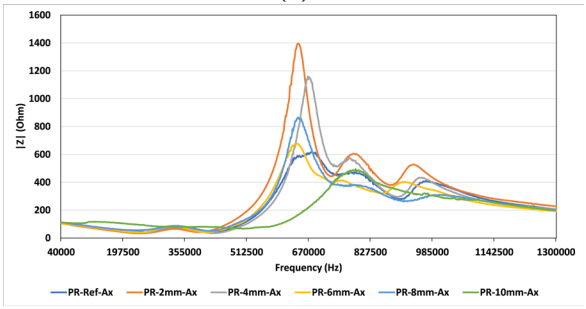

(b)

Fig. 3: Impedance module for the six ceramics fixed in the six plates (the reference plate, and those with holes of 2, 4, 6, 8, and 10 mm) for (a) the radial vibration mode in the frequency range of 150 kHz – 200 kHz, and (b) for the axial vibration mode in the frequency range of 950 kHz – 1.3 MHz.

The RMSD values obtained for the ceramics located in the PR position for the reference plate and the defective samples (with holes of 2, 4, 6, 8, and 10 mm) in the frequency range involving all vibration modes (40 kHz to 1.3 MHz) are shown in Fig. 4(a). The values for the radial vibration mode (150 kHz to 200 kHz) are shown in Fig. 4(b), and for the axial vibration mode (950 kHz to 1.3 MHz) in Fig. 4(c).

The RMSD results for the other ceramics at positions P1, P2, and P3 in all vibration modes (40 kHz to 1.3 MHz), radial modes (150 kHz to 200 kHz), and axial modes (950 kHz to 1.3 kHz) for the reference plate and the defective samples (with holes of 2, 4, 6, 8, and 10 mm) are shown in Tab. 1.

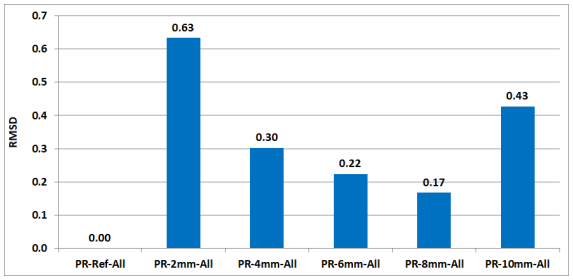

(a)

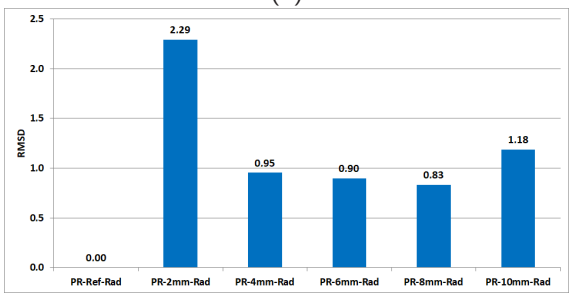

(b)

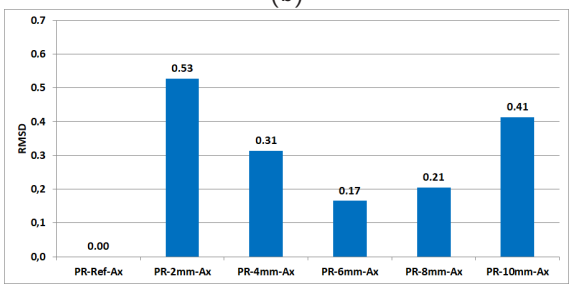

(c)

Fig. 4: RMSD values obtained for the ceramics located in the PR position for the reference plate and the defective samples (with holes of 2, 4, 6, 8, and 10 mm) in the frequency range involving (a) all vibration modes (40 kHz to 1.3 MHz), (b) the radial vibration mode (150 kHz to 200 kHz), and (c) the axial vibration mode (950 kHz to 1.3 MHz).

Conclusion

The results' analysis showed that the RMSD between the samples with defects and the reference sample can be used for material characterization using all the vibration modes of the ceramics or the radial and axial modes alone. Since the radial mode involves a lower frequency range, more straightforward and cost-effective electronic circuits can be designed to operate in this frequency range.

Tab. 1: RMSD values for the ceramics at positions P1, P2, and P3 (see Fig. 2) in all vibration modes (40 kHz to 1.3 MHz), radial mode (150 kHz to 200 kHz), and axial mode (950 kHz to 1.3 kHz) for the reference plate and the defective samples (with holes of 2, 4, 6, 8, and 10 mm).

Ceramics	Position	All modes	Radial mode	Axial mode
Reference	P1	0.00	0.00	0.00
	P2	0.00	0.00	0.00
	P3	0.00	0.00	0.00
2 mm holes	P1	0.20	0.19	0.39
	P2	0.25	0.54	0.66
	P3	0.19	0.51	0.29
4 mm holes	P1	0.26	0.20	0.31
	P2	0.24	0.23	0.78
	P3	0.33	0.41	0.27
6 mm holes	P1	0.63	0.88	0.73
	P2	0.39	0.66	0.79
	P3	0.34	0.72	0.28
8 mm holes	P1	0.52	0.58	0.37
	P2	0.44	0.31	0.49
	P3	0.16	0.34	0.29
10 mm holes	P1	0.29	0.66	0.18
	P2	0.48	0.85	0.41
	P3	0.34	0.95	0.76

Acknowledgements

The authors thank the Brazilian Coordination for the Improvement of Higher Education Personnel (CAPES), grant 001, the National Council for Scientific and Technological Development (CNPq), grant 408274/2021-2, the Federal University of Technology – Paraná (UTFPR), and the Araucaria Foundation for the financial support.

References

[1] P. Cawley, 'The impedance method of non-destructive inspection,' *NDT & E International*, vol. 17, pp. 59–65, 1984. DOI: 10.1016/0308-9126(84)90045-2.

[2] R. Costa and et al., 'Defect detection in aluminum bars using impedance and ultrasonic attenuation,' *IEEE Sensors Journal*, vol. 20, pp. 7400–7413, 2020. DOI: 10.1109/JSEN.2020.2978427.

[3] G. Park and et al., 'Impedance-based health monitoring technique for massive structures and high-temperature structures,' in *Smart Struct. and Mater. Proceedings of the SPIE*, vol. 3670, 1999, pp. 461–469. DOI: 10.1117/12.349760.

[4] X. Dongyu and et al., 'Identifying technology for structural damage based on the impedance analysis of piezoelectric sensor,' *Const. Build. Materials*, vol. 24, pp. 2522–2527, 2010. DOI: 10.1016/j.conbuildmat.2010.06.004.

[5] F. Lefebvre and et al., 'Development of a new ultrasonic technique for bone and biomaterials in vitro characterization,' *Biomed Mater Res*, vol. 63, pp. 441–6, 2002. DOI: 10.1002/jbm.10261.

[6] J. M. Maia and et al., 'Broadband ultrasound attenuation in the calcaneal region: A comparative study of single-position versus scanning systems,' *IEEE Trans. Ultras., Ferroel., and Freq. Control*, vol. 55, pp. 64–73, 2008. DOI: 10.1109/TUFFC.2008.617.

[7] F. Honarvar and A. Varvani-Farahami, 'A review of ultrasonic testing applications in additive manufacturing: Defect evaluation, material characterization, and process control,' *Ultrasonics*, vol. 108, 2020. DOI: 10.1016/j.ultras.2020.106227.

[8] Y. Lu and et al., 'Quantitative assessment of through-thickness crack size based on lamb wave scattering in aluminum plates,' *NDT & E International*, vol. 41, pp. 59–68, 2008. DOI: 10.1016/J.NDTEINT.2007.07.003.

[9] F. Benmeddour and et al., 'Study of the fundamental lamb modes interaction with asymmetrical discontinuities,' *NDT & E International*, vol. 41, pp. 330–340, 2008. DOI: 10.1016/j.ndteint.2008.01.004.

[10] Z. Su and et al., 'Guided lamb waves for identification of damage in composite structures: A review,' *J. of Sound and Vibration*, vol. 295, pp. 753–780, 2006. DOI: 10.1016/j.jsv.2006.01.020.

[11] V. T. Prado and et al., 'Defect detection in anisotropic plates based on the instantaneous phase of signals,' *IEEE Trans. Ultras., Ferroel., and Freq. Control*, vol. 62, pp. 1888–1894, 2015. DOI: 10.1109/TUFFC.2014.006955.

[12] R. C. Mayworm and et al., 'A metrological based realization of time-of-flight diffraction technique,' *Physics Procedia*, vol. 70, pp. 590–593, 2015. DOI: 10.1016/j.phpro.2015.08.029.

DOI 10.5162/Ultrasonic2025/P1.22

High-Power Ultrasound Cleaning for Printed Circuit Heat Exchangers

H.Nasiri[1], A. C.M. Cavalheiro[1], C. M.G. Atehortua[1], N. Tanabi[1], C. A. Burbano Reyna[1], T. F. Oliveira[1], J. H. Lopes[2], M. S.G. Tsuzuki[1], and F.Buiochi[1]
[1]*Escola Politécnica da Universidade de São Paulo, Department of Mechatronics and Mechanical Systems Engineering, São Paulo, Brazil*
[2]*Universidade Federal de Alagoas, Campus Arapiraca, Maceió, Brazil*
h.nasiri.ir@gmail.com

Abstract: Printed Circuit Heat Exchangers (PCHEs) are prone to clogging and difficult to clean using conventional methods. This study investigates high-intensity ultrasound as an effective alternative, applying Langevin transducers to a real PCHE. Ultrasonic vibrations enhanced deposit removal without the need for disassembly. The method is more sustainable, reduces downtime and costs, and offers on-site cleaning.

Keywords: Ultrasound Cleaning, Printed Circuit Heat Exchangers, PCHEs, High Power Transducer.

Introduction

Printed Circuit Heat Exchangers (PCHEs) represent an advanced category of compact heat exchangers, distinguished by their exceptional thermal performance and mechanical robustness [1], [2]. The core of a PCHE consists of thin metal plates, where channels for fluid passage are chemically etched. These plates are then bonded by diffusion, forming a solid block with intricate channels for heat exchange, as shown in Figure 1 (a). Their ability to operate under high-pressure and high-temperature conditions makes them particularly well-suited for demanding industrial environments, such as solar thermal energy systems [3]. Owing to these characteristics, PCHEs have emerged as a compelling option for sectors such as petrochemical processing, where both efficiency and durability in heat exchange are critical. On offshore oil platforms, for example, they are employed during primary processing to cool natural gas using seawater. However, these exchangers are susceptible to clogging, as fouling caused by oily sludge and calcium carbonate that can accumulate in their channels over time, compromising performance and requiring pump overloads or maintenance shutdowns. This incrustation on the channel walls also reduces heat transfer efficiency due to its low thermal conductivity [4].

Cleaning PCHE-type heat exchangers presents a significant challenge due to the small dimensions of the channels through which fluids pass and their intricate internal architecture, which are generally arranged in a zigzag pattern. These channels have a semicircular geometry with dimensions of approximately 2 mm, as shown in Figure 1 (b). These structural characteristics limit the effectiveness of conventional mechanical or chemical cleaning methods, particularly in reaching and removing deposits from deep or narrow passages.

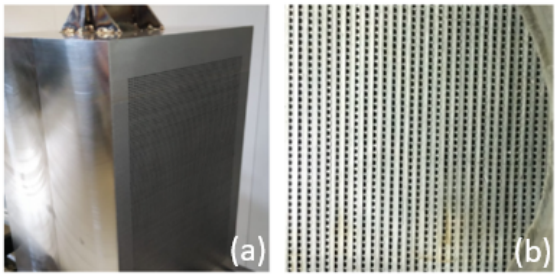

Fig. 1: (a) Core of a Printed Circuit Heat Exchanger (PCHE) ; (b) cross-sectional view highlighting the internal flow passages within the PCHE.

One promising technique for cleaning PCHEs in industry is the application of high-intensity ultrasound waves to produce cavitation in the regions that need to be cleaned. The use of ultrasound for cleaning materials and equipment is a well-established technique, with numerous companies offering cleaning services and the commercial sale of ultrasonic cleaning equipment [5], [6]. However, the mechanical structures of PCHE-type heat exchangers are very complex due to the large number of fluid flow channels with small dimensions and the overall size of the units. This makes cleaning in ultrasonic tanks unsuitable, as cavitation is unlikely to occur uniformly in all areas that require cleaning.

The method presented in this study is a non-invasive strategy for cleaning the internal channels of the PCHE through the application of ultrasonic energy.

DOI 10.5162/Ultrasonic2025/P1.22

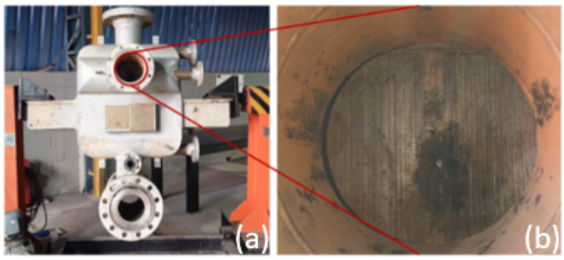

Fig. 2: (a) External view of a Printed Circuit Heat Exchanger (PCHE), showing the main inlet and outlet nozzles; (b) Internal view through the inlet nozzle.

This approach employs high-intensity ultrasonic transducers attached to the outer surface of the equipment. When driven at their resonance frequency, these transducers induce acoustic waves that propagate through the structure, generating localized mechanical stresses and high pressure in the cleaning fluid that fills the channels, causing cavitation that disrupts the adhesion of scale deposits. These dynamic effects promote the detachment of existing scale. Thus, this work proposes to experimentally evaluate the power ultrasound technique applied to the cleaning of the channels of a compact heat exchanger

Materials and Methods

Figure 2 shows the PCHE employed in the tests conducted for cleaning and unclogging its channels using high-power ultrasound. Figure 2 (a) displays a PCHE unit, highlighting its compact and densely packed design, which underscores the practical difficulties associated with maintenance and fouling mitigation. Figure 2 (b) presents an internal view through the inlet nozzle, displaying the small channels of the PCHE, which are designed for high-efficiency heat transfer and operation under extreme thermal and pressure conditions.

Acoustic cavitation enhances the action of detergent/degreaser in cleaning mechanical parts. For acoustic cavitation to occur, the pressure of the ultrasonic wave must reach approximately 100 kPa at frequencies around 20 kHz.

In a complex structure such as cavitation penetration into small orifices, relative to the wavelength, is very limited and thus would not reach the interior of the PCHE. To overcome this limitation, Langevin-type ultrasonic transducers were designed to be directly coupled to the PCHE surface. These transducers were constructed with four rings of piezoelectric ceramic sandwiched between front and rear masses, optimizing acoustic output by promoting longitudinal vibrations in the thickness-extensional mode, at a resonance frequency near 20kHz.

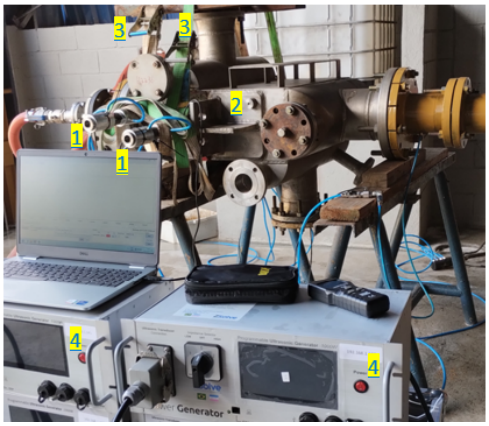

Fig. 3: Experimental setup for applying high-power Langevin transducers to the body of a PCHE-type heat exchanger, where (1) indicates the transducers, (2) the PCHE body, (3) the ratchet straps, and (4) the ultrasonic generators.

The experimental setup for applying ultrasound in the PCHE cleaning process is illustrated in Figure 3. Two high-power Langevin-type ultrasonic transducers (1) were firmly attached to one side of the external surface of the PCHE (2) using ratchet straps (3). Two additional high-power transducers were mounted on the opposite side of the PCHE. The mechanical contact achieved through pressure is enhanced by applying Araldite adhesive to ensure proper acoustic coupling between the flat interfaces formed by the lateral surface of the PCHE block and the tip surface of the transducer's extension rod. The transducers (1) are powered by individual high-power ultrasonic generators (4), with each transducer driven by a dedicated generator. A frequency sweep is performed for each transducer to ensure tuning within its resonance band during operation. This direct coupling is critical for the efficient transmission of ultrasonic waves into the exchanger structure, thereby maximizing the cleaning effect through mechanical vibrations and acoustic cavitation.

Finally, two comparative tests were conducted under identical conditions, using the same water-diluted detergent: one with the application of ultrasonic waves and the other without. These two tests were only performed after circulating the water-detergent mixture for one hour to remove the initial fouling through the conventional cleaning process. This approach was employed to verify the effectiveness of ultrasonic-assisted cleaning through a qualitative visual assessment of the removal of scale and other impurities from within the PCHE channels.

In the first test, without ultrasound—repeating the conventional cleaning process—a sample of the freshly

DOI 10.5162/Ultrasonic2025/P1.22

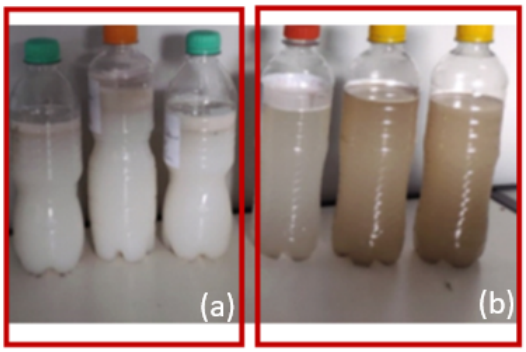

Fig. 4: Comparison of cleaning effectiveness for a PCHE-type heat exchanger: (a) without ultrasonic assistance and (b) with ultrasonic application. The samples collected at the beginning of the process, after 30 minutes, and after 1 hour of operation are positioned from left to right.

circulated mixture inside the PCHE's channels was collected and stored in a labeled PET bottle for later analysis. After 30 minutes of recirculation, another sample was collected and stored, and finally, after 1 hour of recirculation, a third sample was bottled. In the second test, with ultrasound—i.e., with the transducers directly coupled to the surface of PCHE and activated—samples were also collected at the beginning, after 30 minutes, and after 1 hour of recirculation. In both tests, a freshly prepared detergent solution (diluted in water at the same mass ratio) was used to ensure consistency in the cleaning conditions.

Results

As a form of qualitative assessment, the collected samples were subjected to visual inspection following a one-week settling period. Figure 4 presents the appearance of the samples after being left undisturbed on a laboratory bench, allowing for the evaluation of sedimentation behavior and overall cleaning effectiveness.

In Figure 4(a), corresponding to the test without ultrasonic assistance, the cleaning solution appeared more homogeneous and turbid, indicating limited particle separation and less effective scale removal. In contrast, Figure 4(b), representing the sample collected after applying ultrasound during the cleaning process, qualitatively shows more pronounced stratification and increased sediment deposition at the bottom of the containers. This suggests enhanced detachment of impurities and particulates from the internal surfaces of the PCHE channels due to ultrasonic agitation. The visual difference clearly demonstrates the efficacy of ultrasonic waves in improving contaminant dislodgement and suspension, thus validating the positive impact of ultrasonic-assisted cleaning on PCHE performance.

Conclusions

High-intensity ultrasound, applied via Langevin transducers, is an effective and sustainable method for cleaning Printed Circuit Heat Exchangers (PCHEs) without requiring disassembly. The experimental results qualitatively demonstrate that ultrasonic vibrations significantly enhance the removal of deposits, leading to a more effective cleaning process compared to conventional methods. This approach offers benefits such as reduced downtime and costs, and enables on-site cleaning, making it a promising alternative for maintaining PCHE efficiency in industrial applications.

Acklowledgements

This work was supported by CNPq (grants #306.123/2022–3 and #312126/2021-2) and PRH-ANP (grant #5850.0108871.18.9).

References

[1] C. Huang et al. "Review on the characteristics of flow and heat transfer in printed circuit heat exchangers". In: *Applied Thermal Engineering* 153 (2019), pp. 190–205.

[2] J. E. Hesselgreaves, R. Law, and D. Reay. *Compact heat exchangers: selection, design and operation*. Butterworth-Heinemann, 2016.

[3] Y. Ma, G. Xie, and K. Hooman. "Review of printed circuit heat exchangers and its applications in solar thermal energy". In: *Renewable and Sustainable Energy Reviews* 155 (2022), p. 111933.

[4] H. Nasiri et al. "Cleaning of Printed Circuit Heat Exchangers (PCHE) Using High-Power Ultrasonic Transducers". In: *2024 IEEE UFFC Latin America Ultrasonics Symposium (LAUS)*. IEEE. 2024, pp. 1–2.

[5] K. L. Mittal and R. Kohli. *Developments in Surface Contamination and Cleaning: Particle Deposition, Control and Removal*. Elsevier, 2010.

[6] M. O. Lamminen, H. W. Walker, and L. K. Weavers. "Mechanisms and factors influencing the ultrasonic cleaning of particle-fouled ceramic membranes". In: *Journal of membrane science* 237.1-2 (2004), pp. 213–223.

DOI 10.5162/Ultrasonic2025/P1.25

Change of Piezoelectric Signal Generated in Cancellous Bone by Ultrasound Irradiation Associated with Oblique Trabecular Orientation

Atsushi Hosokawa[1]
[1]National Institute of Technology, Akashi College, 679-3 Nishioka, Uozumi, Akashi, Japan,
hosokawa@akashi.ac.jp

Abstract: The piezoelectric signals generated in water-saturated cancellous bone with oblique trabecular orientations were numerically simulated. The waveforms of the piezoelectric signals in cancellous bone and the ultrasound signals through the bone when an ultrasound wave was irradiated were calculated. The simulated results suggested that the piezoelectric waves could primarily depend on the fast and slow waves in the ultrasound signals but could be also affected by the other factors.

Keywords: Cancellous bone, Piezoelectric signal, Trabecular orientation, Fast wave, Slow wave

Introduction

Bone is a piezoelectric material [1], and bone formation can be accompanied by the piezoelectric effects [2]. This mechanism is utilized in accelerating bone fracture healing using ultrasound [3]. To establish an ultrasound healing method for joint bones, it is essential to understand the piezoelectric properties in cancellous bone, which constitutes the majority of the epiphysis. As the ultrasound signals propagated through cancellous bone can change depending on the trabecular orientation [4], it is expected that the piezoelectric signals generated in the bone by ultrasound irradiation can be largely affected by the orientation. In the present study, the piezoelectric signals in water-saturated cancellous bone with oblique trabecular orientations were numerically simulated.

Methods

Numerical simulations of the piezoelectric signals in water-saturated cancellous bone were performed using a piezoelectric finite-difference time-domain (PE-FDTD) method, which is an advanced elastic FDTD method with piezoelectric constitutive equations. The governing equations are as follows [5].

$$\rho \frac{\partial v_i}{\partial t} = \frac{\partial \tau_{ii}}{\partial x_i} + \frac{\partial \tau_{ij}}{\partial x_j} + \frac{\partial \tau_{ik}}{\partial x_k} \tag{1}$$

$$\frac{\partial \tau_{ii}}{\partial t} = (\lambda + 2\mu)\frac{\partial v_i}{\partial x_i} + \lambda \frac{\partial v_j}{\partial x_j} + \lambda \frac{\partial v_k}{\partial x_k} - e_{ii}\frac{\partial E_i}{\partial t} - e_{ji}\frac{\partial E_j}{\partial t} - e_{ki}\frac{\partial E_k}{\partial t} \tag{2}$$

$$\frac{\partial \tau_{jk}}{\partial t} = \mu\left(\frac{\partial v_j}{\partial x_k} + \frac{\partial v_k}{\partial x_j}\right) - e_{il}\frac{\partial E_i}{\partial t} - e_{jl}\frac{\partial E_j}{\partial t} - e_{kl}\frac{\partial E_k}{\partial t} \tag{3}$$

$$\varepsilon_{ii}\frac{\partial E_i}{\partial t} = -e_{ii}\frac{\partial v_i}{\partial x_i} - e_{ij}\frac{\partial v_j}{\partial x_j} - e_{ik}\frac{\partial v_k}{\partial x_k} - \frac{e_{il}}{2}\left(\frac{\partial v_j}{\partial x_k} + \frac{\partial v_k}{\partial x_j}\right) - \frac{e_{im}}{2}\left(\frac{\partial v_k}{\partial x_i} + \frac{\partial v_i}{\partial x_k}\right) - \frac{e_{in}}{2}\left(\frac{\partial v_i}{\partial x_j} + \frac{\partial v_j}{\partial x_i}\right) + \frac{\partial D_i}{\partial t} \tag{4}$$

$$\frac{\partial D_i}{\partial t} = -\sigma_i E_i \tag{5}$$

In Eqs. (1)–(5), the variables are v_i of the particle velocity, τ_{ii} and τ_{ij} of the normal and shear stresses, E_i of the electric field, and D_i of the electric displacement. The constants are ρ of the density, λ and μ of the first and second Lamé coefficients, e_{ij} of the piezoelectric constant, ε_{ii} of the dielectric constant, and σ_i of the conductivity.

The simulation model is shown in Fig. 1. Three-dimensional (3D) X-ray microcomputed tomographic (μCT) images of cancellous bone were obtained from positions with porosities of 0.70 and 0.83 (70 and 83%) of a bovine femur. To create the 3D cancellous bone models with angles θ = 0–90 ° of the major trabecular orientation, each μCT image was rotated at θ, cut into a cube with a side length of 5.7 mm, and binarized into the values of the solid bone and the pore space. The pore spaces were saturated with water.

DOI 10.5162/Ultrasonic2025/P1.25

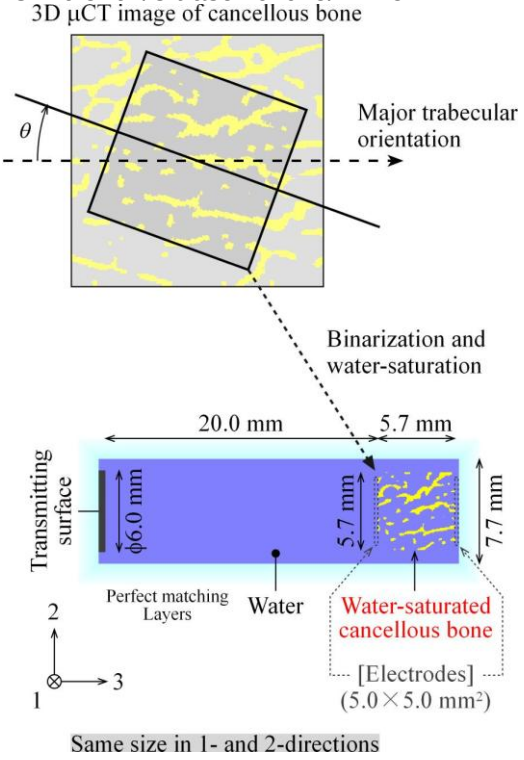

Fig. 1: Numerical model for simulating piezoelectric signals generated in cancellous bone with an oblique angle θ of the major trabecular orientation when an ultrasound wave is irradiated.

Tab. 1: Elastic [6,7] and piezoelectric [8–10] parameters in piezoelectric finite-different time-domain (PE-FDTD) simulations.

	Solid bone	Water
Density ρ (kg/m^3)	1960	1000
1st Lamé coefficient λ (GPa)	14.8	2.2
2nd Lamé coefficient μ (GPa)	8.3	0
Piezoelectric constants (μC/m^2)		
e_{31}, e_{32}, e_{33}	0.21	0
e_{14}, $-e_{25}$	1.32	0
e_{15}, e_{24}	0.26	0
Others	0	0
Dielectric constant ε (nF/m)	50.0	0.7

In the simulation model, the cancellous bone model was located at the position of 20 mm apart from the ultrasound transmitting surface with a diameter of 6.0 mm. The square electrodes with a side of 5.0 mm were assumed to be in the center of the front and back surfaces of the cancellous bone model. However, the electrodes were regarded as perfect conductors, and the elastic properties were ignored. Twenty grids of perfectly matched layers (PMLs) were set at all boundaries surrounding the simulation region. The spatial and temporal intervals were 57 μm and 3 ns, respectively. The elastic [6,7] and piezoelectric [8–10] constant values of the solid bone and water are listed in Tab. 1.

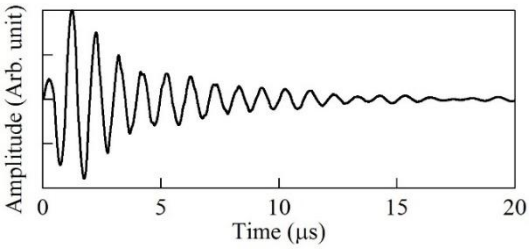

Fig. 2: An input waveform of ultrasound signal irradiated to cancellous bone in piezoelectric finite-difference time-domain (PE-FDTD) simulations.

The input of the irradiated ultrasound signal was the experimental signal emitted from a $Pb(Zr,Ti)O_3$ (PZT) ultrasound transmitter driven by one-cycle burst voltage at 1 MHz, and the waveform is shown in Fig. 2. The output was the piezoelectric signal generated in cancellous bone and the ultrasound signal propagated through the bone. The piezoelectric signal was calculated from the voltage (electric field) induced between the front and back electrodes, and the ultrasound signal was calculated from the normal stress on the surface of the back electrode.

Results and Discussion

The simulated waveforms for the cancellous bone models with porosities of 0.70 and 0.83 are shown in Figs. 3 and 4, respectively; (a) and (b) show the waveforms of the piezoelectric and ultrasound signals, respectively.

It is known that two ultrasound waves of “fast and slow waves” can propagate through water-saturated cancellous bone [11]. The fast and slow waves propagate mainly in the solid bone and the pore space parts, respectively. At the relatively low porosity, the fast wave amplitude becomes larger. Therefore, the fast wave was majorly observed at the porosity of 0.70 in Fig. 3(b). However, both the fast and slow waves were observed at the porosity of 0.83 in Fig. 4(b). Moreover, it is reported that the fast wave speed decreased with the ultrasound angle to the trabecular orientation [12]. Therefore, the first arrival time decreased with the angle θ of the major trabecular orientation. As a result, the overlap of the fast and slow waveforms became larger.

The piezoelectric signal waveforms in Figs. 3(b) and 4(b) were largely different from the ultrasound signal waveforms in Figs. 3(a) and 4(a). This was because the

DOI 10.5162/Ultrasonic2025/P1.25

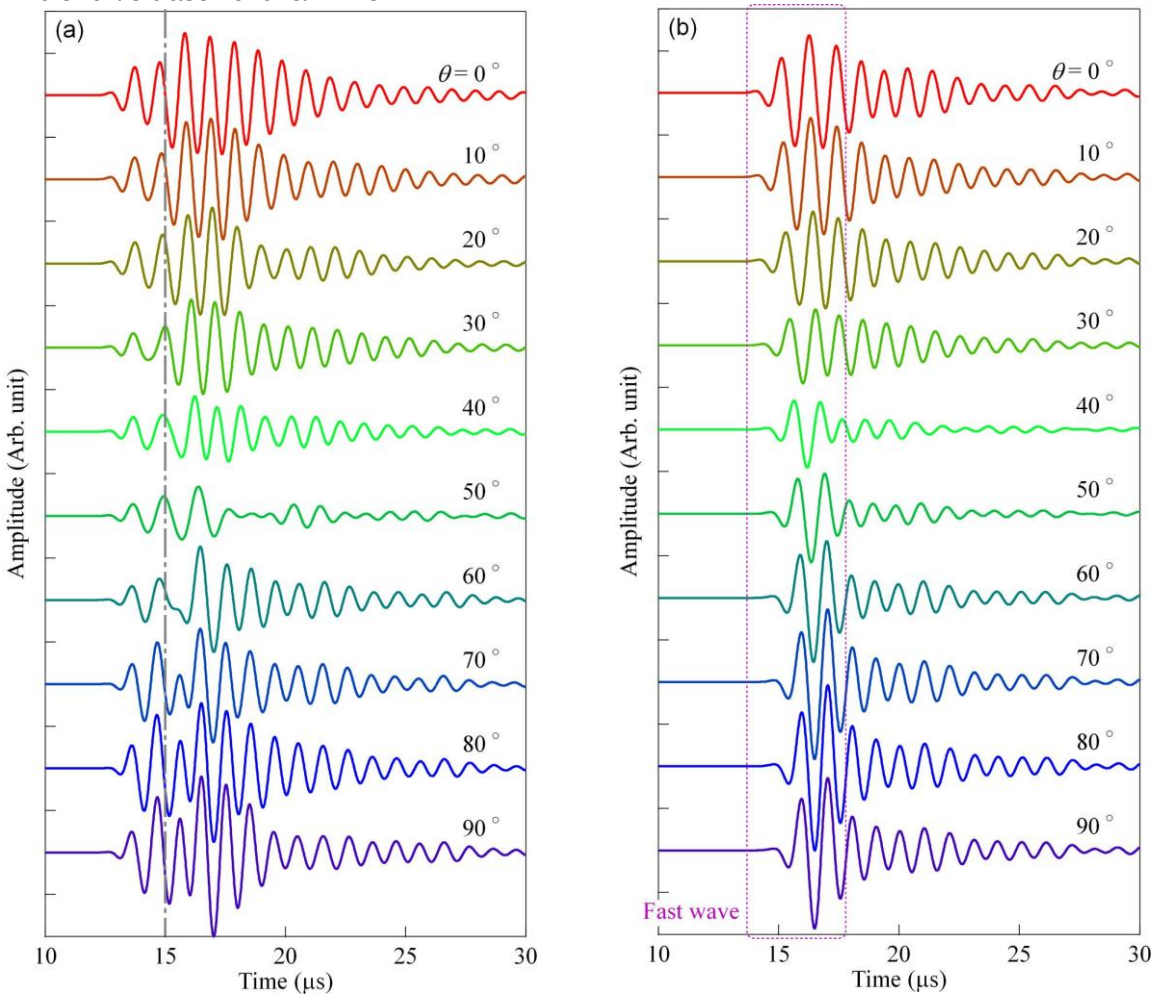

Fig. 3: Calculated waveforms for cancellous bones with a porosity of 0.70 and angles θ = 0–90 ° of the major trabecular orientation in piezoelectric finite-difference time-domain (PE-FDTD) simulations; (a) shows the piezoelectric signals generated in the bones, and (b) shows the ultrasound signals propagated through the bones.

piezoelectric signal detected between the electrodes or between the front and back surfaces of the cancellous bone specimen can be regarded as a superposition of piezoelectric signals generated at the local points in the ultrasound direction. Although it appeared that the piezoelectric signals could be separated into two waves, like the fast and slow waves in the ultrasound signal, the separation times in the signals at the porosities of 0.70 and 0.83 [Figs. 3(a) and 4(a)] were different, being about 15 and 17 μs, respectively. Moreover, the peak time of the wave after the separation time at the porosity of 0.70 increased with the angle θ of the major trabecular orientation, but the time at the porosity of 0.83 was almost constant. This was considered to be because the piezoelectric waves at the porosity of 0.70 could be majorly due to the fast wave, but the piezoelectric wave at the porosity of 0.83 could be majorly due to the slow wave. In the piezoelectric signals at the porosity of 0.83, the waves before 17 μs could be further separated, which was considered to be because the waves due to the fast and slow waves was mixed.

The changes in the piezoelectric signals did not necessarily agree with the changes in the ultrasound signals. The causes for this were considered to be the complex mixture of the piezoelectric waves due to the fast and slow waves, and the properties other than the ultrasound properties.

Conclusions

In the piezoelectric signals, two waves attributed to the fast and slow waves in the ultrasound signals were observed. The changes of the piezoelectric waves did not necessarily depend on only the changes of the fast and slow waves, which was suggested that the piezoelectric signals could be affected by factors other than the ultrasonic signals.

DOI 10.5162/Ultrasonic2025/P1.25

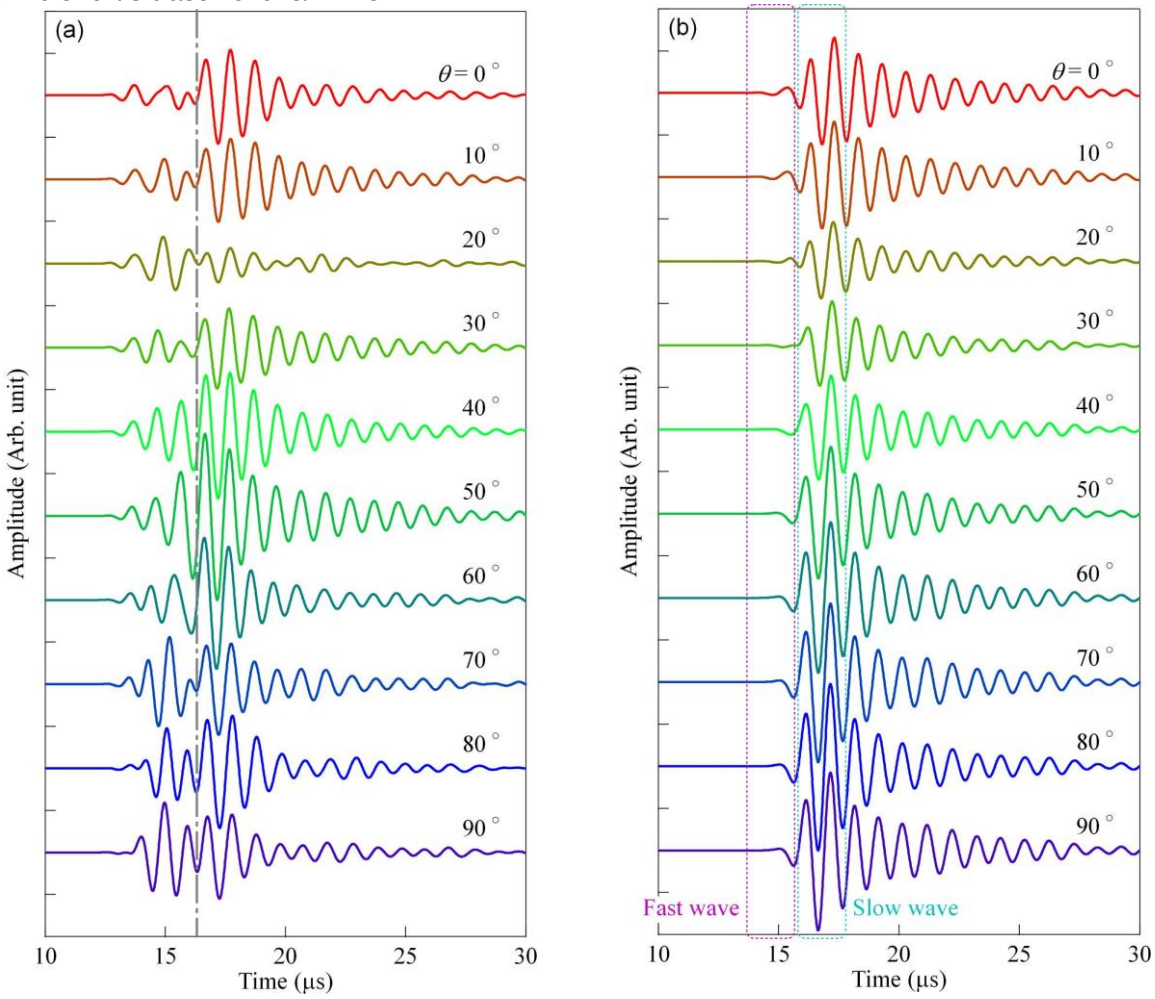

Fig. 4: Calculated waveforms for cancellous bones with a porosity of 0.83 and angles θ = 0–90 ° of the major trabecular orientation in piezoelectric finite-difference time-domain (PE-FDTD) simulations; (a) shows the piezoelectric signals generated in the bones, and (b) shows the ultrasound signals propagated through the bones.

References

[1] E. Fukada and I. Yasuda, Journal of the Physical Society of Japan, vol. 12, pp. 1158–1162, 1957, 10.1143/JPSJ.12.1158.

[2] A. M. Parfitt, Journal of Cellular Biochemistry, vol. 55, pp. 273–286, 1994, 10.1002/jcb.240550303.

[3] L. R. Duarte, Archives of Orthopaedic and Trauma Surgery, vol. 101, pp. 153–159, 1983, 10.1007/BF00436764.

[4] A. Hosokawa and T. Otani, The Journal of the Acoustical Society of America, vol. 103, pp. 2718–2722, 1998, 10.1121/1.418118.

[5] A. Hosokawa, Japanese Journal of Applied Physics, vol. 55, 07KF03, 2016, 10.7567/JJAP.55.07KF03.

[6] S. B. Lang, IEEE Transactions on Biomedical Engineering, vol. 17, pp. 101–105, 1970, 10.1109/TBME.1970.4502706.

[7] J. L. Williams and W. J. H. Johnson, Journal of Biomechanics, vol. 22, pp. 673–682, 1989, 10.1016/0021-9290(89)90017-1.

[8] E. Fukada and I. Yasuda, Japanese Journal of Applied Physics, vol. 3, pp. 117–121, 1964, 10.1143/JJAP.3.117.

[9] S. Saha and P. A. Williams, IEEE Transactions on Biomedical Engineering, vol. 39, pp. 1298–1304, 1992, 10.1109/10.184706.

[10] P. A. Williams and S. Saha, Annals of Biomedical Engineering, vol. 24, pp. 222–233, 1996, 10.1007/BF02667351.

[11] A. Hosokawa and T. Otani, The Journal of the Acoustical Society of America, vol. 101, pp. 558–562, 1997, 10.1121/1.418118.

[12] A. Hosokawa, T. Otani, T. Suzaki, Y. Kubo, and S. Takai, Japanese Journal of Applied Physics, vol. 36, pp. 3233–3237, 1997, 10.1143/JJAP.36.3233.

DOI 10.5162/Ultrasonic2025/P1.31

Study on a Method for Visualizing Hardened Areas Independent of Vibration Direction in Continuous Shear Wave Elastography

Ren Koda[1], Aoi Kuribara[1], Marie Tabaru[2], and Yoshiki Yamakoshi[1]
[1]Gunma University, 1-5-1, Tenjin-cho, Kiryu-shi, Japan
[2]Institute of Science Tokyo, 4259 Nagatsuta-cho, Midori-ku, Yokohama-shi, Japan
koda@gunma-u.ac.jp

Abstract: We propose two continuous shear wave elastography visualization methods to reveal hardened tissue areas regardless vibration direction. Using a tissue-mimicking phantom, vibrations at 78.1 Hz were applied from both the longitudinal and transverse directions relative to the probe. Small-divided-region shear wave velocity imaging consistently identified stiff inclusions under both conditions, while shear strain imaging clearly highlighted their boundaries. Conventional shear wave velocity imaging, in contrast, showed direction-dependent variability.

Keywords: continuous shear wave elastography, shear wave velocity imaging, shear strain imaging, tissue stiffness, ultrasound imaging

Introduction

Because shear wave velocity (SWV)—the speed at which the shear wave propagates through tissue—depends on the stiffness of the medium, various attempts have been made to evaluate the elasticity of biological tissues using shear waves. One of the earliest theoretical studies in this field was conducted by Oestreicher [1].

Later, a technique was developed in which continuous shear waves at around 50 Hz are generated by a compact actuator integrated with an ultrasound probe, allowing measurement of liver elasticity [2]. Subsequently, a practical method known as Shear Wave Elastography (SWE) was established, utilizing impulsive shear waves generated by acoustic radiation force from a focused ultrasound beam [3, 4]. Although safety limits the amplitude of generated shear waves, SWE enables both wave generation and measurement via the same probe and has been widely adopted clinically.

Yamakoshi et al. proposed the continuous SWE (C-SWE) method to visualize tissue elasticity [5]. By applying low-frequency vibrations from a surface actuator, shear waves appear as periodic Doppler signals in color Doppler mode. This method has been applied to musculoskeletal, liver, and mammary tissues, with elasticity inferred from propagation speed [6, 7, 8]. However, C-SWE traditionally assumes that the wave propagates parallel to the element array of the ultrasound probe, an assumption not always met in breast applications. This study investigates two methods for visualizing the stiffened areas independently of the direction of vibration.

Small divided region SWV estimation

When vibrations with frequencies below approximately 1 kHz are applied using a compact shaker, the vibrations propagate through the target medium as shear waves. Simultaneously, if an ultrasonic pulse is transmitted into the target, the backscattered signal received by the same probe is phase-modulated by the Doppler effect.

The ultrasound signal reflected from position (x, z) can be modeled as:

$$y(x,z) = a \exp\{j(2\pi f_0 t + \Delta\varphi(x,z))\} \quad (1)$$

where $\Delta\varphi(x,z)$ represents the Doppler-induced phase modulation:

$$\Delta\varphi(x,z) = \frac{4\pi f_0}{c}\xi_0 \sin(\omega_b t + \theta(x,z)) \quad (2)$$

with: a: amplitude of the ultrasound, f_0: center frequency of the ultrasound, c: speed of sound, ξ_0: displacement amplitude of the shear wave, ω_b: angular frequency of the shear wave, $\theta(x,z)$: local phase of the shear wave.

To demodulate the received ultrasound signal, quadrature detection is performed using a reference signal defined as:

$$r(t) = exp(j2\pi f_0 t) \quad (3)$$

The output of the quadrature demodulation is:

$$Q(x,z) = y(x,z)r*(t) = aexp(j\Delta\phi(x,z)) \quad (4)$$

Here, * denotes complex conjugation.

DOI 10.5162/Ultrasonic2025/P1.31

The Doppler phase component $\Delta\phi(x,z)$ can thus be extracted by:

$$\Delta\phi(x,z) = \tan^{-1}\left(\frac{\mathrm{Im}(Q(x,z))}{\mathrm{Re}(Q(x,z))}\right) \tag{5}$$

To obtain the complex amplitude, a Fourier analysis of the Doppler signal component is performed at the angular frequency ω_b:

$$F(x,z) = \frac{1}{N\Delta t}\int_0^{N\Delta t} \Delta\phi(x,z) exp(j\omega_b t) dt \tag{6}$$

where:

$$\Delta T = \frac{2\pi}{\omega_b} \tag{7}$$

and N is the number of periods for Fourier analysis. By substituting Eq. (2) into Eq. (6), the complex amplitude $F(x,z)$ becomes:

$$F(x,z) = K\exp(j\theta(x,z)) \tag{8}$$

with

$$K = \frac{2\pi f_0 \xi_0}{c} \tag{9}$$

A small-divided-region (SDR) R within the image domain is considered. This region has a width of Δx in the x-direction and Δz in the z-direction,

Let (x_0, z_0) be the center of the region, where a phase reference point A is set. The complex amplitude in the region is multiplied by the complex conjugate of the value at the reference point:

$$\begin{aligned}\Delta F(x,z) &= F(x,z)F^*(x_0,z_0)\\ &= K^2\exp\left[j(\theta(x,z)-\theta(x_0,z_0))\right]\end{aligned} \tag{10}$$

The phase $\theta_e(x,z)$ of $\Delta F(x,z)$ is:

$$\begin{aligned}\theta_e(x,z) &= \tan^{-1}\left(\frac{\mathrm{Im}(\Delta F(x,z))}{\mathrm{Re}(\Delta F(x,z))}\right)\\ &= \theta(x,z) - \theta(x_0,z_0)\end{aligned} \tag{11}$$

Apply a 2D least squares fitting method to $\theta_e(x,z)$ within the region R, and obtain the first-order coefficients a_x and a_z. These represent the phase gradient and correspond to the wave numbers:

$$k_x = a_x, \quad k_z = a_z \tag{12}$$

The shear wave number k, propagation velocity v, and propagation direction ϕ are then given by:

$$k = \sqrt{k_x^2 + k_z^2}, \quad v = \frac{\omega_b}{k}, \quad \phi = \tan^{-1}\left(\frac{k_z}{k_x}\right) \tag{13}$$

By repeating this process while scanning the region across the entire image domain in both the x and z directions, high-resolution estimation of the shear wave propagation parameters can be achieved.

Shear strain estimation

Consider a three-layer structure in which a relatively soft layer is sandwiched between two stiff layers. When sinusoidal displacements are applied to the upper and lower stiff layers in the x-axis direction, their displacements x_1 and x_2 can be described as:

$$x_1 = a_1\sin(\omega t) \tag{14}$$

$$x_2 = a_2\sin(\omega t + \Delta\theta) \tag{15}$$

The shear strain ε generated within the soft intermediate layer due to the differential motion of the stiff layers is given by:

$$\varepsilon = \frac{\Delta x}{L} = \frac{x_1 - x_2}{L} \tag{16}$$

Substituting Eqs. (14) and (15) into Eq. (16), we obtain:

$$\varepsilon = \frac{b\sin(\omega t + \phi)}{L} \tag{17}$$

where the amplitude b and phase ϕ are given by:

$$b = \sqrt{a_1^2 + a_2^2 - 2a_1a_2\cos\Delta\theta} \tag{18}$$

$$\phi = \begin{cases} \tan^{-1}\left(\dfrac{-a_2\sin\Delta\theta}{a_1 - a_2\cos\Delta\theta}\right) \\ \qquad\qquad \text{if } a_1 - a_2\cos\Delta\theta \geq 0 \\ \tan^{-1}\left(\dfrac{-a_2\sin\Delta\theta}{a_1 - a_2\cos\Delta\theta}\right) + \pi \\ \qquad\qquad \text{if } a_1 - a_2\cos\Delta\theta < 0 \end{cases} \tag{19}$$

Therefore, the magnitude of the shear strain induced in the intermediate layer by shear wave propagation is expressed as:

$$|\varepsilon(t)| = \frac{b}{L} \tag{20}$$

Experiments

Two image reconstructions were performed using a linear array ultrasound probe (Finggal Link, Japan) with 128 active elements and a center frequency of 7.5 MHz. Photographs of the experimental setup used for the phantom are shown in Figure 1(a) and 1(b), with the vibration directions of $\theta = 0°$ and $\theta = 90°$, respectively.

An elastography phantom (ELPT-002; OST, Chiba, Japan) was used. It contains five inclusions of varying elasticities and echogenicities embedded in a background material with lower elasticity. These inclusions simulate the Tsukuba elasticity scores (Table 1). Figure 2 shows a schematic diagram of the phantom.

DOI 10.5162/Ultrasonic2025/P1.31

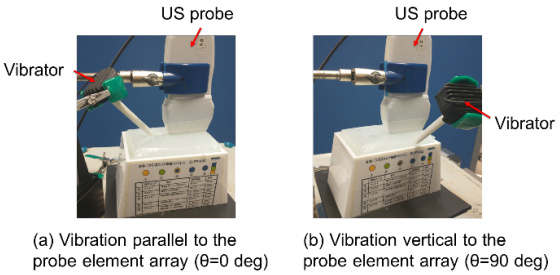

Fig. 1: Vibrator placement for different directions. (a) $\theta = 0°$, (b) $\theta = 90°$

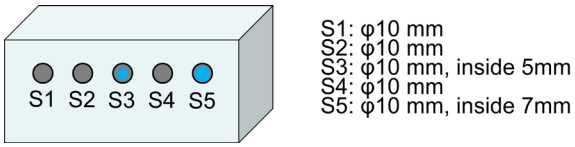

Fig. 2: Schematic image of the tissue-mimicking phantom.

From these, one inclusion corresponding to elasticity score 4 (S4) was selected for imaging. This inclusion has significantly higher stiffness compared to the background.

Results

Figure 3 shows the imaging results of the inclusion with elasticity score 4 under two vibration directions: $\theta = 0°$ (a) and $\theta = 90°$ (b). Images include B-mode, conventional SWV, SDR SWV, and shear strain images in both z and x directions.

The conventional SWV images failed to capture the structural contrast at $\theta = 90°$, whereas SDR SWV maintained visualization consistency across directions. Additionally, shear strain images in both directions exhibited elevated values along inclusion boundaries, regardless of the vibration direction.

Tab. 1: Phantom properties

Score		Brightness	Young's modulus [kPa]
1 (S1)		Low	15
2 (S2)		Low	40
3 (S3)	surroundings	Low	15
	inside	Low	380
4 (S4)		Low	380
5 (S5)	surroundings	stealth	400
	inside	Low	380

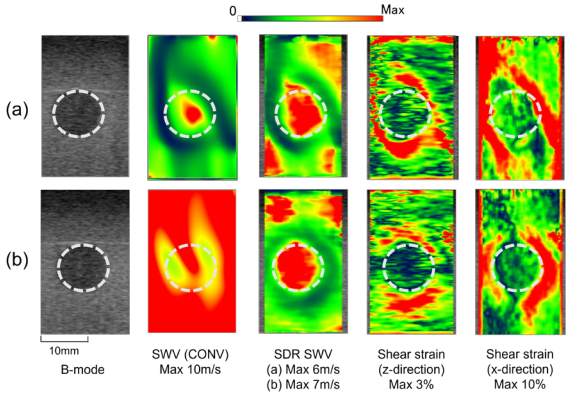

Fig. 3: Imaging results for S4 inclusion under two vibration directions: (a) $\theta = 0°$ and (b) $\theta = 90°$.

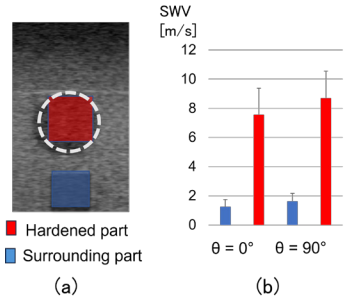

Fig. 4: SDR SWV analysis: (a) ROI setting, (b) Comparison between $\theta = 0°$ and $90°$

Figure 4 shows ROI settings and the SWV values measured within the hardened inclusion and surrounding tissue. The measured velocities were consistent for both vibration directions, closely matching the expected value of 11.22 m/s for the stiff region.

Figure 5 shows results for shear strain. Panel (a) shows the ROI configuration; panels (b) and (c) show z- and x-directional strain respectively. The x-directional strain exhibited overall higher values. There was a consistent and significant contrast between the hardened inclusion and the surroundings in both vibration directions .

Discussion

In this study, it was demonstrated that the two proposed methods enable structural visualization that is independent of the vibration direction. The small-divided-region (SDR) shear wave velocity (SWV) estimation method successfully visualized internal features and similarly, the shear strain method clearly visualized boundary regions, regardless of the vibration direction.

Notably, the shear strain method highlighted large phase differences at the boundary of hardened regions,

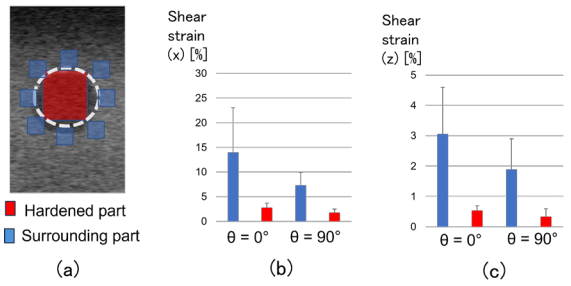

Fig. 5: Shear strain analysis: (a) ROI setting, (b) x-directional shear strain, (c) z-directional shear strain

indicating high shear strain. However, the boundary visualization was not always perfectly aligned, likely due to shear wave refraction effects.

Refraction is influenced by the relationship between excitation direction and target geometry. When there is a large SWV difference between the inclusion and the surrounding medium, the refraction effect becomes more pronounced, resulting in increased variability.

For breast tissue, SWVs for normal breast and malignant lesions have been reported to range from approximately 2.7 to 5.0 m/s. The elastic modulus of normal breast cancer tissue is approximately 22 kPa ([9]), whereas lesions at risk of malignant transformation can reach 74 kPa ([10]). In contrast, the experimental phantom used in this study had a larger SWV contrast, making the results more sensitive to refraction.

Despite improved visualization, the limitations of strain imaging due to unclear tumor boundaries and high variance remain. Future studies will apply directional filters to suppress refractive effects and incorporate simulations and clinical environments to validate and optimize the approach.

Conclusion

In this study, we investigated two methods for visualizing hardened tissue regions independent of vibration direction in continuous shear wave elastography (C-SWE). In phantom experiments, small-divided-region (SDR) SWV estimation visualized internal inclusions consistently, while shear strain imaging highlighted the boundaries of stiff regions. These results demonstrate that both methods can reduce the directional dependency inherent in conventional SWV imaging. Future work will extend this evaluation to in vivo tissues and refine imaging algorithms to reduce refractive artifacts.

Acknowledgement

This work was supported in part by JSPS KAKENHI Grant Number 25K15954, JKA and its promotion funds from KEIRIN RACE.

References

[1] H. L. Oestreicher. "Field and impedance of an oscillating sphere in a viscoelastic medium with an application of biophysics". In: *J. Acoust. Soc. Am.* 23 (1951), pp. 707–714.

[2] L. Sandrin et al. "Transient elastography: A new noninvasive method for assessment of hepatic fibrosis". In: *Ultrasound Med. Biol.* 29 (2003), pp. 1705–1713.

[3] K. Nightingale et al. "Acoustic radiation force impulse imaging: In vivo demonstration of clinical feasibility". In: *Ultrasound Med. Biol.* 28 (2002), pp. 227–235. DOI: 10.1016/s0301-5629(01)00499-9.

[4] J. Bercoff, M. Tanter, and M. Fink. "Supersonic shear imaging: A new technique for soft tissue elasticity mapping". In: *IEEE Trans. Ultrason. Ferroelectr. Freq. Control* 51 (2004), pp. 396–409. DOI: 10.1109/TUFFC.2004.1295425.

[5] Y. Yamakoshi et al. "Shear Wave Imaging of Breast Tissue by Color Doppler Shear Wave Elastography". In: *IEEE Transactions on Ultrasonics, Ferroelectrics, and Frequency Control* 64 (2017), pp. 340–348. DOI: 10.1109/TUFFC.2016.2626359.

[6] R. Koda et al. "Application of continuous shear wave elastography method with multiple frequency selection to liver viscoelasticity measurement". In: *Japanese Journal of Applied Physics* 63 (2024), 04SP82. DOI: 10.35848/1347-4065/ad3ae4.

[7] M. Tabaru et al. "Examination of rapid adjustment system based on screen score obtained using continuous shear wave elastographyt". In: *Journal of Medical Ultrasonics* 51 (2024), pp. 407–418. DOI: 10.1007/s10396-024-01439-7.

[8] N. Tano et al. "Continuous Shear Wave Elastography for Liver Using Frame-to-Frame Equalization of Complex Amplitude". In: *Ultrasonic Imaging* 46 (2024), pp. 197–206. DOI: 10.1177/01617346241247127.

[9] A.Evans et al. "Quantitative shear wave ultrasound elastography: initial experience in solid breast masses". In: *Breast Cancer Res.* 12 (2010), R104.

[10] W. Berg et al. "Shear-wave Elastography Improves the Specificity of Breast US: The BE1 Multinational Study of 939 Masses". In: *Radiology* 262 (2012), pp. 435–449.

DOI 10.5162/Ultrasonic2025/P1.41

Characterizing Elasticity of NiTi Epitaxial Film in Austenitic Phase by Transient Grating Spectroscopy

David Mareš[1], *Kristýna Repček*[2], *Tomáš Grabec*[1], *Jakub Kušnír*[2], *Pavla Stoklasová*[1], *Petr Sedlák*[1], *and Hanuš Seiner*[1]
[1]*Institute of Thermomechanics of the Czech Academy of Sciences, Prague, Czechia*
[2]*Faculty of Nuclear Sciences and Physical Engineering, Czech Technical University in Prague, Prague, Czechia*
david.mares@it.cas.cz

Abstract: We employ transient grating spectroscopy (TGS) with a 7 µm excitation wavelength to analyze anisotropic elasticity of a thin supported film. The high sensitivity of TGS enables detection of multiple surface acoustic modes—Rayleigh, Sezawa (both with strong out-of-plane displacement), and Love (with transverse horizontal displacement)—in a slow-on-fast system of a 3µm thick epitaxial NiTi shape-memory alloy film on MgO, investigated in the austenitic state at 120 °C. Extracting elastic constants from angular dispersions is solved via the Ritz–Rayleigh method, enabling analysis of the cubic elastic constants of the NiTi film and provides valuable insights into the film's properties.

Keywords: transient grating spectroscopy, guided waves, elastic anisotropy, inverse procedure, shape-memory alloy

Introduction-Motivation

Characterizing elasticty of anisotropic thin films with micrometer-scale thickness is challenging. The traditional contact quasi-static techniques of micro- and nanoindentation using Oliver-Pharr [1, 2] analysis provide only limited information on the directional dependence of the elastic response. For this reason, a wide range of laser-ultrasonic approaches have been developed as alternatives, including picosecond ultrasonics, resonant ultrasound spectroscopy, surface-wave spectroscopy, and Brillouin spectroscopy. However, these methods provide only limited information about the elasticity and are often experimentally complex and time-consuming.

We employ transient grating spectroscopy (TGS) [3, 4], a laser-based optical method that relies on interference to achieve high sensitivity and strong k-vector selectivity both in the generation and detection of surface-guided acoustic waves. This approach enables precise measurements of surface acoustic waves (SAWs) at micrometer wavelengths, facilitating the determination of the angular dispersion of wave velocities.

Subsequently, a specifically designed minimization-based inverse procedure, combined with a Ritz-Rayleigh numerical model for elastodynamic properties of layered systems, allows for the precise determination of the elastic constants [5, 6, 7].

This allows us to study wave behavior in anisotropic films grown on anisotropic substrates [6], making it highly useful for non-destructive evaluation of epitaxial films. However, evaluating such layered systems is challenging. In addition to the well-known Rayleigh and Sezawa surface acoustic waves, which exhibit considerable out-of-plane motion, this is also sensitive to detect Love waves and their directional dispersion. Extensive experimental output also makes the inverse problem—extracting elastic constants from measured wave velocities—more complex. The analysis must account for how multiple propagation modes propagate in different directions, often intersecting with each other, and whose intersection points are linked to the very elastic constants being determined.

Methods - experimental setup

Transient grating spectroscopy (TGS), also referred to as impulse stimulated thermal scattering (ISTS) [8], is a laser-ultrasonic method designed for non-contact, non-destructive probing of acoustic properties in solids.It can, however, also be employed for the investigation of thermal properties [9]. The technique combines optical excitation of surface acoustic waves (SAWs) with their optical detection through light diffraction and consequent interference. Such optical heterodyne (interference) detection was first proposed by Maznev et al. [3]. In the present work, we employed the modified optical setup depicted in Figure 1, utilizing the differential heterodyne technique introduced by Verstraeten et al. [8].

In this work, we used TGS setup similar to that in Ref. [4]: SAWs are generated by a Nd:YAG pump laser (1064 nm, 0.55 ns, 200 µJ, 1 kHz) and detected by

DOI 10.5162/Ultrasonic2025/P1.41

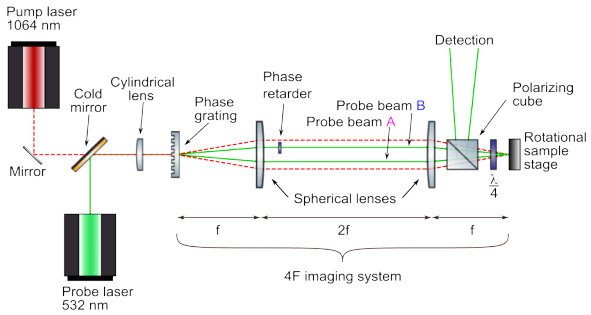

Fig. 1: The optical setup of the TGS method.

a continuous-wave probe laser at 532 nm (80 mW). A transmission grating splits both pump and probe laser beams into their ± 1 diffraction orders, while higher orders are blocked. The first-order beams are projected onto the sample surface using a 4F imaging system, where they interfere to form a periodic intensity pattern. The fringe spacing, and thus the acoustic wavelength, is determined by the incidence angle of the beams and can be easily adjusted by replacing the grating. Each interference fringe acts as a line-like thermoelastic source, launching SAWs with a well-defined wave vector perpendicular to the excitation fringes. The use of a cylindrical lens elongates the excitation pattern, further amplifying the excited k-vector. Because the laser energy is harmonically distributed across a large area, surface damage is avoided, enabling repeated non-destructive measurements, which are ideal for angular-dispersion characterization.

The probe beams, also diffracted into ± 1 orders and recombined on the surface, are sensitive to the transient grating created by the propagating SAWs. The optical setup forms the Littrow configuration, where each probe beam diffracts in the reflection direction of the other, enabling heterodyne detection. Detection is therefore carried out in the phase grating mode by carefully tuning the phase difference between the interfered beams (heterodyne phase $\approx \pi/2$), which maximizes sensitivity to out-of-plane displacements. The signal-to-noise ratio and sensitivity are further enhanced by measuring the intensity using Si photodiodes in a differential setup. Furthermore, since the pump and probe patterns overlap, near-field detection enables the detection of various higher-order modes, including those with very low out-of-plane components. The modulated probe signal, proportional to the instantaneous surface displacement, is captured by an oscilloscope. Averaging thousands of time traces enhances resolution and reduces noise. To determine SAW velocities and angular dispersion, time profiles were obtained for each measured direction. The frequency spectrum of the signal reveals the SAW frequency, from which its velocity is calculated as $v = \lambda f$, with λ determined by the interference pattern.

The angular dispersion of the wave velocities was obtained by rotating the sample with respect to the interference pattern. We carried out a 45° angular scan (with a step of 1°). To measure wave velocities at elevated temperature, a Peltier module was used to achieve a controlled temperature of 120 °C, ensuring that the NiTi film is in its single-crystalline austenite phase.

Methods - numerical

To determine the elastic constants from the measured angular-dependent velocities of guided waves, we have developed an inverse procedure that compares measured dispersive characteristics with theoretical predictions and iteratively adjusts material parameters until good agreement is obtained. For the forward problem, where material parameters are known and velocities are calculated, we use the Ritz-Rayleigh approach – a variational scheme of discretized functional space that converts the continuous wave equation into a discrete eigenvalue problem [5, 10]. This approach enables the calculation of guided-wave modes in generally anisotropic and layered media. However, to determine the elastic constants of a sample, the inverse method must be applied, whereby elasticity is calculated from measured wave velocities. An optimization algorithm is used to update the elastic constants until the misfit function iteratively

$$F(\mathbf{c}) \;=\; \sum_{p} \left(v_p^{\mathrm{cal}}(\mathbf{c_i}) - v_p^{\mathrm{exp}}\right)^2 \;\rightarrow\; \min_{\mathbf{c}}\,. \qquad (1)$$

reaches a minimum. At each iteration, the forward problem is recalculated, producing new dispersion curves that are compared to the experiments. Convergence indicates that the estimated constants reproduce the observed guided-wave dispersion with sufficient accuracy.

Study case

The sample used in this study was a thin film of NiTi shape memory alloy. The film was epitaxially grown [11] by DC magnetron sputtering on a single-crystalline MgO(100) substrate. To reduce epitaxial stress, buffer layers of vanadium and chromium were used, with a combined thickness of 50 nm. The epitaxial relationship between the NiTi austenite (B2 structure) and the MgO substrate was MgO(100)[001] ∥ V/Cr(100)[011] ∥ NiTi B2(100)[011]. This indicates that the austenite unit cell is rotated by 45° around the substrate normal relative to the film, such that of MgO aligns with of the austenite (as shown in Fig. 2a). The film thickness was measured by scanning

DOI 10.5162/Ultrasonic2025/P1.41

electron microscopy on a cross-section prepared by focused ion beam milling using a FEI Helios NanoLab 600i, the determined value being 3060 nm (Figure 2b).

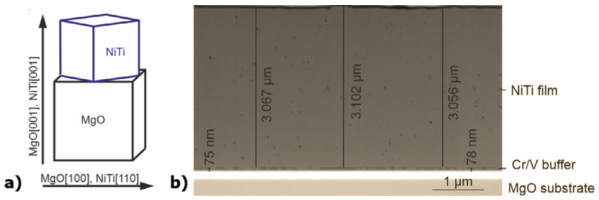

Fig. 2: a) Schematic showing B2 austenite unit-cell orientations of the film with respect to the substrate, b) cross-sectional SEM thickness measurement of the supported 3 µm thick NiTi layer on MgO substrate.

Results and Discussion

In this study, the acoustic wavelength of 7 µm was employed to probe the 3 µm NiTi film. This wavelength was chosen to achieve a balance between the surface confinement and the frequency range of the resulting acoustic signals. Since the acoustic energy of an SAW decays exponentially with depth, over a distance comparable to its wavelength, the 7 µm excitation ensures that a significant portion of the elastic field interacts with the film. Although shorter wavelengths would confine the wave more strictly within the film, they would require finer phase-grating periods, more demanding optical alignment, and higher detector resolution and frequency range. The selected wavelength thus represents an optimized compromise between the sensitivity of the film, the penetration depth, and the experimental practicality.

The TGS velocity map shown in Figure 3a revealed multiple guided modes. Modes were identified through signal strength, angular distribution, and the Ritz-Rayleigh inverse procedure, beginning with estimated elastic constants and the strongest signal corresponding to the Rayleigh-type surface wave. The angular dispersion shows a discontinuity near the middle of the measured angular dispersion. This is caused by a crossing with a Love-type wave with dominantly transverse horizontal polarization. The coupling of this Love-type mode with the Rayleigh-type mode results in a range of measured angles, where both modes are identifiable in the measured spectra. Two peaks corresponding to faster waves, observable across all angles, were identified as Sezawa-type modes. In non-principal crystallographic directions, another Love-type mode was detected via coupling-induced out-of-plane displacement.

NiTi austenite exhibits cubic symmetry, the elasticity of which can be described by three independent constants [12]. However, to allow for an effect of the epitaxial strain, tetragonal symmetry (with six independent elastic constants) was considered for the NiTi film. After the step-by-step identification of the experimentally observed wave modes in the measured angular scan, all six constants were determined. These constants exhibit cubic symmetry, proving that epitaxial strain is negligible and that three constants were sufficient to describe the measured angular dispersion (see the comparison of the experiment and calculation in Figure 3). The resulting elasticity was $c_{11} = 184.7 \pm 1.2$ GPa, $c_{12} = 149.7 \pm 1.3$ GPa, and $c_{44} = 33.19 \pm 0.04$ GPa.

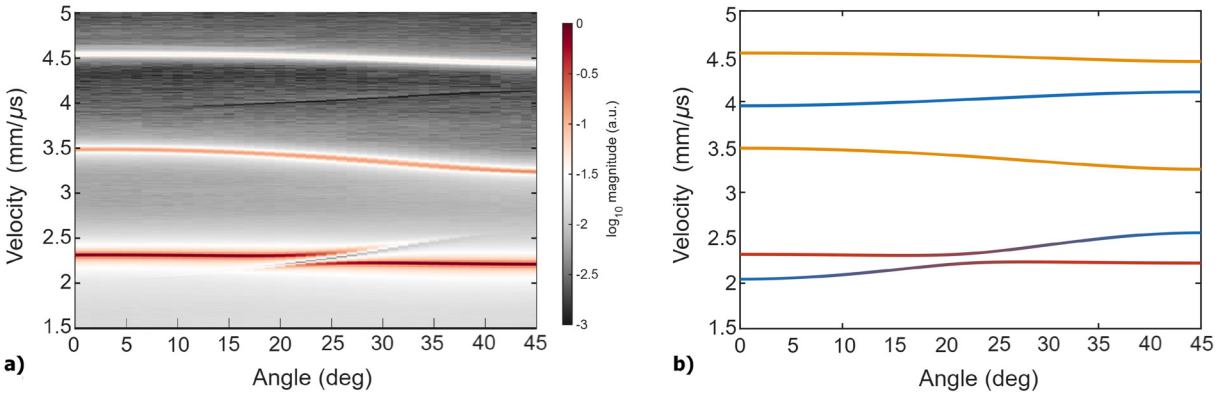

Fig. 3: Velocity maps of the epitaxial NiTi sample at 120 °C (i.e., in austenite) obtained by the angular TGS scan (a) and calculated with the Ritz–Rayleigh forward method with the determined elastic constants (b). The starting point of 0° corresponds to [001] direction of the MgO substrate. Note that the experimental map (a) is color-coded with a logarithmic scale of the signal magnitude. The modes in the calculated map (b) are color-coded as follows: Love-type wave modes are shown in blue, the Rayleigh-type mode in red, and Sezawa-type modes in orange.

Conclusion

In this work, we demonstrated the suitability of TGS for characterizing the elasticity of anisotropic micrometer-thin films on a substrate. We report TGS measurements of guided ultrasonic waves in epitaxially grown 3 µm NiTi thin film on MgO substrate and investigate the single-crystalline austenite phase at elevated temperature. The high sensitivity of TGS to surface-displacement dynamics allowed detection of Rayleigh, multiple Sezawa, and Love-type modes, providing sufficient information to characterize the elastic anisotropy of the film. We further show that the Ritz–Rayleigh numerical approach for guided waves enables solving the multimode inverse problem by single minimization, allowing to assess the elastic constants of the film. The resulting elasticity showed that at 120°C the single-crystalline austenite film remains elastically cubic.

Acknowledgment

This work was financially supported by the Czech Science Foundation [Project No. 22-13462S], Operational Program Johannes Amos Comenius of the Ministry of Education, Youth and Sport of the Czech Republic, within the frame of project Ferroic Multifunctionalities (FerrMion) [Project No.CZ.02.01.01/00/22_008/0004591], co-funded by the European Union and by the Grant Agency of the Czech Technical University [No. SGS25/168/OHK4/3T/14].

References

[1] S. Moyne et al. "Analysis of the thermomechanical behavior of Ti–Ni shape memory alloy thin films by bulging and nanoindentation procedures". In: *Materials Science and Engineering: A* 273-275 (1999), pp. 727–732. ISSN: 0921-5093. DOI: 10.1016/S0921-5093(99)00405-0.

[2] P. D. Tall et al. "Nanoindentation of Ni–Ti Thin Films". In: *Materials and Manufacturing Processes* 22.2 (2007), pp. 175–179. DOI: 10.1080/10426910601062222.

[3] A. A. Maznev, K. A. Nelson, and J. A. Rogers. "Optical heterodyne detection of laser-induced gratings". In: *Opt. Lett.* 23.16 (1998), pp. 1319–1321. DOI: 10.1364/OL.23.001319.

[4] P. Stoklasová et al. "Laser-Ultrasonic Characterization of Strongly Anisotropic Materials by Transient Grating Spectroscopy". In: *Experimental Mechanics* (2021). DOI: 10.1007/s11340-021-00698-6.

[5] P. Stoklasová et al. "Forward and inverse problems for surface acoustic waves in anisotropic media: a Ritz-Rayleigh method based approach". In: *Ultrasonics* 56 (2015), pp. 381–389. DOI: 10.1016/j.ultras.2014.09.004.

[6] T. Grabec et al. "Guided acoustic waves in thin epitaxial films: Experiment and inverse problem solution for NiTi". In: *Ultrasonics* 138 (2024). DOI: 10.1016/j.ultras.2023.107211.

[7] K. Repček et al. "Compliant Lattice Modulations Enable Anomalous Elasticity in Ni–Mn–Ga Martensite". In: *Advanced Materials* 36.39 (2024), p. 2406672. DOI: 10.1002/adma.202406672.

[8] B. Verstraeten et al. "Determination of thermoelastic material properties by differential heterodyne detection of impulsive stimulated thermal scattering". In: *Photoacoustics* 3.2 (2015), pp. 64–77. DOI: 10.1016/j.pacs.2015.05.001.

[9] J. Kušnír et al. "Apparent anisotropic thermal diffusivity measured in cubic single crystals by transient grating spectroscopy". In: *Journal of Applied Physics* 133.12 (2023), p. 125108. DOI: 10.1063/5.0136850.

[10] T. Grabec, P. Sedlák, and H. Seiner. "Application of the Ritz—Rayleigh method for Lamb waves in extremely anisotropic media". In: *Wave Motion* 96 (2020), p. 102567. DOI: 10.1016/j.wavemoti.2020.102567.

[11] K. Lünser et al. "How to grow single-crystalline and epitaxial NiTi films in (100)- and (111)-orientation". In: *Journal of Physics: Materials* 6.3 (May 2023), p. 035002. DOI: 10.1088/2515-7639/acd604.

[12] L. Bodnárová et al. "Elastic Constants of Single-Crystalline NiTi Studied by Resonant Ultrasound Spectroscopy". In: *Shap. Mem. Superelasticity* 11.2 (June 2025), pp. 230–238. ISSN: 2199-3858. DOI: 10.1007/s40830-025-00534-z.

DOI 10.5162/Ultrasonic2025/P1.50

Enhancing Full Waveform Inversion for Ultrasound Imaging with Langevin Stein Variational Gradient Descent: Improved Accuracy and Uncertainty Quantification

Qiang Li[1], *Chengcheng Liu*[1], *and Dean Ta*[1]
[1]*College of Biomedical Engineering, Fudan University, Shanghai 200438, China*
corresponding.li_q@fudan.edu.cn; tda@fudan.edu.cn

Abstract: This study applies Langevin Stein Variational Gradient Descent (LSVGD) to Full Waveform Inversion (FWI) for medical ultrasound imaging. LSVGD enables joint reconstruction of speed of sound (SOS) and spatial uncertainty. Posterior accuracy is validated using a Gaussian mixture model. Applied to a 2D breast phantom, LSVGD achieves reconstruction quality on par with standard FWI, while highlighting uncertainty in heterogeneous regions. Results underscore LSVGD's utility for uncertainty-aware, high-resolution ultrasound imaging.

Keywords: Full waveform inversion, variational inference, uncertainty quantification, medical ultrasound imaging, Bayesian inference

Introduction

FWI is a high-resolution technique increasingly applied in medical ultrasound to recover acoustic tissue properties by minimizing the misfit between measured and simulated wavefields [1]. However, conventional FWI is deterministic and sensitive to the ill-posedness of inverse problems, yielding a single estimate without uncertainty quantification. The lack of uncertainty information limits clinical interpretability, particularly in heterogeneous biological tissues.

To address the limitations, Bayesian inversion reformulates FWI as a probabilistic problem, aiming to infer a posterior distribution over model parameters given the observed data [2]. Variational inference (VI) methods, particularly Stein Variational Gradient Descent (SVGD), approximate the posterior using particle-based updates without assuming a parametric form [3]. Yet, SVGD is prone to mode collapse, limiting its ability to capture multi-modal posteriors [4]. Langevin SVGD (LSVGD) enhances SVGD by introducing stochastic noise from Langevin dynamics, improving posterior exploration [4, 5].

This work introduces LSVGD to medical ultrasound FWI by deriving the log-posterior gradient. Posterior approximation accuracy is validated using a Gaussian Mixture Model. Application to a 2D breast phantom demonstrates accurate SOS reconstruction and pixel-wise uncertainty quantification. Results indicate LSVGD matches standard FWI in accuracy while enabling uncertainty-aware imaging.

Methods

FWI is increasingly being adapted for medical ultrasound imaging to reconstruct detailed maps of acoustic properties, such as SOS, density, attenuation, and others. FWI minimizes the difference between measured and simulated wavefields. The measured data consist of pressure fields from ultrasound transducers, while the simulated data are obtained by solving the acoustic wave equation forward in time. The acoustic wave equation in FWI is

$$m(\boldsymbol{x})\,\frac{\partial^2 p(\boldsymbol{x},t)}{\partial t^2} - \nabla^2 p(\boldsymbol{x},t) = f_s(\boldsymbol{x},t), \quad (1)$$

where $p(\boldsymbol{x},t)$ represents the pressure field at position $\boldsymbol{x}$ and time t, ∇^2 is the Laplacian operator, and $f_s(\boldsymbol{x},t)$ is the source term. The squared slowness $m(\boldsymbol{x})$ is related to the SOS, i.e., $m(\boldsymbol{x}) = 1/c^2(\boldsymbol{x})$. In 2D FWI imaging, the parameter vector $\boldsymbol{m}$ consists of $m(\boldsymbol{x})$ at each position $\boldsymbol{x}$. The vector $\boldsymbol{m}$ is iteratively adjusted to reduce the error between the measured data $\boldsymbol{d}_r^{\text{obs}}$ and the simulated data $\boldsymbol{d}_r^{\text{sim}}$ at each receiver r. The error quantified in FWI is the L_2 norm of the data misfit,

$$\Phi = \frac{1}{2}\sum_r \|\boldsymbol{d}_r^{\text{obs}} - \boldsymbol{d}_r^{\text{sim}}\|_2^2. \quad (2)$$

The gradient of the misfit is computed using adjoint-state methods, which allow for efficient updating of the model parameters.

Standard FWI is formulated as a deterministic optimization problem that aims to find a single best-fit

DOI 10.5162/Ultrasonic2025/P1.50

model by minimizing the misfit between $\boldsymbol{d}_r^{\text{obs}}$ and $\boldsymbol{d}_r^{\text{sim}}$. However, due to the highly nonlinear and ill-posed nature of the problem, conventional FWI yields a single estimate without quantifying uncertainty or confidence. To address this limitation, variational inference (VI)-based FWI reformulates the inversion as a probabilistic problem, aiming to infer a posterior distribution $p(\boldsymbol{m} \mid \boldsymbol{d}^{\text{obs}})$ over possible models given the observed data. VI enables a Bayesian framework,

$$p(\boldsymbol{m} \mid \boldsymbol{d}^{\text{obs}}) = \frac{p(\boldsymbol{d}^{\text{obs}} \mid \boldsymbol{m})\, p(\boldsymbol{m})}{p(\boldsymbol{d}^{\text{obs}})}, \tag{3}$$

where $p(\boldsymbol{m})$ denotes the prior distribution, $p(\boldsymbol{d}^{\text{obs}} \mid \boldsymbol{m})$ is the likelihood model, and $p(\boldsymbol{d}^{\text{obs}})$ is the marginal likelihood that normalizes the posterior. VI approximates the true posterior distribution $p(\boldsymbol{m} \mid \boldsymbol{d}^{\text{obs}})$ by finding a tractable surrogate distribution $q(\boldsymbol{m})$. To quantify the discrepancy between $q(\boldsymbol{m})$ and the true posterior, VI employs the Kullback–Leibler (KL) divergence and minimizes it to ensure the best approximation. The probabilistic formulation allows not only for reconstruction of the mean SOS map but also for pixel-wise uncertainty estimation via the standard deviation of the inferred posterior.

In VI-based FWI, the choice of the form of $q(\boldsymbol{m})$ directly influences the computational complexity and convergence rate. SVGD is a particle-based VI algorithm that approximates posterior distributions using a set of interacting particles $\boldsymbol{m}_i$. SVGD iteratively updates the particles to match the target posterior by minimizing the KL divergence through Stein's identity. SVGD combines the advantages of VI and deterministic optimization, leveraging insights from Stein's method, and does not assume a specific parametric form for $q(\boldsymbol{m})$. A common issue in SVGD is mode collapse, where particles cluster in a single mode, undermining the diversity of the approximation [4]. To address this, LSVGD enhances standard SVGD by introducing a stochastic noise term derived from Langevin dynamics, improving the exploration of the target posterior. LSVGD is a hybrid algorithm inspired by MCMC, combining the deterministic updates of SVGD with Langevin noise for better posterior approximation [5]. The update rule for LSVGD is

$$\begin{aligned}\phi(\boldsymbol{m}) =& \frac{1}{n}\sum_{j=1}^{n}\left[k\left(\boldsymbol{m}_j^t, \boldsymbol{m}\right)\nabla_{\boldsymbol{m}_j}\log p\left(\boldsymbol{m}_j^t \mid \boldsymbol{d}^{\text{obs}}\right) + \right.\\ & \left.\nabla_{\boldsymbol{m}_j} k\left(\boldsymbol{m}_j^t, \boldsymbol{m}\right)\right],\\ \boldsymbol{m}_i^{t+1} =& \boldsymbol{m}_i^t + \epsilon^t \phi(\boldsymbol{m}_i^t) + \sqrt{2\epsilon^t}\boldsymbol{\xi}_t,\end{aligned} \tag{4}$$

where $\boldsymbol{\xi}_t \sim \mathcal{N}(0, \mathbf{I})$ represents standard Gaussian noise and ϵ^t is the step size. The function $k(\boldsymbol{m}_j^t, \boldsymbol{m}) = \exp\left(-\|\boldsymbol{m}_j^t - \boldsymbol{m}\|^2/(2\sigma^2)\right)$ is the Radial Basis Function (RBF) kernel.

To incorporate the LSVGD update rule Eq. (4) into FWI, a critical step is the computation of the gradient of the log-posterior. According to Bayes' theorem Eq. (3), the gradient decomposes into the sum of the gradients of the log-likelihood and the log-prior. For the likelihood term, assuming a Gaussian likelihood yields

$$\log p(\boldsymbol{d}^{\text{obs}} \mid \boldsymbol{m}) \propto -\frac{1}{2}\sum_r \left\|\boldsymbol{d}_r^{\text{obs}} - \boldsymbol{d}_r^{\text{sim}}\right\|^2. \tag{5}$$

Eq. (5) indicates that the gradient of the log-likelihood can be efficiently computed using the adjoint-state method. In contrast, the gradient of the log-prior is analytically tractable when a specific prior distribution is assumed, such as a Gaussian or uniform prior.

LSVGD moves particles $\boldsymbol{m}_i$ to maximize the posterior distribution, which is equivalent to minimizing the negative log-posterior. Applying Bayes' theorem Eq. (3), the objective function is

$$\tilde{\Phi} = -\log p(\boldsymbol{d}^{\text{obs}} \mid \boldsymbol{m}) - \log p(\boldsymbol{m}). \tag{6}$$

For the Gaussian likelihood, Eq. (6) yields a data misfit term and a regularization term,

$$\tilde{\Phi} = \frac{1}{2}\sum_r \left\|\boldsymbol{d}_r^{\text{obs}} - \boldsymbol{d}_r^{\text{sim}}\right\|^2 - \log p(\boldsymbol{m}). \tag{7}$$

Results

To empirically validate the capability of LSVGD in approximating complex posterior distributions, a Gaussian Mixture Model (GMM) comprising three components is constructed as a toy example. The GMM, visualized as a gray curve in Fig. 1(a), is defined as

$$\begin{aligned}p(x) =& 0.2\mathcal{N}(x; -2, 0.5^2) + 0.6\mathcal{N}(x; 2, 0.7^2) + \\ & 0.2\mathcal{N}(x; 0, 1.5^2).\end{aligned}$$

The analytical mean and standard divation of the GMM are 0.8 and 1.831, respectively. LSVGD employs 100 particles initialized from a broad Gaussian distribution $\mathcal{N}(0, 5^2)$ and updates them over 500 iterations using a fixed step size of 5×10^{-2}. The updates utilize AdaGrad to adaptively adjust the learning rate. After reaching the maximum number of iterations, the particle distribution is displayed as green bins in Fig. 1(a). The approximated mean and standard deviation of the particles are 0.814 and 1.826, respectively. Fig. 1(b) illustrates the convergence behavior via the mean squared error (MSE) of both the estimated mean and standard deviation, with MSEs approaching zero. The experiment demonstrates LSVGD's ability to approximate multi-modal distributions, supporting its applicability to more complex inverse problems such as FWI in medical ultrasound imaging.

DOI 10.5162/Ultrasonic2025/P1.50

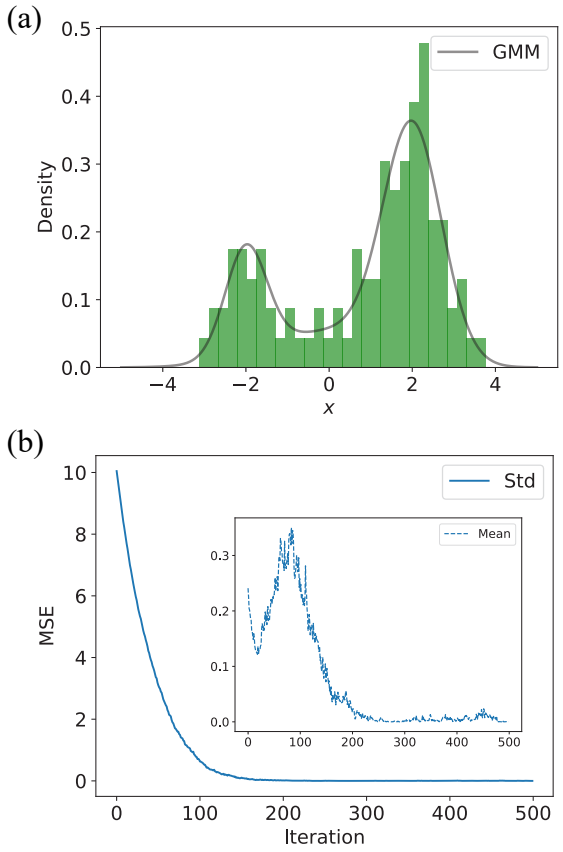

Fig. 1: LSVGD approximates the mean and standard deviation of a GMM. (a) Results of LSVGD with 100 particles. The gray curve represents the target GMM, and the green bins show the particle distribution after 500 iterations. (b) MSEs between the analytical and approximated mean and standard deviation over iterations.

To investigate the performance of LSVGD in FWI for medical ultrasound imaging, a two-dimensional breast phantom model [6] is employed. The background medium is water with a SOS of 1.5 km/s. The breast model includes five tissue types: fat, skin, glandular, ligament, and lesion, with SOS ranging from 1.411 km/s to 1.578 km/s. The simulation domain is discretized on a 351×351 grid with a spatial resolution of $\Delta x = \Delta y = 0.3$ mm. A Courant–Friedrichs–Lewy (CFL) number of 0.53 is adopted, resulting in a time step size of 1×10^{-4} ms. The imaging setup comprises 64 transmitters and 64 receivers, uniformly distributed along a circle of radius 0.51 cm centered within the model domain, as shown in Fig. 2. Each transmitter emits a Ricker wavelet with a center frequency of 0.5 MHz and duration of 0.1 ms.

For LSVGD-based FWI, the process is initialized from a pure water model with a constant SOS

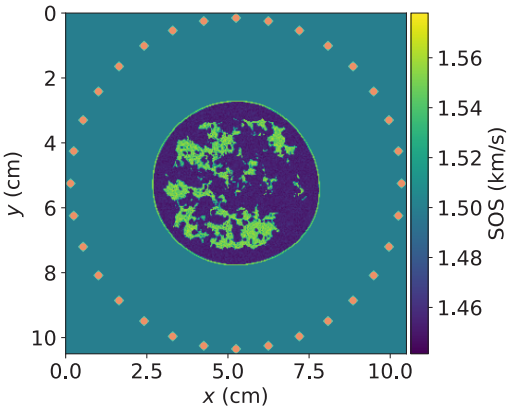

Fig. 2: A two-dimensional breast model. A total of 64 transmitters (orange dots) and 64 receivers (green diamonds) are uniformly distributed along a circle with a radius of 0.51 cm.

$\boldsymbol{c}_0 = 1.5$ km/s. Based on the squared slowness $\boldsymbol{m}_0 = 1/\boldsymbol{c}_0^2$, 20 initial particles are sampled from a Gaussian distribution with mean 0.444 s^2/km^2 and standard deviation 0.01. Given the SOS range of the breast phantom from $c_{\min} = 1.411$ km/s to $c_{\max} = 1.578$ km/s, the squared slowness is constrained within $m_{\min} = 1/c_{\max}^2$ and $m_{\max} = 1/c_{\min}^2$. The inversion employs a quasi-Newton optimization strategy using the L-BFGS-B algorithm with adaptive step size control. The maximum number of iterations is set to 50.

For the converged LSVGD particles, the final SOS distribution is computed for each particle as $\boldsymbol{c}_i = 1/\sqrt{\boldsymbol{m}_i}$. As shown in Fig. 3(a), the reconstructed mean SOS map resolves distinct tissue structures within the breast phantom. The relative error between the reconstructed and ground-truth SOS exhibits a maximum of 6.03% and an average of 0.27%. Fig. 3(b) presents the corresponding pixel-wise uncertainty, quantified by the standard deviation across particles. Notably, higher uncertainty values are observed within heterogeneous tissue regions exhibiting high SOS, indicating the algorithm's sensitivity to structural complexity. The maximum uncertainty reaches 0.056, and the average is 0.012. Areas with elevated uncertainty coincide with regions near the sources and receivers, where reconstruction errors are more pronounced in the mean SOS map.

To provide a baseline for comparison with LSVGD-based FWI, standard FWI is performed using the same experimental setup. The inversion starts from a homogeneous water model with a constant SOS of 1.5 km/s. The optimization is carried out using the L-BFGS-B algorithm, and the maximum number of iterations is set to 50. As shown in Fig. 4, the

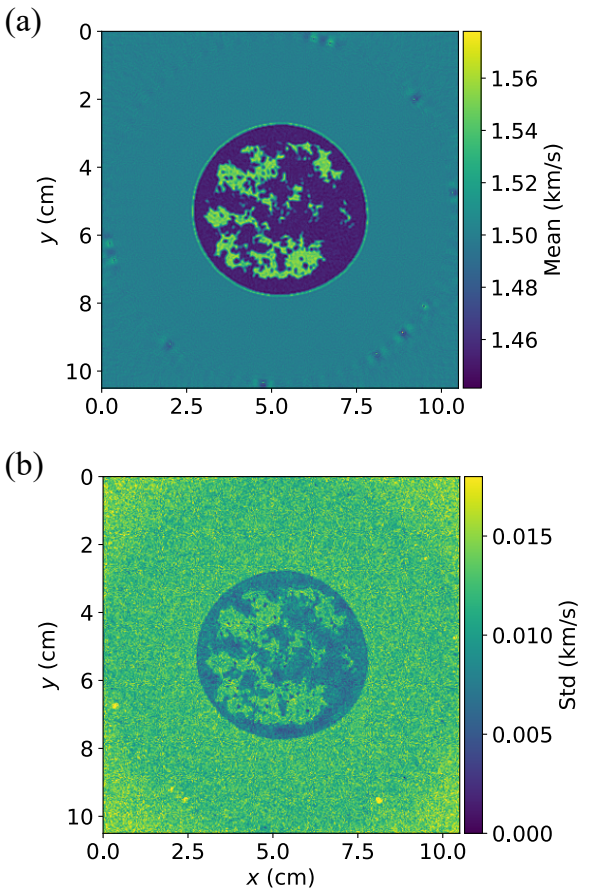

Fig. 3: SOS reconstruction using LSVGD with 20 particles. (a) Mean SOS map. (b) Uncertainty map quantified by standard deviation across particles.

reconstructed SOS map accurately resolves distinct tissue structures. The maximum and average relative errors are 5.06% and 0.21%, respectively. The LSVGD-based FWI attains reconstruction accuracy that is nearly indistinguishable from that of standard FWI, with the added benefit of pixel-wise uncertainty quantification.

Conclusion

This study derives the gradient of the posterior distribution with respect to model parameters and applies LSVGD to FWI in the context of medical ultrasound imaging. The effectiveness of LSVGD in approximating complex posterior distributions is first validated using a GMM. Subsequently, a two-dimensional breast phantom is used to reconstruct the spatial distribution of SOS. The reconstructed mean SOS obtained from LSVGD-based FWI achieves accuracy comparable to that of standard FWI. Moreover, LSVGD provides pixel-wise uncertainty quantification, with elevated uncertainty observed in heterogeneous tissue regions characterized by high SOS, highlighting the sensitivity

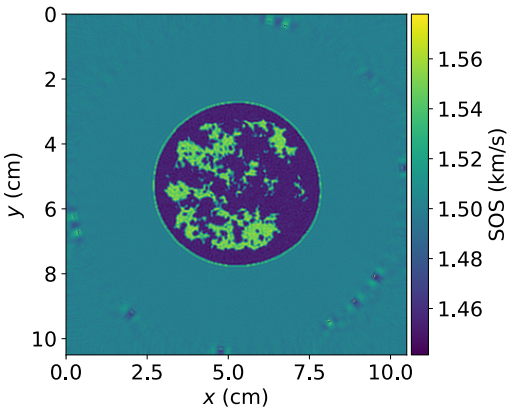

Fig. 4: Reconstructed SOS map using standard FWI.

to structural complexity. The results demonstrate the potential of LSVGD as a powerful tool for uncertainty-aware inversion in biomedical imaging.

Acknowledgements

This work was supported by the National Natural Science Foundation of China (Grant Nos. 12122403, 12034005, and 12327807) and the National Key R&D Program of China (Grant No. 2023YFC2410800). The authors also acknowledge the helpful suggestions provided by Dr. Xin Zhang, the first author of [5].

References

[1] L. Guasch et al. "Full-waveform inversion imaging of the human brain". In: *NPJ digital medicine* 3.1 (2020), p. 28.

[2] O. Bates et al. "A probabilistic approach to tomography and adjoint state methods, with an application to full waveform inversion in medical ultrasound". In: *Inverse Problems* 38.4 (2022), p. 045008.

[3] Q. Liu and D. Wang. "Stein variational gradient descent: A general purpose bayesian inference algorithm". In: *Advances in neural information processing systems* 29 (2016).

[4] D. Wang et al. "Stabilizing training of generative adversarial nets via langevin stein variational gradient descent". In: *IEEE Transactions on Neural Networks and Learning Systems* 33.7 (2020), pp. 2768–2780.

[5] X. Zhang and A. Curtis. "VIP - Variational Inversion Package with example implementations of Bayesian tomographic imaging". In: *Seismica* 3.1 (2024).

[6] F. Li et al. *2D Acoustic Numerical Breast Phantoms and USCT Measurement Data*. Version V1. 2021. DOI: 10.7910/DVN/CUFVKE. URL: https://doi.org/10.7910/DVN/CUFVKE.